Enantioseparation and structural optimisation of β-lactams and stilbene analogues for the treatment of triple negative breast and chemoresistant colorectal cancers

A thesis submitted to the University of Dublin for the degree of Doctor of Philosophy (PhD)

Eavan C. McLoughlin, BSc. (Pharm), MPharm, MPSI, RSci.

Volume 1

The School of Pharmacy and Pharmaceutical Sciences, Trinity College Dublin

2023

Under the supervision of

Asst. Prof. Niamh M. O'Boyle, BSc. (Pharm), PhD, MPSI

Declaration

I declare that this thesis has not been submitted as an exercise for a degree at this or any other university and it is entirely my own work. I agree to deposit this thesis in the University's open access institutional repository or allow the Library to do so on my behalf, subject to Irish Copyright Legislation and Trinity College Library conditions of use and acknowledgement. I consent to the examiner retaining a copy of the thesis beyond the examining period, should they so wish (EU GDPR May 2018).

Eavan McLoughlin

26th August 2022

Acknowledgements

There are far too many people without whom I would never have reached the point of submission going far beyond TBSI and you all know who you are!

I would like to thank my supervisor Dr. Niamh O'Boyle for allowing me the opportunity to undertake this project and for allowing me the flexibility and creativity to pursue many challenges far beyond the scope of the initial plan, inside and outside of the lab. Additionally I would like to express the deepest gratitude to Prof. Mary Meegan for suggesting as far back as 2017 that this was a possibility, encouraging me to consider medicinal chemistry in my future plans and in particular guiding me through the final few months of writing. 'I look forward to great things.' Great things may or may not have been achieved (that part is very much open to debate) but we certainly didn't do too badly in the end without a football field of researchers! I would also like to express sincerest thanks to my co-supervisor Prof. Daniela Zisterer for assistance with all things biochemistry related, use of both the lab and tissue culture facilities in addition to proof reading many drafts of papers and thesis. Thank you!

I would also like to thank Dr. Tamasine Grimes, who became a mentor from my undergraduate years and provided me with a fantastic opportunity to re-visit clinical research mid PhD. Most importantly for teaching me that most people feel like they are rolling down a hill on a bike without the breaks on and that while on occasion you may need to make sacrifices, you really never have to.

To the dynamic duo, John and Manuel, expert NMR specialists, always with solutions yet often annoyingly with more questions; which that said, often led to even better solutions. To John in particular, my work would have never moved forward without your help and exploration. I look forward to seeing your future collaborations! To Brendan for all his work on enantiomer XRDs, dread the word centrosymmetric, dance at the words 3*S*,4*S* or 3*S*,4*R* and cry at the X-ray bill. Thank you for your patience and efforts!

I would like to the technical staff in the School of pharmacy and in particular to Brian Talbot who fixed my rotavap, lamp and Alliance 3 ++ times and was always immediately approachable, accessible and effective.

To Mark, Miriam, Anjali, Kate, Roisín, Niamh, James, Karl, Johannes, Jerry, Jinfan and new recruits Aaron, Aoife and Alina for all the help and company along the way and in particular to Anjali who became excellent counsel during that final slog. To Simon, Ruairí and Helene for pitching in with my organic chemistry towards the end, it was needed! To the biochemistry lab - Ciara, Patricia, Helene and Aidan. I came up with fairly ridiculous questions along the way but was always treated with patience and kindness and indeed tissue culture became a place I looked forward to going to and could find answers to all sorts of problems. I feel privileged and am extremely grateful to have spent the last two years in great company with you all.

A huge thank you to all my students along the way, to Peiwen, Helene, Sophie, Mark, Matt, Philip, Conn, Eldhose, Jack, Nithya, Kealan who each have had a part to play in this thesis. Finally, but not least to Olivia for tremendous independence and patience and early morning tissue culture company.

To Dermot, for teaching me what I am capable of doing if I pool mind and desire together, to actually want something, discipline, how to concentrate and most importantly how to relax and get out of my own head. We may never get it right but we did well when it was good. To Aoife and Karen, our hours together over the last few years were grounding and inspiring to say the least and I hope and look forward to normal service resuming even if it is in a distant future. To queen roommates, Ellis and Lauren, a great source of fun and entertainment in otherwise bizarre times. To Iain, the wise man who once taught me that when a room in your house floods, have another one to go to. Your efforts haven't gone unacknowledged.To all those who shared a run, swim, Deliveroo or procasta-coffee. You each deserve a paragraph in these acknowledgements! To Laura B, Caron, Conall, Clíona, Sorcha, Matthieu, JP, Grace, Eavan McD, Paul and Rachel, Laura and Kunal. To the extended DUHAC family, I am indebted for the company and opportunities along the way over the last four years. We have had an absolutely stellar run and I am proud and honoured to have been a part of

all the great things we have achieved and look forward to seeing the next generation on the rise.

To Poppy and Ellie who were the BEST writing friends. PhD thesis = +++ bonios and peanut butter digestives and numerous dead hedgehogs! Finally to my mother and father, who in recent months have gone above and beyond for me. I don't know what I would do without you both.

Abstract

Triple negative breast cancer (TNBC) is characterised by an extremely aggressive clinical phenotype and minimal expression of typical breast cancer receptors such as the estrogen, progesterone or HER2 receptors.[1, 2] Patient responses to endocrine and HER2 targeted therapies in TNBCs are poor, with pharmacological treatment options limited solely to chemotherapy. Colorectal cancer (CRC) is the third most frequently diagnosed cancer and cause of cancer related deaths worldwide. Despite introduction of targeted therapies, survival rate remains only 12% and only 50% of patients respond to treatment. *Cis* stilbene combretastatin A-4 (CA-4) has demonstrated excellent antimitotic and anticancer activity as a microtubule depolymeriser and colchicine binding site inhibitor (CBSI). The *cis* stilbene structure is 60 times more active as an anti-proliferative agent than the corresponding *trans* CA-4. However the active *cis* conformation readily isomerises into the less active *trans* isomer during storage and *in vivo* metabolism. Introduction of a rigid β-lactam structure in place of CA-4's stilbene bond has been achieved by our group over the last decade as a strategy of *cis* restriction. This overcomes undesirable *cis* to *trans* isomerisation. This chemistry has garnered a large panel of the most potent microtubule destabilising agents reported to date, known as 'the combretazets'. β-lactam derivatives of CA-4 have only been evaluated to date *in vitro* in their racemic forms. This thesis therefore is focused on enantioseparation, characterisation and biochemical evaluation of the enantiopure combretazets. Optimisation of diastereomeric chiral resolution (DR) for enantioseparation of each enantiomer within the β-lactam racemates using amino acid chiral derivatising reagents diastereomer forms has therefore been explored. These enantiomers are structurally designed specifically for dual activity in colorectal and breast cancer cells. A quantitative (q) NMR technique was developed and validated for determining diastereomeric excess following diastereomeric chiral resolution. Chiral resolution proved as a sufficient approach to achieve racemate enantioseparation, yielding up to 95% enantiomeric excess (*ee*). Subsequent biochemical evaluation in a panel of breast cancer, HL-60 human leukaemia and CA-4 resistant HT-29 colorectal cancer cells, determined that the 3*S*,4*S* of the 3-hydroxyl panel and 3*S*,4*R* of the 3-substituted panel are the optimal absolute configurations for maximal anti-proliferative, microtubule destabilising and anti-mitotic activity as the eutomers of racemic enantiomer pairs. Kinetic enzymatic resolution (KR) as a biocatalytic approach for

enantioseparation of β-lactam racemates was also explored to afford a more accessible, sustainable and greener enantioseparative approach. Enantiomers were isolated with *ee* values between 70-99%. Additionally, β-lactam synthesis of the *trans* stilbene anti-angiogenic **P3** structure was explored, employing a pyrazine A ring in place of CA-4's 3,4,5-trimethoxyphenyl A ring and additionally the β-lactam method for *cis* restriction. The **P3** pyrazet β-lactam **151**, isolated in this thesis had superior anti-proliferative activity compared to parent **P3** in a panel of cancer cell lines. This demonstrates potential scope of A ring modifications in order to preserve anti-proliferative activity and illustrates that β-lactam ring insertion has potential to augment bioactivity. In summary, the agents described in this thesis offer potential strategies for future curative and effective management of resistant, advanced and metastatic breast and colorectal cancers and are therefore worthy of further development.

Table of Contents

Chapter 1 - Introduction ... 1
1.1 Introduction to breast cancer ... 2
1.2 Staging and molecular subtypes of breast cancer ... 2
1.2.1 Luminal A versus B BC ... 4
1.2.1.1 Hormone therapies for Luminal A and B BC and limitations with their use ... 4
1.2.2 Progesterone receptor positive (estrogen receptor negative) BC ... 6
1.2.3 HER2 enriched BCs ... 6
1.2.4 Triple negative/Basal like BCs ... 7
1.2.5 Novel treatments for TNBC ... 9
1.3 Colorectal cancer incidence ... 11
1.3.1 Current issues with treatment of colorectal cancer ... 11
1.4 Microtubules as a target for treating cancer ... 13
1.4.1 Structure of the microtubule ... 14
1.4.2 Clinically used microtubule targeting agents ... 15
1.5 Colchicine as a microtubule targeting agent: Historical uses and structure ... 19
1.5.1 The colchicine binding site ... 19
1.5.2 Targeting the colchicine binding site for anti-cancer activity ... 22
1.6 Combretastatin A-4 as a CBSI and anti-angiogenic agent ... 23
1.6.1 Biopharmaceutical issues associated with use of CA-4: solubility ... 24
1.6.2 The prodrug approach ... 25
1.6.2.1 Combretastatin A-4 Phosphate (Fosbretabulin) ... 26
1.6.3 Chemical instability as a biopharmaceutical issue associated with use of CA-4 ... 27
1.6.4 Chemical modifications for augmenting stability of CA-4 ... 28
1.7 β-Lactam cis restricted CA-4 analogues – 'The combretazets' ... 32
1.7.1 Relevance of the combretazets for the treatment of TNBC ... 33
1.7.2 Combretazets as lead analogues for treatment of metastatic chemoresistant colorectal cancer 34
1.8 Rationale for progression of the combretazet family as optically purified enantiomers for the treatment of both breast and colorectal cancers ... 38
1.9 Significance of chirality in modern drug design ... 38
1.10 Chiral synthesis for isolation of enantiopure of β-lactams ... 39
1.11 Chiral resolution of combretazet β-lactam racemates for isolation of enantiomeric pairs ... 41
1.11.1 Diastereomeric chiral resolution using chiral derivatising reagents ... 41
1.11.2 Kinetic resolution using enzymes as biocatalysts ... 42
1.12 Novel anti-angiogenic small molecules designed for the treatment of colorectal cancer: P drugs 43
1.12.1 Further development of stilbene **P3** as a promising radiosensitising agent ... 43
1.13 Synthesis of cis restricted analogues of **P3** ... 45
1.14 Thesis aims ... 46
1.14.1 CA-4 Analogues ... 46
1.14.2 **P3** ... 47
Chapter 2 - Synthesis and chemistry of *trans* β-lactam racemates ... 48
2.1 The β-lactam scaffold in nature and clinical uses ... 49
2.2 Pre-clinical uses of the β-lactam scaffold ... 50
2.3 Precursors for β-lactam synthesis ... 52
2.3.1 Protecting group chemistry ... 52
2.3.2 The TBDMS protecting group ... 53
2.3.3 Benzyl carbamate protecting group ... 54
2.4 Chemistry of β-lactam synthesis via Staudinger reaction ... 56
2.4.1 Staudinger reaction for synthesis of 3-acetoxy-β-lactams ... 60
2.4.2 Optimisation of Staudinger synthesis for isolation of trans β-lactam isomers of 3-acetoxy **17a**. 62
2.4.3 Optimisation of Staudinger synthesis for isolation of trans β-lactam isomers of **18a** ... 65
2.4.4 Application of optimised Staudinger synthesis for isolation of trans β-lactam isomers of 3-hydroxyl combretazet family. ... 67

2.4.5 Synthesis of further trans β-lactams containing the B ring meta hydroxyl or amine substituent group **(24-30, 32, 33, 35, 37,38,40,68,69)**....70
2.4.5.1 Analogues with B ring meta hydroxyl substituent (**24, 26, 30, 33, 38, 39,40, 41**) ...71
2.4.5.2 Further NMR studies of previously reported combretazet **33**....75
2.4.5.3 Analogues with B ring 3-nitro substituent. 76
2.4.5.4 Unexpected isolation of oxazinone derivative and proposed pathways for its synthesis 77
2.4.5.5 Analogues with B ring meta amino substituent....81
2.4.6 Staudinger reaction involving acid activation using triphosgene. 82
2.5 Analysis of stereochemical outcomes by replacing B ring para -OCH_3 with electron withdrawing substituents....84
2.5.1 XRD analysis of **91**....86
2.6 Amide by-products of Staudinger reaction....87
2.7 The Reformatsky reaction....90
2.7.1 Microwave technology versus conventional reflux for Reformatsky synthesis....91
2.7.2 Comparison of isolated yields and stereochemical outcomes for Reformatsky products using conventional reflux versus MAOS....95
Chapter 3 - Optimisation of diastereomeric chiral resolution, 2D EXSY studies and qNMR for β-lactam diastereomer excess determination....99
3.1 Chiral resolution as a method for isolation of enantiopure....100
3.2 Chemistry of β-lactam coupling to amino acid CDRs....101
3.3 NMR spectroscopy as a proposed method for diastereomer purity determination....105
3.3.1 Rotamers/Equilibrating species....105
3.3.2 Chemical exchange experiments....106
3.3.3 Variable temperature experiments....106
3.4 Use of NMR and EXSY spectroscopy for de determination....107
3.5 ^{1}H NMR data for diastereomer mixtures....108
3.5.1 Comparative ^{1}H NMR spectra for diastereomer mixtures **107-113** in H_3 and H_4 region .108
3.6 2D EXSY spectra of **107** and **108** in $CDCl_3$ confirming presence of equilibrating rotamers 111
3.7 VT experiments for diastereomer mixtures **107** and **108** in DMSO-d_6....113
3.8 VT experiments and 2D NOESY spectra for non-proline amino acid CDR diastereomer mixtures **109-113**....116
3.9 Computational data for β-lactam diastereomers....117
3.10 ^{1}H NMR and 2D EXSY spectra for isolated N-Boc-....121
3.11 Application of 2D EXSY spectra in CDCl3 as a qualitative tool for confirmation of resolution 123
3.12 qNMR for calculation of diastereomeric excess for β-lactam diastereomers....126
Chapter 4 - Application of optimised chiral resolution for enantioseparation of β-lactam racemates....129
4.1 Introduction to synthetic routes for chiral resolution using N-Boc-L-proline as a CDR....130
4.1.1 Application of chiral resolution to a panel of 3-hydroxyl racemates....130
4.1.2 Application of 2D EXSY spectroscopy as a qualitative tool to confirm diastereomer ratios for resolved diastereomers of mixtures **114, 116-118, 120-122**....134
4.1.3 qNMR for calculation of de for diastereomers of **114-122**....136
4.2 Hydrazinolysis of diastereomers **114-122** to enantiomers **16EN1 -39EN1** and **16EN2-39EN2**137
4.3 Characterisation of 3-hydroxyl enantiomers....138
4.3.1 XRD studies for **17EN1** and **17EN2**....138
4.4 Application of optimised chiral resolution using esterification of B ring meta hydroxyl group 141
4.5 XRD analysis of **24EN1**....144
4.6 Chiral resolution of 3-phenolic substituted β-lactam analogues....145
4.7 Application of optimised chiral resolution via amide bond derivatisation of the B ring NH_2 substituent....146
4.8 Chiral HPLC to determine enantiomeric excess of isolated analogues....149
4.9 Analysis of drug like properties....152
4.9.3 Bioavailability radar of lead enantiomers....155
4.9.4 Pharmacokinetics....156
4.10 Experimental Calculation of logP values for combretazet enantiomers....160

4.11 Chapter 4 Summary 162
Chapter 5 – Molecular modelling 164
5.1*Introduction to computational studies for β-lactam enantiomers* 165
5.1.1 Introduction to the tubulin-DAMA-colchicine co-crystal structure 1SAO 166
5.1.2 Ligand receptor interactions for CA-4 at the 5LYJ receptor 166
5.2 Methods for computational studies 168
5.2.1 Comparison of energy minimised to XRD structures 168
5.2.3 Preparation of the 1SAO and 5LYJ for docking of enantiomers 171
5.2.4 Docking protocol 171
5.2.5 Validation of docking protocol using 5LYJ 171
5.3 Results and discussion 173
5.3.1 Results of docking for colchicine, **17EN1** and **17EN2** at the CBS of 1SAO 173
5.3.3 Validation of docking protocol using 5LYJ 179
5.3.4 Introduction to scoring functions 181
5.3.5 Comparative docking for **18EN1** and **18EN2** 181
5.3.6 Role of fluorine substitution of **18EN1** for increasing binding affinity at CBS 184
5.3.7 Computational studies for **16EN1** and **16EN2** at the CBS of 1SAO 186
5.3.8 Computational studies for 3-phenyl substituted β-lactams **24EN1** and **24EN2** at the CBS of 1SAO 189
5.4 Conclusions drawn from S values for enantiopure combretazets 193
5.5 Chapter 5 summary and outlook 194
Chapter 6 - Biochemical evaluation of combretazet enantiomers 195
6.1*Rationale for selection of cell lines for preliminary screening* 196
6.1.1.1 MCF-7 cells 196
6.1.1.2 MDA-MB-231 cells 196
6.1.1.3 Hs578T(i)8 cells 196
6.1.1.4 HT-29 cells 197
6.1.1.5 HL-60 cells 197
6.1.1.6 MCF-10-2A non-tumorigenic human breast epithelial cells 197
6.1.2 Experimental details and cell culture 197
6.1.2.1 Breaking out of cells 197
6.1.2.2 Growth and maintenance of cells 198
6.1.2.3 Growth of MCF-7, MDA-MB-231, Hs578T(i)8, HT-29 and HL-60 cells 198
6.1.2.4 Growth of MCF-10-2A cells 198
6.1.2.5 Sub culturing of adherent cells (MCF-7, MDA-MB-231, Hs578T(i)8 and HT-29 cells) 199
6.1.2.6 Sub culturing of HL-60 suspension cells 199
6.1.2.7 Sub culturing of MCF-10-2A cells 199
6.1.2.8 Cryopreservation of cells 199
6.1.2.9 Counting of cells 200
6.2 Resazurin reagent preparation for use as in house AlamarBlue 200
6.3 Optimisation of cell seeding density for cell viability assays using AlamarBlue™ in MCF-7 cells 202
6.4 Optimisation of cell seeding density for cell viability assays using AlamarBlue™ in HS578T(i)8 cells 203
6.5 Measurement of growth inhibitory effects in cell viability/anti-proliferative studies 203
6.5.1.1 Procedure for seeding of cells in 96 well plates and treatment protocol 203
6.5.1.2 Layout of 96 well plate for cell viability assays and procedure 204
6.5.1.3 Measuring cell viability 205
6.5.1.4 Controls used in cell viability experiments 205
6.5.1.5 Treatment doses of test compounds 206
6.5.1.6 IC_{50} determination using GraphPad Prism 206
6.5.1.7 Relative versus absolute IC_{50} values 206
6.6 Cell growth experiment 207
6.7 Tubulin polymerisation studies 207
6.8 Immunofluorescence/confocal microscopy 208
6.9 Cell cycle analysis 208

6.10 Biochemical results 209
6.10.1.1 Anti-proliferative screening of β-lactam racemates and their isolated enantiomers 209
6.10.1.2 Preliminary anti-proliferative activity of the 3-hydroxyl **17** panel in breast cancer cells 209
6.10.1.3 Anti-proliferative activity of 3-hydroxyl panel in three breast cancer cell lines 212
6.10.1.4 Anti-proliferative activity of selected enantiomers in HL-60 human leukemia cell line .215
6.10.1.5 Eudysmic ratios of 3-hydroxyl enantiomers in three breast cancer cell lines.....217
6.10.1.6 Preliminary anti-proliferative screening of enantiomers of **17** in HT-29 colorectal cancer cell lines 219
6.10.1.7 Anti-proliferative activity of 3-hydroxyl enantiomers in HT-29 colorectal cancer cells .221
6.10.1.8 Anti-proliferative activity of 3-substituted enantiomers containing with B ring 3-hydroxy-4-methoxy substitutions in MCF-7 cells.....224
6.10.1.9 Anti-proliferative activity of 3-substituted enantiomers with B ring 3-hydroxy-4-methoxy substitutions in MDA-MB-231 cells.....226
6.10.1.10 Anti-proliferative activity of 3-substituted enantiomers containing with B ring 3-hydroxy-4-methoxy substitutions in Hs578T(i)8 cells 226
6.10.1.11 Anti-proliferative activity of 3-substituted meta hydroxyl analogues in HL-60 human leukemia cell lines 228
6.10.1.12 SAR analysis of eutomers based on cell viability data across four cell lines 228
6.10.1.13 Eudysmic ratios for 3-substituted B ring meta hydroxyl substituted enantiomers..229
6.10.1.14 Biological activities of 3-substituted enantiomers in HT-29 chemoresistant colorectal cancer cell line 230
6.10.1.15 Lead analogue selection for further biochemical analysis based on anti-proliferative findings 233
6.10.1.16 Anti-proliferative screening of 3-phenolic β-lactam racemates.....234
6.10.1.17 Anti-proliferative activity of cis and trans isomers of **28**.....235
6.10.1.18 Anti-proliferative activity of isolated trans isomers **63a**, **63** and **23** 235
6.10.1.19 Anti-proliferative activity of B ring modified β-lactam racemates.....236
6.11 Monitoring of cell growth in MDA-MB-231 cells treated with 3S,4S eutomer **17EN1**.....237
6.12 Tubulin polymerisation assays 240
6.12.1.1 Comparative tubulin polymerisation efficacy of eutomer **17EN1** versus distomer **17EN2** 240
6.12.1.2 Comparative tubulin polymerisation efficacy of **24EN1** versus **24EN2** 242
6.12.1.3 Determination of IC_{50} for tubulin depolymerisation efficacy for **24EN1** 244
6.12.1.4 Comparative tubulin polymerisation assays for β-lactam eutomers with B ring meta substitutions 247
6.12.1.5 Comparative tubulin polymerisation assays for **18EN1** and **18EN2**.....251
6.12.1.6 Calculation of IC_{50} of tubulin polymerisation inhibition for 3S,4S **18EN1** 253
6.13 Cytotoxicity evaluation of enantiomers in non-tumorigenic MCF-10-2A breast cells.....255
6.13.1.1 Cytotoxicity evaluation for enantiomers of **17** in MCF-10-2A cells.....255
6.13.1.2 IC_{50} of **17EN1** and **17EN2** in MCF-10-2A versus MCF-7 cells 256
6.13.1.3 Cytotoxicity for lead eutomers in MCF-10-2A cells 258
6.13.1.4 IC_{50} calculation for eutomers in MCF-10-2A cells 261
6.14 Confocal microscopy.....262
6.14.1.1 **6.14.1** Confocal microscopy of the microtubule network in three breast cancer cell lines following treatment with **17EN1** and **17EN2**.....262
6.14.1.2 Confocal Microscopy of **17EN1** and **17EN2** treated MDA-MB-231 cells.....262
6.14.1.3 Confocal Microscopy of the microtubule network for MCF-7 cells treated with **17EN1** and **17EN2** 264
6.14.1.4 Confocal Microscopy of the Hs578T(i)8 cell microtubule network treated with **17EN1** and **17EN2** 265
6.14.1.5 Confocal microscopy of the microtubule network for breast cancer cells treated with 3S,4R eutomer **24EN1**.....267
6.14.1.6 Confocal microscopy for eutomer **24EN1** in MDA-MB-231 cells.....267
6.14.1.7 Confocal microscopy of the MCF-7 microtubule network treated with **24EN1**.....268
6.14.2 Confocal microscopy of TNBC cells treated with eutomer **18EN1** 269
6.14.3 Confocal microscopy of the microtubule network in HT-29 CA-4 resistant colorectal cancer cells treated with **18EN1** or **24EN1**.....271
6.15 Cell cycle analysis by flow cytometry 273

6.15.1 Cell cycle analysis of MDA-MB-231 TNBC cells following treatment with eutomer **17EN1** 273
6.15.2 Cell cycle analysis of MDA-MB-231 TNBC cells following treatment with **24EN1** 277
6.15.2.1 Cell cycle analysis of Hs578T(i)8 TNBC cells following treatment with **24EN1**..... 280
6.15.3 Cell cycle analysis of HT-29 colorectal cancer cells following treatment with **18EN1** .. 283
6.15.4 Cell cycle analysis of MDA-MB-231 TNBC cells following treatment with **18EN1** 286
6.16 Chapter 6 Summary 289
***Chapter 7* - Kinetic resolution of β-lactam combretazet racemates using *Candida antarctica* lipase B** 260
7.1 Rationale for the use of lipase enzyme mediated kinetic resolution of *β*-lactams racemates 261
7.2 Enantioselectivity values (E values) for KR reactions 262
7.3 Lipase mediated KR of β-lactams and derivatives 263
7.4 Proposed mechanism for CAL-B mediated methanolysis of ester bonds 266
7.5 Preliminary kinetic resolution of 3-acetoxy racemate **17a** using CAL-B 269
7.5.1 Time course analysis of enantiomeric excess for kinetic resolution of **17a**..... 273
7.5.2 Enantioselectivity of CAL-B using methanol as solvent and **17a** as substrate..... 274
7.5.3 Investigating the nucleophilic effects of co-solvent and enzyme content on enantioselectivity of CAL-B with **17a** as substrate..... 275
7.6 Preliminary kinetic resolution of racemate **17** using amano lipase PS..... 277
7.7 Preliminary kinetic resolution of racemate B ring meta substituted 3-acetoxy **18a** using CAL-B 277
7.7.1 Time course analysis of enantiomeric excess for CAL-B mediated KR of **18a** 279
7.8 KR optimisation reactions for **20a** using CAL-B 281
7.10 Preliminary KR of trans **63a** and **23a** 285
7.11 Investigation of lower enzyme and methanol content for KR of B ring meta substituted racemates 286
7.12 Application of optimised KR for the isolation of 3S,4S 3-hydroxyl B ring meta substituted eutomers..... 288
7.13 Double KR for the isolation of 3R,4R 3-acetoxy distomers in >90% ee 292
7.14 Comparison of ee values obtained via chiral diastereomeric resolution versus kinetic enzymatic resolution 293
7.15 Preliminary phosphate prodrug synthesis..... 295
7.16 Conclusions and future outlook..... 298
Chapter 8 -Physiochemical analysis, prodrug synthesis and structural optimisation of Pyrazinib299
8.1 Pyrazinib (**P3**) as a promising radiosensitiser 300
8.2 Solubility issues with **P3** during in vivo pre-clinical animal models 300
8.3 Synthesis of **P3** using conventional reflux 300
8.4 Synthesis of **P3** via MAOS..... 303
8.5 XRD analysis of **P3** 304
8.5.1 Phosphate prodrug synthesis for P3 304
8.5.2 Synthesis of **P3P** using phosphorous oxychloride 305
8.5.2.1 Synthesis of **P3P** using dibenzylphosphite 306
8.5.2.2 Synthesis of P3 dimethyl phosphate (**P3DMP**) using dimethyl phosphite..... 307
8.5.2.3 Removal of dibenzyl groups from **P3DBP** using the McKenna reaction 307
8.5.2.4 Removal of dibenzyl groups using boron tribromide..... 309
8.6 Aqueous solubility of **P3** and **P3P** 309
8.7 Measurement of logP for **P3** and **P3P** 310
8.8 Chemical stability of P3 versus P3P..... 311
8.9 Alkaline phosphatase mediated hydrolysis of **P3P** 311
8.10 Comparison of antiproliferative activity for **P3** versus **P3P** in breast cancer cells 314
8.11 Cell cycle studies for **P3** and **P3P** in MDA-MB-231 cells..... 315
8.12 Molecular modelling for cis and trans **P3**..... 318
8.13 Chemistry of **P3** β-lactam synthesis – 'The Pyrazets'..... 320
8.14 Anti-proliferative evaluation of **151** by National Cancer Institute..... 327
8.15 Chapter summary and outlook..... 330
Chapter 9 - Concluding remarks and future work..... 332
Chapter 10 - Experimental 339
Appendices..... 399

Appendix 1: 400
Appendix 2 403
Appendix 3 405

List of Figures

Figure 1.1: Estimated global prevalence of BC frequency classified by molecular subtype.[35] 3
Figure 1.2: Pathway of estradiol metabolic activation to form genotoxic DNA adducts.[77] 5
Figure 1.3: Small molecules for the treatment of hormone receptor positive BC currently in clinical use. 5
Figure 1.4: Chemotherapeutic agents used in the treatment of TNBC 9
Figure 1.5: Novel small molecules used for treatment of TNBC. 11
Figure 1.6: Diagram of cell cycle detailing interphase (G_1/S/G_2 phases) followed by the 5 stage process of mitosis.[199] 13
Figure 1.7: Microtubule structure from side and top perspectives. Side view: Long, linear protofilaments consisting of αβ-tubulin heterodimers associate laterally. Top view: Association of 13 protofilaments forms the microtubule, a long hollow cylinder.[219] 15
Figure 1.8: Clinically relevant MTAs (vinca alkaloids, taxanes and colchicine) with their binding sites on the αβ tubulin heterodimer. Colchicine binding site illustrated at αβ interface of the tubulin heterodimer. 16
Figure 1.9: The intrinsic apoptotic pathway illustrating the role of Bcl-2 family in MOMP.[236] 17
Figure 1.10: 1SAO's α-tubulin and β-tubulin heterodimer with α-tubulin illustrated in cyan and β-tubulin is illustrated as blue. The T5 and T7 loop re shown in orange and cylindrical H7 and H8 helices shown in yellow and red respectively. White, grey, red, blue and golden yellow carbon = wite, hydrogen = grey, oxygen = red, nitrogen = blue and phosphorous = yellow. DAMA-colchicine = green.[262] 20
Figure 1.11: **A:** Molecular structure of colchicine outlining the 3,4,5-trimethoxy A ring, tropolone B ring and C ring. **B:** Space-filling model of colchicine (green) in the CBS. **C**: Model of DAMA-colchicine bound at the interface of αβ-tubulin. Key binding interactions are with Thrα179 and Valα181 of α-tubulin and Cysβ241 and Asnβ258 of β-tubulin. Colour key: green = carbon; red = oxygen; blue = nitrogen; yellow = sulfur; **D:** *Colchicum autumnale* from which colchicine is isolated. 21
Figure 1.12: Structures of colchicine, CA-4, CA-1 and respective prodrug analogues 23
Figure 1.13: Diagram illustrating the prodrug approach using carriers conjugated to available functional groups amenable to chemical manipulation.[319] 26
Figure 1.14: Isomerisation of *cis* CA-4 to *trans* CA-4 observed during metabolism and storage. 27
Figure 1.15: Biologically active analogues of CA-4.[209, 215, 230, 325, 360, 361, 372, 373] 31
Figure 1.16: Comparison of *cis* CA-4 versus *cis* restricted 3-hydroxyl combretazet β-lactam analogues. *Trans* 3-hydroxyl scaffold illustrated in blue box. 32
Figure 1.17: Plausible mechanism of glucuronidation in HT-29 cells of the phenolic B ring of CA-4 and its corresponding *cis* restricted combretazet *via* UDP-glucuronosyl transferase to an inactive *O*-glucuronide metabolite of CA-4 (left) and racemate **16** (right). 35
Figure 1.18: Parent 3-hydroxyl B ring *meta* hydroxyl substituted analogue (**16**) compared to lead 3-hydroxyl combretazet analogues with modifications at the B ring *meta* position which are active in CA-4 resistant HT-29 cells (**17-23**). *Trans* isomers and one enantiomer of the racemate illustrated.[378, 386, 400] .. 37
Figure 1.19: Synthesis of chiral 1,4-diaryl-3-methylene-2-azetidiones using chiral ligand [(*R,R,R*)-Ph-SKP] for asymmetric allylic amination by Zhou *et al.* 39
Figure 1.20: 3-methylene hydroxyl 3*S*,4*R* cis and 3*R*,4*R* trans enantiomers yielded *via* asymmetric synthesis by Zhou *et al*.[416] 40
Figure 1.21: Structural representation of theoretical *cis* **P3** compared to *cis* CA-4. *Trans* **P3** illustrated for reference. Examples of theoretical β-lactam analogues of **P3** are also illustrated (β-lactam ring highlighted in blue) 46
Figure 2.1: Naturally occurring antimicrobial agents containing the β-lactam scaffold (highlighted in red). 49
Figure 2.2: Semi- and synthetic β-lactams in clinical use. 50
Figure 2.3: XRD of **63a**. Independent molecules in the asymmetric unit of **63a** with atomic displacement shown at 50% probability. Heteroatoms labelled only and hydrogen atoms omitted for clarity. One molecule displays disorder in the acetate groups. *Trans* **63a** illustrated for reference with *trans* configuration at positions 3 and 4 of the β-lactam ring highlighted in blue. 70
Figure 2.4: **A:** ^{1}H NMR Spectrum for **33** at 400 MHz in $CDCl_3$ **B:** Resonance signals for $H_{8'}$, $H_{9'}$ and $H_{10'}$ 76
Figure 2.5: ^{1}H NMR spectrum of oxazinone in $CDCl_3$ at 400 MHz. 80
Figure 2.6: XRD structure of oxazinone (6-benzyl-2-(4-methoxy-3-nitrophenyl)-5-phenyl-3-(3,4,5-trimethoxyphenyl)-2,3-dihydro-4*H*-1,3-oxazin-4-one) **88** with atomic displacement shown at 50% probability. Disordered phenyl ring shown and heteroatoms labelled only. 81
Figure 2.7: Molecular structure of **91** with full atomic labelling. Atomic displacement shown at 50% probability. Displacement at 50% probability. One enantiomer illustrate 86

Figure 2.8: ^{1}H NMR data for **92** in $CDCl_3$ at 400 MHz. XRD structure of **92** with atomic displacement shown at 50% probability illustrated. 87
Figure 2.9: ^{1}H NMR of **78** in $CDCl_3$ at 600 MHz with enlargement of H_3 and H_4 region from δ 4.8 to 5.2 ppm. 97
Figure 3.1: 400 MHz ^{1}H NMR spectra at 25 °C of the H_3 and H_4 region (δ 4.4-5.5 ppm) for diastereomeric mixtures **107** and **108**. A degree of resonance signal overlap is noted for H_4 of **108** in $CDCl_3$ with only three of four signals observed. 109
Figure 3.2: 400 MHz ^{1}H NMR spectra in DMSO-*d*$_6$ of H_3 and H_4 region (δ 4.5-5.8 ppm) for **109-113**. 110
Figure 3.3: 400 MHz 2D EXSY spectra for the β-lactam H_3 and H_4 region (δ 4.5 – 5 ppm) in $CDCl_3$ at 25 °C for **107** and **108**. 112
Figure 3.4: Manual phasing off cross peaks for H_3 and H_4 from 2D EXSY spectra in $CDCl_3$ at 25 °C **A: 107 a: 107a** (H_3) **b**: **107a** (H_4) **c: 107b** (H_3) **d: 107b** (H_4) **B: 108**. **a: 108a** (H_3) **b**: **108b** (H_3) **c: 108a** (H_4), **d: 108b** (H_4) 112
Figure 3.5: Equilibrating rotamers for resolved *N*-Boc-L-proline-derivatised β-lactam diastereomers **108a** and **108b**..... 113
Figure 3.6: 400 MHz ^{1}H NMR spectra in DMSO-*d*$_6$ for H_3 and H_4 (4.3 – 5.8 ppm) region of **A:** D-proline CDR derivatised diastereomer mixture **107 B:** L-proline CDR derivatised diastereomer mixture **108,** as a function of temperature. Proline CH multiplet illustrated in **B** at δ 4.35 ppm for reference with no coalescence observed. 115
Figure 3.7: 400 MHz 2D EXSY spectra at 25 °C and elevated temperatures in DMSO-*d*$_6$ for expanded H_3 and H_4 region of **107** and **108** demonstrating one equivalent independent set of cross peaks for diastereomers in the mixture at 25 °C and a single diastereomeric signal for H_3 and H_4 at elevated temperatures of 95 °C and 85 °C for **107** and **108** respectively. 116
Figure 3.8: VT experiments for diastereomer mixtures **109**, **111, 112** and **113** at 400 MHz in DMSO-*d*$_6$ in H_3 and H_4 region (δ 4.5-5.8 ppm). 119
Figure 3.9: 400 MHz 2D NOESY spectra for H_3 and H_4 region in diastereomeric mixtures **109-113** in DMSO-*d*$_6$ at 25°C..... 120
Figure 3.10: Computational and theoretical model of diastereomeric pairs **108a** and **108b**, **109a** and **109b**, and **111a** and **111b**. Non-covalent intra-molecular π-π interactions indicated by grey dotted lines are present for aromatic moieties of phenylalanine and tryptophan diastereomers only. Hydrogen bonds illustrated as red dotted lines. Representative examples of major rotamers only are illustrated. Atom colours: red = oxygen, grey = carbon, blue = nitrogen. 122
Figure 3.11: **Top:** Overlay of 400 MHz ^{1}H NMR spectra of resolved **108a** (red) and **108b** (green) with diastereomer mixture **108** (blue). Middle: **108a** Bottom: **108b** at 25 °C. Expanded H_3 and H_4 region (δ 4.8-5.5 ppm) in $CDCl_3$ illustrated. 123
Figure 3.12: 400 MHz 2D EXSY spectra at 25 °C for H_3 and H_4 region of **107a**, **107b, 108a** and **108b** in $CDCl_3$. 125
Figure 4.1: Overlay of X-ray crystal structures of **17EN1** and **17EN2** illustrating the 3-hydroxyl orientation at C_3 and C_4 of the β-lactam ring 140
Figure 4.2: HPLC chromatograms for **A:** Achiral chromatogram for *trans* racemate **17**; **B:** chiral chromatogram for *trans* racemate **17**; **C:** Chiral chromatogram for 3*S,*4*S* enantiomer **17EN1**; **D:** Chiral chromatogram for 3*R,*4*R* enantiomer **17EN2** 150
Figure 4.3: HPLC chromatograms for **A:** Achiral chromatogram for *trans* racemate **24**; **B:** chiral chromatogram for *trans* racemate **24**. **C:** Chiral chromatogram for 3*S,*4*R* enantiomer **24EN1**; **D:** Chiral chromatogram for 3*R,* 4*S* enantiomer **24EN2**..... 150
Figure 4.4: Standard curve used for calculating linear equation using standards with known logP. 161
Figure 5.1: Enantiomers of racemates **16, 17, 18** and **24** studied in computational models at the colchicine binding site (CBS). 165
Figure 5.2: DAMA-colchicine (cyan) at the CBS of 1SAO. Red: α helices, yellow: β sheets, blue: loop turns, white: loop ribbons. Atom colours: Red = oxygen, yellow= sulfur. 167
Figure 5.3: The CBS of 1SAO. DAMA-colchicine = green. Atom colours: Red = oxygen, yellow = sulfur, blue = nitrogen. α-Helix = yellow, β-subunit = dark blue[261, 610] 167
Figure 5.4: CA-4 (green) at the CBS of 5LYJ. Hydrogen bonding interaction = dashed green lines.[337] 168
Figure 5.5: Comparison of **A:** 3*S,*4*S* **17EN1** XRD structure (cyan) and energy minimized model (pink) **B:** 3*R,*4*R* **17EN2** XRD structure (green) and energy minimised model (orange). Atom colours: red= oxygen, blue = nitrogen, grey = hydrogen..... 169
Figure 5.6: Validation protocol for database creation for enantiomers prior to computational studies. . 170
Figure 5.7: Validation of protocol for computational studies. 172

Figure 5.8: **A:** DAMA-colchicine (cyan) and colchicine (pink) at the CBS of 1SAO. **B:** Receptor removed on right for clarity. Atom colours: red= oxygen, blue = nitrogen, grey = hydrogen, yellow = sulfur.... 173
Figure 5.9: **17EN1** at the CBS of 1SAO. **A:** DAMA-colchicine (green) and XRD **17EN1** (yellow)**. B:** XRD **17EN1** (yellow) compared to energy minimised **17EN1** (pink) with receptor removed for clarity. Atom colours, red = oxygen, green = hydrogens, blue = nitrogen (*hydrogens illustrated to demonstrate alignment of XRD and energy minimsed structures)* 174
Figure 5.10: 3*R,*4*R* **17EN2** at the CBS of 1SAO. XRD structure (pink) versus energy minimised structure (orange). DAMA-colchicine (green). Receptor removed on right for clarity. Atom colours, red = oxygen, green = hydrogens, blue = nitrogen.... 175
Figure 5.11: **A:** 3*S*,4*S* **17EN1** (yellow) at the CBS of 1SAO compared to 3*R*,4*R* **17EN2** (cyan). Receptor removed on right for clarity. **B:** Comparison of **17EN1 (**yellow) to CA-4 (pink). **C:** Comparison of **17EN2** (cyan) to CA-4. Atom colours, red = oxygen, green = hydrogens, blue = nitrogen.... 177
Figure 5.12: Comparison of **17EN1** versus **17EN2** at the CBS of 1SAO **A: 17EN1** (yellow) **B: 17EN2** (cyan) Red: Hydrophilic pocket interactions. Blue: hydrophobic pocket interactions. Black: neutral pocket interactions. Atom colours: Red= Oxygen, Green = Nitrogen, Blue = Hydrogen 178
Figure 5.13: 5LYJ with CA-4 (cyan), **17EN1** (yellow) and **17EN2** (orange) at the CBS. Atom colours: Red = oxygen, green= hydrogen, blue = nitrogen.... 180
Figure 5.14: **A: 18EN1** (yellow) and CA-4 (cyan) **B: 18EN2** (pink) and CA-4 (cyan) docked at the CBS of 1SAO. Atom colours: Red= oxygen, blue = nitrogen, green = fluorine, grey = hydrogen 182
Figure 5.15: **16EN1** (yellow) and **16EN2 (**cyan) at the CBS of 1SAO. Atom colours: Red = oxygen, Blue = Nitrogen. 187
Figure 5.16: Triplicate studies for **16EN2** at the CBS of 1SAO demonstrating consistent ligand-receptor interactions for each independent replicate, explained by the presence of hydrogen bonding with Metβ259, and Lysβ352. Hydrogen bonds are illustrated as green dotted lines. 188
Figure 5.17: 3*S,*4*R* **24EN1 (**yellow) and 3*R,*4*S* **24EN2 (**cyan) at the CBS of 1SAO. CBS pocked illustrated in light grey. Atom colours: red= oxygen, blue= nitrogen, grey= hydrogen. π-aliphatic interaction illustrated as light blue dashed line. 190
Figure 5.18: 3-phenyl substituent of 3*S,*4*R* **24EN1** with π-aliphatic interaction illustrated as broken blue line between Lysβ254 and the 3-phenyl ring. 190
Figure 5.19: 3*S,*4*S* **16EN1** (cyan) and 3*S,*4*R* **24EN1** (yellow) at the CBS of 1SAO.... 192
Figure 6.1: A representative haemocytometer grid. Cells falling in the outer quadrants are counted. The top left outer quadrant is marked in blue.... 200
Figure 6.2: Schematic representation of the metabolic reduction of blue fluorescent resazurin in AlamarBlue™ to pink resorufin by NADH in living cells.... 201
Figure 6.3: Optimisation of seeding density for alamarBlue™ anti-proliferative assays for MCF-7 cells at 96 hours. Values represent the mean ± SEM for each seeding density performed in triplicate on three independent occasions. Linear range of 1-10 X 10^3 cells/well illustrated 202
Figure 6.4: Optimisation of the seeding density in Hs578T(i)8 breast cancer cells at 96 hours. **A:** 5 X 10^3 - 3 X 10^5 cells/well **B:** Fluorescence intensity at 5 X 10^3 – 4 X 10^4 cells/well illustrating linear range until ~ 4 X 10^3 cells/well. Values represent the mean ± SEM for each seeding density performed in triplicate on three independent occasions.... 203
Figure 6.5: Layout of 96 well plate used for cell viability assays. C_1 = concentration 1. C_2 = concentration 2 etc. 205
Figure 6.6: Cell viability graphs at 72 hours post treatment for **A:** *cis* **17** and *trans* **17s** in MCF-7 cells. **B: 17EN1** versus **17EN2** in MCF-7 cells. **C: 17EN1** versus **17EN2** in MDA-MB-231 cells. **D: 17EN1** versus **17EN2** in Hs578T(i)8 cells.... 211
Figure 6.7: Cell viability graphs for family **18** at 72 hours **A:** MCF-7 breast cancer cells **B:** MDA-MB-231 breast cancer cells. Blue = 3*S,*4*S* **18EN1**, pink = *trans* racemate **18,** green = 3*R,*4*R* **18EN2.** Values represent average of three independent experiments performed in triplicate with error bars representing SEM.... 214
Figure 6.8: Antiproliferative activity at 72 hours for **17EN1** and **17EN2** versus CA-4 in HT-29 chemoresistant colorectal cancer cells. Values represent ± SEM for at least three independent experiments performed in triplicate. 221
Figure 6.9: Antiproliferative activity for eutomers of the 3-hydroxyl eutomer panel in HT-29 cells. Values represent ± SEM for at least three independent experiments performed in triplicate.... 222
Figure 6.10: Cell viability curves for 3*S,*4*R* eutomer **24EN1**, 3*R,*4*S* distomer **24EN2** compared to eutomers **17EN1** and **27EN1 (**structural isomers) in MCF-7 cells at 72 hours. IC_{50} represented by dashed line. Values represent ± SEM for at least three independent experiments performed in triplicate.... 224

Figure 6.11: **A:** Cell viabilities of 3*S,*4*S* eutomer **18EN1** in three breast cancer versus HT-29 cell lines at 72h. **B:** Cell viabilities of 3*S,*4*R* eutomer **24EN1** in three breast cancer versus HT-29 cell lines at 72h. The dotted line represents the IC_{50} value. Values represent ± SEM for at least three independent experiments performed in triplicate. 233
Figure 6.12: Cell growth in MDA-MB-231 cells at 0, 24, 48 and 72 hours when treated with 0.6 % v/v ethanol as vehicle, 10 nM or 15 nM of **17EN1.** Images are representative of three independent experiments performed in triplicate. 239
Figure 6.13: Dose response curves for **A**: **17EN1** and **B: 17EN2** for the *in vitro* tubulin polymerisation assay. Graph selected as a representative example of two independent replicates performed in duplicate. 241
Figure 6.14: Dose response curves for **A: 24EN1** and **B**: **24EN2** for the *in vitro* tubulin polymerisation assay. Graph selected as a representative example of two independent replicates performed in duplicate. 243
Figure 6.15: Dose response curves for **A**: **24EN1** replicate 1 and **B: 24EN1** replicate 2 for *in vitro* tubulin polymerisation assay. **C:** Calculation of IC_{50} as **%** of V_{max} for replicate 1 **D:** Calculation of IC_{50} as **%** of V_{max} for replicate 2 **D:** Calculation of IC_{50} as **%** of final polymer mass for replicate 1 **E:** Calculation of IC_{50} as % of final polymer mass for replicate 2. 246
Figure 6.16: Tubulin polymerisation curves for B ring *meta* substituted 3*S,*4*S* eutomers **18EN1**, **19EN1, 20EN1** and **21EN1** with CA-4 (**A, only**) and paclitaxel as positive controls **A:** 5 μM **B:** 1 μM. Graphs selected as a representative example of two independent replicates performed in duplicate. 248
Figure 6.17: Tubulin polymerisation dose response curves for **18EN1** and **18EN2.** Graph selected is a representative example of two independent replicates performed in duplicate. 252
Figure 6.18: Dose response curves for **A: 18EN1** replicate 1 and **B: 18EN1** replicate 2 for the *in vitro* tubulin polymerisation assay. **C:** Calculation of IC_{50} as **%** of V_{max} for replicate 1 **D:** Calculation of IC_{50} as **%** of V_{max} for replicate 2 **E:** Calculation of IC_{50} as **%** of final polymer mass for replicate 1 **F:** Calculation of IC_{50} as **%** of final polymer mass for replicate 2 254
Figure 6.19: % cellular viability measured using AlamarBlue™ assay for CA-4, **17, 17EN1** and **17EN2** at 72 h in MCF-7 (pink) versus MCF-10-2A (yellow) cells at **A:** 10 nM and **B**: 100 nM. Values represent the average of at least three independent experiments performed in triplicate with error bars representing SEM. Statistical analysis performed using unpaired parametric t tests where ** = $p < 0.002$ *** p = < 0.0002 **** p = <0.0001 257
Figure 6.20: % viability for lead eutomers measured using AlamarBlue™ assay at 72h in MCF-7 (pink) versus MCF-10-2A (yellow) cells at **A:** 1 nM . **B:** 10 nM **C:** 100 nM Values represent averages of at least three independent experiments performed in triplicate with error bars representing SEM. Statistical analysis performed using unpaired parametric t tests where * = $p < 0.03$ ** = $p < 0.002$ *** p = < 0.0002 **** p = <0.0001 260
Figure 6.21: % cellular viability of **24EN1** in MCF-7 versus MCF-10-2A cells at 72 h using the AlamarBlue™ cell viability assay. Values represent averages of at least three independent experiments performed in triplicate with error bars representing SEM. Statistical analysis performed using unpaired parametric t tests where * = $p < 0.03$, *** p = < 0.0002 ****, p = <0.0001. 261
Figure 6.22: Confocal microscopy of the microtubule network in MDA-MB-231 cells. Untreated, vehicle treated (0.6% v/v ethanol) controls paclitaxel (1 μM) and CA-4 (100 nM), 3*S,*4*S* β-lactam eutomer **17EN1** at 10 nM, 50 nM, 100 nM and 500 nM and 3*R,*4*R* β-lactam distomer **17EN2** at 50 nM, 100 nM, 500 nM and 1 μM. Cells were treated for 16 h. Representative confocal micrographs of three independent experiments are shown. Scale bar 100 μm 263
Figure 6.23: Confocal microscopy of the microtubule network in MCF-7 cells. Untreated, vehicle treated (0.6% v/v ethanol), controls paclitaxel (1 μM) and CA-4 (100 nM), 3*S,*4*S* β-lactam eutomer **17EN1** at 10 nM, 50 nM, 100 nM and 500 nM and 3*R,*4*R* β-lactam distomer **17EN2** at 50 nM, 100 nM, 500 nM and 1 μM. Cells were treated for 16 h. Representative confocal micrographs of three independent experiments are shown. Scale bar 100 μM 265
6.24: Confocal microscopy of the microtubule network in Hs578Ti(8) cells. Untreated, vehicle treated (0.6% v/v), controls paclitaxel (1 μM) and CA-4 (100 nM), 3*S,*4*S* eutomer **17EN1** at 10 nM, 50 nM, 100 nM and 500 nM and 3*R,*4*R* distomer **17EN2** at 50 nM, 100 nM, 500 nM and 1 μM. Cells were treated for 16 h. Representative confocal micrographs of three independent experiments are shown. Scale bar 100 μm 266
Figure 6.25: Confocal microscopy of the microtubule network of MDA-MB-231 cells. Untreated, vehicle treated (0.6% v/v ethanol), controls paclitaxel (1 μM) and CA-4 (100 nM), 3*S,*4*R* eutomer **24EN1** at 1 nM, 5 nM, 10 nM and 50 nM. Cells were treated for 16 h. Representative confocal micrographs of three independent experiments are shown. Scale bar: 100 μm. 267

Figure 6.26: Confocal microscopy of the microtubule network of MCF-7 cells. Untreated, vehicle treated 0.6 % (v/v) % ethanol, controls paclitaxel (1 μM) and CA-4 (100 nM), 3*S*,4*R* eutomer **24EN1** at 1 nM, 5 nM, 10 nM and 50 nM. Cells were treated for 16 h. Representative confocal micrographs of three independent experiments are shown. Scale bar: 100 μm. 268
Figure 6.27: Confocal microscopy of the microtubule network of Hs578T(i)8 cells. Untreated, vehicle treated (0.6% v/v), controls paclitaxel (1 μM) and CA-4 (100 nM), 3*S*,4*R* eutomer **24EN1** at 1 nM, 5 nM, 10 nM and 50 nM. Cells were treated for 16 h. Representative confocal micrographs of three independent experiments are shown. Scale bar: 100 μm. 269
Figure 6.28: Confocal microscopy of the microtubule network in MDA-MB-231 cells. Untreated, vehicle treated (0.6% v/v), controls Paclitaxel (1 μM) and CA-4 (100 nM), 3*S*,4*S* eutomer **18EN1** at 1 nM, 5 nM, 1 nM and 50 nM. Cells were treated for 16 h. Representative confocal micrographs of three independent experiments are shown. Scale bar: 100 μm. 270
Figure 6.29: Confocal microscopy of the microtubule network in Hs578T(i)8 cells. Untreated, vehicle treated (0.6% v/v), controls paclitaxel (1 μM) and CA-4 (100 nM), 3*S*,4*S* eutomer **18EN1** at 1 nM, 5 nM, 1 nM and 50 nM. Cells were treated for 16 h. Representative confocal micrographs of three independent experiments are shown. Scale bar: 100 μM 271
Figure 6.30: Confocal microscopy of the microtubule network in HT-29 cells. Untreated, vehicle treated (0.6% v/v), controls paclitaxel (1 μM) and CA-4 (0.1 μM), 3*S*,4*S* eutomer **18EN1** at 1 nM, 5 nM, 10 nM and 50 nM and 3*S*,4*R* eutomer **24EN1** at 1 nM, 5 nM, 10 nM 50 nM. Cells were treated for 16 h. Representative confocal micrographs of three independent experiments are shown. Scale bar: 100 μm bottom. 272
Figure 6.31: **17EN1** induces G_2/M arrest and apoptosis in MDA-MB-231 cells. Cells were treated with either vehicle [1% ethanol (v/v)], or **17EN1** at concentrations of 10, 15, 20, 30, 40, 50 nM or 100 nM for 2, 8, 16, 24, 48 and 72 h. Cells were then fixed, stained with PI, and analysed by flow cytometry. Cell cycle analysis was performed on histograms of gated counts per DNA area (FL2-A). The number of cells with <2N (sub-G_1/G_0), 2N (G_0/G_1), and 4N (G_2/M). DNA content was determined with BD accuri C6. Values represent the mean for three independent experiments. 275
Figure 6.32: **24EN1** induces G_2/M arrest and apoptosis in MDA-MB-231 cells. Cells were treated with either vehicle [1% ethanol (v/v)], or **24EN1** at concentrations of 0.5, 1, 2.5, 5, 8, 10, 25, 50 or 100 nM for 2, 8, 16, 24, 48 and 72 h. Cells were then fixed, stained with PI, and analysed by flow cytometry. Cell cycle analysis was performed on histograms of gated counts per DNA area (FL2-A). The number of cells with <2N (sub-G_1/G_0), 2N (G_0/G_1), and 4N (G_2/M). DNA content was determined with BD accuri C6. Values represent the mean for three independent experiments. 278
Figure 6.33: **24EN1** induces G_2/M arrest and apoptosis in Hs578T(i)8 cells. Cells were treated with either vehicle [1% ethanol (v/v)], or **24EN1** at concentrations of 0.5, 1, 2.5, 5, 8, 10, 25 or 50 nM for 2, 8, 16, 24, 48 and 72 h. Cells were then fixed, stained with PI, and analysed by flow cytometry. Cell cycle analysis was performed on histograms of gated counts per DNA area (FL2-A). The number of cells with <2N (sub-G_1/G_0), 2N (G_0/G_1), and 4N (G_2/M). DNA content was determined with BD accuri C6. Values represent the mean for three independent experiments. 281
Figure 6.34: **18EN1** induces G_2/M arrest and apoptosis in HT-29 cells. Cells were treated with either vehicle [1% ethanol (v/v)], or **18EN1** at concentrations of 0.6 , 1, 5, 10, 25 or 50 nM for 2, 8, 16, 24, 48 and 72 h. Cells were then fixed, stained with PI, and analysed by flow cytometry. Cell cycle analysis was performed on histograms of gated counts per DNA area (FL2-A). The number of cells with <2N (sub-G_1/G_0), 2N (G_0/G_1), and 4N (G_2/M). DNA content was determined with BD accuri C6. Values represent the mean for three independent experiments 284
Figure 6.35: **18EN1** induces G_2/M phase arrest and apoptosis in MDA-MB-231cells. Cells were treated with either vehicle [1% ethanol (v/v)], or **18EN1** at concentrations of 0.6 , 2.5, 5, 10, 25, or 50 nM for 2, 8, 16, 24, 48 and 72 h. Cells were then fixed, stained with PI, and analysed by flow cytometry. Cell cycle analysis was performed on histograms of gated counts per DNA area (FL2-A). The number of cells with <2N (sub-G_1), 2N (G_0/G_1), and 4N (G_2/M). DNA content was determined with BD accuri C6. Values represent the mean for three independent experiments 287
Figure 7.1: **A:** Structural modifications which prevent *cis/trans* isomerisation of CA-4 (β-lactam ring insertion) and increase anti-proliferative activity in CA-4 resistant HT-29 cells (replacement of the B ring *meta* hydroxyl moiety with a halogen or methyl group); **B:** Proposed CAL-B mediated methanolysis of the 3*S*,4*S* 3-acetoxy enantiomer to the 3*S*,4*S* 3-hydroxyl enantiomer. 262
Figure 7.2: Biocatalytic kinetic resolution of racemates using enzymes 263
Figure 7.3: Enantioselective hydrolysis of 3-acetoxy *cis* β-lactam structure in a two-step cascade reaction to the enantioenriched 3-hydroxyl structure in <20% ee followed by enantioselective ring opening to enantiopure taxane side chain precursor in >98% ee.[727] **a:** CAL-B, *i*Pr2O**,** H_2O**,** 60 ºC 264

Figure 7.4: **A:** Lipase PS catalysed enantioselective acylation of β-lactams with vinyl butanoate;[728] **B:** Lipase PS catalysed alcoholysis of the enantioenriched acylate (from **A**) as part of a double resolution strategy to yield the 4*S* enantiomer in >99% *ee*[728] 265
Figure 7.5: Disordered molecular structure of chiral 3-hydroxyl **17EN1** isolated by CAL-B mediated methanolysis in 56% *ee* (**e**ntry 9**,**Table 7.2). Atomic displacement shown at 50% probability and heteroatoms labelled only. 273
Figure 7.6: % *ee* of 3*S,*4*S* 3-hydroxyl **17EN1** and 3*R,*4*R* 3-acetoxy **17aEN2** versus % conversion for entry 9, Table 7.1 274
Figure 7.7**: A:** % *ee* for 3*S,* 4*S* **18EN1** and 3*R,*4*R* 3-acetoxy **18aEN2 (**entry 1**,** Table 7.6**)** determined by chiral HPLC for **B:** entry 2, Table 7.6 280
Figure 7.8: **A:** XRD structure of enantioenriched **18a** with absolute configuration 3*R,*4*R* isolated from CAL-B reactions, entry 2, Table 7.6, crystallised from methanol overnight. 280
Figure 7.9:% conversion of **18a (**Table 7.6**)** and **17a (**Table 7.2**)** using CAL-B (determined by ^{1}H NMR in $CDCl_3$ at 400 MHz) 281
Figure 7.10: XRD for 3*S,*4*S* 3-hydroxyl **22EN1.** Disordered molecular structure with two locations for the trimethoxyphenyl ring (58:42%). Atomic displacement shown at 50% probability and heteroatoms labelled only. 291
Figure 7.11: NMR spectra for dibenzyl phosphate derivative of *3S,*4*S* **140** (70% *ee*) **A:** ^{1}H NMR in $CDCl_3$ at 600 MHz. **B:** ^{31}P NMR spectra at 162 MHz **C:** Blue: PYSCHE for **140 (**dibenzyl phosphate ether of **20EN1**) at 600 MHz in $CDCl_3$ in H_3 and H_4 region illustrating the ^{3}J P-H coupling at δ 5.05 ppm with of 8.5 Hz while H_4 resonates as a singlet. Red: ^{1}H NMR spectrum for H_3 and H_4 at 600 MHz in $CDCl_3$. 297
Figure 8.1: **A: (Left**) **P3** suspended in vehicle A (10% DMSO, 30% EtOH, 60% PBS) and vehicle B (10% DMSO, 30% EtOH, 60% H_2O) at 1 mg/mL. (**Right**) Post vortex **B: P3** dissolved in 99:1 non pharmaceutical grade corn oil: DMSO 300
Figure 8.2: **A:** ^{1} H NMR of **P3** in DMSO-*d*$_6$ at 400 MHz. **B:** ^{13}C NMR of **P3** in DMSO-*d*$_6$ at 100 MHz. 303
Figure 8.3: **A:** Molecular structure of **P3** with atomic displacement shown at 50% probability.**B:** Detail of the intermolecular hydrogen bonding between molecules of **P3** (dotted lines) with atomic displacement shown at 50% probability. 304
Figure 8.4: **A:** ^{1}H NMR spectrum for **P3DBP** in DMSO-*d*$_6$ at 400 MHz. **B**: ^{31}P for **P3DBP** in DMSO-*d*$_6$ at 162 MHz 306
Figure 8.5: **A:** ^{1}H NMR spectrum of **P3MP** in DMSO-*d*$_6$ at 400 MHz. **B:** ^{31}P NMR spectrum of **P3DMP** at 162 MHz. **C:** Spontaneous atmosphere hydrolysis of **P3DMP** to **P3** monomethyl phosphate and ^{1}H NMR in DMSO-*d*$_6$ at 400 MHz after 6 months of storage. **D:** ^{31}P NMR spectra of degraded **P3** monomethyl phosphate **(**blue) versus **P3DMP** in >99% purity (red) 308
Figure 8.6: Calibration curves used for solubility measurements for **A: P3 B: P3P** 310
Figure 8.7: Stability of **P3** and **P3P** at 24 hr and 7 days in phosphate buffers BP at pH values of 4, 7.4 and 9. Two exceptions noted (**P3** pH 7.4 measured at 5 days and **P3P** at pH 9 measured at 23 days due to Covid-restricted lab access). 311
Figure 8.8: Conversion of **P3P** to **P3** by alkaline phosphatase at 37 °C **A:** 5 mL of AP solution (25 DEA units) was added to 5 mL of **P3P** of 0.3 mM stock solution **B:** 5 mL of AP solution (25 DEA units) was added to 10 mL of **P3P** of 0.3 mM stock solution **C:** Enlarged area of **B** from 0-5 minutes 313
Figure 8.9: Antiproliferative activity of prodrug **P3P** (pink) versus **P3** (green) in **A:** MCF-7 cells. **B:** MDA-MB-231 cells. Values represent average of three independent replicates performed in triplicate on three independent occasions. Statistical analysis involved using multiple t-test comparisons corrected for multiple comparisons using the Holm-Sidak method to establish statistical significance with respect to control. * p-value <0.05. *** p-value <0.001. 314
Figure 8.10: Effects of **P3** and **P3P** on the cell cycle in MDA-MB-231 cells. For **P3** cell cycle experiments, cells were treated with vehicle [DMSO 0.5% (v/v)] or **P3** at concentrations of 25, 32.5, 50 or 100 µM. For **P3P** cell cycle experiments, cells were either treated with vehicle (0.6% v/v ethanol) or **P3P** at 10, 20, 25, 32.5, 50 or 100 µM. Cells were treated for 8, 24 or 48 h. Cells were then fixed, stained with PI and analysed by flow cytometry. Cell cycle analysis was performed on histograms of gated counts per DNA area (FL2-A). The number of cells with <2N (sub-G_1), 2N (G_0/G_1), and 4N (G_2/M). DNA content was determined using the BD accuri C6 flow cytometer. Values represent the mean for one experiment. (n=1) 317
Figure 8.11: Structures of *cis* and *trans* CA-4 and **P3** 318
Figure 8.12: Molecular docking studies for *cis* and *trans* **P3** at the CBS of 1SAO **A: *Cis* P3** (pink) and *trans* **P3** (cyan). DAMA-Colchicine is shown in green. CBS binding pocket illustrated in grey. Hydrogen bonding shown as blue dotted lines. **B:** Overlay of *cis* **P3**, *trans* **P3** and DAMA-colchicine with receptor

removed for clarity. **C:**2D Ligand-receptor interaction diagram for *cis* **P3** and **D:** *trans* **P3** ligand interactions**.** Atom colours: Red: oxygen, Blue: Nitrogen, Yellow: Sulfur, Grey: Hydrogen. 319
Figure 8.13: Hypothetical lead analogues of *cis* restricted **P3** β-lactam racemates..... 321
Figure 8.14: ^{1}H NMR of **151** in $CDCl_3$ at 600 MHz illustrating majority presence of *cis* isomer (doublets with ^{3}J = 5 Hz at δ 6.46 and 6.29 ppm) and presence of *trans* isomer (doublets at δ 5.96 and 5.76 ppm with ^{3}J values of 2 Hz). 326
Figure 8.15: Molecular structure of *cis* **151** with atomic displacement shown at 50% probability. Heteroatoms labelled only for clarity. Hydrogen bonding indicated by dotted lines. One enantiomer illustrated. 327
Figure 8.16: Dose-response curves generated by NCI-60 screening for **151** for **A:** breast cancer cell lines **B**: colon cancer cell lines. 328

List of Tables

Table 2.1: 3-Hydroxyl racemates selected as lead analogues[378, 400] 51
Table 2.2: 3-Substituted racemates selected as lead analogues[378, 400, 495] 52
Table 2.3: Preliminary and optimised Staudinger reaction conditions for synthesis of 3-acetoxy-β-lactam **17a** 65
Table 2.4: Staudinger reaction conditions for synthesis of β-lactam **18a.** 67
Table 2.5: Isolated yields for 3-acetoxy and 3-hydroxyl combretazet racemates and stereochemical outcomes.[378, 400] 69
Table 2.6: Isolated yields and stereochemical outcomes for 3-substituted combretazets containing the B ring *meta* hydroxyl substituent.[378, 400, 495] 73
Table 2.7: Yield and stereochemical outcomes for 3-substituted combretazets containing B ring *meta* 3-NO_2 substitutions.[378, 400, 495] 77
Table 2.8: Reduction of *meta* 3-NO_2 B ring substituent to the corresponding 3-NH_2 substituent in β-lactams **32, 35** and **37** and total isolated yields from the Staudinger reaction.[378, 400, 495] 82
Table 2.9: Isolated yields for 3-phenolic substituted β-lactam analogues.[495] 84
Table 2.10: Table of yields for B ring modified β-lactam analogues. 86
Table 2.11: Panel of amides synthesised and general characterisation. 89
Table 2.12: XRD structures for amides 90
Table 2.13: Comparative yields of Reformatsky products isolated *via* conventional reflux and MAOS 95
Table 2.14: Yield of *cis* and *trans* **77** isolated from LC purification of *cis:trans* isomeric mixtures 96
Table 3.1: Integration of H_3 and H_4 resonances on ^{1}H NMR axis for qNMR determination of d.r[1] and *de* values for resolved proline diastereomers **107a**, **107b**, **108a** and **108b**. 127
Table 4.1: Isolated diastereomer mixtures **114-122** and resolved diastereomer (**a** and **b**) yields for 3-hydroxyl β-lactams reported as % yield of original diastereomer mixture. 133
Table 4.2: (Top) 2D EXSY spectra at 400 MHz in $CDCl_3$ for N-Boc-L-proline derivatised diastereomers of **114,** resolved **114a** and **114b** and (bottom) the corresponding ^{1}H NMR spectra in the H_3 and H_4 region (~ δ 4.8-5.5 ppm) 135
Table 4.3: (Top) 2D EXSY spectra for diastereomers of **116,** resolved **116a** and **116b** and (bottom) their corresponding ^{1}H NMR spectra in the H_3 and H_4 region (~ δ 4.8-5.5 ppm) 135
Table 4.4: (Top) 2D EXSY spectra for diastereomers of **117,** resolved **117a** and **117b** and (bottom) their corresponding ^{1}H NMR spectra in the H_3 and H_4 region (~ δ 4.8-5.5 ppm) 136
Table 4.5: Integration of H_3 and H_4 resonances on ^{1}H NMR axis for qNMR determination of d.r[1] and *de* values for resolved proline diastereomers. 137
Table 4.6: Isolated yields for 3-hydroxyl enantiomers 138
Table 4.7: ORTEP representation of the X-ray crystal structures for **17EN1** and **17EN2.** Molecular structure of the majority occupied moiety with atomic displacement shown at 50% probability. Dotted lines indicates intramolecular hydrogen bonding. 139
Table 4.8: Observed optical rotations for enantiomers of **17** and **18** 141
Table 4.9: Yields of isolated diastereomer mixtures **123-131** and their resolved diastereomers (**a** and **b**). 143
Table 4.10: Isolated enantiomer yields for B ring *meta* hydroxy containing hydroxyl analogues 144
Table 4.11: Chiral molecular structure of **24EN1** with atomic displacement shown at 50% probability and heteroatoms labelled only. Dotted lines indicate hydrogen bonding interactions. 145
Table 4.12: Enantiomeric excess (*ee*) for enantiomeric combretazets determined by chiral HPLC. 151
Table 4.13: Physiochemical properties of lead enantiomers calculated using the Swiss ADME webtool. 155
Table 4.14: Bioavailability radar plots for lead enantiomers calculated using the Swiss ADME webtool.[647] 157
Table 4.15: Pharmacokinetic assessment of lead enantiomers using the Swiss ADME webtool.[623] 158
Table 4.16: Assessment of enantiomer drug-likeness using five assessment methods and two drug-like assessment filters; PAINs and Brenk generated using Swiss ADME webtool. [623] 160
Table 4.17: Calculation of retention factor (*k*) and log*k* for standards with known logP 161
Table 4.18: Calculation of logP for enantiomers 162
Table 5.1: Ligand-Receptor Interactions for CA-4, **17EN1** and **17EN2** at the CBS of 1SAO 179
Table 5.2: Ligand-receptor interactions at the CBS of 1SAO **18EN1, 18EN2** and CA-4 184
Table 5.3: Total Number of ligand-receptor binding interactions for **16EN1** and **16EN2** at the CBS of 1SAO 189
Table 5.4: 2D Ligand Interactions for **24EN1** and **24EN2** at the CBS of 1SAO generated by *MOE* 193

Table 5.5: Ranked S values for all enantiomers. Highest scoring enantiomers (**EN1**) shown in bold (black) and highest scoring enantiomers (**EN2**) shown in red..... 194
Table 6.1: Cells/ well and required cells/ mL in initial cell suspension used to seed each cell line..... 204
Table 6.2: Anti-proliferative activity of panel **17** in four CA-4 sensitive cell lines reported as IC_{50} in nM ± SEM [a] 210
Table 6.3: Anti-proliferative activity of 3-hydroxyl racemates and enantiomers (**16,18, 19**) in four CA-4 sensitive cell lines at 72h. IC_{50} [a] reported in nM ± SEM 216
Table 6.4: Anti-proliferative activity for 3-hydroxyl racemates and enantiomers (**20**-**22**) in four CA-4 sensitive cell lines at 72h. IC_{50} reported in nM ± SEM..... 217
Table 6.5: Eudysmic ratios for 3-hydroxyl enantiomers[a] 219
Table 6.6: IC_{50} reported in nM of 3*S* 4*S* eutomer **17EN1** and 3*R,*4*R* distomer **17EN2** and CA-4 in MCF-7 versus HT-29 colorectal cancer cells with relative potency ratios.[a] 220
Table 6.7: IC_{50} values reported in nM for 3-hydroxyl 3*S,*4*S* eutomers and 3*R,*4*R* distomers compared to CA-4 in MCF-7 and HT-29 colorectal cancer cells with respective relative potencies 223
Table 6.8: IC_{50} values reported in nM for B ring *meta* hydroxyl 3-substituted β-lactam racemates and their resolved enantiomers (**24, 27, 30**) 225
Table 6.9: IC_{50} values reported in nM for B ring *meta* hydroxyl β-lactam 3-substituted racemates and enantiomeric β-lactams **33, 39** and **41** 227
Table 6.10: Eudysmic ratios for enantiomers with a β-lactam 3-substitution and 3-hydroxy-4-methoxy substituted B ring[a] 230
Table 6.11: IC_{50} values reported in nM for 3-substituted enantiomers compared to CA-4 in MCF-7 and HT-29 colorectal cancer cells with respective relative potencies. 231
Table 6.12: IC_{50} values reported in nM for 3-phenolic racemates in MCF-7 and MDA-MB-231 cell lines at 72h. 234
Table 6.13: IC_{50} values reported in nM for **28** *cis* and *trans* isomers in MCF-7 and MDA-MB-231 cell lines. 235
Table 6.14: IC_{50} values reported in nM ± SEM for **63a, 63** and **23** in MCF-7 cells at 72h..... 236
Table 6.15: Antiproliferative activity for modified B ring racemates in MCF-7 cells. 237
Table 6.16: Effects of **17EN1, 17EN2** and CA-4 on *in vitro* tubulin polymerisation standardised to vehicle control. Results represent the values from two independent experiments performed in duplicate. 242
Table 6.17: Effects of 3*S,*4*R* eutomer **24EN1,** 3*R* 4*S* distomer **24EN2** and CA-4 on *in vitro* tubulin polymerisation standardised to vehicle control. Results represent the values from two independent experiments performed in duplicate..... 244
Table 6.18: *In vitro* dose response tubulin polymerisation assay for **24EN1**. Values represent average values of two independent experiments performed in duplicate. 247
Table 6.19: IC_{50} values for eutomer **24EN1** calculated as % fold reduction in V_{max} and polymer mass. 247
Table 6.20: Effects on *in vitro* tubulin polymerisation for B ring *meta* substituted 3*S,*4*S* eutomers compared to CA-4. Values represent average values of two independent experiments performed in duplicate. 249
Table 6.21: Effects on *in vitro* tubulin polymerisation for B ring *meta* substituted 3*S,*4*S* eutomers compared to CA-4. Values represent average values of two independent experiments performed in duplicate. 249
Table 6.22: Comparison of anti-proliferative activity for *meta* substituted 3*S,*4*S* eutomers to their microtubule depolymerising activity reported as % reduction in final polymer mass at 1 and 5 μM. 251
Table 6.23: Effects on *in vitro* tubulin polymerisation **18EN1** at 5 μM and **18EN2** at 5 and 10 μM. Values represent average values of two independent experiments performed in duplicate. 252
Table 6.24: Inhibition of *in vitro* tubulin polymerisation for 3*S,*4*S* **18EN1** as a dose response for IC_{50} calculations. Values represent average of two independent experiments performed in duplicate 255
Table 6.25: IC_{50} values for 3*S,* 4*S* **18EN1** calculated as % fold reduction in V_{max} and final polymer mass (OD value) 255
Table 6.26: IC_{50} values for enantiomers of racemate **17** and CA-4 in MCF-7 breast cancer cells versus non-tumorigenic endothelial breast MCF-10-2A cells at 72 h. Values represent the average of at least three independent experiments performed in triplicate ± SEM 257
Table 6.27: IC_{50} values of selected β-lactam enantiomers in ER positive breast cancer cells (MCF-7) versus non-tumorigenic breast cells (MCF-10-2A) 262
Table 6.28**: %** of MDA-MB-231 cells in each stage of cell cycle when treated with **17EN1**. Values represent as the mean for three independent experiments ± SEM. 276

Table 6.29: **%** of MDA-MB-231 cells in each stage of cell cycle when treated with **24EN1**. Values represent as the mean for three independent experiments ± SEM. 279
Table 6.30: **%** of Hs578T(i)8 cells in each stage of cell cycle when treated with **24EN1**. Values represent as the mean for three independent experiments ± SEM. 282
Table 6.31: **%** of HT-29 cells in each stage of cell cycle when treated with **18EN1**. Values represent as the mean for three independent experiments ± SEM. 285
Table 6.32: **%** of MDA-MB-231 cells in each stage of cell cycle when treated with **18EN1**. Values represent as the mean for three independent experiments ± SEM. 288
Table 6.33: Summary table of biochemical data for lead eutomers **18EN1** and **24EN1** 290
Table 7.1: Chiral chromatograms for enantioenriched 3*R,*4*R* 3-acetoxy **17aEN2** and 3*S,*4*S* 3-hydroxyl **17EN1** isolated from entry 6, Table 7.1 purified using LC post-reaction. 270
Table 7.2: CAL-B optimisation reactions using **17a** as substrate. 272
Table 7.3: CAL-B optimisation reactions varying MeOH content using **17a** as substrate. 274
Table 7.4: Optimisation of CALB KR reactions for **17a** varying co-solvent, co-solvent equivalents and enzyme content 276
Table 7.5: Preliminary KR reactions of **17a** using amano Lipase PS, from *Burkholderia cepacia* 277
Table 7.6: CAL-B optimisation reactions for substrate **18a** as substrate. 278
Table 7.7: Chiral chromatograms for 3*R,*4*R* 3-acetoxy **18a** and 3*S,* 4*S* 3-hydroxyl **18** 279
Table 7.8: CAL B optimisation reactions using **20a** as substrate. 283
Table 7.9: Optimisation of KR reactions for *meta* substituted 3-acetoxy β-lactams using CAL-B. 287
Table 7.10: Application of optimised KR procedure to 3-acetoxy β-lactam substrates **17a** -**23a** and **65-66a**. 289
Table 7.11: Isolation of 3-acetoxy 3*R,*4*R* distomers using CAL-B 293
Table 7.12: Comparison of *ee* values obtained using *N*-Boc-L-Proline as the CDR in diastereomeric resolution versus kinetic resolution with lipase enzyme CAL-B. 294
Table 8.1: Experimentally measured logP values for **P3** and **P3P** compared to values obtained using Swiss ADME webtool and clogP. 311
Table 8.2: **%** of MDA-MB-231 cells in each stage of cell cycle when treated with **P3** (25, 32.5, 50 or 100 μM) for 8, 24 or 48 h. Vehicle = DMSO 0.5% v/v. 316
Table 8.3: % of MDA-MB-231 cells in each stage of cell cycle when treated with **P3P** (10, 20, 25, 32.5, 50 or 100 μM) for 8, 24 or 48 h. Vehicle [0.6% v/v ethanol/dH_2O]. 316
Table 8.4: GI_{50} values for **151** in NCI 5-dose screen 328
Table 8.5: GI_{50}, TDI_{50} and LC_{50} values for **P3BL1** in breast cancer cell lines from NCI-60 5 dose screen 330

List of Schemes

Scheme 2.1: Synthesis of silyl ether protect imine **47 a:** Direct protection of imine **46** using TBDSMCl, DBU, anhydrous DCM, inert atmosphere, RT. **b:** Protection of 3-hydroxy-4-methoxybenzaldeyde using TBDMSCl (identical reagents to **a**) to yield **42 c:** 3,4,5-Trimethoxyaniline, ethanol, 90 °C, 4 h. 54
Scheme 2.2: Synthesis of imines **44-56** *via* condensation reaction **a:** ethanol, reflux (90 °C), 3-4h, catalytic quantities of 0.1 M HCl or low intensity ultrasound with a 40 KHz transducer 55
Scheme 2.3: Staudinger reaction mechanism (theory 1) *via* ketene precursor and intramolecular Mannich like [2+2] cycloaddition. Conrotatory and disrotatory ring closure *via* π molecular orbitals yielding an isomeric mixture (*cis* and *trans* β-lactams) illustrated. 57
Scheme 2.4: Staudinger reaction mechanism (theory 2) involving addition of acid chloride and imine to form *cis* acyliminium zwitterion which isomerises to the *trans* zwitterion to yield exclusively *trans* β-lactam. 58
Scheme 2.5: Epimerisation of B ring *para*-nitro substituted 2-azetidinone in Na_2PO_3 basic conditions to a mixture of *cis* and *trans* equilibrating adducts.[419] 59
Scheme 2.6: Routes of *cis* and *trans* β-lactam formation in the Staudinger reaction. **a:** Ketene generated from acid chloride **b:** Imine **c:** pre-*cis* zwitterion **d:** pre-*trans* zwitterion. k_1 = direct ring closure. k_2 pre-*cis* zwitterion isomerisation. $k_{2'}$= reversible isomerization of *trans* zwitterion 60
Scheme 2.7: Staudinger synthesis of 3-acetoxy-β-lactams and hydrazinolysis to 3-hydroxyl β-lactam racemates**.** Reagents and conditions: **a:** Ethanol, reflux, 4h, 0.1M HCl. **b:** acetoxyacetyl chloride, TEA, anhydrous toluene, 100 °C, 5h, inert atmosphere **c:** hydrazine dihydrochloride, TEA, anhydrous methanol, 85 °C, 4h, inert atmosphere. **d:** TBAF, THF, 0 °C, 1h **e:** glacial acetic acid zinc dust, RT, 6 days. Products obtained as racemic mixtures with one enantiomer shown. 62
Scheme 2.8: Mechanism for Staudinger synthesis of 3-acetoxy racemates. 63
Scheme 2.9: Hydrazinolysis of *trans* 3-acetoxy racemates to yield *trans* 3-hydroxyl β-lactams (one enantiomer shown). 69
Scheme 2.10: General synthetic pathway for synthesis of B ring *meta* hydroxyl-, nitro- and amino-substituted β-lactam racemates. **a: Staudinger:** anhydrous toluene, N_2, 100 °C, then TEA, 5h. **b:** triphosgene, anhydrous toluene, 100 °C for 30 minutes, then imine, TEA, 5h. **c: Reformatsky:** Zinc dust, anhydrous benzene, chlorotrimethylsilane, N_2, **47** and substituted ethyl bromoacetate. **d:** glacial acetic acid, zinc dust, N_2, 6 days. **e:** 1:1 ethanol/ethyl acetate, H_2, 10% palladium on carbon, 1-2 h. **f:** anhydrous THF, TBAF (1M in THF) 0 °C, 1-2h. 72
Scheme 2.11: Comparison of **A:** Electronic effects for electron donating B ring *meta* OTBDMS ether favouring *trans* β-lactams **B:** Electronic effects for electron withdrawing B ring *meta* NO_2 favouring *cis* β-lactams. 74
Scheme 2.12: Proposed pathway for oxazinone formation due to dimerisation of ketenes to acylketenes.[528] 78
Scheme 2.13: Proposed pathway for the synthesis of oxazinone **88** under typical Staudinger conditions when excess phenylacetyl chloride is used in effort to synthesise **85** with imine **54**. Competing pathways are indicated by $\mathbf{C_1}$ and $\mathbf{C_2}$ 79
Scheme 2.14: Acid activation of acetic acids to corresponding acid chlorides using triphosgene as acid activator and synthesis of corresponding β-lactams. **a:** 100 °C, anhydrous toluene, 30 minutes at 100°C. **b:** TEA, reflux, 5h. **c:** Pd/C (10%), H_2, ethyl acetate/ethanol (1:1). **d:** TBAF 1M in hexane, anhydrous THF, N_2, 0 °C, 1-2 h 83
Scheme 2.15: Illustration of electron donating properties of the acetoxyacetyl chloride-derived zwitterionic intermediate during the Staudinger reaction. Electron-donating conjugated system illustrated in pink. 85
Scheme 2.16: Competing reactions for formation of β-lactam **70** in the Staudinger reaction (**1**) versus condensation of primary amine 3,4,5-trimethoxyaniline and phenylacetyl chloride (**2)** to form amide **92**.[342] **a:** Staudinger reaction conditions. Acetoxyacetyl chloride, imine, reflux for 20 minutes at 100 °C, then TEA followed by 5 hour reflux. 88
Scheme 2.17: Products formed in Reformatsky reaction using Zn as metal catalyst, and an α-bromo ester as the nucleophile. 92
Scheme 2.18: Synthesis of **27-29** *via* the Reformatksy reaction from ethyl-2-bromoacetate, ethyl-2-bromopropionate and ethyl-2-bromofluoroacetate respectively *via* their OTBDMS protected silyl ethers **76-78**. **a:** Zinc, TMSCl, anhydrous benzene **b:** reflux **c:** β-lactam ring cyclisation. **d:** TBAF in 1M hexane, anhydrous THF, 0 °C, 1-2h. 94
Scheme 3.1: Mechanism of action for coupling of amino acid CDRs to β-lactam**s** using as the peptide coupling reagent. (One diastereomer illustrated isolated as a mixture of diastereomers). 103

Scheme 3.2: Synthesis and resolution of diastereomer mixtures of *trans* β-lactam **17 (107-113**) by coupling with amino acid CDRs. **a:** HBTU, DIPEA, anhydrous MeCN, N_2, rt, 24 hr. Yield = 31-77%. **b:** resolution of diastereomers using gravity and gradient elution of MTBE: n-hexane (2:8-2:1) (relative stereochemistry shown). **c:** Hydrazine dihydrochloride, TEA, MeOH, 0 °C, then reflux for 6h. 104
Scheme 4.1: Esterification routes for addition of *N*-Boc-L-proline as the CDR to combretazet β-lactam racemates. Blue illustrates the 3-hydroxyl route while red illustrates the B ring *meta* hydroxyl route. .. 130
Scheme 4.2: Synthesis of diastereomers and enantiomers of 3-hydroxyl β-lactam**s 18-22, 63, 67a** and **69** by coupling with *N*-Boc-L-proline. **a:** HBTU, DIPEA, anhydrous MeCN, N_2, rt, 24 h; 32-83%. **b:** TBAF 1M in hexane, THF, 0 °C, 1-2h **c:** LC chiral resolution over silica gel with pore size 60 Å, 40-63 μM particle size and 230-400 mesh and gradual gradient of 4:1 n-hexane: MTBE to 2:1 MTBE: n-hexane. **d:** hydrazine dihydrochloride, anhydrous TEA, anhydrous methanol, 85 °C, 4h 131
Scheme 4.3: Synthesis of diastereomer mixtures **123-131,** resolution to 3*S,*4*R* **a** and 3*R,*4*S* **b** diastereomers and hydrazinolysis to their corresponding enantiomers. **a:** HBTU, DIPEA, anhydrous MeCN, N_2, rt, 24h. Yield of diastereomer mixtures: 32-83%. **b:** LC chiral resolution over silica gel with pore size 60 Å, 40-63 μM particle size and 230-400 mesh and gradual gradient of 4:1 n-hexane: MTBE to 2:1 MTBE: n-hexane. **c:** hydrazine dihydrochloride, anhydrous triethylamine, MeOH, 85 °C, 4 h. *(***c** removed both 3-acetoxy and N-Boc-L-proline*)* 142
Scheme 4.4: Routes for esterification of phenolic β-lactams to corresponding diastereomer mixtures .. 146
Scheme 4.5: Route for diastereomer mixture synthesis for combretazet racemates **32, 35** and **37** *via* amide bond formation. **a:** *N*-Boc-L-proline, HBTU, DIPEA, MeCN, N_2, rt, 24h**.** Yield: 0-35% **b:** HOBt, DCC, *N*-Boc-L-proline, DMF. Yield 0-20% 147
Scheme 4.6: Synthesis of amide diastereomer mixtures of B ring *meta* NH_2 substituted β-lactams using DCC and HOBt with **32** derivatised to diastereomer mixture **138** illustrated as a representative example. (One enantiomer and diastereomer shown). 148
Scheme 7.1: The serine hydrolase mechanism mediated by CAL-B using methanol as a nucleophile. Oxyanion residues illustrated in blue. Acylated intermediate illustrated in red. INT_1 = tetrahedral intermediate 1. INT_2.= tetrahedral intermediate 2. 268
Scheme 7.2: Proposed methanolysis of diastereomer mixtures synthesised for chiral resolution using. **a***:* CAL-B 1 mg/mg scale of diastereomer mixture, MeOH, TBME 285
Scheme 7.3: Pathways for KR of **63a** and **23a** using CAL-B. **a:** Reduction of **63a** to **23a** using zinc and glacial acetic acid for 6 days. **b:** KR using CAL-B. 286
Scheme 7.4: Synthesis of **140** as the dibenzyl phosphate ester of **20EN1** *via* Atherton-Todd reaction. [753] **a:** CCl_4 (1.4 eq), ice at 0 °C for 15 minutes in an inert atmosphere, MeCN. Then DMAP, DIPEA and dibenzylphosphite at 0 °C. Then RT overnight. 295
Scheme 8.1: Perkin condensation for synthesis of **P3**. **a:** Acetic anhydride, 180 °C, 4 days **or** microwave on standard power, 160 °C, 5 h. **b:** 1:1 EtOAc/ EtOH with 1M NaOH 301
Scheme 8.2: Proposed mechanism for the Perkin condensation reaction *via* **A:** tautomerisation of 2-methylpyrazine to form a methylene reactive species and **B:** reaction of 2-methylene reactive species with salicaldehyde to afford P3 acetate (blue box). 302
Scheme 8.3: Reaction of **P3** with $POCl_3$. **a:** TEA activates $POCl_3$ to form the reactive TEA-$POCl_3$ complex in anhydrous THF **b: P3** reacts with TEA-$POCl_3$ complex yielding the phosphoro chloridate intermediate and TEA. **c:** Water hydrolyses the phosphorochloridate to the free phosphoric acid. 305
Scheme 8.4: Synthesis of **P3** dibenzyl phosphate (**P3DBP**). CCl_4, 0 °C, N_2, MeCN, 15 minutes with **P3**. Then DMAP, DIPEA, dibenzyl phosphite at 0 °C. Then RT for 24 hours. 306
Scheme 8.5: **a:** Synthesis of **P3DBP** as per Scheme 8.4 **b:** McKenna reaction for debenzylation**.** NaI, Me_3SiCl, 0 °C, N_2 **c:** Debenzylation to **P3P** using BBr_3 (1M in hexane), anhydrous toluene, -10 °C, then 80 °C for 2h, N_2. Then MeOH, 1 h. (Yield 40%) 309
Scheme 8.6: Synthetic routes for synthesis of OTBDMS protected imine **147**. **a:** TBDMSCl, DBU, anhydrous DCM, N_2, RT **b:** breakdown of **146** to 2-aminopyrazine and salicaldehyde **c:** Condensation of 2-aminopyrazine and salicaldehyde in ethanol 90 °C 322
Scheme 8.7: Synthetic routes explored to obtain imines **148-150** and subsequent synthesis of β-lactam **151 a:** Dean Stark apparatus in anhydrous toluene. **b:** Dean Stark apparatus with anhydrous toluene (30 mL) with ethanol as co-solvent. **c**: $TiCl_4$, *n*-butylamine, toluene, 0 °C, then RT overnight. **d:** aminocatalysis: Pyrrolidine (20 mol %), EtOH, 7h, reflux **e:** microwave irradiation: 2-aminopyrazine, substituted aldehyde, 60 minutes. Standard powder (CEM microwave synthesiser) **f:** TEA, toluene, reflux, 5h 322
Scheme 8.8: **A:** Amino catalytic organocatalysed functionalisation of aldehydes using iminium activation with nitrogen based nucleophiles to form imines. **B:** Mechanism of pyrrolidine mediated amino catalytic imine formation through the iminium intermediate.[768] 324

Scheme 8.9: Synthesis of imines *via* a titanium-aldehyde co-ordination complex using $TiCl_4$. Reaction conditions: $TiCl_3$, anhydrous toluene at 0 °C, 2-aminopyrazine, 10 minutes, then *n*-butylamine. RT overnight. 325
Scheme 9.1: Proposed biocatalytic pathway for achieving > 99% *ee* for 3*S*,4*S* eutomers of 3-hydroxyl β-lactam racemates. Pathway carried out and *ee* values determined to date highlighted in red. TBC = to be confirmed. 335
Scheme 9.2: Proposed CA-4-P3 β-lactam hybrid with potential strategies for chiral resolution..... 337
Scheme 9.3: Proposed Perkin condensation synthesis for *cis* **P3**: **a:** *n*-butyl lithium, DIPEA, THF, -78 °C, quench with solid CO_2. **b:** acetic anhydride, TEA, 120 °C, CEM microwave synthesiser, 30 minutes. **c:** Decarboxylation with copper powder, quinoline, 200 °C, 3h..... 337

List of equations

Equation 3.1: Formula for calculation of *de* using ^{1}H NMR axis 126
Equation 4.1: Equation for logP (octanol/water partition coefficient) 153
Equation 4.2: Calculation of retention factor *k* 161
Equation 6.1: Formula for counting of cells using haemocytometer grid. 200

List of abbreviations

^{13}C NMR	carbon 13 NMR
^{19}F NMR	fluorine 19 NMR
^{1}H NMR	proton NMR
AA	anti-angiogenic agents
ABC	ATP binding cassette transporters
ADME	absorption, distribution, metabolism and excretion
ASIS	anisotropic solvent induced shift
ATP	adenosine triphosphate
AUC	area under curve
BBB	blood brain barrier
BBR_3	boron tribromide
BC	breast cancer
BRAC1	breast cancer type 1 susceptibility protein
BRAC2	breast cancer type 2 susceptibility protein
BSA	bovine serum albumin
C18	carbon 18
CA-1	combretastatin A-1
CA-4	combretastatin A-4
CA-4P	combretastatin A-4 phosphate
CADD	computer assisted drug design
CAL-B	*Candida antarctica* lipase B
CBS	colchicine binding site
CBSI	colchicine binding site inhibitor
CBZ	benzyloxycarbonyl
CCl_4	carbon tetrachloride
$CDCl_3$	deuterated chloroform
CDRs	chiral derivatising reagents
CRC	colorectal cancer
CSAs	chiral solvating agents
CYP450	cytochrome P450
DAMA	*N*-deacetyl-*N*-(2-mercaptoacetyl)
D_2O	deuterated water
DAPI	4′,6-diamidino-2-phenylindole
DBU	1,8-diazabicyclo[5.4.0]undec-7-ene
DCC	*N*,*N*'-dicyclohexylcarbodiimide
DCM	dichloromethane
de	diastereomeric excess
DIPEA	*N*,*N*-diisopropylethylamine
DMAP	4-dimethylaminopyridine
DMEM	Dulbecco's minimum essential medium
DMF	dimethylformamide

DMSO	dimethyl sulfoxide
DMSO-d_6	deuterated dimethyl sulfoxide
DPBS	Dulbeccco's phosphate buffered saline
DR	diastereomeric chiral resolution
dr	diastereomer ratio
ee	enantiomeric excess
EGF	epidermal growth factor
EGTA	ethylene glycol-bis(β-aminoethyl ether)-*N*,*N*,*N*′,*N*′-tetraacetic acid
EMT	epithelial to mesenchymal transformation
ER	estrogen receptor
ESI	electrospray ionisation
EXSY	exchange spectroscopy
F_a	fraction absorbed
FACS	flow assisted cell sorting
FBS	foetal bovine serum
FDA	Food and Drug Administration
FITC	fluorescein isothiocyanate
FLEX	flexibility
Fmoc	fluorenylmethyloxycarbonyl
GDP	guanidine diphosphate
GnRH	gonadotropin releasing hormone
GTP	guanidine triphosphate
HBTU	(2-(1*H*-benzotriazol-1-yl)-1,1,3,3-tetramethyluronium hexafluorophosphate/Hexafluorophosphate Benzotriazole Tetramethyl Uronium
HCl	hydrochloric acid
HER2	human epidermal growth factor receptor 2
HIA	human intestinal absorption
HIU	high intensity ultrasound
HMEC-1	immortalised human dermal microvascular endothelial cells
HOBt	1-hydroxybenzotriazole
HPLC	high performance liquid chromatography
HSE	Health Service Executive
IC_{50}	50% inhibitory concentration
ICAM-1	intercellular Adhesion Molecule 1
ICH	International Conference on Harmonisation of Technical Requirements
IL	interleukin
INSATU	unsaturation
INSOLU	insolubility
IR	infrared spectroscopy
ISV	intersegmental vessel assay
KR	kinetic resolution
LAG	liquid assisted grinding

LIPO	lipophilicity
MAOS	microwave assisted organic synthesis
MCF-7	Michigan Cancer Foundation 7 cells
mCRC	metastatic colorectal cancer
Me_3SCl	chlorotrimethylsilane
MeCN	Acetonitrile
MEM	Minimum Essential Medium
MDR	Multidrug resistance
MeOH	methanol
mM	Millimolar
MMFF94s	Merck molecular force field 94s
MRP	multidrug resistant protein
MRP1	multidrug resistant protein 1
MTAs	microtubule targeting agents
MTBE	methyl tertiary butyl ether
N-Boc	*N*-(tertbutoxycarbonyl)
Na_2CO_3	sodium carbonate
NCCP	National Cancer Control Programme
NCI	National Cancer Institute
NCPP	National Cancer Prevention Program.
NEAA	non essential amino acids
nM	nanomolar
NMR	nuclear magnetic resonance
NOESY	nuclear overhauser spectroscopy
OAC	oesophageal adenocarcinoma
OD	optical density
OE33R	radioresistant oesophageal adenocarcinoma cells
P-Gp	p-glycoprotein
P3	Pyrazinib
PAINS	pan assay interference compounds
PARP	poly (ADP-ribose) polymerase
PI	propidium iodide
PIPES	1,4-piperazinediethanesulfonic acid
PK	pharmacokinetics
POLAR	polarity
PR	progesterone receptor
R_f	retention factor
RP	reverse phase
RT	room temperature
SEM	standard error of mean
SERM	selective estrogen receptor modulator
SIZE	size

TBAF	tetra butyl ammonium fluoride
TBDMS	*tert*-butyldimethylsilyl ether
TEA	triethylamine
THF	Tetrahydrofuran
TLC	thin layer chromatography
TMSCl	trimethylsilyl chloride
TNBC	triple negative breast cancer
TTMI	Trinity Translational Medicine Institute
UGT	uridine 5'-diphospho-glucuronosyltransferase
UV	ultraviolet
VCAM-1	vascular cell adhesion molecule 1
VDA	vascular disrupting agent
VEGF	vascular endothelial growth factor
VT	variable temperature
WHO	World Health Organisation
XRD	X-ray diffraction
μM	Micromolar

Thesis outputs: Publications, presentations and awards

Peer reviewed publications:

Malebari, A. M.; Duffy Morales, G.; Twamley, B.; Fayne, D.; Khan, M. F.; **McLoughlin, E. C**.; O'Boyle, N. M.; Zisterer, D. M.; Meegan, M. J., Synthesis, Characterisation and Mechanism of Action of Anticancer 3-Fluoroazetidin-2-ones. *Pharmaceuticals* **2022,** *15* (9), 1044. DOI: 10.3390/ph15091044

McLoughlin, E. C.; O'Brien, J. E.; Trujillo, C.; Meegan, M. J.; O'Boyle, N. M., Application of 2D EXSY and qNMR Spectroscopy for Diastereomeric Excess Determination Following Chiral Resolution of β-Lactams. *ChemistryOpen* **2022,** DOI: 10.1002/open.202200119

Ibrahim, T.S.; Hawwas, M.M.; Malebari, A.M.; Taher, E.S.; Omar, A.M.; O'Boyle, N.M.; **McLoughlin, E**.; Abdel-Samii, Z.K.; Elshaier, Y.A.M.M. Potent Quinoline-Containing Combretastatin A-4 Analogues: Design, Synthesis, Antiproliferative, and Anti-Tubulin Activity. *Pharmaceuticals* **2020**, *13*, 393. DOI: 10.3390/ph13110393

McLoughlin, E.C.; O'Boyle, N.M. Colchicine-Binding Site Inhibitors from Chemistry to Clinic: A Review. *Pharmaceuticals* **2020**, *13*, 8. DOI: 10.3390/ph13010008

Non-peer reviewed publications:

Conference poster:

McLoughlin, E.C.; Valupadasu, N.; O'Boyle, N. A phosphate prodrug of pyrazinib: Improved solubility and antiproliferative activity, in Proceedings of the 7th International Electronic Conference on Medicinal Chemistry, 1–30 November 2021, MDPI: Basel, Switzerland, doi:10.3390/ECMC2021-11438

Conference presentation:

McLoughlin, E.C.; O'Boyle, N. Enantiomeric β-Lactams for the Treatment of Breast Cancer, in Proceedings of the 6th International Electronic Conference on Medicinal Chemistry, 1–30 November 2020, MDPI: Basel, Switzerland, doi:10.3390/ECMC2020-07507

Conference poster:

McLoughlin, E.C.; O'Boyle, N.; Meegan, M. Stories from Staudinger: Synthesis of chiral beta-lactams, in Proceedings of the 5th International Electronic Conference on Medicinal Chemistry, 1–30 November 2019, MDPI: Basel, Switzerland, doi:10.3390/ECMC2019-06402

Oral Presentations:

Synthesis and Chiral Resolution of Trans Configuration Anticancer β-Lactam Enantiomers (YRC05): **29th Annual GP2A Medicinal Chemistry Conference (Online 2021**)

Combretazets: *Enantiomeric β-Lactams for Treatment of Breast Cancer*. **APC 'Frontiers in Research' Seminar Series. March 2021**

Chiral Resolution of Anti-cancer β-Lactam Racemic Derivatives of Combretastatin A-4 using Column Chromatography. RSC BMCS "Synthesis in Drug Discovery and Development", **March 2021**, flash presentation

Poster Presentations:

A comparison of chiral diastereomeric versus kinetic enzymatic resolution for enantioseparation of microtubule depolymerising β-lactams: **30th Annual GP2A Medicinal Chemistry Conference, Dublin 2022**

Chiral Resolution of Anti-cancer β-Lactam Racemic Derivatives of Combretastatin A-4 using Column Chromatography. RSC BMCS "Synthesis in Drug Discovery and Development", **March 2021**, poster presentation

Stories from Staudinger: Synthesis of chiral beta-lactams: **27th Annual GP2A Medicinal Chemistry Conference, Nottingham 2019**

Awards

Registered Scientist (RSci) status awarded by the Royal Society of Chemistry (RSC), November 2022

Trinity Trust Travel Grant (August 2019) for attending the 27th Annual GP2A Medicinal Chemistry Conference in Nottingham

RSC-BMCS (Biological and Medicinal Chemistry Sector) Bursary (February 2020). Attended and presented my work on chiral β-lactam anticancer drugs at the "Synthesis in drug discovery and development" symposium in flash and poster presentation format

MDPI Pharmaceuticals runner up prize for best presentation by early career researcher at the 29th Annual GP2A Medicinal Chemistry Conference, 2021

Chapter 1 - Introduction

1.1 *Introduction to breast cancer*

Cancer is a collection of diseases defined by uncontrolled cell division where damaged cells fail to break down and/or new cellular growth.[3,4] Breast cancer (BC) is the most common female malignancy worldwide.[5-10] According to the World Health Organisation (WHO), in 2020 there were 2.3 million women diagnosed with BC and 685,000 deaths globally. BC is the world's most prevalent cancer.[11,12] Male BC is rare, with less than 1% of all breast cancer cases occurring in men.[13-17] In the USA, BC is the second most common female cancer next to skin cancer. The National Cancer Institute (NCI) estimates that female BC represents 14.8% of all new cancer cases in the USA annually with 281,550 new cases in 2021 and 43,600 deaths.[18] In Ireland, BC is the leading cause of cancer in women according to the Health Service Executive (HSE) in Ireland.[19,20] One in eight women are diagnosed in Ireland with BC during their lifetime.[21] According to the National Cancer Registry, there has been an annual average of 3,053 diagnoses per annum over the period of 2014-2016.[22] The five year survival rate in Ireland has increased from 70% (1994-1999) to 85% (2011-2015). Additionally the five year mortality has halved over this time, declining steadily by 1.8% annually (1994-2016). This trend reflects large improvements in treatment and screening services. However still there have been 723 average deaths annually between 2014 and 2016, indicating that BC treatments require further optimisation. The development of new anti-cancer drugs for the treatment of BC are the focus of this thesis.

1.2 *Staging and molecular subtypes of breast cancer*

BC is a molecularly heterogenous disease. The multiple subtypes of BC with distinct morphologies have clinical implications for the treatment of breast cancer.[23] There are five main types of intrinsic or molecular female BC subtypes, based on gene expression patterns.[24-26] Staging of BC is based on the TNM system; the degree of nearby tissue invasion (T), spread to the lymph nodes (N) and metastasis (M).[27] Stage I-III BCs have spread into nearby lymph nodes while stage III also invades muscle tissue. Metastatic or stage IV breast cancers are defined as those that have spread beyond lymph nodes of breast tissue and travelled to other locations in body.[28-30] Since 2019 the American Joint Committee on Cancer incorporates additional characteristics as part of the TNM system. These characteristics include tumour grade, estrogen receptor (ER), progesterone receptor (PR) and HER2 (human epidermal growth factor receptor 2) status in addition to oncotype DX scores which are genomic tests designed to predict the genetic risk factor

for BC recurrence.[31,32] Typically immunohistochemistry (IHC) of the estrogen receptor (ER), progesterone receptor (PR), human epidermal growth factor receptor 2 (HER2R) and Ki67 as a cellular marker for proliferation,[33] determine BC subtypes. IHC is therefore invaluable as a prognostic marker with receptor expression patterns determining the clinical course of treatment.[34] There are four main molecular subtypes of BC, outlined in Figure 1.1, accompanied by their global prevalence.[35] Estrogen receptor positive (ER +) breast cancers consist of the two subtypes, luminal A and luminal B. Both are linked with good prognoses of 80-85% 5 year survival.[36-38] In contrast, estrogen receptor negative (ER –) subtypes consist of human epidermal growth factor receptor 2 positive cancers (HER2 +), basal like and triple negative breast cancers (TNBC). Each of these BCs are much more challenging to treat. Both are linked with poor 5 year survival of 50-60%.[36,39, 40] TNBCs are a heterogenous tumour group, defined by negative immunohistochemical staining for ER, progesterone receptor (PR) while also lacking HER2 overexpression.[41-43] Although TNBC and basal like cancers are terms used interchangeable, they are not synonymous terms.[44, 45] Basal like cancers often demonstrate the triple negative immunophenotype. However basal like caners express proteins that are absent in truly TNBC. Basal-like cancers express cytokeratin CK5/6, CK14 CK17, caveolin-1, p63 and epidermal growth factor receptor (EGFR), reflecting the mammary gland basal component.[46] While the majority of TNBCs often exhibit basal-like phenotypes while basal like tumours are often also triple negative, not all basal like cancers lack total gene expression of ER, PR and HER2. Conversely not all TNBCs demonstrate basal-like phenotypes in gene expression array analysis.[47] Truly TNBCs are however, widely regarded as devoid of hormone receptors.[48]

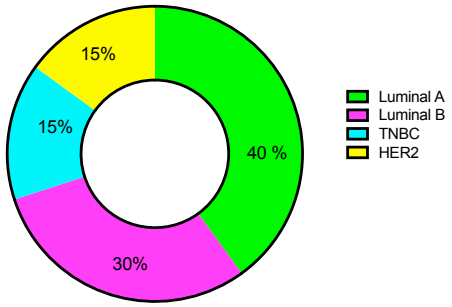

Figure 1.1: Estimated global prevalence of BC frequency classified by molecular subtype.[35]

1.2.1 *Luminal A versus B BC*

Luminal A BC is characterised by high expression of hormone receptors expressing the ER, PR or both.[49, 50] Luminal A and luminal B BC subtypes differentiated by Ki-67 % expression levels.[51-54] Ki-67 as a nuclear antigen expressed in growth and synthesis phase of the cycle, is reported as a proliferation marker in all cancer types.[55] Ki-67 is associated with cell proliferation where cancers expressing increased % levels of Ki-67 are considered to have poorer prognostic factors.[56-58] While the clinical role of Ki-67 is not established, high expression levels are often considered as a positive predictive factor for response to chemotherapy.[33] A Ki-67 gene expression level of <20% defines luminal A versus luminal B subtypes.[59] Both luminal A and B cancers grow slowly, are treatable by endocrine/hormone therapy and have the best prognoses.[60,61] Luminal A cancers typically have better prognosis than luminal B cancers.[54,62] In Ireland between 2003 and 2015, 79% of females diagnosed BCs were ER or PR positive.[22] Luminal B may express the HER2R. However it is much more commonly HER2R negative. Luminal B cancers grow faster than luminal A, are less common, prognosis is poorer and are associated with higher grade of nodal metastasis than luminal A.[63,64]

1.2.1.1 *Hormone therapies for Luminal A and B BC and limitations with their use*

Estradiol, acting through the ER, stimulates mammary cell proliferation, errors in DNA replication and cellular mutations.[65-67] Quinone metabolites of estrogen may also act as genotoxic agents binding to DNA as toxic adducts causing cancerous growth (Figure 1.2).[68] ER positive BCs are excellent candidates for endocrine therapy such as the selective estrogen receptor modulators (SERM) tamoxifen as adjuvant therapy (Figure 1.3).[69] Aromatase enzyme inhibition using anastrozole, letrozole or exemestane (Figure 1.3) may be used as alternative anti-estrogen therapies.[70,71] Gonadotropin releasing hormone analogues include Gosarelin (Zoladex®)[72] or Leuprolin (Prostap®).[73, 74] Alternatively the ER antagonist, Fulvestrant, which prevents dimerisation of ER monomers to accelerate receptor degradation,[75] is reserved as second line agents in cases of treatment failure (Figure 1.3).[76]

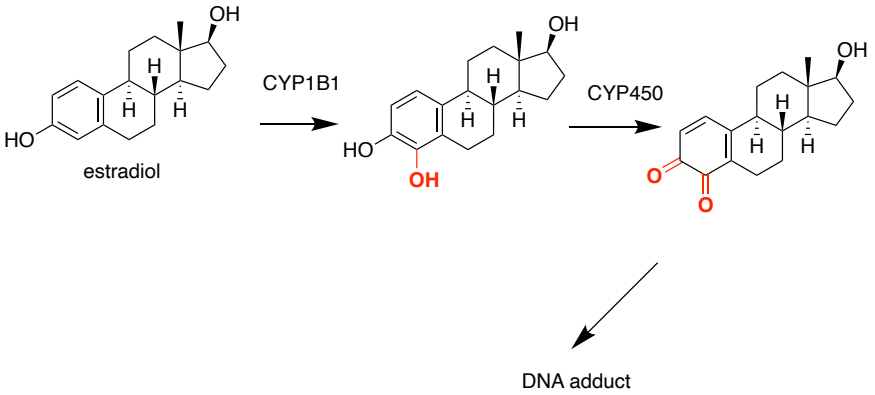

Figure 1.2: Pathway of estradiol metabolic activation to form genotoxic DNA adducts.[77]

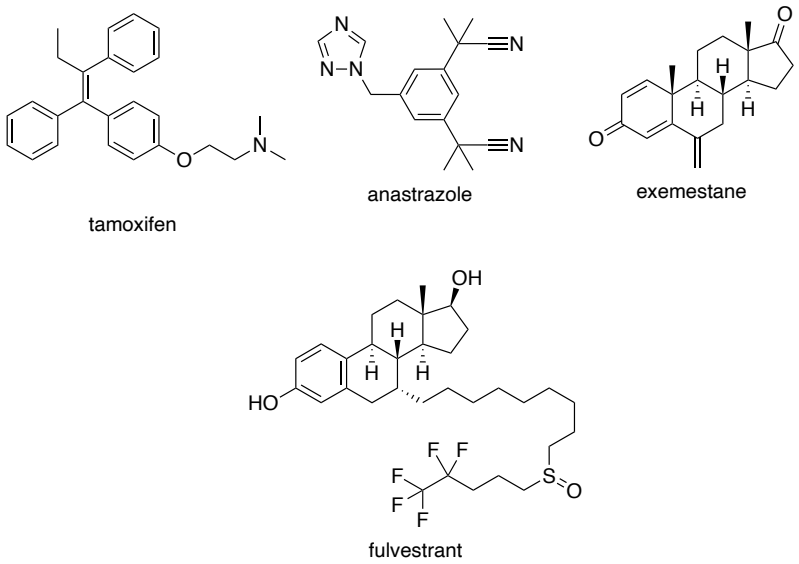

Figure 1.3: Small molecules for the treatment of hormone receptor positive BC currently in clinical use

Typically ER positive breast tumours are extremely responsive to endocrine treatment.[78] Endocrine agents reduce the risk of death in hormone receptor positive BC by 40%.[7] However some ER positive BCs do not respond adequately to endocrine therapy with resistance widely reported.[78-80] *De novo* resistance refers to tumours that do not respond to endocrine manipulation during primary treatment.[81] Other tumours may develop acquired or secondary resistance and/or become refractory to treatment following successful initial response.[82, 83] A third of women treated with tamoxifen will develop resistance to the drug within 2-5 years of ongoing treatment.[69, 84] Additionally, long term use of endocrine therapy is associated with risk of endometrial cancer.[85] Eventually

resistance develops to endocrine agents, rendering them ineffective for long term use.[86] Anti-cancer agents discussed in this thesis are designed primarily for TNBC, but also for the treatment of BC which does not respond to endocrine therapy, *i.e* for applications in hormone receptor positive BCs that have become resistant to these agents.

1.2.2 *Progesterone receptor positive (estrogen receptor negative) BC*

Expression of both ER and PR status are strongly associated since the PR is reliant on ER signalling.[87] Therefore it is typical for hormone responsive BCs to express both receptors, accounting for over 50% of all BC. More invasive single hormone receptor expressing BC are rarer. They account for approximately 15-20% of all BCs. This subtype is generally ER + and PR -, a phenotype associated with rapid growth and reduced endocrine therapy sensitivity.[88,89] Tumours which express the PR but not the ER are uncommon, comprising of only 1-8% of hormone expressing BCs.[90] This unique sub-population in the past was considered as a result of poor tissue fixation techniques in IHC assays. The proportion in this cohort therefore have decreased with the progressive optimisation of IHC methods.[91] On the converse to this argument, due to development of molecular biology techniques, increasing evidence supports the existence of an ER- and PR + subtype.[92] Anti-progesterone therapies are not currently reported. 30% of this subgroup express receptor tyrosine kinase 2 (ERBB2) and are candidates for treatment with tyrosine kinase inhibitors *e.g* erlotinib, sunitinib *etc.*[93, 94] Moreover the effectiveness of tamoxifen in hormone receptor negative (ER- and PR-) BC is much lower than in ER- and PR+ breast cancer, where ER-/PR+ BC patients can benefit from tamoxifen therapy.[95] The role of progesterone in the progression of BC remains controversial,[96, 97] a potential reason for absence of agents targeting the PR.[98]

1.2.3 *HER2 enriched BCs*

HER2 expressing cancers are found in 1 of 5 BCs.[99] The HER2R (also known as erbB2) belongs to a family of receptor tyrosine kinases, activated upon dimerisation in normal cells. Activation enables a rich network of cell signalling pathways to control cell growth, differentiation and cellular motility.[100-102] HER2 is responsible for activation of the PI3k/AKt 'survival' cell signalling pathway which prevents cellular proliferation by inhibiting programmed cell death or apoptosis.[103] Tumorigenic actions of HER2 include cellular proliferation and metastasis.[104] HER2R expressing cancers grow faster than luminal cancers, fail to respond to endocrine therapy and therefore have poorer

prognoses.[105] They are however often responsive to targeted therapies such as anti-HER2 therapy.[106] HER2 currently represents one of the most appropriate BC targets for targeted therapy with trastuzumab (Herceptin), a monoclonal antibody directed against the extracellular domain of the HER2R.[107] HER2R+ BCs may however fail to respond to anti-HER2R therapy due to obstacles preventing trastuzumab binding to HER2, upregulation of HER2R downstream signalling pathways or failure to trigger an immune-mediated mechanism to destroy the tumour cells once the HER2R is bound to the antibody.[108] Anti-cancer agents discussed in this thesis are relevant in specific instances.

1.2.4 *Triple negative/Basal like BCs*

As discussed in Section 1.2, TNBC and basal like BC are typically both characterised by an extremely aggressive clinical phenotype in addition to minimal expression of typical BC receptors *i.e* ER, PR and HER2R.[109] Both TNBC and basal like BC are associated with poorest prognosis of all BCs.[43, 110-114] However basal and TNBCs are classified differently on a molecular level. Approximately 15-20% of BC are triple negative.[111,115,116] It is characterised by shorter overall survival with greatest risk of visceral and/or brain metastases.[114,117] TNBCs are most frequent in women under the age of 40 years and in those with germ line breast cancer susceptibility gene type 1 and type 2 (BRCA1/2) mutations.[25, 26, 118,119] Since BRCA1/2 function to maintain genome integrity by repairing DNA double strand breaks, mutations resulting in functional disruption to the BRCA1/2 proteins impact tightly regulated cellular processes which lead to progression toward cancer.[120] 19.5% of women suffering from TNBC harbour these mutations.[43, 121, 122] Chemotherapy is the only available pharmacological treatment for TNBC.[123] Patient responses to endocrine and HER2 targeted therapies in TNBCs are poor, and effective targeted therapy has not been well-established.[124] Classes of chemotherapy used in TNBC include the DNA intercalating anthracyclines [doxorubicin and epirubicin], the taxanes as microtubule stabilising microtubule targeting agents [(MTAs) docetaxel and paclitaxel] and the nitrogen mustard family of alkylating agents [carboplatin and cyclophosphamide (Figure 1.4)]. Chemotherapy is also usually associated with a plethora of non-specific side effects.[125]

The monoclonal antibody, bevacizumab (Avastin®), is licensed as a combination treatment for metastatic BC where taxanes or anthracyclines are considered inappropriate.[126-128] Bevacizumab as a vascular disrupting agent (VDA) binds to vascular endothelial growth factor (VEGF), preventing vasculogenesis and angiogenesis mediated by binding of VEGF to its receptor, VEGFR. Bevacizumab inhibits the formation of new tumour vasculature and therefore reverses tumour growth.[129]

The National Cancer Prevention Programme (NCPP) provides general consensus regimens for current treatment of TNBC in Ireland. Examples of currently used clinical regimens include neoadjuvant (pre-surgical) treatment with carboplatin and paclitaxel as weekly cycles 1-4, followed by doxorubicin and cyclophosphamide as cycles 5-8.[130] Other examples include gemcitabine and carboplatin therapy for treatment of locally recurrent metastatic TNBC[131] (Figure 1.4). Advanced regimens using NCPP guidelines include bevacizumab monotherapy, capecitabine monotherapy, cyclophosphamide in combination with oral methotrexate, 5-fluorouracil monotherapy or docetaxel monotherapy (Figure 1.4). Each of these options are associated with an element of toxicity.[132] TNBC has the greatest death rates of all molecular subtypes in first 5 years following initial diagnosis. Recurrence is also common.[133] In Stage IV TNBC, chemotherapy is the primary option for treatment but often fails to respond to options discussed above.[134] Agents discussed in this thesis which act independently of hormone receptors are invaluable as alternative options for TNBC to fulfil this gap in clinically available treatment options for TNBC.

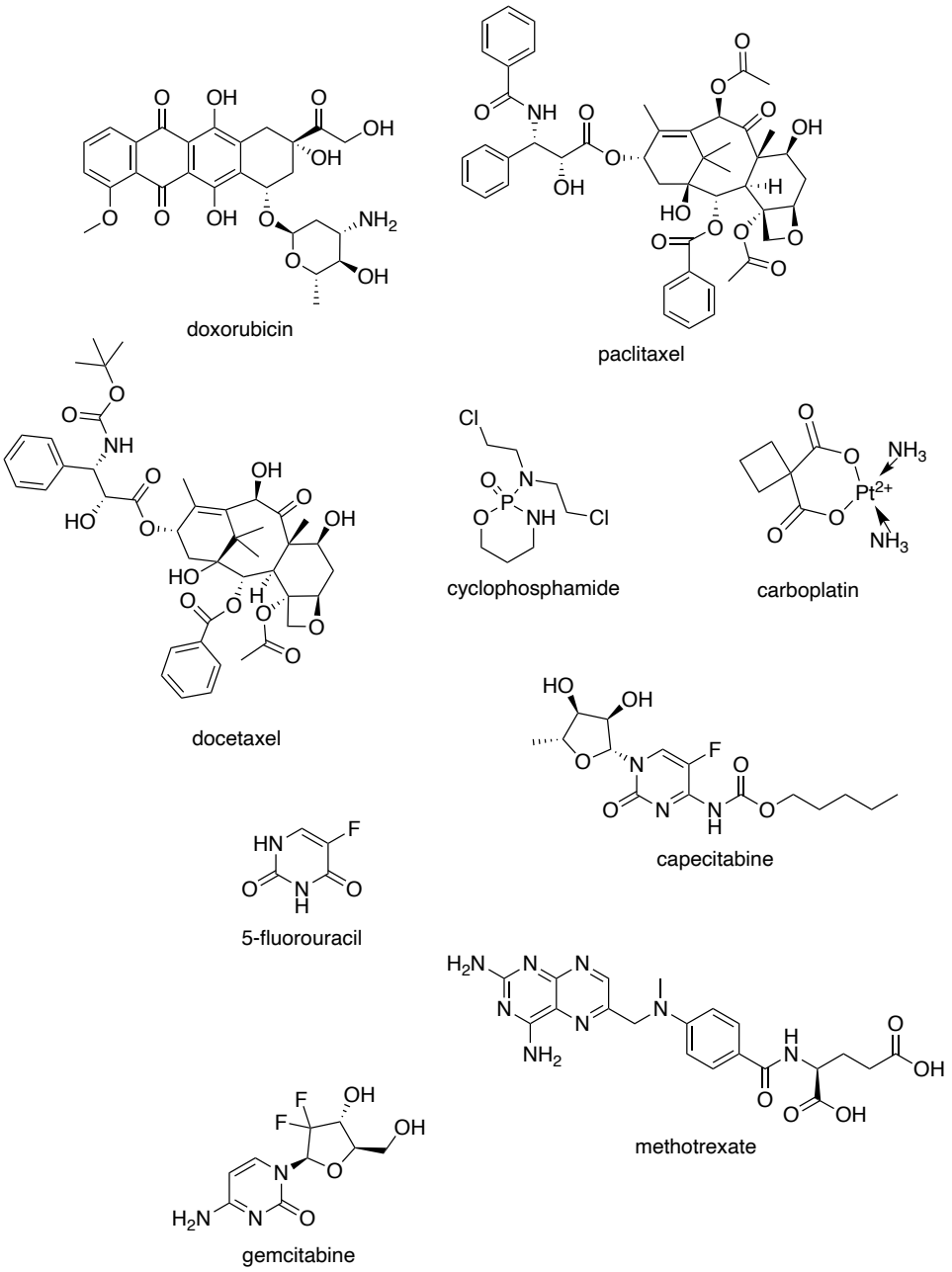

Figure 1.4: Chemotherapeutic agents used in the treatment of TNBC

1.2.5 *Novel treatments for TNBC*

Several agents are now in the pipeline for treatment of TNBC. The most recent drugs approved by European Medicines Agency (2015-2021) for treatment of all BC [including HER2-targeted drugs, CDK 4/6 inhibitors, PIK3CA inhibitors, PARP inhibitors, immunotherapy drugs and antibody-drug conjugates (ADCs)] have been reviewed.[135] Poly (ADP-ribose) polymerase (PARP) inhibitors target key enzymes involving single strand breaks in cellular DNA.[136,137] Cells with deficient BRCA1 activity are particularly

sensitive to PARP inhibition.[138] Iniparib, olaparib and veliparib are PARP inhibitors that are now in clinical evaluation for the treatment of TNBC (Figure 1.5). Olaparib was first approved in 2014 for the treatment of ovarian cancers with BRCA mutations,[139] and is now also approved in the EU as monotherapy or in combination therapy as Lynparza® for adjuvant early treatment of HER2 negative high risk breast cancer.[140] Olaparib has also demonstrated promising outcomes in phase II trials for treatment of chemotherapy refractory advanced BC in patients carrying the BRCA1 and BRCA2 mutations.[59,141,142] A phase II trial evaluated iniparib in combination with gemcitabine/carboplatin. Addition of iniparib to standard gemcitabine/carboplatin therapy augments the DNA damaging effects of platinum-based chemotherapy and improves mean survival time with minimal toxicity.[143,144] Veloparib (Figure 1.5) has also demonstrated success in combination with temozolomide in phase II trials for metastatic BRCA1 and 2 deficient BCs.[145] Promising anti-angiogenic agents directed against VEGF include the tyrosine kinase inhibitor and anti-angiogenic agent sunitinib (Figure 1.5), which has been evaluated in one phase II trial in patients previously treated with anthracycline and/or taxane chemotherapy.[146-148] Sunitinib demonstrated excellent responses in the TNBC subgroup.

Epidermal growth factor receptor (EGFR) is also a viable target for treatment of TNBC. The anti-EGFR agent cetuximab has been evaluated both as monotherapy and additionally in combination with carboplatin in phase II trials for metastatic basal-like TNBC. Monotherapy of cetuximab demonstrated moderate success in chemotherapy refractory TNBC. However a combination of cetuximab with carboplatin produced partial responses in 71% of patients.[149] The EGFR tyrosine kinase inhibitor erlotinib (Figure 1.5) has also demonstrated activity in combination with capecitabine and docetaxel.[150]

The antibody drug conjugate sacituzumab govitecan, a TROP2-targeted antibody (Trodelvy®) linked with its cytotoxic payload, topoisomerase I inhibitor SN-38, is now approved for previously treated metastatic TNBC.[151, 152] Ladiratuzumab vedotin, the zinc transporter LIV-1 targeted antibody (often overexpressed in BC)[153] linked to monomethyl auristatin E, a potent microtubule-disrupting agent is now approved for locally advanced or metastatic TNBC.[154,155] Despite these aforementioned advances,

there remains a need for addition of novel agents to the arsenal of chemotherapies available for the treatment of advanced and metastatic TNBC.[156]

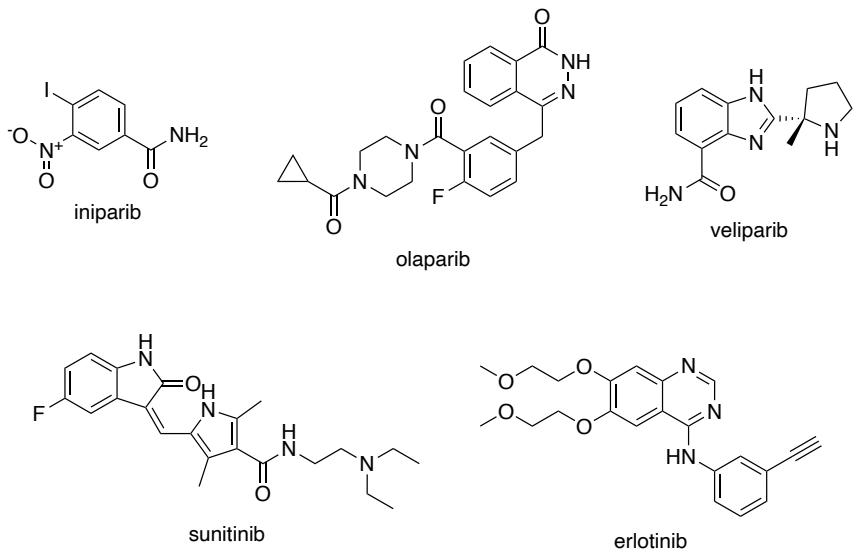

Figure 1.5: Novel small molecules used for treatment of TNBC

1.3 *Colorectal cancer incidence*

Colorectal cancer (CRC) is the third most frequently diagnosed cancer and cause of cancer related deaths worldwide.[157, 158] During 2020, CRC resulted in 419,536 deaths amongst females and 515,637 deaths in males worldwide.[159] This is largely due to lack of therapeutic strategies and increasing incidence rates.[5, 157, 159-165] In 2020, CRC accounted for 10% of global cancer incidence rates and 9.4% of cancer deaths. This global number is predicted to reach 3.2 million cases by 2040.[157, 166] Advancements in survival rates for metastatic CRC (mCRC) patients and understanding of its pathophysiology require a wider variety of treatment options for advanced disease.[160]

1.3.1 *Current issues with treatment of colorectal cancer*

There are currently many challenges associated with treatment of CRC. Mainstays of colorectal cancer therapy involve use of cytotoxic and cytostatic chemotherapies.[163] The first successful agent was the fluoropyrimidine, 5-fluoruracil [5-FU, (Figure 1.4)], recognised in 1990 as demonstrating superior anti-cancer properties over surgery alone.[167] Since the introduction of 5-FU as an adjuvant therapy to surgical resection, many other cytotoxic drugs have emerged for CRC chemotherapy regimens including capecitabine, irinotecan and oxaliplatin.[168] Treatment with targeted therapies or precision

medicine (treatments targeting proteins and biochemical pathways responsible for aberrant cell division)[169] has become the mainstay of CRC treatment with anti-angiogenic agents that target VEGF and EGF (bevacizumab and cetuximab).[170-174] VEGF promotes growth of CRC by stimulating release of pro-angiogenic factors that enable tumour blood supply, endothelial cell mitogenesis, vascular permeability, extra-cellular matrix degradation and endothelial cell migration.[175,176] Despite introduction of targeted therapies, survival rate remains only at 12%.[5, 177] While bevacizumab is currently the standard of care for mCRC, only 50% of patients respond to treatment.[178-180] Combining targeted anti-VEGF therapy (biologics) with chemotherapy (cytotoxic chemicals), prolongs progression free survival of mCRC patients, but only by an average of 4.7 months.[181,182] Additionally, treatment with bevacizumab is also accompanied by high-risk significant side effects such as hypertension, proteinuria and bowel perforation, with the possibility of inadequate clinical response.[183-185]

Despite decades of research, the mainstay of mCRC treatment remains based on cytotoxic chemotherapy regimens such as FOLFOX (folinic acid, 5-FU, oxaliplatin)[182,186] and FOLRIRI (folinic acid, 5-FU and irinotecan). Both regimens demonstrate only modest clinical outcomes, even as first line treatment.[187] As an example, treatment of unresectable colorectal cancer is empirically treated with FOLFOX as first line therapy.[188, 189] However resistance to FOLFOX occurs in 40% of colorectal cancers, mediated by a plethora of processes including enhanced repair of damaged DNA, altered expression of oncogenes, decreased drug import and enhanced efflux, apoptotic evasion and enhanced tolerance to platinum adduct accumulation.[190,191] Resistance to oxaliplatin, a third generation platinum drug used as first line treatment for CRC, is mediated by enhanced expression of ATP binding cassette transporter ABCG2, a multidrug resistance (MDR) protein causing efflux of chemotherapeutic agents, reducing intracellular concentration and rendering chemotherapeutic regimens ineffective.[192]

As survival has improved for patients with mCRC, there is an increased need for effective and well-tolerated therapies in third and subsequent lines of treatment.[193] Potential failure of anti-angiogenic therapy combined with both risk of significant drug related side effects and resistance are major impediments to successful treatment of CRC with

chemotherapy. While re-challenge with oxaliplatin and EGFR targeted therapies may provide some benefit, conventional chemotherapeutic agents such as 5-FU, irinotecan, capecitabine and gemcitabine are much less effective in mCRC in second line treatment.[64]

Options for treating refractory mCRC, while limited, are currently expanding. A new oral multi-kinase inhibitor, regorafenib, targeting angiogenic kinases including VEGFR2, tyrosine kinase, immunoglobulin-like and EFF-like domains 2 and others, is now indicated for refractory mCRC.[194-196] Regorafenib prolongs survival and reduces death by 23%.[197] There remains scope for augmenting strategies for the treatment of mCRC and novel agents are discussed in this thesis.

1.4 *Microtubules as a target for treating cancer*

The cell cycle is divided into two main stages. Interphase is the first of the two stages, with the cell preparing for cell division (G_1/S/G_2 phases), followed by mitosis. Mitosis is a five step process involving prophase, prometaphase , metaphase, anaphase, telophase and finally cytokinesis as the fifth and final stage. Cytokinesis is responsible for division of cellular DNA to create two daughter cells (Figure 1.6).[198]

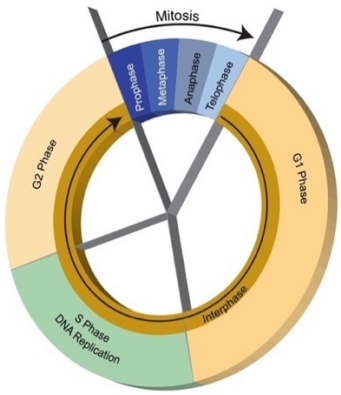

Figure 1.6: Diagram of cell cycle detailing interphase (G_1/S/G_2 phases) followed by the 5 stage process of mitosis.[199]

Mitosis is an important target of many anti-cancer drugs including microtubule depolymerisers, due to the loss of normal cell cycle controls in malignant versus non-tumorigenic cells.[200] Since the rate of mitosis is much larger in tumorigenic versus non-

tumorigenic cells,[201] targeting mitosis offers potential for semi-selective targeting of cancer tissues mediating selective apoptosis of tumour cells, while limiting unwanted side effects associated with apoptosis of healthy cells.[200, 202, 203] Microtubules are major components of the eukaryotic cytoskeleton, mediating chromosomal separation during mitosis through formation of the mitotic spindle.[204,205] When cells enter mitosis, the rate of microtubule growth increases up to 100-fold. Rapid microtubule dynamics are highly sensitive to modulation by anti-mitotic agents.[206] Mitosis is a crucial and selective anti-cancer target for anti-mitotic agents due to the much faster rate of cell division in cancer cells in comparison to non-tumorigenic cells.[203,207,208] Microtubules are the targets of a wide variety of chemically diverse microtubule targeting agents (MTAs) which have been used with great success as chemotherapeutic agents in the treatment of cancer to date. The microtubule as a target for the treatment of TNBC and colorectal are the focus of anti-mitotic agents described in this thesis.

1.4.1 *Structure of the microtubule*

Microtubules are described as 'dynamic polymers', composed of α and β tubulin monomers as the tubulin heterodimer (Figure 1.7).[208-210] Tubulin is a globular protein composed of αβ heterodimers as the principle building block of the microtubule structure. α and β tubulin are both 50 kDa in size and share 40% identity in amino acid homology.[211, 212] Each microtubule consists of α and β tubulin heterodimer assembled together, associated in head-to-tail format to make up the linear protofilament. Thirteen protofilaments associate laterally and wind together to form a 24 nm diameter, long, hollow cylinder known as the microtubule.[213, 214] The microtubule is a polar structure with a fast growing positive end and a slow growing negative end (Figure 1.7).[215] Microtubules alternate between periods of growth and shrinkage in what is known as 'dynamic instability', undergoing periods of polymerisation and depolymerisation, continually assembling and disassembling inside the cell. This occurs through reversible addition of guanosine triphosphate (GTP)-bound tubulin at the positive pole to the β-subunit and removal of guanosine diphosphate (GDP)-bound tubulin at the negative pole. This dynamic state is determined by the rate of addition of GTP to β-tubulin. Hydrolysis of GTP to GDP weakens tubulin's binding affinity for adjacent tubulin molecules and favours depolymerisation of the microtubule. As long as GTP-bound tubulin units are added more rapidly than hydrolysis to GDP, a GTP cap at the positive pole is retained

and microtubules continue to grow. If the addition rate of GTP-bound tubulin slows, GTP at the negative end is hydrolysed and results in rapid depolymerisation.[216,217] The majority of microtubule-binding agents (MTAs) bind to β-tubulin, suppressing microtubule dynamics and causing blockade at the metaphase-anaphase (metaphase involves metaphase, in which the chromosome movement toward the equatorial plane of the spindle while anaphase involves separation of chromatids to the opposite sides of cell)[199] transition during mitosis, known as G_2/M phase arrest, which leads to apoptosis and cell death.[206,218]

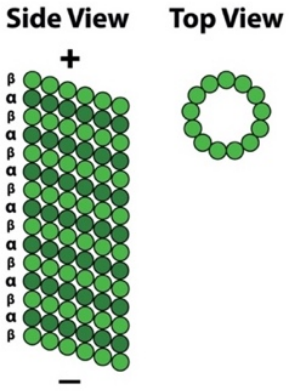

Figure 1.7: Microtubule structure from side and top perspectives. Side view: Long, linear protofilaments consisting of αβ-tubulin heterodimers associate laterally. Top view: Association of 13 protofilaments forms the microtubule, a long hollow cylinder.[219]

1.4.2 *Clinically used microtubule targeting agents*

Microtubule targeting agents (MTAs) interact with tubulin at a number of different binding sites. The four main sites/domains within the tubulin heterodimer are as follows: the laulimalide, taxane/epithilone,[220] colchicine and vinca alkaloid sites (Figure 1.8).[209,221, 222] Two main sites targeting α tubulin are described; the pironetin site[223] and the recently described gatorbulin (2021) site, also at the αβ interface close to the CBS.[224] A novel agent, cevipabulin has been identified as binding to this site.[225] A total of 27 distinct binding sites have been identified on the tubulin heterodimer using computational and crystallographic approaches with 56 chemically diverse fragments now determined as interacting with tubulin.[226] There is therefore further scope for rationale design of many potential MTAs targeting this wide variety of binding sites.

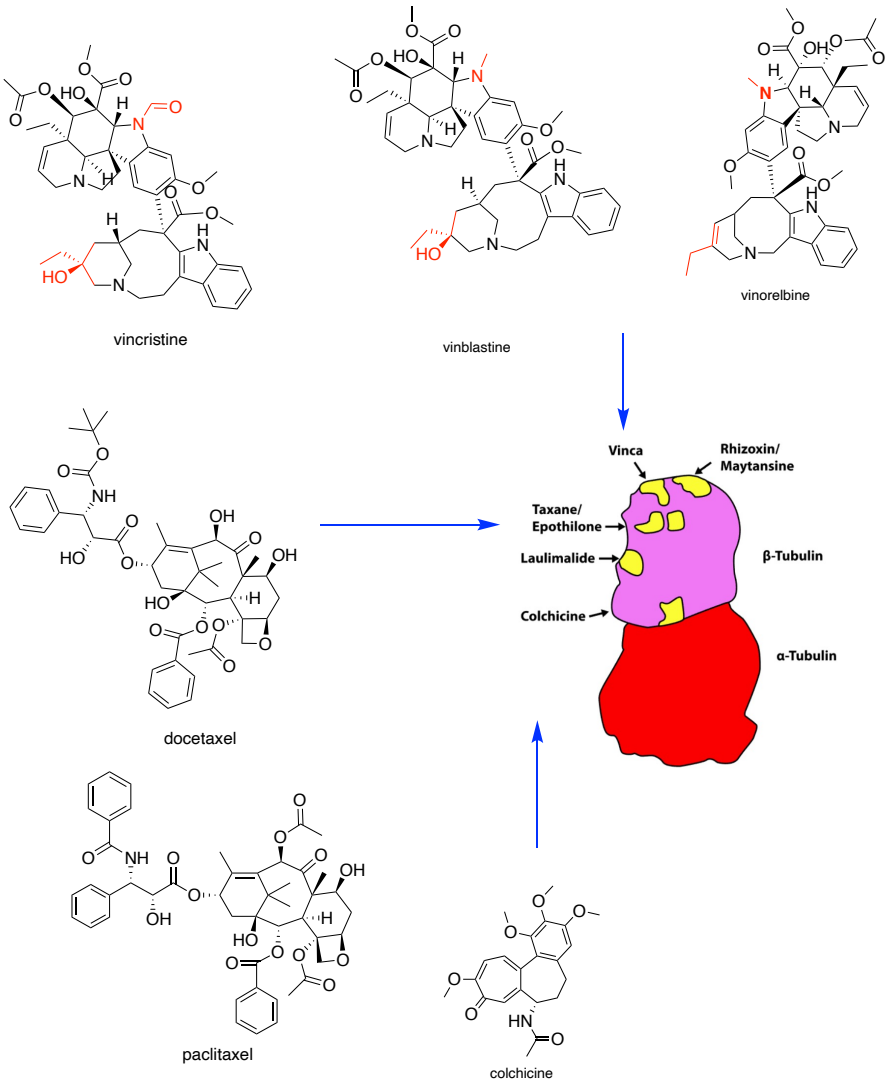

Figure 1.8: Clinically relevant MTAs (vinca alkaloids, taxanes and colchicine) with their binding sites on the αβ tubulin heterodimer. Colchicine binding site illustrated at αβ interface of the tubulin heterodimer.

In cancer cells, MTAs suppress microtubule dynamics and induce programmed cell death or apoptosis *via* the mitochondrial intrinsic pathway (Figure 1.9). The ability of MTAs to induce apoptosis was first identified by Bhalla *et al* in 1993[227] as the primary mechanism of paclitaxel-mediated cytotoxic effects in myeloid leukaemia cells.[228] Two routes for apoptosis are known, the intrinsic (Figure 1.9) and extrinsic pathway or death receptor pathway.[229,230] Mitochondria are crucial cell organelles mediating the success of chemotherapy. Their membrane permeabilisation [mitochondrial outer membrane permeabilisation (MOMP)] is responsible for the on/off switch of apoptosis. Permeabilisation mediates release of caspases, cytochrome c and formation of the

apoptosome.[231] MOAP is the point of no return in the process of apoptosis and it is carefully regulated by the balance of pro- and anti-apoptotic molecules of the Bcl-2 family.[232, 233] The Bcl-2 family is divided into three groups based on

1. Anti-apoptotic (Bcl-2-Bcl-$X_{L,}$ Mcl-1 etc.)
2. Pro-apoptotic (BAD, BID etc.)
3. Pore formers (BAK, BAX, BOK)

The interactions of the Bcl-2 family members dictate whether MOMP will occur.[234,235] Proapoptotic members of the Bcl-2 family cause MOMP while anti-apoptotic proteins (Bcl-2 and Mcl-1) inhibit cytochrome C release to prohibit apoptosis (Figure 1.9).

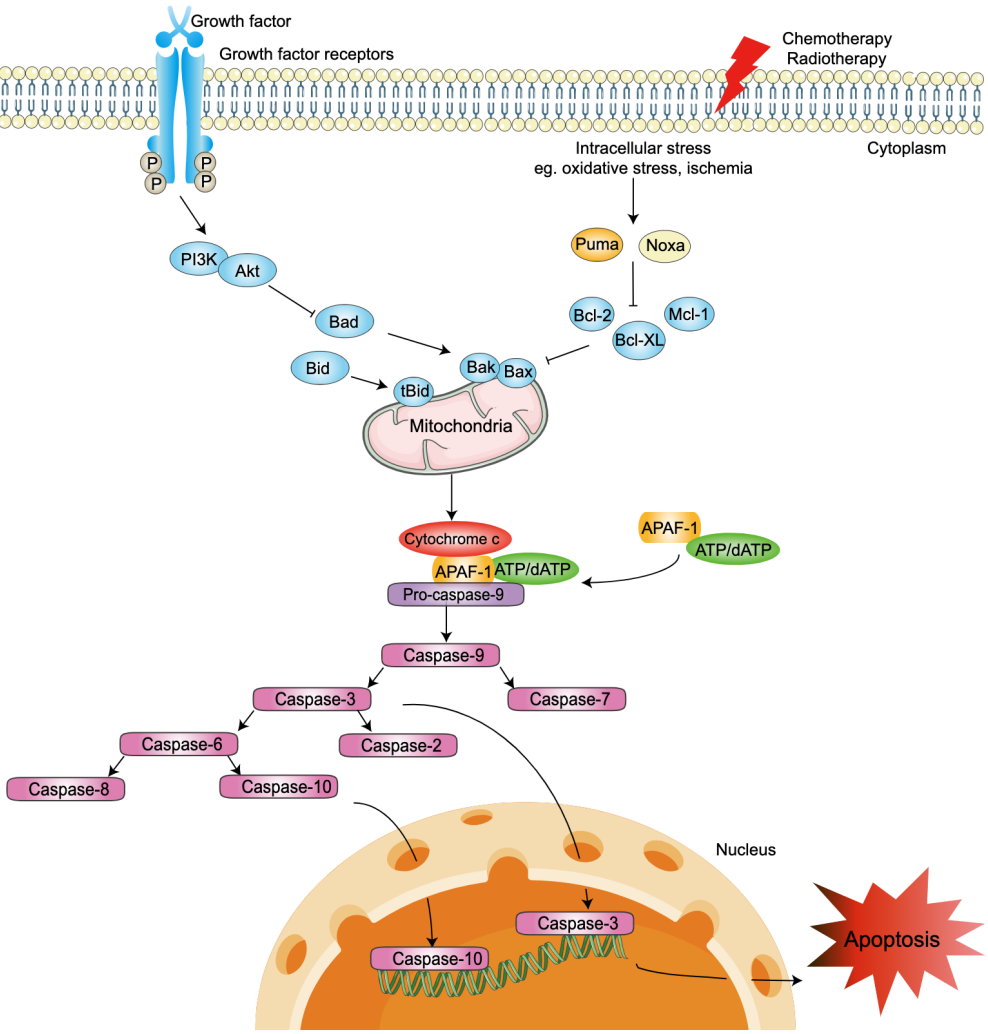

Figure 1.9: The intrinsic apoptotic pathway illustrating the role of Bcl-2 family in MOMP.[236]

MTAs and most chemotherapeutics mediate their activity through the intrinsic apoptotic pathway *via* caspase activation and cytochrome C release.[237] Additionally, MTAs influence the expression of Bcl-2 family members, composed of 30 proteins which are divided into pro- and anti-apoptotic proteins. MTAs modulate expression and activity of pro-apoptotic members of the Bcl-2 panel, upregulating pro-apoptotic proteins BAD, PUMA, BAX and BAK, observed following vinca alkaloid and taxane treatment.[238, 239] Treatment with MTAs initiates hyperphosphorylation and post translational inactivation of the anti-apoptotic Bcl-2 member of the Mcl-1 family,[240-242] causing apoptotic mediated cell death.[243,244]

It is their ability to induce apoptosis in endothelial cells which mediates the excellent anti-angiogenic and anti-vascular properties of MTAs.[245, 246] Our research focuses on targeting the colchicine binding site, with colchicine binding site inhibitors (CBSIs).[226]

MTAs are categorised into two groups: agents inducing microtubule polymerisation such as the taxanes, epothilones, and laulimalide (macrolide isolated in trace amounts from marines sponge),[247] or agents inducing depolymerisation including colchicine, the vinca alkaloids, and maytansine. Paclitaxel and docetaxel are members of the taxane class which are microtubule-stabilising agents. Vincristine, vinblastine and vinorelbine are members of the vinca alkaloids and are microtubule-destabilising agents. Both classes are the most successful tubulin targeting anti-cancer drugs known to date [209, 248] as powerful inducers of apoptosis due to their microtubule inhibition, anti-angiogenic and vascular disrupting properties.[249] The taxanes and vinca alkaloids are routinely used to treat a wide variety of malignancies in the clinical setting, such as breast cancer, non-small cell lung carcinoma, ovarian cancer, gastroesophageal cancer, germ cell tumours, as well as cancers of the head and neck.[250]

The molecular structures of clinically used MTAs and their binding sites on the αβ tubulin heterodimer are illustrated in Figure 1.8. This thesis focuses predominantly on microtubule-destabilising CBSIs with high affinity for the colchicine-binding site (CBS) at the αβ interface of the tubulin heterodimer (Figure 1.8).

1.5 *Colchicine as a microtubule targeting agent: Historical uses and structure*

Colchicine (**A,** Figure 1.11) is a tricyclic alkaloid extracted from the plant *Colchicum autumnale* also known as the autumn crocus or 'poisonous meadow saffron' (**D,** Figure 1.11). Colchicine has been used as a medicine throughout history with its first therapeutic use described almost 3000 years ago.[251] Therapeutic efficacy for colchicine ranges from acute flares of gout, gouty arthritis[252, 253] to familial Mediterranean fever,[254] Bechet's disease and recurring pericarditis with effusion.[255] Experimental uses include the treatment of acute coronary syndromes,[256] utilising colchicine's inhibition of the NLRP3 inflammasome protein complex. This novel pathway independent of colchicine's microtubule targeting effects suggests that colchicine has additional therapeutic effects in addition to its potent anti-mitotic potential.[257, 258] Colchicine's non-specific targeting of microtubules in non-tumorigenic cells results in mitotic arrest in healthy tissues and multi-organ dysfunction.[259] While an economical chemotherapeutic option, its narrow therapeutic index and the development of MDR precludes its use as an anti-cancer agent.[260]

1.5.1 *The colchicine binding site*

The CBS lies in the intermediate domain at the interface of α and β subunits (**B,** Figure 1.11). It was first characterised in 2004 by Ravelli *et al* using X-ray crystallography. 1SAO is a 3.5 Å X-ray structure of αβ-tubulin in complex with *N*-deacetyl-*N*-(2-mercaptoacetyl) colchicine (DAMA-colchicine) and illustrates the structure of the CBS binding pocket of 4–5 Å in diameter. The volume of the CBS site is mediated by helix 7 (H7) of β-tubulin containing Cysβ241, loop 7 (T7) and helix 8 [H8 (Figure 1.10)] . DAMA-colchicine binds to β-tubulin at the interface with α-tubulin and subsequently inhibits tubulin polymerisation. The important trimethoxyphenyl ring of colchicine is orientated deep within the β-tubulin subunit in close proximity to Cysβ241.[261] At the CBS, colchicine is surrounded by helix 7 of β-tubulin (Figure 1.10).

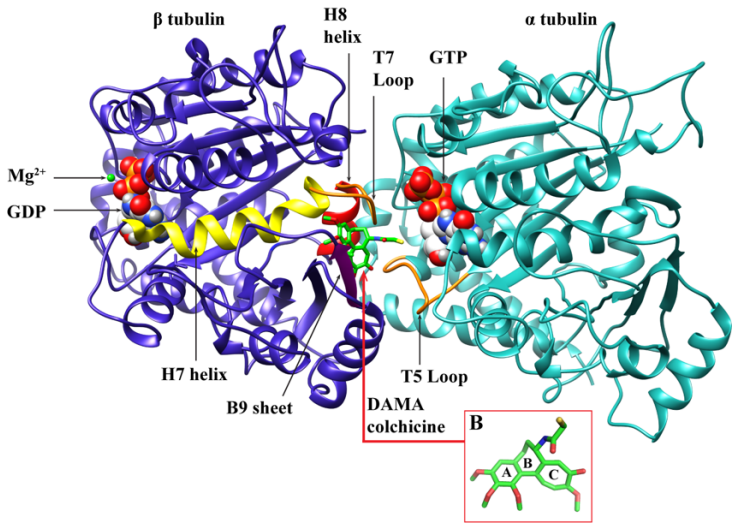

Figure 1.10: 1SAO's α-tubulin and β-tubulin heterodimer with α-tubulin illustrated in cyan and β-tubulin is illustrated as blue. The T5 and T7 loop re shown in orange and cylindrical H7 and H8 helices shown in yellow and red respectively. White, grey, red, blue and golden yellow carbon = wite, hydrogen = grey, oxygen = red, nitrogen = blue and phosphorous = yellow. DAMA-colchicine = green.[262]

Cysβ241 hydrogen bonds with the trimethoxyphenyl ring of colchicine while Thrα179 and Valα181 of α-tubulin form hydrogen bonds with the tropolone C ring (**A,**Figure 1.10).[263] Upon colchicine binding to tubulin, the essential straight conformation of the αβ-tubulin heterodimer is lost resulting in curved tubulin heterodimers. A steric clash between colchicine and α-tubulin inhibits microtubule assembly.[261] Lateral contacts of adjacent αβ-subunits necessary to maintain heterodimer interactions are lost in this configuration. As the quantity of lateral contacts decreases, microtubules progressively disassemble.

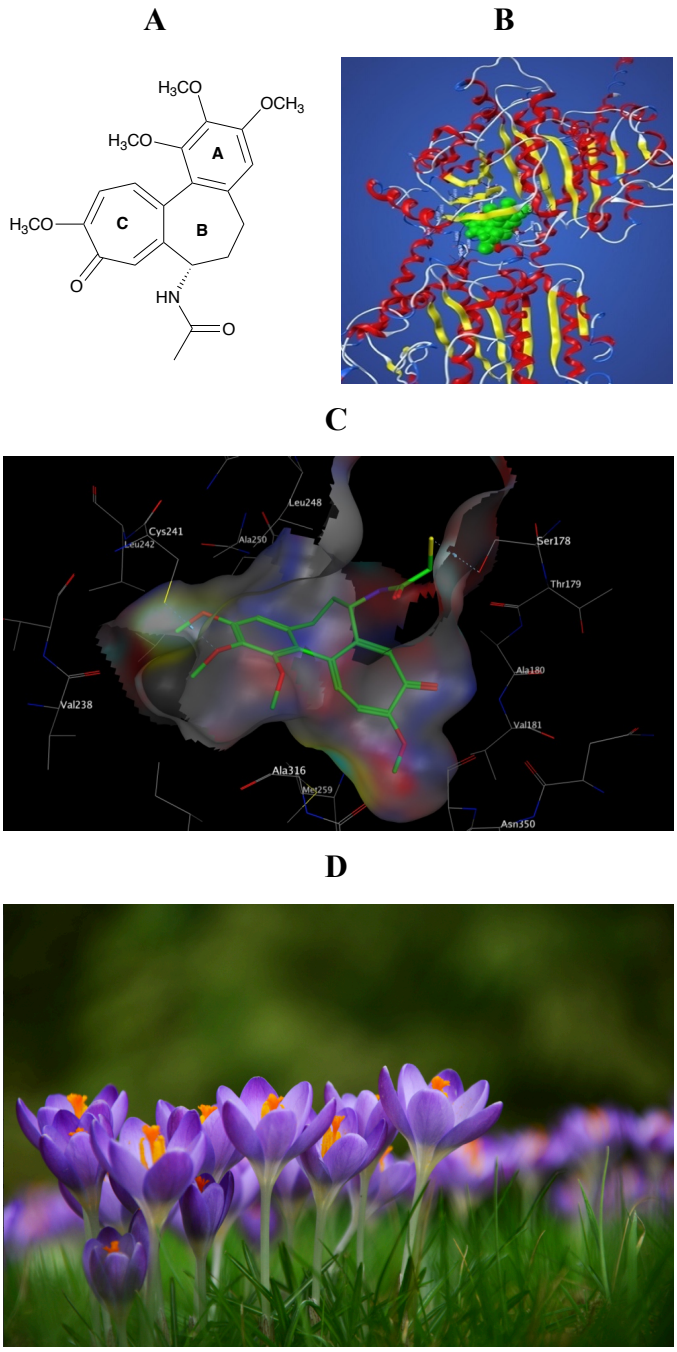

Figure 1.11: **A:** Molecular structure of colchicine outlining the 3,4,5-trimethoxy A ring, tropolone B ring and C ring. **B:** Space-filling model of colchicine (green) in the CBS. **C**: Model of DAMA-colchicine bound at the interface of αβ-tubulin. Key binding interactions are with Thrα179 and Valα181 of α-tubulin and Cysβ241 and Asnβ258 of β-tubulin. Colour key: green = carbon; red = oxygen; blue = nitrogen; yellow = sulfur; **D:** *Colchicum autumnale* from which colchicine is isolated.

1.5.2 *Targeting the colchicine binding site for anti-cancer activity*

There are several advantages of targeting the CBS using CBSIs, including inhibition of angiogenesis and overcoming multidrug resistance (MDR). Angiogenesis is one of the hallmarks of cancer playing a critical role supplying solid tumours with blood, adequate oxygen and nutrients enabling tumour growth beyond dormant state.[264] In the process of angiogenesis, endothelial cells invade surrounding basement membrane and migrate toward a pro-angiogenic stimulus and proceed to proliferate to provide additional cells for new blood vessel growth.[202, 265, 266] Microtubules are critical mediators of this process regulating both endothelial cell shape and proliferation.[267] Tumour vasculature is responsible for growth, invasion, metastasis and additional response or resistance to various chemotherapeutics. Therefore targeting angiogenesis is an excellent strategy to treat human cancer.[268] It is widely reported that MTAs have vascular disrupting effects.[269] They cause prominent changes in endothelial cell morphology which is followed by rapid *in vivo* vascular collapse.[270, 271] The taxanes, combretastatins, vinca alkaloids and colchicine are known to exert anti-angiogenic and vascular disruption.[272] There are several advantages associated with targeting tumour vasculature using vascular disrupting agents (VDAs) such as MTAs.[273, 274] VDAs target the tumour's established vasculature leading to haemorrhagic necrosis and subsequent cell death.[275] VDAs are particularly advantageous as they cause vascular shutdown, oxygen and nutrient deprivation and necrosis of the tumour core.[276-279]

In the context of treating resistant cancers such as triple negative breast cancer (TNBC) and chemoresistant colorectal cancers, the CBS serves as an invaluable anti-cancer target. While colchicine's anti-vascular effects are only observed at doses approaching or exceeding the maximum tolerated dose, this property does not exclude the use of its scaffold as a template for generation of potent anti-cancer derivatives. This thesis focuses on the development of agents selectively targeting the CBS of cancer cells and other anti-angiogenic agents for the treatment of hormone resistant cancers, *i.e* TNBC, and those which are resistant to traditional chemotherapy, *i.e* drug-resistant colorectal cancers, to overcome the non-specific microtubule depolymerising effects and toxicity associated with colchicine.

1.6 *Combretastatin A-4 as a CBSI and anti-angiogenic agent*

The combretastatins are a group of diaryl stilbenoid natural products which were isolated by Pettit *et al* in 1989 from the bark of the South African willow tree, *Combretum caffrum*.[280] Stilbenes are C6-C2-C6 carbon skeletons and phytoalexins produced by plants for protection in response to disease, injury or stress.[281] Stilbenes are small molecular structures, derived from biosynthetic pathways involving a combination of the phenylalanine and polymalonate route where stilbene synthase is the last key enzyme in biosynthesis of the stilbene structure.[282] Many stilbene structures isolated from nature have yielded promising medicinal properties.[283] *Combretum caffrum* was used for decades as a remedy for ailments ranging from heart and worm remedies, wound dressings and scorpion stings by the Xhosa tribe in South Africa.[284] Pettit *et al* first demonstrated that isolates from the bark of *Combretum caffrum* were active as an anti-cancer against murine lymphocytic leukaemia cell lines (P-388).[285-287] This antiproliferative activity was later attributed to the combretastatin A series of compounds. In total, among 17 original natural combretastatins isolated, two *cis* stilbene or A compounds with an alkene bond separating A and B rings, combretastatin A-4 (CA-4), and combretastatin A-1 [CA-1 (Figure 1.12)] have attracted profound interest over many years as the most potent combretastatin analogues.[288]

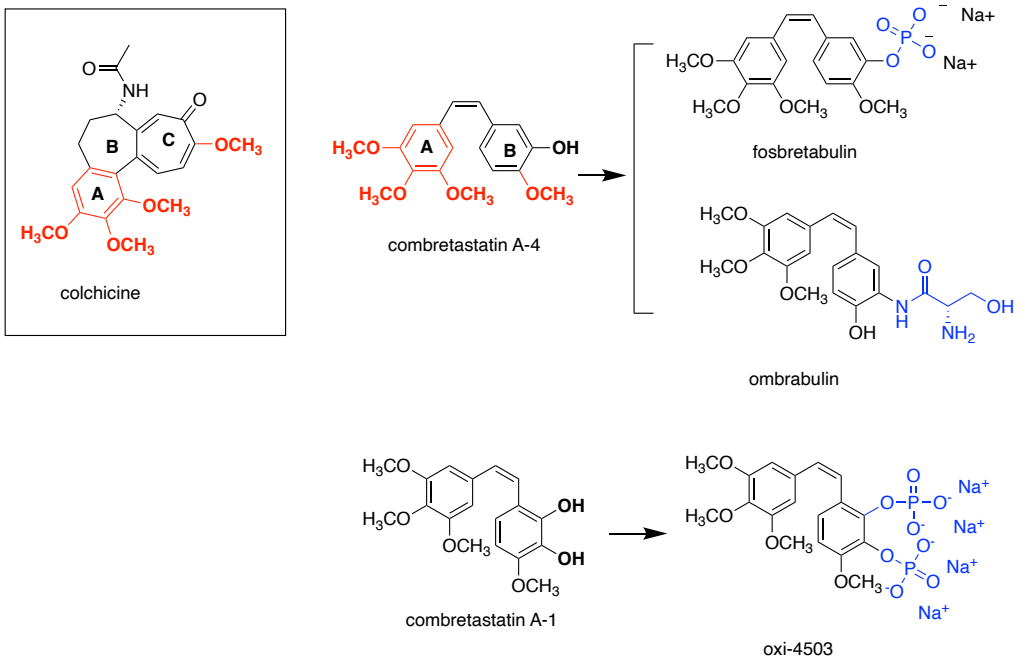

Figure 1.12: Structures of colchicine, CA-4, CA-1 and respective prodrug analogues

The *cis* stilbene CA-4 (Figure 1.12) has excellent antimitotic and anticancer activity as a microtubule-depolymeriser and CBSI.[287, 289] CA-4 is structurally related to colchicine with the phenyl A and B rings tilted at a 50-60° angle to each other, linked in *cis* geometry by a stilbene double bond. Both colchicine and CA-4 contain the crucial 3,4,5-trimethoxyphenyl A ring system. Binding in similar orientation to colchicine at the CBS, CA-4 is potent at low nanomolar concentrations across a wide variety of cancer cell lines.[290] CA-4 typically inhibits cancer proliferation with a 50% inhibitory rate (IC_{50}) between of 1-10 nM and microtubule polymerisation from 2-3 μM.[291, 292] VDAs are an attractive option as cancer treatments since non-tumorigenic angiogenesis occurs in a limited number of situations, for example during wound healing and the menstrual cycle. Therefore, angiogenesis is a selective anti-cancer target associated with limited systemic toxicity. CA-4 has potent anti-vascular and anti-angiogenic effects as a VDA.[293] The sodium phosphate derivative, CA-4P or fosbretabulin (Figure 1.12) inhibits tumour blood flow and leads to vascular shutdown at concentrations 10-fold lower than its maximum tolerated dose.[278] CA-4 disrupts endothelial cell-specific junctional molecule vascular endothelial cadherin (VE-cadherin), inhibiting endothelial cell migration and capillary tube formation.[276] CA-4 targets the tumour core *via* occlusion of the tumour vasculature resulting in hypoxic-induced necrosis.[294] This mechanism is unlike many other VDAs which generally target peripheral tumour cells only. CA-4 is therefore associated with low MDR in tumour cells on account of its anti-vascular activity at the tumour core.[276] Additionally, CA-4 is active against multidrug resistant cell lines and therefore is a promising adjunctive chemotherapeutic agent.[285-287, 295-297]

1.6.1 *Biopharmaceutical issues associated with use of CA-4: solubility*

Translation of CA-4 towards clinical use is limited by two major obstacles, its poor water solubility and therefore poor oral bioavailability.[259, 278, 297] The antiproliferative and vascular damaging properties of CA-4 have prompted attempts to overcome bioavailability issues using conventional prodrug strategies, including synthesis of CA-4 sodium phosphate (CA-4P, fosbretabulin) to augment aqueous solubility.[298, 299]

1.6.2 *The prodrug approach*

Prodrugs are bio-reversible, often inactive drug derivatives which are re-converted to active parent drug *in vivo.*[300] Prodrugs are considered as a masking pro-moiety or drug carrier. Due to chemical lability of the prodrug moiety, *in vivo* bioconversion releases the active metabolite or drug. Contemporary small molecules are often associated with undesirable physiochemical properties limiting drug delivery to the biological target. Structural modifications and early implementation of prodrug strategies typically speeds up the clinical development of drug products.[301-311] The prodrug approach (Figure 1.13) overcomes biopharmaceutical barriers associated with absorption, distribution, metabolism and excretion (ADME).[300, 302, 304-308, 312-317] Modification towards the prodrug form is considered by regulating bodies as the formation of a new chemical entity, requiring new pre-clinical evaluation. Therefore starting from the point of a prodrug expedites drug development, saving time and money.[306, 314, 318] Approximately 10% of all marketed drugs worldwide are prodrugs.[300] Additionally, the prodrug approach may also improve stability and pharmacokinetic properties of parent drug candidates.[310]

Carrier-linked prodrugs undergo enzymatic or non-enzymatic cleavage to release the active drug. Phosphate prodrugs are an example of a carrier-linked prodrug. Addition of the carrier enables solubilisation of the parent molecular for delivery in parental solutions in addition to traversing of gastrointestinal membranes that the parent drug cannot due to poor aqueous solubility. The phosphate prodrug is subject to phosphatase mediated cleavage *in vivo* once exposed to phosphatase enzymes.[302] A good orally bioavailable prodrug modification results in intracellular hydrolysis of prodrug carrier without extracellular hydrolysis (Figure 1.13). Phosphate pro-drug derivatisation ensures excellent chemical stability and rapid bioconversion *in vivo* to the parent drug by phosphatases present in the intestinal brush border or in the liver (Figure 1.13).[308] For the purposes of this thesis, pro-drug derivatisation aims to increase aqueous solubility for the purposes parenteral drug administration and progression toward *in vivo* and pre-clinical models only rather than the design of an orally bioavailable drug which is depicted in Figure 1.13.

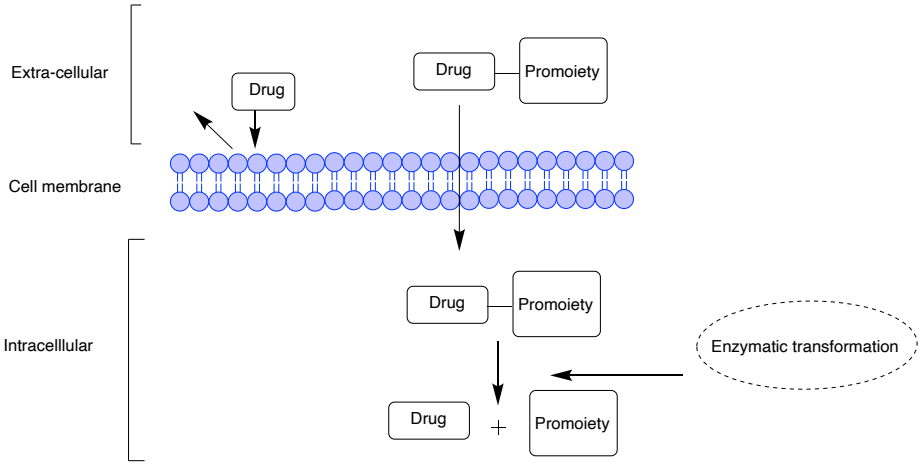

Figure 1.13: Diagram illustrating the prodrug approach using carriers conjugated to available functional groups amenable to chemical manipulation.[319]

Pettit *et al* were the first to describe phosphate prodrugs of both CA-4 and CA-1 (Figure 1.12).[320] Initial attempts to synthesise prodrug derivatives of CA-4 involved addition of a serinamide to CA-4's B ring hydroxyl group, creating an analogue known as AVE8062. AVE8062 is an amino acid prodrug which was marketed by Sanofi as ombrabulin. The more aqueous soluble serine derivative is cleaved *in vivo* by aminopeptidases to release the active CA-4 parent analogue.[297] Another successful phosphate salt derivative is CA-1 diphosphate (CA-1P) or Oxi4503. Semi-selective release at the tumour site takes place for both CA-4P and CA-1P prodrugs, which are converted to their respective parent analogues seven times faster in tumour and liver cells than in blood.[321] The phosphate prodrug, fosbretabulin (CA-4P) is of increasing therapeutic interest for the potential treatment of tumours with acquired drug resistance.[290]

1.6.2.1 Combretastatin *A-4 Phosphate* (*Fosbretabulin*)

CA-4P (fosbretabulin) has undergone several phase I/II/III clinical trials[178,322,323] and designated orphan drug status by the EMA for the treatment of platinum resistant ovarian cancer as the sodium phosphate salt (Figure 1.12).[320,324, 325] Fosbretabulin tromethamine improves outcomes for platinum-resistant ovarian cancers in combination with carboplatin and paclitaxel.[324] The FDA have also approved fosbretabulin as an orphan drug for treatment of anaplastic thyroid cancer, medullary thyroid cancer and stage IV papillary or follicular thyroid cancers as a VDA.[326] Since March 2016, CA-4P has also gained orphan drug approval for the treatment of gastro-entero-pancreatic neuroendocrine tumours.[325] While it has not been approved for therapeutic use as

monotherapy due to conformational instability and short half-life,[327] further clinical evaluation is underway using in combinatorial regimens with approved cancer therapies.[328, 329]

1.6.3 *Chemical instability as a biopharmaceutical issue associated with use of CA-4*

The second limitation associated with clinical use of CA-4 which is not overcome by chemical conversion to the phosphate prodrug, CA-4P, is its poor metabolic and chemical stability.[298, 330] CA-4 can exist in two geometric configurations as either the *cis* and *trans* stilbene (Figure 1.14). Only the *cis* configuration is a potent anti-mitotic agent. Computational studies have demonstrated that the *cis* structure is crucial for optimal binding at the CBS. The *cis* stilbene structure is 60 times more active as an anti-proliferative agent than the corresponding *trans* CA-4.The essential non-coplanar configuration of the trimethoxyphenyl A with the B ring (discussed in detail in Chapter 5), which is maintained by the *cis* double bond moiety, is lost upon isomerisation (Figure 1.14). Moreover the active *cis* conformation readily isomerises into the less active *trans* isomer during storage and *in vivo* metabolism.[331] This is liable to occur *via* a free radical process in presence of free radical generator such as light or CYP450 enzymes during metabolism.[332] Photoisomerisation radical induced *Z-E* conversion occurs by proceeding through a π to π* excited state of π alkene electrons (Figure 1.14).[333] This isomerisation to the *trans* form causes a dramatic reduction in both microtubule depolymerising, anti-mitotic and antitumour activity, attributed to *trans* CA-4's unfavourable binding orientation at the CBS, with much lower affinity relative to *cis* CA-4 (discussed in detail in Chapter 5). [209, 210,208, 334-339]

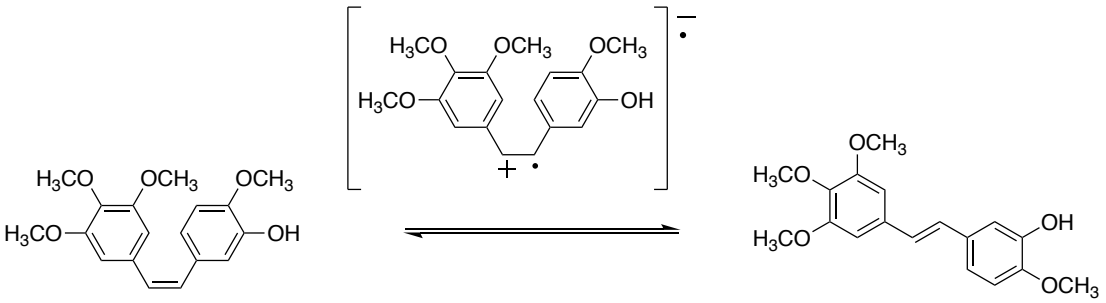

Figure 1.14: Isomerisation of *cis* CA-4 to *trans* CA-4 observed during metabolism and storage.

1.6.4 *Chemical modifications for augmenting stability of CA-4*

CA-4's structural simplicity renders it amenable to structural manipulation for enhancing its chemical stability and therefore bioactivity. Stringent structural requirements are known for colchicine's CBS binding affinity. The binding between the 3,4,5-trimethoxyphenyl A ring and β-tubulin is largely responsible for CBS affinity and therefore degree of CBS inhibition. CBS affinity is also modulated by interactions between the oxygen atoms on colchicine's tropolone ring.[299] While modification of colchicine's A ring result in loss of binding affinity, B and C ring structural modifications are possible and are widely reported in the literature with representative examples discussed below.[340,341]

SAR studies have demonstrated that the following are crucial for tubulin depolymerising effects of CA-4:

1) 3,4,5-trimethoxyphenyl-subsituted ring A.
2) 3-hydroxy-4-methoxyphenyl-substituted ring B.
3) *Cis* double bond separating the two phenyl rings.[342,331, 343]

Insertion of a heteroatom has potential to modify pharmacodynamic and pharmacokinetic properties, including lipophilicity, polarity, aqueous solubility, potency and selectivity.[344] A number of heterocyclic bridging CA-4 analogues have been prepared with aim of restricting the *cis* configuration of A and B rings to provide optimal geometry for interaction with the CBS. *Cis* restriction has been achieved using a plethora of analogues including many heterocyclic derivatives such as thiazoles,[345, 346] imidazoles,[295, 347-351] pyrroles,[352, 353] oxazoles *etc*.[354, 355] This thesis focuses on utilising the β-lactam scaffold as a method for CA-4's *cis* restriction, achieved by Meegan *et al* over the last two decades.[356-359] A selection of successfully *cis* restricted CA-4 analogues using a variety of *cis* restriction approaches are illustrated in Figure 1.15. Modification of the *cis* stilbene linker has also resulted in increased chemical stability with respect to CA-4, for example the chalcone scaffolds synthesised by Ducki *et al* (**1,** Figure 1.15).[360, 361] Phenstatin (**2,** Figure 1.15) is a synthetic analogue of serendipitous discovery, with the double bond replaced by a carbonyl moiety.[301,362] *Iso*CA-4 analogues (**3,** Figure 1.15) replaces CA-4's *Z* 1,2-ethylene bridge with a 1,1-ethylene bridge as a chemically stable bioisostere.[363, 364] The dihydronapthalene molecular scaffold has been used to synthesise

two chemically stable CA-4 derivatives KGP03 (**4**) and KG413 (**5,** Figure 1.15), incorporating the phenstatin linker.[362,365,366]

An interesting and novel approach to increasing the site selectivity of CA-4 analogues and improving chemical stability involves delivery of CA-4 as a photo responsive azo analogue (**6** and **7,** Figure 1.15).[367] Issues with tissue selectivity are addressed by designing a series of potent photo-responsive analogues where CA-4's alkene bond is replaced by an azobenzene structure (**6** and **7**, Figure 1.15).[368] Photopharmacology is a potentially powerful tool to selectively target chemotherapy towards cancer cells. It involves controlling biological functions by applying light to localised areas, overcoming poor drug delivery specificity to achieve accurate *in vivo* selectivity.[369-371] Using UV light of λ 400 nm at the tumour site, following drug administration and distribution, the inactive *trans* isomer (**6,** Figure 1.15) is converted to *cis* bioactive derivative (**7,** Figure 1.15). The *cis* isomer is 550 times more active than corresponding *trans* azo-CA-4 parent molecule.[367]

3,4-Diaryl substituted *1H*-pyrazoles have also successfully been employed to replace CA-4's ethylene bridge with increased stability and similar potency (**8** and **9,** Figure 1.15).[372, 373] Introduction of a methyl at the *N*-1 position of the pyrazole ring in a series of 1,4-substituted-3-(3,4,5-trimethoxyphenyl)-5-aminopyrazole analogues of CA-4 (**9**, Figure 1.15) gave rise to low nanomolar IC_{50} values of 17 nM and 31 nM in ovarian cancer and TNBC cells respectively.[374] Niu *et al* have replaced the alkene of CA-4 with a benzosuberene ring structure to yield **10** (Figure 1.15) with an IC_{50} of 6.9 nM in the ovarian cancer cell line, SK-OV-3. The phosphate prodrug of **10** (**11,** Figure 1.15) demonstrated a dose-dependent vascular shutdown as a VDA.[375] The 1,2,4-triazole-3-carboxamide scaffold has also been used to replace the stilbene double bond of CA-4, (**12,** Figure 1.15) resulting in an IC_{50} of 4 nM in HL-60 cells, an excellent example of fluorine introduction to CA-4's B ring to augment anti-proliferative activity (Figure 1.15).[376] Fluorine substitutions of CA-4's B ring are explored in this thesis with aim of emulating these findings of augmented microtubule depolymerising effects upon fluorine atom addition.

O'Boyle *et al* have synthesised a library of piperazine conjugates, using Perkin condensations. Through addition of the piperazine moiety to the *cis* stilbene structure, problematic *cis* to *trans* isomerisation has been overcome (**13,** Figure 1.15). The piperazine analogues had sub-micromolar IC_{50} values in MCF-7 cells. Most recently, the [1,2,4]triazolo[1,5-a]pyrimidine nucleus has been used to replace CA-4's alkene bond as a strategy for *cis* restriction yielding IC_{50} values in low nanomolar range in MDA-MB-231 TNBC cells for **14** and **15** of 0.051 and 0.061 μM (Figure 1.15).[377]

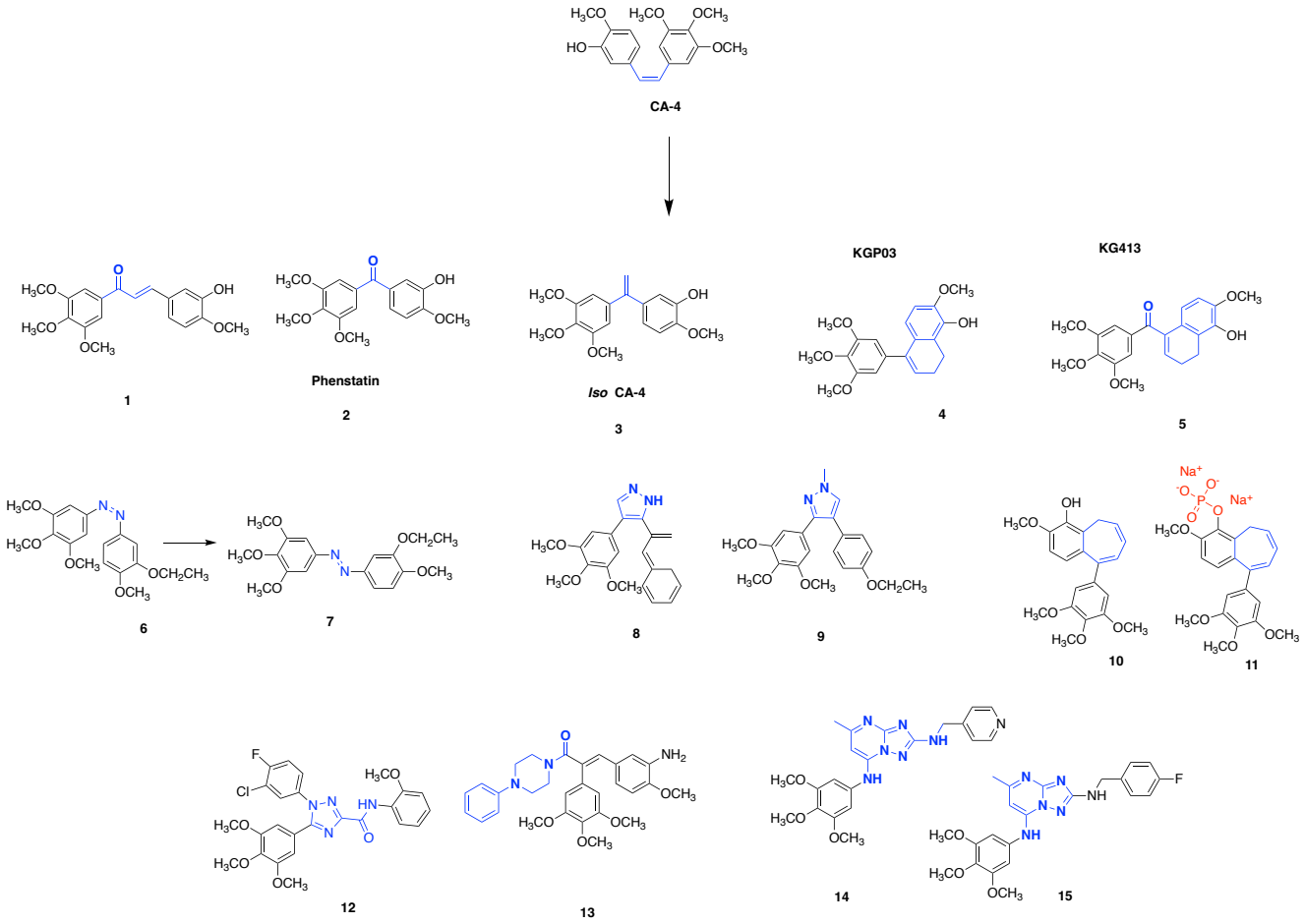

Figure 1.15: Biologically active analogues of CA-4.[209, 215, 230, 325, 360, 361, 372, 373]

1.7 *β-Lactam cis restricted CA-4 analogues – 'The combretazets'*

Introduction of a rigid β-lactam structure in place of CA-4's stilbene bond has been achieved by our group and many others over the last decade,[378-380] enabling similar structural arrangement between CA-4's two A and B aromatic rings in non-coplanar *cis* conformation to overcome the undesirable *cis* to *trans* isomerisation (Figure 1.16).[357, 381-384] This chemistry has produced a large library of extremely potent anti-cancer analogues known as 'the combretazets' with sub micromolar IC_{50} values across a wide variety of cell lines including MCF-7 breast cancer, MDA-MB-231 TNBC, HT-29 colorectal cancer and HL-60 leukemia cells.[357, 381-383] The combretazets are a series of potent antiproliferative and microtubule destabilising β-lactam *cis* restricted analogues of CA-4, which have greater or equivalent microtubule depolymerisation activity with respect to parent CA-4 (Figure 1.16).[357] Prior to our development of combretazet panel it was known that β-lactam-containing compounds possessed antiproliferative activity.[385, 386] To date, the combretazets have been synthesised and evaluated *in vitro* as their racemates and occasionally as a *cis:trans* isomeric mixture. For β-lactams substituted at the 3- and 4-positions (highlighted in red, Figure 1.16), two possible stereochemical outcomes during chemical synthesis may be possible depending on the orientation of the H_3 and H_4 protons (discussed further in Chapter 2). For many of our analogues, the *trans* isomer has more potent antiproliferative activity than the corresponding *cis* derivative (Figure 1.16).

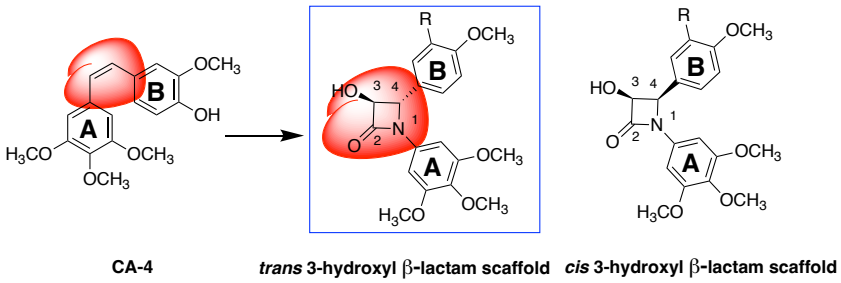

Figure 1.16: Comparison of *cis* CA-4 versus *cis* restricted 3-hydroxyl combretazet β-lactam analogues. *Trans* 3-hydroxyl scaffold illustrated in blue box.

1.7.1 *Relevance of the combretazets for the treatment of TNBC*

Overall survival rates in TNBC remain lower than all other forms of BC. Treatment options for TNBC lag behind those for hormone responsive breast cancers. More than a third of metastatic BC patients present with primary resistance to taxanes, *i.e* failing to respond to chemotherapy on initial treatment.[387] The development of resistance to both the vinca alkaloids and taxanes as major pillars for the treatment of TNBC also represents a major limitation in overall response for TNBC cancer patients.[388] This thesis aims to evaluate the combretazets in their enantiopure forms as CBSIs in addition to other *cis* stilbene derivatives as potentially applicable therapeutic agents for the treatment of TNBC, due to their mechanism of action which is independent of hormone and HER2 receptor status.

Multidrug resistance (MDR) is mediated by overexpression of the ATP-dependent drug efflux pump, p-glycoprotein (P-gp).[389] P-gp transports anti-cancer agents out of cells, away from their intended target.[390] One of the major impediments for the use of MTAs is the overexpression of the MDR1 gene encoding for P-gp in tumour cells, which limits the efficacy of MTAs as cytotoxic agents by decreasing intracellular drug levels.[391] Overexpression of P-gp is correlated with poor response and treatment failure to the taxanes and vinca alkaloids.[389] Due to P-gp mediated drug efflux, tumours that overexpress P-gp are often resistant toward taxane and vinca alkaloid based treatment regimens.[392,393,394] Additionally, expression of mutant β-tubulin III isoforms gives rise to taxane and vinca alkaloid resistance, specifically towards paclitaxel and vinorelbine.[395] Exploration of the combretazat β-lactam family using computational studies suggests that these analogues evade and are not substrates of P-gp mediated efflux. CBSIs also remain unaffected by the expression pattern of β-tubulin (Chapter 4).[396] Agents targeting the CBS at the αβ interface of tubulin are therefore exceptionally promising anti-cancer targets for the treatment of metastatic and chemoresistant TNBC and specifically for circumventing issues associated with MDR either as an adjunctive or alternative treatment to mainstay clinical regimens.[397-399]

1.7.2 *Combretazets as lead analogues for treatment of metastatic chemoresistant colorectal cancer*

Both CA-4 and the B ring *meta* substituted hydroxyl combretazet panel have minimal antiproliferative activity in refractory HT-29 colorectal cancer cells. Chemoresistant HT-29 cells overexpress the drug metabolising enzyme, uridine 5-diphospho-glucuronosyl transferase (UGT).[378, 400] UGTs are major phase II metabolising enzymes, responsible for catalysing the conjugation of UDP-glucuronic acid to drug molecules containing hydroxyl moieties.[401] Glucuronidation involves covalent addition of glucuronic acid to a chemical and is widely regarded as the most common mammalian conjugation pathway mediating drug metabolism. UGT mediated glucuronidation therefore contributes to drug resistance in colon cancer cells due to rapid clearance of hydroxyl containing anti-cancer derivatives as their inactive *O*-glucuronide metabolites (Figure 1.17).[402] A co-enzyme form of glucuronic acid, uridine 5-dipospho-α-*D*-glucuronic acid (UDP-glucuronic acid) is added in the glucuronidation process. This is biosynthesised from α-*D*-glucose-*D*-phosphate (glucose) by phosphorylase catalysed conversion to a nucleotide sugar which is then oxidised to the corresponding carboxylic acid by UDP dehydrogenase. Therefore UDP glucuronic acid contains *D*-glucuronic acid at the anomeric carbon (Figure 1.17).[403]

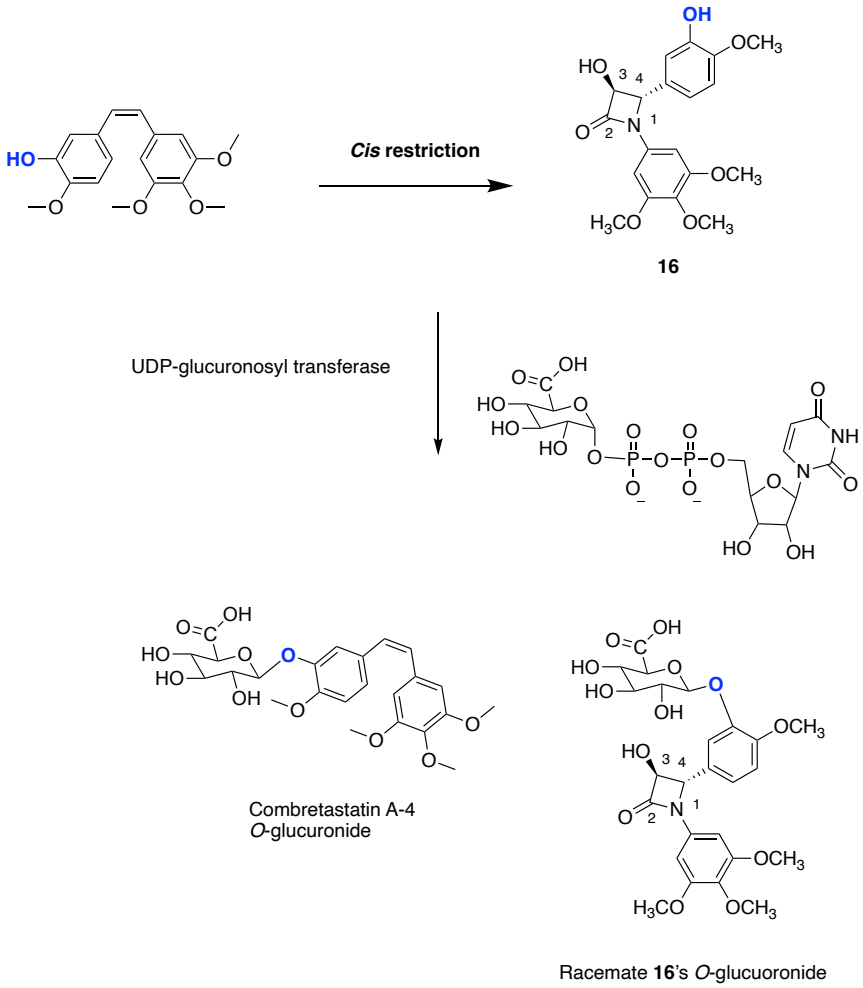

Figure 1.17: Plausible mechanism of glucuronidation in HT-29 cells of the phenolic B ring of CA-4 and its corresponding *cis* restricted combretazet *via* UDP-glucuronosyl transferase to an inactive *O*-glucuronide metabolite of CA-4 (left) and racemate **16** (right).

While combretazet analogues containing the B ring *meta* 3-hydroxyl substituent (**16,** Figure 1.18) are reported as extremely potent anti-proliferative agents in MCF-7 and MDA-MB-231 breast cancer cells, formation of *O*-glucuronide metabolites by UGT1A9 and UGT1A6 enzymes is suggested as contributing to rapid clearance of both CA-4 and B ring *meta* hydroxyl containing combretazets,[404-407] reducing their efficacy in HT-29 cells.[408, 409] Combretazet analogues designed for maximum antiproliferative activity in breast cancer cells bearing the B ring *meta* hydroxyl (**16**, Figure 1.18), are inactive in chemo resistant HT-29 cells.[378, 400] Deletion of the B ring *meta* hydroxyl group or substitution with an amine significantly increases activity in CA-4 refractory HT-29 cells.[328] Recent work has evaluated a subset of B ring *meta* hydroxyl deletions or substituted combretazets *in vitro*, including halogen or methyl moieties *in vitro* (**17-22,**

Figure 1.18).[378, 400] Interestingly, the 3-hydroxyl analogues were determined (**17-22,** Figure 1.18) are the most potent combretazet analogues designed to date in HT-29 colorectal cancer cells, despite known inactivation of the B ring *meta* hydroxyl substituents. The parent 3-hydroxyl analogue bearing the B ring *meta* hydroxyl substituent (**16,** Figure 1.18) is 40 times less active than the corresponding 3-hydroxyl analogue where the B ring *meta* hydroxyl is deleted (**17,** Figure 1.18). This indicates that it is the B ring *meta* phenol versus the 3-hydroxyl alcohol site which is the favoured site for glucuronidation. **23** has been synthesised by Sun *et al* only as the *cis* isomer. **23** has not yet been isolated or undergone *in vitro* evaluation in its *trans* form.[386] This panel of 3-hydroxyl analogues successfully circumvents *meta* hydroxyl metabolism by substitution of the hydroxyl with methyl or halogen substituents [F (**18**), Cl (**19**), CH_3 (**20**) or H (**17**) (Figure 1.18)] with racemates demonstrating potent IC_{50} values in low nanomolar range in HT-29 cells. Analogues **17-22** are the focus of this thesis for development as anti-cancer agents with dual activity against CA-4 resistant colorectal cancers and TNBC, reported to date as their racemates.[378, 400] Additionally attempts will be made to synthesise **23** in the *trans* configuration for further biochemical evaluation.

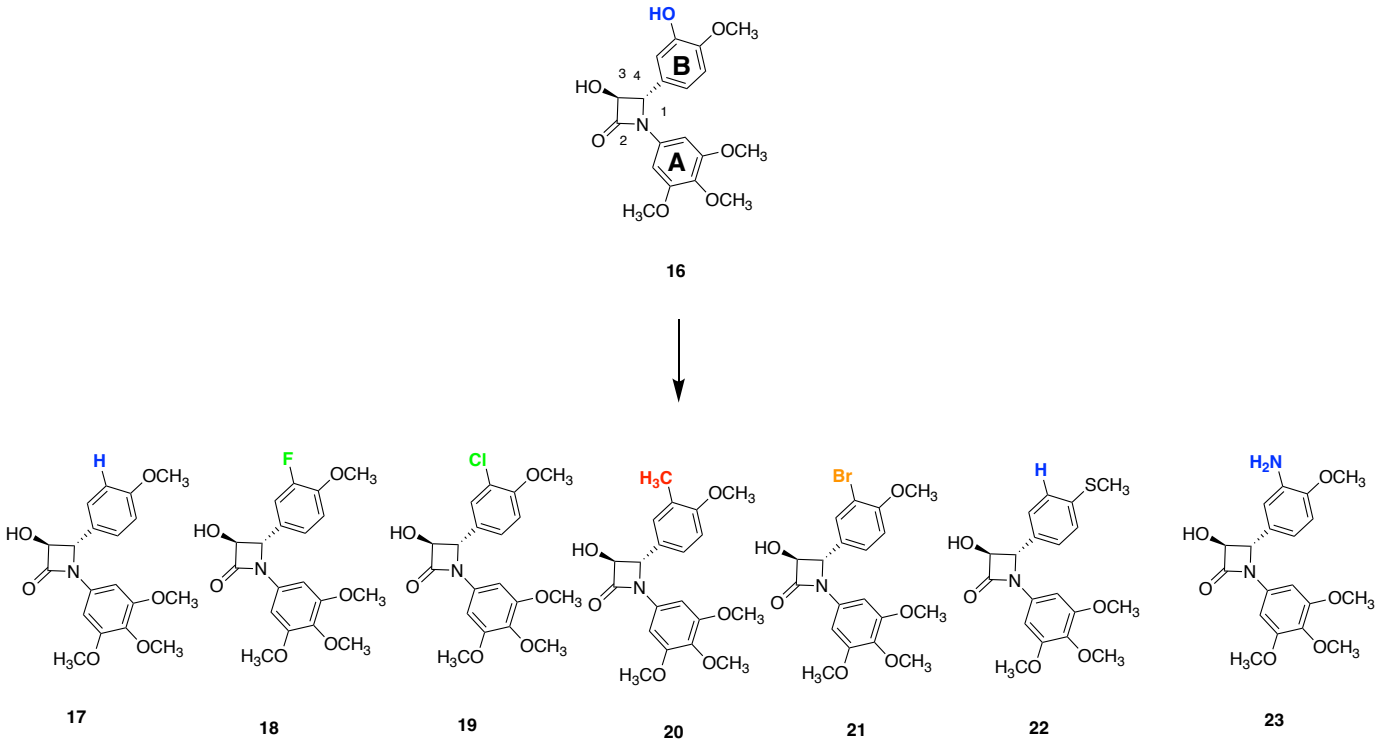

Figure 1.18: Parent 3-hydroxyl B ring *meta* hydroxyl substituted analogue (**16**) compared to lead 3-hydroxyl combretazet analogues with modifications at the B ring *meta* position which are active in CA-4 resistant HT-29 cells (**17-23**). *Trans* isomers and one enantiomer of the racemate illustrated.[378, 386, 400]

1.8 *Rationale for progression of the combretazet family as optically purified enantiomers for the treatment of both breast and colorectal cancers*

To date, β-lactam derivatives of CA-4 by our group have been synthesised and evaluated *in vitro* as racemates only.[359, 378, 400] Considerations required for progression of the combretazets towards pre-clinical studies and eventual clinical evaluation includes achieving both isomeric (*trans*) and optical purities. Greene *et al* and more recently Malebari *et al* have demonstrated that *trans* isomers are superior as antiproliferative agents.[357, 410] Additionally, stereocentres exists at H_3 and H_4 of the β-lactam ring. Two possible isomers [*cis* and/or *trans* (Figure 1.16)] and their enantiomer pairs gives rise to four potentially bioactive compounds varying in anti-proliferative activity. The rational next step in pre-clinical development is the isolation of *trans* enantiomers and comparative biological evaluation to determine the therapeutic efficacy and toxicity of eutomer versus distomer *i.e* the more potent versus the less potent enantiomers respectively. Resolution of enantiomers and comparison of their potencies is the principal focus of this thesis.

1.9 *Significance of chirality in modern drug design*

Chirality holds a significant weighting in the drug discovery and design process. The physical and chemical properties of enantiomers are virtually identical in achiral environments. However once placed in a chiral environment, *e.g*, amongst biological receptors, the reactivities of enantiomers usually differ. The eutomer is designated as the enantiomer with the desired effect while the distomer is associated with poorer activity, no activity or alternatively detrimental biological effects. More recently distomers have been defined as pollutants or contaminants.[411] For new chiral drugs, the choice between using a racemate versus the eutomer must be based on critical evaluation of chiral properties of both enantiomers including therapeutic activity and toxicology.[412] Since 1992, drug design and regulatory guidelines have placed emphasis on optical purity. Early drug design now requires evaluation of the eudysmic ratio, *i.e* the difference in biological activity between eutomer versus distomer. FDA guidelines compel the early consideration of stereochemistry during lead development.[411, 413] Currently the FDA allows drug companies to develop and market a drug as a racemate or single enantiomer where rationale behind such decisions are extensively investigated and documented in drug approval applications.[413] Similarly the International Conference on Harmonisation of Technical Requirements (ICH) Q6A guidelines, published in 2001, regarding chiral

drug quality, considers the distomer as an impurity whose contribution to the racemate's efficacy and safety must be established.[414] The last three decades have witnessed rapid growth in field of chirality and the pitfalls associated with failure to recognise the importance of its role in drug development. The incentive for enhancing and advancing the area of chiral separation and asymmetric synthesis will continue to be an important area of focus in drug design.

1.10 *Chiral synthesis for isolation of enantiopure of β-lactams*

Recently Zhou *et al* have employed asymmetric synthesis with phosphine-based chiral catalysts [(*R,R,R*)-Ph-SKP] to synthesise a wide variety of enantiopure β-lactams with subsequent biological evaluation *in vitro* and also *in vivo* in human xenograft model of ovarian cancer. Enantiomers of 3-hydroxyl methyl *cis* and *trans* β-lactam CA-4 analogues have been synthesised as *cis* 3*S*,4*R* and *trans* 3*R*,4*R*. A Morita-Baylis-Hillman condensation of substituted aromatic aldehydes with ethyl acrylate in base was employed to form racemic adducts which were then acylated as starting materials for asymmetric allylic amination. Racemic adducts were then reacted with aromatic amines as the nucleophile, $Pd_2(dba)_3$ and [(*R,R,R*)-Ph-SKP] as the chiral catalyst (Figure 1.19).[415, 416]

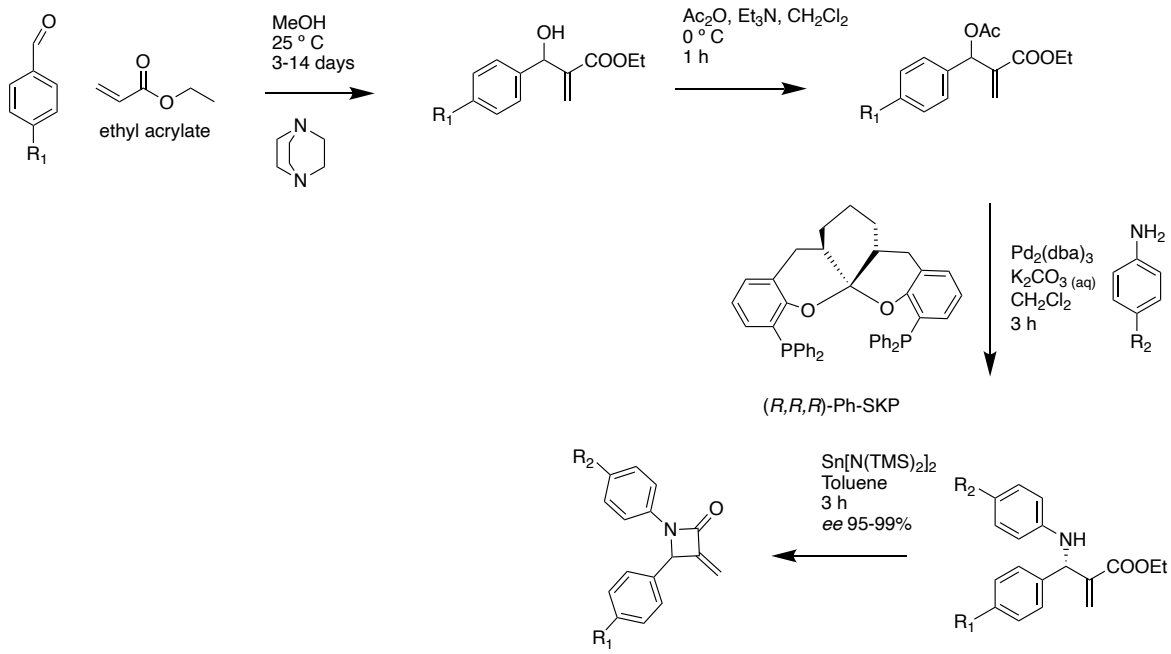

Figure 1.19: Synthesis of chiral 1,4-diaryl-3-methylene-2-azetidiones using chiral ligand [(*R,R,R*)-Ph-SKP] for asymmetric allylic amination by Zhou *et al*.

This reaction was successful in greater than 90% yield while also achieving excellent enantioselectivity [>99% enantiomeric excess (*ee*)].[416] These asymmetric aminated adducts were then cyclised to the corresponding β-lactam scaffold using $Sn[N(TMS)_2]_2$ in toluene at reflux temperatures to yield a final β-lactam substituted with an alkene the 3-position of the β-lactam ring. This 3-alkene substitution served as a functional group for chemical manipulation to provide a panel of enantiomers for biological evaluation (Figure 1.19). The most potent 3*R,*4*R* 3-methylhydroxyl enantiomer demonstrated superior potency in MDA-MB-231 cells with an IC_{50} of 16 nM in comparison to 182 nM of the *cis 3S,*4*R* relative (Figure 1.20). Despite an excellent asymmetric approach to yield optically purified β-lactams of CA-4 in both impressive isolated yields and *ee*, the 3*S*,4*S* enantiomer of the 3-hydroxyl family have not yet been reported by means of asymmetric synthesis. This thesis therefore seeks to isolate both enantiomers of the 3-hydroxyl combretazets and other β-lactam racemates by the alternative route of *trans* β-lactam resolution to isolate both enantiopure forms (*i.e* the 3*R,*4*R* and novel 3*S,*4*S* enantiomers). Two approaches will be explored: diastereomeric chiral resolution *via* derivatisation to the corresponding diastereomer pairs using chiral derivatising reagents [CDRs (Chapter 3 and 4)] and kinetic resolution (Chapter 7), using a biocatalytic approach with lipase enzymes. Proceeding on from enantioseparation using either or both methods, subsequent comparative biological evaluation will aim to determine the eutomer versus distomer.

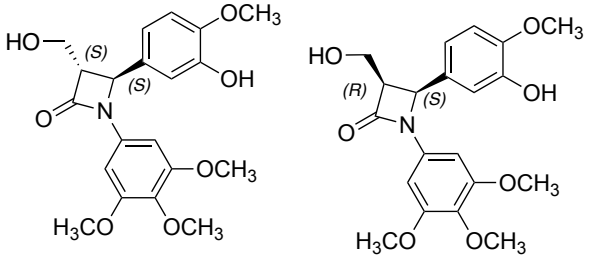

Figure 1.20: 3-methylene hydroxyl 3*S*,4*R* cis and 3*R*,4*R* trans enantiomers yielded *via* asymmetric synthesis by Zhou *et al*.[416]

1.11 *Chiral resolution of combretazet β-lactam racemates for isolation of enantiomeric pairs*

Chiral resolution involves separation of individual enantiomers from their racemic mixtures.[417] The synthesis of organic compounds with a stereocentre is one of the most challenging tasks in modern organic synthesis. Amongst the possibilities for enantioseparation are diastereomeric and kinetic enzymatic resolution procedures. Both diastereomeric and enzymatic methods are pursued in this thesis based on approaches previously documented in the literature.[291,418,419] By resolving both eutomer and distomer, this thesis aims to determine the absolute configurations of both enantiomers, calculate their eudysmic ratios, and evaluate cytotoxicity for both enantiomers in non-tumorigenic cells.

1.11.1 *Diastereomeric chiral resolution using chiral derivatising reagents*

Chiral resolution offers a solution for isolation of all four enantiomers of both *cis* and *trans* isomers of the β-lactam combretazets through purification of individual *cis* and *trans* isomeric racemates using liquid chromatography (LC) followed by resolution of each racemate. Chiral resolution explored in this thesis involves separation of individual enantiomers from a racemic mixture by derivatising to diastereomers using a CDR.[420, 291] Using this technique, the racemate can be synthesised using conventional chemistry and subsequently separated on the basis of different physiochemical properties of derivatised diastereomer pairs.[291,420] Tripodi *et al* have reported a chiral resolution procedure using *N*-Boc-L-proline as the CDR applied to 3-hydroxyl β-lactam derivatives of CA-4.[291] Dextrorotary enantiomers were over 10 times more potent than the corresponding levorotatory enantiomers with IC_{50} values in low nanomolar range across a panel of cancer cell lines. This evidence serves as a plausible reason to pursue the chiral resolution of combretazet enantiomers for further comparative biochemical evaluation. Despite successful isolation of both *trans* enantiomers of two dextrorotatory and two levorotatory *trans* 3-hydroxyl β-lactam derivatives, the absolute configurations or comparative tubulin polymerisation studies have not yet been reported for 3-hydroxyl β-lactam enantiomers. The Tripodi method will serve as a starting point for optimisation of the chiral resolution procedure employed in this thesis for isolation of combretazet enantiomers.

1.11.2 *Kinetic resolution using enzymes as biocatalysts*

Alternatively kinetic enzymatic resolution (KR) may be employed as a biocatalytic method for enantioseparation β-lactams. KR is based on partial transformation of a racemic starting material toward a chiral product, yielding enantioenriched starting material (discussed in detail in Chapter 7).[421,422] If a racemate is subjected to KR, chiral discrimination occurs within the chiral environment of the enzyme active site. One enantiomer is often the preferential substrate of the enzyme and therefore converted at a faster rate.[423] KR may result in partial or complete resolution depending on the enantioselectivity or E value which is discussed further in Chapter 7. The biocatalytic approach for preparation of enantiomerically pure chiral compounds is considered a mature technology of asymmetric induction.[422,424] A number of industrial processes employ biocatalysts in organic synthesis to ensure highly selective, efficient, sustainable and economical outputs.[425,426] The serine hydrolase class (Enzyme Commission number EC 3) are valuable biocatalytic enzymes due to substrate specificity and commercial availability.[427-430] Within the hydrolase family, the lipase or triacylglycerol subset (EC 3.1.1.3) are considered most useful due to their precision in terms of stereoselectivity in unnatural environments.[431-433] The ability of lipases to discriminate between enantiotopic groups makes them invaluable tools for the preparation of enantiopure compounds.[416,434,435] Hydrolases are extremely versatile for synthetic purposes, capable of catalysing many synthetic transformations in both aqueous medium and organic solvents, at higher temperatures of up to 100°C.[436,437] Lipases have an extremely broad substrate specificity due to their ability to change the active site conformation through an induced fit model, assuming a wide array of conformations to accommodate substrates of various sizes and complexities.[438-440] Lipase enzymes are also excellent candidates for solvent free and green mechanoenzymatic mediated reactions.[441] *Candida antarctica* amino lipase B (CAL-B) has recently been reported for isolation of both enantiomeric precursors of propranolol in high *ee*, activated through mechanical force, using a ball and mill apparatus.[442] Lipases carry out enantioselective reactions through hydrolytic or esterification reactions or alternatively formation of amide bonds.[443] Lipase mediated enzymatic hydrolysis of esters have produced > 90% *ee* in chiral products.[444] They are also known to mediate aminolysis, acidolysis and alcoholysis.[445] The use of lipases to produce enantiopure combretazets is as a strategy for KR is discussed in Chapter 7.

1.12 *Novel anti-angiogenic small molecules designed for the treatment of colorectal cancer: P drugs*

Vascular targeted therapies (VTT) are composed of VDAs and anti-angiogenic agents (AAs). Although both drug classes target tumour vasculature, their mechanism of action differs significantly. VDAs can be distinguished from AAs as compounds that directly destroy the tumour vasculature while the latter impede formation of new vessel growth. Since VDAs target tumour cores, a peripheral rim of vessels remains, which contributes to treatment resistance. There is therefore strong rationale combining VDAs regimens with AA agents or alternatively other chemotherapeutics to augment anti-cancer treatment response.[446, 447]

The stilbene AA pyrazinib [**P3** (Figure 1.21)] originally supplied and extensively investigated by our collaborators, is therefore also explored in this thesis with specific emphasis on modifying its physiochemical properties. Prodrug exploration will be discussed with aim of improving drug-likeness and clinical viability. Chemical screens have identified quininib [**Q1** (2-[(*E*)-2-(quinolin-2-yl)vinyl]phenol) (Figure 1.21)] as a small molecule and potent anti-angiogenic quinoline derivative both *in-vitro* and *in-vivo*.[448, 449] The **P** or pyrazine series have been derived from quininib (Figure 1.21) and extensively investigated for treatment of oesophageal adenocarcinoma (OAC).[450,451] **P3** is a pyrazine derivative with radiosensitising properties and AA activity.[451] Resistance to traditional radiotherapy in OAC is common and positively correlated to tumour burden and size.[452] OAC radioresistance is thought to be closely associated with oxygen content in the tumour microenvironment, dysfunctional cellular energetics,[453] angiogenesis[454] and pro-inflammatory mediators.[455] **P3** influences each of the aforementioned factors and is therefore a promising adjunctive drug candidate as a radiosensitising agent for radiotherapy.

1.12.1 *Further development of stilbene **P3** as a promising radiosensitising agent*

Pyrazinib is currently in development by our collaborators at Trinity Translational Medicine Institute (TTMI) as an adjunctive radiosensitising agent for the treatment of OAC.[450] Treatment regimens for OAC focus on neoadjuvant treatment with either chemotherapy alone or chemotherapy in combination with radiation prior to surgical resection of tumours. While neoadjuvant combination chemotherapy and radiotherapy is

shown to have a higher overall survival rate,[456-458] 70-80% of patients do not respond to radiation treatment in the neoadjuvant setting. This delays surgical resection and results in patients receiving toxic doses of both chemotherapy and radiation with little therapeutic gain.[459,460,461] There are currently no markers to predict response to radiotherapy, which is often inversely correlated with tumour burden.[452] Three main factors are identified as drivers of radioresistance in OAC: altered energy metabolism, upregulated inflammation and angiogenesis.[60, 453, 454]

A number of chemotherapies and radiotherapies rely on oxygen in the tumour microenvironment to exert their cytotoxic effects by formation of oxygenated free radicals. Oxygen itself is a potent radiosensitiser required for maximal response to radiotherapy.[462] Oxygenated cells are more susceptible to cell death versus hypoxic cells.[463] The oxygen content in the tumour micro-environment of a radioresistant tumour is typically limited.[464] Altered energy metabolism in presence of minimal oxygen content in the tumour microenvironment is a hallmark of cancer and determinant of radioresponsiveness.[465] Aerobic glycolysis or 'the Warburg effect' is a primary feature of cancer cells involving altered energy metabolism with the less effective anaerobic glycolytic pathway preferentially used to make ATP even in aerobic conditions through breakdown of glucose to pyruvate and facilitates cancer cell survival.[466] Lynam-Lennon *et al* have demonstrated that radioresistant cancer cells demonstrate altered oxidative phosphorylation, metabolic rates and mitochondrial function. Excess cellular energy consumption results in depleted oxygen supplies further limiting oxygen availability in tumour microenvironment rendering radiotherapy less effective in more aggressive tumours that participate in 'aerobic glycolysis'.[453] Since the use of bevacizumab as an AA as mainstay of treatment for both colorectal cancers and OAC further limits the supply of oxygen to the tumour itself, response to radiotherapy is diminished thus potentially enhancing radioresistance.[467] This counter argument to the use of anti-angiogenic agents is of concern for patients with larger tumour burdens who rely on success of radiotherapy prior to surgical resection in the neoadjuvant setting.[450]

Promisingly in a model of hypoxic radioresistance, **P3** successfully reduced the fraction of radioresistant OAC (OE33R) cells which were treated with 4 gray (Gy) irradiation, demonstrating **P3**'s potential to stimulate radioresponsiveness in radioresistant cancer cells.[451] **P3** is a promising lead analogue for treatment of radioresistant tumours and

prevention of radioresistance where AA agents must be used, *e.g* as combination therapy with bevacizumab.

Inflammation is another factor contributing to radioresistance.[468, 469] IL-6 and cytokine family members are linked to radioresistance in OAC.[451] Administration of IL-8 and IL-6 neutralising antibodies sensitises tumours towards radiotherapy.[470] **P3** reduces secretion levels of pro-inflammatory interleukins IL-6, IL-8, IL-4 and IL-3 in OE33R radioresistant cells.[451] **P3** has also demonstrated anti-angiogenic activity in zebrafish ISV screens. **P3** (10 μM) reduced the intersegmental vessel number in zebrafish as an *in vivo* model of angiogenesis, by 67%.[451] The effect of combining **P3** with bevacizumab (Avastin) may enhance both efficacy of radiotherapy through radiosensitisation in addition to augmenting synergistic anti-angiogenic activity in combination with bevacizumab.

P3's *in vivo* performance to date has not reproduced results which have been observed *in vitro* potentially attributed to its biopharmaceutical issues such as extremely poor observed aqueous solubility. Quantitative measurements of **P3**'s physiochemical properties including solubility and stability in addition to prodrug derivatisation using the phosphate prodrug approach are explored in this thesis with aim of synthesising a more clinically viable analogue of **P3**.

1.13 *Synthesis of cis restricted analogues of **P3***

Cis **P3** has not been synthesised or biologically evaluated to date. While *trans* **P3** does not have known antiproliferative activity, the structural similarity of *cis* **P3** with *cis*-CA-4 (Figure 1.21) combined with the knowledge of *cis*-CA-4's inactivation upon isomerisation to the *trans* isomer warrants further investigation of *cis* **P3** as a potential CBSI. This thesis will investigate *cis* restriction of **P3**'s A and B rings using a similar strategy β-lactam mediated *cis* restriction strategy prior employed to create the panel of combretazets. Theoretical β-lactam analogues of **P3** are illustrated in Figure 1.21.

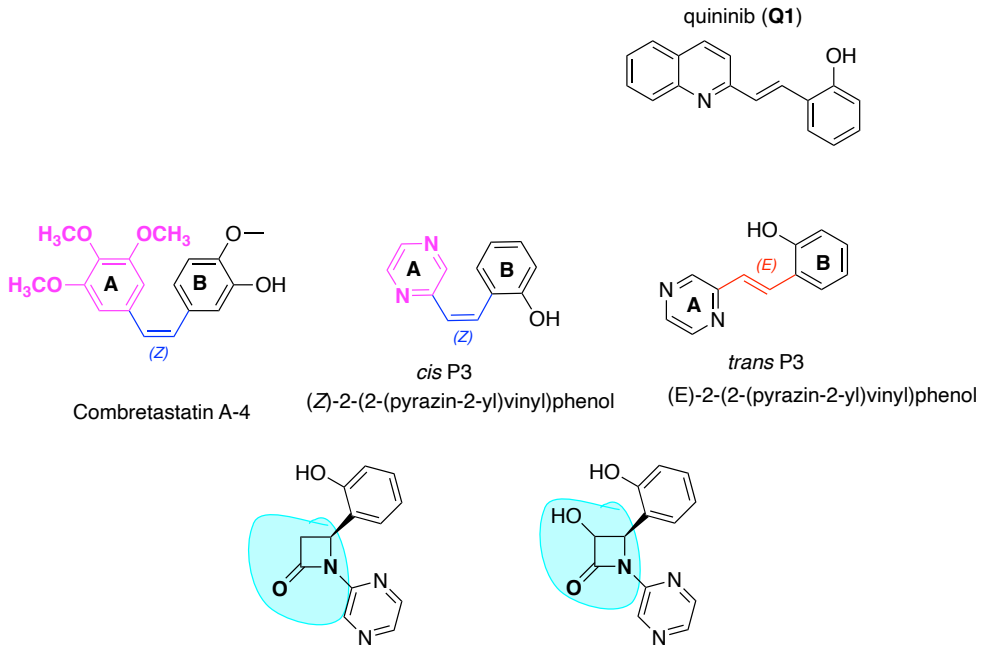

Figure 1.21: Structural representation of theoretical *cis* **P3** compared to *cis* CA-4. *Trans* **P3** illustrated for reference. Examples of theoretical β-lactam analogues of **P3** are also illustrated (β-lactam ring highlighted in blue)

1.14 *Thesis aims*

1.14.1 *CA-4 Analogues*

This thesis aims to:

- Synthesise a panel of *trans* configuration β-lactam combretazets for resolution of optically purified enantiomers.
- Select appropriate CDRs for diastereomeric chiral resolution and isolation of enantiopure β-lactams.
- Kinetic resolution using serine hydrolase lipase enzymes to catalyse enantioselective reactions.
- Characterise enantiomers using:
    - Chiral HPLC
    - X-ray crystallography
- Computational studies to postulate on binding modes of enantiomers as a predictive tool for determining eutomer versus distomers.

- Biochemical evaluation of enantiomers in a panel of cancer cell lines in addition to evaluation of cytotoxicity in non-tumorigenic MCF-10-2A breast epithelial cells.
- Determine microtubule-depolymerising activity using both the tubulin polymerisation assay and immunofluorescence/confocal microscopy as complimentary techniques
- Evaluate the cell cycle for lead enantiomers and determination of G_2/M phase arrest and apoptosis.

1.14.2 *P3*

The thesis also aims to:

- Synthesise **P3** as a starting material for solubility and stability analysis in addition to prodrug synthesis.
- Modify the physicochemical properties of **P3** *via* phosphate prodrug synthesis accompanied by comparative stability and solubility measurements of **P3** versus its phosphate prodrug.
- Evaluate biochemical activities of the phosphate prodrug of **P3** compared to parent **P3.**
- Molecular modelling of *cis* and *trans* **P3** to determine CBS activity for both isomeric forms.
- *Cis* restriction of **P3** *via* β-lactam insertion and subsequent biochemical evaluation of **P3** β-lactam racemates.

Chapter 2 - Synthesis and chemistry of *trans* β-lactam racemates

2.1 *The β-lactam scaffold in nature and clinical uses*

The 2-azetidinone is the core scaffold within the β-lactam class of anti-microbial agents, composed of a four membered heterocyclic lactam containing three carbon atoms and one nitrogen atom(Figure 2.1). Penicillin was first discovered by Alexander Fleming in 1929 as *Penicillium* mould from cultures of *Staphlycoccous sp*.[471,472] Today the β-lactam class are the most widely prescribed antibiotics, accounting for over 50% of antibiotic prescriptions in the world.[473, 474] The β-lactam scaffold has since been found in many natural products such as the penicillins V and G, cephalosporin C,[475,476] clavulanic acid,[477] thienamycin,[478,479] tabtoxin,[480] norcardicin A[481] and sulfacezin[482] (Figure 2.1).

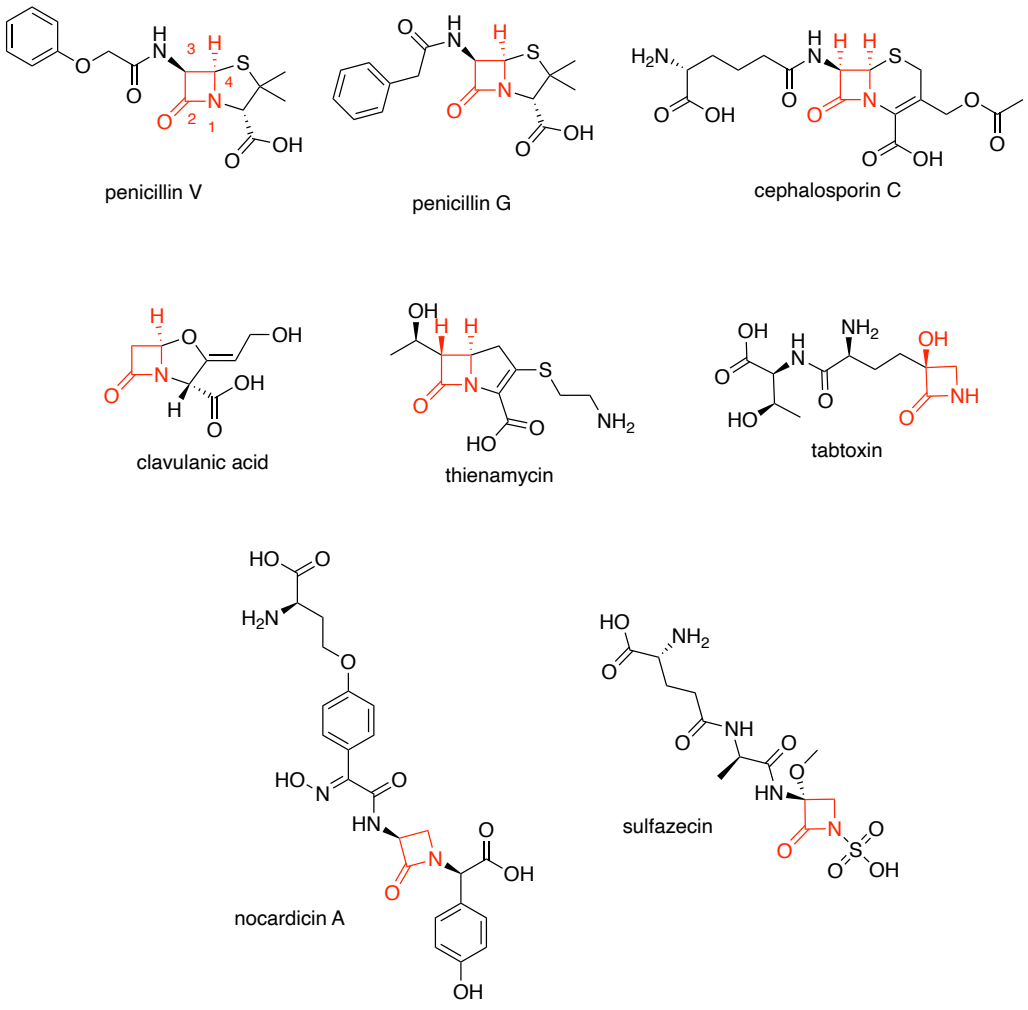

Figure 2.1: Naturally occurring antimicrobial agents containing the β-lactam scaffold (highlighted in red).

Biosynthetically produced β-lactams such as penicillin V, G, cephalosoporin C etc. (Figure 2.1) have catalysed a new era of semi-and synthetically produced analogues, to combat emerging antimicrobial resistance *e.g* thienamycin. Anti-microbial β-lactams in clinical use are classified as five subgroups: penicillins (*e.g* amoxicillin), cephalosporins (*e.g*. ceftazime), clavams (*e.g* clavulanic acid,) carbapenem (*e.g* meropenem and ertapenem) and monocyclic β-lactams [*e.g* aztreonam (Figure 2.2)].[483]

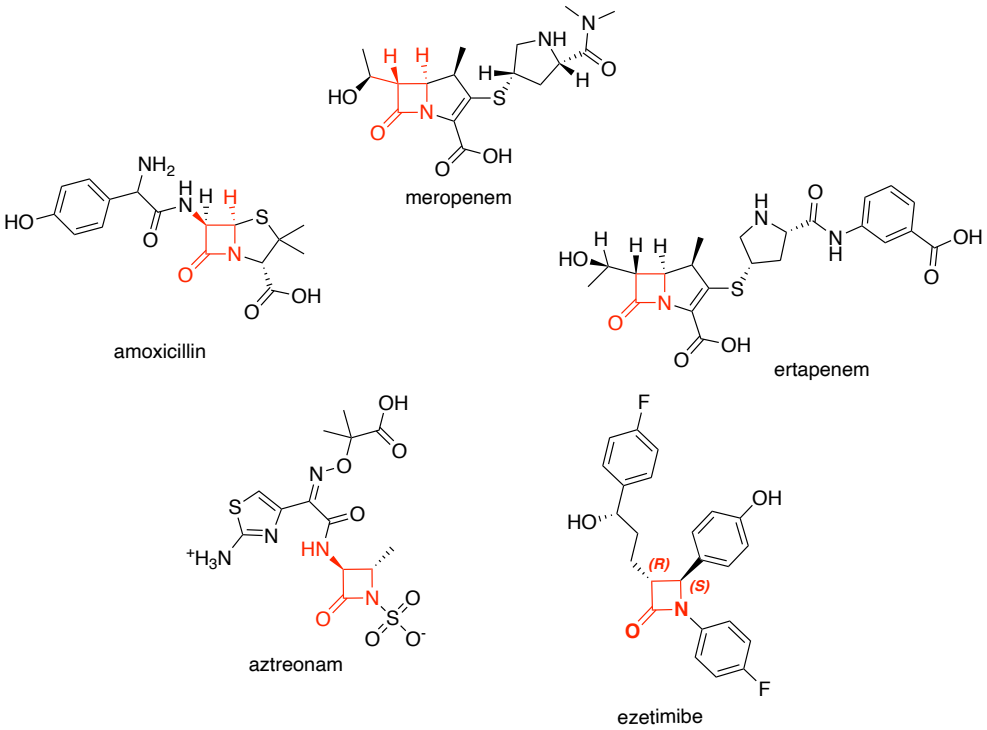

Figure 2.2: Semi- and synthetic β-lactams in clinical use.

2.2 *Pre-clinical uses of the β-lactam scaffold*

The β-lactam scaffold has been extensively investigated as a synthon for the preparation of various heterocyclic analogues for diverse biological applications. Clinical uses now extend beyond anti-microbial activity *e.g* ezetimibe which is marketed as the enantiopure 3*R*,4*S* form as a cholesterol absorption inhibitor (Figure 2.2).[484-486] Several efforts for synthetic development of β-lactams as anti-malarials are also reported.[487-489] *N*-methylthiolated β-lactam structures were reported over two decades ago as selective inducers of apoptosis in tumour cells as anti-cancer agents.[490-492] As mentioned in the introduction to this thesis (Chapter 1) Meegan *et al* and many others have reported a wide variety of *cis* restricted CA-4 analogues by replacing CA-4's alkene bond with the β-

lactam ring, thus overcoming chemical lability and its undesirable *cis* to *trans* isomerisation. [291, 360, 366-368, 386, 493, 494] These analogues are amongst the most potent tubulin depolymerising agents synthesised and reported to date. Selected 3-substituted analogues previously synthesised by O'Boyle *et al*,[495] Malebari *et al*,[378, 400] Greene *et al*[357] and Wang *et al*[359] with excellent *in vitro* activity reported for the racemates, were chosen as lead analogues for resolution towards their enantiopure form in this thesis (Table 2.1 and Table 2.2).

Table 2.1: 3-Hydroxyl racemates selected as lead analogues[378, 400]

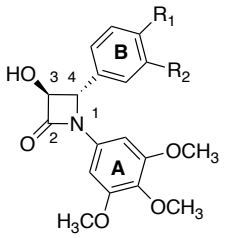

Compound	R_1	R_2
16	OCH_3	OH
17	OCH_3	H
18	OCH_3	F
19	OCH_3	Cl
20	OCH_3	CH_3
21	OCH_3	Br
22	SCH_3	H

Lead analogues (Table 2.1 and Table 2.2) were selected based on two characteristics.

1) Prior biochemical data demonstrating antiproliferative IC_{50} values of < 50 nM in MCF-7 breast cancer cells.[357, 359, 378, 382, 383, 400]
2) A hydroxyl or nitro amenable to synthetic reduction toward an amino functional group available for diastereomer derivatisation through esterification or amide bond formation in preparation for diastereomeric chiral resolution. (Chapter 3 and 4)

Three stereochemical outcomes in synthesis of the 2-azetidinone scaffold are possible, *cis, trans* or isomeric mixtures are possible during β-lactam synthesis. Isolation of the *trans* β-lactam racemates is explored in this chapter with the following aims:

1) Purification of *trans* β-lactams from isomeric mixtures using liquid chromatography (LC) synthesised *via* Staudinger (Section 2.4) and Reformatsky reactions (Section 2.7) as main routes for β-lactam synthesis in this thesis.
2) Optimisation of Staudinger and Reformatsky conditions for exclusive synthesis of the *trans* β-lactam isomers to maximise isolated yields for progression toward chiral (Chapter 3 and 4) and kinetic resolution (Chapter 7).

Table 2.2: 3-Substituted racemates selected as lead analogues[378, 400, 495]

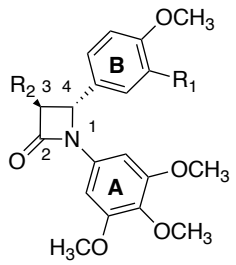

Compound	R_1	R_2	Compound	R_1	R_2
24	OH		**33**	OH	
25	NO_2		**34**	NO_2	
26	OH	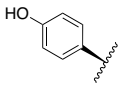	**35**	NH_2	
27	OH	H	**36**	NO_2	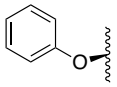
28	OH	CH_3	**37**	NH_2	
29	OH	F	**38**	OH	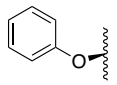
30	OH		**39**	OH	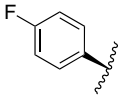
31	NO_2		**40**	OH	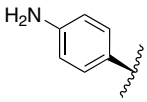
32	NH_2		**41**	OH	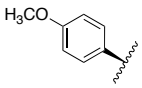

2.3 *Precursors for β-lactam synthesis*

2.3.1 *Protecting group chemistry*

Many combretazet analogues contain the B ring *meta* hydroxyl substituent (Table 2.2) which requires protection at early stages prior to β-lactam synthesis using the Staudinger

reaction. A synthetic route yielding highest purity of protected imine precursors is required due to the the imine bond's (N=CH) acid lability preventing their purification over silica gel.[496-498] Selective protection of the *meta* hydroxyl group of 3-hydroxy-4-methoxybenzaldaldehyde followed by imine formation (route A, Scheme 2.2) yields purer imines in higher yield compared to direct protection of hydroxyl substituted imines (route B, Scheme 2.2).[358, 384] Two protecting groups were used for hydroxyl protection in this thesis, the *tert*-butyldimethyl silyl ether and benzyl ether groups. For amine protection at the β-lactam 3-position the benzyl carbamate group was employed (**40,** Table 2.2).

2.3.2 *The TBDMS protecting group*

Silyl protecting groups are widely used in organic chemistry.[499, 500] The *tert*-butyldimethylsilyl (TBDMS) protecting group is one of the most popular due to superior stability compared to trimethylsilyl (TMS) ethers,[499] 10^4 times more hydrolytically and acid stable than TMS.[501,502] Reaction of *tert*-butyldimethylsilylchloride (TBMSCl) with the phenolic hydroxyl occurs in the presence of the base 1,8-diazabicycloundec-7-ene (DBU) *via* the highly reactive silylating *N-tert*-butyl dimethylsilyl-DBU.[502,503] Phenolic aldehyde protection with TBDMS and DBU is reported by our group in excellent yields and high purity.[378, 495, 504] High yields of 80-90% for **42** (Scheme 2.1) were obtained as a yellow oil in >90% purity for condensation with 3,4,5-trimethoxyaniline to the corresponding OTBDMS protected imine **47** without further purification (Scheme 2.1). TBDMS protected hydroxyl groups are stable under the Staudinger reaction conditions (Section 2.4). Once the desired β-lactam derivative has been isolated, the TBDMS protecting group is removed in the presence of a fluoride ion source such as tetra *n*-butyl ammonium fluoride (TBAF). Since the Si-F bond strength is stronger by 30 kcal/mol than the Si-O bond, removal by nucleophilic attack of the fluoride anion on the Si atom occurs readily and rapidly.[502, 503]

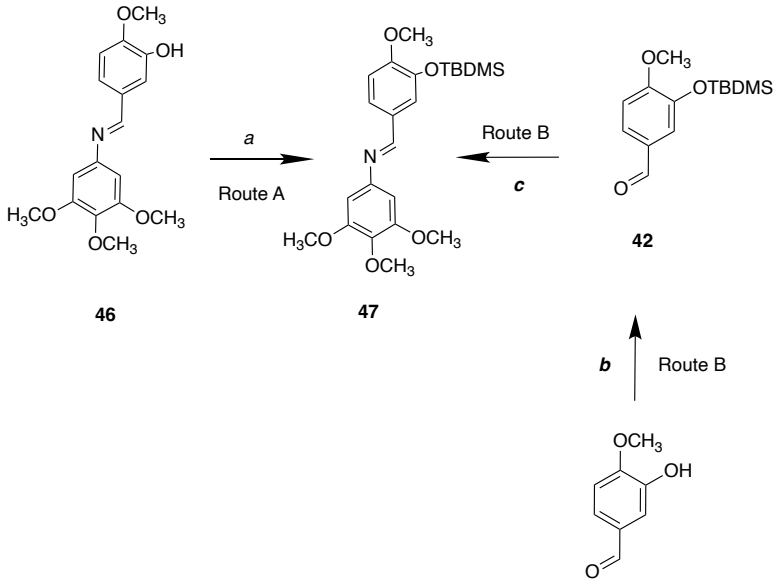

Scheme 2.1: Synthesis of silyl ether protect imine **47 a:** Direct protection of imine **46** using TBDSMCl, DBU, anhydrous DCM, inert atmosphere, RT. **b:** Protection of 3-hydroxy-4-methoxybenzaldeyde using TBDMSCl (identical reagents to **a**) to yield **42 c:** 3,4,5-Trimethoxyaniline, ethanol, 90 °C, 4 h.

2.3.3 *Benzyl carbamate protecting group*

The benzyl carbamate protecting group was selected for protection of precursor 4-aminophenylacetic acid employed in the synthesis of analogue **40** to yield the benzyl protected analogue **43** (Scheme 2.10). The benzyloxycarbonyl (CBZ) group is one of the most common amine protecting groups utilised in synthetic transformations due to ease of introduction, stability under acidic and basic conditions and ease of removal *via* simple hydrogenolytic conditions using palladium as a metal catalyst.[505] This route was selected since it has been shown that reaction of 4-nitrophenylacetyl chloride did not yield the desired 3-amino β-lactam.[495] The benzyl carbamate group was introduced in aqueous media using 4-aminophenylacetic acid, sodium bicarbonate (Na_2CO_3) as the base, dioxane as co-solvent and benzyl chloroformate. The desired 4-benzyloxycarbonyl aminophenylacetic acid product, **43a** was obtained in > 75% yield.

2.3.4 *Imines*

Imines or Schiff bases contain a CH=N moiety and are key precursors for the synthesis of the β-lactam scaffold enabling both insertion of the β-lactam ring nitrogen in addition to the 3,4,5-trimethoxyaniline A and 4-methoxy aryl substituted B rings, essential for CBS activity.[506] Imines **44**-**56 (**Scheme 2.2) were readily prepared using condensation reactions *via* nucleophilic attack of the aromatic primary amine's lone pair of electrons

on the electropositive carbon of carbonyl containing compounds *e.g* an aldehydes (Scheme 2.2). This panel of imines was obtained in high yields (70-95%) *via* condensation of appropriately substituted aldehyde with 3,4,5-trimethoxyaniline under reflux conditions in ethanol in presence of catalytic quantities of 0.1 M HCl (Scheme 2.2). 3,4,5-Trimethoxyaniline is a highly activated primary amine due to the electron donating methoxy groups. Removal of water using either the Deak Stark apparatus, drying agents ($MgSO_4$) or molecular sieves was therefore not necessary for condensation to proceed.[507] Imines also readily condensed at room temperature overnight in ethanol to form a bright yellow precipitate which were subsequently filtered to afford the pure material in >90% yield. B ring *meta* fluorine substituted **45** was also obtained using low intensity ultrasound with a 40 KHz transducer containing sonicator. Imines were observed as off-white/yellow precipitates in < 1 hour in the minimum volume of cold ethanol (10-20 mL) on a 10 mmol scale at 25 °C using the Branson Ultrasonic 2510 cleaning sonicator. Confirmation of imine formation is readily observed by the CH singlet of the CH=N bond at δ 8.4 ppm on the ^{1}H NMR spectrum. [508]

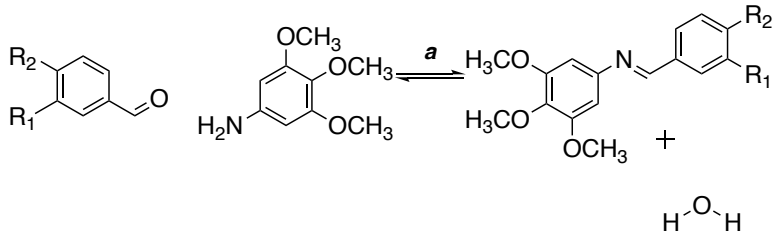

44 R_1 = H, R_2 = OCH_3
45 R_1 = F, R_2 = OCH_3
46 R_1 = OH, R_2 = OCH_3
47 R_1 = OTBDMS, R_2 = OCH_3
48 R_1 = Cl, R_2 = OCH_3
49 R_1 = CH_3, R_2 = OCH_3
50 R_1 = H, R_2 = SCH_3
51 R_1 = H, R_2 = F
52 R_1 = H, R_2 = NO_2
53 R_1 = Br, R_2 = OCH_3
54 R_1 = NO_2, R_2 = OCH_3
55 R_1 = H, R_2 = OCH_2CH_3
56 R_1 = H, R_2 = SCH_2CH_3

Scheme 2.2: Synthesis of imines **44-56** *via* condensation reaction **a:** ethanol, reflux (90 °C), 3-4h, catalytic quantities of 0.1 M HCl or low intensity ultrasound with a 40 KHz transducer

Two synthetic routes were investigated for synthesis of OTBDMS protected **47.** The addition of the TBDMS protecting group to imine **46** to yield **47** failed to yield desired imine in required % purity (**a,** Scheme 2.1). Aqueous work up resulted in CH=N bond hydrolysis towards precursor aldehyde and amine. **Route b** (Scheme 2.1) involved protection of 3-hydroxy-4-methoxy benzaldehyde with TBDMSCl followed by condensation of **42** with 3,4,5-trimethoxyaniline (**c,** Scheme 2.1) to yield **47**. Racemate **47** was isolated in 60-70% total yield and in >90% purity. **Route b** (Scheme 2.1) was therefore selected as the synthetic method of choice for isolation of silyl protected **47**.

The successful addition of the silyl ether protecting group was confirmed by two characteristic signals on the ^{1}H NMR spectrum; a singlet at δ 0.17 ppm integrating to 6H for silyl ether methyl protons (2× CH_3) and singlet at δ 1.00 ppm integrating to 9H of the *t*-butyl methyl protons (3×CH_3).

2.4 *Chemistry of β-lactam synthesis via Staudinger reaction*

The Staudinger reaction is one of the most common synthetic strategies for β-lactam synthesis.[386, 509-515] Its reaction mechanism has been extensively investigated to explain stereoselective synthesis. Two major theories exist regarding the nature of ring cyclisation during the Staudinger reaction.[514] The first theory involves *in situ* generation of a ketene formed from the appropriate acid chloride in the presence of base *e.g* triethylamine (TEA), which catalyses the loss of the chloride anion leaving group (Scheme 2.3). Ketene formation has been observed in the Staudinger reaction, monitored by IR absorption of the -C=C=O at 2100 cm^{-1} when analysed at <100 K.[516] Nucleophilic attack of the imine nitrogen on the sp-hybridized carbon atom of the ketene forms a transition state zwitterionic structure. An electrocyclic [2+2] cycloaddition reaction occurs next due to the 4π electron system of the zwitterionic intermediate (Scheme 2.3). If this occurs *via* conrotatory ring closure, exclusively *cis* isomer is formed where as a mixture of disrotatory and conrotatory (Scheme 2.3) ring closure will give rise to isomeric mixtures.

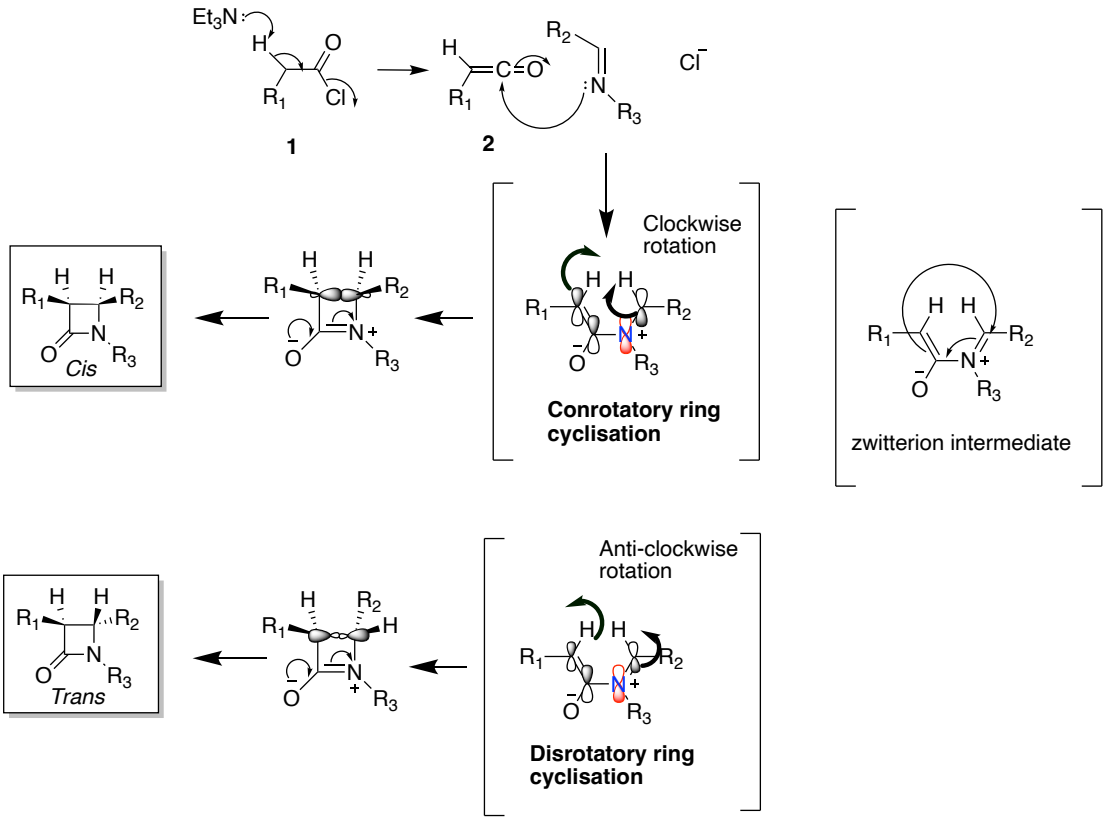

Scheme 2.3: Staudinger reaction mechanism (theory 1) *via* ketene precursor and intramolecular Mannich like [2+2] cycloaddition. Conrotatory and disrotatory ring closure *via* π molecular orbitals yielding an isomeric mixture (*cis* and *trans* β-lactams) illustrated.

The second theory considers a stepwise reaction involving nucleophilic attack of the imine nitrogen on the sp^2-hybridised carbon of the acid chloride, resulting in the an acyl-iminium intermediate zwitterion (**57**, Scheme 2.4), which then cyclises to form the 2-azetidinone ring. This mechanism proceeds if the acid chloride and imine react prior to the addition of TEA as the catalytic base. An equilibrium is set up between the *N*-acyliminium chloride zwitterion **57** and **58** (Scheme 2.4).[517] Isomerisation of the *cis* zwitterion to the corresponding *trans* form may occur prior to addition of base. TEA catalyses proton loss from **58** to form the enolate structure **59**. Intermediate **59** then undergoes cycloaddition through an intramolecular biomolecular S_N2 nucleophilic substitution reaction (Scheme 2.4).[518] The rate of ring closure determines stereochemical outcome as exclusively *cis*, *trans* or alternatively a mixture of isomers.[511] Rapid ring closure may prohibit *cis* zwitterion isomerisation to the desirable *trans* form yielding predominantly *cis* β-lactam product.

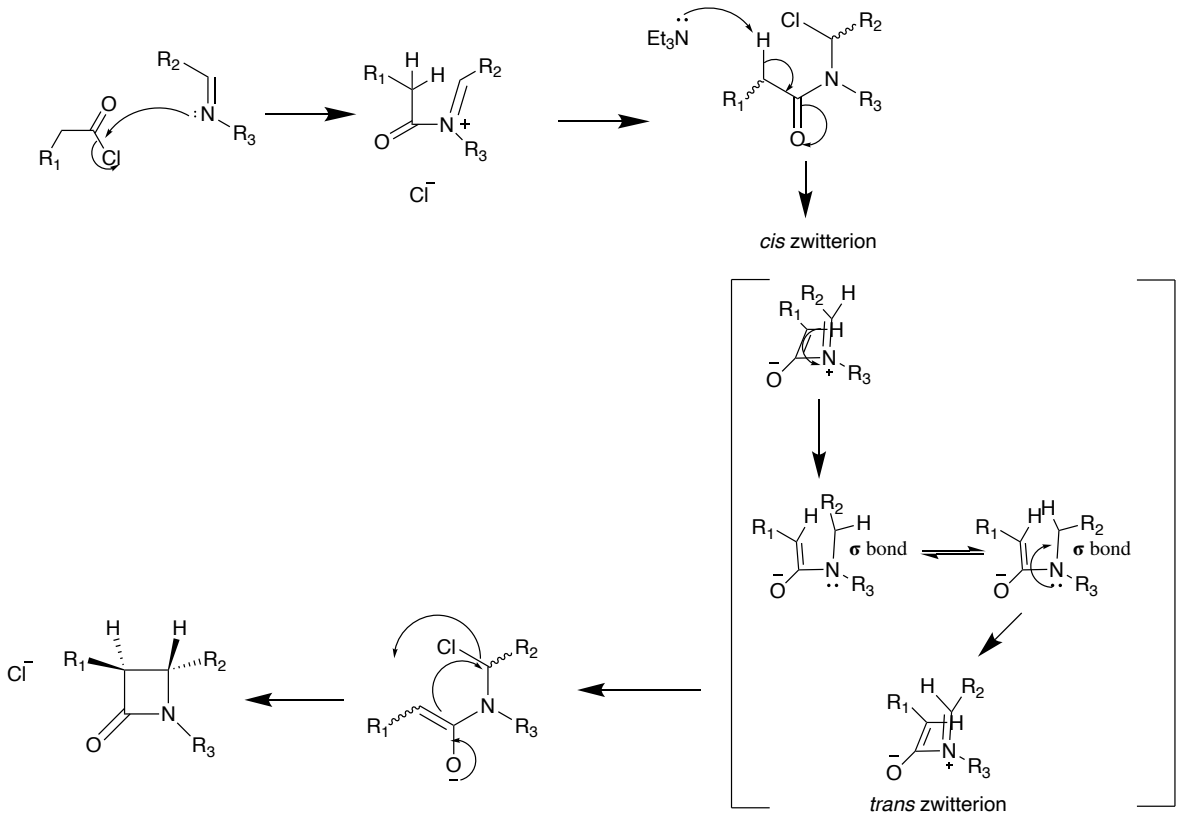

Scheme 2.4: Staudinger reaction mechanism (theory 2) involving addition of acid chloride and imine to form *cis* acyliminium zwitterion which isomerises to the *trans* zwitterion to yield exclusively *trans* β-lactam.

Isomerisation of *cis* to *trans* β-lactam products are not widely reported in the literature. *N*-Aryl-2-azetidinones do not isomerise after hours of UV irradiation, but instead suffer from enhanced degradation.[519] Isolated reports of epimerisation of the 3-hydroxyl β-lactams are reported in the literature. The interconversion of *cis* isomer to a mixture of *cis:trans* mixtures has been explained by unusual potassium phosphate base-catalysed ring opening of 3-hydroxyl analogue (**60**, Scheme 2.5) of the β-lactam C_3-C_4 bond to yield the benzylic carbanion (**61**, Scheme 2.5). The formation of this carbanion is favoured due to its extra stability on account of an electron-withdrawing B ring 4-nitro substitution. The β-lactam ring is then re-generated by nucleophilic attack on the carbonyl carbon in either *trans* (**62**) or *cis* (**60**) configuration (Scheme 2.5).[419]

While epimerisation of 3-hydroxyl β-lactams is possible,[419] it has not been observed or reported by Meegan *et al.*[357, 410, 504] Relative *cis:trans* ratios for lead analogues are determined by reaction conditions (temperature, solvent and choice of base). Order of reagent addition and substitution patterns on the acid chloride and/or imine precursors also influence stereochemical outcomes.[520] Optimisation of the Staudinger reaction is necessary to minimise the less biologically active *cis* isomer and maximise the available yield of *trans* racemate for the resolution procedure.

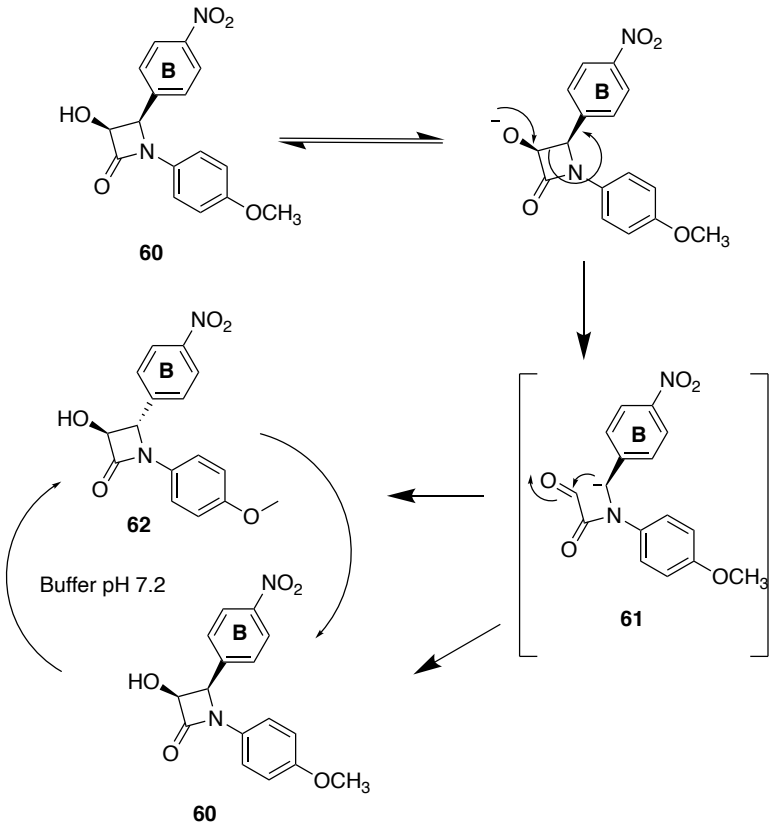

Scheme 2.5: Epimerisation of B ring *para*-nitro substituted 2-azetidinone in Na_2PO_3 basic conditions to a mixture of *cis* and *trans* equilibrating adducts.[419]

Stereoselectivity of the reaction is controlled by two competing factors:[521]

1. Direct ring closure upon acylation of the imine (k_1, Scheme 2.6).
2. Isomerisation of the pre-*cis* zwitterion to the pre-*trans* zwitterion (k_2, Scheme 2.6).[521]

The rate of k_2' is negligible due to steric and geometric favourability between groups R_1 and R_2 in configuration **d** (Scheme 2.6). The rate of direct ring closure (k_1) is determined

by the electronic effects and the substitution patterns on both ketene and imine precursors.

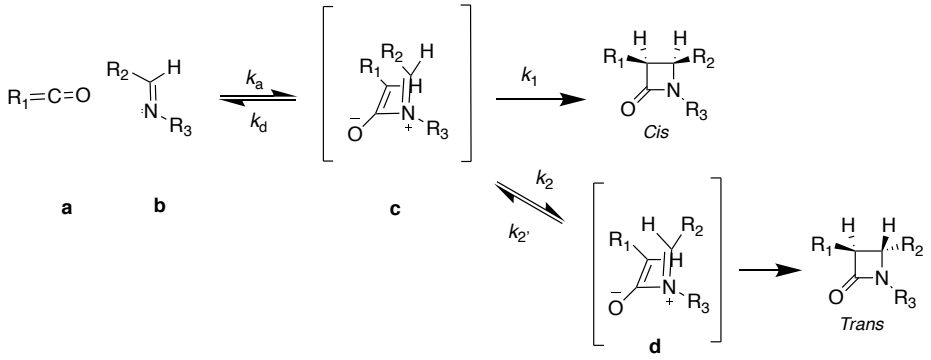

Scheme 2.6: Routes of *cis* and *trans* β-lactam formation in the Staudinger reaction. **a:** Ketene generated from acid chloride **b:** Imine **c:** pre-*cis* zwitterion **d:** pre-*trans* zwitterion. k_1 = direct ring closure. k_2 pre-*cis* zwitterion isomerisation. $k_{2'}$= reversible isomerization of *trans* zwitterion

Electron donating groups on the acid chloride (and therefore ketenes) accelerate ring closure, favouring k_1. In contrast, electron withdrawing groups decelerate the rate of ring closure, favouring k_2 (**c** to **d**, Scheme 2.6) prior to conrotatory electrocyclic ring closure to afford *trans* β-lactams.[522] Acetoxyacetyl chloride is employed for synthesis of the 3-hydroxyl racemates. Since an acetoxy group is electron-withdrawing, it was anticipated that Staudinger reactions would favour k_2 (Scheme 2.6) and result in predominantly *trans* isomers. An electron withdrawing group on the imine will accelerate the rate of ring closure (k_1, Scheme 2.6) favouring formation of the *cis* isomer due to enhancement of the zwitterion's electrophilicity rendering it more susceptible to S_N2 attack by the enolate nucleophile during ring closure.[520, 521] Conclusions are drawn as follows:

1) The relative stereochemistry of β-lactam products is determined by the rate of ring closure, favouring *cis* stereochemical outcomes if $k_1 > k_2$.
2) If $k_2 = k_1$ a mixture of *cis* and *trans* isomers will be formed.
3) Staudinger reaction conditions which favour k_2 versus k_1 should favour formation of the *trans* isomer.[520, 521]

2.4.1 *Staudinger reaction for synthesis of 3-acetoxy-β-lactams*

The preparation of 3-acetoxy-β-lactam racemates employed the Staudinger reaction between acetoxyacetyl chloride, the relevant imine and TEA as the catalytic base (Scheme 2.7). The order of addition of reagents determined the stereochemical outcome

and relative *cis:trans* isomer ratios for **17a**. Preliminary synthesis involved the addition of acetoxyacetyl chloride and imine **44** to anhydrous toluene at 0 °C. TEA was added immediately after warming from 0 °C to room temperature. Despite using the electron withdrawing acetoxyacetyl chloride which was anticipated to favour predominantly *trans* stereochemical outcomes, a 51:49 *cis:trans* ratio was observed, **(entry 1**, Table 2.3) determined using the crude ^{1}H NMR spectrum at 400 MHz in $CDCl_3$ and ^{3}J values for β-lactam H_3 and H_4 doublets. Geometric isomers of β-lactam structures are easily distinguished on using the β-lactam H_3 and H_4 resonances (Scheme 2.7), characteristically split by one another into doublets. *Cis* isomers resonate with larger ^{3}J values of 4-5 Hz, in comparison to smaller values of 1.8-2 Hz for the corresponding *trans* isomers.[385, 514] Stereochemical outcomes were determined using integration of the H_3 resonance and normalising to 100%. **17a** was isolated in 61% yield using preliminary reaction conditions (**entry 1**, Table 2.3). The isomeric β-lactam mixture was treated with hydrazine dihydrochloride and TEA in anhydrous methanol (**c,** Scheme 2.7) to yield the free 3-hydroxyl isomeric racemate in 55% overall yield. The *cis* and *trans* isomeric mixture of **17** required LC purification resulting in only 33% of *trans* 3-hydroxyl β-lactam (**17**). Emphasis was placed on determining optimal conditions for large scale synthesis of exclusively the *trans* isomer of **17** prior to synthesis of the remainder of the 3-acetoxy panel [**16a-22a** and **63a, 64a** and **65a** (Scheme 2.7)]. A detailed reaction mechanism for the Staudinger reaction is illustrated in Scheme 2.8.

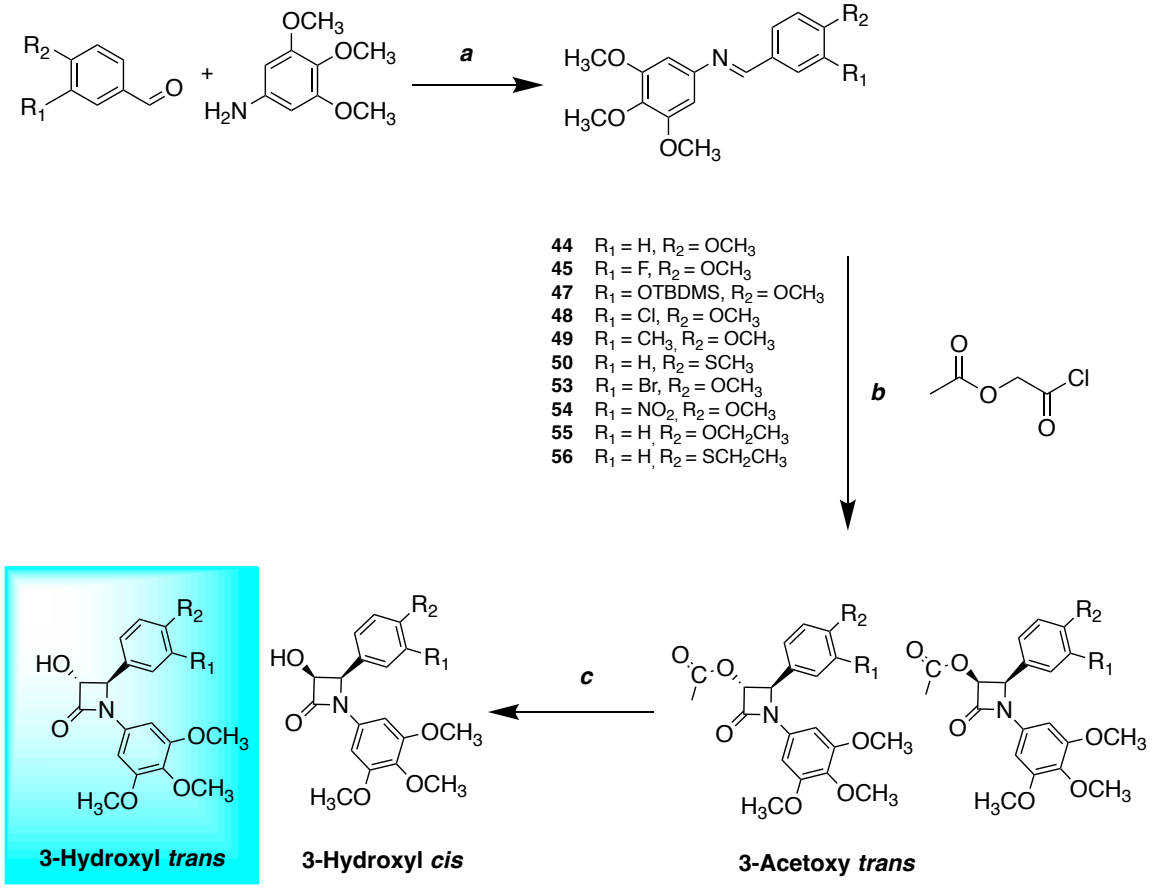

44 $R_1 = H$, $R_2 = OCH_3$
45 $R_1 = F$, $R_2 = OCH_3$
47 $R_1 = OTBDMS$, $R_2 = OCH_3$
48 $R_1 = Cl$, $R_2 = OCH_3$
49 $R_1 = CH_3$, $R_2 = OCH_3$
50 $R_1 = H$, $R_2 = SCH_3$
53 $R_1 = Br$, $R_2 = OCH_3$
54 $R_1 = NO_2$, $R_2 = OCH_3$
55 $R_1 = H$, $R_2 = OCH_2CH_3$
56 $R_1 = H$, $R_2 = SCH_2CH_3$

d
67 $R_1 = OTBDMS$, $R_2 = OCH_3$
16 $R_1 = OH$, $R_2 = OCH_3$
17 $R_1 = H$, $R_2 = OCH_3$
18 $R_1 = F$, $R_2 = OCH_3$
19 $R_1 = Cl$, $R_2 = OCH_3$
20 $R_1 = CH_3$, $R_2 = OCH_3$
21 $R_1 = Br$, $R_2 = OCH_3$
22 $R_1 = H$, $R_2 = SCH_3$
e
63 $R_1 = NO_2$, $R_2 = OCH_3$
23 $R_1 = NH_2$, $R_2 = OCH_3$
65 $R_1 = H$, $R_2 = OCH_2CH_3$
66 $R_1 = H$, $R_2 = SCH_2CH_3$

16a $R_1 = OTBDMS$, $R_2 = OCH_3$
17a $R_1 = H$, $R_2 = OCH_3$
18a $R_1 = F$, $R_2 = OCH_3$
19a $R_1 = Cl$, $R_2 = OCH_3$
20a $R_1 = CH_3$, $R_2 = OCH_3$
21a $R_1 = Br$, $R_2 = OCH_3$
22a $R_1 = H$, $R_2 = SCH_3$
e
63a $R_1 = NO_2$, $R_2 = OCH_3$
23a $R_1 = NH_2$, $R_2 = OCH_3$
65a $R_1 = H$, $R_2 = OCH_2CH_3$
66a $R_1 = H$, $R_2 = SCH_2CH_3$

Scheme 2.7: Staudinger synthesis of 3-acetoxy-β-lactams and hydrazinolysis to 3-hydroxyl β-lactam racemates. Reagents and conditions: **a:** Ethanol, reflux, 4h, 0.1M HCl. **b:** acetoxyacetyl chloride, TEA, anhydrous toluene, 100 °C, 5h, inert atmosphere **c:** hydrazine dihydrochloride, TEA, anhydrous methanol, 85 °C, 4h, inert atmosphere. **d:** TBAF, THF, 0 °C, 1h **e:** glacial acetic acid zinc dust, RT, 6 days. Products obtained as racemic mixtures with one enantiomer shown.

2.4.2 *Optimisation of Staudinger synthesis for isolation of trans β-lactam isomers of 3-acetoxy **17a**.*

In order to minimise *cis* yields and favour the formation of 3-acetoxy *trans* **17a** as the prerequisite for chiral resolution, further optimisation of the Staudinger reaction was

carried out. (**entries 2-7**, Table 2.3) During initial optimisation reactions, undesirable *cis* yields between 32 and 51% were observed **(entries 1-4,** Table 2.3) accompanied by problematic co-elution of *cis* and *trans* isomers during LC purification of 3-acetoxy isomeric mixtures.

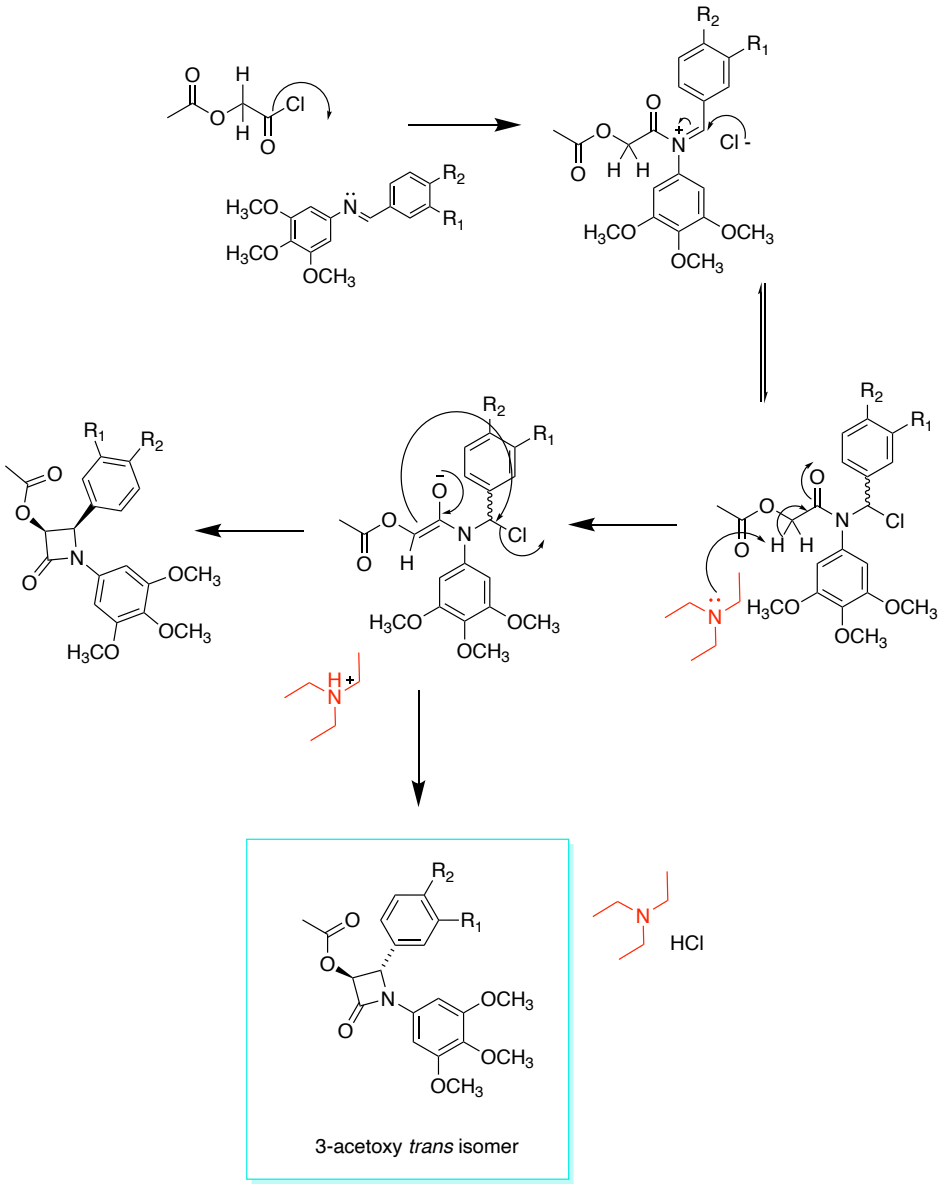

Scheme 2.8: Mechanism for Staudinger synthesis of 3-acetoxy racemates.

The order of reagent addition is reported to influence stereochemical outcomes of the Staudinger reaction. Slow dropwise addition of acid chloride at low temperatures into a solution of imine and base solution is reported in the literature as heavily favouring the formation of exclusively *cis* β-lactams.[515] Therefore time points of reagent addition

were next investigated. The final series of Staudinger optimisation reactions investigated stereochemical outcomes by modifying duration of reaction of acetoxyacetyl chloride and imine **44** prior to addition of base (**entries 5** and **6**, Table 2.3). For entries **5-7** (Table 2.3), acetoxyacetyl chloride was added directly to anhydrous toluene at 0 ºC. Imine **44** was subsequently added to the vessel and heated to reflux for either 45 (**entry 5**, Table 2.3) or 20 minutes (**entry 6** and **7**, Table 2.3) at 100 ºC prior to addition of the TEA. Excellent and almost exclusively *trans* product (94-97%) was observed. Comparative crude ^{1}H NMR spectra demonstrated minimal degradation of imine into parent *para*-anisaldehyde (7% aldehyde: 93% β-lactam) for **entry 6** compared to **entry 5** (45% aldehyde: 55% β-lactam). Lower degradation of precursor imine resulted in increased isolated yield of *trans* 3-acetoxy- β-lactam **17a** from 46% to 58% **(entry 5** versus **6**, Table 2.3). Reaction conditions for **entry 6 (**Table 2.3) was therefore selected as most optimal. **Entry 7 (**Table 2.3) demonstrated that increasing the reaction scale from 5 to 10 mmol accompanied by an increase in solvent volume yielded 60% of 3-acetoxy- intermediate **17a** for proceeding toward resolution optimisation (Chapter 3).

Table 2.3: Preliminary and optimised Staudinger reaction conditions for synthesis of 3-acetoxy-β-lactam **17a**

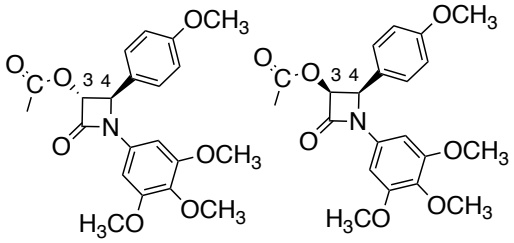

trans ***cis***

Entry	Scale (mmol)	Conditions	*Cis: trans* yield[2]	Isolated yield %
1	5	**a**[3]	51:49	60
2	5	**b**[3]	42:58	Nd
3	5	**c**[3]	32: 68	Nd
4	5	**d**[3]	34:66	Nd
5	5	**e**[3]	4:96	46
6	5	**f**[3]	5:95	58
7	10	**f**[4]	3:97	60

a Imine and acetoxyacetyl chloride at 0 °C. TEA added at room temperature followed by heating to 100 °C.
b Imine and acetoxyacetyl chloride at 0°C. TEA added between 25-100 °C.
c Imine, acid chloride and TEA together at 0°C followed by immediate transfer to 100 °C.
d Imine, acetoxyacetyl chloride followed by TEA at 100 °C.
e Acetoxyacetyl chloride followed by imine at 0 °C. Reflux at 100 °C for 45 minutes followed by dropwise addition of TEA.
f Acetoxyacetyl chloride followed by imine at 0 °C. Reflux at 100 °C for 15-20 minutes followed by dropwise addition of TEA.

One enantiomer illustrated for 3-acetoxy-β-lactam isomers. [2] Calculated from ^{1}H NMR in $CDCl_3$ at 400 MHz; integration of H_3 and H_4 and normalising to 100%. [3] Toluene volume = 50 mL. [4] Toluene volume = 150 mL. Nd = Not determined.

2.4.3 *Optimisation of Staudinger synthesis for isolation of trans β-lactam isomers of 18a*

Staudinger optimisation reactions were also carried out for a second 3-acetoxy-substrate, the B ring *meta* fluorine substituted **18a.** The proportion of *cis* product of **17a** varied between 3-51% (Table 2.3). In contrast, *cis* yields for **18a** were more sensitive to reaction conditions, ranging from 7-80% (Table 2.4). Dropwise addition of TEA while increasing from room temperature to 100 °C resulted in an 80% *cis* yield for **18a** (**entry 4**, Table 2.4), contrasting 42% *cis* yield for **17a** observed using the same conditions (**entry 2**, Table 2.4). Stereochemical outcomes for **18a** appear more sensitive to temperature of TEA addition compared to **17a**. Addition of all three reagents including TEA at reflux resulted in a 45% *cis* yield (**entry 3,** Table 2.4**)** versus previously

described 80% isolated when TEA was added approaching reflux [temperature between 0-100 °C) (**entry 4,** Table 2.4)]. Introduction of the electron withdrawing fluorine atom at the *meta* position of the B ring favours higher *cis* yield for **18a** with respect to **17a**, despite similar size and isosteric nature to the electroneutral hydrogen atom of **17a**. The electron withdrawing fluorine may increase the reactivity of the *N*-acyl-iminium zwitterion, promoting an increased rate of cyclisation rather than pre-*cis* zwitterion isomerization to pre-*trans* zwitterion.

Addition of acid chloride to anhydrous toluene prior to imine (**45**) addition at 0 °C which was followed by heating to reflux and stirring for 20 minutes with subsequent dropwise addition of TEA, gave rise to an excellent *cis*:*trans* outcome of 7:93 accompanied by an excellent isolated yield of 48% (**entry 5**, Table 2.4). Yield was further increased to 58% by reducing the reaction scale from 7.5 mmol (**entry 5**, Table 2.4) to 5 mmol (**entry 6**, Table 2.4)

Table 2.4: Staudinger reaction conditions for synthesis of β-lactam **18a.**

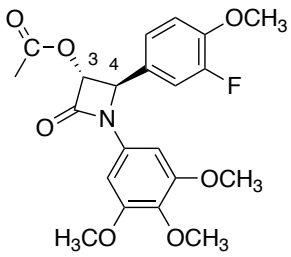

trans

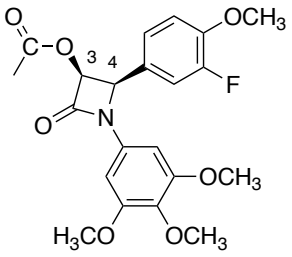

cis [1]

Entry	Scale (mmol)	Conditions	*Cis: trans* yield[2]	Isolated yield %
1	5	**a** [3]	7:93	24
2	10	**b**[3]	36:64	27
3	5	**c**[3]	45:58	37
4	10	**d**[3]	80:20	41
5	7.5	**e**[3]	7:93	48
6	5	**e**[3]	5:95	58
7	7.5	**e**[4]	6:84	68
8	15	**e**[4]	15:85	29

a Imine and acetoxyacetyl chloride at 0 °C. TEA added dropwise over 2-5 minutes at 100 °C.
b Imine and acetoxyacetyl chloride at 0°C. TEA added as one aliquot at RT. Reaction then heated to 100 °C.
c Imine, acid chloride and TEA added together at 0°C followed by immediate transfer to 100 °C.
d Imine, acid chloride and TEA added together at 100 °C.
e Imine, acid chloride and TEA added together at 0°C followed increasing temperature from 0°C to 100 °C

[1]One enantiomer illustrated for each 3-acetoxy- β-lactam isomer. [2]Calculated from ^{1}H NMR in $CDCl_3$ at 400 MHz *via* integration of H_3 and H_4 protons followed by normalisation to 100%. [3] Toluene volume = 50 mL.[4] Toluene volume = 150 mL

Increasing the reaction scale to 7.5 mmol reaction in an increased solvent volume 150 mL of toluene (**entry 7**, Table 2.4) yield 68% of isolated **18a**. Previous reactions on a 7.5 mmol scale in 50 mL of toluene (typical volume of a Staudinger reaction) yielded only 48% of isolated **18a (entry 5**, Table 2.4). When carried out on a 15 mmol scale, lower yields were isolated (29%) and the *cis* ratio was greater [15% (**entry 8,** Table 2.4)]. 7.5 mmol was determined as the optimal scale for **18a** synthesis in 150 mL of toluene.

2.4.4 *Application of optimised Staudinger synthesis for isolation of trans β-lactam isomers of 3-hydroxyl combretazet family.*

The remainder of the 3-acetoxy β-lactam panel (**16a-22a**, **63a, 65a** and **66a**) were synthesised using the optimised Staudinger method (**entry 6**, Table 2.3). Stereochemical

outcomes are listed in Table 2.5. The optimised Staudinger method resulted in moderate to excellent yields for 3-acetoxy racemates from 36 (**22)** – 73% (**19)** (Table 2.5). Stereochemical yields were favourable with > 80% *trans* yield observed for all crude 3-acetoxy β-lactams (Table 2.5). Treatment of 3-acetoxy- β-lactam intermediates with hydrazine dihydrochloride yielded the final 3-hydroxyl β-lactam racemates accompanied by release of acetohydrazide as a by-product (Scheme 2.9). Yields were moderate to good (32-57%, Table 2.5) with the exception of **63a**. Racemate **63a** was susceptible to apparent degradation resulting in poor yield (16%) of 3-hydroxyl **63** (Table 2.5). This was possible due to the highly reactive aromatic B ring *meta*- NO_2. In the presence of hydrazine and base it may be reduced to the corresponding aniline derivative.[523] Degradation products were not however characterised in the present work. Sufficient yield of **63** was isolated for biological evaluation as the racemate of the *trans* isomer. **65a** and **66a** were not isolated from their corresponding 3-acetoxy protected structures using hydrazine dihydrochloride (Scheme 2.9). The 3-hydroxyl structures **65** and **66** (Table 2.5) were yielded using lipase enzymes *via* biocatalytic kinetic resolution which is discussed in Chapter 7.

Table 2.5: Isolated yields for 3-acetoxy and 3-hydroxyl combretazet racemates and stereochemical outcomes.[378, 400]

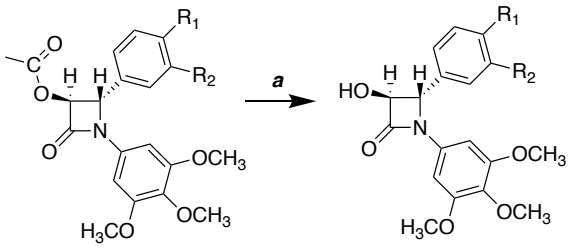

Code	R_1	R_2	3-acetoxy yield (%)	*Cis:trans* ratio[2]	3-hydroxyl yield[1] (%)
17	OCH_3	H	58%	3:97	56%
18	OCH_3	F	68% [3]	6:94	54%
67a	OCH_3	OTBDMS	60%	3:97	43%
19	OCH_3	Cl	72%	5:95	57%
20	OCH_3	CH_3	49%[4]	4:96	46%
21	OCH_3	Br	63%	5:95	44%
22	SCH_3	H	36%	11:89	32%
63	OCH_3	NO_2	60%	16:84	16%
65	OCH_2CH_3	H	45%	20:80	Nd
66	SCH_2CH_3	H	40%	5:95	Nd

All reactions carried out on 5 mmol scale unless annotated.
[1] Total isolated yield from Staudinger reaction. [2] Stereochemical outcome measured using crude ^{1}H NMR in $CDCl_3$ at 400 MHz for 3-acetoxy structures. [3] 7.5 mmol scale. [4] 10 mmol scale Nd: not determined. One enantiomer only illustrated. **a:** hydrazine dihydrochloride, TEA and methanol.

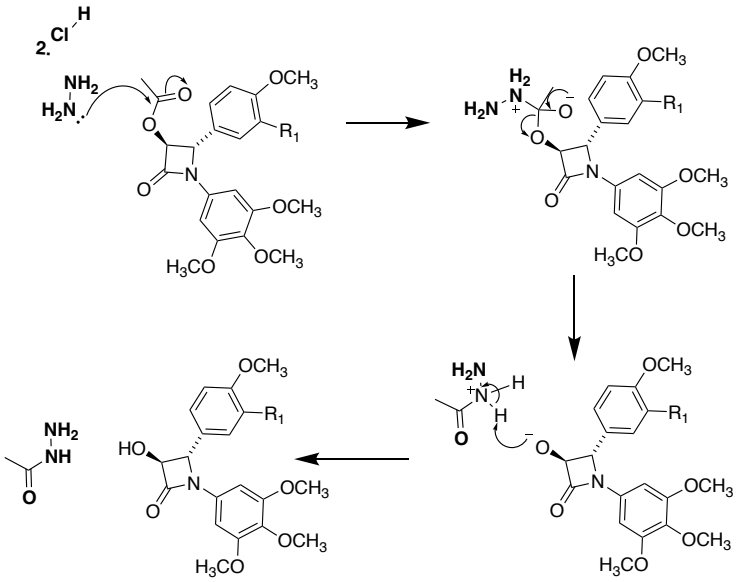

Scheme 2.9: Hydrazinolysis of *trans* 3-acetoxy racemates to yield *trans* 3-hydroxyl β-lactams (one enantiomer shown).

2.4.4.1 *Novel trans **63** and **63a***

3-Acetoxy compound **63a** (Table 2.5) is a novel *trans* racemate previously evaluated *in vitro* only as the *cis* isomer and synthesised *via* a one pot Staudinger reaction of acid chloride, imine and TEA in DCM by Sun *et al*.[386] Excellent anti-proliferative activity in the nanomolar range for **63**'s *cis* isomer has been reported (IC_{50} of 97 nM in MCF-7 breast cancer cells). The corresponding 3-amino-4-methoxyphenyl analogue was superior to the corresponding *cis* nitro substituted analogue (IC_{50} of 81 nM).[386] Since it is known that *trans* isomers are far superior for anti-proliferative activity, stereochemical outcomes for **63a** using the optimised method were investigated. 84% *trans* isomer was observed in the crude product (Table 2.5), exceeding the % of *trans* isomer (0%) previously reported.[386] The XRD structure for **63a** demonstrates the *trans* orientation of H_3 and H_4 protons (Figure 2.3).

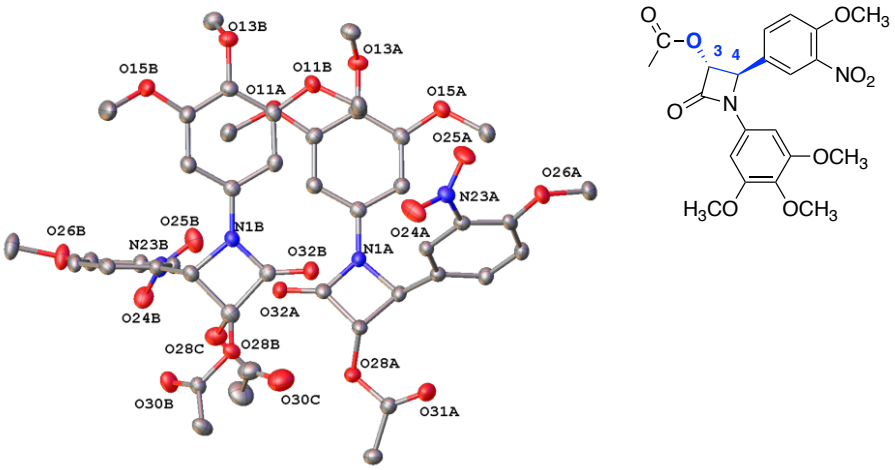

Figure 2.3: XRD of **63a**. Independent molecules in the asymmetric unit of **63a** with atomic displacement shown at 50% probability. Heteroatoms labelled only and hydrogen atoms omitted for clarity. One molecule displays disorder in the acetate groups. *Trans* **63a** illustrated for reference with *trans* configuration at positions 3 and 4 of the β-lactam ring highlighted in blue.

2.4.5 *Synthesis of further trans β-lactams containing the B ring meta hydroxyl or amine substituent group **(24-30, 32, 33, 35, 37,38,40,68,69)**.*

Two other scaffolds were selected for diastereomeric chiral resolution. Both scaffolds contained an appropriate handle for diastereomer derivatisation and were reported as extremely potent 3-racemates.[357, 359,495] These analogues contained either a B ring *meta* 3-hydroxyl (Section 2.4.5.1) or nitro which was then reduced to an amine substituent

(Sections 2.4.5.3 and 2.4.5.5). Scheme 2.10 illustrates the general pathway for synthesis of these analogues.

2.4.5.1 *Analogues with B ring meta hydroxyl substituent* ***(24, 26, 30, 33, 38, 39,40, 41)***

The reaction pathway for synthesis of B ring *meta* hydroxyl substituted combretazet racemates is illustrated by **a** and **f**, Scheme 2.10 synthesised *via* the TBDMS protected phenolic imine **47** (**a,** Scheme 2.10). Isolated yields were poor [average of 30% (Table 2.6)] compared to the 3-hydroxyl β-lactam panel [average of 44% (Table 2.5)] using identical and optimised Staudinger reaction conditions (Section 2.4.2 and 2.4.3). TBDMS intermediate β-lactam racemates were purified using LC prior to TBDMS removal, using TBAF 1M in THF (**f**, Scheme 2.10). Fluoride anion mediated de-protection of TBDMS was rapid, reaching completion in under 1 hour.

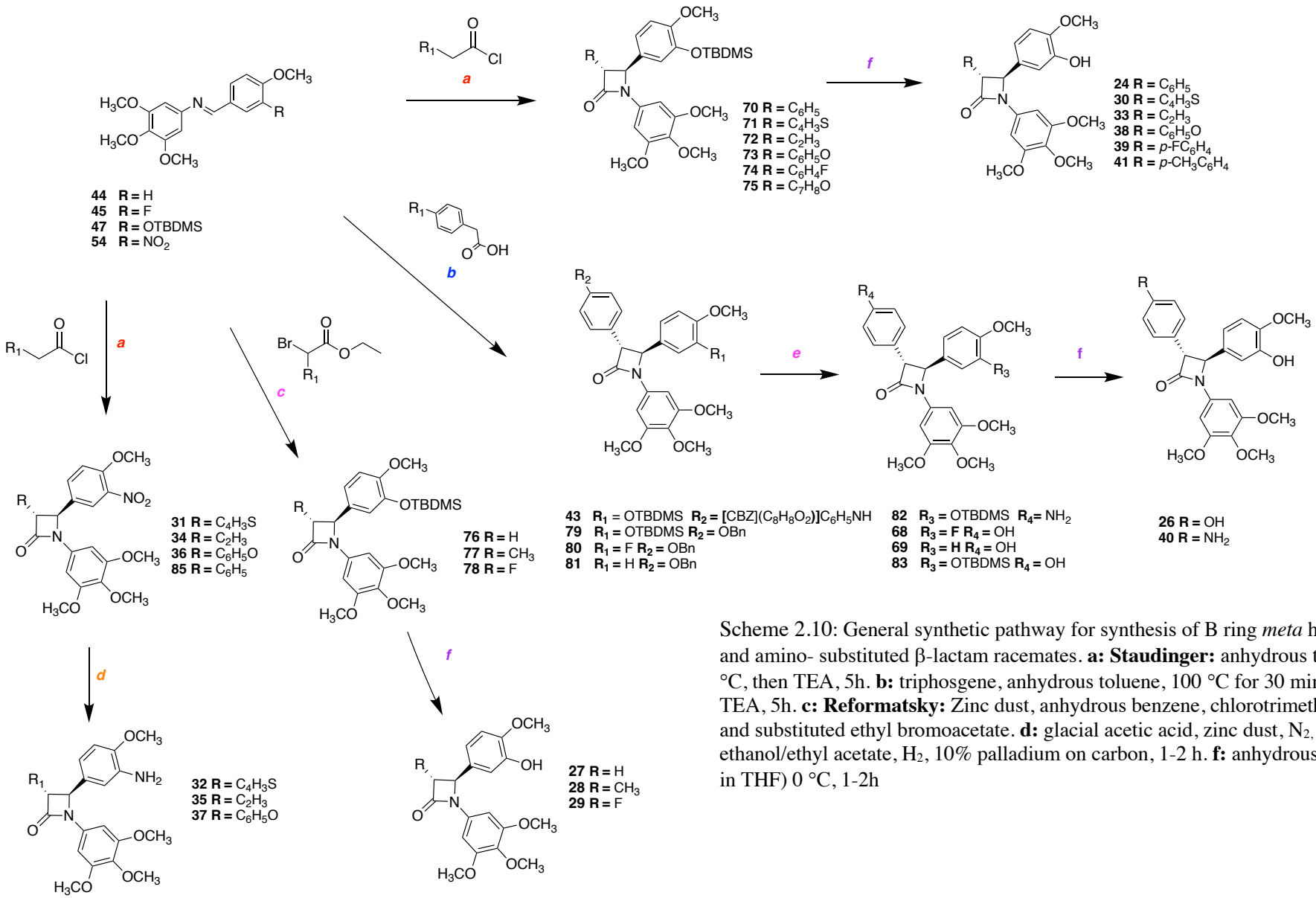

Scheme 2.10: General synthetic pathway for synthesis of B ring *meta* hydroxyl-, nitro- and amino- substituted β-lactam racemates. **a: Staudinger:** anhydrous toluene, N_2, 100 °C, then TEA, 5h. **b:** triphosgene, anhydrous toluene, 100 °C for 30 minutes, then imine, TEA, 5h. **c: Reformatsky:** Zinc dust, anhydrous benzene, chlorotrimethylsilane, N_2, **47** and substituted ethyl bromoacetate. **d:** glacial acetic acid, zinc dust, N_2, 6 days. **e:** 1:1 ethanol/ethyl acetate, H_2, 10% palladium on carbon, 1-2 h. **f:** anhydrous THF, TBAF (1M in THF) 0 °C, 1-2h

Table 2.6: Isolated yields and stereochemical outcomes for 3-substituted combretazets containing the B ring *meta* hydroxyl substituent.[378, 400, 495]

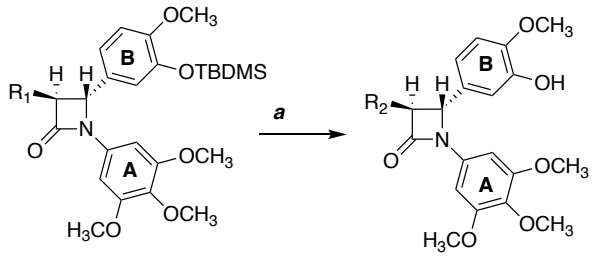

Code	R_1	R_2	Yield from Staudinger reaction (%)	Yield of racemate[1] (%)	Ratio of *cis:trans* isomers[3]
24	C_6H_5	C_6H_5	32	18	6:94
30			58	32	0:100
33	C_2H_3	C_2H_3	Nd[2]	28	0:100
38	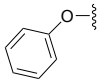	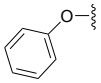	37	32	9:91
39	*p*-F(C_6H_4)	*p*-F(C_6H_4)	42	40	10:90
40	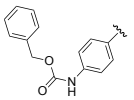	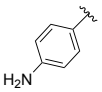	37	Not isolated[2]	0:100
41	*p*-$OCH_3(C_6H_4)$	*p*-$OCH_3(C_6H_4)$	57	43	0:100

a: anhydrous THF, TBAF (1M in THF) 0 °C, 1-2h. [1] Total isolated yield from Staudinger synthesis. [2]Yield too poor for isolation of pure material. [3]Calculated from ^{1}H NMR in $CDCl_3$ at 400 MHz *via* integration of H_3 and H_4 protons followed by normalisation to 100%. ***a:*** anhydrous THF, TBAF 1M in THF, 0 °C, 1-2h.

B ring *meta* hydroxyl substituted racemates were synthesised in favourable *trans* yield [90% - 100% (Table 2.6)]. 3-Phenoxy substituted analogue **38** was synthesised in 91:9 *trans*:*cis* isomer yield (Table 2.6), previously only reported by Greene *et al* as a mixture of isomers (75:25 *cis:trans*).[357] This increase in % of *trans* isomer for β-lactam **38** with respect to previously cited values supports the hypothesis that the optimised reaction favour *trans* stereochemical outcomes predominantly and proceeds through the *N*-acyliminium chloride zwitterion which may isomerise to the *trans* isomer prior to ring cyclisation once TEA is added (Scheme 2.4 and Scheme 2.6).

Silyl ethers are electron-donating in nature[524] and are reported to stabilise oxocarbenium cation intermediates at their anomeric carbon intermediates in silyl assisted glucosylation.[525] High yields of the *trans* isomer observed on the ^{1}H NMR spectra of crude TBDMS protected B ring *meta* hydroxyl intermediates is explained by the electron-donating nature of silyl ether OTBDMS, which assists the stability of the acyliminium zwitterion. Donation of the oxygen's lone pair of electrons through the conjugated B ring system results in a higher electron density within the delocalised π-electron system. This delocalised π electron system has potential to stabilise the site susceptible to intramolecular nucleophilic attack during ring cyclisation (**A**, Scheme 2.11). The net result is a slower rate of ring cyclisation and opportunity for isomerisation of the *N*-acyl-iminium chloride zwitterion to the desirable *trans* isomer.

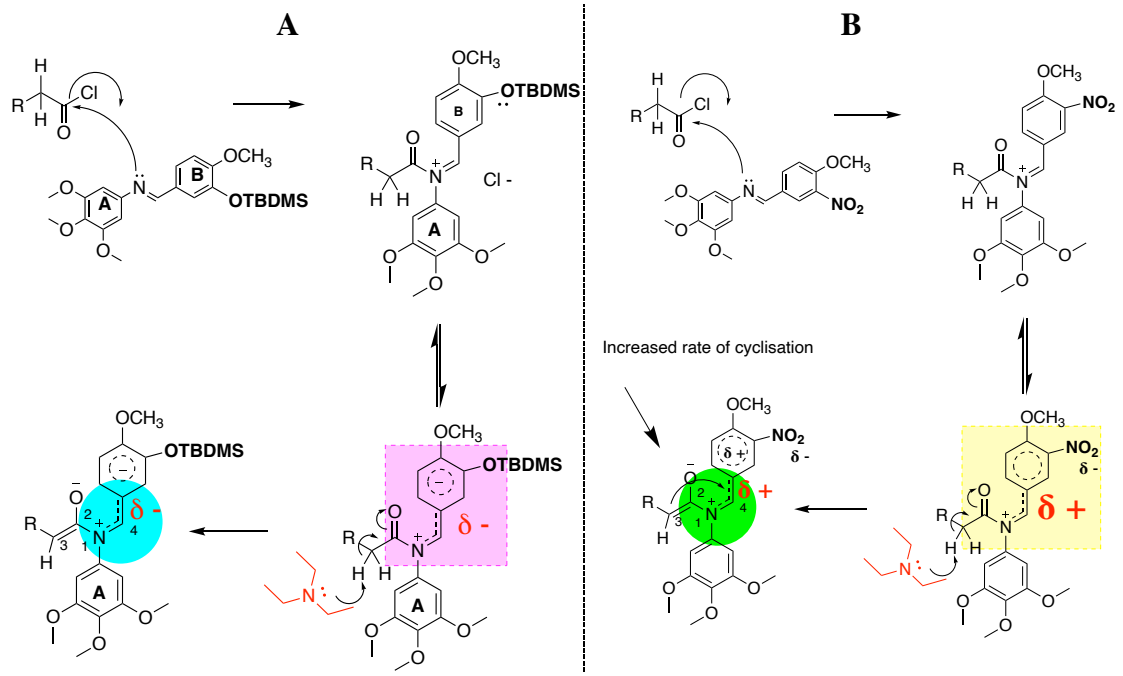

Scheme 2.11: Comparison of **A:** Electronic effects for electron donating B ring *meta* OTBDMS ether favouring *trans* β-lactams **B:** Electronic effects for electron withdrawing B ring *meta* NO_2 favouring *cis* β-lactams.

Racemate **40** was synthesised *via* the benzylcarbamate-protected 3-aminophenyl and B ring *meta* OTBDMS protected analogue **43**. Palladium catalysed hydrogenolysis was required for benzylcarbamate deprotection (**e**, Scheme 2.10) followed by TBAF-mediated removal of TBDMS from **82** to generate the phenolic *meta* hydroxyl of **40** (Scheme 2.10). Since both synthetic steps required purification, the yield of final racemate **40** was too low for further progression toward chiral resolution.

2.4.5.2 *Further NMR studies of previously reported combretazet* ***33***

The vinyl bond at position 3 of compound **33** demonstrates interesting ^{3}J *cis* and *trans* coupling in addition to ^{2}J geminal coupling which differs from the typical *trans* β-lactam hydrogen doublet presentation (Figure 2.4). Complex multiplets are observed at δ 6.03, 5.39 and 5.33 ppm, assigned to $H_{8'}$, $H_{10'}$ and $H_{9'}$ respectively. The apparent multiplet at δ 6.03 ppm is characterised as a triplet of doublets, with $H_{8'}$ coupling to $H_{9'}$ with a *cis* ^{3}J coupling constant of 10 Hz while also coupling to $H_{10'}$ by the *trans* ^{3}J coupling constant of 17 Hz. Lastly $H_{8'}$ couples to $H_{3''}$ with a ^{3}J value of 2.2 Hz. The resonances at δ 5.39 and 5.33 ppm are assigned to geminal vinyl protons $H_{9'}$ and $H_{10'}$ as doublets of triplets split by geminal ^{2}J coupling of 1.8 Hz. For $H_{10'}$ which resonates more downfield at δ 5.39 ppm, this doublet is further coupled to $H_{8'}$ by a larger *trans* coupling constant of 17 Hz. In contrast, for $H_{9'}$, the doublets are coupled with $H_{8'}$ with a smaller cis ^{3}J coupling constant of 10.3 Hz (**B,** Figure 2.4)

A

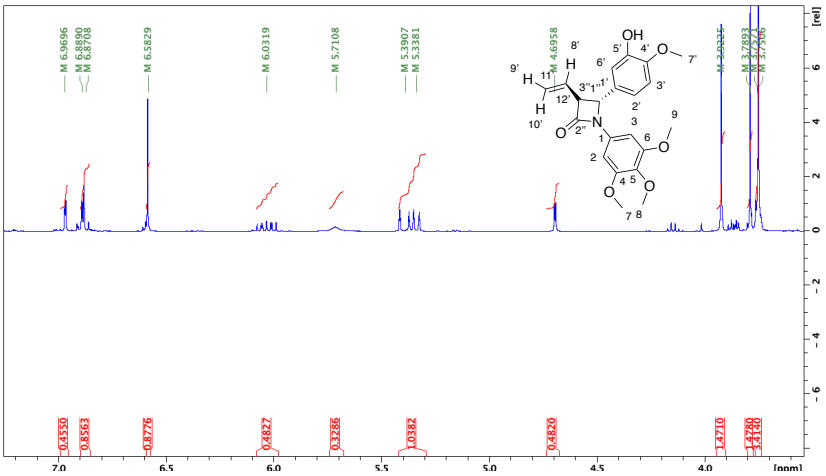

B

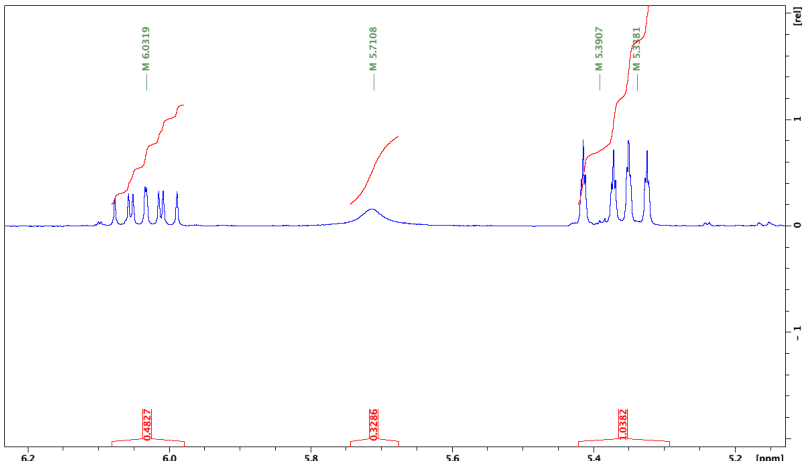

Figure 2.4: **A:** ^{1}H NMR Spectrum for **33** at 400 MHz in $CDCl_3$ **B:** Resonance signals for $H_{8'}$, $H_{9'}$ and $H_{10'}$

2.4.5.3 *Analogues with B ring 3-nitro substituent.*

Replacement of the B ring *meta* 3-hydroxyl with an electron withdrawing nitro substituent resulted in a much higher *cis* yield (racemates **31** and **36,** Table 2.7) with respect to the corresponding B ring *meta* hydroxyl substituted relatives (**30** and **38,** Table 2.6). Comparing the 3-thiophene β-lactams **31** (nitro-substituted, Table 2.7) and **30** (hydroxyl-substituted, Table 2.6) a larger *cis* proportion of 16% for **31** was observed versus 100% *trans* product for racemate **30**. Both racemate **36** (Table 2.7) and **38** (Table

2.6) are 3-phenoxy substituted. *Cis* yield was 61% for **36** but only 9% for **38**. The presence of an electron withdrawing *meta* nitro substituent on the imine's B ring appears to favour immediate ring cyclisation in the *cis* configuration, increasing *cis* yield for both **36** and **31**. The influence of the electron withdrawing *meta* NO_2 group is illustrated in **B,** Scheme 2.11 and can be compared to donating effect of OTBDMS (**A,** Scheme 2.11).

The larger *cis* yield for racemate **36** (61%) compared to **31**(16%) may be attributed to the electron donating phenoxyacetyl chloride versus weaker electron donating properties of the 3-thiophene substituent.[526] While thiophene is a π electron donor, it is however amongst the weaker of heterocyclic electron donors (furans > pyrroles > thiophene > pyridine[527]) and much weaker than the more strongly electron donating 3-phenoxy substitution (Table 2.7).

Table 2.7: Yield and stereochemical outcomes for 3-substituted combretazets containing B ring *meta* 3-NO_2 substitutions.[378, 400, 495]

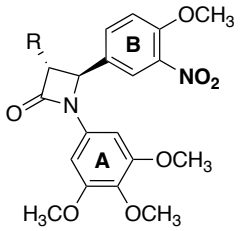

Code	R	Yield from Staudinger (%)	*Cis:trans* ratio
31		40%	16:83
34	C_2H_3	11%	0:100
36	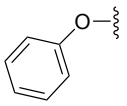	36%	61:39
85	C_6H_5	Not isolated[1]	Not isolated[1]

2.4.5.4 *Unexpected isolation of oxazinone derivative and proposed pathways for its synthesis*

β-Lactam **85 (**Scheme 2.10) was not isolated although observed in very minor yields on ^{1}H NMR of the crude reaction mixture. Instead, an oxazinone structure (**88,** Scheme 2.13) [6-benzyl-2-(4-methoxy-3-nitrophenyl)-5-phenyl-3-(3,4,5-trimethoxyphenyl)-2,3-

dihydro-4*H*-1,3-oxazin-4-one] (Scheme 2.13 and Figure 2.5), was serendipitously discovered. The oxazinone structure was confirmed by XRD analysis (Figure 2.6). Oxazinone structures have previously been reported in the literature. One study reports 40% yield of the unexpected oxazinone during preparation of 3-alkyl β-lactams in solid state Staudinger reactions. Imines were tethered to an fmoc-Gly-Wang resin with a large excess of acid chloride employed. An oxazinone product is explained by dimerisation of ketenes to form of acyl ketenes in presence of large acid chloride excess. In this proposed pathway, the extremely reactive acylketene reacts with the imine dienophile in a [4+2] Diels-Alder reaction (Scheme 2.12).[528] Another study isolated a series of highly substituted 1,3-oxazin-4-one derivatives in attempts to synthesise novel *N*-benzyl-3,4-diaryl substituted 2-azetidinone derivatives as anti-bacterial agents.[529] Biochemical activity for oxazinones isolated from Staudinger reactions are not reported.[529] However efavirenz as an anti-retroviral for the prevention and treatment of HIV contains an oxazinone moiety, which is essential for its metabolism by CYP2B6, demonstrating that oxazinones are not inert structures and are reactive in biological systems.[530]

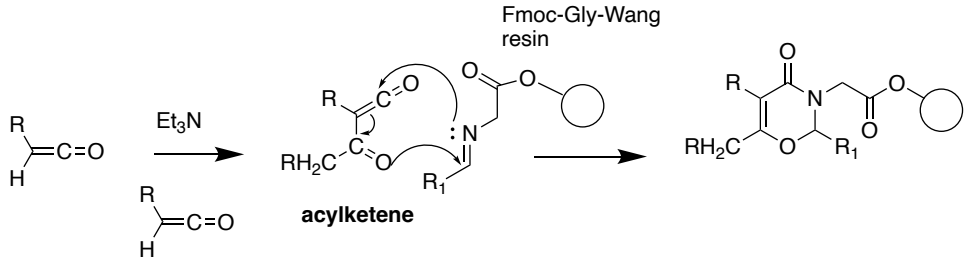

Scheme 2.12: Proposed pathway for oxazinone formation due to dimerisation of ketenes to acylketenes. [528]

Oxazinone structures would be anticipated in crude Staudinger product for all crude β-lactams if the Diels-Alder mechanism outlined in Scheme 2.12 was the principal source of formation. This thesis proposes an alternative mechanism (Scheme 2.13), since **88** was only observed with use of imine **54** in efforts to synthesise **85,** indicating that the electron withdrawing properties of the B ring *meta* nitro substituent of **54** play a role. Scheme 2.13 suggests that oxazinone formation does not proceed *via* the Diels-Alder reaction proposed in Scheme 2.12. Instead Scheme 2.13 suggests that the excess phenylacetyl chloride contributes to the six-membered ring formation of oxazinone (**88**) *via* a double addition of the acid chloride. This mechanism proposes that in the presence of

triethylamine, the acid chloride forms a ketene which reacts with the imine [**54, a**, (Scheme 2.13)] forming zwitterion **86** (**b**, Scheme 2.13). Instead of ring cyclisation, a competing reaction occurs in the presence of excess acid chloride, involving addition of a second equivalent of phenylacetyl chloride with the zwitterion intermediate. The carbanion of the zwitterion acts as a nucleophile to react with carbonyl of a second ketene molecule to form a second zwitterion, **87** (**c**, Scheme 2.13).[342] This second zwitterion cyclises originating from the negative oxygen anion to the positive iminium moiety (**d**, Scheme 2.13).

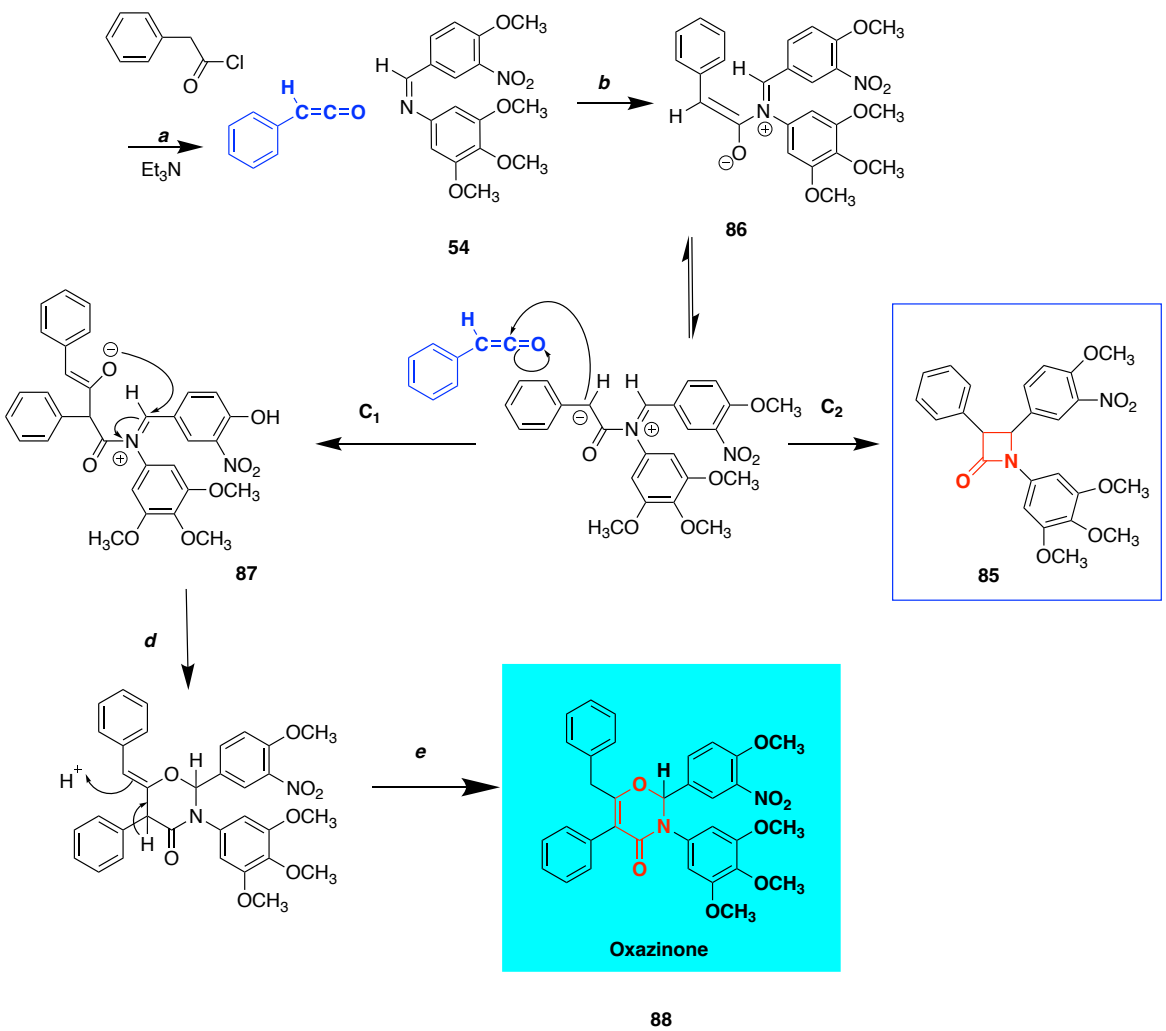

Scheme 2.13: Proposed pathway for the synthesis of oxazinone **88** under typical Staudinger conditions when excess phenylacetyl chloride is used in effort to synthesise **85** with imine **54**. Competing pathways are indicated by $\mathbf{C_1}$ and $\mathbf{C_2}$

The net result of addition of the second acid chloride instead of ring cyclisation is the formation of a six-membered oxazinone ring (**88**) instead of the four-membered β-lactam

(**85**) (**d**, Scheme 2.13). A simple proton abstraction in presence of base TEA and electron rearrangement results in the final oxazinone (**88**) product (**e**, Scheme 2.13). The presence of β-lactam (**85**) in the crude mixture was observed by observation of typical *trans* doublets at δ 4.95 and at δ 4.3 ppm with *J* values of 2.6 Hz, characteristic of the *trans* isomer. The ratio of oxazinone (**88**) to β-lactam (**85**) was determined by integrating the 2H A ring singlet at δ 6.56 ppm for the oxazinone structure and δ 6.54 ppm for H_3 of the β-lactam ring on ^{1} H NMR in $CDCl_3$ at 400 MHz and normalising to 100%. 62% of crude yield was determined as oxazinone while only 38% as β-lactam **85**. β-Lactam **85** was not isolated in its pure form on account of difficult chromatographic separation and low yield.

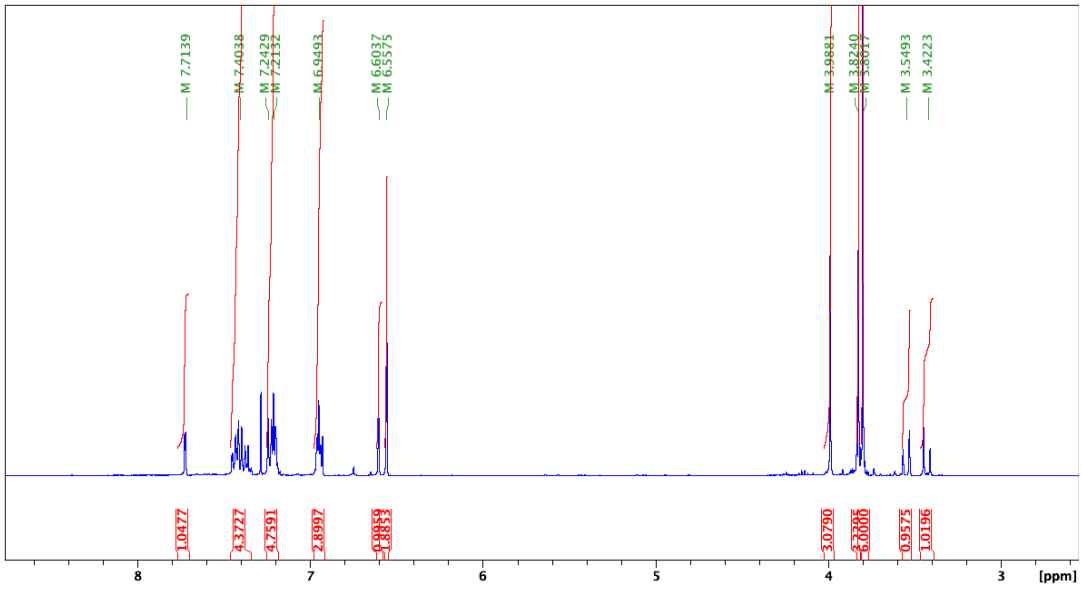

Figure 2.5: ^{1}H NMR spectrum of oxazinone in $CDCl_3$ at 400 MHz.

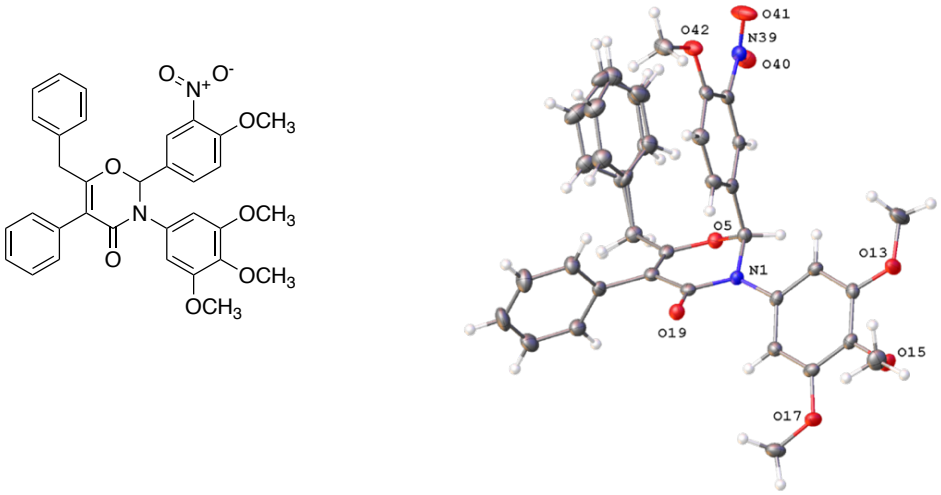

Figure 2.6: XRD structure of oxazinone (6-benzyl-2-(4-methoxy-3-nitrophenyl)-5-phenyl-3-(3,4,5-trimethoxyphenyl)-2,3-dihydro-4*H*-1,3-oxazin-4-one) **88** with atomic displacement shown at 50% probability. Disordered phenyl ring shown and heteroatoms labelled only.

2.4.5.5 *Analogues with B ring meta amino substituent*

The evidence for use of the nitro group in therapeutic agents is contradictory, considered both a pharmacophore but also a toxicophore.[531] Drugs containing the nitro group have potential to induce severe toxicity and are associated with genotoxicity and mutagenicity.[531, 532] For this reason use of the nitro group in drugs is typically avoided. Nitro compounds require enzymatic bio-reductive transformation to induce both therapeutic and cytotoxic effects which is mediated by *in vivo* nitro reductases using NADPH. This involves formation of a nitroso derivative, a nitro radical anion, a nitroxyl radical and hydroxylamine, followed by the bioactive primary amine. Radical anions, nitroso groups and hydroxylamines react with biomolecules to exert mutagenic effects.[533, 534] Toxicity is attributed to such toxic metabolites and their carcinogenic and mutagenic effects.[533] Since the fate of the nitro moiety *in vivo* is bio-reduction to the primary amine, for this reason, in this thesis, the nitro β-lactam analogues were reduced synthetically (Table 2.8 and **d**, Scheme 2.10) to bypass *in vivo* toxicity associated with use of the nitro group. Mild reduction of amino-containing analogues was achieved using the corresponding nitro analogue with zinc dust and glacial acetic acid over a period of six days. Racemates were isolated [**32**, **35** and **37** (Table 2.8)] with aim of using the NH_2 as a handle for amide derivatisation during chiral resolution to the corresponding diastereomers.

Table 2.8: Reduction of *meta* 3-NO_2 B ring substituent to the corresponding 3-NH_2 substituent in β-lactams **32, 35** and **37** and total isolated yields from the Staudinger reaction.[378, 400, 495]

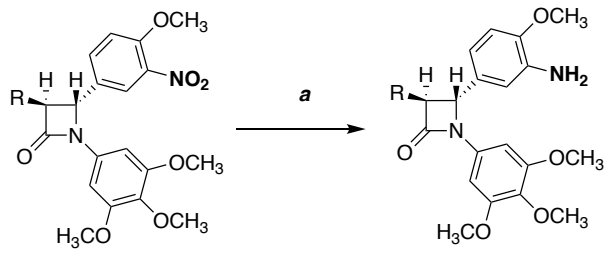

Code	R	Total yield from Staudinger reaction (%)
32	C_4H_3S	11%
35	C_2H_3	20%
37[357, 359, 495]	C_6H_5O	Nd[1]

a: Zinc dust, glacial acetic acid, 6 days. [1]Yield too low for calculation

2.4.6 *Staudinger reaction involving acid activation using triphosgene.*

Where the relevant acid chloride was not available commercially, an acid activation step was carried out using triphosgene [bis(trichloromethyl)carbonate]. Triphosgene is a highly efficient acid activator for β-lactam synthesis using ketene-imine cycloadditions.[535, 536] Other acid activating agents include ethyl chloroformate,[537] trifluoroacetic anhydride,[538] *p*-toluenesulfonyl chloride,[539] phosphorous derived reagents,[540, 541] Mukaiyama reagent[542] and cyanuric chloride.[543] Triphosgene was chosen due to prior successful application in the synthesis of 3-phenolic and 3-aminophenyl combretazets. Triphosgene is added to anhydrous toluene at 100 °C in presence of relevant acetic acid in a ratio of 1:3. Heating results in decomposition to three phosgene molecules which proceed to activate the acetic acid to the corresponding acid chloride (Scheme 2.14).[544] Reactions were carried out as one-pot *in situ* reactions. The imine and catalytic base were added after a 30 minute acid activation period followed by further reflux for 5 hours for synthesis of the desired β-lactam. (4-Benzyloxyphenyl)acetic acid was activated to the corresponding acid chloride for the synthesis benzyl ether protected precursors [**79**, **80**, **81**, Scheme 2.10]. Similarly, the 4-benzyloxycarbonylaminophenyl acetic acid was activated using triphosgene for the synthesis of analogue **40** (Table 2.6) as the benzyl carbamate and TBDMS protected **43** (Scheme 2.14).

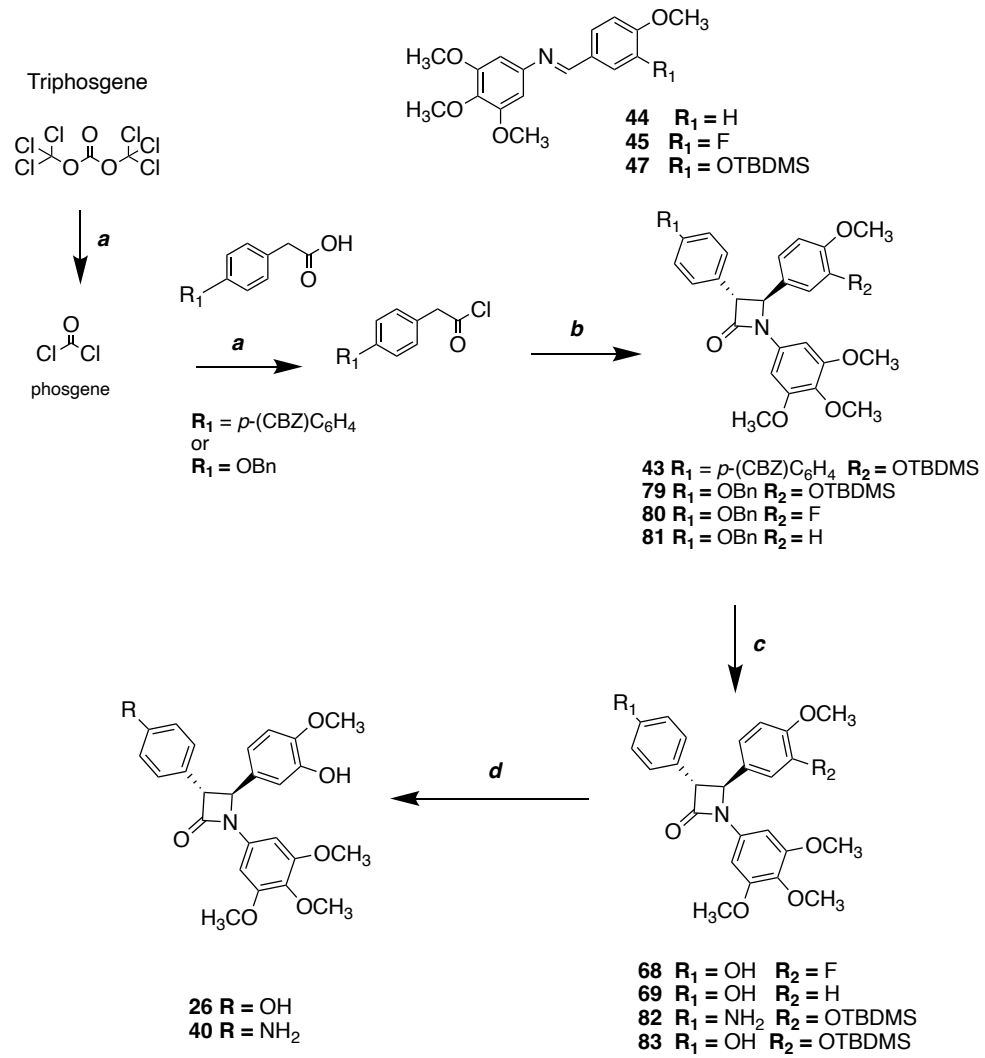

Scheme 2.14: Acid activation of acetic acids to corresponding acid chlorides using triphosgene as acid activator and synthesis of corresponding β-lactams. **a:** 100 °C, anhydrous toluene, 30 minutes at 100°C. **b:** TEA, reflux, 5h. **c:** Pd/C (10%), H_2, ethyl acetate/ethanol (1:1). **d:** TBAF 1M in hexane, anhydrous THF, N_2, 0 °C, 1-2 h

β-Lactam **26** (Scheme 2.14) was selected as lead analogue due to its potent IC_{50} value previously reported in MCF-7 cells of 0.4 nM.[495] Additionally two novel 3-phenolic analogues were synthesised with deletion (**69**) and fluorine substitution (**68**) of the B ring *meta* hydroxyl position, designed to overcome chemoresistance in HT-29 cells.[378, 400] All phenolic analogues were synthesised as the benzyloxy-protected phenol at C-3 ([**79**, **80** and **81**, (Scheme 2.14)] which were reduced H_2, Pd/C to the corresponding phenolic derivative (**d**, Scheme 2.14).

Table 2.9: Isolated yields for 3-phenolic substituted β-lactam analogues.[495]

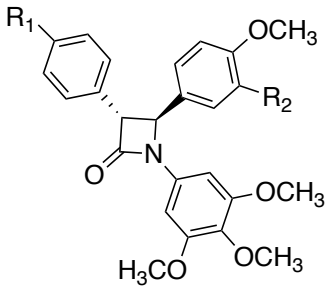

Code	R_1	R_2	Yield from Staudinger (%)	Code	R_1	R_2	Yield of final racemate (%)
79	OBn	OTBDMS	29[1]	**26**	OH	OH	10
80	OBn	F	24[2]	**68**	OH	F	18
81	OBn	H	Nd[3]	**69**	OH	H	13

[1]Reaction carried out on 10 mmol scale. [2]Reaction carried out on 5 mmol scale. [3]Hydrogenated without purification.

2.5 *Analysis of stereochemical outcomes by replacing B ring para -OCH_3 with electron withdrawing substituents*

Stereochemical outcomes for 3-hydroxyl β-lactams of the Staudinger reaction with replacement of the B ring *para*-OCH_3 with an electron withdrawing fluorine (**89**, Table 2.10) or nitro group (**90**, Table 2.10) were investigated. The effects of the acid chloride was also explored by comparing *cis:trans* ratios for two B ring *para*- nitro substituted racemates, 3-hydroxyl **90** and 3-phenyl substituted **91** (Table 2.10). The fluorine analogue **89** was isolated in predominantly *trans* yield [*cis:trans* ratio of 8:92 **(**Table 2.10)]. In contrast B ring *para*-nitro substituted **90** had a higher proporotion of *cis* isomer [1:1 *cis:trans* (Table 2.10)]. *Cis* proportions were lower (20%) for **91** which employed phenylacetyl chloride rather than acetoxyacetyl chloride used to synthesised **90**. A higher *cis* yield was anticipated for **91** using electron donating phenylacetyl chloride due to increased nucleophilicity of the zwitterion in contrast to the electron withdrawing properties of acetoxyacetyl chloride which should favour *trans* β-lactams accordingly.[545] This suggests that acetoxyacetyl chloride may have electron donating properties during the ring cyclisation stages. A proposed mechanism is outlined in Scheme 2.15. Due to electron withdrawing properties of the ester moiety, acetoxyacetyl chloride is electron

withdrawing in its native form and in the final 3-acetoxy β-lactam structure. In contrast the zwitterionic form is a conjugated system (Scheme 2.15) with potential for electron delocalisation due to oxygen's mesomeric effects. Due to π electron delocalisation in the zwitterionic form, the nucleophilicity of the ketene component within the zwitterion increases the rate of β-lactam ring cyclisation and potentially explains a higher than anticipated *cis* yield (Scheme 2.15). The *cis* yield for **91** (20%, Table 2.10) was greater than B ring *meta* hydroxyl substituted relative **24** (6%, Table 2.6) demonstrating that the electronic effects of precursor imines influence *cis:trans* outcomes in the Staudinger reaction.

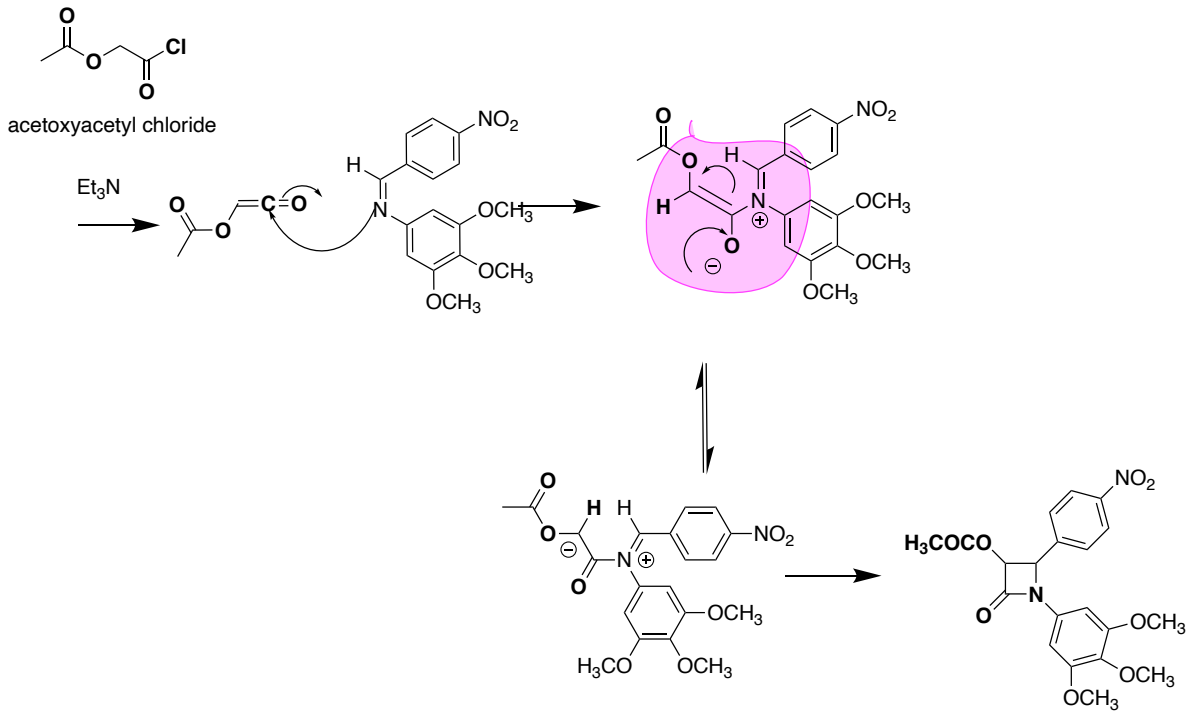

Scheme 2.15: Illustration of electron donating properties of the acetoxyacetyl chloride-derived zwitterionic intermediate during the Staudinger reaction. Electron-donating conjugated system illustrated in pink.

Table 2.10: Table of yields for B ring modified β-lactam analogues.

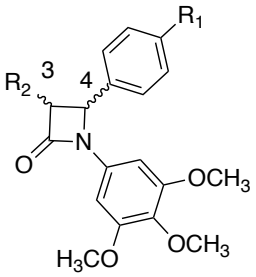

Code	R_1	R_2	*Cis: trans* ratio	Isolated yield from Staudinger (%)	Overall yield (%)
89	F	OH	8:92	30	11
90 ***trans***	NO_2	OH	50:50	Nd[1]	6
90 ***cis***	NO_2	OH	50:50	Nd[1]	1.6
91	NO_2	C_6H_5	20:80	48	48

[1]Not determined. Isolated as a mixture of 3 -hydroxyl *cis* and *trans* enantiomers and purified at the 3-hydroxyl stage

2.5.1 *XRD analysis of **91***

An XRD study was carried out on racemic analogue **91** demonstrating a triclinic unit cells with the 4-nitro group evident in B ring (Figure 2.7). The crystal structure was collected as centrosymmetric space group with chiralities identified as 3*R*,4*S* and 3*S*,4*R* for each enantiomer within the mixture.

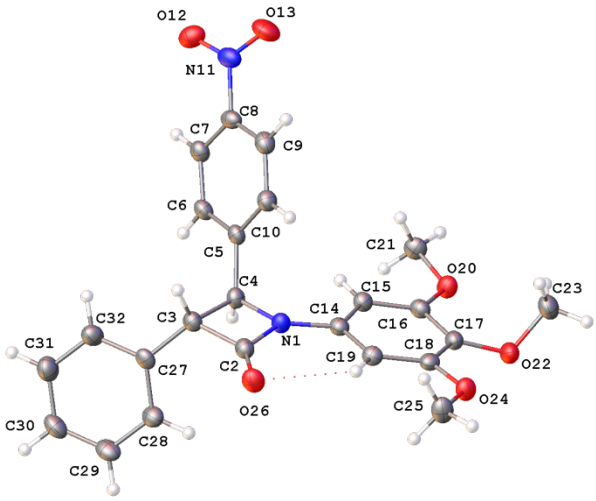

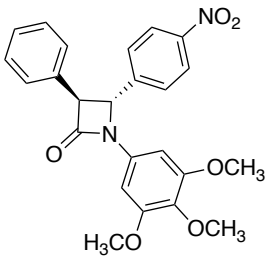

Figure 2.7: Molecular structure of **91** with full atomic labelling. Atomic displacement shown at 50% probability. Displacement at 50% probability. One enantiomer illustrate

2.6 *Amide by-products of Staudinger reaction*

A 3,4,5-trimethoxy containing compound was discovered as a by-product from synthesis of racemate **70**. The ^{1}H NMR spectra of the purified powder demonstrated the presence of a phenyl ring in the δ 6.7-7.4 ppm region and trimethoxy A ring in the δ 3.7-3.9 ppm region. The absence of any β-lactam hydrogens in the H_3 and H_4 δ 4-6 ppm region indicated that the 2-azetidinone **70** structure was not present. Additionally, a broad singlet was present at δ 7.02 ppm suggestive of presence of either OH or NH (Figure 2.8). A ^{15}N HSQC was obtained at 60.8 MHz demonstrating the presence the nitrogen heteroatom's NH bond at δ 167.8 ppm on ^{15}N NMR in $CDCl_3$. The corresponding proton resonated at δ 7.02 ppm, characteristic of a secondary amine. HRMS resulted in a mass of 302.138685 [M + H^+]. XRD analysis of **92** confirmed the structure as an amide (Figure 2.8).

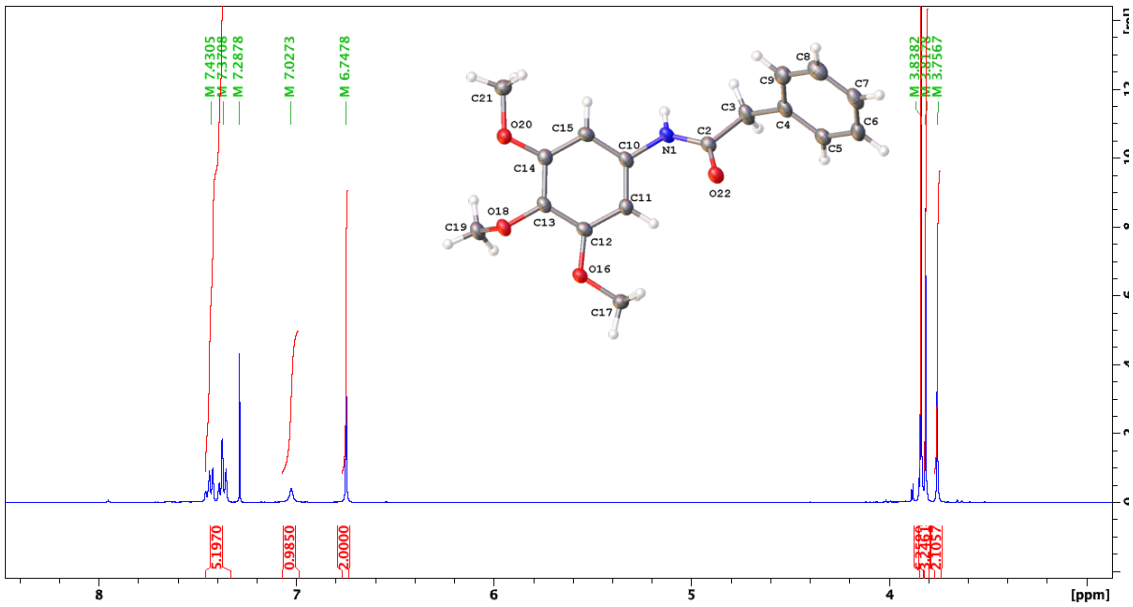

Figure 2.8: ^{1}H NMR data for **92** in $CDCl_3$ at 400 MHz. XRD structure of **92** with atomic displacement shown at 50% probability illustrated.

Evidence of similar structures were observed on ^{1}H NMR of crude mixtures for **17a**, **38** and **79**. Acetoxyacetyl chloride was used for **17a**, 4-(benzyloxyphenyl)acetic acid for **79** and phenoxyacetyl chloride used in the case of **73**. Scheme 2.16 proposes that the amides are formed by reaction of the acid chloride directly with 3,4,5-trimethoxyaniline as a side reaction during Staudinger synthesis of β-lactam structures. The presence of water in

reaction vessel influences the breakdown of imine into aldehyde and primary amine (3,4,5-trimethoxyaniline). Upon addition of acid chloride, two alternative reactions happen simultaneously; the first being the Staudinger cycloaddition to relevant β-lactam and the second being the reaction of the imine breakdown product with the relevant acid chloride to form amide by-products (Scheme 2.16).[342]

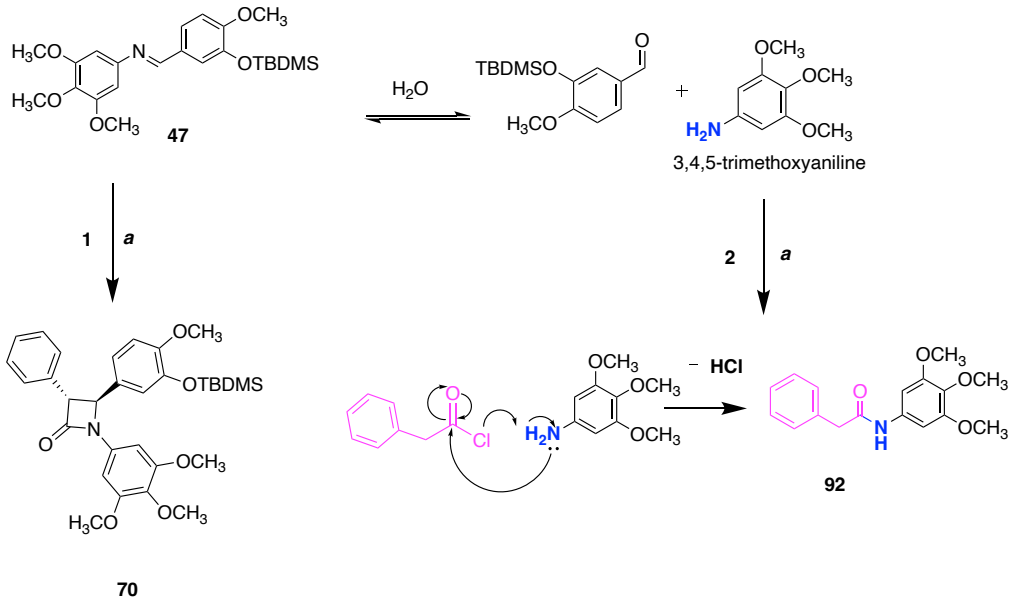

Scheme 2.16: Competing reactions for formation of β-lactam **70** in the Staudinger reaction (**1**) versus condensation of primary amine 3,4,5-trimethoxyaniline and phenylacetyl chloride (**2**) to form amide **92**.[342] **a:** Staudinger reaction conditions. Acetoxyacetyl chloride, imine, reflux for 20 minutes at 100 °C, then TEA followed by 5 hour reflux.

A base independent reaction occurs mediated by nucleophilic attack of the primary amine's lone pair of electrons on the δ + carbonyl carbon of the acid chloride to promote departure of chloride leaving group as hydrogen chloride to form amide structures in the presence of water which mediates imine breakdown. To demonstrate the proposed reaction mechanism (**2**, Scheme 2.16), a series of reactions were carried out involving direct reaction of acid chloride and 3,4,5-trimethoxyaniline in toluene at room temperature without the addition of anhydrous TEA as base. Amides readily condensed at room temperature in < 2 hours. Table 2.11 lists the panel of amides synthesised in high yields (53-89%) which were re-crystallised from hot ethanol in purity of > 90%, determined by RP-HPLC. Amides were synthesised with the aim of determining their potential anti-proliferative activity.

Table 2.11: Panel of amides synthesised and general characterisation.

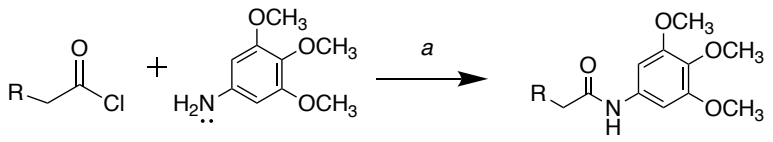

Code	R	Yield (%)	R_f [1]	Melting Point (°C)	IR NH band (cm^{-1})	Purity[3]
92		78	0.47	173-176	3294	95%
93		64	0.21	137	3313	94%
94		53	0.42	178-179	3277	94%
95		89	0.63	144-145	3287	95%
96		66	0.47	152-153	3260	95%
97	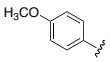	78	0.37	174-175	3330	95%

All reactions were carried out on 2.5 mmol scale. [1] TLC on silica gel (Merck TLC silica plates alumnium F_{254}), mobile phase: 1:1 *n*-hexane: ethyl acetate. **a:** Anhydrous toluene, RT, 1-2 hours.

Table 2.12: XRD structures for amides

Code	Structure	XRD Structure [1]	Detail of hydrogen bonding[2]
93	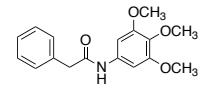	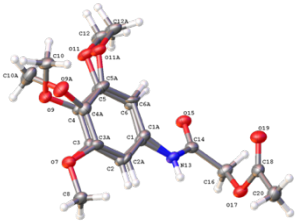	Not observed
94	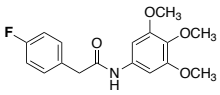	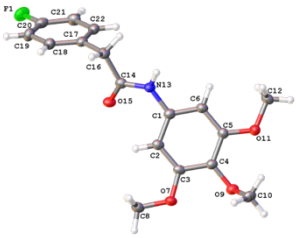	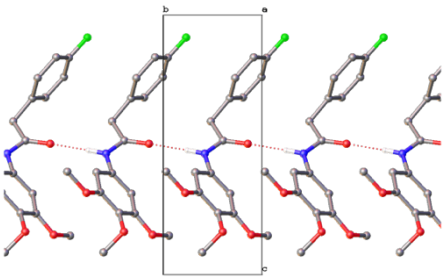
95	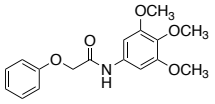	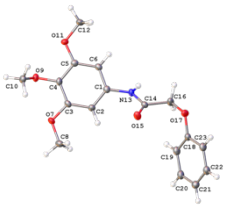	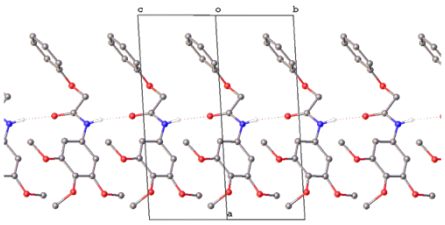
96	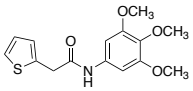	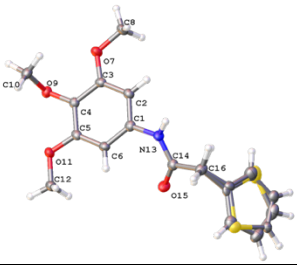	Not observed
97	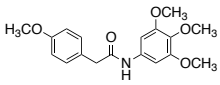	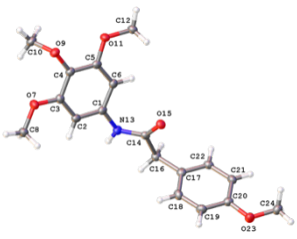	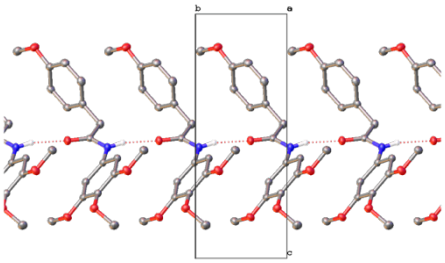

[1]Molecular structure of **93-97** with atomic displacement shown at 50% probability [2] Detail of hydrogen bonding synthon shown normal to the c-axis

2.7 *The Reformatsky reaction*

The Reformatsky reaction is an organometallic reaction involving formation of β-hydroxy esters. It is mediated by metallic zinc with α-haloesters as nucleophiles and aldehydes or ketones as electrophilic substrates.[546, 547-549] The Reformatsky reaction was

first introduced in 1887 initially as a zinc mediated formation of β-hydroxyalkanoates[550] and now extends beyond use of aldehydes and ketones as electrophiles. Many other catalysts in addition to zinc are now used and the reaction is now defined as oxidative metal insertions into carbon-halogen bonds activated by carbonyl related groups in vicinal positions.[551] A reactive enolate is formed due to an equilibrium reaction between the product formed upon oxidative insertion of a metal ion between C-halogen bond of α-haloester. The enolate's alkene double bond is an incredibly reactive nucleophile, responsible for C-C bond formation by attacking the electrophilic carbon of the carbonyl containing substrate. The departure of the halogen and metal atom gives rise to the final β-hydroxy ester product.[549] Electrophilic substrates also include imines. Therefore the Reformatsky reaction in an excellent tool for β-lactam scaffold synthesis which was first described by Gilman and Speeter.[552]

2.7.1 *Microwave technology versus conventional reflux for Reformatsky synthesis*

The Reformatsky reaction (Scheme 2.17) is usually carried out at reflux temperatures by adding a carbonyl substrate and bromo ester simultaneously to a suspension of zinc in benzene. Ultrasonic irradiation has been used as an alternative source of energy for Reformatsky reactions[547,553] ordinarily accomplished by heating by both low intensity ultrasound[554] and also high intensity ultrasound.[450,555] Microwave assisted organic synthesis (MAOS) is particularly beneficial for isolating higher yields accompanied by shorter reaction times and lower environmental impact.[556, 557] For example; reflux to achieve synthesis of **76** and **77** (Table 2.13) required 6-8 hours while MAOS resulted in β-lactam product in relatively similar yields after only 30 minutes at 100 °C. MAOS operates on premise of dielectric volumetric heating as an alternative heat source resulting in faster reaction rates as a result of more uniform heat distribution. Dielectric heating takes advantage of the medium's ability to channel electromagnetic radiation into heat which occurs as dipole ions present in reaction mixture align in applied electric field and attempt to re-align with oscillating electric field. Due to molecular friction and dielectric losses, heat is generated or lost in this process and this drives chemical reactions forward.[558, 559]

When imines react with α-haloesters, a mixture of products is formed; the final cyclised β-lactam or the corresponding β-amino ester or alternatively a mixture of both products.

[555] In the Reformatksy reaction, the δ^+ CH=N imine carbon is the electrophile undergoing nucleophilic attack by the activated δ^- moiety α to the halogen of the α-haloester (Scheme 2.17).

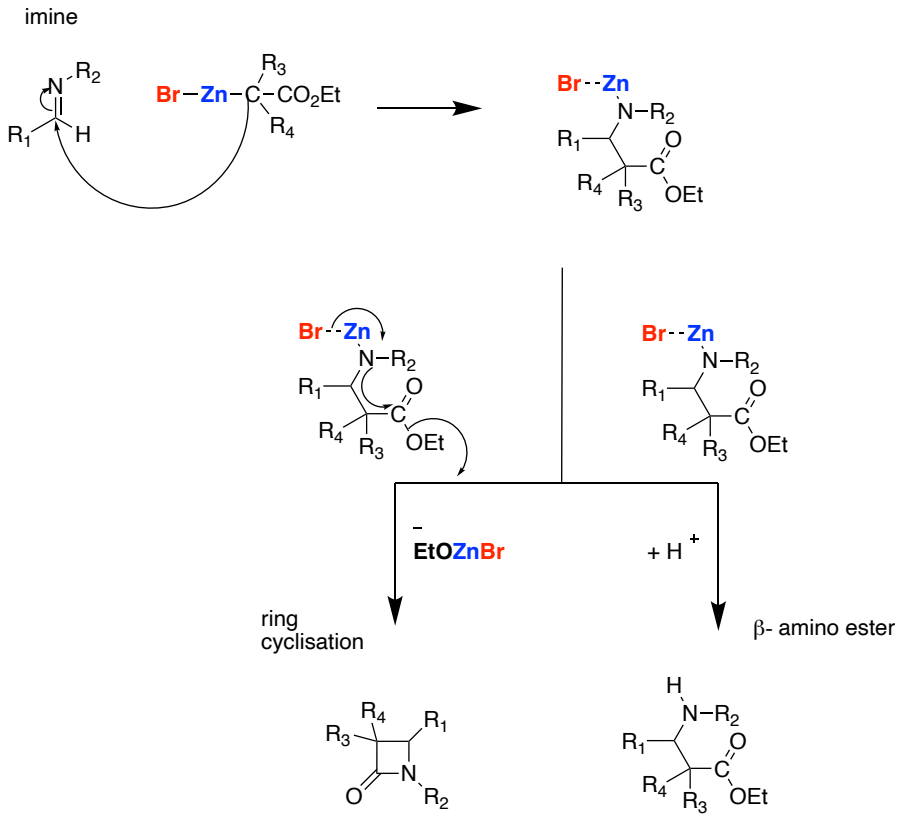

Scheme 2.17: Products formed in Reformatsky reaction using Zn as metal catalyst, and an α-bromo ester as the nucleophile.

Reformatsky reactions were carried out for this project using both conventional reflux and microwave conditions. Zinc dust was activated with trimethylchlorosilane (TMSCl) to remove zinc oxide.[560] Microwave synthesis using the Discover CEM microwave synthesiser reduced the reaction time from 8 hours to 30 minutes. Another previously reported advantage due to benzene's carcinogenicity[448] was the reduction in reaction volume from 20 mL to 4 mL. Zinc activation times were shorter using MAOS rather than conventional reflux (2 versus 5 minutes).

Three racemates (**27**, **28** and **29**) were synthesised using the Reformatsky reaction (Scheme 2.18). Stereochemical and isolated yields obtained *via* microwave synthesis were compared to conventional reflux. These analogues were selected based on their known anti-proliferative potency in MCF-7 cells.[384] Racemate **28** (Scheme 2.18) is

reported as an extremely potent racemate but only as a 2:1 *cis:trans* mixture (IC_{50} value of 10 nM in MCF-7 cells).[384] Isolation of exclusively the *trans* isomer of **28** (Scheme 2.18) was anticipated to significantly increase biological activity. Efforts therefore focused on LC purification of the isomeric mixture obtained *via* Reformatsky synthesis for **28** and its OTBDMS precursor **77** (Scheme 2.18).

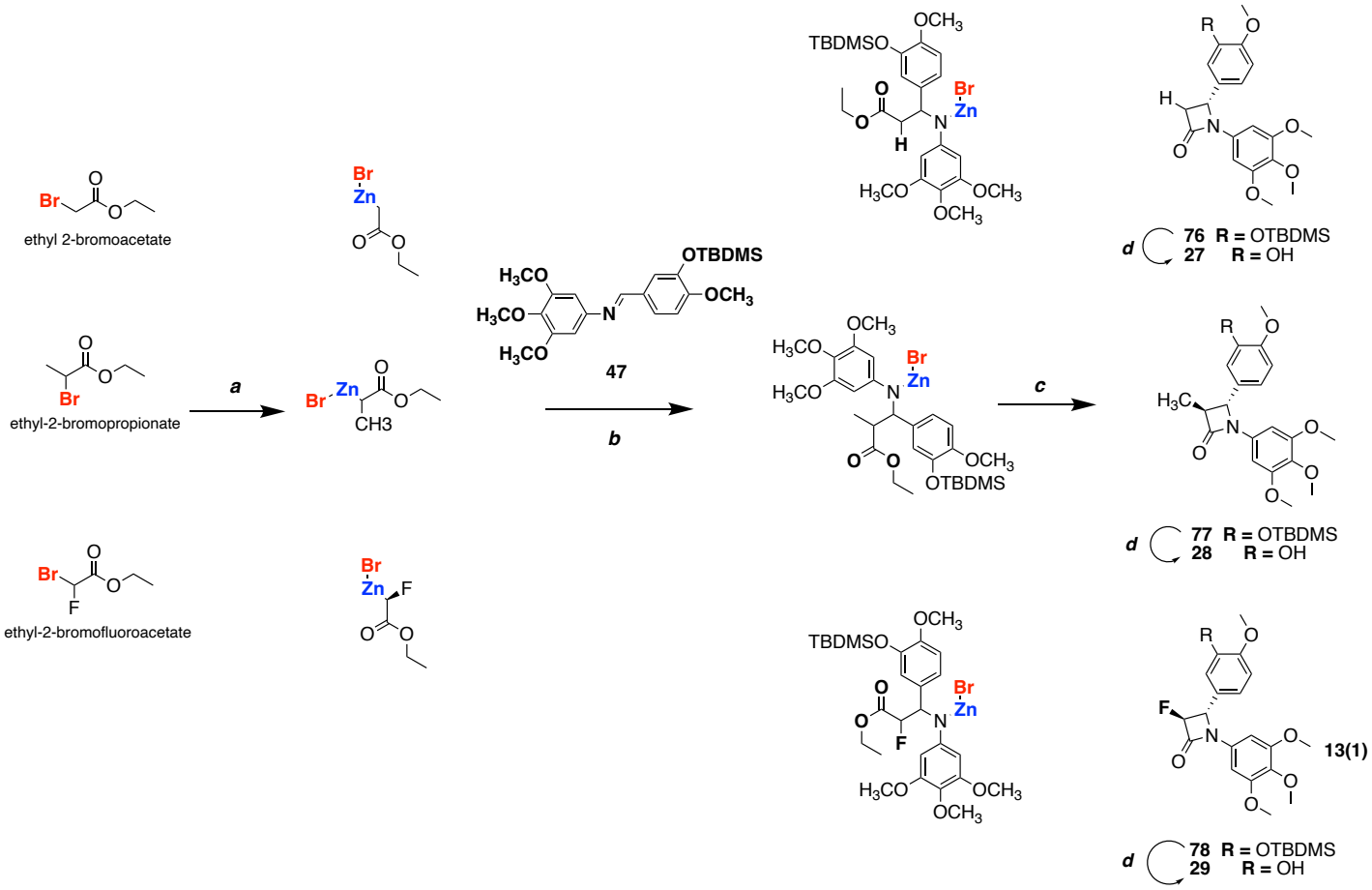

Scheme 2.18: Synthesis of **27-29** *via* the Reformatksy reaction from ethyl-2-bromoacetate, ethyl-2-bromopropionate and ethyl-2-bromofluoroacetate respectively *via* their OTBDMS protected silyl ethers **76-78**. **a:** Zinc, TMSCl, anhydrous benzene **b:** reflux **c:** β-lactam ring cyclisation. **d:** TBAF in 1M hexane, anhydrous THF, 0 °C, 1-2h.

Racemates **76-78** were synthesised using corresponding α-haloesters and silyl ether protected **47** (Scheme 2.18) which were de-protected to the free B ring *meta* 3-hydroxy derivative as the final racemate.

2.7.2 *Comparison of isolated yields and stereochemical outcomes for Reformatsky products using conventional reflux versus MAOS*

Racemates **76** and **77** (Scheme 2.18) were isolated using both reflux and MAOS. MAOS was advantageous in reducing the reaction time and solvent volume. Isolated yields were consistently higher for conventional reflux (Table 2.13). Isolated yields for **76** using reflux was 40% compared to 17% for MAOS. The isolated yield for **77** using reflux was 63% versus 39% for MAOS. Racemate **78** was not successfully synthesised or isolated through conventional reflux. MAOS returned 52% yield for **78** (Table 2.13). Despite higher yields achieved for both **76** and **77** using conventional reflux, repetition of MAOS mediated reactions was a more optimal way for isolation of large quantities of **77** with shorter reaction times.

Table 2.13: Comparative yields of Reformatsky products isolated *via* conventional reflux and MAOS

Code	Reflux			MAOS		
	Scale (mmol)	**Yield %**	***Cis: trans* ratio**	**Scale (mmol)**	**Yield %**	***Cis: trans* ratio**
76	7	40	Na	5	17	Na
77	5	63	75:25	5	39	42:58
78	5	Not isolated	Not isolated	3	52	0:100

NA = not applicable

MAOS consistently returned a higher *trans* yield for **77** compared to conventional reflux (Table 2.13). A 58% *trans* yield was observed using MAOS compared to 25% for conventional reflux. Separation by TLC of *cis* and *trans* isomers was not achieved for **28** following de-silylation to the phenolic *meta* 3-hydroxyl on the B ring. Both isomers had identical R_f values prohibiting separation using LC. In contrast, separation of the TBDMS protected isomers was possible using gradient and gravity elution over silica gel (3:1 to 2:1 *n*-hexane: ethyl acetate). Yields of **77** *cis* and **77** *trans* isomers are detailed in Table 2.14. Only 2% (87 mg) of *trans* **77** was separated from the isomeric mixture while 3%

(110 mg) of *cis* isomer was purified (Table 2.14). De-silylation of the *cis* and *trans* isomers to their final B ring *meta* substituted hydroxyl racemates provided 40 mg of *trans* **28** (71:29 *trans*:*cis*) and 50 mg of *cis* **28** (15:85 *trans:cis*) for biological evaluation, previously only evaluated as a 2:1 *cis:trans* isomeric mixture (Table 2.14).[384] Preparative TLC was also explored, to determine if separation could be achieved. This was limited by sample loading size and band overlap for *cis* and *trans* isomers. The initial *cis* ratio (62%) was reduced only to 56% using preparative TLC. *Trans* **28** was not carried forward for chiral resolution due to limited isolated yield and poor isomeric purity [71%, (Table 2.14)]. Only **27** and **29** were considered as suitable starting materials for chiral resolution.

Table 2.14: Yield of *cis* and *trans* **77** isolated from LC purification of *cis:trans* isomeric mixtures

Isomer	R_f [1]	Yield mg (mmol) %[2]	Isomeric purity*	Yield after de-silylation mg (mmol) %[2]
Trans	0.69	87 (0.18) 2%	71%	40 (0.11) 3%
Cis	0.66	110 (0.23) 3%	85%	50 (0.13) 4%

[1]2:1 *n*-hexane: ethyl acetate. [2] Initial scale of LC purification was 3.5 mmol.

*% of *cis* and *trans* isomer in isolated yields respectively *i.e* maximum *trans* or *cis* proportion isolated in thesis

Use of benzene as the reaction solvent complicated interpretation of crude **78** on ^{1}H NMR spectrum due to anisotropic solvent induced[561] mediated downfield shifts of H_3 and H_4 resonances due to residual benzene present. Benzene is an anisotropic solvent due to its π electron delocalisation. When a compound is dissolved in an anisotropic solvent versus an isotropic solvent such as $CDCl_3$, NMR resonances shift. This is known as ASIS (anisotropic solvent induced shifts).[561] Fluorine coupling at position 3 of the β-lactam ring to both H_3 and H_4 was observed for **78** and **29**. H_3 and H_4 of **78** resonate as apparent double doublets at δ 5.14 (H_3) and δ 4.85 ppm (H_4). The ^2J geminal fluorine coupling constant for 3-F to H_3 is large and typical of F-H *J* values of 48 Hz in combination with typical *trans* β-lactam coupling constants observed of 2.2 Hz. H_4 couples with a smaller ^3J F coupling constant of 25 Hz. (Figure 2.9) Interesting fluorine coupling is observed between quaternary C_2 of the β-lactam ring carbonyl and 3-F of 25.6 Hz on the ^{13}C NMR

spectrum. C-F coupling is also observed for both C_3 (195 Hz) and C_4 (21 Hz). 3-Fluoro substituted racemate **29** was isolated using MAOS in sufficient yield of 56%. However purification of **29** remained an issue due to contamination with residual β-amino acid which was not removed using LC. **29** was therefore unsuitable as a candidate for progression toward chiral resolution.

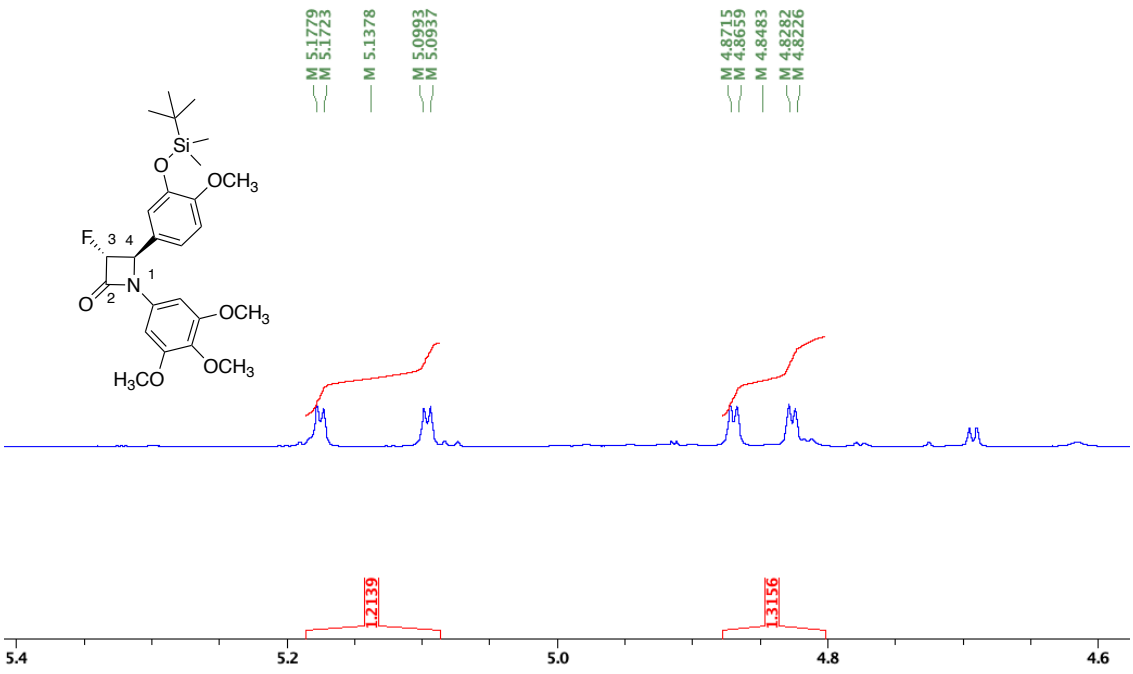

Figure 2.9: ^{1}H NMR of **78** in $CDCl_3$ at 600 MHz with enlargement of H_3 and H_4 region from δ 4.8 to 5.2 ppm.

2.8 *Summary*

The synthesis of a diverse range of β-lactam racemates was described with emphasis on optimising crude and isolated *trans* yields. Successful separation of *cis* and *trans* isomers was achieved by LC in addition to optimising the stereoselective synthesis of exclusively *trans* isomers for many analogues including the 3-hydroxyl substituted β-lactams, B ring *meta* hydroxyl and NH_2 containing analogues. Additionally novel phenolic analogues **68** and **69**, 3-hydroxyl **63**, 3-methyl *cis* and *trans* Reformatsky products **28** in addition to B ring analogues **89-91** have been isolated for *in vitro* biological evaluation as anti-proliferative agents. A number of racemates did not return adequate yield or purity for progression *e.g* **40,** *trans* **28** and **29**. Future work will involve synthesis and isolation of

greater yields for resolution to their enantiomeric forms. Novel oxazinone **(88)** and amides (**92-97**) as by-products from the Staudinger reaction were also isolated and will also be evaluated for their antiproliferative activity. The chemistry described in this chapter serves as an optimal starting point for progression towards diastereomeric and kinetic chiral resolution of combretazet enantiomers for comparative biological evaluation.

Chapter 3 - Optimisation of diastereomeric chiral resolution, 2D EXSY studies and qNMR for β-lactam diastereomer excess determination

3.1 *Chiral resolution as a method for isolation of enantiopure β-lactam combretazets*

Preliminary optimisation of diastereomeric chiral resolution for enantiopure β-lactam isolation from their racemic forms is explored in this chapter for racemate **17** as the most structurally simple 3-hydroxyl analogue. Direct or indirect techniques are options for resolution of enantiomeric mixtures. Direct methods employ chiral chromatographic separation while indirect methods separate enantiomers using optically active CDRs.[562, 563] While direct chiral chromatographic separations using preparative HPLC are among the best methods for enantiomer isolation, this strategy is typically limited by high instrumentations costs and sample loading limitations.[564] Indirect techniques are extremely economical for small scale preparative isolation of enantiomers preliminary *in vitro* evaluation.[565] As mentioned in Chapter 1, asymmetric catalysis has yielded optically pure β-lactams but only as isomeric mixtures, where the *cis* isomer is a significantly less potent anti-proliferative agent than the desirable enantiopure *trans* isomer.[415, 416,566] This chapter pursues an alternative method for isolation of the enantiopure *trans* isomers of β-lactams of **17** (Scheme 3.2). LC chiral resolution following synthesis of *trans* β-lactams racemates is employed. *Trans* racemates are resolved as the corresponding diastereomer derivatives trialing a series of amino acids CDRs.[291] There is a plethora of data on the use of CDRs for indirect separation of enantiomers using HPLC[567] and extensively reported for enantiopure isolation of L-amino acids.[568,569] Amino acids, peptide and peptidomimetics have been employed as chiral selectors for enantioresolution as chiral mobile phase additives using both TLC and HPLC.[570, 571] However, the use and selection of amino acids as CDRs themselves for chiral resolution is not widely reported.[291] Considering previous work demonstrating augmented solubility of β-lactam racemates *via* amino acid prodrug formation,[380] a series of *N*-protected amino acids including *N*-Boc-L-proline were chosen as CDRs for derivatisation of β-lactam **17**. Dual aims of trialling a panel of amino acid CDRs included *in situ* LC chiral resolution of enantiopure β-lactams of **17** and as their derivatised amino acid prodrugs.[380] Resolving powers amongst the panel of *N*-protected amino acid CDRs chosen differed significantly and are discussed in detail in this chapter.

Diastereomer mixtures of **17** (Scheme 3.1) were not readily resolved on achiral reverse phase HPLC. HPLC could not therefore be employed to confirm diastereomer purity or

excess (*de)*[572] following LC chiral resolution. This chapter describes enantiomers derivatisation to the corresponding amino acid CDR protected diastereomers, LC resolution of diastereomers, confirmation of purity using qualitative 2D exchange spectroscopy (EXSY) spectra followed by diastereomeric excess (*de)* determination using quantitative NMR (qNMR) spectroscopy.

3.2 *Chemistry of β-lactam coupling to amino acid CDRs*

Esterification at the 3-hydroxyl position of the β-lactam ring for **17** using selected *N*-protected amino acids was achieved using (2-(1*H*-benzotriazol-1-yl)-1,1,3,3-tetramethyluronium hexafluorophosphate (HBTU), *N,N*-diisopropylethylamine (DIPEA) and acetonitrile (MeCN) at room temperature under inert conditions for 24 hours **(**Scheme 3.2). The mechanism for HBTU mediated coupling is illustrated in Scheme 3.1. The carboxylate anion of the amino acid (**99**, Scheme 3.1) attacks the imide carbon of HBTU (**98,** Scheme 3.1) to form the first HOBt ester of the reaction (**100**, Scheme 3.1). An anionic benzotriazole *N*-oxide is displaced (**101,** Scheme 3.1) which is itself a nucleophile and attacks the carbonyl of activated amino acid (**102,** Scheme 3.1) to yield intermediate **103.** A urea by-product (**104**, Scheme 3.1) is subsequently displaced from intermediate **103** to yield an activated HOBt ester (**105,** Scheme 3.1). Hydrolysis of the HOBt ester by the 3-hydroxyl alcohol moiety of β-lactam **106** yields the desired amino acid diastereomer mixture with displacement of the benzotriazole *N*-oxide.

Diastereomeric mixtures **107-113** (Scheme 3.2) were successfully synthesised in moderate to good yields (31- 77%). Coupling of *N-tert*-butoxycarbonyl-L-histidine and β-lactam **17** was unsuccessful. A preliminary LC purification for separation of the diastereomer mixture from other reaction products was first required. The subsequent resolution of purified diastereomer mixtures employed gravity LC over laboratory grade silica gel to obtain maximum resolution and minimal diastereomer co-elution. Sufficient resolution of diastereomers was achieved using a slow and gradual gradient of 4:1 *n*-hexane: MTBE (methyl *tert*-butyl ether) to 2:1 MTBE: *n*-hexane. Esterification and LC chiral resolution was first trialled with *N*-Boc-D-proline as the CDR yielding diastereomer mixture **107** in 52% yield.

During LC resolution, diastereomers eluting first as herein referred to as **a** and the second diastereomer **b**. *E.g* the first diastereomer eluting of **107** is **107a** while second is **107b** (Scheme 3.2). Success of D-proline diastereomer LC resolution was limited due to significant diastereomer co-elution of **107a** with **107b**, prohibiting progression to the corresponding enantiomers of (+) and (-) **17**. Only 15% of **107a** and 5% of **107b** from their original **107** diastereomer mixture[342] were isolated and only as partially resolved diastereomers determined using TLC. Using the corresponding *N*-Boc-L-proline CDR, a much higher isolated yield of 77% was achieved for diastereomer mixture **108**. LC chiral resolution of **108** resulted in successful isolation of purified diastereomers **108a** and **108b** in good yields of 32% and 37% for progression towards their 3-hydroxyl enantiomers (+) **17** and (-) **17** (Scheme 3.2) using hydrazine dihydrochloride, triethylamine and methanol for removal of the CDR. For all other amino acid CDRs trialled (**109-113**, Scheme 3.2) separation of diastereomers was not achieved on TLC or LC using identical conditions of MTBE:*n*-hexane.

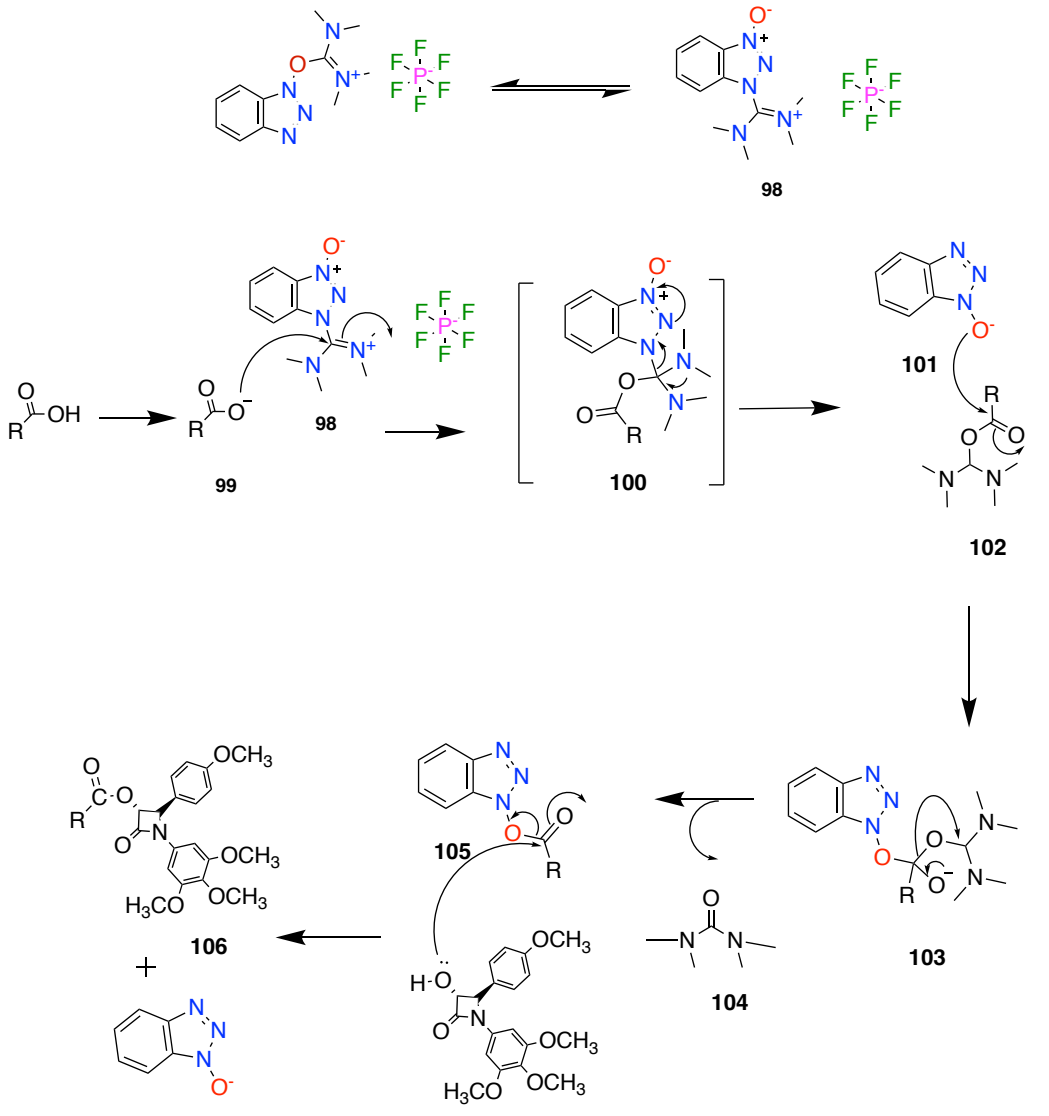

Scheme 3.1: Mechanism of action for coupling of amino acid CDRs to β-lactams using as the peptide coupling reagent. (One diastereomer illustrated isolated as a mixture of diastereomers).

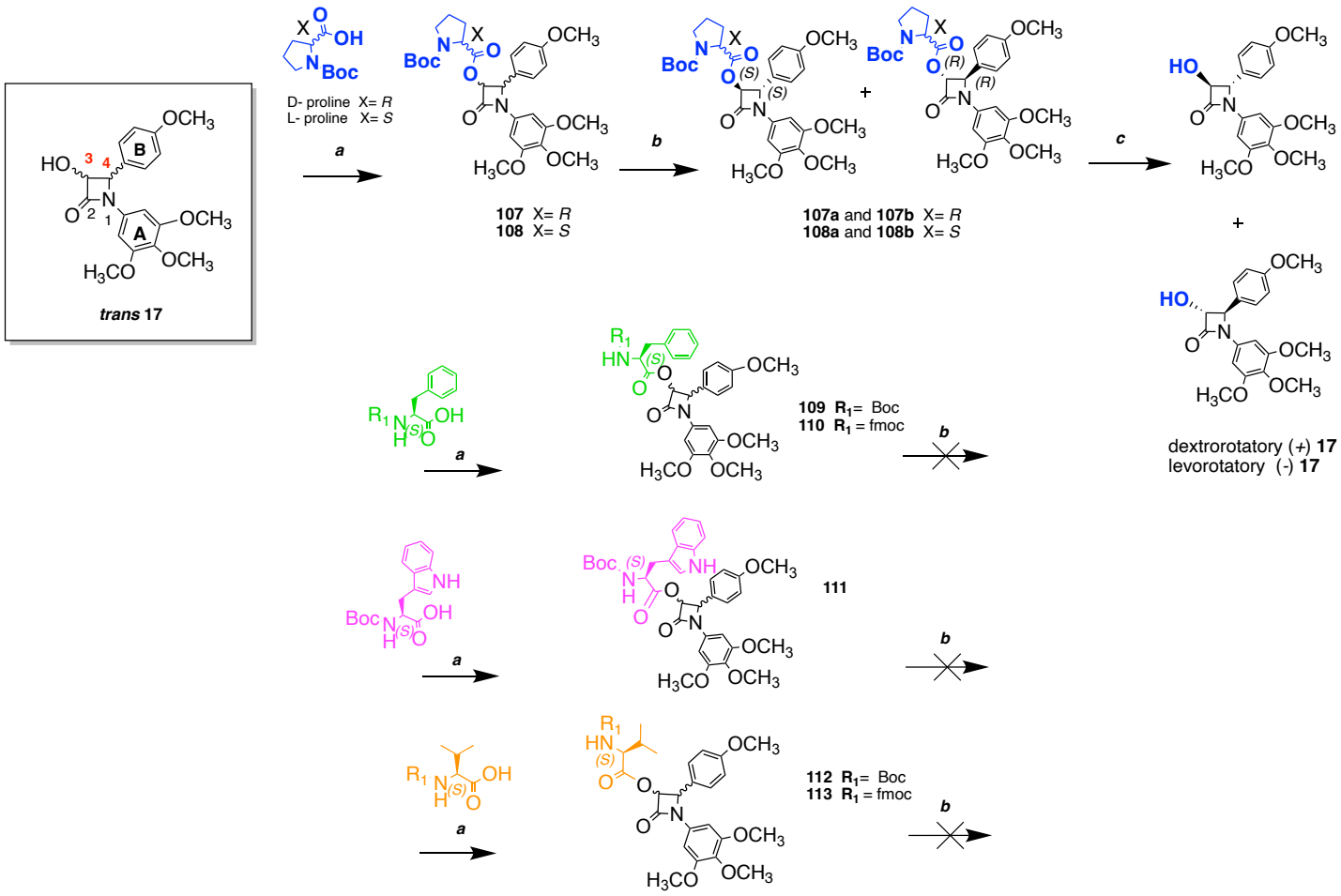

Scheme 3.2: Synthesis and resolution of diastereomer mixtures of *trans* β-lactam **17** (**107-113**) by coupling with amino acid CDRs. **a:** HBTU, DIPEA, anhydrous MeCN, N_2, rt, 24 hr. Yield = 31-77%. **b:** resolution of diastereomers using gravity and gradient elution of MTBE: n-hexane (2:8-2:1) (relative stereochemistry shown). **c:** Hydrazine dihydrochloride, TEA, MeOH, 0 °C, then reflux for 6h.

3.3 *NMR spectroscopy as a proposed method for diastereomer purity determination*

A suitable method was required to establish the diastereomeric excess (*de*) of purified diastereomers following LC chiral resolution (**b,** Scheme 3.2). ^{1}H NMR spectroscopy typically serves as a robust and reliable primary analytical tool for acquisition of purity, orthogonal to HPLC,[573] particularly when HPLC is associated with drawbacks such as inability to detect inorganic impurities, water content, solvent residues and co-eluting compounds with similar retention times to analyte in question.[574-576] NMR using chiral solvating reagents (CSAs), *e.g* chiral lanthanide shift reagents, is widely reported in particular by Wenzel *et al*, for enantiodifferentiation, *ee* calculations and absolute configuration determination[577] and involves non-covalent association of analyte enantiomers with the CSA.[578, 579] CSAs are advantageous as their only pre-requisite is their physical addition to analyte of interest. However unlike CDRs which derivatise parent racemate, CSAs form non-covalent adducts and therefore do not aid separation of enantiomers using LC. NMR analysis using CSAs for enantiopurity analysis has been acknowledged for decades but is largely surpassed by chromatographic enantioseparation technology.[578-581] Enantiopure chromatographic separation is based on the principle of adsorption of two enantiomers of the compound of interest by an enantiopure adsorbent which is often difficult due to extremely subtle differences in analyte enantiomers or diastereomers.[582] In this study chiral HPLC failed to adequately separate diastereomers of **107** or **108 (**Scheme 3.2), requiring alternative methods of *de* analysis. In this respect qNMR was proposed as useful, as a well-established method for purity determination to provide a method for calculation of *de* following LC chiral resolution.[583-586]

3.3.1 *Rotamers/Equilibrating species*

Conformational isomers are known rotamers and are stereoisomers produced by rotation around σ bonds.[587] Rotamers are often rapidly converting or equilibrating at room temperature. Rotation around the single σ bond is restricted and therefore an energy barrier exists to interconversion.[588] The appearance on ^{1}H NMR spectroscopy of equilibrating species such as rotamers complicates analysis of reaction products.[589] Equilibrating species are distinguished from non-equilibrating species *i.e* diastereomer pairs using 2D NOESY, EXSY outcomes and variable temperature (VT) experiments in this chapter. Equilibrating species or rotamers formed due to addition of protecting

groups are known to create complex ^{1}H NMR presentations. Rotamers are often distinguishable as independent molecules due to their high kinetic barrier to rotation.[291, 590, 591]

3.3.2 *Chemical exchange experiments*

Chemical exchange experiments have the ability to distinguish between equilibrating conformers.[591, 592] Hu *et al* have demonstrated the use of 1D NOESY for distinguishing between rapidly equilibrating rotamers in the presence of non-equilibrating diastereomers of Boc-protected valine desipeptides, due to their resonances being well resolved from one another.[591] Resonances under significant exchange demonstrate same phase negative peaks on the 1D NOE difference spectrum due to inversion transfer.[591, 593] Additionally 2D gradient NOESY spectra may detect chemical exchange in the format of the 2D EXSY spectrum. Rotameric exchange may be observed by phasing the diagonal of the 2D NOESY spectrum and obtaining either an EXSY (exchange and same phase) or NOESY (through space and opposite phase) outcome. This has been applied most recently to determine equilibrating *E* and *Z* isomers of conjugated enamino carbonyl systems. The presence of EXSY cross peaks indicative of equilibrating isomers, with protons undergoing chemical exchange are reported as *same* phase signals with the diagonal of the EXSY spectrum.[592] Qualitative EXSY studies are highly advantageous for precious materials as a non-destructive technique which can be carried out with standard NMR concentration samples (10-50 mM) without loss of material.[594,591] Preinstalled and common pulse sequences on NMR instruments ensure that the NOESY/EXSY method combined with regular ^{1}H NMR are readily accessible.

3.3.3 *Variable temperature experiments*

A series of VT or coalescence experiments were carried out in DMSO-d_6 to support confirmation of rotameric presence provided by EXSY outcomes. Where intramolecular exchange occurs between rotamers *i.e* rotation around a bond, coalescence principles predict that as temperature rises, resonance signals exchanging with one another will broaden towards coalescence, a process which occurs below the rotational energy barrier and eventually resonate as a sharp single signal once this rotational energy barrier has been overcome.[595] At room temperature, the energy barrier to intramolecular rotation is large with exchange frequencies being small and slow for ^{1}H NMR to observe different

magnetic nuclei with differing Larmor frequencies within each rotamer of an exchanging pair.[596] NMR can detect different magnetic nuclei within an exchanging pair. In contrast, at elevated temperatures NMR can no longer distinguish between rotamers due to fast exchange. Although resonance signals of diastereomers may alter marginally with increasing temperature, the crucial difference in a VT experiment is that diastereomer resonance signals will never coalesce as temperature is increased.[597]

3.4 *Use of NMR and EXSY spectroscopy for de determination*

NOESY and EXSY spectra are identical experiments used for different purposes.[598,599] While NOESY spectra detect through space and non-bonded correlations, through spin lattice relaxation, it may also detect chemical exchange, so called the EXSY or exchange spectroscopy spectrum. EXSY spectra are useful for detecting coherence transfer through chemical or confirmational exchange as a homonuclear shift correlated spectrum. EXSY spectra demonstrate off diagonal responses for spins in chemical exchange when the rate of exchange is greater or equal to the T_1 relaxation time. Quantitative 2D EXSY can be used to deduce kinetics or rates of exchange by recording a series of EXSY spectra with different mixing times in combination with VT studies,[598, 600] reviewed in detail by Perrin and Dwyer.[601] Relative intensities of cross peaks on an EXSY spectrum gives an indication of relative rate, *i.e* slow exchange will generate intense cross peaks.[602]

The use of NMR spectroscopy is emerging as a popular technique for diastereomer ratio determination.[603,604] The plausibility of calculating diastereomeric ratios (dr) using the EXSY technique is suggested by Hussaini *et al* and most recently an approach for *in situ* monitoring of the diastereoselectivity of peptide coupling has been reported using ^{31}P or ^{1}H NMR integration, accurately determining diastereomer ratios in crude reaction mixtures.[605] The possibility of utilising NMR for the calculation of *de* following LC chiral resolution for complex β-lactam mixtures is therefore plausible.[592, 606] In this chapter, qualitative EXSY is used in tandem with ^{1}H NMR to confirm diastereomer separation, calculate diastereomeric ratios and *de* values respectively.[594,591]

This thesis employs qualitative visual confirmation of diastereomeric separation using 2D EXSY spectra which were used to assign resonances to H_3 and H_4 in tandem with quantitative integration of H_3 and H_4 on the ^{1}H NMR axis using qNMR. This method

enables accurate and precise *de* calculation as a novel qNMR strategy, confirming the success of the chiral resolution.

3.5 *^{1}H NMR data for diastereomer mixtures*

Both diastereomeric mixtures **107** and **108** and their respective isolated diastereomers (**107a**, **107b** and **108a**, **108b**) demonstrated complex ^{1}H NMR spectra preventing purity or diastereomeric excess (*de)* estimation from preliminary ^{1}H NMR analysis (Figure 3.1). Adjunctive NMR experiments, including 2D NOESY/EXSY studies and variable temperature (VT) experiments were required for resolved diastereomers, their parent diastereomer mixtures and other unresolved diastereomer mixtures **107-113**. Such experiments sought to understand the spectroscopic behaviour of proline-derivatised diastereomers and distinguish between diastereomer resonances of **107** and **108** versus exchange signals. This was needed to establish a reliable method for H_3 and H_4 characterisation in order to determine *de* values when analysing ^{1}H NMR spectra of resolved **107a**, **107b**, **108a** and **108b**.

3.5.1 *Comparative ^{1}H NMR spectra for diastereomer mixtures **107-113** in H_3 and H_4 region*

The ^{1}H NMR spectra of the proline derivatised diastereomer mixtures (**107** and **108**) were analysed in $CDCl_3$ and DMSO-d_6 (Figure 3.1). In each solvent and for both mixtures **107** and **108**, additional resonances in the H_3 and H_4 β-lactam region (δ 4.5 – 5.8 ppm) were observed, raising the question of both diastereomer and rotamer presence in proline diastereomer mixtures. Proline diastereomers appear to behave spectroscopically in NMR solvents as if they are chemically exchanging (Figure 3.1).

Additional resonances are not observed for the H_3 and H_4 region for phenylalanine-, tryptophan- and valine-derivatised diastereomer mixtures (**109-113**, Scheme 3.2) in either $CDCl_3$ or DMSO-d_6 (Figure 3.2). Only four anticipated diastereomeric H_3 and H_4 resonances are observed for **109-113**. Since the ^{1}H NMR spectra for diastereomer mixtures **109-113** are not complex, rotamers were suggested as absent. Comparative chemical exchange experiments, including 2D EXSY and VT studies were carried out to investigate possibility of exchange for proline diastereomer mixtures **107** and **108** versus presence of diastereomeric resonances only for all other diastereomeric mixtures (**109-113**).

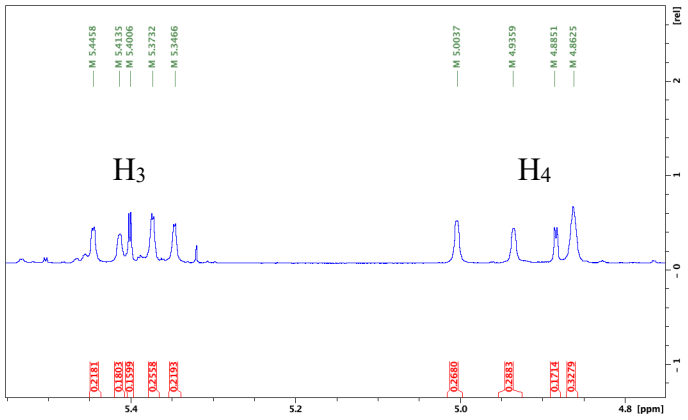

107, $CDCl_3$

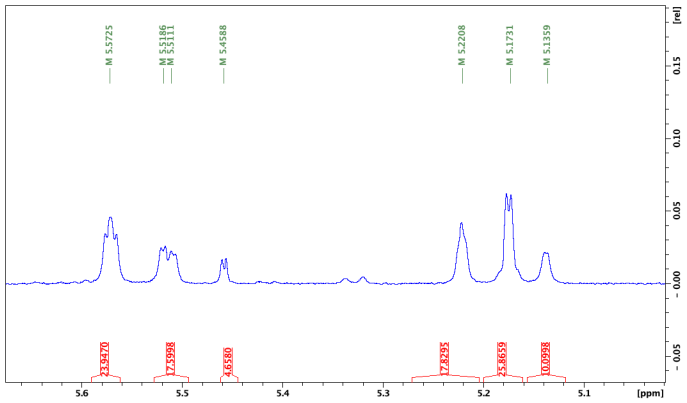

107, DMSO-d_6

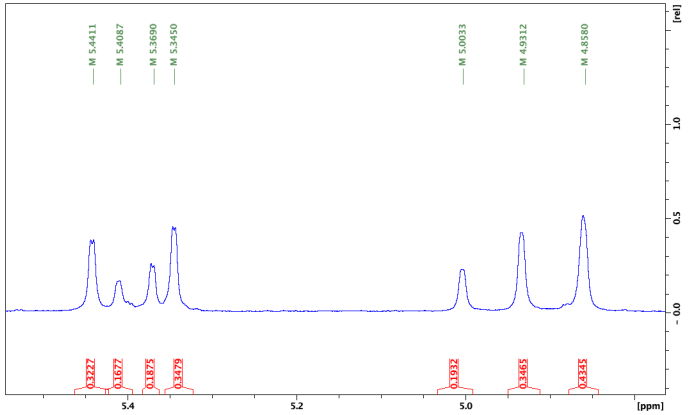

108, $CDCl_3$

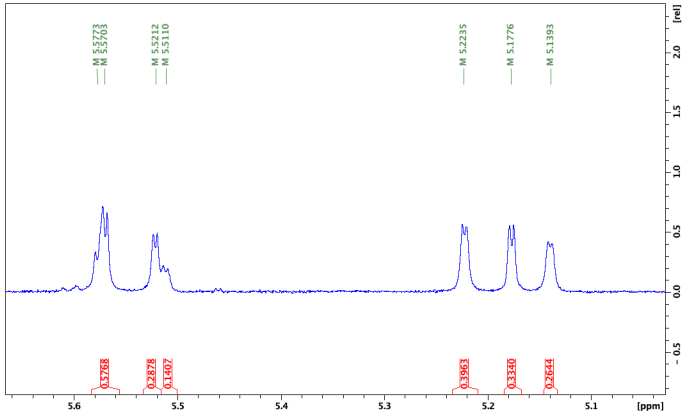

108, DMSO-d_6

Figure 3.1: 400 MHz ^{1}H NMR spectra at 25 °C of the H_3 and H_4 region (δ 4.4-5.5 ppm) for diastereomeric mixtures **107** and **108**. A degree of resonance signal overlap is noted for H_4 of **108** in $CDCl_3$ with only three of four signals observed.

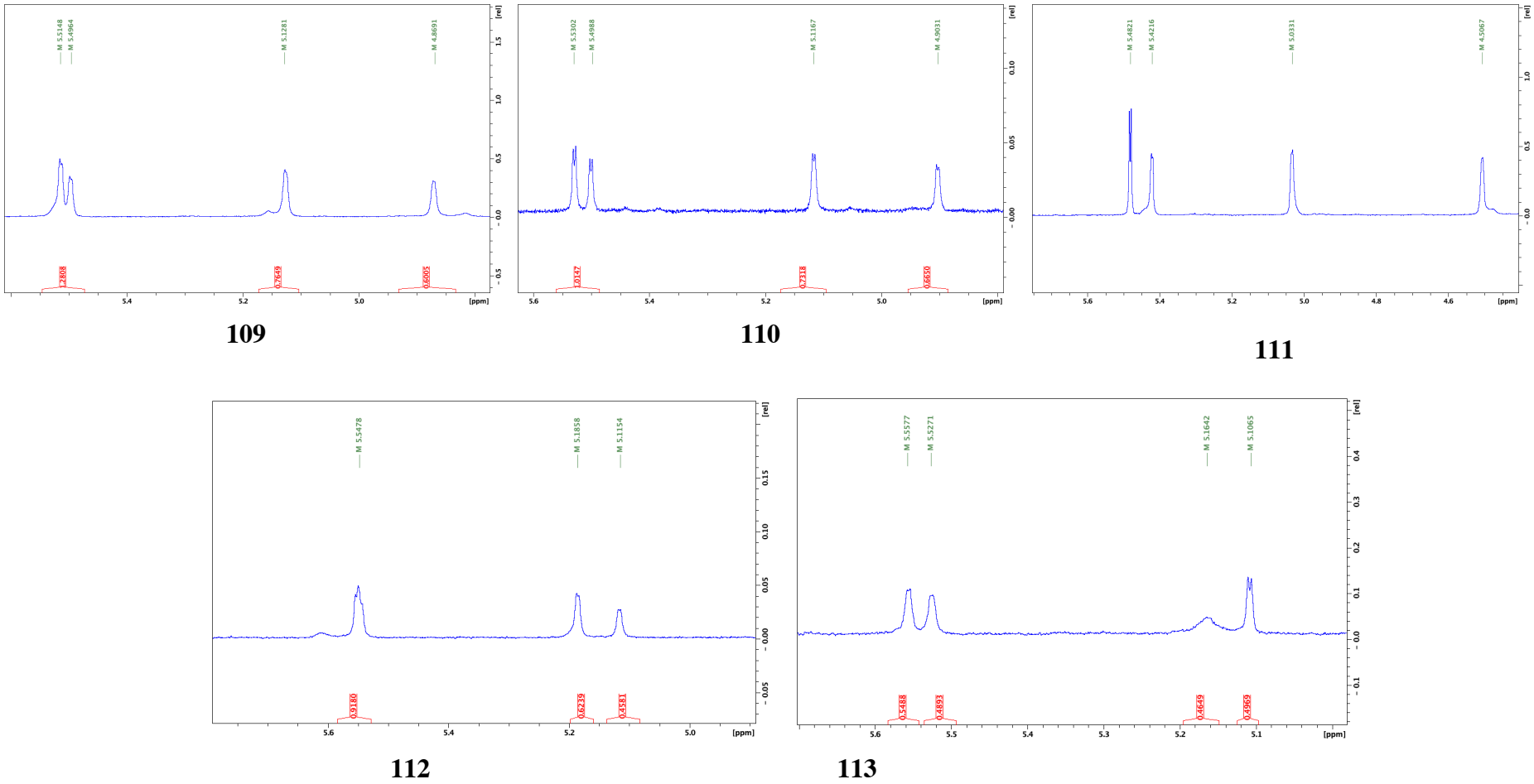

Figure 3.2: 400 MHz ^{1}H NMR spectra in DMSO-d_6 of H_3 and H_4 region (δ 4.5-5.8 ppm) for **109-113**.

3.6 *2D EXSY spectra of **107** and **108** in $CDCl_3$ confirming presence of equilibrating rotamers*

EXSY spectra were collected using 2 scans per increment, 2048 X 256 time domains, a mixing time of D8/500 m/s and the NOESY gpphp pulse programme (phase sensitive NOESY) from the Bruker pulse library. 2D EXSY spectra were obtained for **107** and **108** in $CDCl_3$ and DMSO-d_6 (Figure 3.7) to further investigate the additional H_3 and H_4 resonances of the ^1H NMR spectra (Figure 3.1). Equilibrating rotamers are identified and confirmed by observation of cross peaks off the diagonal of the 2D EXSY spectrum for both **107** and **108** in both solvents. (Figure 3.7) Hence, the complex presentation in the expanded H_3 and H_4 region on ^1H NMR in $CDCl_3$ (Figure 3.1) is accounted for by both diastereomeric and exchanging rotamer signals, detectable on ^1H NMR at 25 °C. Furthermore both **107** and **108** demonstrate independent equilibrating exchange signals in $CDCl_3$ only. This was not observed in DMSO-d_6 (Figure 3.7). In $CDCl_3$ each of the H_3 and H_4 diastereomer resonances were observed with resolved and exchanging rotamer cross peaks, as two independent sets of cross peaks on the 2D EXSY spectra, one for each diastereomer (Figure 3.3). $CDCl_3$ was therefore considered as the optimal solvent for qualitative confirmation of proline diastereomer purity following LC chiral resolution using 2D EXSY spectra of resolved diastereomers. A successful resolution procedure should demonstrate one single set of cross peaks on the 2D EXSY spectrum if sufficient diastereomer purity is achieved.

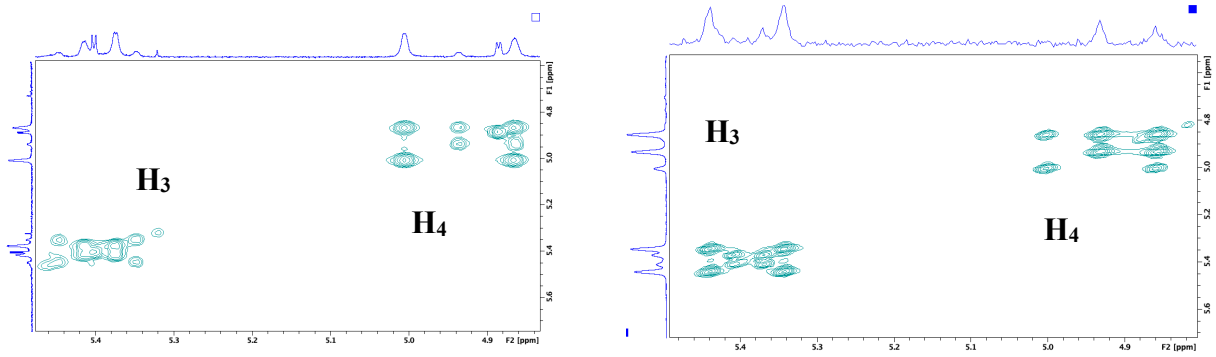

2D EXSY of **107** in $CDCl_3$

2D EXSY of **108** in $CDCl_3$

Figure 3.3: 400 MHz 2D EXSY spectra for the β-lactam H_3 and H_4 region (δ 4.5 – 5 ppm) in $CDCl_3$ at 25 °C for **107** and **108**.

A

B

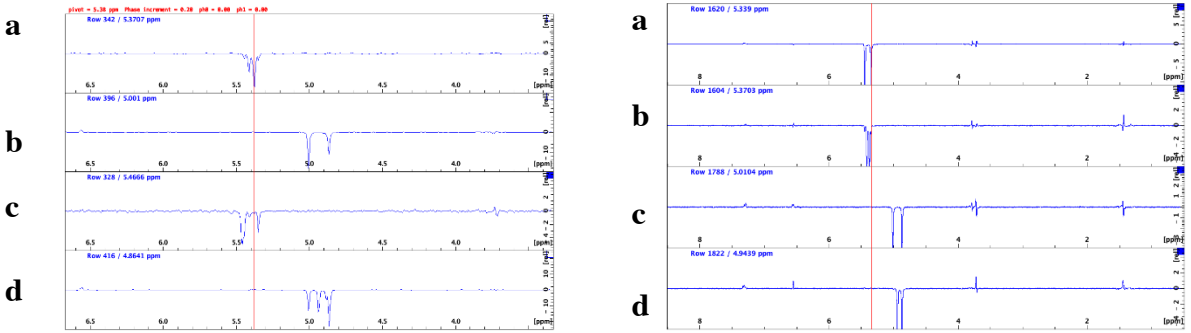

Figure 3.4: Manual phasing off cross peaks for H_3 and H_4 from 2D EXSY spectra in $CDCl_3$ at 25 °C **A: 107 a: 107a** (H_3) **b**: **107a** (H_4) **c: 107b** (H_3) **d: 107b** (H_4) **B: 108**. **a: 108a** (H_3) **b**: **108b** (H_3) **c: 108a** (H_4), **d: 108b** (H_4)

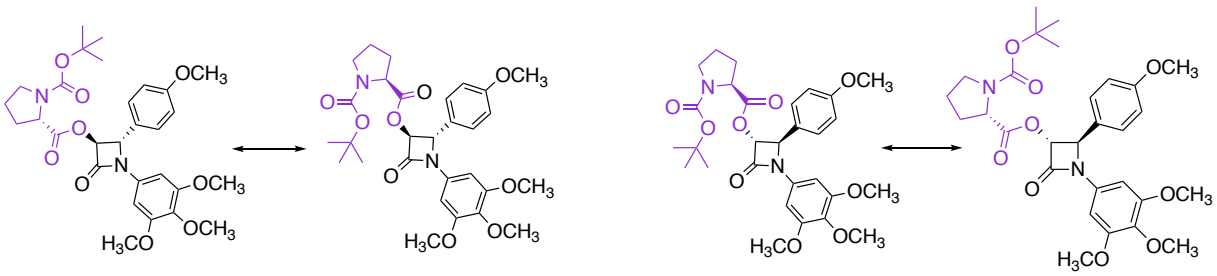

Figure 3.5: Equilibrating rotamers for resolved *N*-Boc-L-proline-derivatised β-lactam diastereomers **108a** and **108b**

Rotamers were unequivocally confirmed for both **107** and **108** using a similar method to Hussaini *et al via* manual phasing of the 2D EXSY cross peaks. Standard zero order and first order phase correction was employed to get pure absorption signals. Manual phasing of cross peaks resulted in same phase signals as the diagonal (Figure 3.4).[592] At least two same phase signals are observed for each cross peak indicative of a minimum of two rotamers present for each diastereomer. A structural representation of potential rotamer conformations for diastereomers of **108** is illustrated in Figure 3.5.

3.7 *VT experiments for diastereomer mixtures **107** and **108** in DMSO-d_6*

VT experiments were carried out for proline diastereomer mixtures **107** and **108** in DMSO-d_6 (Figure 3.6). At lower temperatures of 25 °C equilibrating rotamers are detectable on ^{1}H NMR, observed as cross peaks off the diagonal on 2D EXSY spectra for both **107** and **108** (Figure 3.6). At elevated temperatures ^{1}H NMR no longer distinguishes between rotamers due to very fast exchange resulting in coalescence of equilibrating resonances. With each progressive increase in temperature, notable changes occur in the H_3 and H_4 region for both **107** and **108** (Figure 3.6). For diastereomer mixture **108**, coalescence at 60 °C to broad singlets is observed for both H_3 and H_4 at δ 5.2 and δ 5.5 ppm respectively. Exchange broadening of 25-30 Hz observed for apparent singlets of H_3 and H_4. At higher temperatures of 80 and 90 °C in the H_3 and H_4 region, this exchange broadening is no longer observed (green and purple, **B,** Figure 3.6). H_4

resonated as a doublet with a ^{3}J value of 1.8 Hz while exchange broadening for H_3 is reduced to 3.6 Hz at 80 and 90 °C (green and purple, **B,** Figure 3.6). Visualisation of both diastereomers within the mixture in absence of exchange signals was anticipated in the ^{1}H NMR spectrum of **107** and **108** at elevated temperatures. However DMSO-d_6 does not distinguish between individual diastereomers of either diastereomer mixture **107** or **108**. Only one set of H_3 and H_4 resonances are present. Resolution of diastereomer resonances was not observed even in absence of rotameric resonances at either 80 and 90 °C. (green and purple, **B**, Figure 3.6). At 25 °C only equilibrating rotamers are distinguished in DMSO-d_6 with only one set of cross peaks on 2D EXSY spectra for diastereomer mixtures **107** and **108** (Figure 3.7). In contrast to $CDCl_3$, which detects both rotamers and diastereomer pairs for **107** and **108** on ^{1}H NMR (Figure 3.1) and 2D EXSY spectra (Figure 3.3) DMSO-d_6 cannot be used as a solvent for calculation of diastereomeric ratios. Individual diastereomers have identical resonances on ^{1}H NMR and 2D EXSY spectra using DMSO-d_6 (Figure 3.7). $CDCl_3$ was therefore determined as the solvent choice for qualitative analysis of resolved diastereomers utilising rotameric resonance signals for H_3 and H_4 on 2D EXSY spectra and the ^{1}H NMR for *de* calculations as a qNMR technique.

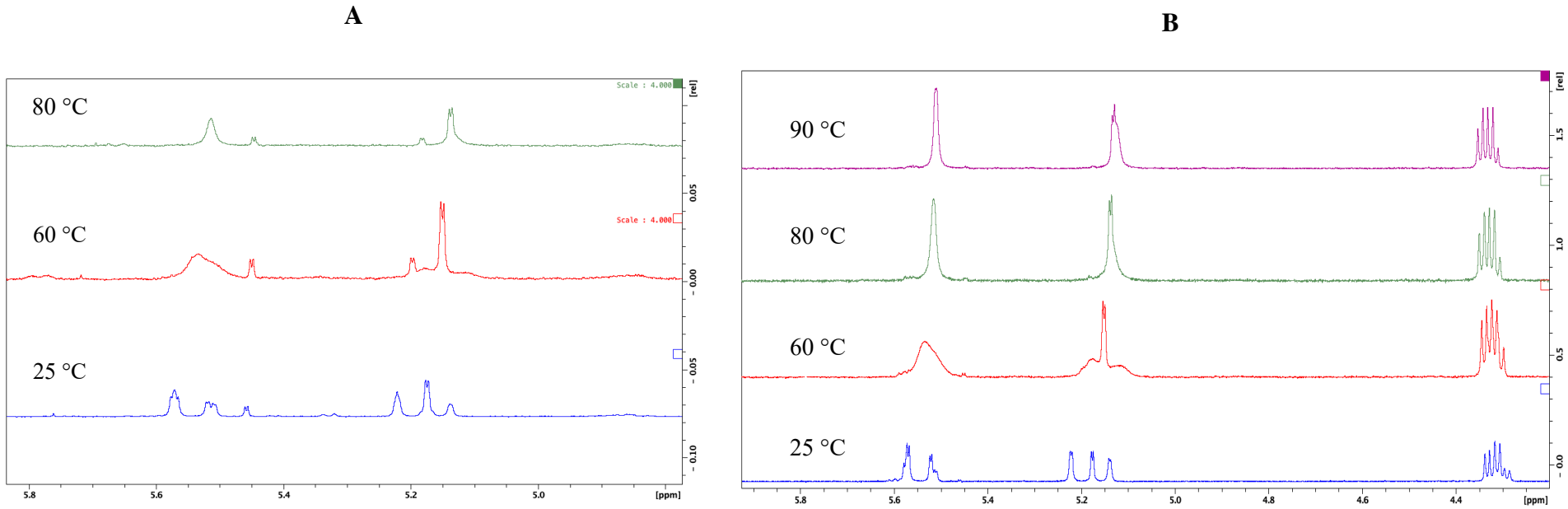

Figure 3.6: 400 MHz ^{1}H NMR spectra in DMSO-d_6 for H_3 and H_4 (4.3 – 5.8 ppm) region of **A:** D-proline CDR derivatised diastereomer mixture **107 B:** L-proline CDR derivatised diastereomer mixture **108,** as a function of temperature. Proline CH multiplet illustrated in **B** at δ 4.35 ppm for reference with no coalescence observed.

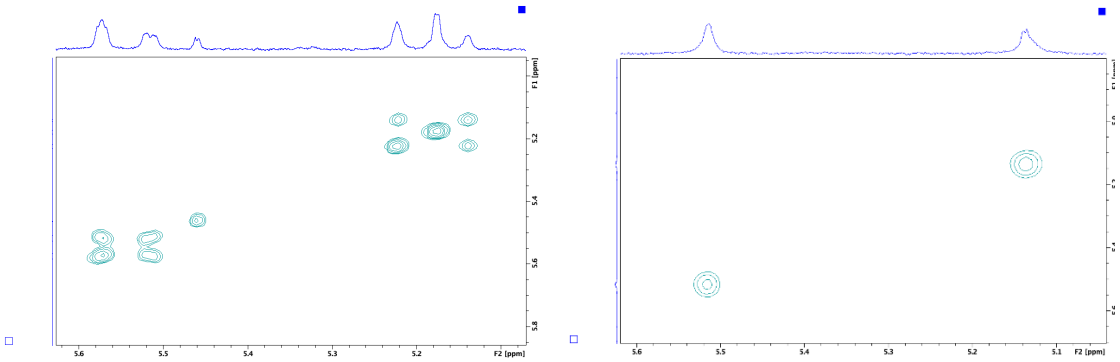

2D EXSY of **107** at 25 °C

2D EXSY of **107** at 95 °C

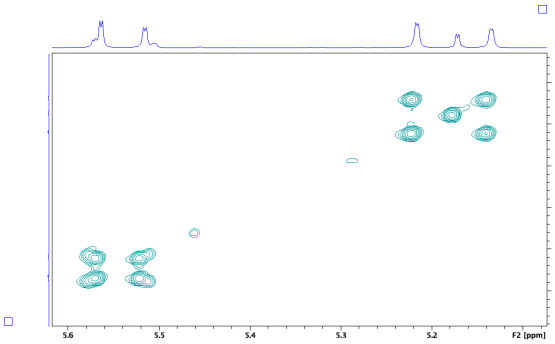

2D EXSY of **108** at 25 °C

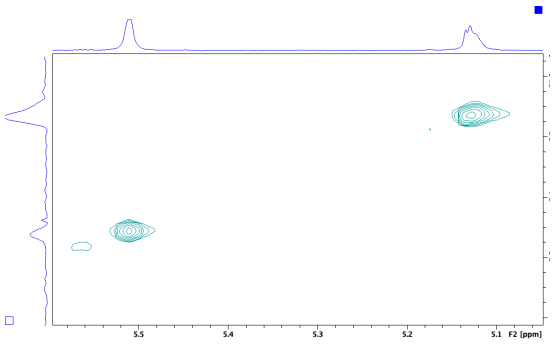

2D EXSY of **108** at 85 °C

Figure 3.7: 400 MHz 2D EXSY spectra at 25 °C and elevated temperatures in DMSO-d_6 for expanded H_3 and H_4 region of **107** and **108** demonstrating one equivalent independent set of cross peaks for diastereomers in the mixture at 25 °C and a single diastereomeric signal for H_3 and H_4 at elevated temperatures of 95 °C and 85 °C for **107** and **108** respectively.

3.8 *VT experiments and 2D NOESY spectra for non-proline amino acid CDR diastereomer mixtures* ***109-113***

VT experiments confirmed absence of major rotamers for diastereomer mixtures **109-113**. Minor evidence of equilibrating rotamers will be discussed which was observed for valine diastereomer mixtures **112** and **113**. Evidence of equilibrating rotamers on 2D NOESY (Figure 3.9) or on VT spectra (Figure 3.8) for CDR conjugates **109-111** due to absence of H_3 and H_4 resonance coalescence at elevated temperatures. This contrasts observations for proline diastereomer mixtures **107** and **108** with evident and progressive coalescence in the H_3 and H_4 region (Figure 3.6). Minor evidence of

coalescence is observed for valine diastereomer mixture **112** and **113** in the H_4 and B ring regions [δ 5.11 and 7.37-7.42 ppm respectively (Figure 3.8)]. Coalescence was observed in VT experiments while cross peaks indicative of equilibrating rotamers were not observed on 2D NOESY studies for valine diastereomers. This indicates that VT experiments are more sensitive for rotamer detection than 2D chemical exchange studies. Nevertheless exchange for valine diastereomers is faster and therefore more subtle than successfully resolved proline diastereomers (*i.e* the *N*-Boc-D- and L- proline diastereomer mixtures **107** and **108**) which hold the unique spectroscopic property of slow conformational exchange with equilibrating rotamers which are readily observed on both ^{1}H NMR (Figure 3.2) and 2D EXSY spectra in $CDCl_3$ and DMSO-d_6. Taken together, results from ^{1}H NMR, 2D NOESY (Figure 3.9) and VT experiments (Figure 3.8) confirm that equilibrating rotamers are absent in diastereomeric mixtures **109-111** prepared using *N*-Boc-L-phenylalanine, *N*-Boc-L-tryptophan and fmoc- L - phenylalanine. It is possible that the unique property of slow exchange for proline diastereomers **107** and **108** may influence separation of proline diastereomers during LC chiral resolution compared to other non-proline diastereomer mixtures which do not form rotamers in $CDCl_3$ or DMSO-d_6.

3.9 *Computational data for β-lactam diastereomers*

A computational study was carried out for selected *N*-Boc protected amino acid diastereomers **[108, 109,** and **111 (**Figure 3.10)**]** by Dr. Cristina Trulijo of the School of Chemistry, Trinity College Dublin. This study was carried out to examine the process of rotamer exchange, unique to proline diastereomers of β-lactam **17**, but not observed for other amino acid diastereomers. Intramolecular non-covalent interactions (NCIs) are not observed between the L-proline CDR and β-lactam scaffold of **17**, potentially explaining rotamer presence. The absence of non-covalent intramolecular π-π stacking interactions between CDR and β-lactam scaffold of **17**, due to proline's non-aromatic structure, may enable free rotation of the proline ring for **107** and **108,** therefore enabling exchange and rotamer formation. The aromatic amino moieties for phenylalanine (**109**) and tryptophan (**111**) have potential to form intramolecular π–π NCIs with the β-lactam scaffold of **17**

(Figure 3.10). These intramolecular π–π interactions between the CDR and β-lactam scaffold of **01** for diastereomers of **109** and **111** stabilise phenylalanine (**109**) and indole (**111**) aromatic rings, limiting their free rotational capacity to prevent exchange.

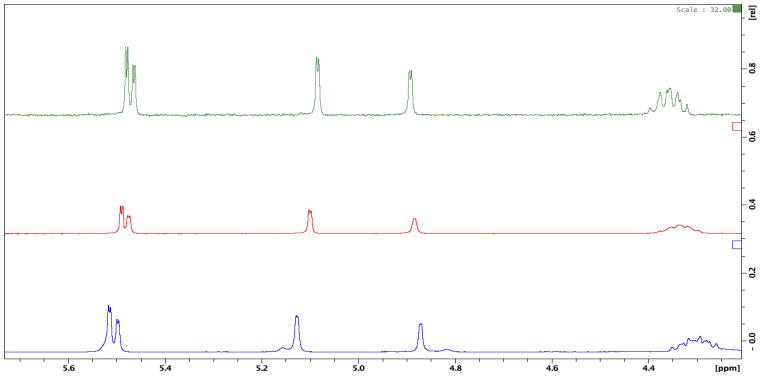

109, Blue: 25 °C, red: 60 °C, green: 80 °C

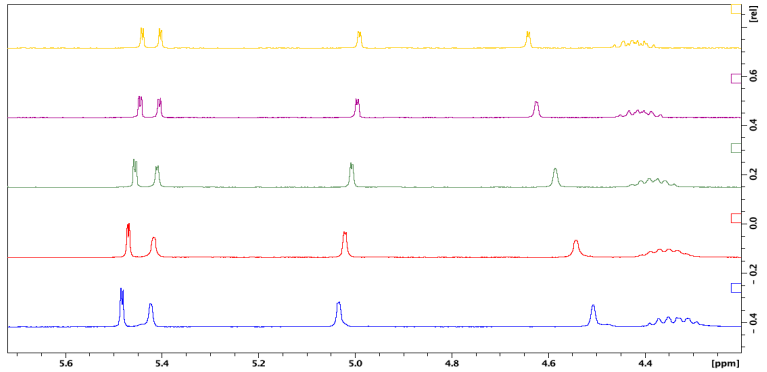

111, Blue: 25 °C, red: 40 °C, green: 60 °C, purple: 80 °C, yellow: 90 °C

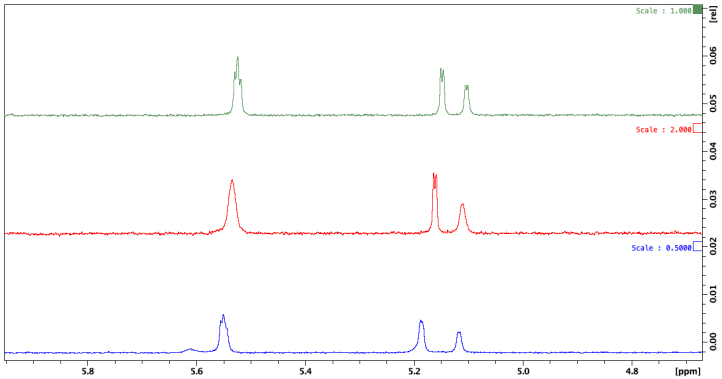

112, Blue: 25 °C, red: 60 °C, green: 80 °C

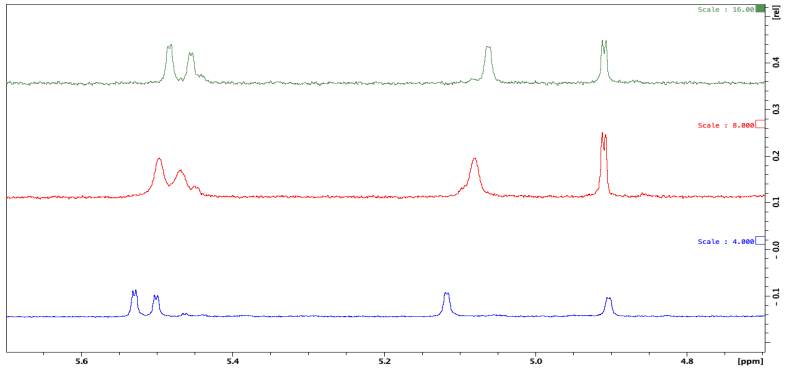

113, Blue: 25 °C, red: 60 °C, green: 80 °C

Figure 3.8: VT experiments for diastereomer mixtures **109**, **111, 112** and **113** at 400 MHz in DMSO-d_6 in H_3 and H_4 region (δ 4.5-5.8 ppm).

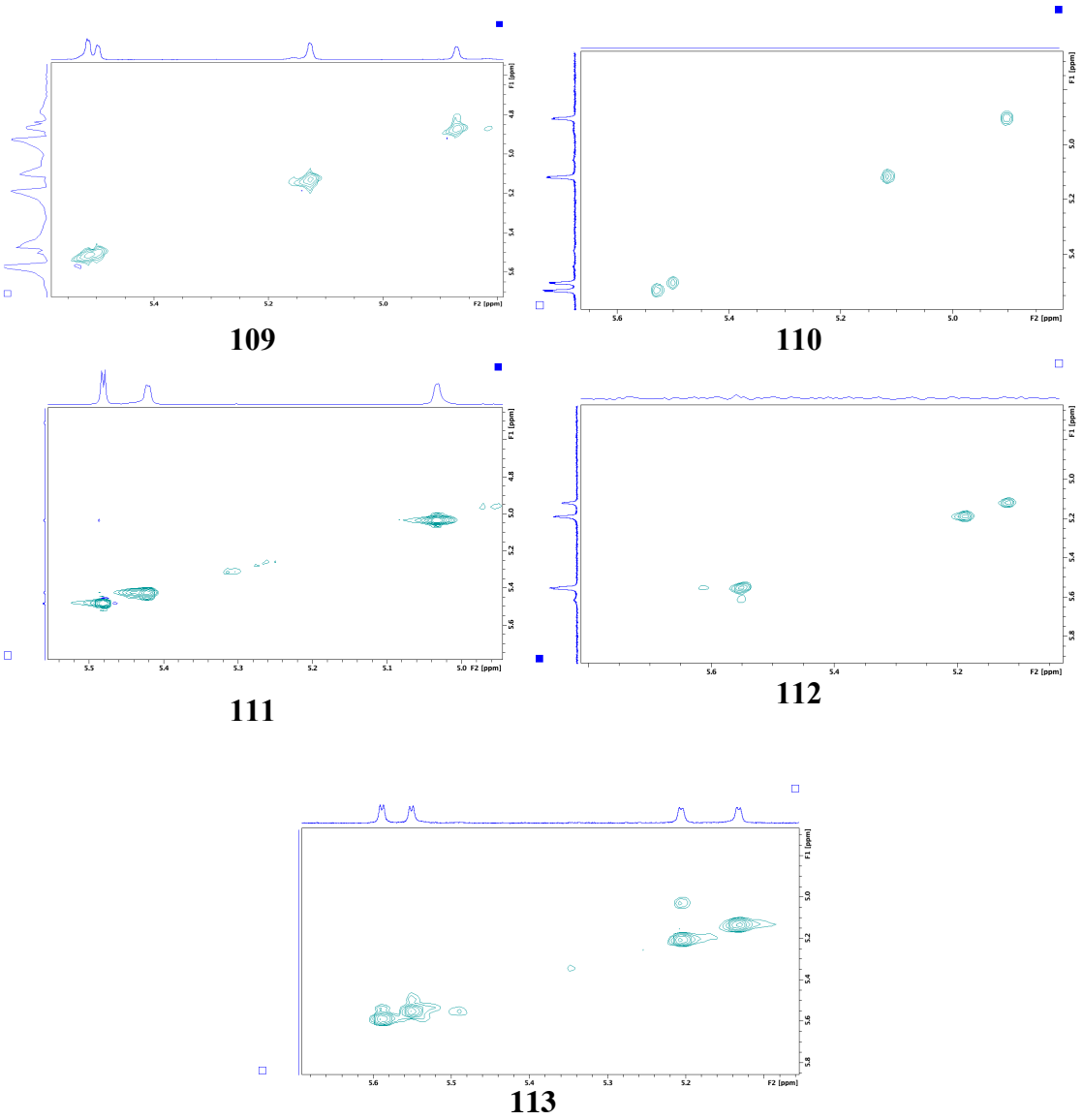

Figure 3.9: 400 MHz 2D NOESY spectra for H_3 and H_4 region in diastereomeric mixtures **109-113** in DMSO-d_6 at 25°C.

Steric effects are traditionally considered as major factors for consideration in computational models since electronic energies of non-bonded atoms increases exponentially with decreasing distance. However in recent years NCIs are more widely regarded as factors influencing organocatalytic reaction selectivity.[607, 608] NCIs have previously been reported as major determinants of the stereoselectivity for histamine complexes.[609]

Major conformers for these diastereomers (**109a**, **109b**, **111a** and **111b**) arise on account of non-covalent π–π interactions which stabilise one predominant conformation (Figure 3.10). Notwithstanding the complexities associated with accurate computational predictions of structures where NCIs in addition to steric effects are possible, the β-lactam diastereomer models illustrated in Figure 3.10 which demonstrates these NCI π–π interactions gives rise to a plausible explanation for major conformational exchange observed in the H_3 and H_4 region only for proline diastereomers (Figure 3.1) but not for non-proline CDRs on ^{1}H NMR (Figure 3.2) or 2D NOESY studies (Figure 3.9). Due to the non-aromatic structure of valine, π–π interactions were not possible between the amino acid CDR and the β-lactam ring in diastereomeric mixtures **112** and **113**, explaining why valine diastereomers were the only non-proline diastereomer mixtures with minor evidence of exchange on 2D NOESY/EXSY and VT experiments (Figure 3.9 and Figure 3.8).

3.10 *^{1}H NMR and 2D EXSY spectra for isolated N-Boc-* L *- and* D *- proline diastereomers*

Both **107** and **108** were successfully resolved using LC with superior resolution and minimal diastereomer co-elution of **108a** and **108b** using *N*-Boc-L-proline as the CDR. Significant co-elution of **107a** and **107b** reduced isolated yields to 15% for **107a** and 5% for **107b**. On the other hand 32% and 37% of the original diastereomer mixture was resolved for **108a** and **108b** respectively. *N*-Boc-L-proline was therefore determined as the optimal CDR for resolution of 3-hydroxyl β-lactam **17**. Direct comparison of the ^{1}H NMR axis of **108a** and **108b** by overlaying the ^{1}H NMR spectra for isolated diastereomer mixture **108a** (red, Figure 3.11) and **108b** (green, Figure 3.11) with parent diastereomer mixture **108** (blue, Figure 3.11) demonstrates unique resonances for H_3 and H_4 of **108a** and **108b**, inferring successful resolution. Two major resonances are observed for both H_3 and H_4, representing exchanging rotamer pairs for each isolated diastereomer. Identification and quantification of the H_3 and H_4 rotameric and diastereomeric resonances allowed application of a qNMR approach for accurate *de* calculations discussed in this chapter.

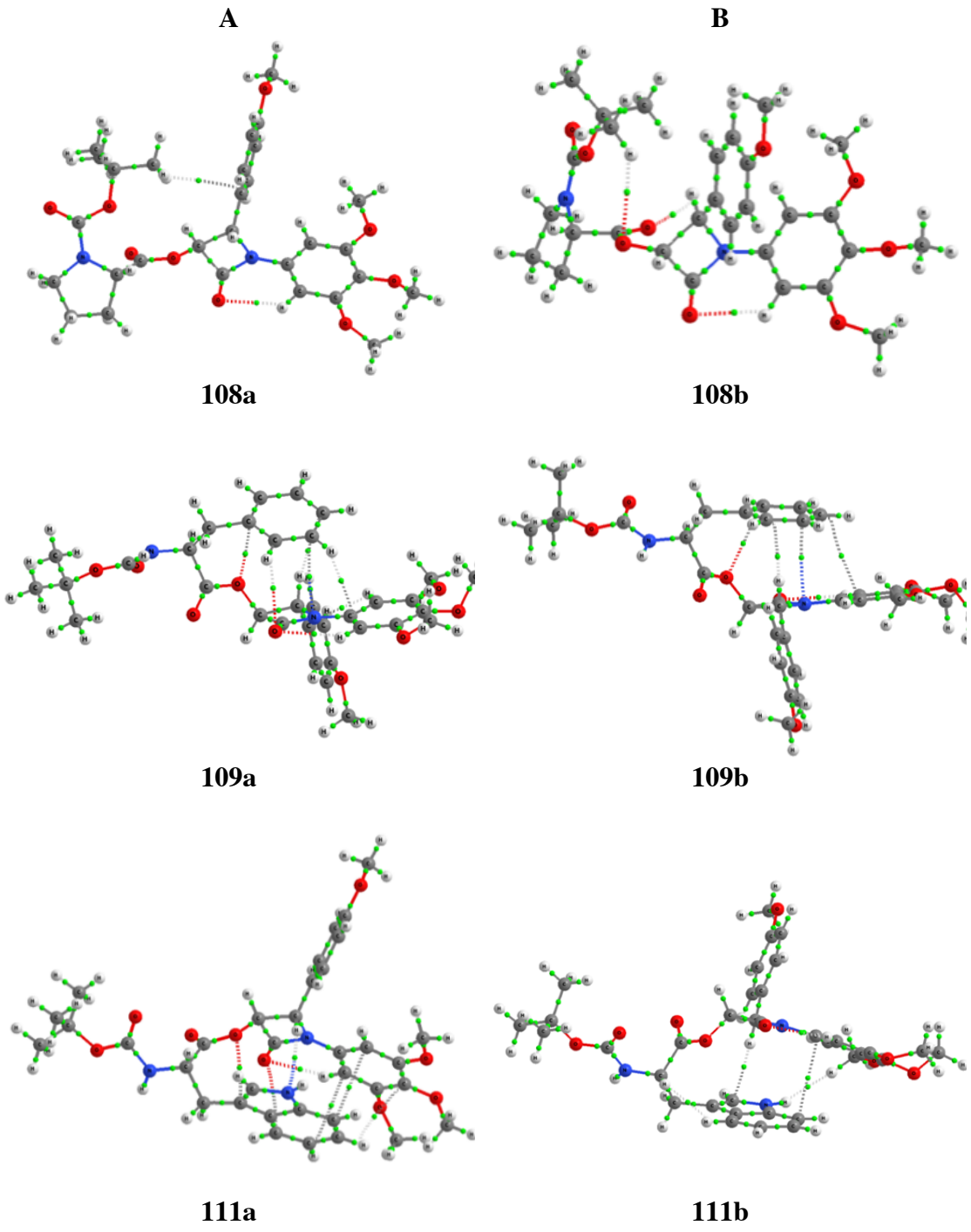

Figure 3.10: Computational and theoretical model of diastereomeric pairs **108a** and **108b**, **109a** and **109b**, and **111a** and **111b**. Non-covalent intra-molecular π-π interactions indicated by grey dotted lines are present for aromatic moieties of phenylalanine and tryptophan diastereomers only. Hydrogen bonds illustrated as red dotted lines. Representative examples of major rotamers only are illustrated. Atom colours: red = oxygen, grey = carbon, blue = nitrogen.

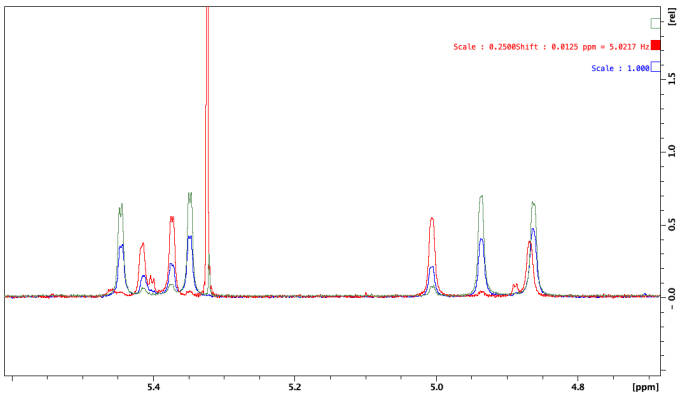

108 (blue), **108a** (red), **108b** (green)

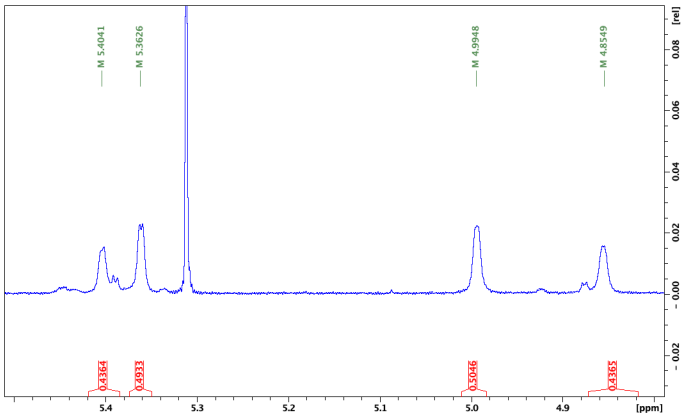

108a

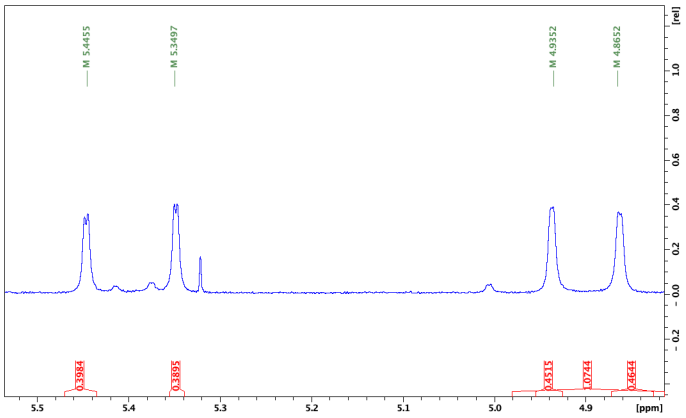

108b

Figure 3.11: **Top:** Overlay of 400 MHz ^{1}H NMR spectra of resolved **108a** (red) and **108b** (green) with diastereomer mixture **108** (blue). Middle: **108a** Bottom: **108b** at 25 °C. Expanded H_3 and H_4 region (δ 4.8-5.5 ppm) in $CDCl_3$ illustrated.

3.11 *Application of 2D EXSY spectra in CDCl3 as a qualitative tool for confirmation of resolution*

Equilibrating rotamers for each diastereomer have enabled use of 2D EXSY spectra as a qualitative tool to visually estimate diastereomeric purity (*de*) following chiral resolution. Comparing 2D EXSY of isolated diastereomers serves as a qualitative and

visual tool for confirmation of diastereomer purity following LC chiral resolution of β-lactam proline diastereomers. 2D EXSY spectra for isolated **107a, 107b, 108a** and **108b** in $CDCl_3$ are compared in Figure 3.12. Co-elution during LC chiral resolution is evident on the 2D EXSY spectra for **107a** and **107b**. One major set of cross peaks is accompanied by the minor presence of a second set for resolved D-proline diastereomer derivatives, indicative of incomplete LC chiral resolution of diastereomer mixture **107** with presence of a second diastereomer and its exchanging rotamers. In contrast, only one set of cross peaks are present on 2D EXSY spectra for **108a** and **108b** (Figure 3.12). This contrasts the 2D EXSY spectrum obtained for parent diastereomer mixture **108** (Figure 3.3) with two independent sets of cross peaks. 2D EXSY spectra support use of *N*-Boc-L-proline as the most optimal CDR studied for resolution of β-lactam **17**.

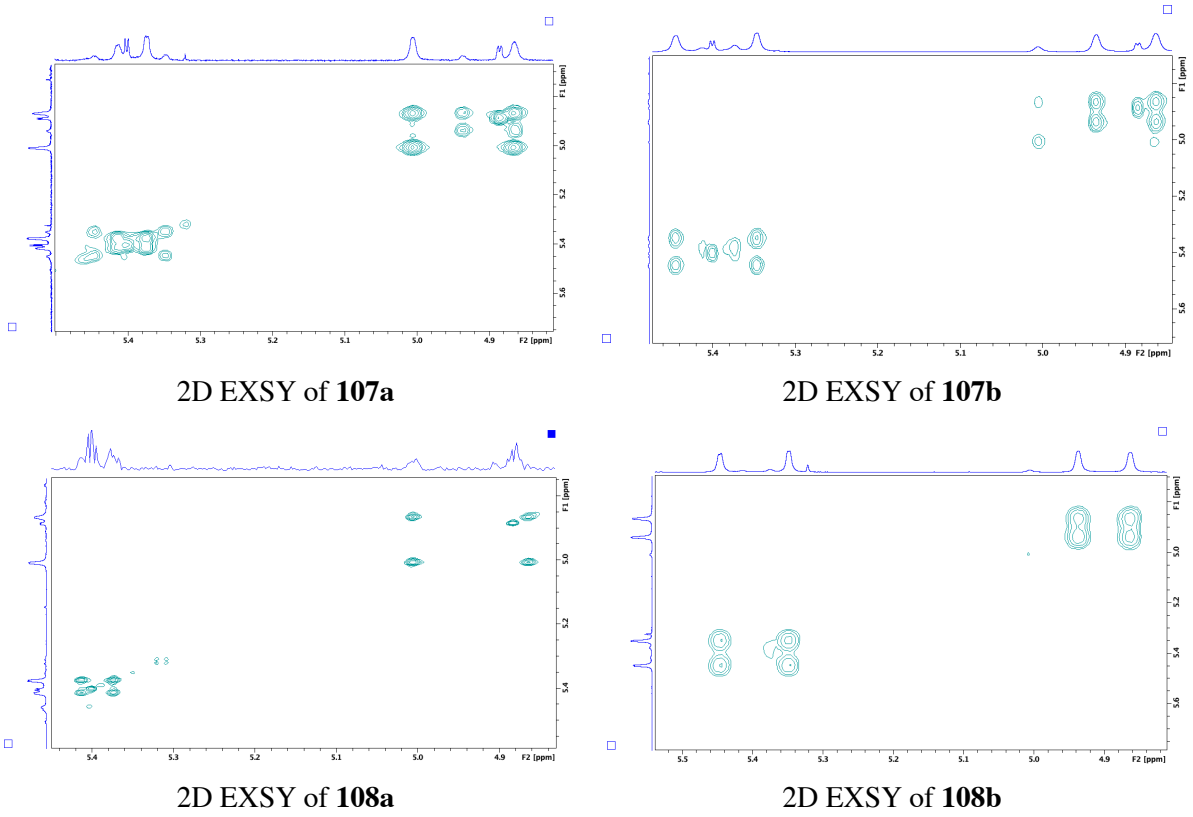

Figure 3.12: 400 MHz 2D EXSY spectra at 25 °C for H_3 and H_4 region of **107a**, **107b, 108a** and **108b** in $CDCl_3$.

3.12 *qNMR for calculation of diastereomeric excess for β-lactam diastereomers*

By virtue of seeking a robust method for structural characterisation of the H_3 and H_4 β-lactam resonances in resolved diastereomers, a quantitative (q) NMR approach for *de* calculation was developed. This qNMR strategy accurately and precisely reports diastereomeric purity in the format of a *de* value, in line with IUPAC guidelines for *de* calculation (Equation 3.1).[572] qNMR ^{1}H experiments utilised a 90° excitation pulse and a 60 second recycle delay between scans to allow the spins to return to equilibrium ensuring 5 times the T_1 (spin lattice relaxation) was exceeded. Distinguishing between diastereomeric and rotameric resonances for H_3 and H_4 protons of the β-lactam ring using 2D EXSY studies (Figure 3.3 and Figure 3.12) has enabled integration of H_3 and H_4 diastereomeric resonances and calculation of *de* values for resolved diastereomers (Table 3.1). *De* values were obtained independently for H_3 and H_4 of resolved diastereomers **107a**, **107b**, **108a** and **108b** and reported as the average of both H_3 and H_4 integrations (Table 3.1 and Equation 3.1). The *de* value for L-proline **108a** of 90% is far superior to 63% for the corresponding D-proline derivatised **107a**. Similarly L-proline derivatised **108b** was isolated in superior *de* of 74% compared to 45% for D-proline derivatized **107b** further validating the *N*-Boc-L-proline CDR as the most optimal amino acid evaluated for the chiral resolution of β-lactam **17**.

$$\% \; de = \mathrm{D1}\ (\text{integrals for rotamers of diastereomer 1*}) - \mathrm{D2}\ (\text{integrals for rotamers of diastereomer 2*})$$

D1 = major diastereomer
D2 = minor diastereomer

** integrals for rotamers of both diastereomer normalised to 100% prior to insertion into formula*

Equation 3.1: Formula for calculation of *de* using ^{1}H NMR axis

^{1}H NMR spectroscopy for determination of *de* values of resolved diastereomers as a qNMR tool for **108a** and **108b** was validated by comparison to *ee* values of 94% and 71% obtained for 3-hydroxyl enantiomers (+) **17EN1** and (-) **17EN2** (Scheme 3.2) respectively using chiral HPLC (discussed in detail in Chapter 4). Similar values obtained for both *de* measured using qNMR and *ee* of final enantiomers using chiral

HPLC (discussed further in Chapter 4) for **108a** and **108b** underpins the utility of this qNMR method for quantitative determination of accurate *de* values following diastereomer resolution using LC.

Table 3.1: Integration of H_3 and H_4 resonances on ^{1}H NMR axis for qNMR determination of d.r[1] and *de* values for resolved proline diastereomers **107a**, **107b**, **108a** and **108b**.

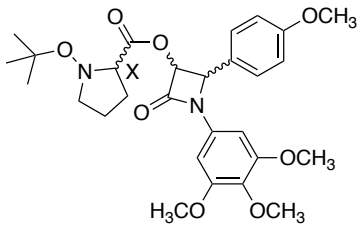

Code	X	d.r (H_3)[1] (D1:D2)	*de* % (H_3)	d.r (H_4)[1] (D1:D2)	*de* % (H_4)	*de* % (average of H_3 and H_4 *de*)	*ee* %[3]
107a	*R*	83:17	66	80:20	60	63	Nd[4]
107b	*R*	73:27	46	72:28	44	45	Nd[4]
108a	*S*	94:6	88	96:4	92	90	94
108b	*S*	86:14	72	88:12	76	74	71

[1] d.r (diastereomeric ratio) is the ratio of the percentage of one diastereomer in a mixture (D1) to that of the other (D2). D1 and D2 are calculated as the integrals of rotamers for the major and minor diastereomers, respectively, normalised to 100%.[572]
[2] *de* = D1 – D2
[3] *ee* (enantiomer excess) calculated using chiral HPLC analysis of enantiomers **17EN1** and **17EN2**
Nd = not determined

3.14 *Chapter 3 summary and outlook*

A series of diastereomer mixtures of β-lactam **17** were prepared with aim of selecting the optimal CDR for the resolution of **17** in the form of amino acid derivatised diastereomer mixtures. D- and L-proline derivatised mixtures **107** and **108** were the only diastereomer mixtures that were both successfully resolved and showed strong evidence of rotamer exchange in all NMR experimental conditions using both $CDCl_3$ and DMSO-d_6. *N*-Boc-L-proline was determined as the optimal CDR in this study. Theoretical computational

models of selected diastereomers demonstrated that intramolecular π-interactions between the aromatic CDRs [phenylalanine (**109**) and tryptophan (**111**)] and β-lactam scaffold of **17** may prevent the formation of rotamers. 2D EXSY spectra served as a visual and qualitative tool to determine diastereomeric purity in resolved diastereomers. Successful characterisation of H_3 and H_4 rotamer versus diastereomer resonances in $CDCl_3$ has enabled use of quantitative integration as a robust qNMR method for determination of *de* values. Future work will involve application of the optimised LC chiral resolution in tandem with qualitative 2D EXSY and qNMR spectroscopy for *de* calculations to a library of 3-hydroxyl β-lactam analogues of biological interest. In principle, this method of LC chiral resolution in conjunction with qNMR is widely applicable and of synthetic relevance for racemates bearing an hydroxyl moiety for resolution and confirmation of diastereomeric purity.

Chapter 4 - Application of optimised chiral resolution for enantioseparation of β-lactam racemates

4.1 *Introduction to synthetic routes for chiral resolution using N-Boc-L-proline as a CDR*

Following chiral resolution of 3-hydroxyl β-lactam enantiomers of **17** (Chapter 3), the logical progression involved application of this optimised chiral resolution procedure to a panel of combretazet β-lactam racemates synthesised in Chapter 2. Two alternative routes for chiral resolution are pursued in this chapter. Firstly, a continuation of the chiral resolution described in Chapter 3, involving esterification at the 3-hydroxyl position was applied to β-lactams **16, 18-22**, **63** and **89** (Scheme 4.1 and Table 4.1). Secondly, esterification of the B ring *meta* hydroxyl group is also explored to yield diastereomers and subsequently enantiomers of 3-substituted combretazets (Scheme 4.3).

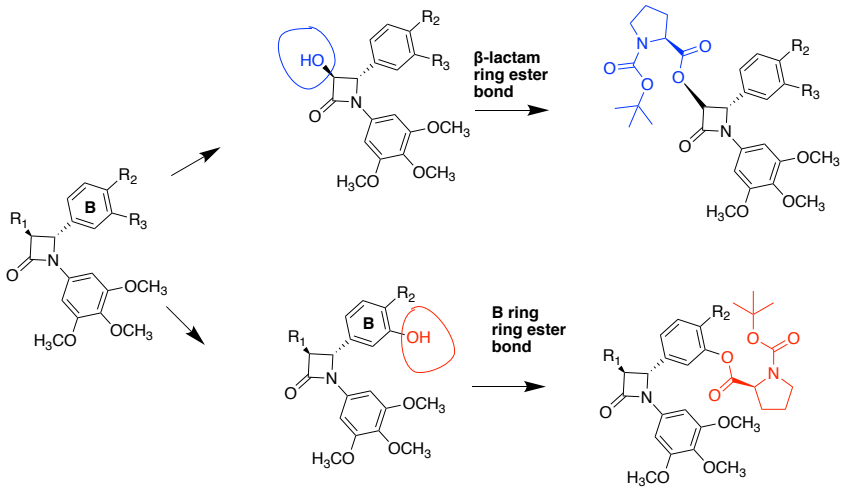

Scheme 4.1: Esterification routes for addition of *N*-Boc-L-proline as the CDR to combretazet β-lactam racemates. Blue illustrates the 3-hydroxyl route while red illustrates the B ring *meta* hydroxyl route.

4.1.1 *Application of chiral resolution to a panel of 3-hydroxyl racemates*

The optimised chiral resolution procedure described in Chapter 3 was successfully applied to a panel of 3-hydroxyl racemates (Table 4.1). Scheme 4.2 outlines a general procedure for coupling of *N*-Boc-L-proline to 3-hydroxyl β-lactam racemates **18-22** and **67a**, **63** and **89** (**a,** Scheme 4.2) followed by purification as diastereomer pairs and subsequent resolution to the corresponding 3*S*,4*S* and 3*R*,4*R* diastereomers (**b,**Scheme 4.2). Hydrazinolysis of the CDR affords the 3*S*,4*S* and 3*R*,4*R* enantiomers (absolute configurations identified by XRD of final enantiomers) using hydrazine dihydrochloride, catalysed by TEA (**c,**Scheme 4.2).

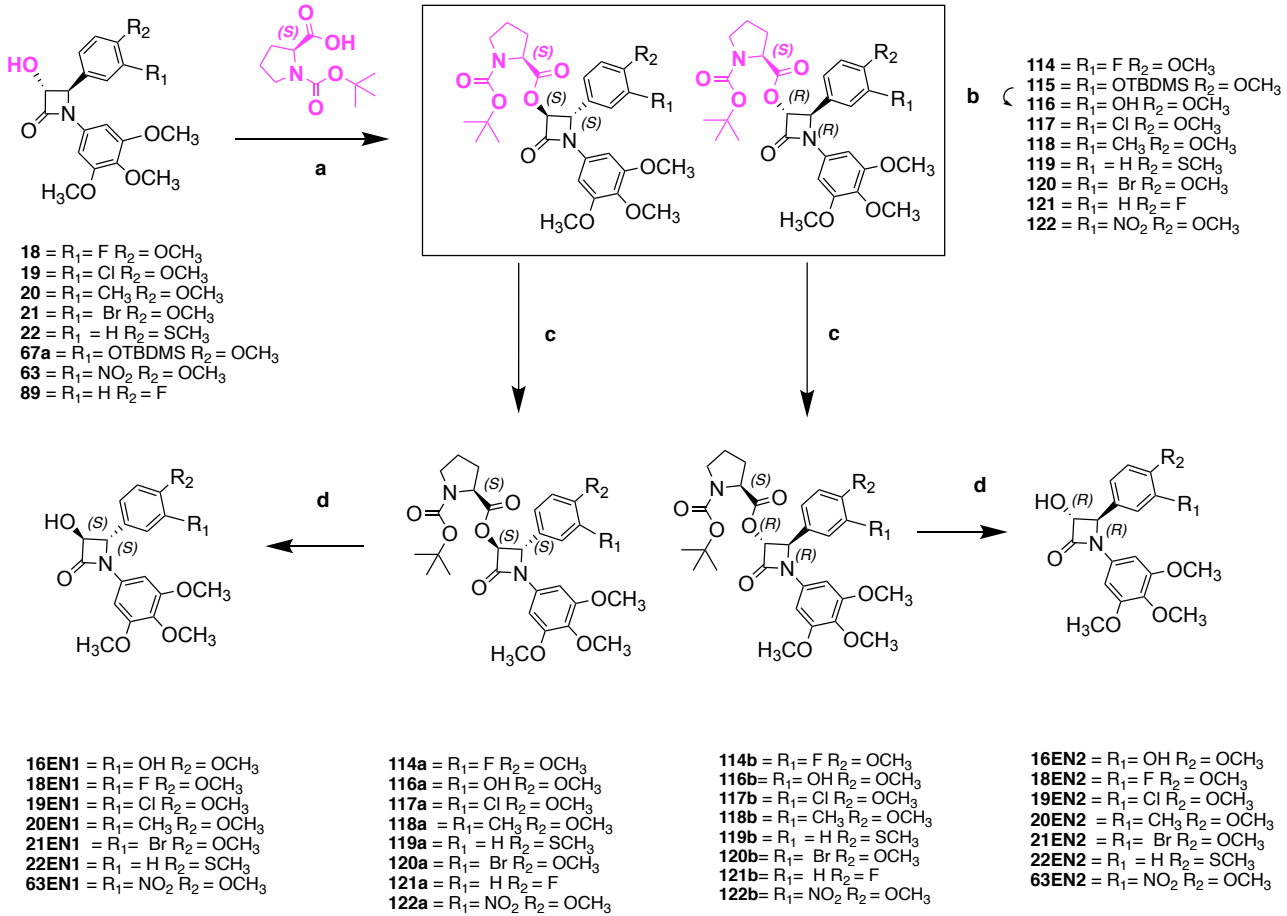

Scheme 4.2: Synthesis of diastereomers and enantiomers of 3-hydroxyl β-lactam**s 18-22, 63, 67a** and **69** by coupling with *N*-Boc-L-proline. **a:** HBTU, DIPEA, anhydrous MeCN, N_2, rt, 24 h; 32-83%. **b:** TBAF 1M in hexane, THF, 0 °C, 1-2h **c:** LC chiral resolution over silica gel with pore size 60 Å, 40-63 µM particle size and 230-400 mesh and gradual gradient of 4:1 n-hexane: MTBE to 2:1 MTBE: n-hexane. **d:** hydrazine dihydrochloride, anhydrous TEA, anhydrous methanol, 85 °C, 4h

Esterification using *N*-Boc-L-proline as the CDR required initial purification to separate the diastereomer mixture using flash LC with mobile phase of 1:1 *n*-hexane:ethyl acetate. This was carried out prior to resolution **(a**, Scheme 4.2). Isolated yields for diastereomer mixtures were mild to moderate ranging from 32% for **119** to 77% for **114** and 83% for **122**. For resolution of **16** to **116a** and **116b**, the chemistry involved esterification of 3-hydroxyl position of TBDMS protected **67a** to yield **115** as a mixture of OTBDMS protected diastereomers (Scheme 4.2). R_f values were > 0.8 due to the non-polar nature of the -OTBDMS moiety. Resolution of diastereomers bearing the TBDMS protecting group was therefore not achieved on TLC (2:1 MTBE: *n*-hexane), as the eluent failed to produce gradual separation of diastereomers due. De-silylation of the -OTBDMS using TBAF in THF (**b,** Scheme 4.2) to afford the free B ring *meta* hydroxyl substituted proline diastereomers **116**, and resolution using conditions described in **c**, Scheme 4.2 yielded **116a** and **116b** in 20% and 17% yields respectively (Table 4.1). Chiral resolution using the optimised LC procedure developed in Chapter 3 was achieved for a panel of 3-hydroxyl racemates albeit in poor to moderate yields for resolved β-lactam diastereomers (6-45%, Table 4.1)

Considering the requirement for progression towards their corresponding enantiomers for further *in vitro* biochemical analysis (**c,** Scheme 4.2), the use of chiral resolution as a strategy for enantiomer isolation while modest was considered as sufficient. Poor yields obtained *via* LC chiral resolution were attributed to the following issues:

1) The available amount of *trans* β-lactam racemate as a starting reactant limited the isolated diastereomer mixture yield.
2) Esterification chemistry requires a pre-requisite LC purification of the crude diastereomer mixture prior to chiral resolution.
3) Co-elution of the first diastereomer (**a**) often limits the available yield of second eluting diastereomer (**b**).

Table 4.1: Isolated diastereomer mixtures **114-122** and resolved diastereomer (**a** and **b**) yields for 3-hydroxyl β-lactams reported as % yield of original diastereomer mixture.

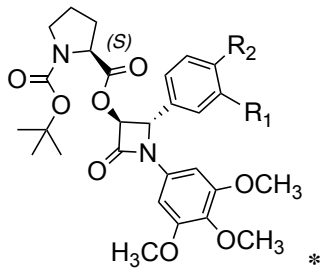

*

Code	R_1	R_2	Diastereomer mixture yield[1] %	Diastereomer a yield[2,3] %	Diastereomer b yield[2,4] %
114	F	OCH_3	80	45	24
116	OH	OCH_3	82	20	17
117	Cl	OCH_3	61	37	12
118	CH_3	OCH_3	58	37	6
119	H	SCH_3	32	27	12
120	Br	OCH_3	61	26	12
121	H	F	44	50	34
122	NO_2	OCH_3	82	40	25

[1] Reaction scale varied for each reaction depending on available yield of racemate.
[2] % Isolated yields for resolved diastereomers refer to % of original diastereomer mixture.
[3] Diastereomer a is the first eluting diastereomer.
[4] Diastereomer b is the second eluting diastereomer. *one diastereomer shown

For example, the success of the esterification of the 3-hydroxyl diastereomers and purification of the resulting diastereomer mixtures was varied. For example, **22**, only 32% was isolated as the pure diastereomer mixture **119 (a,** Scheme 4.2). In contrast 58% of **118** was isolated as the diastereomer mixture with 37% was resolved as **118a** while only 6% was isolated as the second eluting diastereomer **118b** (Table 4.1). For all other analogues, the trend of significant second diastereomer (**b**) loss also occurred, due to co-elution during LC chiral resolution. Isolated yields of **a** diastereomers ranged from 26% (**120a**) to 50% (**121a**) while those for **b** diastereomers were modest ranging from 6% (**119b**) to 34% [**121b** (Table 4.1)]. **114** and **121** were resolved in superior yield with respect to all other 3-hydroxyl analogues with 45% resolved for **114a** and 24% for **114b** and 50% and 34% isolated for **121a** and **121b** respectively (Table 4.1). Moderate yields of 37% for both B ring *meta* chlorine **117a** and *meta* methyl substituted **118a** were also resolved. The quantity of *meta* nitro-substituted **122a** and **122b** was too low for further reduction to the desired *meta* - NH_2 substituted

diastereomers. **63EN1** did not progress further for cell viability screening due to presence of the cytotoxic NO_2 moiety. Future work could involve reduction of the *meta*-nitro substituted diastereomer mixture prior to resolution and hydrazinolysis toward their enantiomeric forms. Additionally, **121a** and **121b** were not carried forward for isolation as the corresponding enantiomers due to preliminary cell viability data demonstrating poor anti-proliferative activity (Chapter 6).

4.1.2 *Application of 2D EXSY spectroscopy as a qualitative tool to confirm diastereomer ratios for resolved diastereomers of mixtures **114, 116-118, 120-122***

The 2D EXSY spectra at 400 MHz in $CDCl_3$ for representative examples of the L-proline derivatised 3-hydroxyl diastereomer mixtures **114, 116** and **117** in $CDCl_3$ are illustrated in Table 4.2, Table 4.3 and Table 4.4. Two independent sets of cross peaks are evident for each diastereomeric mixture of **114, 116** and **117**. A combination of cross peaks off the diagonal of the 2D EXSY spectrum, in addition to H_3 and H_4 resonance multiplication, is indicative of the presence of both diastereomers and equilibrating rotamers for the remainder of the 3-hydroxyl derivatised diastereomer panel. Therefore it was possible to use the 2D EXSY spectra for isolated diastereomers as visual and qualitative confirmation of successful LC diastereomer resolution. 2D EXSY spectra also assisted in the characterisation of H_3 and H_4 resonances in preparation for qNMR and *de* calculation of resolved fractions as outlined in Chapter 3.

Table 4.2: (Top) 2D EXSY spectra at 400 MHz in $CDCl_3$ for N-Boc-L-proline derivatised diastereomers of **114,** resolved **114a** and **114b** and (bottom) the corresponding ^1H NMR spectra in the H_3 and H_4 region (~ δ 4.8-5.5 ppm)

114	**114a**	**114b**
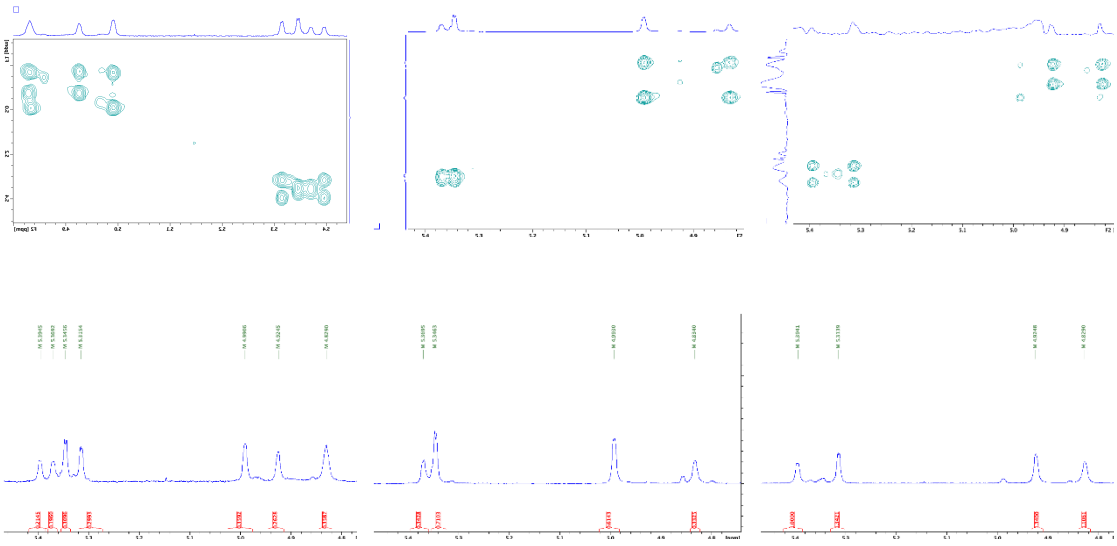		

Table 4.3: (Top) 2D EXSY spectra for diastereomers of **116,** resolved **116a** and **116b** and (bottom) their corresponding ^1H NMR spectra in the H_3 and H_4 region (~ δ 4.8-5.5 ppm)

116	**116a**	**116b**
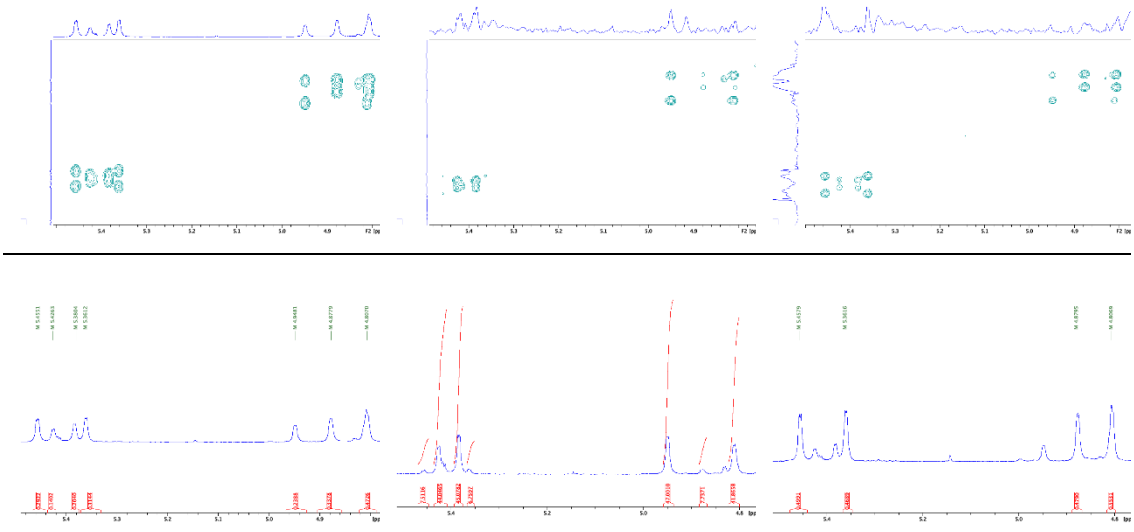		

Table 4.4: (Top) 2D EXSY spectra for diastereomers of **117,** resolved **117a** and **117b** and (bottom) their corresponding ^{1}H NMR spectra in the H_3 and H_4 region (~ δ 4.8-5.5 ppm)

117	**117a**	**117b**
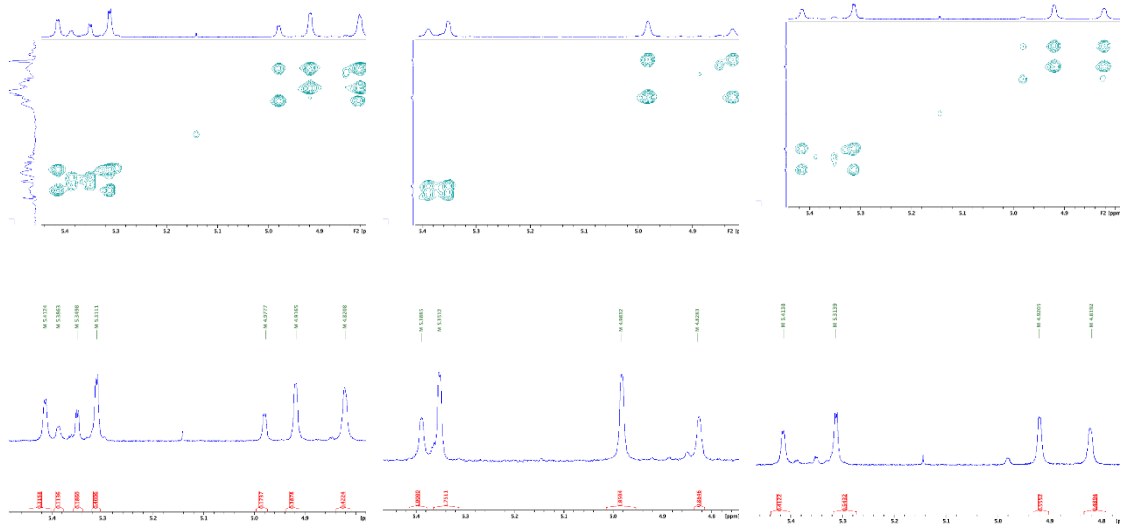		

4.1.3 *qNMR for calculation of de for diastereomers of **114-122***

qNMR experiments were carried out as described in Chapter 3. *De* values for **a** diastereomers ranged from 62-100% (average *de* value of 83%, Table 4.5) while those of **b** diastereomers as anticipated, were poorer based on qualitative observations from 2D EXSY spectra. *De* values for **b** diastereomers ranged from 51-83%. qNMR derived *de* values (Table 4.5) in tandem with 2D EXSY spectra (Table 4.2, Table 4.3 and Table 4.4) determined that diastereomer resolution was sufficient for progression to the corresponding enantiomers. **119a** and **119b** were also carried forward despite their low yield prohibiting accurate analysis by qNMR and 2D EXSY methods.

Table 4.5: Integration of H_3 and H_4 resonances on ^1H NMR axis for qNMR determination of d.r[1] and *de* values for resolved proline diastereomers.

Code	**d.r (H_3)[1] (D1:D2)**	***de* (H_3)**	**d.r (H_4)[1] (D1:D2)**	***de* (H_4)**	***De* (average H_3 and H_4 *de*)**
114a	93:7	86%	90:10	81	83%
114b	84:16	67%	86:14	72%	70%
116a	88:12	78%	86:14	76%	77%
116b	79:21	58%	75:25	50%	54%
117a	100:0	10%	100:0	10%	100%
117b	86:14	72%	86:14	72%	72%
118a	82:18	64%	81:19	60%	62%
118b	77:23	54%	74:26	48%	51%
120a	99:1	98%	99:1	98%	98%
120b	90:10	80%	93:7	86%	83%
122a	87:13	73%	91:9	89%	81%
122b	85:15	70%	92:8	84%	77%

[1] d.r (diastereomeric ratio) is the ratio of the percentage of one diastereomer in a mixture (D1) to that of the other (D2). D1 and D2 are calculated as the integrals of rotamers for the major and minor diastereomers, respectively, normalised to 100%.[572]

[2] *de* = D1 – D2

* **119a, 119b, 121a** and **121b** not determined

4.2 *Hydrazinolysis of diastereomers **114-122** to enantiomers **16EN1 -39EN1** and **16EN2-39EN2***

The proline CDR was removed using **c,** Scheme 4.2 *via* hydrazinolysis. Enantiomers were isolated in yields of 50-65% (Table 4.6).

Table 4.6: Isolated yields for 3-hydroxyl enantiomers

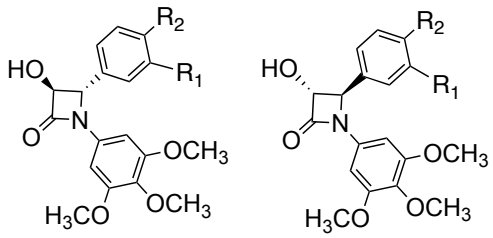

(+) **EN1** (-) **EN2**

Code	R_1	R_2	Enantiomer 1 yield (EN1)[1] %	Enantiomer 2 yield (EN2)[1] %
16	OH	OCH_3	30	18
17	H	OCH_3	30	66
18	F	OCH_3	46	67
19	Cl	OCH_3	71	70
20	CH_3	OCH_3	35	41
21	Br	OCH_3	76	65
22	H	SCH_3	48	27
63	NO_2	OCH_3	25	Not isolated

[1]Yield for hydrazinolysis

4.3 *Characterisation of 3-hydroxyl enantiomers*

Characterisation of 3-hydroxyl enantiomers included crystallisation to determine the absolute configuration at H_3 and H_4 positions of β-lactam ring, measuring optical rotations and enantiomeric excess (*ee*) determination using chiral HPLC. Additionally the drug-like properties of lead eutomers (determined in Chapter 6 during anti-proliferative assays) were evaluated. LogP values were experimentally measured for selected enantiomeric pairs.

4.3.1 *XRD studies for **17EN1** and **17EN2***

X-ray crystal studies were carried out on **17EN1** and **17EN2**, crystallised from ethanol over a period of four weeks, to determine their absolute configuration at H_3 and H_4 of the β-lactam ring (Table 4.7). **17EN1** (Figure 4.1) crystallised as an orthorhombic unit cell with crystal size of 0.32 x 0.04 x 0.03 mm^3 and final unit cell dimensions of a = 5.0080[342] Å, b = 12.5611(5) Å and c = 28.0822(12) Å. Chirality of *S* was calculated at the 3 position

using the absolute structure or flack parameter of -0.02(17). **17EN2** (Figure 4.1) crystallised also as an orthorhombic unit cell with crystal size of 0.51 x 0.06 x 0.05 mm^3 and final unit cell dimensions of a = 5.0067[342] Å, b = 12.5609(6) Å and c = 28.0863(13) Å. The opposite chirality of *R* was calculated at the 3 position using the absolute structure or flack parameter which is 0.1(19). X- ray structures confirm torsional angles between the A and B ring in close agreement with colchicine and CA-4, reported as 53 °[261,610] and 55 °[611,612] respectively. The A/B ring torsional angle was found to be 52.5 ° for **17EN1**. In contrast the torsional angle for **17EN2** was -56.3° demonstrating a different orientation of the B ring of **17EN2** compared to **17EN1**. XRD structures confirm 3*S*,4*S* as the absolute configuration for **17EN1** and 3*R*,4*R* for **17EN2** (Table 4.7). Crystallisation of the remaining enantiomers was not possible due to low yield. 3*S*,4*S* was assigned as the general absolute configuration for 3-hydroxyl **EN1** enantiomers while 3*R*,4*R* was assigned to **EN2**.

Table 4.7: ORTEP representation of the X-ray crystal structures for **17EN1** and **17EN2.** Molecular structure of the majority occupied moiety with atomic displacement shown at 50% probability. Dotted lines indicates intramolecular hydrogen bonding.

Enantiomer	Absolute Configuration	Structure	X ray ORTEP representation
17EN1	3*S*,4*S*	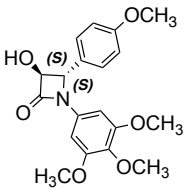	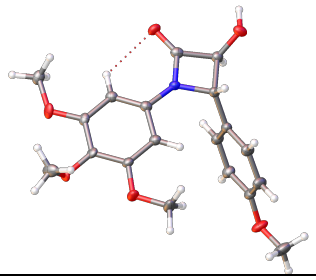
17EN2	3*R*,4*R*	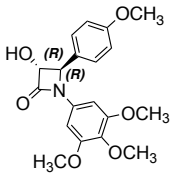	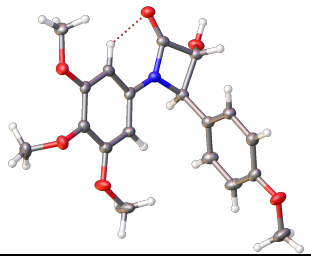

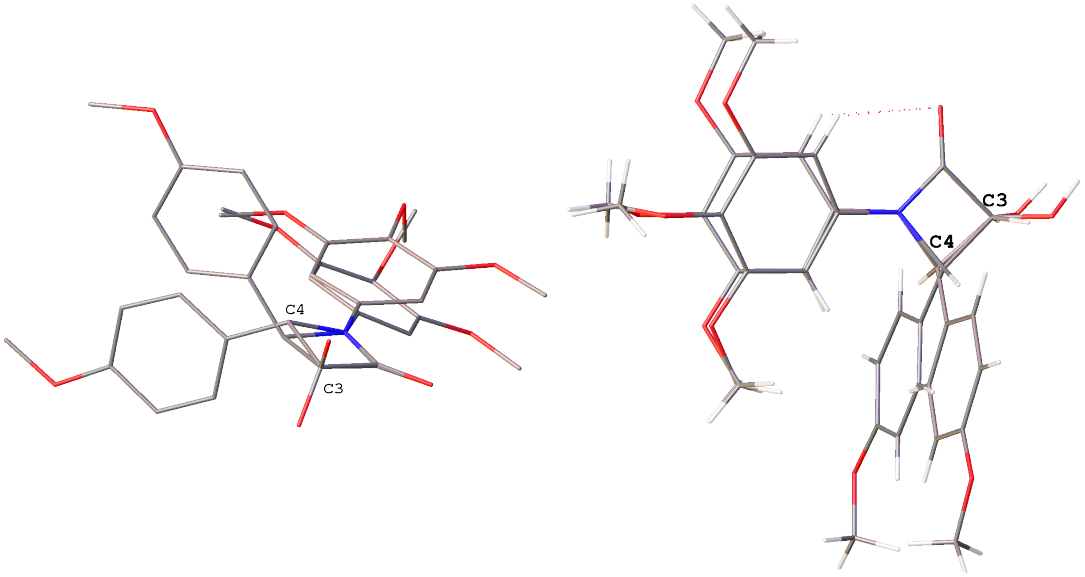

Figure 4.1: Overlay of X-ray crystal structures of **17EN1** and **17EN2** illustrating the 3-hydroxyl orientation at C_3 and C_4 of the β-lactam ring

4.3.2 *Optical rotations for **17EN1**, **17EN2**, **18EN1** and **18EN2***

Polarimetry is a facile method for determination of racemic forms or enantioenrichment. Plane polarised light is created by passing ordinary light (typically 589 nm from the D line of a sodium lamp) of one wavelength (*i.e* monochromatic light) through a polarising device which selects for only a single magnetic and electrical vector oscillating in a single plane.) Light passes through the analyte within the sample cell and the detector determines the degree of rotation. Rotation to the right is dextrorotatory and is annotated with a + value while to the left is levorotatory and assigned a – value. Optical rotations depend on concentration, temperature, solvent and wavelength. Due to temperature dependency of readouts, optical rotations are measured at constant temperature of 20 °C. The specific rotation or $[\alpha]\frac{20}{D}$ is a fundamental property of a chiral molecule with 100% *ee*. Enantiomeric pairs have equal and opposite specific rotations while racemates do not rotate plane polarised light. Enantiomers of **17** and **18** were the only enantiomeric pairs with sufficient yield available for calculation of optical rotations. Observed rotations only were calculated, since *ee* was not known. Specific rotations are not known for **17EN1**, **17EN2**, **18EN1** and **18EN2** since *ee* values obtained *via* LC chiral resolution were not 100%. Observed optical rotations however indicate that the 3*S*,4*S* enantiomer (**EN1**) is dextrorotatory while the 3*R*,4*R* enantiomer (**EN2**) is levorotatory (Table 4.8).

Table 4.8: Observed optical rotations for enantiomers of **17** and **18**

Code	Concentration (g/ mL)	Observed α	Observed α at 1g/ mL
17EN1	0.004	+ 0.09	+ 25.14
17EN2	0.004	-0.1	-25.38
18EN1	0.004	+ 0.07	+ 22.15
18EN2	0.003	- 0.04	- 17

4.4 *Application of optimised chiral resolution using esterification of B ring meta hydroxyl group*

The second route for esterification and chiral resolution involved coupling of *N*-Boc- L-proline to the B ring *meta* hydroxy moiety (Scheme 4.3). This was successfully trialled for *trans* **24** to isolate the diastereomer mixture **124 (**Scheme 4.3)**. 124a** and **124b** were resolved in 26% and 21% yield respectively (Table 4.9). Chiral resolution was subsequently successfully applied to a panel of B ring *meta* hydroxyl substituted analogues enabling access the enantiomers of extremely potent 3-substituted racemates previously synthesised by Meegan *et al*.[357, 359, 382, 495] Although esterification was achieved for the majority of the panel of B ring *meta* hydroxyl substituted racemates (Table 4.9), resolution of 3-phenoxy substituted *trans* **129** and 3-fluoro substituted **126** was unsuccessful. **123a** and **123b** were also synthesised as the 3-acetoxy diastereomer analogues (**123**) by coupling of the *N*-Boc-L- proline to the TBDMS deprotected B ring *meta* hydroxyl substituent of **67b**. 26% and 21% were resolved for 3-acetoxy protected **123a** and **123b** respectively (Table 4.9). CDR coupling to the B ring *meta* hydroxyl position proved an equally efficient route for isolation of enantiomers **16EN1** and **16EN2**. Racemate **41** is a novel analogue designed and synthesised on due to success of the corresponding phenolic racemate **26** as the most potent β-lactam reported to date.[495] Diastereomers of **41** were successfully synthesised as the mixture **131** and resolved in yields of 18% and 22% as **131a** and **131b** respectively.

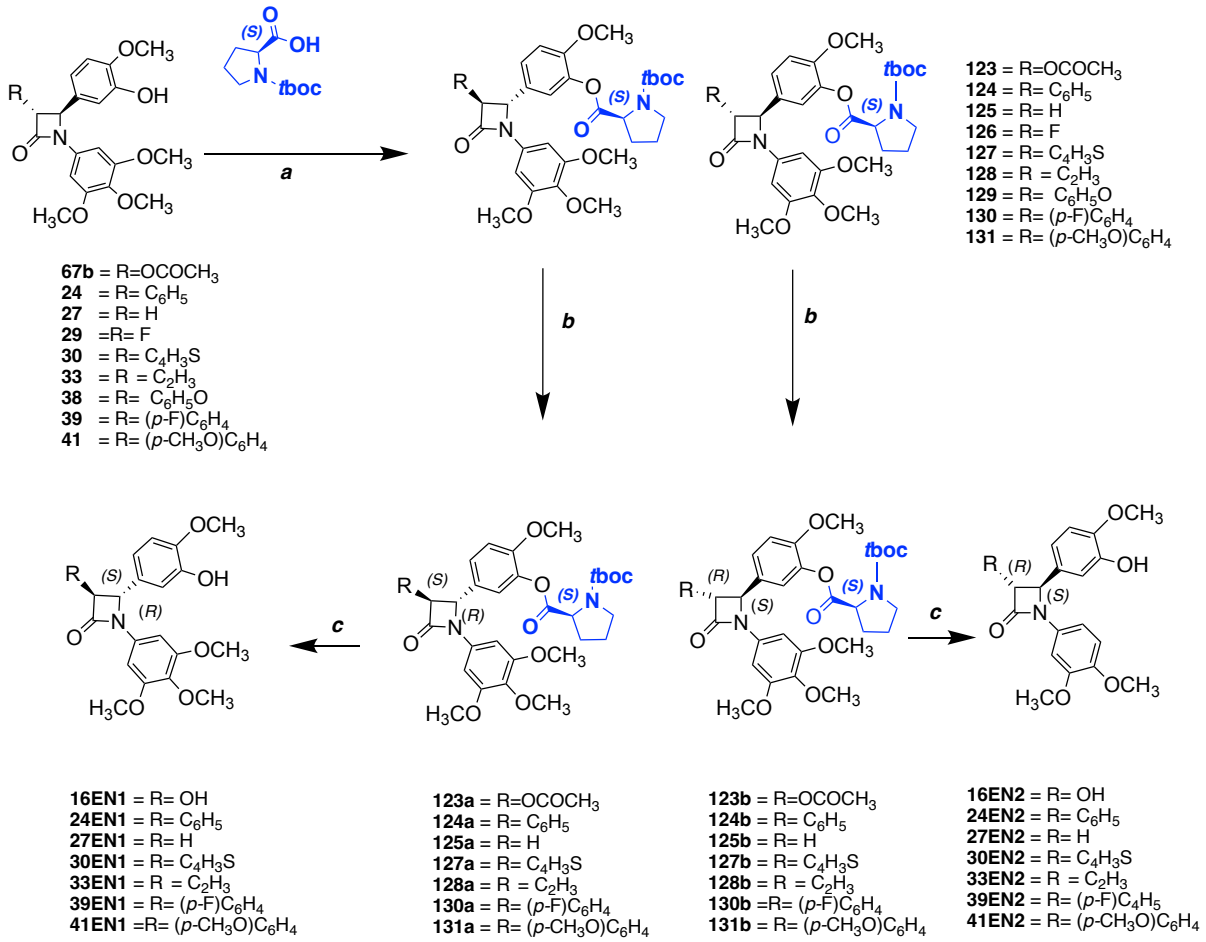

Scheme 4.3: Synthesis of diastereomer mixtures **123-131,** resolution to 3*S*,4*R* **a** and 3*R*,4*S* **b** diastereomers and hydrazinolysis to their corresponding enantiomers. **a:** HBTU, DIPEA, anhydrous MeCN, N_2, rt, 24h. Yield of diastereomer mixtures: 32-83%. **b:** LC chiral resolution over silica gel with pore size 60 Å, 40-63 µM particle size and 230-400 mesh and gradual gradient of 4:1 n-hexane: MTBE to 2:1 MTBE: n-hexane. **c:** hydrazine dihydrochloride, anhydrous triethylamine, MeOH, 85 °C, 4 h. *(***c** removed both 3-acetoxy and N-Boc-L-proline*)*

Esterification chemistry outlined in Scheme 4.3 resulted in poor to moderate yields for proline derivatised diastereomer mixtures [7-65%, (average 37%) (Table 4.9)], which was considerably lower than corresponding yields isolated for the 3-hydroxyl derivatised diastereomers (average 63%) (Table 4.9)]. The esterification chemistry was therefore more optimal for resolving 3-hydroxyl β-lactams. Co-elution of diastereomers was also a limiting issue for the B ring *meta* hydroxyl route of esterification (Scheme 4.2 and Scheme 4.3). Nevertheless yields of resolved isolated B ring *meta* hydroxyl diastereomers ranged from 11 – 40% [average 21%, (Table 4.9)] and were sufficient for progression towards hydrazinolysis to their corresponding enantiomers **(c,** Scheme 4.3).

Table 4.9: Yields of isolated diastereomer mixtures **123-131** and their resolved diastereomers (**a** and **b**).

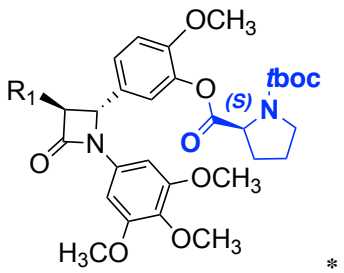

*

Code	R_1	Diastereomer mixture yield[1] %	Diastereomer a yield[2,3] %	Diastereomer b yield[2,4] %
123	$OCOCH_3$	65	26	21
124	C_6H_5	57	26	21
125	H	53	15	14
126	F	26	Not isolated	Not isolated
127	C_4H_3S	7	14	20
128	C_2H_3	43	40	33
129	C_6H_5O	11	Not isolated	Not isolated
130	C_6H_4F	37	11	15
131	C_7H_8O	35	18	22

[1] Reaction scale varied for each reaction depending on available yield of racemate.
[2] % Isolated yields for resolved diastereomers refer to % of original diastereomer mixture.
[3] Diastereomer **a** is the first eluting diastereomer.
[4] Diastereomer **b** is the second eluting diastereomer.
* one diastereomer shown

Although rotamers were observed on 2D EXSY and ^{1}NMR spectra of 3-hydroxy-4-methoxy B ring containing proline derivatised diastereomers **124, 125, 127** and **131** (Table 4.9), the complex presentation of the ^{1}H NMR axis prohibited use of qNMR and qualitative EXSY studies as a method for determining their *de*. Confirmation of successful resolution therefore relied on chiral HPLC to determine *ee* of the final enantiomers.

4.4.2 *Hydrazinolysis of 3-hydroxy-4-methoxy B ring containing proline derivatized diastereomers to their corresponding enantiomers*

B ring *meta* hydroxyl esterified diastereomers (Table 4.9) were hydrazinolysed to corresponding enantiomers (**c,** Scheme 4.3) in yields of 38 – 86% (Table 4.10).

Table 4.10: Isolated enantiomer yields for B ring *meta* hydroxy containing hydroxyl analogues

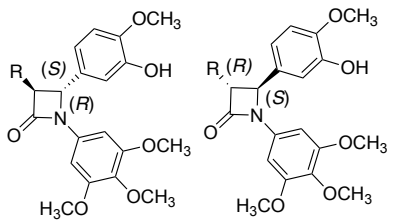

Code	R	Enantiomer 1 yield (EN1) %	Enantiomer 2 yield (EN2) %
16	$OCOCH_3$	50	61
24	C_6H_5	43	38
27	H	58	80
30	C_4H_3S	63	72
33	C_2H_3	38	Not isolated
39	(*p*-F)C_6H_4	86	81
41	(*p*-CH_3)C_6H_4	85	61

4.5 *XRD analysis of **24EN1***

XRD analysis was carried out for **24EN1** as a representative example of the 3-hydroxy-4-methoxy substituted B ring containing enantiomers to determine absolute configuration at the H_3 and H_4 positions of the β-lactam ring. The chiral molecular structure of **24EN1** was obtained from its orthorhombic crystal and the absolute

configuration was determined to be 3*S*, 4*R* based on flack parameter of -0.4 (Table 4.11).

Table 4.11: Chiral molecular structure of **24EN1** with atomic displacement shown at 50% probability and heteroatoms labelled only. Dotted lines indicate hydrogen bonding interactions.

Enantiomer	Absolute Configuration	Structure	Chiral XRD structure
24EN1	3*S*,4R	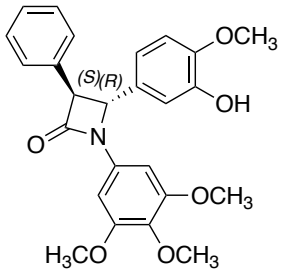	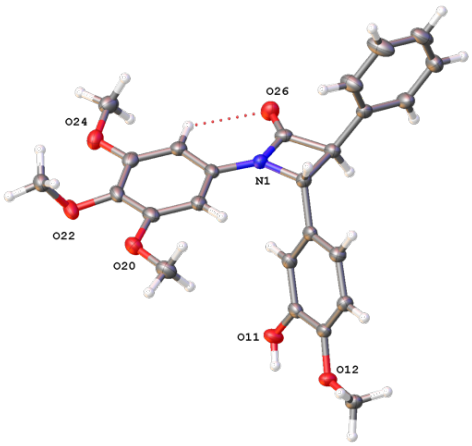

4.6 *Chiral resolution of 3-phenolic substituted β-lactam analogues*

It was desirable to apply the optimised chiral resolution procedure to phenolic analogues **26, 68** and **69**, in particular for **26** due to its reported potency as the most potent β-lactam racemate to date.[495] Additionally **68** and **69** were designed for optimised antiproliferative activity in CA-4 resistant HT-29 cells. The phenol at position 3 of the β-lactam ring was chosen as a starting point for esterification with amino acid CDRs as a common moiety in **26, 68** and **69**. Esterification was successful for racemates **68** and **69** confirmed by ^{1}H NMR yielding **133** and **134** (Scheme 4.4). However, attempted esterification of TBDMS protected **79** with *N*-Boc-L-proline did not yield **132** as the desired diastereomer mixture (**a,** Scheme 4.4). A second route was trialled *via* esterification of the benzyloxy protected **83**'s B ring *meta*-hydroxyl (**b,** Scheme 4.4). The proline protected diastereomer mixture **132** was not observed or isolated. Resolution of diastereomers was not achieved for phenolic esterified proline diastereomers **133** or **134** using standard resolution mobile phase of 2:1 MTBE: *n*-hexane. *N*-Boc- L -phenylalanine was also trialled as the CDR for resolution of racemate **68**. Esterification chemistry was successful yielding **135.** Resolution towards isolated diastereomers **135a** and **135b** was not however achieved in

keeping with findings from Chapter 3 for phenylalanine diastereomers of **17** (**109** and **110,** Scheme 3.1) which were not resolved using LC.

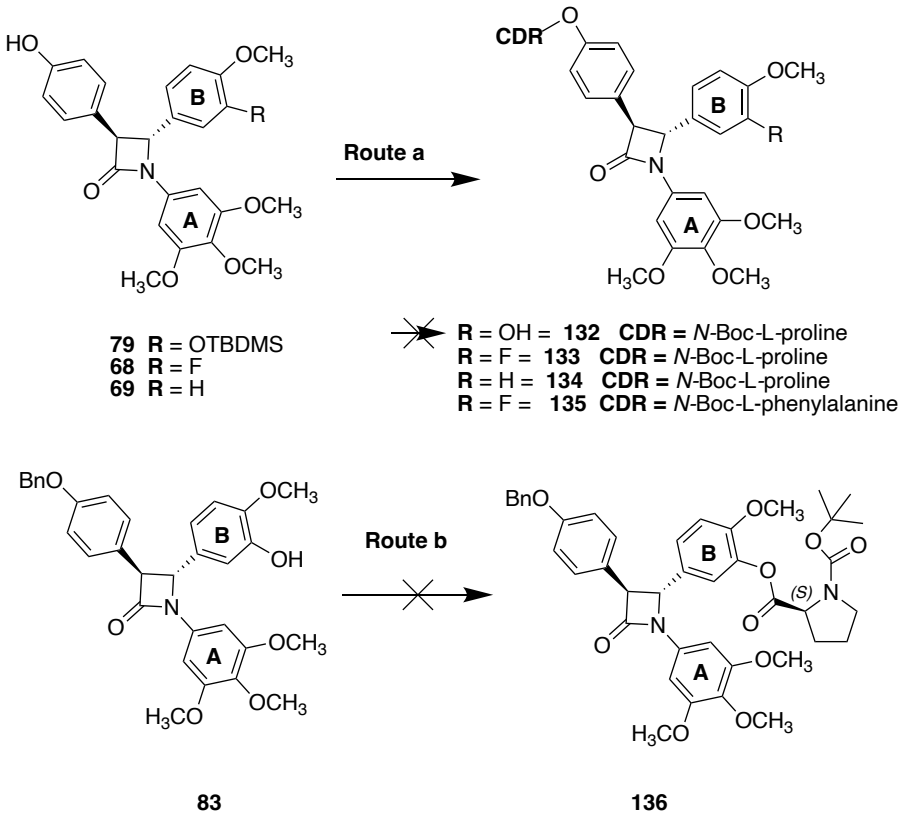

Scheme 4.4: Routes for esterification of phenolic β-lactams to corresponding diastereomer mixtures

4.7 *Application of optimised chiral resolution via amide bond derivatisation of the B ring NH_2 substituent*

Three analogues containing a B ring *meta* amine substituent were selected for resolution (Scheme 4.5). The chiral resolution procedure employed the amine as a point of attachment for *N*-Boc-L-proline. Two alternative synthetic approaches were applied for analogues **32, 35** and **37 (a** and **b,** Scheme 4.5). Route **a** (Scheme 4.5) employed an identical procedure as for esterification of 3-hydroxyl B ring *meta* hydroxyl substituted combretazets. An isolated yield of 35% was obtained for diastereomer **138** from racemate **32**. **139** was not observed or isolated from racemate **35**. The isolated yield of 3-phenoxy substituted **137** from **37** was negligible (<1%).

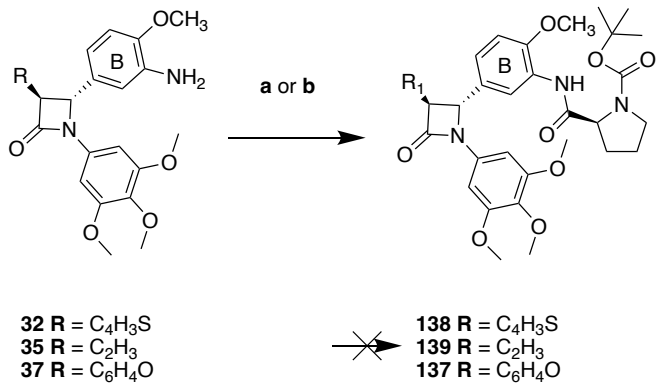

Scheme 4.5: Route for diastereomer mixture synthesis for combretazet racemates **32, 35** and **37** *via* amide bond formation. **a:** *N*-Boc-L-proline, HBTU, DIPEA, MeCN, N_2, rt, 24h**.** Yield: 0-35% **b:** HOBt, DCC, *N*-Boc-L-proline, DMF. Yield 0-20%

The second approach to yield amide derivatised diastereomers is outlined in route **b,** Scheme 4.5. Racemate **32** was dissolved in dimethylformamide (DMF) under inert conditions followed by addition of 1-hydroxybenzotriazole (HOBt), dicyclohexylcarbodiimide (DCC) and *N*-Boc-L-proline. DCC is commonly used to prepare both esters and amides from carboxylic acids with HOBt employed as an additive to reduce racemisation.[613,614] The nucleophilic imine of DCC decarboxylates the amino acid CDR to the carboxylate anion which as a nucleophile reacts with the now electrophilic carbon of DCC (**140,** Scheme 4.6) affording intermediate **141 (**Scheme 4.6). The electrophilic intermediate **141 (**Scheme 4.6) reacts with the nucleophilic oxygen of HOBt's *N*-oxide anion to form the activated HOBt ester (**142,** Scheme 4.6) and dicyclohexylisourea as an insoluble by-product (filtered away during reaction work up). The nucleophilic β-lactam (**32,** Scheme 4.6) then reacts with the carbonyl of proline-HOBt activated ester (**142,** Scheme 4.6) eliminating HOBt and affording the desired amide diastereomer mixture **138**.[615,616] **138** was isolated in lower yield of 20% using **b,** Scheme 4.6 compared to 35% isolated using route **a (**Scheme 4.6**)**.

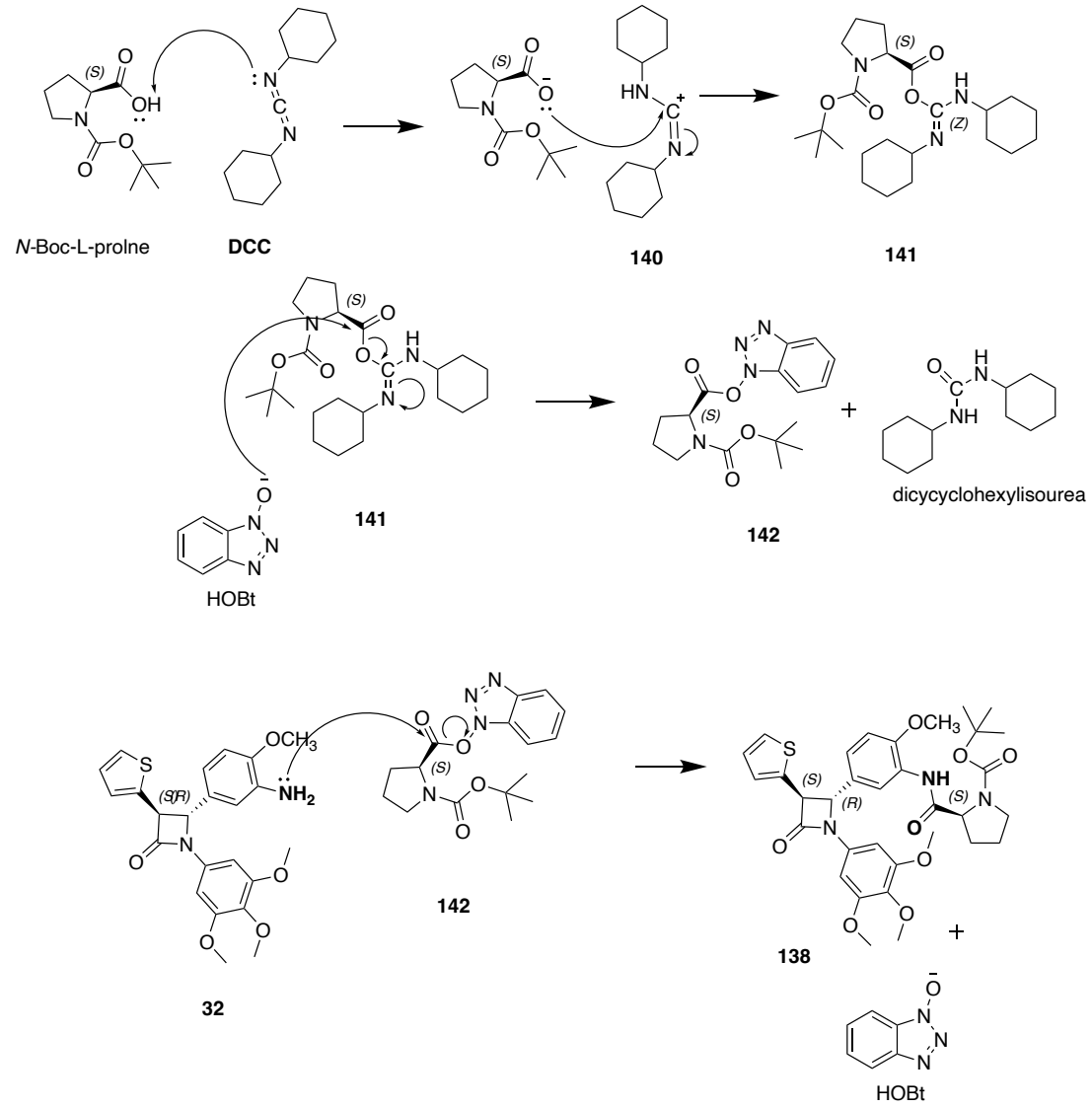

Scheme 4.6: Synthesis of amide diastereomer mixtures of B ring *meta* NH_2 substituted β-lactams using DCC and HOBt with **32** derivatised to diastereomer mixture **138** illustrated as a representative example. (One enantiomer and diastereomer shown).

Only route **a** (Scheme 4.6) was trialled for synthesis of **137** due to low available yield of racemate **37** (<1%). HRMS confirmed the desired mass of 636.2384 calculated for $C_{33}H_{38}N_3O_8S$ and 646.278552 calculated for $C_{35}H_{40}N_3O_9$ (APCI [M-H^+]) for **138** and **137** respectively. An amide NH signal was observed for **138** on ^{15}N NMR (60.8 MHz in $CDCl_3$) at δ 117.8 ppm in line with literature values reported for amide NH resonances.[617] Neither route **a** or **b** (Scheme 4.6) yielded diastereomer mixture **139**. Diastereomer separation was not achieved for either amide diastereomers **137** or **138** using the optimised chiral resolution procedure. Amide bonds are more rigid than ester bonds with

a higher rotational energy barrier due to their planar geometry and ability to form resonance structures.[618] This explains the absence of rotamers on ^{1}H NMR for amide diastereomers. Importantly amide bonds are extremely resistant to hydrolysis with respect to esters,[619, 620] requiring heat and aqueous acid or base for prolonged periods to afford the desirable free hydroxyl.[621] Amide bonds are stable in neat trifluoroacetic acid.[622] Progression toward enantiomers *via* CDR aminolysis would require extensive optimisation in order to prevent β-lactam ring opening under such harsh conditions. For this reason chiral resolution of amide diastereomers did not progress beyond initial isolation of **137** and **138.**

4.8 *Chiral HPLC to determine enantiomeric excess of isolated analogues*

Chiral HPLC was carried out on racemates and their isolated enantiomers using the chiral stationary phase column, Chrompak-IH-3 (150 x 4.6 mm) supplied by Chiral Technologies Europe with a Chiral- IH-3 guard column utilising an immobilised chiral polysaccharide stationary phase (*tris(S)*-a-*methylbenzylcarbamate*). Experimental details are described in Chapter 10. Chiral HPLC chromatograms were compared to achiral chromatograms for families of **17** and **24** as representative examples illustrated in Figure 4.2 and Figure 4.3. For 3-hydroxyl racemates, the 3*S*,4*S* **EN1** enantiomer eluted first followed by 3*R*,4*R* **EN2**. Achiral HPLC chromatograms for racemates demonstrate a single elution for both enantiomers versus two enantiomers present in a 1:1 ratio on chiral HPLC chromatograms. **(A** and **B,** Figure 4.2 and Figure 4.3) *Ee* values are presented in Table 4.12. *Ee* values were compared to *de* values obtained using qNMR and found to be in an acceptable range of error (1-4%) in comparison to chiral HPLC derived *ee* values. Consistently across all enantiomeric pairs, **EN2** enantiomers had lower *ee* values on account of diastereomer co-elution during the LC chiral resolution procedure. LC chiral resolution resulted in poor *ee* for analogues such **20EN1** (66% *ee*) and **27EN1** (46% *ee*). These analogues were selected as the focus of kinetic resolution to determine if an alternative resolution method would result in greater enantioenrichment (Chapter 7).

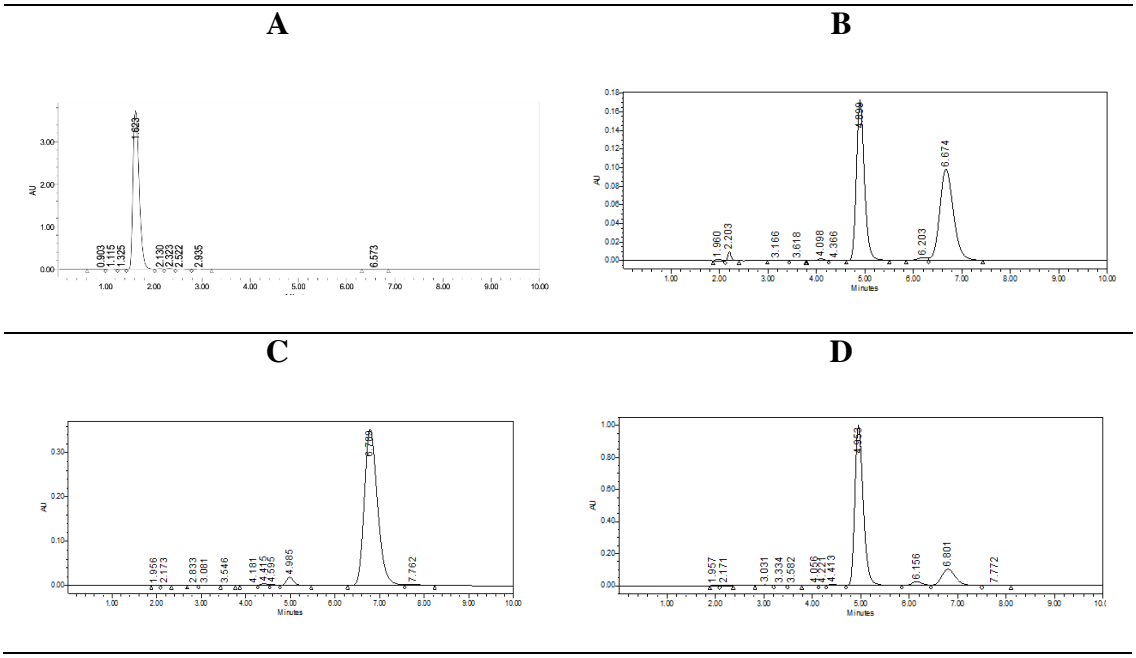

Figure 4.2: HPLC chromatograms for **A:** Achiral chromatogram for *trans* racemate **17**; **B:** chiral chromatogram for *trans* racemate **17**; **C:** Chiral chromatogram for 3*S*,4*S* enantiomer **17EN1**; **D:** Chiral chromatogram for 3*R*,4*R* enantiomer **17EN2**

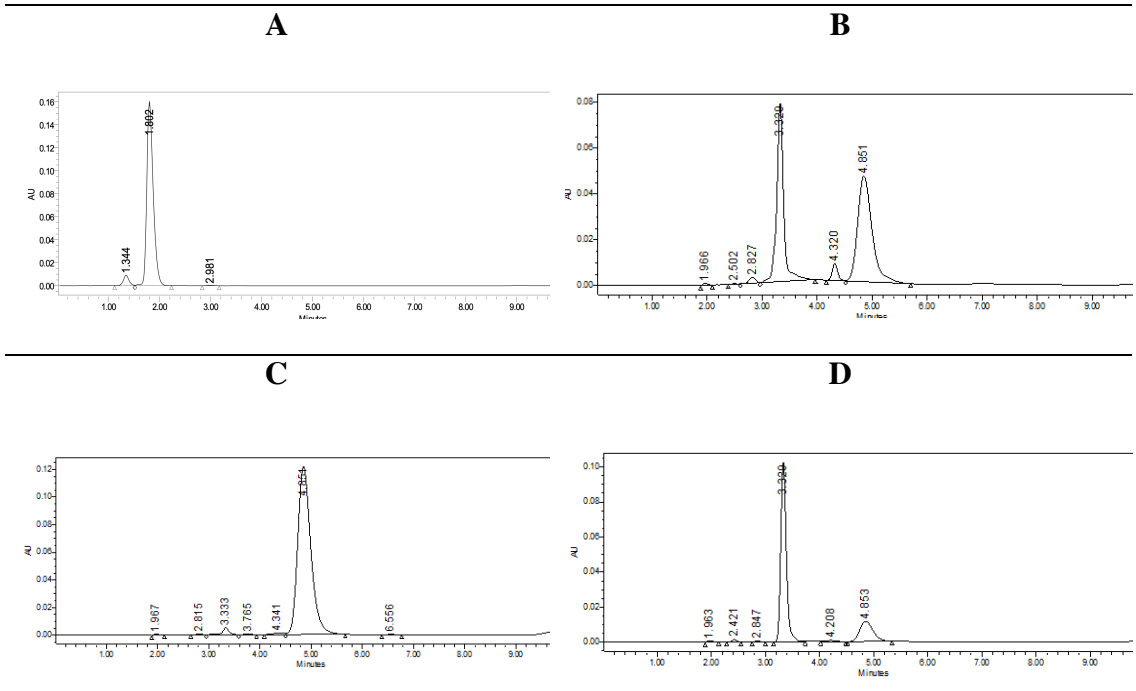

Figure 4.3: HPLC chromatograms for **A:** Achiral chromatogram for *trans* racemate **24**; **B:** chiral chromatogram for *trans* racemate **24**. **C:** Chiral chromatogram for 3*S*,4*R* enantiomer **24EN1**; **D:** Chiral chromatogram for 3*R*, 4*S* enantiomer **24EN2**

Table 4.12: Enantiomeric excess (*ee*) for enantiomeric combretazets determined by chiral HPLC.

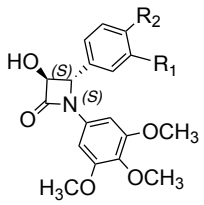

16EN1 = R_1= OH R_2 = OCH_3
17EN1 = R_1= H R_2 = OCH_3
18EN1 = R_1= F R_2 = OCH_3
19EN1 = R_1= Cl R_2 = OCH_3
20EN1 = R_1= CH_3 R_2 = OCH_3
21EN1 = R_1= Br R_2 = OCH_3
22EN1 = R_1 = H R_2 = SCH_3

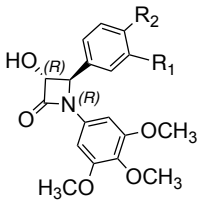

16EN2 = R_1= OH R_2 = OCH_3
17EN1 = R_1= H R_2 = OCH_3
18EN2 = R_1= F R_2 = OCH_3
19EN2 = R_1= Cl R_2 = OCH_3
20EN2 = R_1= CH_3 R_2 = OCH_3
21EN2 = R_1= Br R_2 = OCH_3
22EN2 = R_1 = H R_2 = SCH_3

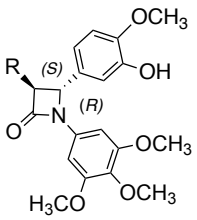

24EN1 = R= C_6H_5
27EN1 = R= H
30EN1 = R= C_4H_3S
33EN1 = R = C_2H_3
39EN1 = R= (*p*-F)C_6H_4
41EN1 = R= (*p*-CH_3O)C_6H_5

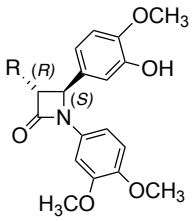

24EN2 = R= C_6H_5
27EN2 = R= H
30EN2 = R= C_4H_3S
33EN2 = R = C_2H_3
39EN2 = R= (*p*-F)C_6
41EN2 = R= (*p*-CH_3

Compound	Major Peak(%)	Minor Peak (%)	*ee* (%)[1]	*de* (%)[2]
16EN1 (*S*,*S*)	88	12	**75**	77
16EN2 (*R*,*R*)	70	30	**41**	54
17EN1 (*S*,*S*)	97	3	**94**	90
17EN2 (*R*,*R*)	85	14	**71**	74
18EN1 (*S*,*S*)	90	11	**79**	83
18EN2 (*R*,*R*)	87	12	**75**	70
19EN1 (*S*,*S*)	96	5	**91**	100
19EN2 (*R*,*R*)	89	11	**78**	72
20EN1 (*S*,*S*)	8	17	**66**	62
20EN2 (*R*,*R*)	75	25	**50**	51
21EN1 (*S*,*S*)	100	24	**76**	98
21EN2 (*R*,*R*)	100	4	**96**	83
22EN1 (*S*,*S*)	92	8	**84**	Nd
22EN2 (*R*,*R*)	93	8	**85**	Nd
24EN1 (*S*,*R*)	98	2	**96**	Nd
24EN2 (*R*,*S*)	79	21	**59**	Nd
27EN1	81	19	**61**	Nd
27EN2	73	27	**45**	Nd
30EN1(*S*,*R*)	100	0	**100**	Nd
30EN2 (*R*,*S*)	78	22	**56**	Nd
33EN1 (*S*,*R*)	93	7	**85**	Nd
41EN1 (*S*,*R*)	93	7	**89**	Nd
41EN2 (*R*,*S*)	62	38	**23**	Nd

[1] *ee* calculated using major peak – minor peak
[2] *de* = D1 – D2 calculated using qNMR and diastereomer intermediates

4.9 *Analysis of drug like properties*

To determine the biopharmaceutical suitability for lead combretazet enantiomers (determined using anti-proliferative assays in Chapter 6), an *in silico* cheminformatic analysis was carried out using the Swiss ADME webtool, followed by experimental determination of logP values. Chapter 6 has determined that the 3*S*,4*S* 3-hydroxyl **EN1** enantiomer and 3*S*,4*R* 3-substituted enantiomers are the eutomers of their enantiomer pairs. Therefore only **EN1** enantiomers were of interest for *in silico* screening.

4.9.1 *In silico cheminformatic analysis*

The physicochemical properties of lead enantiomers were evaluated using the free Swiss ADME webtool designed for computer aided drug designed (CADD).[623] Traditional ways to estimate the fate of a drug when administered to a patient are considered by its pharmacokinetic (PK) profile. PK is defined by the National Cancer Institute (NCI) as the drug's activity in the body over a period of time. PK includes processes of absorption (A), distribution in the body and localisation in tissues (D), metabolism (M) and excretion (E). [624,625] ADME factors impact a drug's access to the target site of action.[626] Computer models are valid alternatives to experimental procedures to determine ADME parameters,[627] particularly when synthetic accessibility is difficult.[628] A high attrition rate of drug candidates during clinical trials due to poor ADME parameters of drug candidates now necessitates evaluation of ADME at preliminary stages in drug development to mitigate risk of PK related failure during clinical phases.[629,630]

4.9.2 *Physicochemical properties and lipophilicity*

Molar refractivity and lipophilicity are properties which influence receptor binding, cellular uptake and bioavailability. Molar refractivity is defined as the molar volume corrected by the refractive index and represents the size and polarizability of a fragment or molecule.[631,632] Ghose *et al* propose suitable ranges for 'drug-like' molecules of 40 – 130 m^3/mol.[633] Molar refractivities for enantiomers range from 98.05 (**18EN1**) – 136.86 (**41EN1**) m^3/mol (Table 4.13). **41EN1** was the only enantiomer outside criteria for molar refractivity for optimal drug-like properties.

Polar surface area (PSA) is defined as the polar surface area of a molecule arising from oxygen, nitrogen and hydrogen atoms.[634] A major challenge in early lead optimiaation in drug discovery is the balance between permeability and water solubility. The more polar a molecule, the less permeable it becomes, reducing diffusion potential across gastrointestinal and cell membranes and overall exposure at target site of action. Topological polar surface area (TPSA) is a method of describing polarity enabling calculation of PSA based on addition of tabulated data for surface contributions of polar fragments within a molecule. It may be used for rapid screening of bioavailability for virtual libraries of analogues.[635] The favourable range for TPSA is broadly defined from 0-140 $Å^2$.[636] It is suggested that < 140 $Å^2$ is a good indicator of intestinal absorption while < 60 $Å^2$ results in BBB permeation.[637] Hence, >70 $Å^2$ and < 130 $Å^2$ are ideal TPSA values for drug like candidates. Each enantiomer fulfils this criteria ranging from 77.46 **(17EN1, 18EN1, 33EN1, 20EN1, 39EN1, 24EN1, 33EN1** and **39EN1**) to 105.70 [**30EN1** (Table 4.13)].

Hydrophobicity is an important drug parameter determining drug permeation, passive drug diffusion and therefore final potency of a molecule. Excessive lipophilicity mediates sub-optimal bioactivity due to poor solubility and poor access to the target site.[638] The descriptor of lipophilicity is the partition coefficient *P* , the partition between two immiscible solvents, *n*-octanol and water. Lipophilicity is quoted as logP; defined by Equation 4.1.

$$\mathbf{LogP} = \mathbf{LogP}_{\mathbf{o/w}} = \text{Log } C_O / C_w$$

C_O = concentration in *n*-octanol
C_w = concentration in water

Equation 4.1: Equation for logP (octanol/water partition coefficient)

The Swiss ADME model defines a molecule as 'drug like' if it falls within the range of -0.7 to + 5.0. Each enantiomer falls within this range. **24EN1** has a high consensus logP of 3.56 which may limit its progression in the parent form towards *in vivo* models due to solubility issues. However the B ring *meta* hydroxyl of **24EN1** is available for derivatisation towards the phosphate prodrug. Solubility data previously reported

demonstrates that racemate **24** displayed no detectable level of solubility in comparison to its corresponding phosphate prodrug with aqueous solubility measured at 0.3 mg/mL, above the minimum requirement of 0.05 mg/ mL for drug like candidates.[380] A similar derivitisaiton has potential to increase aqueous solibility for **24EN1** thus ensuring its clinical viability.

Table 4.13: Physiochemical properties of lead enantiomers calculated using the Swiss ADME webtool.

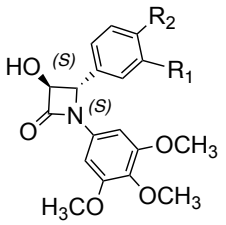

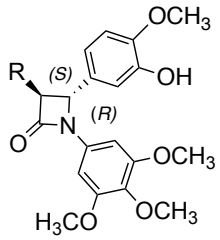

16EN1 = R_1= OH R_2 = OCH_3
17EN1 = R_1= H R_2 = OCH_3
18EN1 = R_1= F R_2 = OCH_3
19EN1 = R_1= Cl R_2 = OCH_3
20EN1 = R_1= CH_3 R_2 = OCH_3
21EN1 = R_1= Br R_2 = OCH_3
22EN1 = R_1 = H R_2 = SCH_3

24EN1 = R= C_6H_5
27EN1 = R= H
30EN1 = R= C_4H_3S
33EN1 = R = C_2H_3
39EN1 = R= (*p*-F)C_6H_4
41EN1 = R= (*p*-CH_3O)C_6H_5

	MR (m^3/ mol)	TPSA ($Å^2$)	Log P [1]	Water Solubility (mg/mL)	Water Solubility Class	GI Absorption
16EN1	100.12	97.69	1.62	5.79e-02	Soluble	High
17EN1	98.09	77.46	2.02	1.43e-02	Moderately Soluble	High
18EN1	98.05	77.46	2.31	8.16e-03	Moderately soluble	High
19EN1	103.10	77.46	2.55	4.05e-03	Moderately soluble	High
20EN1	103.06	77.46	2.34	6.25e-03	Moderately soluble	High
21EN1	105.79	77.46	2.62	2.87e-03	Moderately soluble	High
22EN1	103.32	95.53	2.56	6.57e-03	Moderately soluble	High
24EN1	123.44	77.46	3.56	6.14e-05	Poorly soluble	High
27EN1	98.95	77.46	2.35	8.44e-03	Moderately soluble	High
30EN1	121.32	105.70	3.55	3.39e-04	Poorly soluble	High
33EN1	108.09	77.46	2.86	5.77e-03	Moderately soluble	High
39EN1	123.40	77.46	3.87	3.50e-05	Poorly soluble	High
41EN1	136.86	86.69	3.03	5.42e-05	Poorly soluble	High

MR = molar refractivity, TPSA = topological surface area, [1]consensus logP derived from three independent methods

4.9.3 *Bioavailability radar of lead enantiomers*

The bioavailability radar is an excellent graphical tool for rapid assessment of drug likeness. It takes into account six physiochemical properties: lipophilicity (LIPO), size (SIZE), polarity (POLAR), solubility (INSOLU), degree of saturation within compound (INSATU) and flexibility (FLEX). A range for each axis has been defined for each descriptor from data published by Ritchie *et al* [639] and Lovering *et al* [640] The pink area is defined as the suitable range for oral bioavailability (Table 4.14). Lead analogues must

fall entirely within the pink boundary for consideration as drug-like molecules.[623] Each of the lead β-lactam eutomers was within the defined range with drug-likeness. The 3-hydroxyl family, **16EN1, 17En1, 18EN1, 19EN1** and **20EN1** fall further within the border than their 3-phenyl (**24EN1**), 4-fluorophenyl (**39EN1**) and 4-methoxyphenyl (**41EN1**) substituted relatives. The 3-hydroxyl scaffold is more favourable as a drug-like scaffold compared to other 3-substiuted analogues.

4.9.4 *Pharmacokinetics*

P-glycoprotein (p-gp) and CYP450 enzymes impact the pharmacokinetics properties of drug molecules. P-gp is the most extensively studied ATP binding cassette (ABC) transporter mediating efflux of toxins and xenobiotics *e.g* drug molecules out of cells.[641] Many drug interactions involve both P-gp and CYP3A4. Three major ABC efflux pump transporters play a role in MDR in cancer: P-gp, multidrug-resistance protein 1 (MRP1) and breast cancer resistance protein (BCRP).[642] P-gp is the most extensively studied in terms of resistance to chemotherapy.[643] In a study of 118 anti-cancer agents, over 95% had a negative correlation between efficacy in cancer cells and p-gp expression.[644] Cancer cells up-regulate p-gp expression as an adaptive response to evade chemotherapy mediated cell death.[645] The benefits of combining a p-gp inhibitor with chemotherapeutic regimens to reduce MDR mediated drug efflux is limited and associated with poor clinical outcomes due to risk of toxicity.[645] For example, ciclosporin as a p-gp inhibitor is also a potent immunosuppressant and results in undesirable systemic toxicity.[646] Therefore analogues which are estimated to evade P-gp efflux are advantageous. Enantiomers **19EN1**, **21EN1, 22EN1** and **33EN1** are extremely promising chemotherapeutics due to P-gp efflux evasion (Table 4.15) and therefore may evade MDR development.

Table 4.14: Bioavailability radar plots for lead enantiomers calculated using the Swiss ADME webtool.[647]

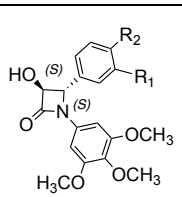

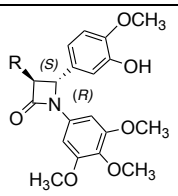

16EN1 = R_1= OH R_2 = OCH_3
17EN1 = R_1= H R_2 = OCH_3
18EN1 = R_1= F R_2 = OCH_3
19EN1 = R_1= Cl R_2 = OCH_3
20EN1 = R_1= CH_3 R_2 = OCH_3
21EN1 = R_1= Br R_2 = OCH_3
22EN1 = R_1 = H R_2 = SCH_3

24EN1 = R= C_6H_5
27EN1 = R= H
30EN1 = R= C_4H_3S
33EN1 = R = C_2H_3
39EN1 = R= (*p*-F)C_6H_4
41EN1 = R= (*p*-CH_3O)C_6H_5

16EN1	17EN1	18EN1	19EN1
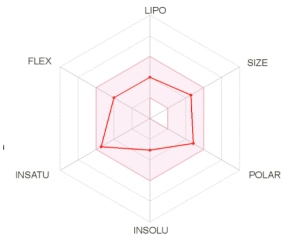	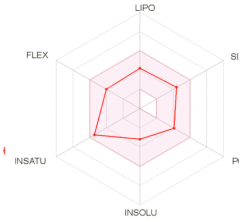	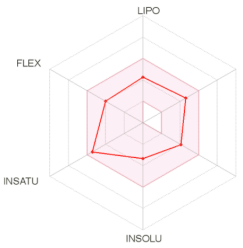	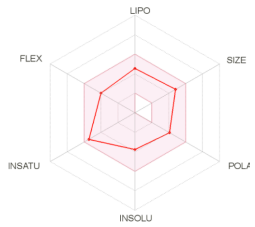
20EN1	**21EN1**	**22EN1**	**24EN1**
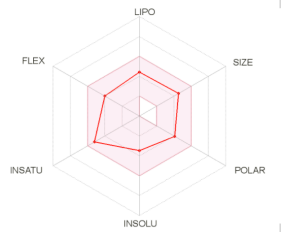	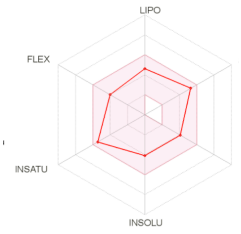	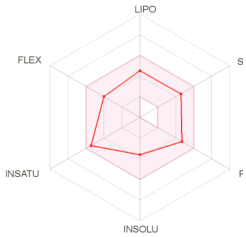	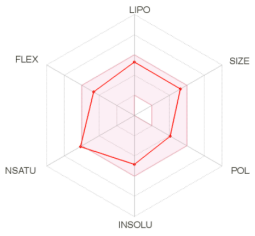
27EN1	**30EN1**	**33EN1**	**39EN1**
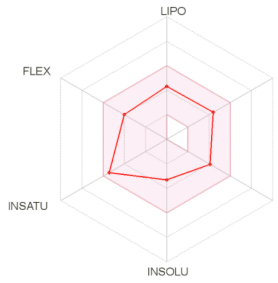	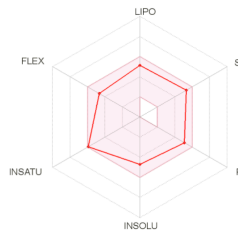	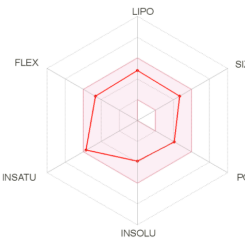	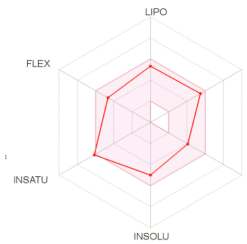
41EN1			
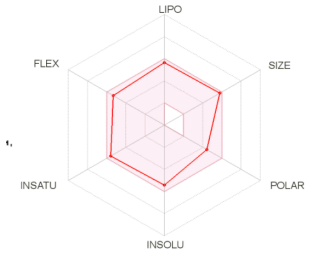			

Range of acceptance for oral bioavailability: LIPO: -0.7 < LogP < + 5.0, SIZE: 150 g/mol < molecular weight <500 g/mol, POLAR: 20 $Å^2$ < TPSA < 130 $Å^2$, INSOLU: 0 < LogS < 6, INSATU: 0.25 < Fraction of carbons Sp^3 < 1, FLEX: 0 < # of rotatable bonds < 9 [639, 640]

Table 4.15: Pharmacokinetic assessment of lead enantiomers using the Swiss ADME webtool.[623]

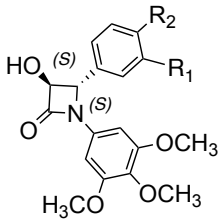

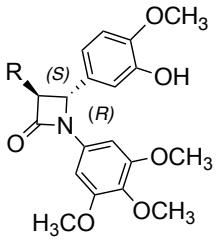

16EN1 = R_1= OH R_2 = OCH_3
17EN1 = R_1= H R_2 = OCH_3
18EN1 = R_1= F R_2 = OCH_3
19EN1 = R_1= Cl R_2 = OCH_3
20EN1 = R_1= CH_3 R_2 = OCH_3
21EN1 = R_1= Br R_2 = OCH_3
22EN1 = R_1 = H R_2 = SCH_3

24EN1 = R= C_6H_5
27EN1 = R= H
30EN1 = R= C_4H_3S
33EN1 = R = C_2H_3
39EN1 = R= (*p*-F)C_6H_4
41EN1 = R= (*p*-CH_3O)C_6H_5

Compound	P-gp Substrate	CYP1A2 inhibitor	CYP2C19 inhibitor	CYP2C9 Inhibitor	CYP2D6 inhibitor	CYP3A4 inhibitor
16EN1	Yes	No	No	No	Yes	No
17EN1	Yes	No	No	No	Yes	No
18EN1	Yes	No	No	No	Yes	No
19EN1	**No**	No	Yes	Yes	Yes	No
20EN1	Yes	No	No	No	Yes	No
21EN1	**No**	No	Yes	No	Yes	Yes
22EN1	**No**	No	Yes	No	Yes	No
24EN1	Yes	No	Yes	Yes	Yes	Yes
27EN1	Yes	Yes	Yes	No	Yes	No
30EN1	Yes	No	Yes	Yes	Yes	Yes
33EN1	**No**	No	Yes	Yes	Yes	No
39EN1	Yes	No	Yes	Yes	Yes	Yes
41EN1	Yes	No	Yes	No	Yes	Yes

4.9.5 *Drug like assessment methods*

Drug-likeness describes a molecule's potential of becoming an oral drug based on bioavailability. It was first described by Lipinski in 2001.[648] Lipinski's rule of 5 is a set of four criteria required for good permeability and absorption widely known as the rule of five (RO5). [649] 90% of orally active drugs reaching phase II clinical trials fulfil Lipinski's RO5. Failure of a new drug molecule to meet the RO5 criteria is associated with a high probability of failure in clinical phases due to poor oral bioavailability.[650] Since Lipinski there have been many developments on the meaning of 'drug-like' which are accounted for by the Swiss ADME webtool *e.g* Ghose (Amgen),[633] Veber (GSK),[651] Egan (Pharmacia)[652] and Muegge (Bayer) [653]and many further developments.[654] Drug

likeness calculators embedded in the Swiss ADME webtool enable access to an invaluable *in silico* consensus view of drug-likeness for the panel of eutomers designed in this thesis (Table 4.16). Pan assay interference compounds (PAINS) are chemical compounds that often meet drug- criteria using drug-likeness assessment methods. However during high throughput screening these compounds are liable to produce false positives amongst real hits. For example, they may interfere in receptor binding interactions by forming aggregates or alternatively they react with proteins. Certain fragments may have potential to interfere with assay signalling. The PAINS filter is designed to identify problematic moieties. Any compound yielding a PAINS alert in isolation has the potential to produce promising data suggestive of an optimisable hit but is considered a poor choice for drug development.[655] Fortunately no lead enantiomer returned an alert. Thus the biological data produced in this thesis can be relied on rather than as a result of off-target interferences identified in PAINS screening. The BRENK filter defines drug likeness according to the following criteria:

1) Absence of unwanted groups.
2) Lead like properties.
3) Limited complexity.

Unwanted compounds include potentially mutagenic groups such as NO_2 moieties and groups that are expected to have unfavourable pharmacokinetic profiles.[656]

Only one compound (**41EN1**) returned an alert due to molecular weight (MW) of > 480 and a molar refractivity of > 130.[631] All other enantiomers are considered drug-like and did not give rise to structural alerts using the PAINS filter. **33EN1** returned a structural alert using the BRENK filer due to its 3-vinyl moiety. **41EN1** and **33EN1** are therefore ruled out for further progression as lead enantiomers while all other enantiomers are promising drug candidates (Table 4.16).

Table 4.16: Assessment of enantiomer drug-likeness using five assessment methods and two drug-like assessment filters; PAINs and Brenk generated using Swiss ADME webtool. [623]

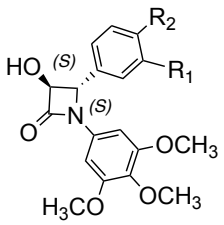

16EN1 = R_1= OH R_2 = OCH_3
17EN1 = R_1= H R_2 = OCH_3
18EN1 = R_1= F R_2 = OCH_3
19EN1 = R_1= Cl R_2 = OCH_3
20EN1 = R_1= CH_3 R_2 = OCH_3
21EN1 = R_1= Br R_2 = OCH_3
22EN1 = R_1 = H R_2 = SCH_3

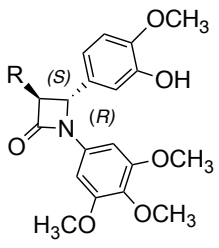

24EN1 = R= C_6H_5
27EN1 = R= H
30EN1 = R= C_4H_3S
33EN1 = R = C_2H_3
39EN1 = R= (*p*-F)C_6H_4
41EN1 = R= (*p*-CH_3O)C_6H_5

Compound	Lipinski	Ghose	Veber	Egan	Muegge	PAINS	Brenk
17EN1	+	+	+	+	+	0 alert	0 alert
18EN1	+	+	+	+	+	0 alert	0 alert
16EN1	+	+	+	+	+	0 alert	0 alert
24EN1	+	+	+	+	+	0 alert	0 alert
19EN1	+	+	+	+	+	0 alert	0 alert
20EN1	+	+	+	+	+	0 alert	0 alert
21EN1	+	+	+	+	+	0 alert	0 alert
22EN1	+	+	+	+	+	0 alert	0 alert
24EN1	+	+	+	+	+	0 alert	0 alert
27EN1	+	+	+	+	+	0 alert	0 alert
33EN1	+	+	+	+	+	0 alert	1 alert[1]
39EN1	+	+	+	+	+	0 alert	0 alert
41EN1	+	-[2]	+	+	+	0 alert	0 alert

+ = no alerts - = alerts, [1]vinyl bond present , [2]MW> 480

4.10 *Experimental Calculation of logP values for combretazet enantiomers*

The logP of selected enantiomer pairs **17EN1** and **17EN2, 16EN1** and **16EN2,** and **27EN1** and **27EN2** were calculated as representative examples of the panel of combretazet enantiomers. A HPLC method previously reported by Valkó *et al* was employed.[657] HPLC is a suitable means of reliably and accurately determining compound concentrations in solvents and thus can be used as a method of determining octanol-water partition coefficient. This is based on the compound's chromatographic retention time which is a property of its distribution between mobile and stationary phases. Using this procedure, partition coefficients are independent of concentration,

where *k* is the retention factor (Equation 4.2). LogK can then be plotted against standards with known logP values (Table 4.17) to form a linear calibration (Figure 4.4) which is then used to calculate logP values of novel compounds.

$$k = (T_r - T_0)/T_0$$

T_r = retention time of analyte

T_0 = retention time of initial unretained peak

Equation 4.2: Calculation of retention factor *k*

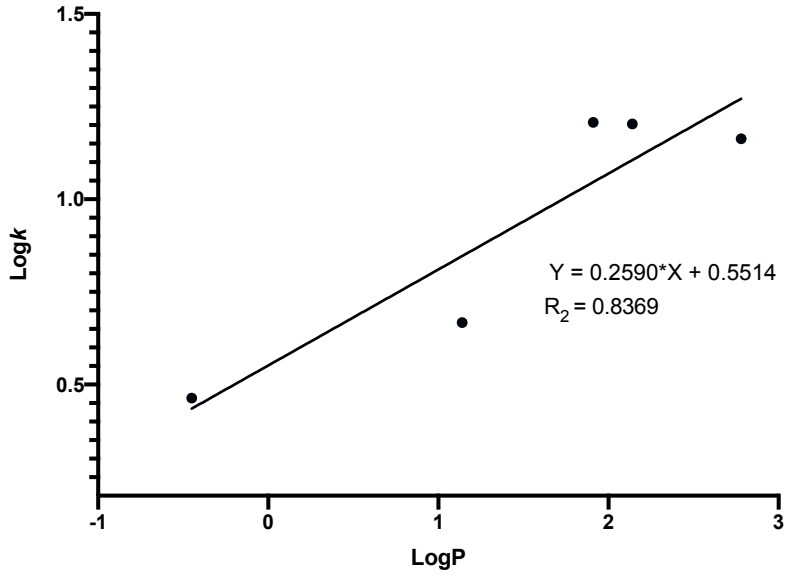

Figure 4.4: Standard curve used for calculating linear equation using standards with known logP.

Table 4.17: Calculation of retention factor (*k*) and log*k* for standards with known logP

Standards	**T_r (minutes)**	**T_0 (minutes)**	**k** $(T_r-T_0)/T_0$	**Log*k***	**LogP** (known)
Adenine[658]	3.91	1	2.91	0.46	-0.45
Colchicine[659]	5.64	1	4.64	0.67	1.14
Glipizide[660]	17.1	1	16.1	1.21	1.91
Indole[658]	16.98	1	16.0	1.20	2.14
Naproxen[661]	15.57	1	14.6	1.16	2.78

Conditions: Mobile phase of 80:20 H_2O: MeCN and reverse phase C18 BDS Hypersil. Injection volume of 10 μL and flow rate of 1 mL/min. λ of detection = 254 nm.

17EN1 and **17EN2** have logP values of 2.51 fulfilling drug-like criteria discussed previously. Calculated logP values are similar to values predicted by the Swiss ADME webtool. **16EN1** and **16EN2** were measured with a lower logP of 1.07 (Table 4.18). Increased partition in water layers is plausibly imparted by the additional B ring *meta* hydroxyl group. A logP of 1.07 for **16EN1** is comparable to 0.90 and 1.69 predicted by ChemDraw and the Swiss ADME webtool respectively (Table 4.18). **27EN1** and **27EN2** were also measured with drug-like logP values of 1.99 (Table 4.18). As mentioned previously CA-4 phosphate has shown success in overcoming solubility issues encountered during formulation of CA-4[662] while maintaining excellent anti-proliferative activity.[324, 325, 414] It is plausible that similar chemical modifications for β-lactam eutomers would facilitate a decrease in measured logP values, thus increasing aqueous solubility, ameliorating formulation and drug delivery potential while also maintaining excellent anti-proliferative activity.

Table 4.18: Calculation of logP for enantiomers

Code	T_r	T_0	k $(T_r-T_0)/T_0$	Log*k* (y value)	Experimental Calculated logP	cLogP (ChemDraw) [663]	Log P consensus (Swiss ADME) [623, 664]
17EN1	16.9	1	15.9	1.20	2.51	1.81	2.02
17EN2	16.90	1	15.9	1.20	2.51	1.81	2.02
16EN1	7.42	1	6.42	0.81	0.99	0.90	1.62
16EN2	7.46	1	6.42	0.81	1.00	0.90	1.62
27EN1	12.7	1	11.7	1.07	1.99	1.16	2.35
27EN2	12.7	1	11.7	1.07	1.99	1.16	2.35

4.11 *Chapter 4 Summary*

In summary, the optimised chiral resolution developed in Chapter 3 was applied to a panel of 3-hydroxyl combretazet β-lactam analogues whose *de* values were accurately estimated using 2D EXSY spectra and quantitatively calculated subsequently using the optimised qNMR approach also discussed in Chapter 3. The optimised chiral resolution method was also successfully applied to 3-hydroxy-4-methoxy substituted B ring combretazets. However the qNMR method did not prove useful for *de* calculation for these analogues. Chiral resolution was also trialled unsuccessfully with 3-phenolic and

B ring *meta* NH_2 substituted analogues. Given the excellent potency reported for racemate **26** in the literature**,** future work should focus on isolation of **26'**s eutomer. *Ee* values for enantiomers isolated in this thesis *via* LC chiral resolution were moderate to high (50-95%). XRD studies confirm that for the 3-hydroxyl family, the absolute configuration is 3*S*,4*S* for **EN1** and 3*R*,4*R* for **EN2**. XRD for **24EN1** confirmed that the absolute configurations for 3-substituted analogues is 3*S*, 4*R* for **EN1** and by extrapolation *3R*,4*S* for **EN2**. The panel of 3-hydroxyl analogues demonstrated excellent drug like properties using the Swiss ADME webtool and additionally for their experimentally derived logP values, inferring that they are extremely promising drug-like candidates for future clinical progression. Modification towards the phosphate or amino acid prodrug derivatives in future work *via* their hydroxyl functional groups is a potential strategy to ensure ease of formulation, drug delivery and therefore potential for progression toward pre-clinical and clinical *in vivo* studies.

Chapter 5 – Molecular modelling for enantiopure combretazets

5.1 *Introduction to computational studies for β-lactam enantiomers*

Computational approaches have previously reported the binding interactions of many combretazets at the CBS at the αβ interface of tubulin.[359, 378, 400] Prior to carrying out computational studies for the series of combretazet enantiomers, docking orientations of racemate **17** were first explored for two tubulin heterodimer receptors; 1SAO[610] and 5LYJ.[337] Additionally the docking procedure for computational studies was also optimised by re-docking native ligands at the colchicine binding site (CBS) to ensure reliability and validity of docking output. Molecular modelling studies for selected β-lactam enantiomer pairs were then carried out inclusive of **16, 17, 18** and **24** (Figure 5.1).

Molecular modelling aimed to determine both the binding orientations and ligand-receptor interactions for each enantiomer and predict eutomer from distomer prior to biochemical evaluation for subsequent rationalisation of comparative *in vitro* biochemical activity.

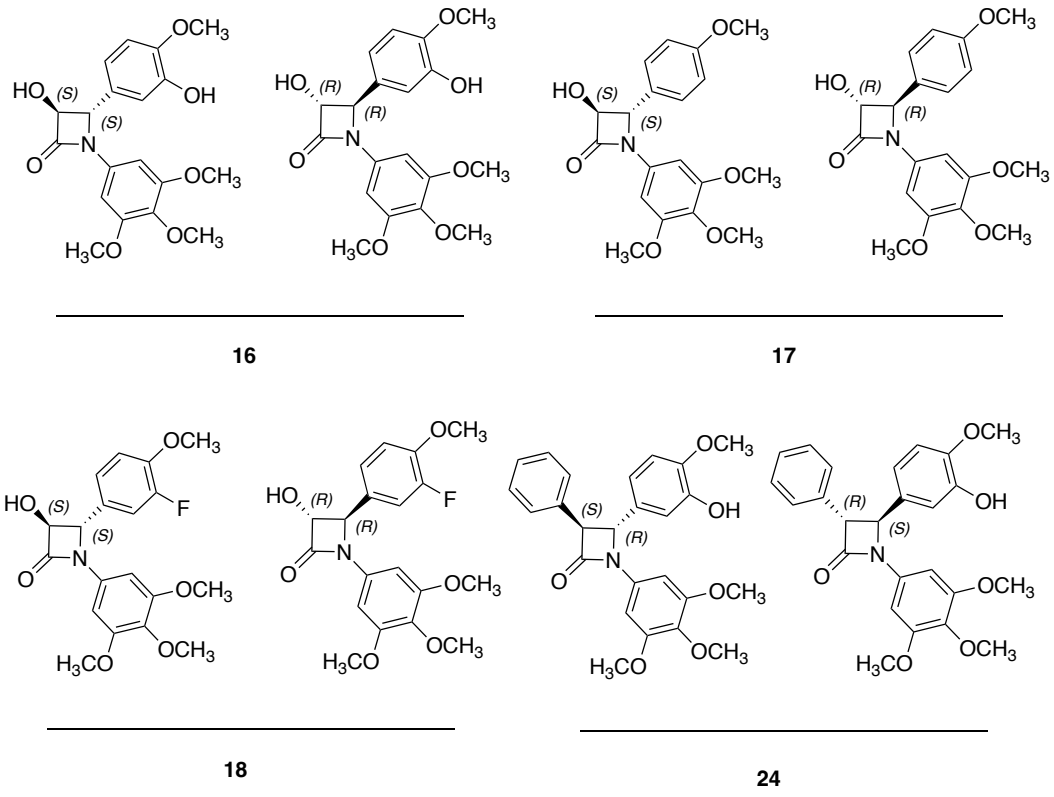

Figure 5.1: Enantiomers of racemates **16, 17, 18** and **24** studied in computational models at the colchicine binding site (CBS).

5.1.1 *Introduction to the tubulin-DAMA-colchicine co-crystal structure 1SAO*

1SAO is a tubulin *N*-deacetyl-*N*-(2-mercaptoacetyl)-colchicine (DAMA-colchicine) X-ray co-crystal structure of 3.58 Å resolution with DAMA-colchicine bound at the CBS,[261, 610] composed of a head to tail assembly of two tubulin heterodimers with a curvature maintained by an α helix sheet. The CBS lies at the αβ interface of tubulin (Figure 5.2) and is predominantly buried within the intermediate domain of the β-subunit enclosed by strands S8, S9, loop T7 and helices H7 and H8 (Figure 5.3). Colchicine also interacts with the T5 loop of the α subunit. When colchicine binds to free tubulin, a steric clash between Asnα101, GTP and Valα181 prevents the critical switching of the H7α - helix to a straight orientation. The α-subunit is also prohibited from occupying the geometry that would allow the required straight conformation and lateral contact assembly for polymerisation (Figure 5.2 and Figure 5.3).[261, 610]

5.1.2 *Ligand receptor interactions for CA-4 at the 5LYJ receptor*

Cis CA-4 prevents tubulin assembly by preventing curved to straight tubulin switch and proceeding to induce de-polymerisation as a microtubule destabiliser.[337, 338] Gaspari *et al* have published 5LYJ, an X-ray co crystal of CA-4 at the CBS of the tubulin hetereodimer of 2.4 A° resolution. *Cis* CA-4 at the 5LYJ CBS binds deep in the hydrophobic pocket of the CBS with its trimethoxyphenyl A ring held in place by β-subunit residues Valβ238, Cysβ241, Leuβ242, Alaβ250, Leuβ255, Alaβ316, Ileβ318, Alaβ354 and Ileβ378.The B ring is stacked between two polar residues, Asnβ359 and Lysβ352 and stabilized by six hydrophobic residues; Thrα179, Alaα180, Valα181, Metβ259, Alaβ316, Asnβ349. CA-4 forms hydrogen bonds between its B ring meta 3-hydroxyl and the amide nitrogen of Valα181 and Thrα179[338] **(**Figure 5.4). *Cis* CA-4 is bound to the CBS, enclosed by the residues βS8, βS9, loop βT7, helices βH7 and βH8 of β-tubulin and also the loop αT5 of α tubulin. These receptor residues are considered as key reference comparators for enantiomers studied in this thesis.

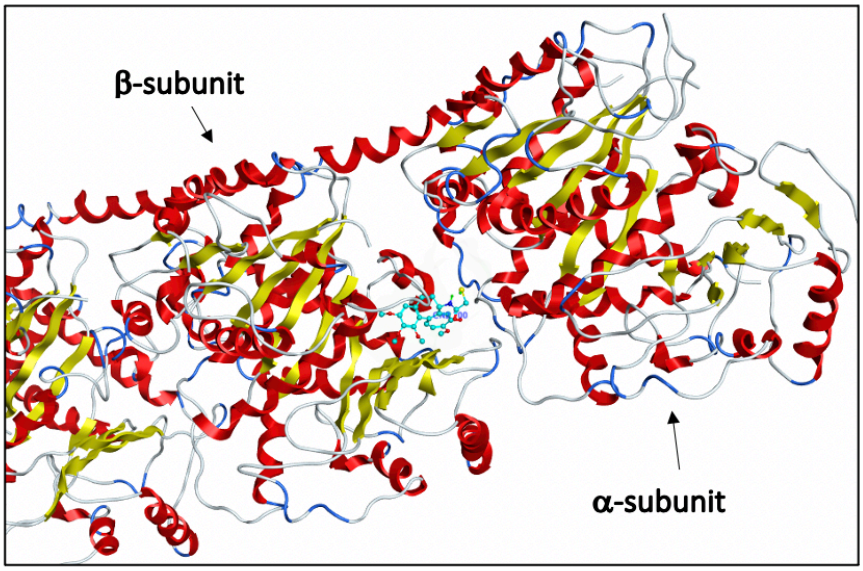

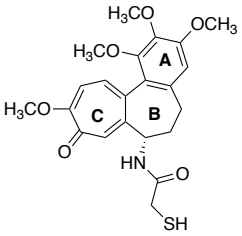

Figure 5.2: DAMA-colchicine (cyan) at the CBS of 1SAO. Red: α helices, yellow: β sheets, blue: loop turns, white: loop ribbons. Atom colours: Red = oxygen, yellow= sulfur.

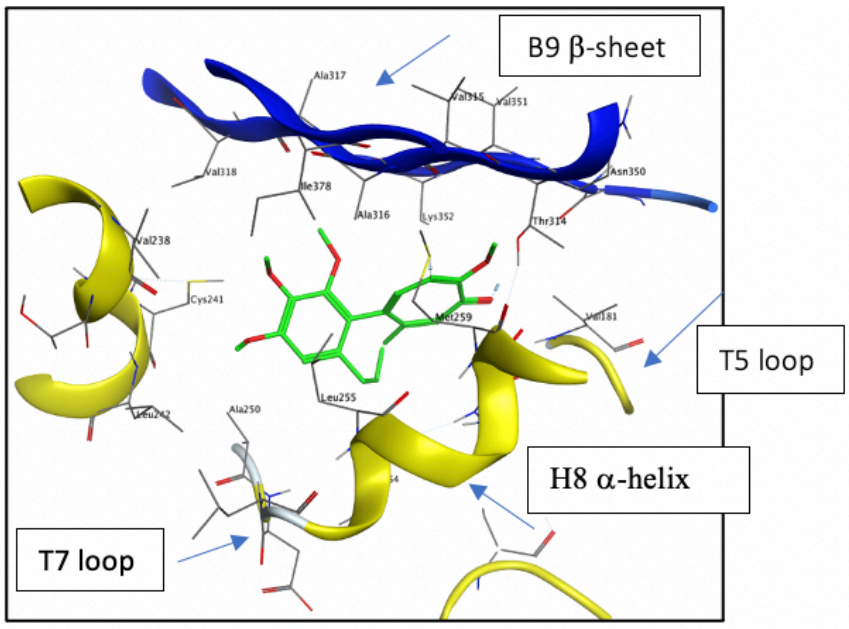

Figure 5.3: The CBS of 1SAO. DAMA-colchicine = green. Atom colours: Red = oxygen, yellow = sulfur, blue = nitrogen. α-Helix = yellow, β-subunit = dark blue[261, 610]

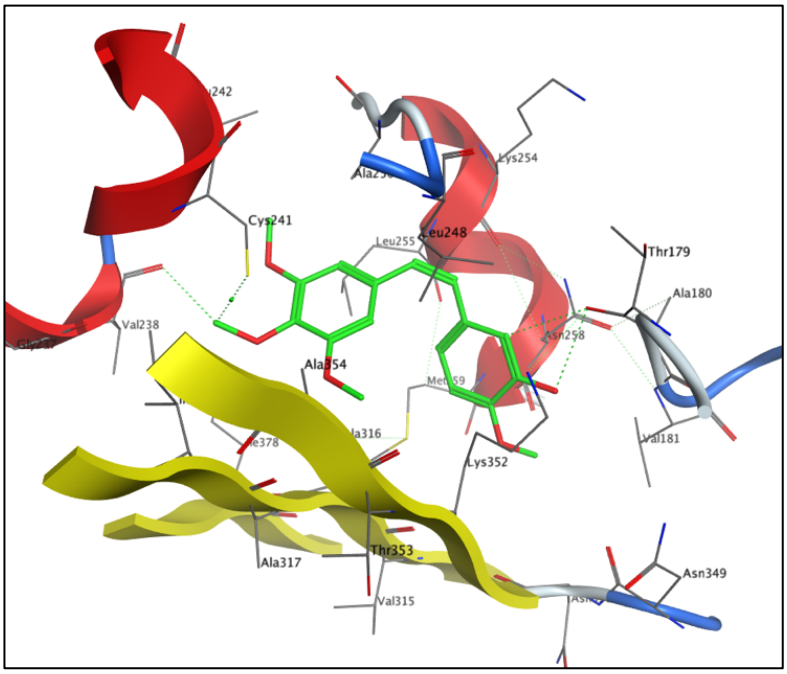

Figure 5.4: CA-4 (green) at the CBS of 5LYJ. Hydrogen bonding interaction = dashed green lines.[337]

5.2 *Methods for computational studies*

The *MOE* 2019.0102 software package was used alongside XQuartz 2.7.11 for computational studies.[665, 666]1SAO and subsequently the 5LYJ co-crystal structures were employed to investigate docking orientations of resolved enantiomers.[610, 337] Both of these structures were available for import into the *MOE* 2019.0102 software package *via* the RCSB.pdb protein data bank.[610, 337] ChemDraw Professional 16.0.1.4 was used to construct enantiomer structures, colchicine and CA-4 structures as .SDF files.[663] The .SDF file formats were then imported into *MOE*. *MOE* was then used to generate energy minimised structures where XRD files were unavailable, using the Merck Molecular force field (MMFF94s). MMFF94s was chosen due to its ability to planarise delocalised trigonal nitrogen atoms and is considered as a better estimation of molecular geometry.[667]

5.2.1 *Comparison of energy minimised to XRD structures*

In order to investigate likeness of energy minimised structures using *MOE* and MMFF94s forcefield with XRD structures, the XRD structures available for 3*S*,4*S* **17EN1** and 3*R*,4*R* **17EN2** were compared to energy minimised geometries. .SDF derived

energy minimised enantiomers versus original crystal structures demonstrated good agreement in ligand-receptor interactions and orientation for **17EN1** and **17EN2**. Superimposition illustrates minor difference in the orientation of the 4-methoxy B ring (Figure 5.5). Energy minimised structures due to absence of XRD structures were employed for computational studies for enantiomers of **16, 19** and **24** [XRD structures not obtained at the time of writing with XRD structure for **24EN1** reported since (Chapter 4)].

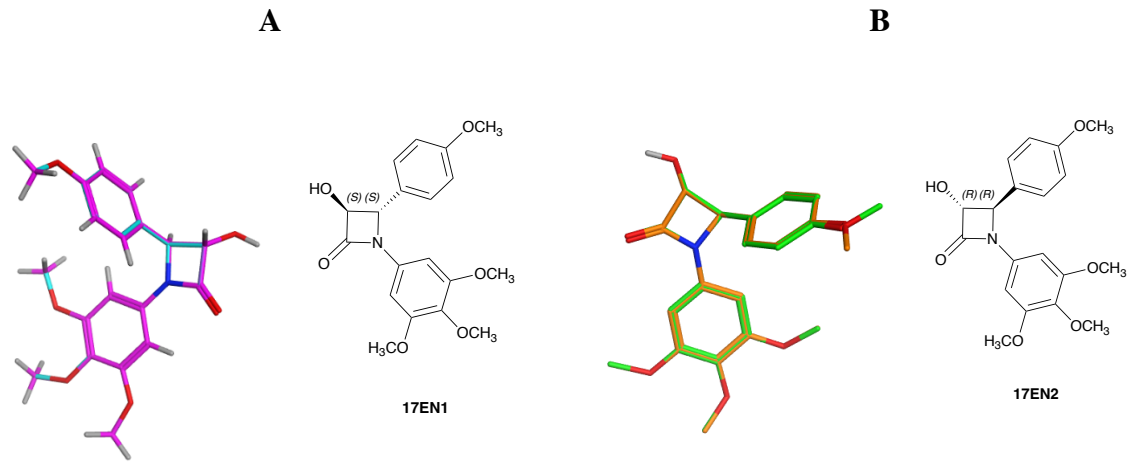

Figure 5.5: Comparison of **A:** 3*S*,4*S* **17EN1** XRD structure (cyan) and energy minimized model (pink) **B:** 3*R*,4*R* **17EN2** XRD structure (green) and energy minimised model (orange). Atom colours: red= oxygen, blue = nitrogen, grey = hydrogen

5.2.2 *Database creation of enantiomers for docking studies*

A database for docking studies was constructed as a .mdb file, creating by uploading .sdf files for enantiomers into *MOE,* followed by energy minimisation of each enantiomers within the.mdb file. XRD structures for **17EN1** and **17EN2** were also added to the .mdb database. The validation process for creation of enantiomer databases is outlined as the flow chart of Figure 5.6.

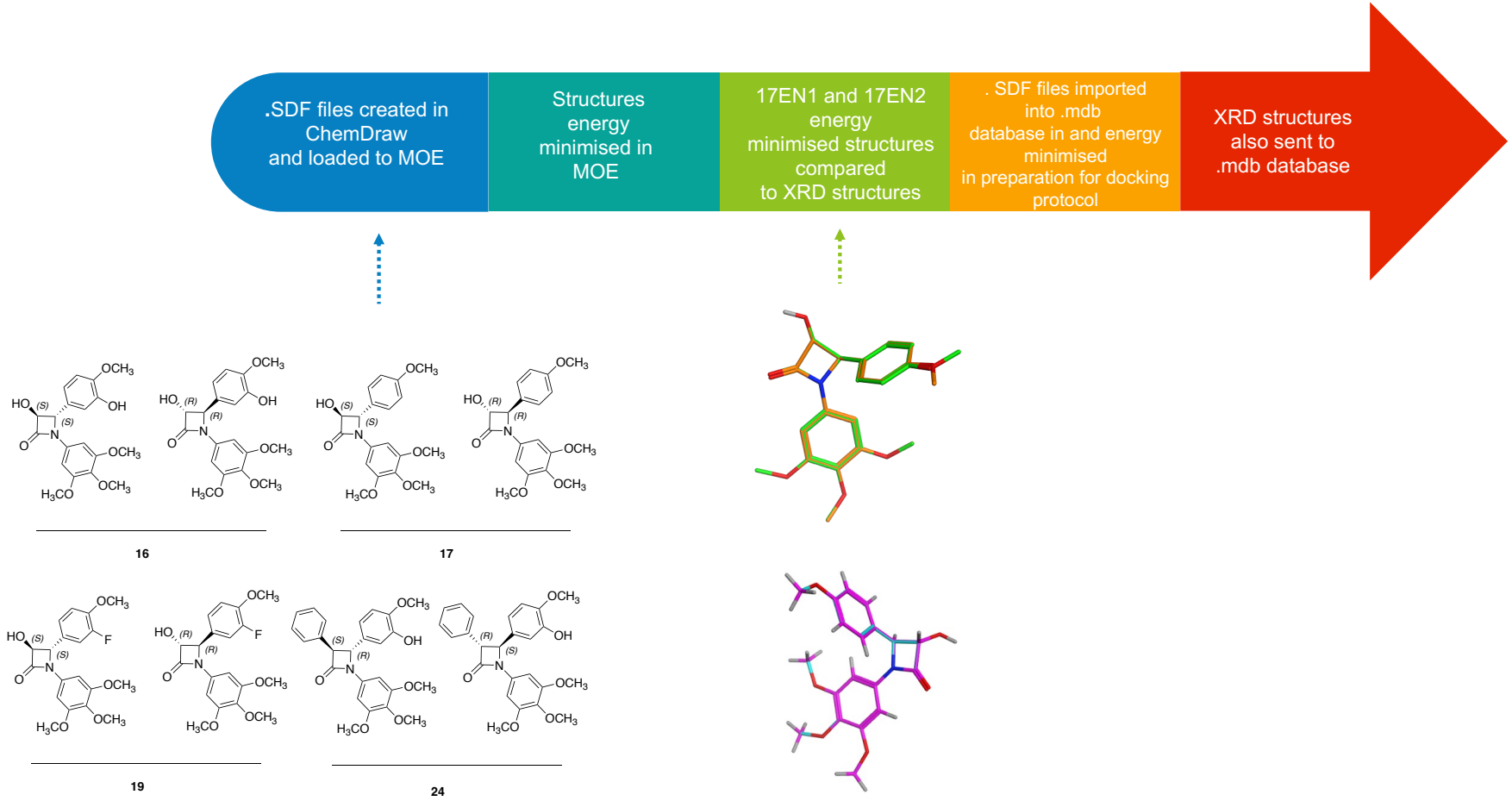

Figure 5.6: Validation protocol for database creation for enantiomers prior to computational studies.

5.2.3 *Preparation of the 1SAO and 5LYJ for docking of enantiomers*

1SAO was prepared for docking by using the 'add hydrogens', 'correct' and 'type and fix potential' options in *MOE*. The pH for docking studies is set by default to pH 7.4. DAMA-colchicine and CA-4 were selected as ligands to define the active site for docking of β-lactam enantiomers at the CBS of both 1SAO and 5LYJ. The proteins preparation was finalised using the QuickPrep option available in *MOE*.

5.2.4 *Docking protocol*

An initial docking protocol in *MOE* was explored using **17EN1, 17EN2** accompanied by CA-4 and DAMA-colchicine at the CBS of 1SAO. Colchicine was included to ensure that ligand-receptor binding interactions were similar and repdroducible as the native ligand, DAMA-colchicine.[668] The number of placements and refinements were initially set at 100 and 30 respectively. Each conformation was subsequently docked and scored using the London dG score. The top binding poses were refined using the GBVI/WSA dG method.[667] XRD structures were docked at the CBS for enantiomers of **17** and compared to ligand-receptor interactions of their energy minimised models to further validate the use of energy minimised models in absence of XRD files for enantiomers. The procedure for validation of the docking protocol is outlined in the flow chart of Figure 5.7. The number of placements and refinements were increased and set to 200 each to increase the reliability of data obtained. All docking studies were also carried out in triplicate to investigate reproducibility of ligand-receptor interactions in independent simulations. The lowest energy confirmations (determined by *S* scores) are reported in this chapter.

5.2.5 *Validation of docking protocol using 5LYJ*

To validate the reliability of the ligand-receptor interactions reported using 1SAO as the protein of choice for computational studies, enantiomers were also studied at the CBS of 5LYJ.[342] Validation using 5LYJ involved docking of colchicine, CA-4, **17EN1** and **17EN2**. Observation of similar receptor-ligand interactions for 5LYJ comparable to 1SAO strengthened the reliability of docking outputs obtained using 1SAO.

Figure 5.7: Validation of protocol for computational studies.

5.3 *Results and discussion*

5.3.1 *Results of docking for colchicine, **17EN1** and **17EN2** at the CBS of 1SAO*

Key ligand-receptor interactions are preserved for colchicine at the CBS of 1SAO when compared to native DAMA-colchicine. Colchicine's trimethoxyphenyl A ring interacts with Cysβ241 and Valβ318 (pink, **A** and **B,** Figure 5.8) consistent with native DAMA-colchicine (cyan, **A** and **B,** Figure 5.8).

A **B**

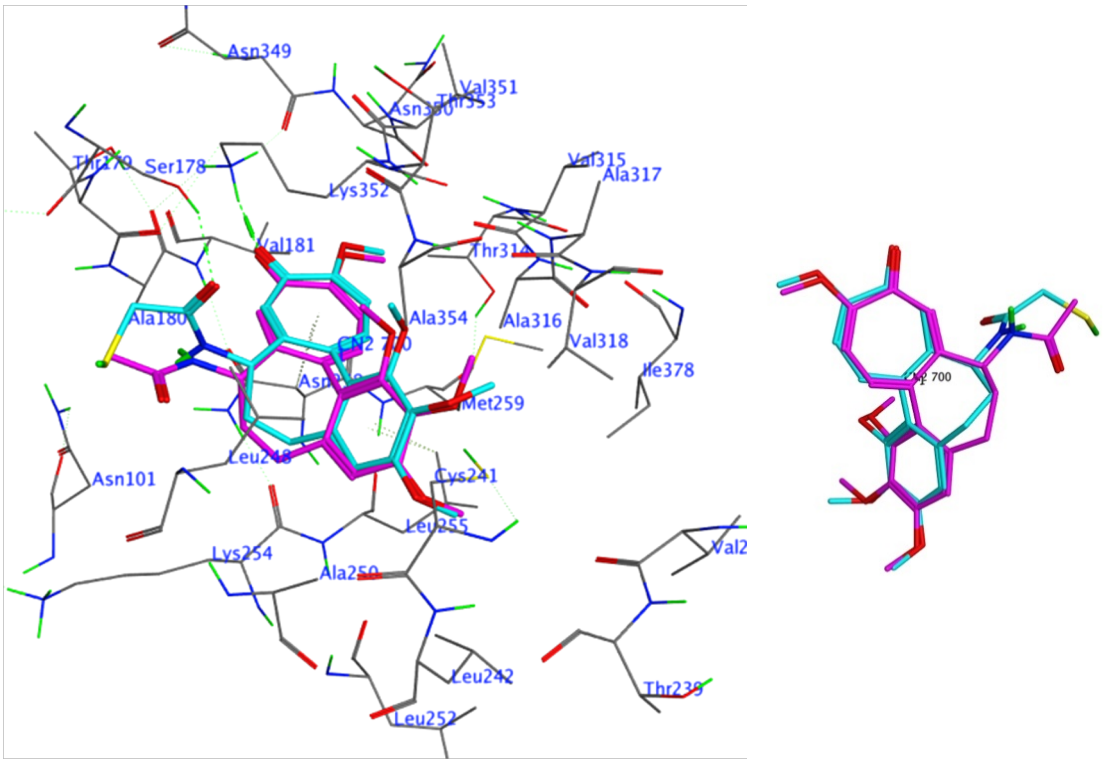

Figure 5.8: **A:** DAMA-colchicine (cyan) and colchicine (pink) at the CBS of 1SAO. **B:** Receptor removed on right for clarity. Atom colours: red= oxygen, blue = nitrogen, grey = hydrogen, yellow = sulfur

17EN1's XRD structure demonstrates comparable ligand-receptor interactions for the trimethoxyphenyl A ring of both **17EN1 (A,** yellow, Figure 5.9) and DAMA-colchicine. **(A, green,** Figure 5.9) The XRD structure for **17EN1 (B,** yellow, Figure 5.9) also demonstrated identical ligand-receptor interactions to its energy minimised structure (**B,** pink, Figure 5.8) as the final validation for use of *MOE* generated energy minimised structures in molecular modelling studies.

3*S*,4*S* **17EN1** binds within the β subunit comparable to DAMA-colchicine, interacting with Cysβ241 and Valβ318. Cysβ241 and Val β318 tubulin variants have reduced sensitivity towards colchicine.[261] Therefore binding orientations with preferential binding orientations toward the β subunit mediate the magnitude of CBS affinity, translating toward microtubule depolymerising and anti-proliferative potency.[261, 338]

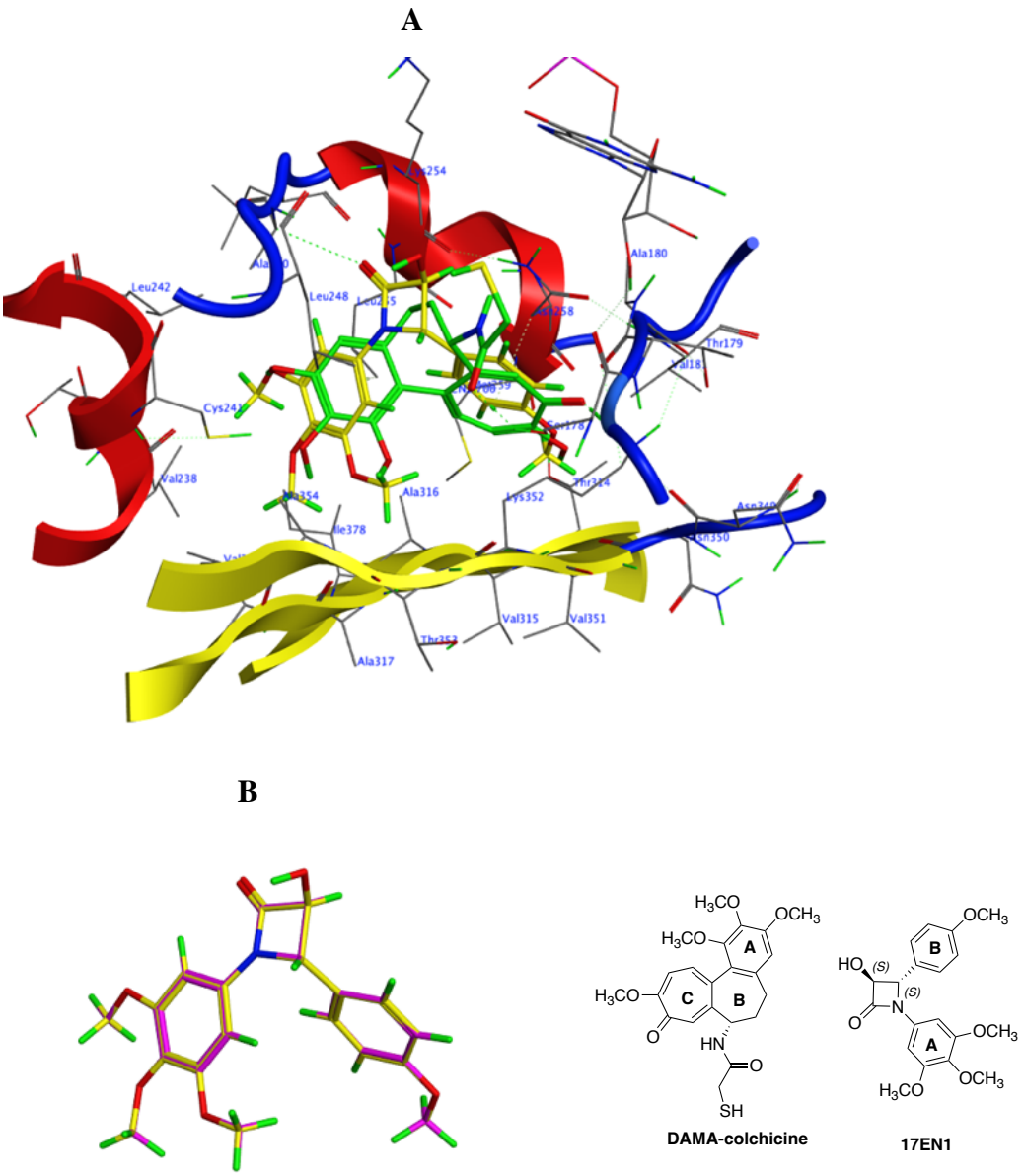

Figure 5.9: **17EN1** at the CBS of 1SAO. **A:** DAMA-colchicine (green) and XRD **17EN1** (yellow)**. B:** XRD **17EN1** (yellow) compared to energy minimised **17EN1** (pink) with receptor removed for clarity. Atom colours, red = oxygen, green = hydrogens, blue = nitrogen (*hydrogens illustrated to demonstrate alignment of XRD and energy minimsed structures)*

Minor disagreements were observed between ligand-receptor interactions for the XRD structure of **17EN2**'s XRD versus its energy minimised model (Figure 5.10). This gave rise to preliminary evidences of inconsistent docking configuration and ligand-receptor interactions for the 3*R*,4*R* 3-hydroxyl enantiomers at the CBS of 1SAO. Based on inconsistent findings for the 3*R*,4*R* 3-hydroxyl enantiomers, all docking studies were carried out in triplicate in order to determine the reproducibility of ligand-receptor interactions for enantiopure combretazets during independent replicates in computational models.

Initial modelling of 3*R*,4*R* **17EN2** illustrated a less favourable binding orientation with respect to 3*S*, 4*S* **17EN1**. The crucial trimethoxyphenyl A ring was observed as oriented away from the β-subunit (pink, Figure 5.10) and in the opposite direction to both DAMA-colchicine (green, Figure 5.10) and **17EN1**'s A ring (yellow, Figure 5.9). The orientation of **17EN2**'s A ring abolishes the critical interactions with β subunit residues Cysβ241 and Valβ318.

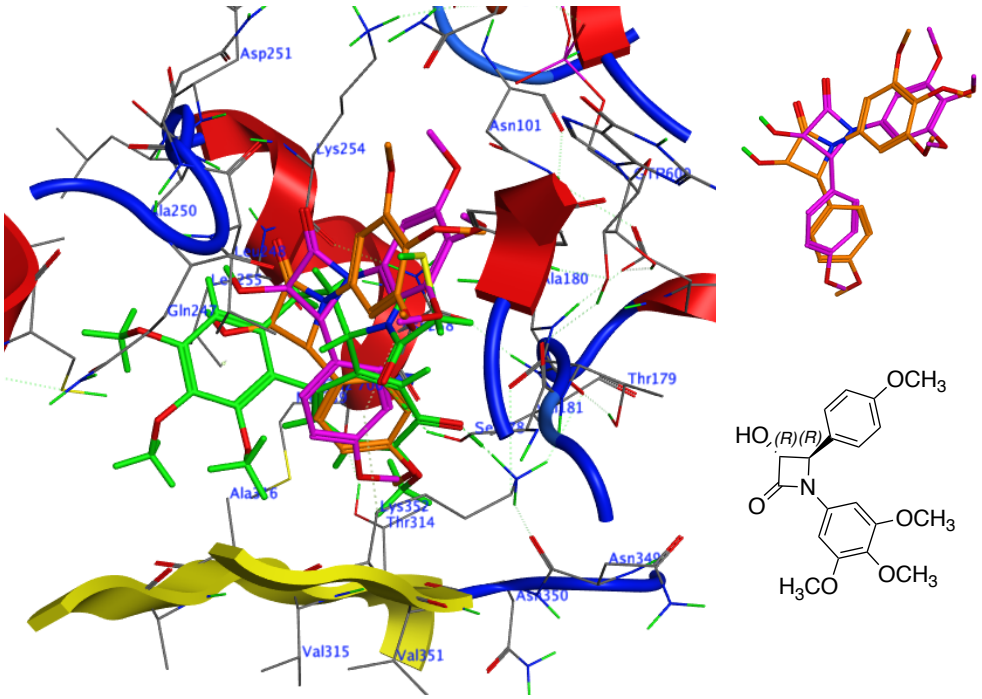

Figure 5.10: 3*R*,4*R* **17EN2** at the CBS of 1SAO. XRD structure (pink) versus energy minimised structure (orange). DAMA-colchicine (green). Receptor removed on right for clarity. Atom colours, red = oxygen, green = hydrogens, blue = nitrogen

5.3.2 *Comparative modelling for **17EN1** and **17EN2** at the CBS of 1SAO*

A second study was carried out which involved docking of **17EN1** and **17EN2** simultaneously at the CBS of 1SAO according to the flowchart outlined in Figure 5.7. This study was carried out to demonstrate the impact of opposite absolute configuration on binding orientations at the CBS. Docking results are illustrated in Figure 5.11. Comparative docking illustrates the unfavourable docking configuration for 3*R*,4*R* **17EN2**, binding again in the opposite orientation to **17EN1** with its B ring overlaying the A ring of **17EN1**. **17EN1**'s carbonyl oxygen forms a hydrogen bond with Alaβ250, 2.41 Å away. This is a critical interaction previously reported by Malebari *et al* for the combretazets at the CBS of 1SAO. [359] The carbonyl group of **17EN2** instead is directed outside oriented the binding pocket and away from the β-subunit at 180° in the opposite direction to **17EN1**. Rather than the critical stabilizing interaction with Alaβ250 which was observed for **17EN1** (yellow, Figure 5.9), the 3-hydroxyl of **17EN2** participates in a hydrogen bonding interaction with the carbonyl of Alaβ317 1.86 Å away. Due to the opposite orientation of **17EN2's** phenyl rings, the critical trimethoxyphenyl moiety cannot participate in the essential hydrophobic interactions with Cysβ241 and Valβ318.

Additionally docking output for **17EN2** obtained during comparative computational studies versus **17EN1** (Figure 5.11) has a different set of ligand-receptor interactions in comparison to initial docking (Figure 5.10) which both employed identical docking protocols as outlined in Figure 5.7. By comparison **17EN1**'s ligand-receptor interactions are consistent with findings from the initial docking study (Figure 5.9). This trend gives rise to further evidence of inconsistent binding orientations for the 3*R*, 4*R* **17EN2** enantiomer, inferring poorer stability at the CBS. Additionally, in triplicate studies, **17EN2** was observed with varying and inconsistent quantities and orientation ligand-receptor interactions in each independent study, a trend which was not observed for **17EN1**.

3*S*,4*S* **17EN1**'s A ring overlays with CA-4's. Its A and B rings bind in a non-planar and similar orientation to CA-4's A and B rings, with the critical β-lactam ring overlaying the *cis* stilbene moiety of CA-4. The B-ring methoxy moieties for both CA-4 and **17EN1**

overlay and interact with hydrophobic Valβ181 and basic Lysβ352 (**B,** yellow, Figure 5.11). In contrast the A ring for **17EN2** (A, cyan, Figure 5.11) does not align with the A ring of **17EN1** (**A,** yellow, Figure 5.11) but overlays CA-4's B ring (**C**, cyan, Figure 5.11). Figure 5.12 illustrates the CBS binding pocket in grey, with comparative illustration of the favourable docking orientation for **17EN1** (yellow, Figure 5.12) versus unfavourable orientation for **17EN2** (pink, Figure 5.12).

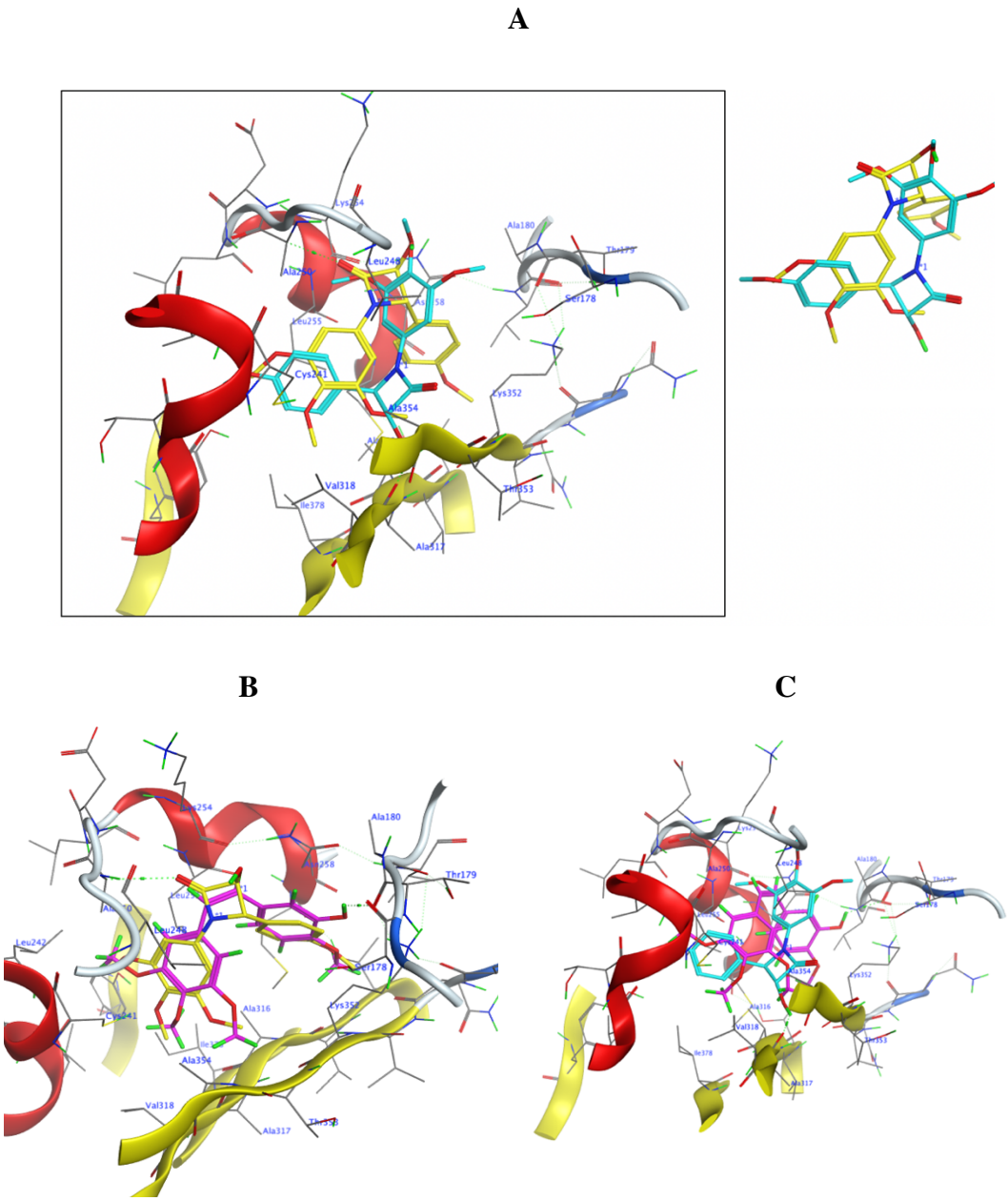

Figure 5.11: **A:** 3*S*,4*S* **17EN1** (yellow) at the CBS of 1SAO compared to 3*R*,4*R* **17EN2** (cyan). Receptor removed on right for clarity. **B:** Comparison of **17EN1** (yellow) to CA-4 (pink). **C:** Comparison of **17EN2** (cyan) to CA-4. Atom colours, red = oxygen, green = hydrogens, blue = nitrogen.

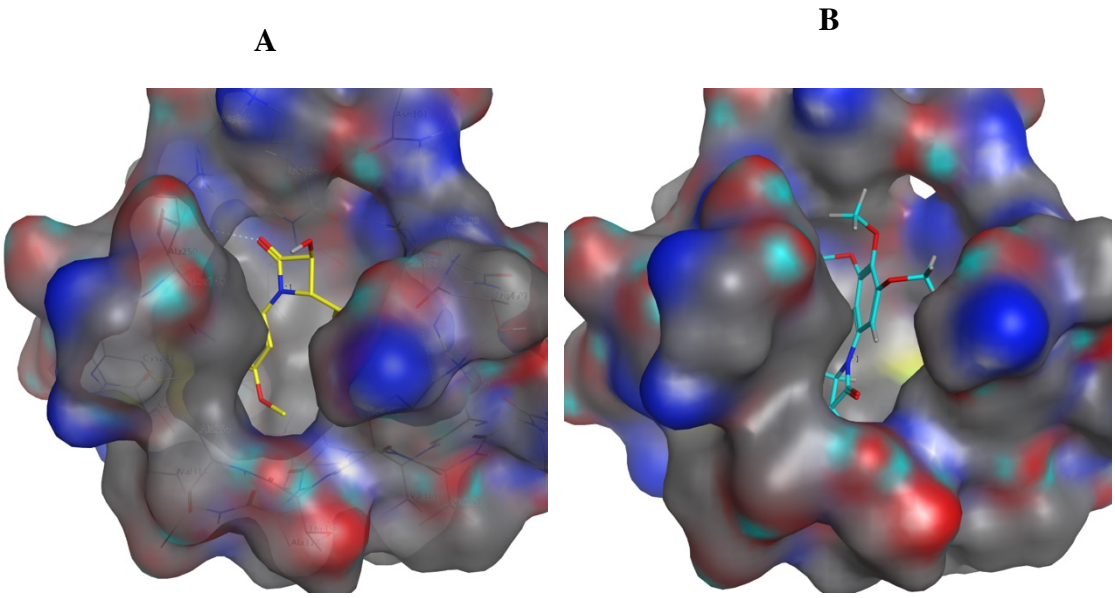

Figure 5.12: Comparison of **17EN1** versus **17EN2** at the CBS of 1SAO **A: 17EN1** (yellow) **B: 17EN2** (cyan) Red: Hydrophilic pocket interactions. Blue: hydrophobic pocket interactions. Black: neutral pocket interactions. Atom colours: Red= Oxygen, Green = Nitrogen, Blue = Hydrogen

A comparative analysis of ligand-receptor interactions was carried out for **17EN1, 17EN2** and CA-4 at the CBS of 1SAO. **17EN1** has the largest number of ligand-receptor interactions with 24 in total compared to 23 for CA-4 and 18 for **17EN2** (Table 5.1). The binding orientation for **17EN2** results in a loss in quantity of ligand-receptor residue interactions, with absence of Valβ318 as one of CA-4's critical interacting residues. This may translate to poor CBS affinity, poorer microtubule depolymerising and anti-proliferative activity.

Table 5.1: Ligand-Receptor Interactions for CA-4, **17EN1** and **17EN2** at the CBS of 1SAO

Compound	Predicted Polar Interactions	Hydrophobic Interactions	Total Predicted Binding Interactions
CA-4	1. Asnβ258 2. Asnβ350 3. Lys β352 4. Thrβ353 5. Thrβ314 6. Thrα179 7. Cysβ241 8. Lys β254	1. Ileβ378 2. Alaβ317 3. Valβ315 4. Alaα180 5. Valβ351 6. Valα181 7. Alaβ316 8. Metβ259 9. Valβ318 10. Leuβ255 11. Leuβ248 12. Leuβ242 13. Valβ238 14. Alaβ250 15. Alaβ254	23
17EN1 (3*S*,4*S*)	1. Asnα101 2. Thrα179 3. Asnβ258 4. Lysβ352 5. Asnβ350 6. Asnβ349 7. Lys β254 8. Thrβ353 9. Cysβ241 10. Aspβ251	1. Valβ351 2. Valβ181 3. Valβ315 4. Alaβ317 5. Alaβ354 6. Metβ259 7. Alaβ316 8. Valβ318 9. Ileβ378 10. Valβ238 11. Leuβ242 12. Leuβ248 13. Leuβ255 14. Alaβ250	24
17EN2 (3*R*,4*R*)	1. Lys β254 2. Aspα101 3. Aspβ251 4. Serα178 5. Thrα179 6. Thrβ353 7. Lysβ352 8. Tyrβ202 9. Cysβ241	1. Leuβ248 2. Ileβ378 3. Alaβ317 4. Alaβ316 5. Alaβ354 6. Leuβ242 7. Valβ238 8. Alaβ250 9. Leuβ255	18

5.3.3 *Validation of docking protocol using 5LYJ*

5LYJ was used as a control protein to confirm validity of ligand-receptor interactions observed at the CBS of 1SAO for **17EN1** and **17EN2**, as process of the docking protocol outlined in Figure 5.7. Figure 5.13 illustrates the 5LYJ co-crystal structure and native

ligand, *cis* CA-4 (cyan, Figure 5.13), at the active site. Ligand-receptor interaction output for **17EN1** in both 1SAO (**A,** yellow, Figure 5.11 and Figure 5.12) and 5LJY (yellow, Figure 5.13) are consistent and in close agreement. **17EN2** differed however in ligand-receptor interactions observed at the CBS of 1SAO (**B, cyan,** Figure 5.12) and 5LYJ (Figure 5.13). The variability for **17EN2**'s binding configurations and ligand-receptor interactions suggest that the 3*R*,4*R* absolute configuration does not complement the CBS binding pocket in the same manner as the 3*S*,4*S* configuration to enable a fixed and consistent docking orientation. This has also been observed and reported for the less active *trans* CA-4. Tubulin does not stabilise *trans* CA-4 to the same extent as *cis*-CA-4. The tubulin-*cis*-CA-4 complex is more stable by 4.5kcal.mol^{-1} equivalent to a 20,000 fold increase in tubulin binding affinity.[338,669] Future work may involve measuring and comparing the binding affinities of enantiomers of opposite absolute configurations. Following validation of the docking protocol outlined in flowchart Figure 5.7, 1SAO was chosen as the main receptor for further computational studies in line with literature previously published by Meegan *et al*.[359, 378, 400]

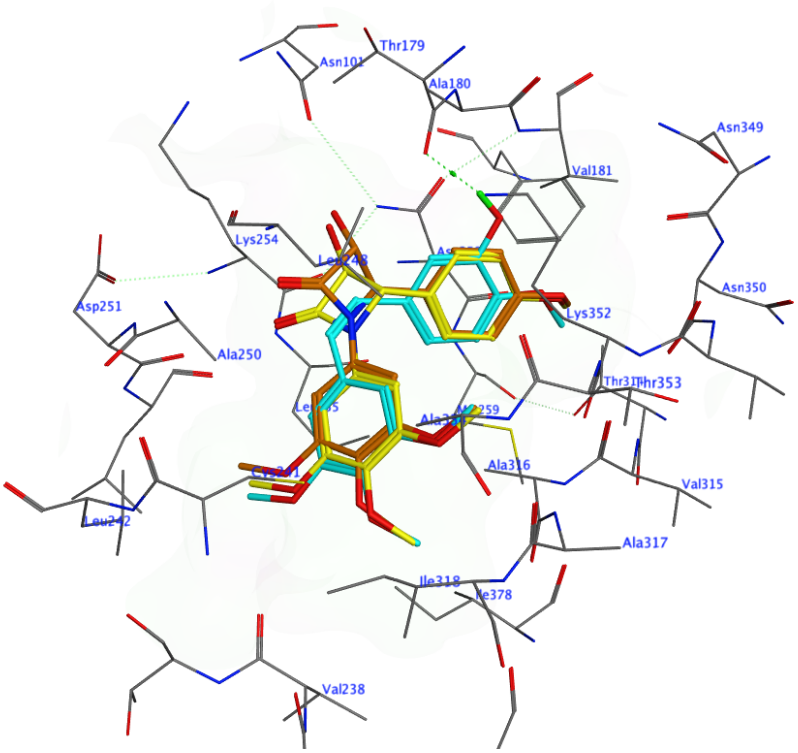

Figure 5.13: 5LYJ with CA-4 (cyan), **17EN1** (yellow) and **17EN2** (orange) at the CBS. Atom colours: Red = oxygen, green= hydrogen, blue = nitrogen.

5.3.4 *Introduction to scoring functions*

Scoring functions or *S* values are used in computational studies to predict the strength of non-covalent interactions and therefore binding affinity of a ligand at a receptor site.[670, 671] Scoring is a process of evaluating a particular pose as a mathematical model that counts the number of favourable intermolecular interactions such as polar, hydrophobic interactions and hydrogen bonds. The scoring is a prediction of the ligands free energy of binding and therefore allows for ranking of compounds according to their favourable interaction for a particular receptor.[672] A lower *S* value is indicative of lower energy of binding and therefore better binding affinity. *S* values can be used to determine the binding mode and site of a ligand, predict binding affinity and therefore identify promising drug leads for a given protein target.[673]

17EN1 consistently yielded a lower *S* value than **17EN2**. The lowest scoring function of -8.7823 for **17EN1** versus - 7.9197 of **17EN2** indicates increased stability for the 3*S,* 4*S* enantiomer at the CBS (Table 5.5). Comparing *S* values for **17EN1** versus **17EN2** rationalises the inconsistent binding orientation of **17EN2**, inferring that **17EN2** relatively is less energetically stable at the CBS with poorer receptor affinity with respect to **17EN1**.

5.3.5 *Comparative docking for **18EN1** and **18EN2***

B ring *meta* fluorine substituted enantiomers **18EN1** and **18EN2** were next docked at the CBS of 1SAO. Figure 5.14 demonstrates the binding orientation for both **18EN1** and **18EN2**. The 3*S*,4*S* **18EN1** enantiomer docks favourably with the trimethoxyphenyl A ring oriented toward the β subunit (**A,** Figure 5.14) while **18EN2**'s A ring is instead oriented towards the opening of the CBS binding pocket and fails to interact with the key β subunit residues Cysβ241, Valβ238 and Valβ318 (**B,** Figure 5.14). These observations are in line with findings observed for **17EN1** and **17EN2** (Figure 5.10, Figure 5.11, Figure 5.12).

For comparison, both **18EN1** and **18EN2** were studied alongside CA-4 (**A**, cyan, Figure 5.14). **18EN1'**s trimethoxyphenyl A ring is closely aligned (**A**, yellow, Figure 5.14) with the A ring of CA-4. Similarly to the non-coplanar orientation of CA-4's A and B rings (**A**, **cyan,** Figure 5.14), **18EN1**'s aromatic A and B rings are non-planar with a dihedral

angle of 46.9 °. (**A**, yellow, Figure 5.14) **18EN1**'s critical β-lactam ring overlays the *cis* stilbene moiety of CA-4. **18EN2**'s (**B,** pink, Figure 5.14) β-lactam moiety points away and perpendicular from the *cis* stilbene structure of CA-4 (**B, cyan,** Figure 5.14) demonstrating that the 3*R*,4*R* absolute configuration is not favourable for maintaining the desirable *cis* CA-4's orientation at the CBS. CA-4's *meta* hydroxyl hydrogen bonds to Thrα179, 2.03 Å away.

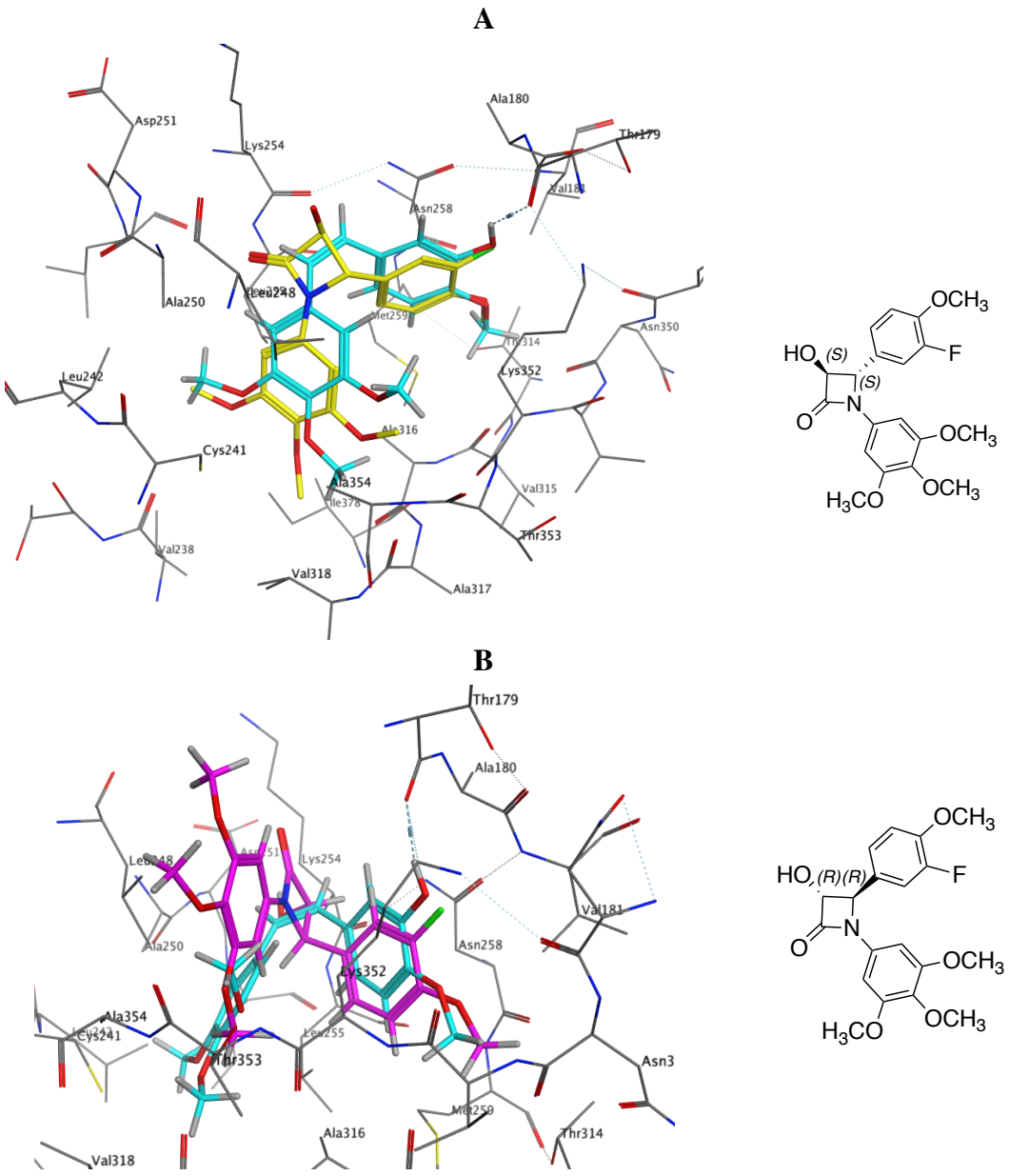

Figure 5.14: **A: 18EN1** (yellow) and CA-4 (cyan) **B: 18EN2** (pink) and CA-4 (cyan) docked at the CBS of 1SAO. Atom colours: Red= oxygen, blue = nitrogen, green = fluorine, grey = hydrogen

The fluorine atom of the B ring which lies in close proximity with Thrα179 and has potential to halogen bond or non-covalently interact with this residue. Furthermore the carbonyl oxygen of **18EN1** forms a critical hydrogen bond with the α carbon's hydrogen on the residue Alaβ250, 2.41 Å away (**A,** yellow, Figure 5.14) which was also observed for **17EN1** (Figure 5.11). This critical interaction with Alaβ250 was again not observed for **18EN2** (**B,** pink, Figure 5.14). **18EN2** instead demonstrated backwards docking with respect to **18EN1**. At the surface of the binding pocket, **18EN1** is not visible on due to deep burial within the CBS. In contrast, the trimethoxyphenyl A ring for **18EN2** is observed oriented out of the pocket with its β-lactam carbonyl oriented at the opening of the CBS. These are two key structural interactions likely to reduce the microtubule depolymerising activity for 3*R*,4*R* **18EN2** with respect to 3*S*,4*S* **18EN1** (Figure 5.14). **18EN1** also has a superior number of interacting residues (24) compared to 22 for CA-4 and 21 for **18EN2** (Table 5.2), further underpinning its potential increased affinity at the CBS relative to the 3*R*,4*R* configuration of **18EN2**. **18EN1** and **18EN2** were also studied in triplicate studies. All three replicates demonstrated similar binding orientation for **18EN1**. **18EN2** however demonstrated an inconsistent binding orientation for each independent replicate in keeping with findings observed for **17EN2**.

The *S* values for *meta* fluorine substituted **18EN1** and **18EN2** are -8.9461 and -8.6614 respectively. These values for both 3*S*,4*S* and 3*R*,4*R* enantiomers are lower than the corresponding *S* values for the *meta* unsubstituted **17EN1** and **17EN2** [-8.7823 and -7.9197 respectively, (Table 5.5)] indicating that the addition of the *meta* 3-fluoro substituent to the B ring of the 3-hydroxyl enantiomers is advantageous for increasing the ligand-receptor interactions independent of absolute configuration.

Conclusions on important ligand-receptor interactions which result in optimal binding at the CBS for enantiomers of **17** and **18** are as follows:

1) The position of the trimethoxyphenyl A ring towards the hydrophobic pocket deep within the β subunit in addition to proximity and interaction with three important residues; Cysβ241, Valβ238 and Valβ318.
2) Hydrogen bonding of the β-lactam carbonyl to the Alaβ250 residue.
3) The B ring orientation towards Thrα179 with the *meta* fluorine substitution having the advantage of additional halogen bonding to the carbonyl of Thrα179.

Table 5.2: Ligand-receptor interactions at the CBS of 1SAO **18EN1, 18EN2** and CA-4

Compound	Predicted Polar Interactions	Hydrophobic Interactions	Total Predicted Binding Interactions
CA-4	3 Lys β352 4 Thrα179 5 Asnβ258 6 Asnβ350 7 Thrβ314 8 Cysβ241 9 Lysβ254 10 Thrβ353	1. Alaα180 2. Valα181 3. Valβ318 4. Valβ315 5. Leuβ255 6. Alaβ316 7. Metβ259 8. Valβ238 9. Leuβ248 10. Leuβ242 11. Alaβ250 12. Alaβ354 13. Valβ351 14. Alaβ317	22
18EN1 (3*S*,4*S*)	1. Lys β352 2. Asnβ258 3. Thrβ353 4. Lysβ254 5. Thrβ314 6. Thrα179 7. Asnβ350 8. Cysβ241 9. Serα178 10. Glnβ247	1. Ileβ378 2. Alaβ354 3. Alaα180 4. Valβ318 5. Leuβ255 6. Valα181 7. Valβ315 8. Valβ317 9. Alaβ316 10. Leuβ242 11. Valβ238 12. Alaβ250 13. Leuβ248	23
18EN2 (3*R*,4*R*)	1. Lysβ254 2. Thrβ314 3. Thrβ353 4. Glnβ247 5. Serα178 6. Lysβ352 7. Thrα179 8. Asnβ258 9. Asnβ349 10. Asnβ350	1. Valβ315 2. Metβ259 3. Alaβ250 4. Leuβ248 5. Alaβ354 6. Alaβ317 7. Leuβ255 8. Alaα180 9. Valα181 10. Alaβ316 11. Valβ351	21

5.3.6 *Role of fluorine substitution of **18EN1** for increasing binding affinity at CBS*

Substitution of hydrogen for a fluorine atom is a common method employed in medicinal chemistry to enhance ligand to protein binding. Although charactersed by

electronegativity, fluorine can participate in hydrogen bonding as a hydrogen bond acceptor.[674] Similarity of the C-F and C-H bond length in addition to similar van der Waals radii enables substitution of a hydrogen with a fluorine atom without increasing the molecular size of drug molecule while potentially enhancing ligand affinity and selectivity. As an effective isostere in place of CA-4's B ring *meta* hydroxyl moiety, fluorine can act as a hydrogen bond acceptor with potentially the Thrα179 residue.[675] Halogens due to their high electron density function as electron donating sites or nucleophiles.[676] Fluorine atoms prefer hydrogen bonding over halogen bonding.[677] Replacement of the *meta* hydroxyl with a fluorine also has the advantage of preventing B ring *meta* hydroxyl metabolism *via* glucuronidating enzymes, thus enabling microtubule depolymerising activity in HT-29 cells. Malebari *et al* have demonstrated a 1300 fold increase in potency for racemate **19** versus **16**, due to **19**'s reduced susceptibility to glucuronidation on deletion of this B ring *meta* hydroxyl atom and replacement with the fluorine halogen atom.[378, 400]

A C-F bond is more resistant towards metabolism with higher energy of 116 kcal/mol relative to a C-H bond of 99 kcal/mol. An increase in metabolic inertness in certain fluorine substituted compounds is observed compared to their C-H counterparts. The comparative anti-proliferative activity for **18EN1** and **18EN2** versus B ring *meta* hydroxyl substituted **16EN1** and **16EN2** in HT-29 cells is discussed in Chapter 6. Additionally fluorine introduces an element of hydrophilicity to otherwise hydrophobic compounds. Since hydrophobic compounds are particularly sensitive to oxidation by liver enzymes (e.g. CYP450s), metabolic oxidation may potentially be overcome by introducing a fluorine atom.[675]

The B ring *meta* fluorine substituted **18EN1** has a lower and more energetically favourable *S* value of -8.9461 versus the corresponding unsubstituted 3-hydroxyl enantiomer, **17EN1** with an *S* value of -8.7823 (Table 5.5). Hydrogen bonding between the *meta* fluorine substitution for either **18EN1** or **18EN2** was not directly observed (Figure 5.14). Close contact between the fluorine and various C-H and N-H bonds of residues at the α subunit however were observed. C-F…H-C interactions are considered as weak hydrogen bonding interactions. Vargas *et al* have demonstrated that an aromatic fluorine substituted thrombin inhibitor had enhanced positive polarisation of the

hydrogen atom *ortho* to the fluorine substituent which in turn increased hydrophobic interactions with nearby tryptophan residue on its target receptor.[678] The C-H bond *ortho* to the fluorine in **18EN1** is in relatively close proximity to Alaα180 and Valα181 hydrophobic residues which may participate in these non-covalent interactions resulting in enhanced CBS affinity reflected by its lower *S* score relative to **17EN1** (Table 5.5). Vargas *et al* also suggest that basic interactions of the fluorine atom with an asparagine polar residue augments biological activity with respect to non-fluorinated parent compound.[678] The fluorine atom in both **18EN1** and **18EN2** lies in close proximity to both basic residues Asnβ258 and Lysβ352, ~2 A° away from the hydrogen of the NH_3^+ of its side chain. Each of these factors may result in enhanced anti-proliferative activity of fluorine substituted **18EN1** versus **17EN1**.

5.3.7 *Computational studies for **16EN1** and **16EN2** at the CBS of 1SAO*

Enantiomers of **16** are the closest structural β-lactam relation to stilbene parent CA-4, containing an identical 3-hydroxy-4-methoxy substituted B ring in addition to the conserved 3,4,5-trimethoxyphenyl A ring. Both enantiomers for **16** are illustrated in Figure 5.1 and Figure 5.15. **16EN1** demonstrated similar binding orientation and maintained comparable ligand-receptor interactions to the previously discussed enantiomers **17EN1** and **18EN1** (Figure 5.13 and Figure 5.14). **16EN2 (**cyan, Figure 5.15) was observed at the CBS in an opposite orientation to **16EN1 (**yellow, Figure 5.15) with the trimethoxyphenyl A ring emerging from the CBS pocket, in line with earlier observations for 3*R*,4*R* **17EN2** (pink**,** Figure 5.11) and **18EN2 (**cyan, Figure 5.15), failing to make the essential interactions deep within the β subunit at the CBS.

The lowest scoring *S* value for **16EN1** was -8.9775 which is lower but similar to the lowest *S* score for **18EN1** (-8.946) and superior to the lowest S score for **17EN1** [-8.7823, (Table 5.5)]. This favourable *S* value may be due to the B ring *meta* hydroxyl of **16EN1**, 3.35 A° away from the Thrα179 backbone oxygen (Figure 5.16), an interaction known to stabilise CA-4 at the CBS *via* hydrogen bonding.[669] The interactions of Lysβ352 or Thrα179 with **16EN1** may contribute to enhanced affinity at the CBS. **16EN1** in replicate studies demonstrated relatively consistent ligand-receptor interactions. In replicates where the B ring's *meta* hydroxyl was oriented away from Thrα179 oxygen and the NH_3^+ of the Lysβ352 side chain, the S score was higher and less

stable. This indicates that the optimal binding orientation to ensure maximum CBS affinity for the B ring *meta* hydroxyl and bioisosteres such as the fluorine atom of **18EN1**, is toward the Thrα179 oxygen and the NH_3^+ of the Lysβ352 side chain.

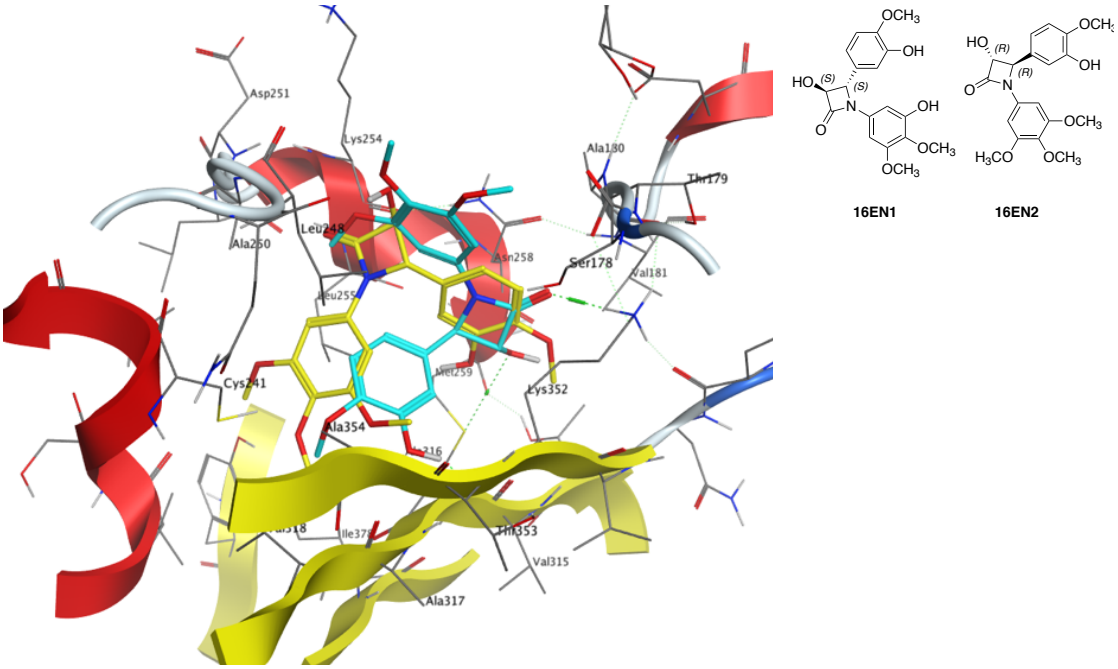

Figure 5.15: **16EN1** (yellow) and **16EN2** (cyan) at the CBS of 1SAO. Atom colours: Red = oxygen, Blue = Nitrogen.

In contrast to **17EN2** and **18EN2** which demonstrated different ligand-receptor interactions for each replicate in triplicate docking simulations, each replicate of **16EN2** afforded comparable and consistent binding orientations as the first 3*R*,4*R* 3-hydroxyl enantiomer demonstrating this property. This unique property of **16EN2** is explained by three hydrogen bonds (Figure 5.16) which were not observed for either **17EN2** (Figure 5.11) or **18EN2** (Figure 5.14). Stabilising hydrogen bonds observed for **16EN2** are as follows and are illustrated in Figure 5.16:

1) The β-lactam carbonyl hydrogen bonds to the NH_3^+ of Lysβ352 side chain.
2) The B ring *meta* hydroxyl hydrogen bonds to the carbonyl of Lysβ352's backbone which is possibly the most critical stabilising interaction due to absence of OH in **19EN1** and **17EN1**.

3) The β-lactam ring 3-hydroxyl hydrogen bonds to the sulfur of Metβ259 2.8 A° away.

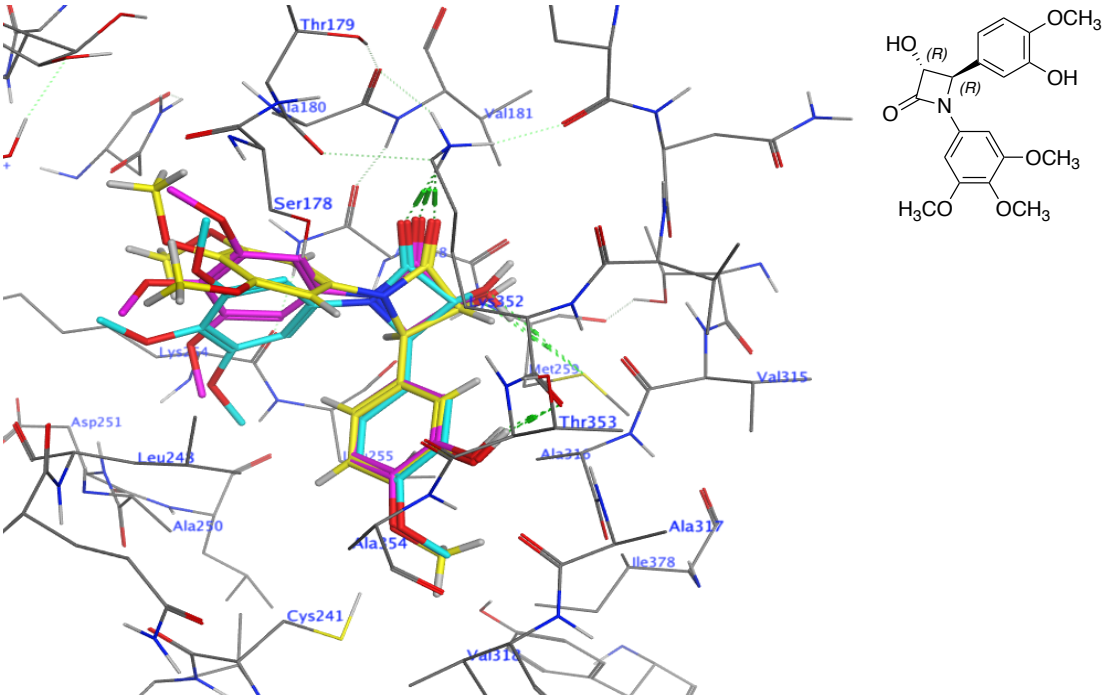

Figure 5.16: Triplicate studies for **16EN2** at the CBS of 1SAO demonstrating consistent ligand-receptor interactions for each independent replicate, explained by the presence of hydrogen bonding with Metβ259, and Lysβ352. Hydrogen bonds are illustrated as green dotted lines.

Despite the stability of **16EN2**'s B ring due hydrogen bonding interactions illustrated in Figure 5.15 and Figure 5.16, key interactions for the trimethoxyphenyl A ring are abolished. The Cysβ241 residue is > 7.3 Å away from **16EN2** (Figure 5.16) compared to 1.89 Å for **16EN1** (Figure 5.15). The important Valβ318 residue is also 12.8 Å away from **16EN2** (Figure 5.16) compared to 3.1 Å for **16EN1** (Figure 5.15). The total number of binding interactions (20) for **16EN2** is lower than **16EN1** [24, (Table 5.3)] in similar trend to previous observations for enantiomers of **17** and **18** (Table 5.1 and Table 5.2).

Table 5.3: Total Number of ligand-receptor binding interactions for **16EN1** and **16EN2** at the CBS of 1SAO

Compound	Predicted Polar Interactions	Hydrophobic Interactions	Total Predicted Binding Interactions
16EN1 (3*S*, 4*S*)	1) Lys β254 2) Thrα179 3) Asnβ258 4) Lysβ352 5) Asnβ349 6) Thr β353 7) Asnβ350 8) Cysβ241 9) Asnβ251	1) Ileβ378 2) Valβ318 3) Alaβ317 4) Valβ238 5) Leuβ242 6) Alaβ250 7) Leuβ248 8) Valα181 9) Alaα180 10) Metβ259 11) Leuβ255 12) Valβ351 13) Alaβ316 14) Alaβ354 15) Valβ315	24
16EN2 (3*R*, 4*R*)	1) Serα178 2) Thr β353 3) Lysβ352 4) Thrα179 5) Asnβ258 6) Lys β254 7) Asnβ251 8) Cysβ241	1) Alaβ354 2) Alaα180 3) Ileβ378 4) Alaβ317 5) Valβ315 6) Valα181 7) Alaβ316 8) Metβ259 9) Leuβ255 10) Valβ318 11) Leuβ248 12) Alaβ250	20

5.3.8 *Computational studies for 3-phenyl substituted β-lactams **24EN1** and **24EN2** at the CBS of 1SAO*

3-Phenyl substituted enantiomers of **24** with the 3-hydroxy-4-methoxy substituted B ring were next docked at the CBS of 1SAO. XRD analysis of **24EN1** has confirmed its absolute configuration as 3*S*,4*R* (Chapter 4). Molecular modelling studies of **24EN1** at the CBS of 1SAO demonstrated that the 3*S*,4*R* enantiomer binds in similar orientation to the 3-hydroxyl 3*S*,4*S* series. The carbonyl of **24EN1** of the β-lactam ring was observed oriented towards the Alaβ250 of the β-subunit, in keeping in finding observed for 3*S*,4*S* enantiomers (yellow, Figure 5.17). Additionally, an additional arene – hydrogen (π-aliphatic) interaction occurs between the hydrophobic portion of Lysβ254's side chain

and the 3-phenyl β-lactam substituent (Figure 5.18). All major ligand interactions for 3*S*,4*R* **24EN1** are consistent with those described for the 3-hydroxyl 3*S*,4*S* enantiomers (Table 5.4).

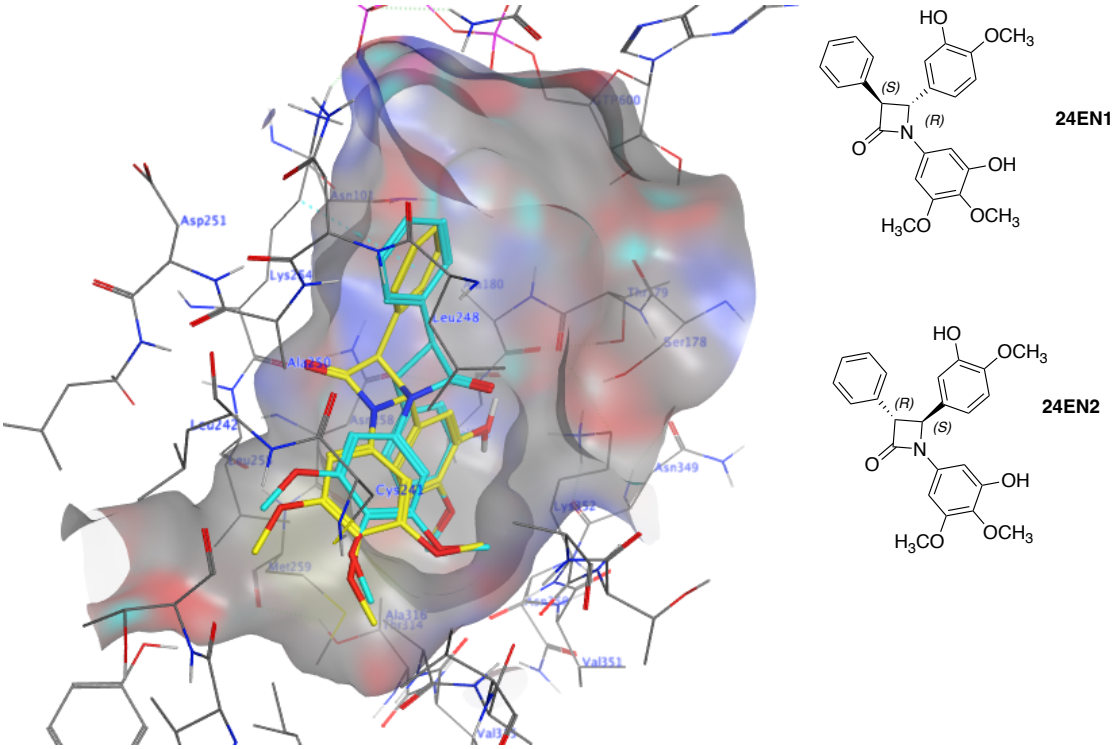

Figure 5.17: 3*S*,4*R* **24EN1** (yellow) and 3*R*,4*S* **24EN2** (cyan) at the CBS of 1SAO. CBS pocked illustrated in light grey. Atom colours: red= oxygen, blue= nitrogen, grey= hydrogen. π-aliphatic interaction illustrated as light blue dashed line.

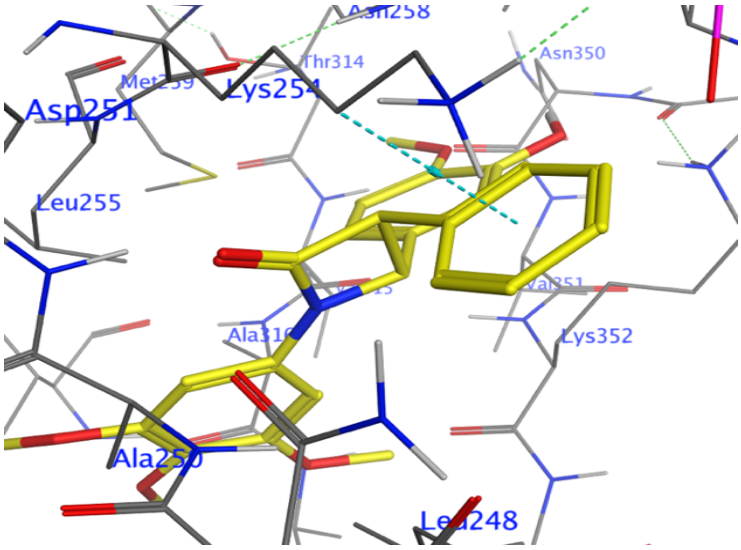

Figure 5.18: 3-phenyl substituent of 3*S*,4*R* **24EN1** with π-aliphatic interaction illustrated as broken blue line between Lysβ254 and the 3-phenyl ring.

The *S* value of -10.2684 (Table 5.5) for **24EN1** is the lowest and most energetically favourable of all enantiomers thus far, suggesting that the 3-phenyl substituent and specifically the π-aliphatic interaction in combination with the 3*S*,4*R* absolute configuration enhances the binding affinity at the CBS when compared to corresponding structurally related 3-hydroxyl enantiomer, **16EN1,** whose lowest scoring S value was observed as -8.9775 (Table 5.5). **24EN1** was therefore next studied in computational models alongside **16EN1** to demonstrate its superior ligand-receptor interactions (Figure 5.19). Both **16EN1** and **24EN1** demonstrated identical A and B ring ligand-receptor binding interactions. The additional stabilising factor for **24EN1** between the CH_2 hydrogen of Lysβ254's side chain and its 3-phenyl ring substituent of the β-lactam ring was absent for **16EN1 (**Figure 5.19). By comparison, the 3-hydroxyl of **16EN1** is oriented out of the CBS pocket in absence of major receptor-ligand interactions, providing no additional stability. This suggests that the aromatic substitution at the 3 position of the β-lactam ring which forms a π- aliphatic stabilising interaction (Figure 5.18) is favourable for CBS binding.

O'Boyle *et al* have demonstrated that while the 3-phenyl substitution on the β-lactam ring is extremely potent (IC_{50} in nanomolar range) in MCF-7 breast cancer cells, extension of this group to a wide range of carbocyclic and heterocyclic analogues demonstrates poor biological activity. The 3-thiophene substitution was tolerated and demonstrated excellent anti-proliferative activity (IC_{50} in low nanomolar range) while introduction of larger substituents at this position led to substantial decreases in biological activity. For example, a diphenyl modification resulted in an IC_{50} of 47.5 μM, 1-naphthyl had an IC_{50} of 11.2 μM and 2-naphthyl had an IC_{50} of 2.47 μM. Due to lower *S* value of 3-phenyl substituted β-lactam **24EN1** compared to 3-hydroxyl 3*S*,4*S* enantiomers **16EN1, 17EN1** and **18EN1** (Table 5.5), there is scope for introduction of larger heterocyclic substituents with respect to the 3-hydroxyl moiety. Substitution however may be limited to one aromatic or heterocyclic ring.[504]

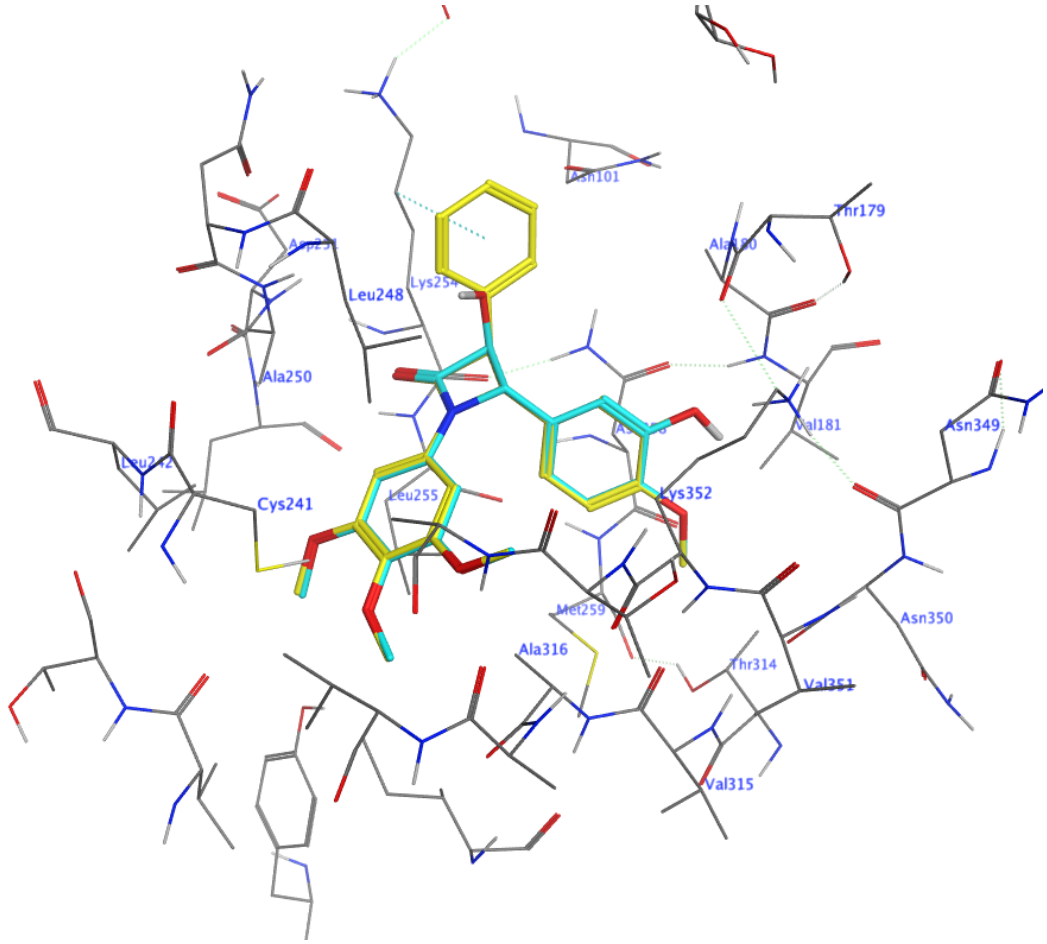

Figure 5.19: 3*S*,4*S* **16EN1** (cyan) and 3*S*,4*R* **24EN1** (yellow) at the CBS of 1SAO.

The *S* value of -9.401 for **24EN2** is much lower than for 3*R*,4*R* 3-hydroxyl enantiomers whose values ranged from -7.51 to -8.66 (Table 5.5). **24EN2** also has a lower *S* value than any of the 3*S*,4*S* 3-hydroxyl enantiomers (-8.7823, - 8.946, -8.9975 for **17EN1, 18EN1** and **16EN1** respectively). Comparing *S* values as an indicator of CBS binding affinity, and therefore microtubule polymerising and/or anti-proliferative potency, suggests greater activity for the less optimal enantiomer **24EN2** with respect to any of the 3-hydroxyl enantiomers. These findings will be further investigated and discussed in Chapter 6. The balance between hydrophobic versus polar interactions is quite different for **24EN1** versus its distomer **24EN2**. **24EN1** interacts with 10 and 15 polar and hydrophobic residues respectively where as the less potent **24EN2** interacts with 13 and 12 respectively. However the total number of binding interactions for both enantiomers of **24** [25, (Table 5.4)]. This contrasts the 3-hydroxyl β-lactam enantiomers where the less favoured 3*R*,4*R* enantiomers consistently had a lower quantity of binding interactions compared to the favourable 3*S*,4*S* enantiomers. Biological evaluation for

24EN2 will determine if such superior receptor-ligand interactions and excellent *S* scores will give rise to enhanced anti-proliferative potency versus the 3-hydroxyl panel, further underpinning potential importance of the π-aliphatic non-covalent interactions illustrated in Figure 5.18.

Table 5.4: 2D Ligand Interactions for **24EN1** and **24EN2** at the CBS of 1SAO generated by *MOE*

Compound	Predicted Polar Interactions	Hydrophobic Interactions	Total Predicted Binding Interactions
24EN1 (3S, 4*R*)	1. Lysβ254 2. Thrα179 3. Asnβ258 4. Asnα101 5. Thrβ314 6. Asnβ350 7. Lysβ352 8. Cysβ241 9. Thrβ353 10. Aspβ251	1. Valα181 2. Valβ315 3. Alaα180 4. Alaβ354 5. Valβ318 6. Valβ238 7. Alaβ317 8. Ileβ378 9. Leuβ242 10. Alaβ250 11. Alaβ316 12. Metβ259 13. Leuβ248 14. Leuβ255 15. Leuβ248	25
24EN2 (3*R*, 4*S*)	1. Serα178 2. Asnα101 3. Asnβ258 4. Asnβ350 5. Thrβ314 6. Asnβ349 7. Aspβ251 8. Lysβ352 9. Cysβ241 10. Lysβ254 11. Thrβ353 12. Thrα179 13. GTPC600	1. Alaα180 2. Valβ351 3. Alaβ316 4. Metβ259 5. Leuβ255 6. Alaβ250 7. Leuβ248 8. Valα181 9. Ileβ378 10. Valβ315 11. Alaβ317 12. Alaβ180	25

5.4 *Conclusions drawn from S values for enantiopure combretazets*

A summary of the lowest scoring *S* values for each enantiomer studied is presented in Table 5.5**.** The 3-phenyl **24EN1** enantiomer ranks lowest in terms of *S* value. Interestingly, the second enantiomer of **24** demonstrated a lower *S* value than any of the 3-hydroxyl derivatives suggesting that a phenyl ring at the 3-position may enhance

binding affinity at the CBS. The 3-hydroxyl compounds are predicted to bind in the following order of CBS affinity based on their scoring function: **16EN1, 18EN1** and **17EN1**.

Table 5.5: Ranked S values for all enantiomers. Highest scoring enantiomers (**EN1**) shown in bold (black) and highest scoring enantiomers (**EN2**) shown in red

Ranking	Enantiomer Code	S value
1	**24EN1**	**-10.2684**
2	**24EN2**	**-9.4014**
3	**16EN1**	**-8.9775**
4	**18EN1**	**-8.9461**
5	**17EN1**	**-8.7823**
6	**18EN2**	**-8.6614**
7	**16EN2**	**-8.1835**
8	**17EN2**	**-7.9187**

5.5 *Chapter 5 summary and outlook*

In summary for the 3-hydroxyl enantiomers, the 3*S*,4*S* absolute configuration is anticipated as the eutomer with more potent microtubule depolymerising effects due to superior orientation at the CBS with respect to the corresponding 3*R*,4*R* enantiomer, predicted as the distomer. Similarly the 3*S*,4*R* absolute configuration of 3-phenyl **24EN1** is anticipated as the eutomer. Since *S* values for **24EN1** are superior to any of the 3-hydroxyl eutomers, it is anticipated that this enantiomer may have superior biological activity of all enantiomers from molecular modelling studies. Anti-proliferative screening of enantiomers will next be presented in Chapter 6 with aim of validating computational findings.

Chapter 6 - Biochemical evaluation of combretazet enantiomers

6.1 *Rationale for selection of cell lines for preliminary screening*

The MCF-7, MDA-MB-231 and Hs578T(i) cell lines were chosen as *in vitro* models of breast cancer for anti-proliferative screening of enantiomers. HL-60 cells were selected as a human leukaemia cell line to demonstrate that the activity β-lactam enantiomers is not limited to breast cancer. HT-29 cells were chosen for screening of enantiopure β-lactams specifically designed for anti-proliferative activity in CA-4 resistant colorectal cancer cells. MCF-10-2A cells were selected as a model of non-tumorigenic *in vitro* breast epithelial cells for evaluation of the cytotoxicity of combretazet enantiomers.

6.1.1.1 *MCF-7 cells*

The MCF-7 or Michigan Cancer Foundation-7 human adenocarcinoma cell line was selected as a preliminary *in vitro* screen for β-lactam racemates and their enantiomers.[111] The MCF-7 cell line is a hormone positive human breast cancer cell line with the estrogen receptor (ER), progesterone receptor (PR) and glucocorticoid receptors (GR) derived from the pleural effusion of a 69-year old caucasian female with metastatic breast cancer.[679,680] MCF-7 cells are a useful *in vitro* breast cancer model for studies of hormone responsive breast cancers due to their expression of the ER.[679,681]

6.1.1.2 *MDA-MB-231 cells*

The MDA-MB-231 cell line serves as an *in vitro* model for invasive and late stage TNBC, lacking the ER, PR and HER2 receptor.[682] MDA-MB-231 cells were isolated from the pleural effusion of a 51 year old Caucasian female.[683] Metastasis is a multifactorial process whereby non-tumorigenic breast epithelial tissue undergoes transformation towards migration and invasion, referred to as the epithelial to mesenchymal transition (EMT).[684] MDA- MB-231 cells accurately represent the EMT associated with cancer progression as an *in vitro* model of TNBC.[685]

6.1.1.3 *Hs578T(i)8 cells*

The Hs578T(i)8 cell line is an isogenic subclone from the parental Hs578T cell line which is 3-fold more invasive and 2.5 fold more migratory than the parental cell line.[686] Rapid cellular proliferation is observed during tissue culture requiring low seeding densities and frequent passaging to prevent over confluency.

6.1.1.4 *HT-29 cells*

The HT-29 cells line is a human colorectal adenocarcinoma isolated from a primary tumour of a 44 year old Caucasian female.[687] HT-29 cells grow in monolayers after seeding followed by clustering and growth into multiple layers. HT-29 cells were chosen for exploration of the anti-proliferative effects of the panel of B ring *meta* substituted enantiomers isolated in Chapter 4.[378,400]

6.1.1.5 *HL-60 cells*

HL-60 cells are promyeoloblasts leukamia cells isolated from the peripheral blood of a 36-year-old caucasian female with acute promyelocytic leukemia. HL-60 cells grow in suspension rather than the panel of adherent cancer cells described above.[688]

6.1.1.6 *MCF-10-2A non-tumorigenic human breast epithelial cells*

MCF-10-2A are non tumorigenic human epithelial breast cells derived from parental MCF-10A cells through culturing in serum free medium with low calcium ion concentration. [689] A selection of the most potent enantiomers were selected for screening in MCF-10-2A cells to measure their cytotoxic effects. MCF-10-2A cells grow in 3D colonies and form domes in confluent cultures.

6.1.2 *Experimental details and cell culture*

6.1.2.1 *Breaking out of cells*

When not in culture, cells were stored in a liquid nitrogen vapour phase at temperature of -178 °C, preserved in 0.5 mL of 10%/90% DMSO and foetal bovine serum (FBS). Cells were thawed using pre-warmed media (100-200 μL) in a sterile laminar flow unit. Resuspended media and cells were transferred to a sterile 50 mL falcon tube followed by centrifugation at 200 *g* for 5 minutes. The supernatant was discarded to remove the DMSO content and pellet re-suspended in growth medium prior to transferring into a T25 tissue culture flask. Cells were incubated in a 5:95 % CO_2/ O_2 sterile environment at 37 °C until the required confluency was reached.

6.1.2.2 *Growth and maintenance of cells*

Cells were incubated in a 5:95 % CO_2/ O_2 atmosphere until 60-80% confluency. Cells were then sub-cultured to prevent cell death or genetic drift due to cellular mutations and alterations in protein expression when cultured in over confluent monolayers. Sub-culturing cells below 70% confluency maintains the integrity of conclusions derived from experimental results.

6.1.2.3 *Growth of MCF-7, MDA-MB-231, Hs578T(i)8, HT-29 and HL-60 cells*

The MCF-7 cell line was cultured in Eagles Minimum Essential Medium (MEM) (Gibco™ MEM, Glutamax™ Gibco, 41090-036).[690] The media was supplemented with 10% FBS (Gibco, foetal bovine serum, qualified, heat inactivated, US, 16140-071), 5 mL of 100 units/mL and 100 μg/mL of penicillin/streptomycin (Gibco, 15140-122) in addition to 1% of 100 X non-essential amino acids [NEAA) (Merck, M7145)]. MDA-MB-231 cells and HT-29 cells were grown in Dulbecco's Modified Eagles Medium (DMEM) high glucose with Glutamax™ (Gibco, 10566-016) supplemented with 10% FBS and 100 units/mL and 100 μg/mL of penicillin/streptomycin. Hs578T(i)8 cells were also grown in the same media, with additional supplementation of insulin [0.01 mg/mL (Merck, 10516-5mL)]. The Caucasian promyelotic leukemia HL-60 cell line were cultured in RPMI 1640 with Glutamax™ (Gibco, 61870-036) supplemented with 10% FBS and 100 units/mL and 100 μg/mL of penicillin/ streptomycin.

6.1.2.4 *Growth of MCF-10-2A cells*

MCF-10-2A cells were cultured in medium designed to support the growth of non tumorigenic breast epithelial cells. The growth medium consisted of (DMEM) high glucose with Glutamax™ (470 mL) with 5% horse serum [25 mL (Gibco, 16050-122)], 5 mL of 100 units/mL and 100 μg/mL of penicillin/streptomycin and additives of epidermal growth factor (EGF) 20 ng/ mL (Peprotech 1mg, E9644) resuspended at 100 μg/ mL in sterile dH_2O, 0.5 μg/ mL hydrocortisone of (Sigma #H-0888, 1g) resuspended at 1 mg/mL in 70% ethanol, 100 ng/ mL of cholera toxin (Sigma #C-8052, 4 mg) resuspended at 1 mg/ mL in sterile dH_2O, 10 μg/ mL of insulin (Sigma #19278-5 mL, 10 mg/mL) in addition to 100 units/mL and 100 μg/mL of penicillin/streptomycin.

6.1.2.5 *Sub culturing of adherent cells (MCF-7, MDA-MB-231, Hs578T(i)8 and HT-29 cells)*

Media was removed from the flask and cells were washed with room temperature sterile dulbecco's phosphate buffered saline (DPBS) to prevent interference of the media with trypsinisation. 1-3 mL of sterile Trypsin-EDTA solution (TrypLE™ Express Enzyme (1X) with phenol red, 12605-010 and 12605-028) was added and incubated for approximately 5 minutes at 37 °C. 5-10 mL of media was then added to neutralise the trypsin prior to transferring the suspension of cells to a falcon tube (50 mL) and centrifuging at 200 *g* for 5 minutes. The supernatant was discarded from the cell pellet and the pellet was then re-suspended in the required volume of media. Re-suspended cells were sub cultured at the required ratio and transferred to the required sterile tissue culture flask (T75 or T175) at the relevant seeding density. Cells were sub cultured at minimum on two independent occasions prior to experimental use following breaking out after cryo-preservation.

6.1.2.6 *Sub culturing of HL-60 suspension cells*

The media was removed from flask and transferred to sterile falcon followed by centrifugation at 200 *g* for 5 minutes. The supernatant was discarded and pellet re-suspended in growth medium. Cells were then counted and seeded into a sterile T175 flask at a seeding density of 5 X 10^6 cells in 25 mL of growth medium (RPMI).

6.1.2.7 *Sub culturing of MCF-10-2A cells*

MCF-10-2A cells were sub-cultured using an identical procedure as employed for adherent cells (Section 6.2.3) until the centrifugation stage. Since MCF-10-2A cells do not pellet well during centrifugation trypsin was instead diluted with media and sub-cultured from the diluted trypsin/media solution.

6.1.2.8 *Cryopreservation of cells*

The procedure for cryopreservation or freezing of cell pellets involved centrifugation at 200 *g* of the freshly trypsinised cells, removal of media and resuspension in the freezing medium. (9:1 FBS: DMSO) Thereafter 0.5 mL was aliquoted into sterile cryotubes and placed at -78 °C, for a minimum of 2 hours. Frozen cells were then transferred to the liquid nitrogen vapour phase in an environmental temperature of -178 °C for long term storage.

6.1.2.9 *Counting of cells*

A 3 X 3 haemocytometer was used to count cells for cell counting. The quantity of cells in each of the outer quadrants (1-4) was counted manually. A clean coverslip was applied to the haemocytometer (Figure 6.1). 10 µL of freshly suspended cells was added to the haemocytometer underneath the coverslip. Cells touching the top and left hand sides were excluded from the count but cells touching the right and bottom were included. (Equation 6.1) was used to calculate the quantity of cells per mL of suspension.

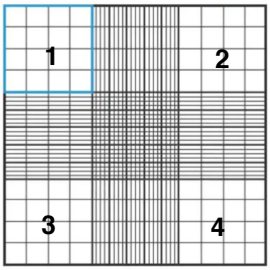

Figure 6.1: A representative haemocytometer grid. Cells falling in the outer quadrants are counted. The top left outer quadrant is marked in blue.

$$\frac{\text{Number of Cells in Quadrants (1–4)}}{4} \text{ X } 10^4 \text{ X dilution factor} = \text{Number of cells/ mL}$$

Equation 6.1: Formula for counting of cells using haemocytometer grid.

6.2 *Resazurin reagent preparation for use as in house AlamarBlue*

Cell viability assays employed the use of the alamarBlue™ cell viability reagent to determine the anti-proliferative effect of β-lactam enantiomers. The active chemical in alamarBlue™, resazurin, is a cell permeable, non- toxic and water soluble redox indicator or dye used to quantify viable cells.[374, 691] In its native form, resazurin is a blue substance. When added to living cells it is irreversibly reduced to the pink fluorescent resorufin (Figure 6.2). The quantity of resorufin produced is proportional to the number of viable cells relative to vehicle control. The number of viable cells can readily be measured using a microplate fluorometer with a λ 560 nm excitation and λ 590 nm emission filter set.[692] The incubation period is typically 3-5 hours to ensure adequate reduction and colorimetric change. Fluorescence intensity at end of a 72 h treatment period is measured and converted to a % cell viability with respect to vehicle treated cells. Dead cells are not able to reduce

resazurin to resorufin.[693, 694] Cell viability assays using AlamarBlue™ therefore allow for quantitative determination of viable cell proportions with reference to vehicle control wells which are considered as 100% viable. The vehicle control consists of 0.6% v/v ethanol. DMSO 0.5% v/v was used for poorly soluble analogues.

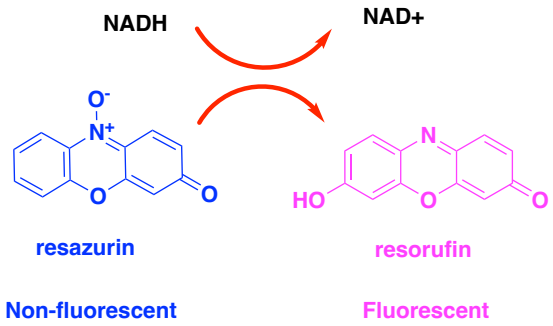

Figure 6.2: Schematic representation of the metabolic reduction of blue fluorescent resazurin in AlamarBlue™ to pink resorufin by NADH in living cells

Commercial resazurin may be purchased as the alamarBlue™ cell viability reagent. (Invitrogen™, DAL1100). Due to shortage of the commercially available form from suppliers, the black/blue resazurin dry powder was also purchased and reconstituted. (TCI, 1g, R0203). The concentration in commercial product [Life Technologies, Inc. Cat #DAL1100) is reported as a 440 µM solution of resazurin (0.011% w/v)].[695] Other sources determine that the concentration of reagent should be approximately 0.015 – 0.05% w/v. [696]

Resazurin (110 mg) was dissolved in sterile PBS (100 mL) as a 0.11 % w/v stock solution and filtered through a 0.2 µm filter in the laminar flow into a sterile light protected container. Two stocks were then prepared:

1. 1:10 dilution (in sterile DPBS) to yield a 440 µM solution (0.011% w/v).[695]
2. 1:5 dilution to yield an 880 µM solution (0.022% w/v).

The final volume of AlamarBlue™ used in a typical cell viability assay is 10 % v/v *i.e* 20 µL added to 200 µL as a 1:100 dilution. Absorbance values of both resazurin stocks (0.011% w/v and 0.022% w/v) were measured as 1:100 dilutions (20µL in 200 µL of media) on a microplate reader and compared to commercial AlamarBlue™. The average

fluorescent microplate readings of the 0.011% w/v and 0.022% w/v solution were 600-800 and 1000-1300 respectively with the latter in line with the blank absorbance obtained with commercial AlamarBlue™. The final resazurin concentration for in house reconstitution was 0.022% w/v.

6.3 *Optimisation of cell seeding density for cell viability assays using AlamarBlue™ in MCF-7 cells*

The validity of the AlamarBlue™ assay relies on a linear correlation between the fluorescence intensity and cell density. A seeding density experiment was carried out to determine the linear range of fluorescence intensity for MCF-7 cells. MCF-7 cells were seeded at densities from 1000-40,000 cells/well in 96 well plates (Greiner CELLSTAR® , 655180) in MEM (200µL). Cells were incubated at 37 °C in the dark with 5% CO_2 for a total of 96 hours (to account for 24 hour seeding period and 72 hour treatment of a typical cell viability assay). Five hours prior to the final time point of 72 hours, alamarBlue™ (20 µL) was added. After 96 hours, fluorescence was then measured on a microplate reader (FLUOstar Optima, BMG Labtech, Offenburg, Germany) at an excitation wavelength of 544 nm and an emission wavelength of 590 nm. Results were plotted using GraphPad Prism 8 for MacOs (June 2020). A linear correlation between cell density was observed from 1000-10,000 cells per well with a correlation coefficient (R^2) of 0.9 (Figure 6.3). 5000 cells/ well was determined as the optimal density in line with literature values for cell viability studies using MCF-7 cells.[378]

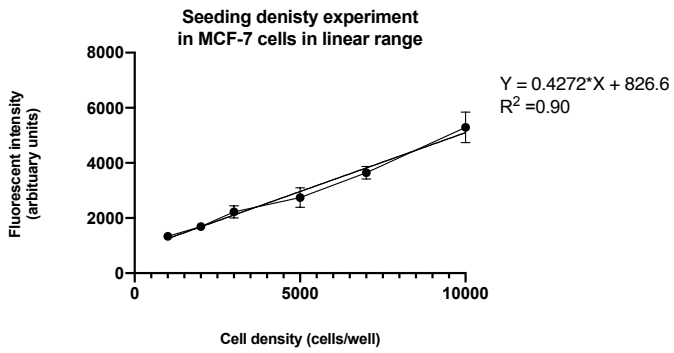

Figure 6.3: Optimisation of seeding density for alamarBlue™ anti-proliferative assays for MCF-7 cells at 96 hours. Values represent the mean ± SEM for each seeding density performed in triplicate on three independent occasions. Linear range of 1-10 X 10^3 cells/well illustrated

6.4 *Optimisation of cell seeding density for cell viability assays using AlamarBlue™ in HS578T(i)8 cells*

Due to the aggressive proliferation of the Hs578T(i)8 cells [686] a seeding density experiment was carried out to determine the optimal seeding density which prevents over confluency at the end of a 96 hour cell viability assay (24 hour seeding and 72 hour treatment periods). Cells were seeded in at 500-30,000 cells per well. The range of linearity extended to 5000 cells/well reflected by the R_2 value of 0.81. (**B,** Figure 6.4) However cells became overconfluent at 96 hours at densities as low as 3000 cells/well. 2500 cells per well (12,500 cells/mL) was chosen as the optimal seeding density. Seeding density experiments were not required for all other cell lines employed for viability assays since accurate documentation of the appropriate seeding density has already been documented in the literature by Malebari *et al*.[378, 400]

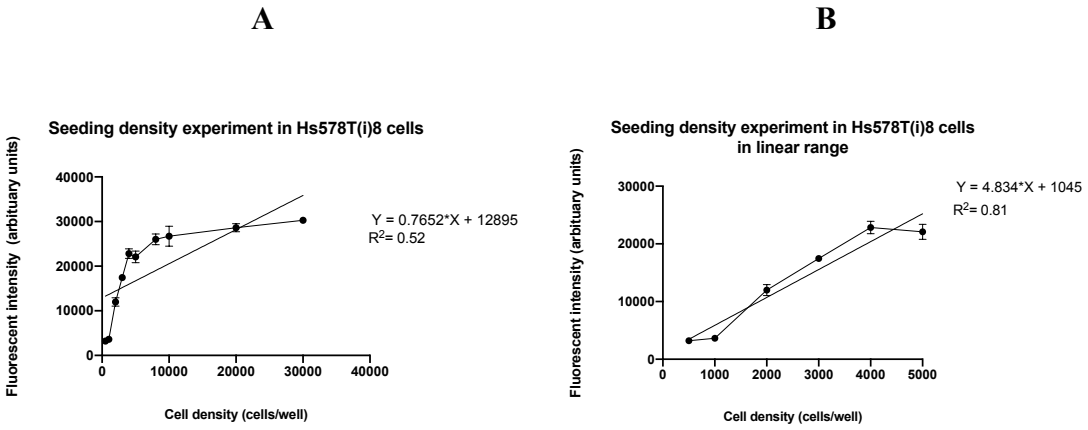

Figure 6.4: Optimisation of the seeding density in Hs578T(i)8 breast cancer cells at 96 hours. **A:** 5 X 10^3 - 3 X 10^5 cells/well **B:** Fluorescence intensity at 5 X 10^3 – 4 X 10^4 cells/well illustrating linear range until ~ 4 X 10^3 cells/well. Values represent the mean ± SEM for each seeding density performed in triplicate on three independent occasions

6.5 *Measurement of growth inhibitory effects in cell viability/anti-proliferative studies*

6.5.1.1 *Procedure for seeding of cells in 96 well plates and treatment protocol*

MCF-7, MDA-MB-231, HL-60, HT-29 and Hs578T(i)8 cells were seeded in sterile transparent flat bottom 96 well plates. Seeding densities selected are outlined in Table 6.1.[359] Due to IC_{50} values in low and sub nanomolar ranges for β-lactam enantiomers, a narrow treatment range was required in order to accurately measure their anti-proliferative activity. A modified approach for seeding and treating was explored to

reduce standard error. Cells were seeded in media (100 μL) per well in contrast to previous work which seeded at 200 μL per well.[378, 379] For ethanol based vehicles, test compound (8 μL) dissolved in vehicle was first added to media (392 μL) in a sterile microcentrifuge tube. Drug and media (100 μL) were subsequently added to the relevant wells in triplicate. If DMSO was employed as the drug vehicle, to facilitate a final concentration of 0.5% v/v independent of DMSO's cytotoxic effects, the drug in 100% DMSO (4 μL) was added to media (396 μL). 100 μL of this media and drug solution was added to the relevant wells in triplicate yielding a final concentration of 0.5% v/v.

Table 6.1: Cells/ well and required cells/ mL in initial cell suspension used to seed each cell line.

Cell line	Cells/well	Cells/mL	Final cells/ mL following treatment
MCF-7	5000	50,000	25,000
MDA-MB-231	5000	50,000	25,000
HL-60	40,000	400,000	200,000
HT-29	10,000	100,000	50,000
Hs578T(i)8	2500	25,000	12,500
MCF-10-2A	5000	50,000	25,000

6.5.1.2 *Layout of 96 well plate for cell viability assays and procedure*

Media only (200 μL) was added to each of the wells on the border of the plate to prevent evaporation of media from inner wells. Cells suspended in media (100 μL) were added to each of the 60 inner wells (Figure 6.5). After a 24 hour pre-treatment period, cells were then treated with the desired drug concentration in media (Section 6.6.1). Cells were then incubated for a further 72 hours.

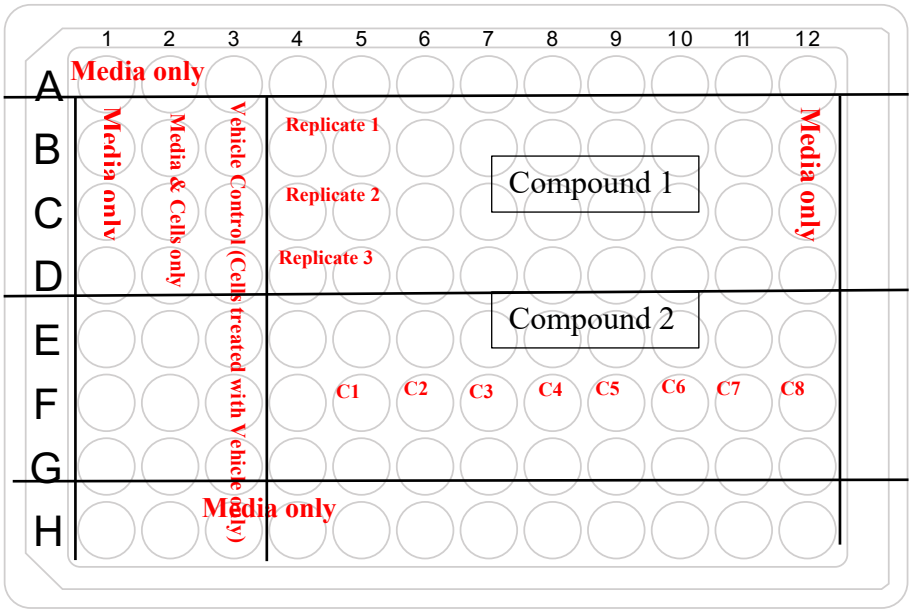

Figure 6.5: Layout of 96 well plate used for cell viability assays. C_1 = concentration 1. C_2 = concentration 2 etc.

6.5.1.3 *Measuring cell viability*

5 hours before the assay completion at 72 hours (67 hours), commercial alamarBlue™ (20 µL) or reconstituted resazurin (0.022% v/v in sterile PBS) was added to each well, inclusive of the blank wells containing media only. Plates were wrapped in tinfoil to protect from light and incubated until 72 hours post drug treatment. Fluorescence intensity of the 96 well plate is then read at an excitation λ of 544 nm and an emission λ of 590 nm. Untreated wells are considered as 100% cell viability. Blank fluorescent values from media only are measured and taken away from each well to account for background fluorescence. Vehicle treated wells are expressed as a % of the untreated wells. The fluorescent intensity of treatment wells is compared to vehicle treated wells and expressed as a percentage cell viability.

6.5.1.4 *Controls used in cell viability experiments*

CA-4 was used as a positive control and compared to literature values. Vehicle controls were measured for each independent assay [0.5% v/v 100% DMSO or 0.6 % v/v dH_2O/ethanol (1:2)].

6.5.1.5 *Treatment doses of test compounds*

A 10 mM stock solution was serial diluted to 1 mM, 100 μM and 10 μM. The 10 μM solution resulted in a final concentration of 0.1 μM (100 nM) following cell treatment (1:100 dilution). This 10 μM stock was used as a stock for further serial dilutions toward low nanomolar range. 100 μM and 0.1 nM were used as the highest and lowest concentrations [final test concentrations of 1 μM (10^{-6} M) and 0.001 nM (10^{-12} M) *i.e* C_1 and C_8, (Figure 6.5)] Six other test concentrations around the expected IC_{50} were also used as C_2-C_7 (Figure 6.5). Average IC_{50} values were considered acceptable when the SEM was < 1/3 of the IC_{50} value.

(1:2)].

6.5.1.6 *IC_{50} determination using GraphPad Prism*

The raw fluorescence data obtained from the microplate reader (FLUOstar Optima BMG Labtech, Offenburg, Germany) was transferred into Microsoft Excel. Blank readings (media (200 μL) and AlamarBlue™ (20 μL) were subtracted from vehicle control and test compound wells to obtained the corrected fluorescent reading. Test compounds were then expressed as a % cell viability with respect to corrected vehicle control well. Cell viability values were transferred to GraphPad Prism with concentrations expressed in M. Concentrations in M was then transformed in GraphPad Prsim to log[M]. A dose response curve was plotted as log(M) versus response using three parameters (three values) to yield the reported IC_{50} values.

6.5.1.7 *Relative versus absolute IC_{50} values*

The relative IC_{50} is the concentration corresponding to a response midway between the lower and upper plateaus of a cell viability curve. In contrast the absolute IC_{50} is the response corresponding to a 50% reduction in cell growth with respect to the vehicle control *i.e* the mean of or midway between the 0% and 100% controls. Despite achieving an apparent 50% reduction relative to a stable 100% viability value in this thesis. For anti-proliferative assays, the absolute IC_{50} cannot be reported. This is due to the absence of a 0% control viability value, which cannot be obtained due to apparent resistant of 10-30% of residual cells when treated with combretazet analogues. Guidelines for accurate reporting of IC_{50} estimations state that where there is a possibility of >/ 5% error

in the IC_{50} calculation apparent absolute IC_{50} values should be reported as relative data.[697] Relative IC_{50} values are the most commonly reported. This compares to the absolute IC_{50} which is more commonly referred to using the GI_{50} abbreviation. The GI_{50} is more commonly employed for analogues that slow cellular growth and describes the concentration required to reduce total cell population to 50%.[698] In this thesis, all IC_{50} values are considered as relative rather than absolute, with the aim of selecting the most potent and lead analogue amongst the panel analysed.

6.6 *Cell growth experiment*

MDA-MB-231 cells were seeded at 5000 cells/well in a 96 well plate and treated 24 hours post seeding with either 0.6 % v/v ethanol as vehicle control or **17EN1** at concentrations of 10 and 15 nM. Immediately after treatment, plates were placed in an 5% CO_2 incubator at 37 °C and monitored using Incucyte®, taking photographs every 2 hours until 72 hours post treatment.

6.7 *Tubulin polymerisation studies*

The polymerisation of purified bovine tubulin was monitored using the kit, BK006 V3.0, purchased from Cytoskeleton Inc. (October 2020). Tubulin polymerisation reactions were carried out using 100 μL of tubulin (3 mg/ mL) in general tubulin buffer (80 mM PIPES pH 6.9, 0.5 mM EGTA, 2mM $MgCl_2$) 1 mM GTP and 10% glycerol buffer, collectively labelled 'tubulin polymerisation buffer'. Bovine tubulin resuspended in tubulin polymerisation buffer was added to wells of a half well 96 well plate (100 μL). Tubulin was re-suspended at 0 °C. The microplate reader (Softmax Pro 340 spectrophotometer) was pre-set to 37 °C. Tubulin polymerisation was subsequently commenced by adding the plate at 0 °C to the microplate reader at 37 °C. Light is scattered proportionally to the concentration of polymerised microtubules in the assay. Tubulin assembly was monitored turbidimetrically by measuring the optical density (OD) value at 340 nm. OD readings were taken every 30 seconds for 62 minutes. Tubulin was either incubated with paclitaxel (10 μM) as a polymerising positive control, CA-4 used as a depolymerising positive control, test enantiomer or vehicle [DMSO (0.5% v/v)]. We gratefully acknowledge Dr. Vincent Kelly for the use of the Softmax Pro 340 microplate reader.

6.8 *Immunofluorescence/confocal microscopy*

Confocal microscopy was used to study effects of enantiomers on the cytoskeleton of MCF-7, MDA-MB-231, Hs578T(i)8 cells and HT-29 cells. Cells were seeded on sterilised 18 mm glass coverslips in 12 well plates (Cellstar®, 665180) at a seeding density of 1 x 10^5 cells/ mL (1 mL/ well). After 24 h cells were treated with either 0.6 % v/v ethanol as the vehicle control, CA-4 (100 nM) or paclitaxel (1 μM) as tubulin depolymerising and polymerising controls respectively. Test concentrations for enantiomers were selected around the IC_{50} value. Following incubation for 16 hours, cells were washed twice with PBS (pre-warmed to 37 °C to prevent tubulin disintegration) and fixed in 4% formaldehyde in dH_2O for 15 minutes at 37 °C. Following fixation, cells were washed with PBS supplemented with Tween 0.1% v/v (PBST 0.1% v/v) three times and permeabilised with triton X-100 (0.5% v/v in PBS). Cells were washed with PBST (0.1% v/v) three times and treated with blocking buffer (3% bovine serum albumin (BSA) in PBST (0.1% v/v). Cells were then incubated anti-α-tubulin FITC antibody (clone DM1A) (Sigma, F2168) as a 1:100 dilution in bovine serum albumin (BSA), in the dark overnight at 4 °C (16-24 h). Cells were washed with PBST (0.1% v/v) three times followed by incubation with Alexa Fluor™ 488 goat anti-mouse IgG (Invitrogen, A11001) as a 1:2000 dilution in BSA for 1 h (room temperature). Following incubation cells were washed three times with dH_2O. Coverslips were removed, surface water on surface of cell samples dried and mounted in Ultra Cruz® Mounting Media (Santa Cruz Biotechnology, Santa Cruz, CA, 10 sc-24941), containing 4,6-diamino-2-phenolindol dihydrochloride (DAPI). Images were captured by Leica SP8 confocal microscopy with Leica application suite X software. All images per replicate were collected on the same day using identical parameters. Each experiment was performed as three independent replicates on three independent occasions.

6.9 *Cell cycle analysis*

MDA-MB-231 cells were seeded at 1 x 10^5 cells/mL (2 mL) in sterile 6 well plates (Greiner cellstar®, 657160) for 24 hours prior to treatment with 0.6 % v/v ethanol as vehicle or test compound. At the relevant time point (2, 8, 16, 24, 48 or 72 hours) cells were collected by removing media, washing with PBS and retaining both supernatant and media. Cell monolayers were then trypsinised with Trypsin-EDTA solution (TrypLE™ Express Enzyme (1X) with phenol red, 12605-010 and 12605-028). The supernatant was

removed and washed again with PBS. All layers were retained in a 15 mL falcon tube and centrifuged at 200 *g* for 5 min. The supernatant was removed and pellet re-suspended in 50 μL of ice cold 1 X PBS. 1 mL of 70% ice cold ethanol in PBS (1X) was added prior to fixing cells overnight at -20 °C. Fixed cells were then centrifuged at 700 *g* for 10 minutes prior to removal of supernatant and re-suspension in 200 μL of 1 X PBS. 12.5 μL of DNase-free RNase A and 37.5 μL of 1 mg/ mL of propidium iodide (Sigma-Aldrich, P4170, 25g) dissolved in dH_2O was added before incubation in the dark at 37°C for 30 minutes. The DNA content of samples were measured by fluorescence activated cell sorting (FACS) analysis using the BD Accuri C6 flow cytometer and software at 488 nM gated for 10,000 events *i.e* cells/experimental group. We gratefully acknowledge Dr. Barry Moran for assistance and advice on flow cytometry experiments.

6.10 *Biochemical results*

6.10.1.1 Anti-proliferative screening of β-lactam racemates and their isolated enantiomers

Anti-proliferative evaluation of β-lactam racemates and their enantiomers was carried out in MCF-7 breast cancer cells in preliminary screening. Subsequently the most potent enantiomer pairs were evaluated in MDA-MB-231 and Hs578T(i)8 TNBC breast cancer cells as *in vitro* models of aggressive metastatic BC. Additionally selected enantiomer pairs were evaluated in HT-29 cancer cells to demonstrate the anti-proliferative activity of B ring *meta* substituted analogues in CA-4 resistant colorectal cancer cell lines. The most potent eutomers were then screened in acute promyelocytic leukaemia HL-60 cells.

6.10.1.2 *Preliminary anti-proliferative activity of the 3-hydroxyl **17** panel in breast cancer cells*

Both geometric isomers of **17** were evaluated in MCF-7 cells confirming superior biological activity of the *trans* isomer[357] which was greater than four times more potent than *cis* **17** (IC_{50} of 13 versus 60 nM (Table 6.2). Comparative anti-proliferative activity for *cis* and *trans* isomers of **17** is illustrated in **A,** Figure 6.6. *Trans* enantiomers **17EN1** and **17EN2** demonstrated largely different anti-proliferative activity in MCF-7 cells. 3*S,* 4*S* **17EN1** was determined as the more potent eutomer with an IC_{50} of 4 nM compared to 32 nM for the 3*R,* 4*R* distomer (Table 6.2). This anti-proliferative data for enantiomers of *trans* **17** in MCF-7 cells complements the molecular modelling data discussed in

Chapter 5, which predicted that the 3*S*,4*S* enantiomer would result in superior CBS affinity and therefore anti-proliferative activity (Figure 5.5). **17EN1** has comparable biological activity to CA-4 (in house IC_{50} of 5 nM in line with literature values).[357, 359, 378, 400] Further investigation on the comparative biological effects of the 3*S*,4*S* and 3*R*,4*R* **17** enantiomers were next carried in MDA-MB-231 cells. Again **17EN1** was superior to both *trans* **17** and 3*R*, 4*R* **17EN2** with an extremely potent IC_{50} of 8 nM in MDA-MB-231 which is superior to CA-4's in house IC_{50} of 11 nM (Table 6.2). Both enantiomers of *trans* **17** were also screened in the invasive and metastatic like Hs578T(i)8 cell line.[686, 113]

Table 6.2: Anti-proliferative activity of panel **17** in four CA-4 sensitive cell lines reported as IC_{50} in nM ± SEM [a]

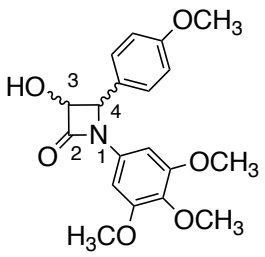

Code	3*X*[1]	4*X*[1]	MCF-7	MDA-MB-231	Hs578T(i)8	HL-60
***Trans* 17**	Racemate	Racemate	13.20 ± 0.37	13.56 ± 3.24	Nd	Nd
***Cis* 17**	Racemate	Racemate	60.28 ± 17.72	Nd	Nd	Nd
17EN1	*S*	*S*	4.69 ± 1.72	7.93 ± 2.5	4.64 ± 2.81	3.04 ± 0.10
17EN2	*R*	*R*	31.66 ± 1.11	48.60 ± 17.75	46.41 ± 17.16	Nd
CA-4 [b]			5.33 ± 2.11	11.33 ± 4.32	4.618 ± 1.38	1.378 ± 0.30

[a] IC_{50} values are half maximal inhibitory concentrations required to inhibit growth at 72 h following treatment. Values represent ± SEM for at least three independent experiments performed in triplicate. [b] The IC_{50} values for CA-4 are in line with literature values. [291, 357, 359, 378, 400] Nd = not determined [1] 3*X*,4*X* refers to absolute configuration.

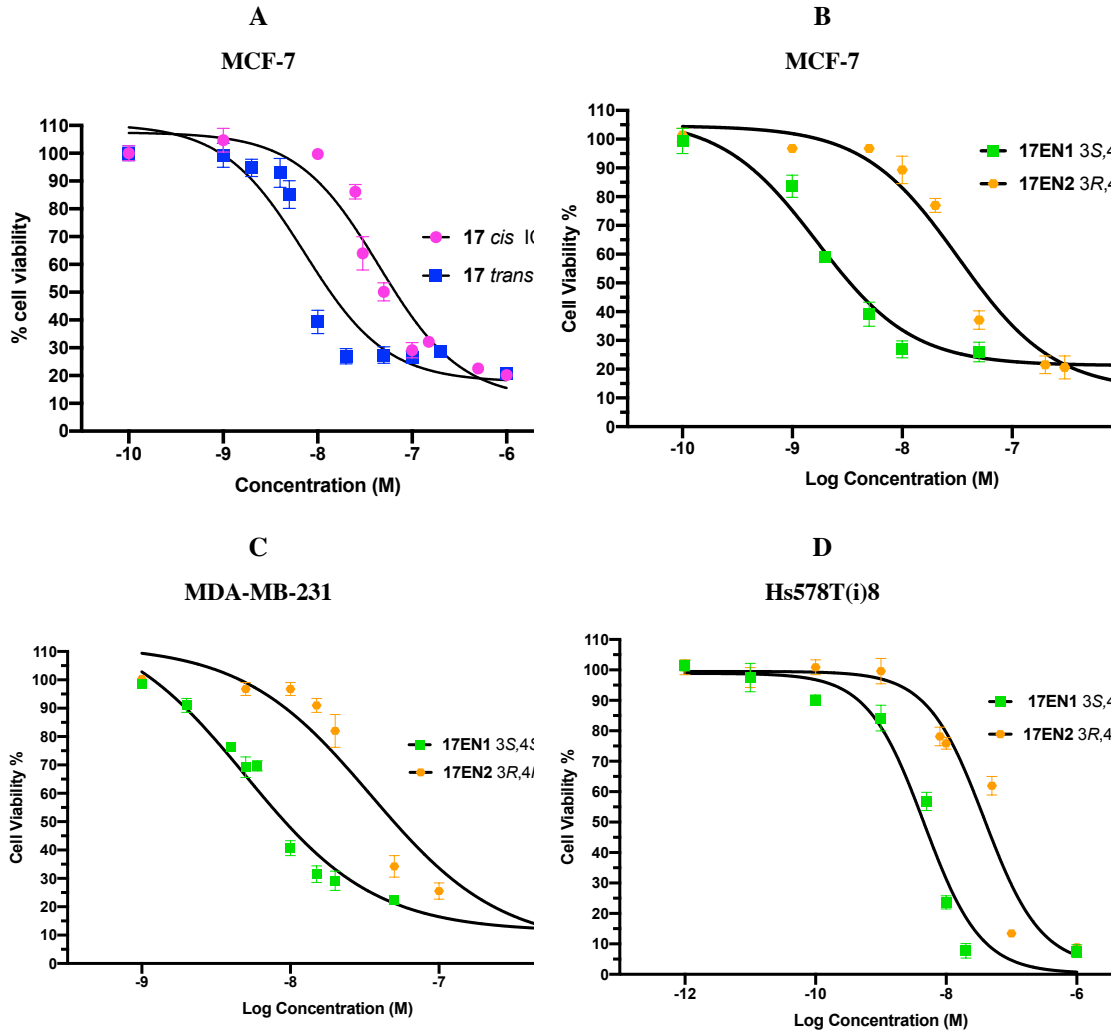

Figure 6.6: Cell viability graphs at 72 hours post treatment for **A:** *cis* **17** and *trans* **17s** in MCF-7 cells. **B: 17EN1** versus **17EN2** in MCF-7 cells. **C: 17EN1** versus **17EN2** in MDA-MB-231 cells. **D: 17EN1** versus **17EN2** in Hs578T(i)8 cells

17EN1 had comparable and slightly superior anti-proliferative activity in the more aggressive Hs578T(i)8 versus the MDA-MB-231 TNBC cell line [IC_{50} of 5 and 8 nM respectively (Table 6.2)] underpinning its mechanism of action as an microtubule targeting CBSI, preferentially targeting more rapidly proliferating cells. **17EN1** is a promising lead analogue as a CBSI whose mechanism of action is independent of hormone receptors for future development in TNBC cell lines. Cell viability graphs for **17EN1** versus **17EN2** in three breast cancer cell lines are illustrated in **B**, **C** and **D**, Figure 6.6. **17EN1** also demonstrated excellent activity in HL-60 cells (IC_{50} of 3 nM) and therefore has potential application for the treatment of leukaemia

6.10.1.3 *Anti-proliferative activity of 3-hydroxyl panel in three breast cancer cell lines*

The remainder of the 3-hydroxyl enantiomer panel were screened in MCF-7 and MDA-MB-231 cells (Table 6.3 and Table 6.4). The 3*S*,4*S* enantiomer was consistently determined as the eutomer with superior anti-proliferative activity versus 3*R*,4*R* distomers. All eutomers were superior in potency than parent racemates. Of the entire panel of 3-hydroxyl β-lactams, B ring *meta* fluorine substituted **18EN1** demonstrated the best potency in MCF-7 cells (IC_{50} of 0.26 nM, Table 6.3). The cell viability curves and comparative antiproliferative activity for **18, 18EN1** and **18EN2** are illustrated in Figure 6.7. Eutomer **18EN1** is 30 and 10 times more potent than *trans* racemate **18** in MCF-7 and MDA-MB-231 cells respectively (Table 6.3). The distomer **18EN2** had IC_{50} values of 18.13 and 33.92 nM in MCF-7 and MDA-MB-231 cells, with poorer antiproliferative activity with respect to parent racemate **18** [IC_{50} of 8.36 and 7.18 nM in MCF-7 and MDA-MB-231 cells, (Table 6.3)]. Two other 3*S*,4*S* enantiomers, **16EN1** and **20EN1** also had sub nanomolar IC_{50} values in MCF-7 cells [0.80 and 0.66 nM respectively (Table 6.3 and Table 6.4)]. **18EN1** remained however the most potent enantiopure 3-hydroxyl β-lactam across all breast cancer cell lines.

Approximately 25% of all drugs approved by the FDA in 2020 contained a fluorine atom and are considered fluoro-pharmaceuticals.[699] The first fluoro-pharmaceutical marketed was fludrocortisone acetate (Fluorinef™), a synthetic corticosteroid containing a fluorine atom at the stereogenic 9α-position in 1954. Globally more than 340 marketed drugs (20% of the market) contain at least one fluorine atom.[700] As discussed in Chapter 5,

substitution with a fluorine atom is increasingly employed to enhance binding affinity of lead analogues with the desired target protein with aim of increasing potency[675] and target selectivity of a drug by modifying properties such as pKa, lipophilicity, hydrophobic interactions, conformation and membrane permeability. Oral bioavailability and half-life may also be improved.[701]

Fluorophilic binding sites on the CBS *e.g* a proteins hydroxyl moiety (C-F…H-O) or alternatively interactions with amides, phenyl moieties, sulphydryl or carboxyl groups,[702] may contribute to stabilisation of the **18EN1** drug-receptor complex.[703] **18EN1** was the only 3-hydroxyl eutomer with sub nanomolar potency in MDA-MB-231 cells [IC_{50} of 0.7 nM, (Table 6.3)], demonstrating that addition of the fluorine atom is excellent for enhancing anti-proliferative activity in the TNBC cell line. This compliments findings for **18EN1** in computational studies (Figure 5.14) which was found to have a lower S value of -8.95 compared to *meta* unsubstituted **17EN1,** with a larger S value of -8.78 indicative of poorer CBS affinity with respect to **18EN1** (Table 5.5).

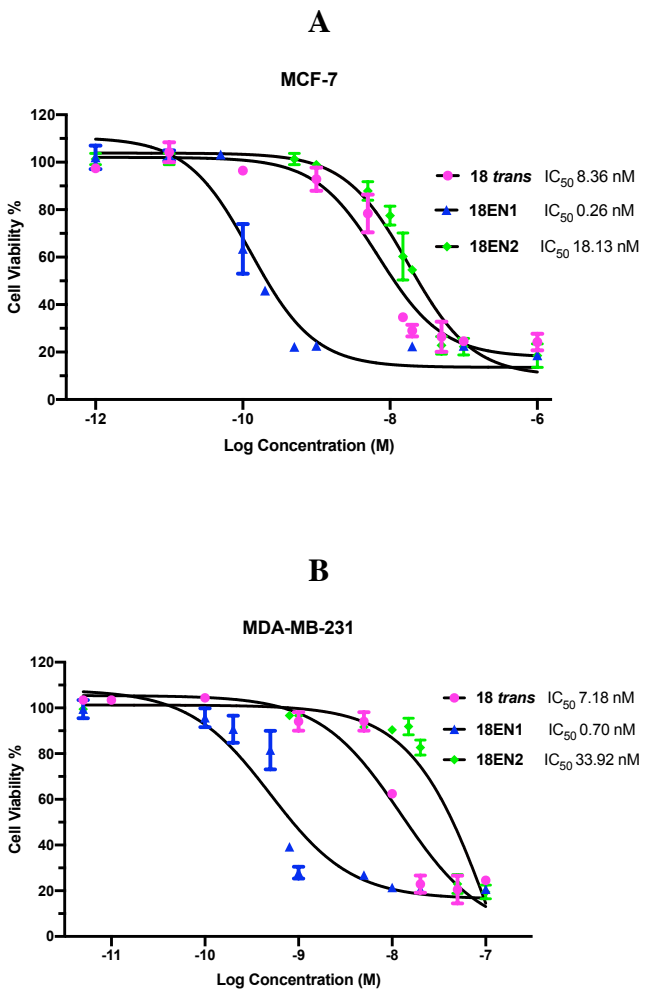

Figure 6.7: Cell viability graphs for family **18** at 72 hours **A:** MCF-7 breast cancer cells **B:** MDA-MB-231 breast cancer cells. Blue = 3*S*,4*S* **18EN1**, pink = *trans* racemate **18,** green = 3*R*,4*R* **18EN2.** Values represent average of three independent experiments performed in triplicate with error bars representing SEM

16EN1 also displayed excellent activity in MDA-MB-231 cells with an IC_{50} approaching sub nanomolar range of 1.48 nM (Table 6.3). B ring *meta* bromine substituted eutomer **21EN1** also had better activity in MDA-MD-231 than in MCF-7 cells with an IC_{50} of 1.74 nM versus 2.08 nM respectively (Table 6.4). Similarly B ring *meta*- methyl substituted **20EN1** had good activity as third most active eutomer in MDA-MB-231 cells [IC_{50} of 2.44 nM, (Table 6.4)]. **39EN1** with the isosteric *para*-methyl sulfide B ring substitution in place of **17EN1**'s *para*-methoxy was marginally more active than **17EN1** in MDA-MB-231 cells with an IC_{50} of 7.56 nM (Table 6.4) compared to 13 nM for parent racemate **17** (Table 6.2). Both B ring *meta* unsubstituted eutomers, [**17EN1** and **22EN1** (Table 6.2 and Table 6.4)] had weaker activity than the *meta* halogen substituted β-

lactams [**18EN1**, **19EN1**, **21EN1,** (Table 6.3 and Table 6.4)], B ring *meta* hydroxyl substituted **16EN1** or methyl substituted **20EN1** (Table 6.4), demonstrating that addition of a halogen or methyl substituent at the B ring *meta* position is advantageous for anti-proliferative activity. A selection of enantiomer pairs were screened in the aggressive Hs578T(i)8 TNBC cell (**16, 18, 19, 20** and **22**). Enantiomers were consistently and comparably potent in the more aggressive Hs578T(i)8 cell line (Table 6.3 and Table 6.4). For example, **18EN1** had IC_{50} values 0.26and 0.32 nM in MCF-7 and Hs578T(i)8 cells respectively with a slightly poorer IC_{50} value of 0.70 nM in MDA-MB-231 cells (Table 6.3). **16EN1, 19EN1** and **20EN1** also each had sub nanomolar IC_{50} values in Hs578T(i)8 cells (Table 6.3 and Table 6.4). This data demonstrates that the Hs578T(i) TNBC cell line is highly susceptible to the anti-proliferative effects of the 3-hydroxyl 3*S*,4*S* eutomers. Comparable anti-proliferative data in the Hs578T(i)8 cell line with respect to hormone responsive MCF-7 cells for the 3-hydroxyl eutomers is promising, due to the highly aggressive nature of these TNBC cells.

6.10.1.4 *Anti-proliferative activity of selected enantiomers in HL-60 human leukemia cell line*

Four β-lactam 3*S*,4*S* eutomers, **16EN1, 18EN1, 19EN1** and **20EN1** were evaluated in HL-60 cells. The IC_{50} values of 0.27 nM, 0.19 nM, 1.16 nM and 0.41 nM for **18EN1, 16EN1, 19EN1** and **20EN1** (Table 6.3 and Table 6.4) respectively were all superior to CA-4 (in house IC_{50} value of 1.38 nM) demonstrating their potential application as anti-cancer agents for the treatment of leukemia

Table 6.3: Anti-proliferative activity of 3-hydroxyl racemates and enantiomers (**16,18, 19**) in four CA-4 sensitive cell lines at 72h. IC_{50} [a] reported in nM ± SEM

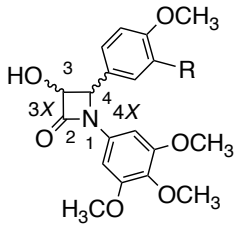

Code	R	3*X*[1]	4*X*[1]	MCF-7	MDA-MB-231	Hs578T(i)8	HL-60
16	OH	Racemate	Racemate	3.24 ± 1.62	6.21 ± 1.06	Nd	Nd
16EN 1	OH	*S*	*S*	**0.80 ± 0.16**	**1.48 ± 0.75**	**0.69 ± 0.34**	**0.19 ± 0.02**
16EN 2	OH	*R*	*R*	4.88 ± 1.56	16.03 ± 2.33	4.94 ± 1.84	Nd
18	F	Racemate	Racemate	8.36 ± 1.41	7.18 ± 2.76	**Nd**	**Nd**
18EN 1	F	*S*	*S*	**0.26 ± 0.15**	**0.70 ± 0.05**	**0.32 ± 0.08**	**0.27 ± 0.17**
18EN 2	F	*R*	*R*	18.13 ± 2.55	33.92 ± 3.45	15.11 ± 5.55	Nd
19	Cl	Racemate	Racemate	1.89 ± 0.93	18.64 ± 7.31	Nd	Nd
19EN 1	Cl	*S*	*S*	**1.11 ± 0.36**	**12.98 ± 6.65**	**0.40 ± 0.06**	**1.16 ± 0.31**
19EN 2	Cl	*R*	*R*	51.78 ± 17.96	63.67 ± 20.30	49.75 ± 4.71	Nd
CA-4[b]				5.33 ± 2.11	11.33 ± 4.32	4.62 ± 1.38	1.38 ±0.30

[a] IC_{50} values are half maximal inhibitory concentrations required to inhibit growth at 72h. Values represent ± S.E.M for at least three independent experiments performed in triplicate.[b] The IC_{50} values for CA-4 are in line with literature values. [291, 357, 359, 378, 400, 416, 415] Eutomer highlighted in bold. [1] 3*X*,4*X* refers to absolute configuration of enantiomers

Table 6.4: Anti-proliferative activity for 3-hydroxyl racemates and enantiomers (**20**-**22**) in four CA-4 sensitive cell lines at 72h. IC_{50} reported in nM ± SEM

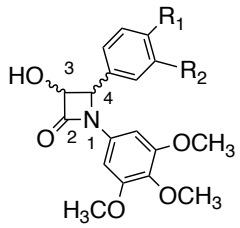

Code	R_1	R_2	3*X*[1]	4*X*[1]	MCF-7	MDA-MB-231	Hs578T(i)8	HL-60
20	OCH_3	CH_3	Racemate	Racemate	5.21 ± 1.48	6.46 ± 1.79	**Nd**	**Nd**
20EN1	OCH_3	CH_3	*S*	*S*	**0.66 ± 0.31**	**2.44 ± 0.99**	**0.20 ± 0.06**	**0.41 ± 0.09**
20EN2	OCH_3	CH_3	*R*	*R*	34.68 ± 12.03	45.01 ± 4.60	13.95 ± 2.30	**Nd**
21	OCH_3	Br	Racemate	Racemate	5.64 ± 2.17	2.19 ± 1.24	**Nd**	**Nd**
21EN1	OCH_3	Br	*S*	*S*	**2.08 ± 0.92**	**1.74 ± 0.90**	**Nd**	**Nd**
21EN2	OCH_3	Br	*R*	*R*	40.73 ± 7.53	87.24 ± 18.58	**Nd**	**Nd**
22	SCH_3	H	Racemate	Racemate	8.36 ± 1.4	16.24 ± 5.75	**Nd**	**Nd**
22EN1	SCH_3	H	*S*	*S*	**3.66 ± 0.81**	**7.56 ± 4.75**	**1.67 ± 0.81**	**Nd**
22EN2	SCH_3	H	*R*	*R*	29.85 ± 2.12	60.15 ± 21.66	20.81 ± 6.22	**Nd**
CA-4[b]					5.33 ± 2.11	11.33 ± 4.32	4.62 ± 1.38	1.38 ± 0.23

[a] IC_{50} values are half maximal inhibitory required to inhibit cell growth. Values represent ± SEM for at least three independent performed in triplicate. [b] The IC_{50} values for CA-4 are in line with literature values.[291, 357, 359, 378, 400] Eutomer highlighted in bold. [1] 3*X*,4*X* refers to absolute configuration of enatiomers. Nd= not determined

6.10.1.5 *Eudysmic ratios of 3-hydroxyl enantiomers in three breast cancer cell lines*

The eudysmic ratios calculated for enantiomeric pairs in breast cancer cell lines consistently demonstrated a difference in biological activities between eutomer and distomer (Table 6.5). The magnitude of the eudysmic ratios varied between enantiomeric pairs which could be attributed to either degree of diastereomer co-elution during diastereomeric LC chiral resolution and final *ee* values, or alternatively substitution at the B ring *meta* position which influences the binding affinity of eutomer versus distomer. The relative activity for enantiomers of **17** is similar across all three cell lines [6-10, (Table 6.5)**]** The eudysmic ratios for **18EN1** and **18EN2** are much larger compared

to enantiomers of **17** (70, 48 and 47 in MCF-7, MDA-MB-231 and Hs578T(i)8 cells) demonstrating that the difference in anti-proliferative activity between eutomer **18EN1** and distomer **18EN2** is greatly influenced by addition of *meta* fluorine substituent to the B ring (Table 6.5)]. Enantiomers of **19** have a much larger differential anti-proliferative activity in Hs578T(i)8 cells with a eudysmic ratio of 125 compared to 47 and 5 in MCF-7 and MDA-MB-231 cells. A similar trend is observed for enantiomers of **20** with the largest eudysmic ratio of 67 observed in Hs578T(i)8 cells compared to 52 and 18 in MCF-7 and MDA-MB-231 cells respectively. The magnitude of difference for enantiomers of **16** is smaller and consistent with a range of 7-11 in Hs578T(i)8 and MDA-MB-231 cells respectively. Enantiomers of **22** have smaller and consistent eudysmic ratios, from 8 to 13 in keeping with findings for its isosteric relatives **17.** This data suggests that the *meta* halogen or methyl substitution is beneficial for CBS affinity for 3*S*,4*S* 3-hydroxyl enantiomers and results in larger eudysmic ratios than the corresponding unsubstituted enantiomers (Table 6.5).

Table 6.5: Eudysmic ratios for 3-hydroxyl enantiomers[a]

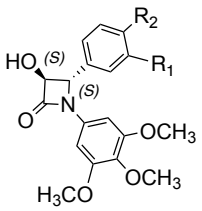

16EN1 = R_1= OH R_2 = OCH_3
17EN1 = R_1= H R_2 = OCH_3
18EN1 = R_1= F R_2 = OCH_3
19EN1 = R_1= Cl R_2 = OCH_3
20EN1 = R_1= CH_3 R_2 = OCH_3
21EN1 = R_1= Br R_2 = OCH_3
22EN1 = R_1 = H R_2 = SCH_3

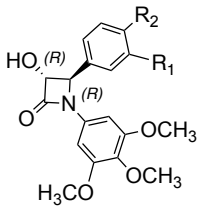

16EN2 = R_1= OH R_2 = OCH_3
18EN2 = R_1= F R_2 = OCH_3
17EN2 = R_1= H R_2 = OCH_3
19EN2 = R_1= Cl R_2 = OCH_3
20EN2 = R_1= CH_3 R_2 = OCH_3
21EN2 = R_1= Br R_2 = OCH_3
22EN2 = R_1 = H R_2 = SCH_3

Code	MCF-7	MDA-MB-231	Hs578T(i)8	*ee* eutomer (EN1)	*ee* distomer (EN2)
17EN2 : 17EN1[a]	7	6	10	94	71
18EN2 : 18EN1[a]	70	48	47	79	75
16EN2 : 16EN1[a]	6	11	7	75	41
19EN2 : 19EN1[a]	47	5	125	91	78
20EN2 : 20EN1[a]	52	18	67	66	50
21EN2 : 21EN1[a]	19	50	Nd	76	96
22EN2 : 22EN1[a]	8	8	13	84	85

[a] Eudysmic ratio calculated by the ratio of distomer IC_{50}: eutomer IC_{50}

6.10.1.6 *Preliminary anti-proliferative screening of enantiomers of **17** in HT-29 colorectal cancer cell lines*

17EN1 and **17EN2** were also screened in CA-4 resistant HT-29 colorectal cancer cells. Good antiproliferative activity was anticipated due to deletion of the B ring *meta* hydroxyl substituent present on **16EN1** as discussed in Chapter 1. Both **17EN1** and **17EN2** demonstrated excellent anti-proliferative activity in HT-29 cells with IC_{50} values of 8 and 224 nM respectively compared to 5209 nM for CA-4 (Table 6.6). These findings are in agreement with reported data suggesting that deletion of CA-4's B ring *meta* hydroxyl is advantageous for augmenting biological activity in HT-29 colorectal cells.[378, 400] The relative potency of 0.001 for CA-4 in MCF-7 cells versus HT-29 (Table 6.6) demonstrates its HT-29 cell resistance. In contrast the relative potency between MCF-7 and HT-29 cells for **17EN1** is 0.610, demonstrating comparable relative activity in both

cell lines by virtue of the B ring *meta* hydroxyl deletion. **17EN1** is therefore a suitable candidate for both aggressive breast cancers in addition to HT-29 CA-4 resistant colorectal cancers. As the less active 3*R*,4*R* distomer, **17EN2**'s IC_{50} of 220 nM (Table 6.6), is also superior to CA-4 in HT-29 cells, despite its unfavourable absolute configuration for optimal CBS activity. The cell viability curves for **17EN1** and **17EN2** versus CA-4 in HT-29 cells are illustrated in Figure 6.6.

Table 6.6: IC_{50} reported in nM of 3*S* 4*S* eutomer **17EN1** and 3*R*,4*R* distomer **17EN2** and CA-4 in MCF-7 versus HT-29 colorectal cancer cells with relative potency ratios.[a]

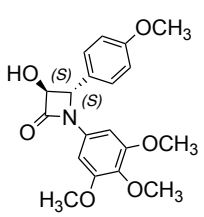

17EN1

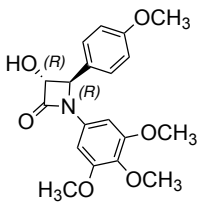

17EN2

Compound Code	MCF-7	HT-29	Relative potency[a]
17EN1	4.69 ± 1.72	7.75 ± 2.15	0.610
17EN2	31.66 ± 1.11	225.6 ± 35.28	0.140
CA-4[b]	5.33 ± 2.11	5209 ± 956.8	0.001

Values represent ± SEM for at least three independent experiments performed in triplicate.
[a] IC_{50} in MCF-7 cells / IC_{50} in HT-29 cells [b] The IC_{50} values for CA-4 are in line with literature values. [291, 357, 359, 378, 400, 416]

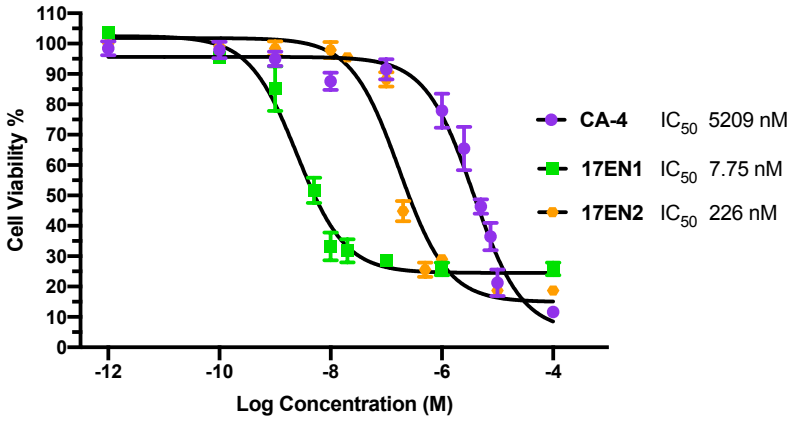

Figure 6.8: Antiproliferative activity at 72 hours for **17EN1** and **17EN2** versus CA-4 in HT-29 chemoresistant colorectal cancer cells. Values represent ± SEM for at least three independent experiments performed in triplicate.

6.10.1.7 *Anti-proliferative activity of 3-hydroxyl enantiomers in HT-29 colorectal cancer cells*

16EN1 as the B ring *meta* hydroxyl substituted eutomer had poor anti-proliferative activity in HT-29 cells (IC_{50} value of 226 nM, (Table 6.9)] Substituting the *meta* B ring hydroxyl yielding B ring *meta* fluorine substituted analogue, **18EN1,** chlorine substituted **19EN1,** methyl substituted **20EN1** and bromine substituted **21EN1** resulted in excellent activity in HT-29 cells with IC_{50} values of 0.53, 1.41, 0.77 and 1.44 nM respectively (Table 6.7) in addition to excellent anti-proliferative IC_{50} values in TNBC cells (Table 6.3 and Table 6.4). **22EN1** also had good antiproliferative activity in HT-29 cells with an IC_{50} of 5.82 nM (Table 6.9), comparable to its isosteric relative **17EN1** [IC_{50} of 7.7 nM, (Table 6.6)]. The relative antiproliferative activities for each eutomer in HT-29 cells are illustrated in Figure 6.9 and are compared to CA-4. While **16EN1** had better biological activity than CA-4 in HT-29 cells its anti-proliferative activity was much poorer when compared to the corresponding *meta* substituted **18EN1, 20EN1, 21EN1, 33EN1**) and unsubstituted **17EN1** and **22EN1** relatives (Figure 6.9). This confirmed previous findings by Malebari *et al*, suggesting that replacement or deletion of the *meta* hydroxyl of both CA-4 and **16EN1** sensitises CA-4 resistant HT-29 cells to the microtubule depolymerising and anti-proliferative effects of the combretazet racemates.[378, 410] This thesis observed the same for both enantiopure eutomers and distomers of these previously reported racemates (Figure 6.9).

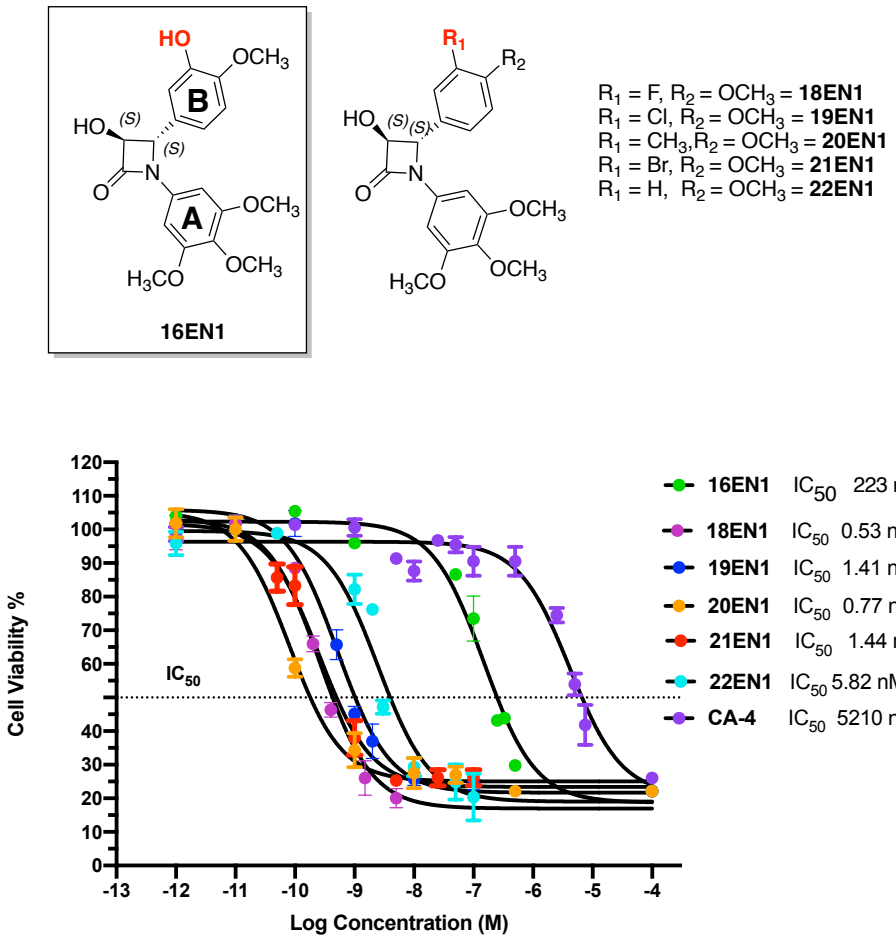

Figure 6.9: Antiproliferative activity for eutomers of the 3-hydroxyl eutomer panel in HT-29 cells. Values represent ± SEM for at least three independent experiments performed in triplicate.

While **18EN1** and other B ring substituted analogues were designed with intention of optimising antiproliferative activity in HT-29 colorectal cancer cells, its relative potency in MCF-7 compared to HT-29 cells of 0.49 (Table 6.7) demonstrates its potential as a lead analogue for dual activity in both breast and colorectal cancers. Relative potencies of 0.78, 0.86, 1.44 and 0.62 for 3-hydroxyl eutomers **19EN1, 20EN1, 21EN1** and **22EN1** (Table 6.7) demonstrate that their anti-proliferative activity is retained in HT-29 cells. These values care more favourable than **16EN1** which demonstrated a relative potency of 0.003 (Table 6.7). The poor relative potency for **16EN1** illustrates its significantly diminished anti-proliferative activity in HT-29 cells, due to presence of the undesirable B ring *meta* hydroxyl, suspectable to metabolic inactivation mediated by UDP-

glucuronyl transferase. The *meta* halogen and methyl substituted *3S*,4*S* eutomers are therefore dual candidates for the development against both breast and CA-4 resistant colorectal cancers.

Table 6.7: IC_{50} values reported in nM for 3-hydroxyl 3*S*,4*S* eutomers and 3*R*,4*R* distomers compared to CA-4 in MCF-7 and HT-29 colorectal cancer cells with respective relative potencies .

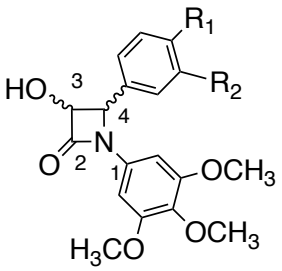

Code	R_1	R_2	MCF-7	HT-29	Relative potency[a]
16EN1	OCH_3	OH	0.80 ± 0.16	236.1 ± 36.5	0.003
16EN2	OCH_3	OH	4.89 ± 1.56	624.2 ± 88.4	0.008
18EN1	OCH_3	F	0.26 ± 0.15	0.53 ± 0.33	0.49
18EN2	OCH_3	F	18.13 ± 2.55	24.4 ± 6.0	0.730
19EN1	OCH_3	Cl	1.11 ± 0.36	1.41 ± 0.29	0.78
19En2	OCH_3	Cl	51.8 ± 18.0	59.1 ± 8.83	0.88
20EN1	OCH_3	CH_3	0.66 ± 0.31	0.77 ± 0.28	0.86
20EN2	OCH_3	CH_3	34.7 ± 12.03	37.63 ± 9.63	0.93
21EN1	OCH_3	Br	2.08 ± 0.92	1.44 ± 0.34	1.44
21EN2	OCH_3	Br	40.7 ± 7.53	47.7 ± 15.4	0.86
22EN1	SCH_3	H	3.66 ± 0.81	5.82 ± 1.66	0.63
22EN2	SCH_3	H	29.9± 2.12	51.91 ± 7.01	0.58
CA-4[a]	-	-	5.33 ± 2.11	5209 ± 956.0	0.001

Values represent ± SEM for at least three independent experiments performed in triplicate. [a] IC_{50} in MCF-7 cells / IC_{50} in HT-29 cells [a] The IC_{50} values for CA-4 are in line with literature values. [291, 357, 359, 378, 400, 416, 415]

6.10.1.8 *Anti-proliferative activity of 3-substituted enantiomers containing with B ring 3-hydroxy-4-methoxy substitutions in MCF-7 cells*

The antiproliferative activities of the B ring *meta* hydroxyl substituted analogues were evaluated. 3*S*,4*R* **24EN1** had an IC_{50} of 0.033 nM assigned as the eutomer while 3*R*,4*S* **24EN2** had an IC_{50} of 2.58 nM in MCF-7 cells. (Table 6.8) Both eutomer and distomer were extremely active in MCF-7 cells. As predicted by *S* values obtained in computational studies in Chapter 5 (Table 5.5), the 3-phenyl substituted distomer of 3-phenyl substituted racemate **24**, **24EN2**, had superior anti-proliferative activity in MCF-7 cells (IC_{50} of 2.579 nM) than any of the 3-hydroxyl distomers [4.88-51.78 nM, (Table 6.3 and Table 6.4)]. Additionally the distomer **24EN2** is more potent than 3*S*,4*S* eutomer **17EN1** [IC_{50} of 2.58 (Table 6.9) versus 4.69 nM (Table 6.2)]. The additional π-CH_2 interaction at the CBS between the 3-phenyl substitution of both **24EN1** and **24EN2** and the Lysβ254 residue as discussed in Chapter 5 (Figure 5.18), is highly advantageous for augmenting anti-proliferative activity. The 3-unsubstituted eutomer **27EN1** as the structural isomer of 3*S*,4*S* **17EN1** (Table 6.2) was also much less potent than 3*R*,4*S* distomer **24EN2** with an IC_{50} of 4.259 nM (Table 6.8), comparable to **17EN1** [IC_{50} of 4.69 nM in MCF-7 cells (Table 6.2)]. This is illustrated by cell viability curves for eutomer **24EN1** and distomer **24EN2** compared to structural isomers **17EN1** and **27EN1** in Figure 6.10.

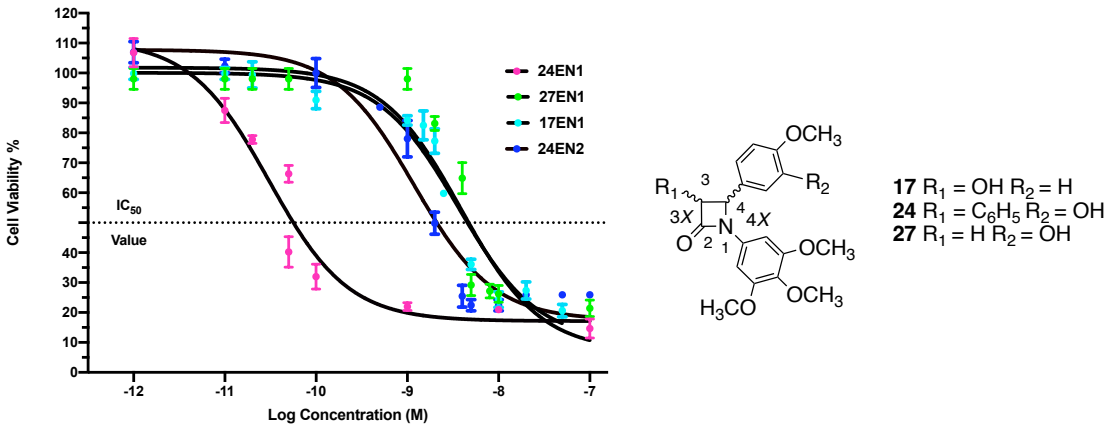

Figure 6.10: Cell viability curves for 3*S*,4*R* eutomer **24EN1**, 3*R*,4*S* distomer **24EN2** compared to eutomers **17EN1** and **27EN1** (structural isomers) in MCF-7 cells at 72 hours. IC_{50} represented by dashed line. Values represent ± SEM for at least three independent experiments performed in triplicate.

Table 6.8: IC_{50} values reported in nM for B ring *meta* hydroxyl 3-substituted β-lactam racemates and their resolved enantiomers (**24, 27, 30**)

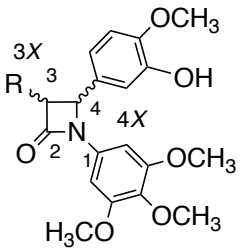

Code	R	$3X^1$	$4X^1$	MCF-7	MDA-MB-231	Hs578T(i)8	HL-60
24	C_6H_5	Racemate	Racemate	0.78 ± 0.35	2.51 ± 1.22	Nd	Nd
24EN1	C_6H_5	*S*	*R*	0.03 ± 0.01	0.68 ± 0.33	0.27 ± 0.06	0.16 ± 0.06
24EN2	C_6H_5	*R*	*S*	2.58 ± 1.50	4.49 ± 4.32	3.09 ±0. 85	Nd
27	H	NA	Nd	17.45 ± 5.37	17.82 ± 4.77	Nd	Nd
27EN1	H	NA	Nd	4.26 ± 0.19	4.37 ± 1.16	2.82 ± 0.56	Nd
27EN2	H	NA	Nd	23.8 ± 4.22	29.1 ± 2.17	17.7 ± 3.96	Nd
30	C_4H_3S	Racemate	Racemate	1.47 ± 0.41	4.81 ± 1.16	Nd	Nd
30EN1	C_4H_3S	*S*	*R*	0.04 ± 0.01	0.41 ± 0.18	0.048 ± 0.01	Nd
30EN2	C_4H_3S	*R*	*S*	12.2 ± 3.00	35.4 ± 7.83	7.88 ± 0.84	Nd
CA-4[a]				5.33 ± 2.11	11.3 ± 4.32	4.62 ± 1.38	1.38 ± 0.30

IC_{50} values are half maximal inhibitory concentrations required to inhibit cell growth. Values represent ± SEM for at least three independent experiments performed in triplicate.[a] The IC_{50} values for CA-4 are in line with literature values. [291, 357, 359, 378, 400] 3*X*, 4*X* refers to absolute configuration for enantiomeric derivatives. Na = not applicable, Nd = not determined

3-Thiophene substituted eutomer **30EN1** was extremely potent in MCF-7 cells with its IC_{50} determined as 0.04 nM (Table 6.8). However poor solubility was noted upon dissolution in desired vehicle ethanol (60% v/v). Further modification towards a more water soluble analogue would be required prior to progression of **30EN1** as a lead analogue, in keeping with findings published for the racemate as the phosphate prodrug.

33EN1, 39EN1 and **41EN1** also had excellent activity in MCF-7 cells [IC_{50} values of 0.42, 0.27 and 0.14 nM respectively (Table 6.9)]. All eutomers of the 3-substituted analogues were superior to CA-4 in MCF-7 cells.

6.10.1.9 *Anti-proliferative activity of 3-substituted enantiomers with B ring 3-hydroxy-4-methoxy substitutions in MDA-MB-231 cells*

Comparable IC_{50} values are observed for **27EN1** and **41EN1** in both MCF-7 [4.26 nM (Table 6.8) and 0.14 nM (Table 6.9)] to MDA-MB-231 cells [4.37 nM (Table 6.8) and 0.15 nM (Table 6.9)]. IC_{50} values for all other eutomers were marginally less potent in MDA-MB-231 compared to MCF-7 cells. All B ring *meta* hydroxyl substituted eutomers however were extremely potent in MDA-MB-231 cells with IC_{50} values in sub nanomolar range [0.679 nM, 0.412 nM , 0.298 nM and 0.947 nM for **24EN1, 30EN1, 33EN1** and **39EN1 (**Table 6.8 and Table 6.9)].

6.10.1.10 *Anti-proliferative activity of 3-substituted enantiomers containing with B ring 3-hydroxy-4-methoxy substitutions in Hs578T(i)8 cells*

27EN1 is the least active of all 3-substituted B ring *meta* containing hydroxyl eutomers across three breast cancer cell lines [$IC_{50} > 1$ nM, (Table 6.8)]. Nevertheless, its IC_{50} in Hs578T(i)8 cells is nearly two fold more potent than in MCF-7 and MDA-MB-231 cells. All other eutomers had IC_{50} values superior to their IC_{50} values in either MCF-7 or MDA-MB-231 cells in the more aggressively proliferating Hs578T(i)8 cell line [0.268 nM, 0.048 nM, 0.035 nM, 0.534 nM and 0.071 nM for **24EN1, 30EN1, (**Table 6.8), **33EN1, 39EN1** and **41EN1 (**Table 6.9) respectively] demonstrating at least comparable and potentially superior anti-proliferative potency in the aggressive Hs578T(i)8 TNBC cell line.

Table 6.9: IC_{50} values reported in nM for B ring *meta* hydroxyl β-lactam 3-substituted racemates and enantiomeric β-lactams **33, 39** and **41**

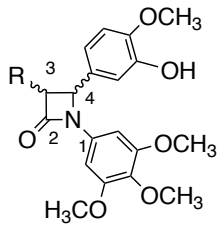

Code	R	3*X*[1]	4*X*[1]	MCF-7	MDA-MB-231	Hs578T(i)8	HL-60
33	C_2H_3	Racemate	Racemate	5.29 ± 3.0	7.91 ± 2.23	Nd	Nd
33EN1	C_2H_3	*S*	*R*	0.42 ± 0.16	0.30 ± 0.09	0.04 ± 0.02	0.09 ± 0.02
33EN2	C_2H_3	*R*	*S*	Nd	Nd	Nd	Nd
39	C_6H_4F	Racemate	Racemate	6.45 ± 1.67	18.8 ± 6.06	Nd	Nd
39EN1	C_6H_4F	*S*	*R*	0.27 ± 0.09	0.95 ± 0.36	0.54 ± 0.22	0.48 ± 0.19
39EN2	C_6H_4F	*R*	*S*	16.82 ± 3.25	40.96 ± 13.73	4.86 ± 2.11	Nd
41	C_7H_7O	Racemate	Racemate	1.04 ± 0.3	7.27 ± 4.13	Nd	Nd
41EN1	C_7H_7O	*S*	*R*	0.14 ± 0.09	0.15 ± 0.03	0.07 ± 0.02	0.05 ± 0.01
41EN2	C_7H_7O	*R*	*S*	3.52 ± 1.3	7.81 ± 3.0	3.41 ± 0.98	Nd
CA-4[a]				5.33 ± 2.11	11.3 ± 4.32	4.62 ± 1.38	1.38 ± 0.30

IC_{50} values are half maximal inhibitory concentrations required to inhibit cell growth. Values represent ± SEM for at least three independent experiments performed in triplicate.[a] The IC_{50} values for CA-4 are in line with literature values.[291, 357, 359, 378, 400, 416, 415] [1]3*X*, 4*X* refers to absolute configuration for enantiomeric derivatives. Na = not applicable, Nd = not determined

6.10.1.11 *Anti-proliferative activity of 3-substituted meta hydroxyl analogues in HL-60 human leukemia cell lines*

Four 3-substituted B ring *meta* hydroxyl substituted eutomers were screened in HL-60 cells. IC_{50} values were all in sub nanomolar range with values of 0.158 nM for **24EN1** (Table 6.8) and 0.092 nM, 0.481 nM and 0.045 nM for **33EN1, 39EN1** and **41EN1** (Table 6.9) respectively.

6.10.1.12 *SAR analysis of eutomers based on cell viability data across four cell lines*

Cell viability findings in tandem with computational data (Chapter 5) demonstrate that substitution at the 3-position with a phenyl moiety is advantageous for increasing CBS affinity, microtubule depolymerising activity and therefore anti-proliferative potency compared to the corresponding 3-hydroxyl relatives. For example, **24EN1** and **16EN1** both contain 3-hydroxyl-4-methoxy substituted B rings and differ only in their 3-substitution with a 3-phenyl or 3-hydroxyl moiety on the β-lactam ring respectively. Computational data demonstrates that an additional and stabilising π-aliphatic interaction between the 3-phenyl moiety of **24EN1** and the adjacent Lysβ254 of the CBS (Figure 5.18) is not present for **16EN1** (Figure 5.19). **24EN1** had increased CBS affinity, reflected by its lower *S* value (Table 5.5) and importantly its more potent IC_{50} values (Table 6.8) with respect to **16EN1 (**Table 6.7). The antiproliferative activity for **24EN1** is 24 times greater than **16EN1** in MCF-7 cells [0.03 nM (Table 6.8) versus 0.81 nM (Table 6.7)], > 2 times in MDA-MB-231 cells (0.679 versus 1.48 nM) and > 2.5 times Hs578T(i)8 cells [0.268 nM versus 0.697 nM, (Table 6.7 and Table 6.8)].

The 3-vinyl substituted enantiomer, **33EN1**, was also extremely potent in breast cancer cells lines [IC_{50} values of 0.034-0.415 nM (Table 6.9)] and in the HL-60 cell line [IC_{50} of 0.092 nM, (Table 6.9)]. This suggested that an alkene at position 3 of the β-lactam ring is also advantageous, potentially due to increased hydrophobic bonding at the CBS. Wang *et al* have reported that the vinyl moiety has potential to hydrogen bond with the Lysβ352 residue. [359] However the vinyl moiety returned a structural alert during Swiss ADME analysis using the BRENK filter (Chapter 4). **33EN1** was therefore not considered for further biochemical analysis.

Addition of the 4-fluoro- substituent on the 3-phenyl position decreased biological activity across all cell lines for **39EN1** while the 4-methoxy substituent of **41EN1** resulted in comparable activity to 3-phenyl substituted **24EN1** (Table 6.8 and Table 6.9). Modification of the *para* position on the phenyl substituent at position 3 of the β-lactam was sensitive to alterations in anti-proliferative activities for the β-lactam enantiomers, potentially due to interactions with polar residues at the β subunit of the CBS.

6.10.1.13 *Eudysmic ratios for 3-substituted B ring meta hydroxyl substituted enantiomers*

Eudysmic ratios for the 3-substituted enantiomers are presented in Table 6.10. The largest comparative difference in antiproliferative activity is observed for 3-thiophene enantiomers of **30** with eudysmic ratios of 277, 86 and 166 in MCF-7, MDA-MB-231 and Hs578T(i)8 cells. The eudysmic ratio for enantiomers of **24** is largest in MCF-7 cells (78) compared to MDA-MB-231 and Hs578T(i)8 cell lines (7 and 12 respectively). The eudysmic ratios for 3-unsubsituted **27** are much smaller and consistent (6,7 and 6) across three breast cancer cell lines. Eudysmic ratios are therefore larger for enantiomers with favourable 3-substitutions. Since 3-unsubstituted enantiomers of **27** have much poorer biological activity compared to the majority of the 3-substituted analogues (Table 6.8 and Table 6.9), this would suggest that a 3-substitution greatly enhances anti-proliferative activity for eutomers due to enhanced affinity at the CBS mediated by hydrophilic and hydrophobic ligand-receptor interactions of the 3-substitution of the β-lactam ring.

Table 6.10: Eudysmic ratios for enantiomers with a β-lactam 3-substitution and 3-hydroxy-4-methoxy substituted B ring[a]

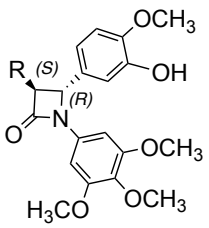

24EN1 R = C_6H_5
27EN1 R = H
30EN1 R = C_4H_3S
39EN1 R = (*p*-F)C_6H_4
41EN1 R = (*p*-CH_3O)C_6H_4

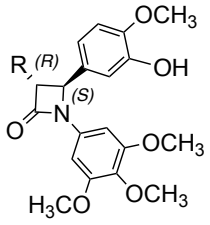

24EN2 R = C_6H_5
27EN2 R = H
30EN2 R = C_4H_3S
39EN2 R = (*p*-F)C_6H_4
41EN2 R = (*p*-CH_3O)C_6H_4

Code	MCF-7	MDA-MB-231	Hs578T(i)8	*ee* eutomer (En1)	*ee* distomer (En2)
24EN2 / 24EN1	78	7	12	99	58
27EN2 / 27EN1	6	7	6	61	45
30EN2 / 30EN1	277	86	166	100	56
39EN2 / 39EN1	62	43	9	Nd	Nd
41EN2 / 41EN1	25	54	47	89	23

[a] Eudysmic ratio calculated by the ratio of distomer IC_{50}: eutomer IC_{50}

6.10.1.14 *Biological activities of 3-substituted enantiomers in HT-29 chemoresistant colorectal cancer cell line*

Each of the B ring *meta* hydroxyl substituted eutomers were much less active in HT-29 cells compared to excellent anti-proliferative activity in low nanomolar range in MCF-7 cells. reflected by relative potency ratios listed in Table 6.11. **27EN2** had the poorest anti-proliferative activity of all 3-substituted enantiomers in CA-4 chemoresistant HT-29 cells with an IC_{50} of 4.9 μM comparable to the diminished anti-proliferative activity of 5.2 μM for CA-4. The corresponding eutomer **27EN1** while twice as potent as distomer **27EN2** had a poor IC_{50} of 2.36 μM (Table 6.11). While **27EN1** was much more active than both **27EN2** and CA-4 in HT-29 cells, both enantiomers have relative ratios of 0.002 and 0.005 respectively, demonstrating significantly poorer anti-proliferative activity in HT-29 cells versus MCF-7 breast cancer cells (Table 6.11). Eutomer **24EN1** [IC_{50} in of 28.4 nM in HT-29 cells, (Table 6.11)] was much more active than **27EN1** but

had much poorer potency than the corresponding IC_{50} in MCF-7 breast cancer cells [0.033 nM (Table 6.8)]. Antiproliferative activity was reduced by a factor of a thousand [relative potency of 0.001 (Table 6.11)]. Although **24EN1** was more potent than **27EN1** in HT-29 cells, relative potencies were comparable with values of 0.001 and 0.002 respectively **(**Table 6.11). Each enantiomer has a relative potency of <1, ranging from 0.0001 for **30EN1** to 0.189 for **39EN2,** indicating that the presence of B ring *meta* hydroxyl substitution is not optimal for anti-proliferative activity in HT-29 cells (Table 6.11).

Table 6.11: IC_{50} values reported in nM for 3-substituted enantiomers compared to CA-4 in MCF-7 and HT-29 colorectal cancer cells with respective relative potencies.

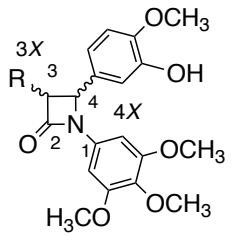

Code	R	MCF-7	HT-29	Eudysmic ratio in HT-29 cells	Relative potency[a]
24EN1	C_6H_5	0.03 ± 0.01	28.4 ± 4.28	-	0.001
24EN2	C_6H_5	2.58 ± 1.50	395.0 ± 90.7	14	0.007
27EN1	H	4.26 ± 0.19	2362.2 ± 872.7	-	0.002
27EN2	H	23.8 ± 4.2	4925.5 ± 1137.7	2	0.005
30EN1	C_4H_3S	0.04 ± 0.01	329.4 ± 87.7	-	0.0001
30EN2	C_4H_3S	12.2 ± 3.0	772.0 ± 501.3	2	0.015
39EN1	C_6H_4F	0.27 ± 0.09	7.62 ± 2.44	-	0.036
39EN2	C_6H_4F	16.82 ± 3.25	89.21 ± 6.36	12	0.189
41EN1	C_7H_7O	0.14 ± 0.09	5.10 ± 0.88	-	0.03
41EN2	C_7H_7O	3.52 ± 1.30	25.3 ± 5.79	5	0.14
CA-4[b]		5.33 ± 2.11	5209 ± 956.8	-	0.001

Values represent ± SEM for at least three independent experiments performed in triplicate. [a] IC_{50} in MCF-7 cells / IC_{50} in HT-29 cells [b] The IC_{50} values for CA-4 are in line with literature values. [291, 357, 359, 378, 400]

To demonstrate the relative biological activity of B ring *meta* substituted analogues and 3-substituted B ring *meta* hydroxyl analogues in breast versus HT-29 cancer cell lines, cell viability curves for **18EN1** and **24EN1** are presented (**A** and **B,** Figure 6.11). The IC_{50} of *meta* fluorine B ring substituted *3S,*4*S* eutomer **18EN1** in HT-29 cells is comparable in MCF-7 and Hs578T(i)8 cells [IC_{50} 0.53 nM versus 0.26 nM and 0.32 respectively (Table 6.7 and Table 6.3)] and more potent than in MBA-MB-231 cells (IC_{50} 0.70 nM,Table 6.3) (**A**, Figure 6.11)]. However 3*S,*4*R* eutomer **24EN1** is much less active in HT-29 cells than in breast cancer cells (**B,** Figure 6.11) with IC_{50} values of 0.033 nM, 0.679 nM and 0.269 nM in MCF-7, MDA-MB-231 and Hs578T(i)8 cells respectively (Table 6.8) compared to 28.4 nM in HT-29 cells (Table 6.11).While **24EN1** appears to maintain a certain degree of biological activity in HT-29 cells measured during anti-proliferative cell viability assays [IC_{50} of 28.4 nM, (Table 6.11)] this was not observed during immunofluorescence confocal microscopy where cells are seeded at higher seeding densities of 200,000 cells per well in a 12 well plate (Section 6.9) and treated for 16 hours compared to 10,000 cells per well in a 96 well plate and 72 hour treatment used in cell viability assays (Section 6.6). Tubulin depolymerisation activity was not observed for **24EN1** in HT-29 cells in confocal microscopy experiments. (Section 6.15).

Poor antiproliferative activity was observed for **30EN1** in HT-29 cells [IC_{50} of 329 nM (Table 6.11)] compared to its extremely potent IC_{50} values of 0.044 nM, 0.412 nM and 0.0474 nM in MCF-7, MDA-MB-231 and Hs578T(i)8 breast cancer cells respectively (Table 6.8). 4-Fluoro- and 4-methoxyphenyl eutomers **39EN1** and **41EN1** retained a degree of anti-proliferative activity in cell viability assays with IC_{50} values of 7.62 nM and 5.10 nM respectively (Table 6.11) despite the presence of the unfavourable B ring *meta* hydroxyl group.

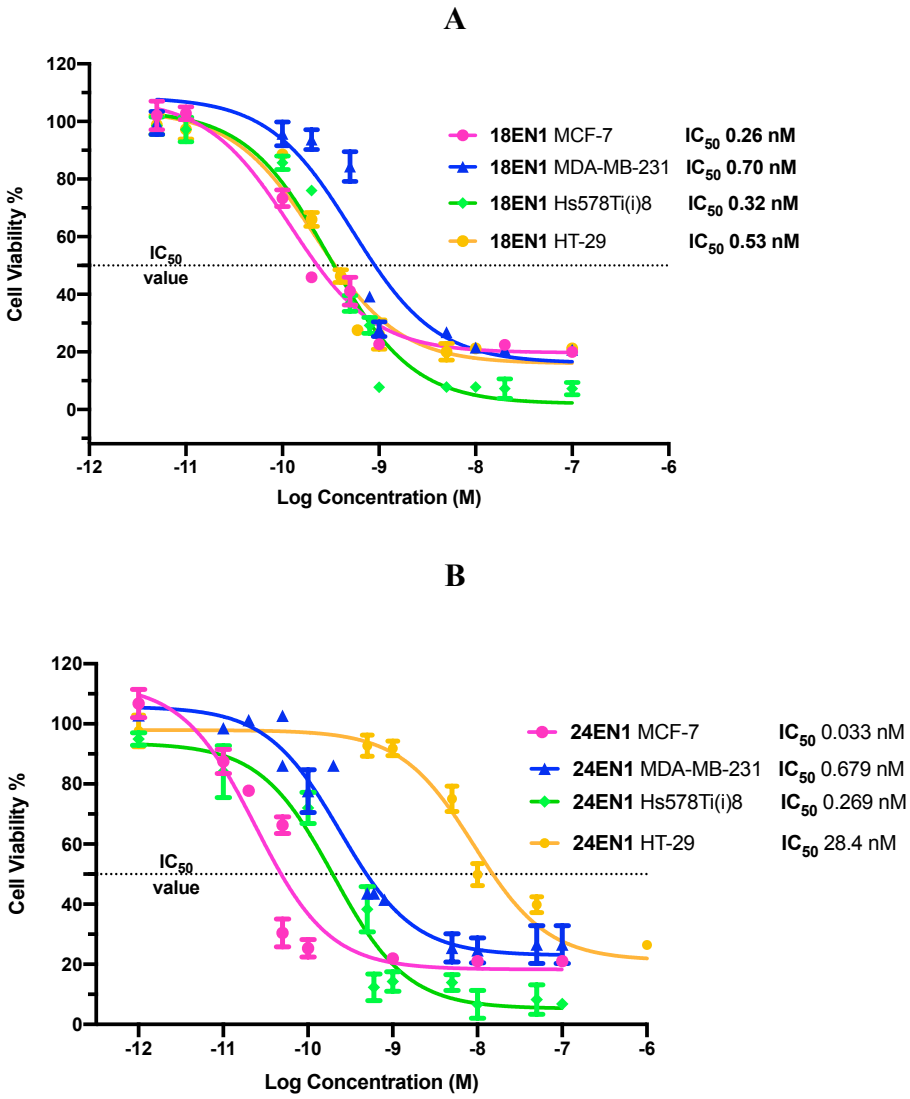

Figure 6.11: **A:** Cell viabilities of 3*S*,4*S* eutomer **18EN1** in three breast cancer versus HT-29 cell lines at 72h. **B:** Cell viabilities of 3*S*,4*R* eutomer **24EN1** in three breast cancer versus HT-29 cell lines at 72h. The dotted line represents the IC_{50} value. Values represent ± SEM for at least three independent experiments performed in triplicate.

6.10.1.15 *Lead analogue selection for further biochemical analysis based on anti-proliferative findings*

17EN1 and **17EN2** were selected as lead analogues for comparative biochemical studies as the first enantiomer pair isolated. **18EN1** was chosen as the most potent 3*S*,4*S* eutomer from the 3-hydroxyl enantiopure panel for further development as dual anti-cancer agents in breast and CA-4 resistant colorectal cancers. **24EN1** has been extensively studied as the racemate[328] and was selected as the lead 3*S*,4*R* eutomer for development as a CBSI

for TNBC due to its extremely potent anti-proliferative activity and absence of structural alerts using the Swiss ADME webtool (Chapter 4).

6.10.1.16 *Anti-proliferative screening of 3-phenolic β-lactam racemates*

Racemate **26** is the most potent β-lactam racemate synthesised to date by O'Boyle *et al*.[495] Phenolic racemates were not resolved using the LC chiral resolution procedure described in Chapter 4. Nevertheless the racemic forms were screened *in vitro* for antiproliferative activity alongside novel phenolic analogues, **68** and **69** (Table 6.12). **26** was most potent [IC_{50} of 0.44 nM and 0.73 nM in MCF-7 and MDA-MB-231 cells respectively, (Table 6.12)]. Both **68** and **69** were less potent [IC_{50} values of 6.3 nM and 6.84 nM in MCF-7 cells (Table 6.12)] compared to parent **26**. Since enantiomers were not isolated, **26, 68** and **69** did not progress for screening in HT-29 cells. Future work should focus on method development for resolution of **26**'s eutomer as the most potent β-lactam racemate evaluated in this thesis. Eutomers of **68** and **69** where isolated in future studies are potential candidates for further development for activity in HT-29 cells due to deletion and replacement of **26**'s B ring *meta* hydroxyl substitution for **68** and **69** respectively.

Table 6.12: IC_{50} values reported in nM for 3-phenolic racemates in MCF-7 and MDA-MB-231 cell lines at 72h.

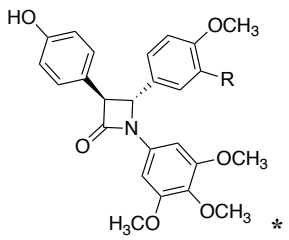

Code	R	MCF-7	MDA-MB-231
26	OH	0.44 ± 0.23	0.73 ± 0.30
68	F	6.3 ± 1.9	47.2 ± 14.3
69	H	6.84 ± 1.8	14.32± 1.11
CA-4 [a]	-	5.33 ± 2.11	11.33± 4.32

Values represent mean ± SEM of at least three independent experiments performed in triplicate.[a] The IC_{50} values for CA-4 are in line with literature values. [291, 357, 359, 378, 400, 416, 415] * one enantiomer shown

6.10.1.17 *Anti-proliferative activity of cis and trans isomers of **28***

Previous work published by Carr *et al* evaluated **28** as an isomeric mixture in 67% *cis* yield. IC_{50} values were reported as 10 nM and 47 nM in MCF-7 and MDA-MB-231 cells respectively.[384] In this thesis, **28** has been isolated as both *cis* (85% *cis* isomer purity) and *trans* isomers (71% *trans* isomer purity). IC_{50} values of 4.31 and 20.1 nM for *trans* **28** were observed in MCF-7 and MDA-MB-231 cells. The *cis* isomer was much less active with an IC_{50} value of 31.1 nM in MCF-7 cells (Table 6.13). *Trans* **28** is the structural isomer of 3-hydroxyl racemate **20**. IC_{50} values were comparable to **20** in MCF-7 cells [5.21 nM (Table 6.4)]. **20** was more potent in MDA-MB-231 cells than *trans* **28** [IC_{50} of 6.96 nM (Table 6.4) versus 20.1 nM (Table 6.13)]. Enantiomers of *trans* **28** were not isolated due to poor yields which limited progression towards chiral resolution. Additionally, its isomeric purity was poor, contaminated with 29% residual *cis* isomer. For these reasons further progression of *trans* **28** was not considered.

Table 6.13: IC_{50} values reported in nM for **28** *cis* and *trans* isomers in MCF-7 and MDA-MB-231 cell lines.

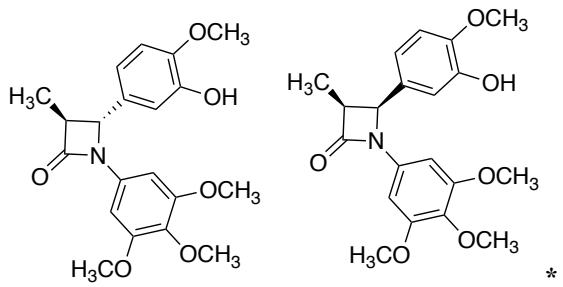

*

Code	MCF-7	MDA-MB-231
Trans **28**	4.31 ± 0.39	20.1 ± 7.61
*Cis **28***	31.1 ± 1.76	Nd
CA-4 [a]	5.33 ± 2.109	11.3 ± 4.32

Values represent mean ± SEM for at least three independent experiments with three unique cell passage numbers performed in triplicate.[a] The IC_{50} values for CA-4 are in line with literature values.[291, 357, 359, 378, 400, 416, 415] * one enantiomer shown for each of the *cis* and *trans* isomers. *Trans* **28** = 71:29 *trans:cis*. *Cis* **28** = 85:15 *cis:trans*.

6.10.1.18 *Anti-proliferative activity of isolated trans isomers **63a, 63** and **23***

Racemates **63** and **23** are previously reported in the *cis* configuration.[704] In this thesis they were evaluated *in vitro* for their anti-proliferative activity in MCF-7 cells in the

trans configuration (Table 6.14). The 3-acetoxy intermediate **63a** demonstrated good activity in MCF-7 cells with an IC_{50} of 28.3 nM. (Table 6.14) 3-Hydroxyl racemate **63** had an IC_{50} of 19.5 nM, superior to 97 nM observed by Sun *et al* for its corresponding *cis* isomer.[704] A 5-fold improvement in antiproliferative activity was therefore observed *via* trans isolation. Reduction of the nitro of racemate **63** to the corresponding amine (**23**) resulted in excellent activity in MCF-7 cells with an IC_{50} of 8.61 nM (Table 6.14) which is 10 fold greater than 81 nM reported by Sun *et al* for the *cis meta* amino substituted isomer.[704] However poor yields for both **63** and **23** limited progression towards enantiomers of either **63** or **23.**

Table 6.14: IC_{50} values reported in nM ± SEM for **63a, 63** and **23** in MCF-7 cells at 72h

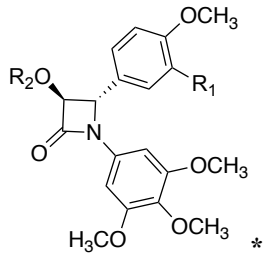

*

Code	R_1	R_2	MCF-7
63a	NO_2	$COCH_3$	28.3 ± 1.53
63	NO_2	H	19.5 ± 6.56
23	NH_2	H	8.61 ± 3.73
CA-4 [a]			5.33 ± 2.11

Values represent mean ± SEM for at least three independent experiments performed in triplicate.[a] The IC_{50} values for CA-4 are in line with literature values.[291, 357, 359, 378, 400, 416, 415] * one enantiomer shown

6.10.1.19 *Anti-proliferative activity of B ring modified β-lactam racemates*

Racemates with replacement of the B ring 4-methoxy by a nitro or a fluorine at the *para* position of the B ring resulted in a substantial loss in biological activity (Table 6.15). IC_{50} values in MCF-7 cells were 12.66 μM, 11.03 μM and 0.96 μM for *trans* isomers of racemates **89, 90** and **91.** Despite poor bioactivity, these values offer invaluable SAR information on the optimal substitution at the β-lactam ring 3-position. Replacing the 3-hydroxyl of **16** with the 3-phenyl of **91** resulted in an 11-fold increase in potency [IC_{50}

of 11.03 μM versus 0.96 μM (Table 6.15)]. This supports computational findings determining that the 3-phenyl substitution of the β-lactam ring will improve anti-proliferative activity of the combretazets due to the π-CH_2 stacking between the 3-phenyl aromatic ring and Lysβ254 at the CBS.

Table 6.15: Antiproliferative activity for modified B ring racemates in MCF-7 cells.

Compound Structure	Code	% Viability in at 1 μM	% Viability in at 5 μM	% Viability at 10 μM	IC_{50} (μM) ± SEM
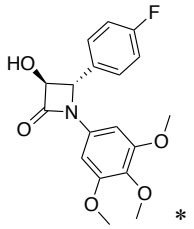	**89**	101.8 ± 5.8	58.4 ± 10.4	47.8 ± 15.5	12.7 ± 2.54
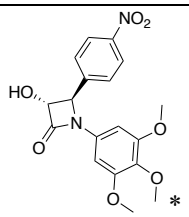	**90**	95.3 ± 8.4	81.3 ± 11.1	53.3 ± 19.0	11.0 ± 2.6
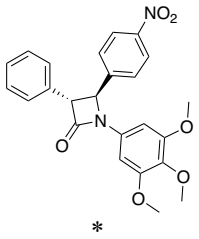	**91**	42.7 ± 6.03	34.4 ± 2.9	20.3 ± 3.8	0.96 ± 0.29

Values represent mean ± SEM for at least three independent experiments performed in triplicate. *one enantiomer shown.

6.11 *Monitoring of cell growth in MDA-MB-231 cells treated with 3S,4S eutomer **17EN1***

The growth of MDA-MB-231 cells treated with **17EN1** was monitored using Incucyte® taking photographs every 2 hours post treatment until 72 hours (Figure 6.12). Two concentrations of **17EN1** in approximate range of the IC_{50} value were chosen (10 nM and 15 nM, Figure 6.12). At time zero cells were sparsely populated. The appearance of vehicle control treated cells was similar to cells treated with **17EN1**. A reduction in cellular proliferation was observed at 24 hours between cells treated

with **17EN1 (**15 nM). At 48 hours a reduction in proliferation between cells treated with a lower concentration of **17EN1 (**10 nM) compared to vehicle treated cells was observed. No further growth occurred between 24-48 hours for cells treated with 15 nM of **17EN1.** At 72 hours vehicle control treated cells were confluent in contrast to cells treated with 10 nM of **17EN1** which had not yet reached confluency. Cells treated with 15 nM appeared shrivelled and apoptotic like while those treated with 10 nM retained the spindle like morphology of MDA-MB-342 cells despite the reduced confluency relative to vehicle control observed at 72 h (Figure 6.12). **17EN1** may reduce the migration potential of MDA-MB-231 cells below concentrations which cause cells to die and become apoptotic.

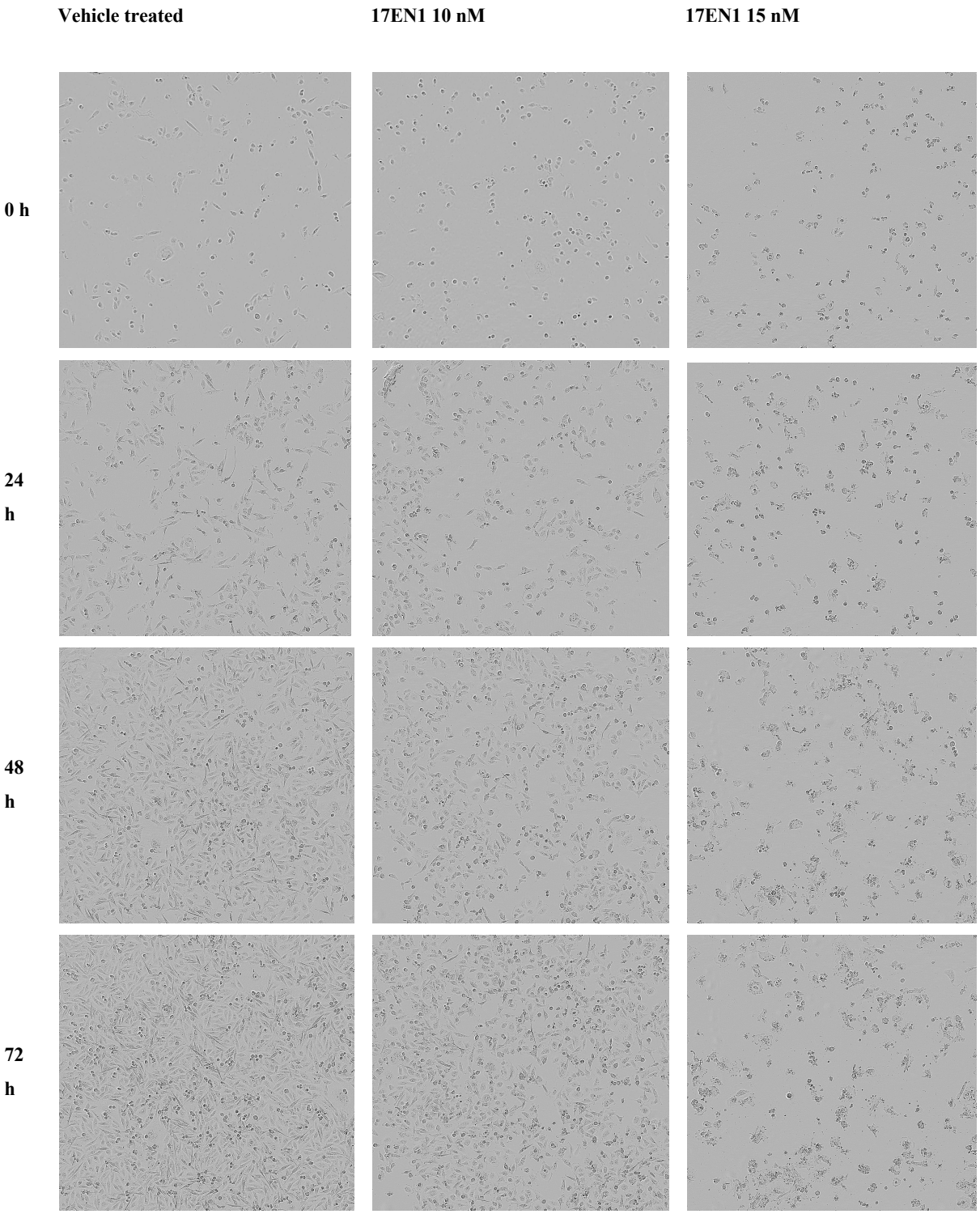

Figure 6.12: Cell growth in MDA-MB-231 cells at 0, 24, 48 and 72 hours when treated with 0.6 % v/v ethanol as vehicle, 10 nM or 15 nM of **17EN1.** Images are representative of three independent experiments performed in triplicate.

6.12 *Tubulin polymerisation assays*

Comparative tubulin polymerisation studies were carried out for eutomer **17EN1** versus distomer **17EN2** to investigate the potential microtubule depolymerising effects of the distomer. 3-Phenyl eutomer **24EN1** and distomer **24EN2** were also investigated in addition to calculation of the IC_{50} of tubulin depolymerisation for **24EN1.** Comparative tubulin polymerisation analysis was carried out for B ring *meta* substituted analogues targeting HT-29 cells with subsequent comparative analysis of **18EN1** with its distomer **18EN2**. A dose response was also carried out for **18EN1** to calculate its microtubule depolymerising IC_{50} value. CA-4 and paclitaxel (10 μM) were used as positive controls and DMSO as the vehicle control. The effect on tubulin assembly was monitored in a Spectramax 340PC spectrophotometer at 340 nm at 30 s intervals for 62 minutes at 37 °C.

6.12.1.1 *Comparative tubulin polymerisation efficacy of eutomer **17EN1** versus distomer **17EN2***

The effects of **17EN1** compared to **17EN2** were evaluated alongside representative microtubule depolymeriser CA-4.[705-707] CA-4 has previously been reported as inhibiting tubulin polymerisation by 35% at 1 μM while 10 μM abolished activity.[708] The final optical density (OD) value was recorded as an indicator of final polymer mass and % reduction of the final OD value with respect to vehicle value recorded. The fold reduction for area under curve (AUC) for each tubulin polymerisation graph is also detailed in Table 6.16. The V_{max} value offers the most sensitive indicator of tubulin/ ligand interactions and is calculated most accurately using the value obtained from microplate reader.[709] *V*max the maximum velocity of tubulin polymerisation in mOD/minute. Fold changes in V_{max} for each compound were calculated with respect to vehicle control and compared to one another (Table 6.16).

CA-4 (10 μM) reduced V_{max} of tubulin polymerisation by a factor of 2, AUC by a factor of 3 and caused a reduction in % of final OD by almost 50%. At the same concentration (10 μM), **17EN1** was superior to CA-4 (10 μM) for all three parameters, reducing V_{max} greater than 5 fold, AUC by 17 fold and final OD by 88%. **17EN1 (**5 μM) had equivalent microtubule depolymerising activity to CA-4 (10μM). These findings infer that **17EN1**

at 10 μM and as low as 5 μM, is superior to CA-4 (10 μM) as a microtubule depolymeriser (Table 6.16 and **A,** Figure 6.13).

17EN2 was not observed to have microtubule depolymerising activity. This confirms computational findings (Chapter 5) which predicted that the 3*R*,4*R* absolute configuration is unfavourable for optimal CBS activity. While the tubulin polymerisation assay suggested that **17EN2** is not a tubulin inhibitor, it may also act as a microtubule polymeriser which is observed on **B,** Figure 6.13 by greater polymerisation with respect to vehicle control. Immunofluorescence microscopy was therefore required to further investigate the effects of **17EN2** on the cytoskeletal network in cultured cells and is discussed in Section 6.15.

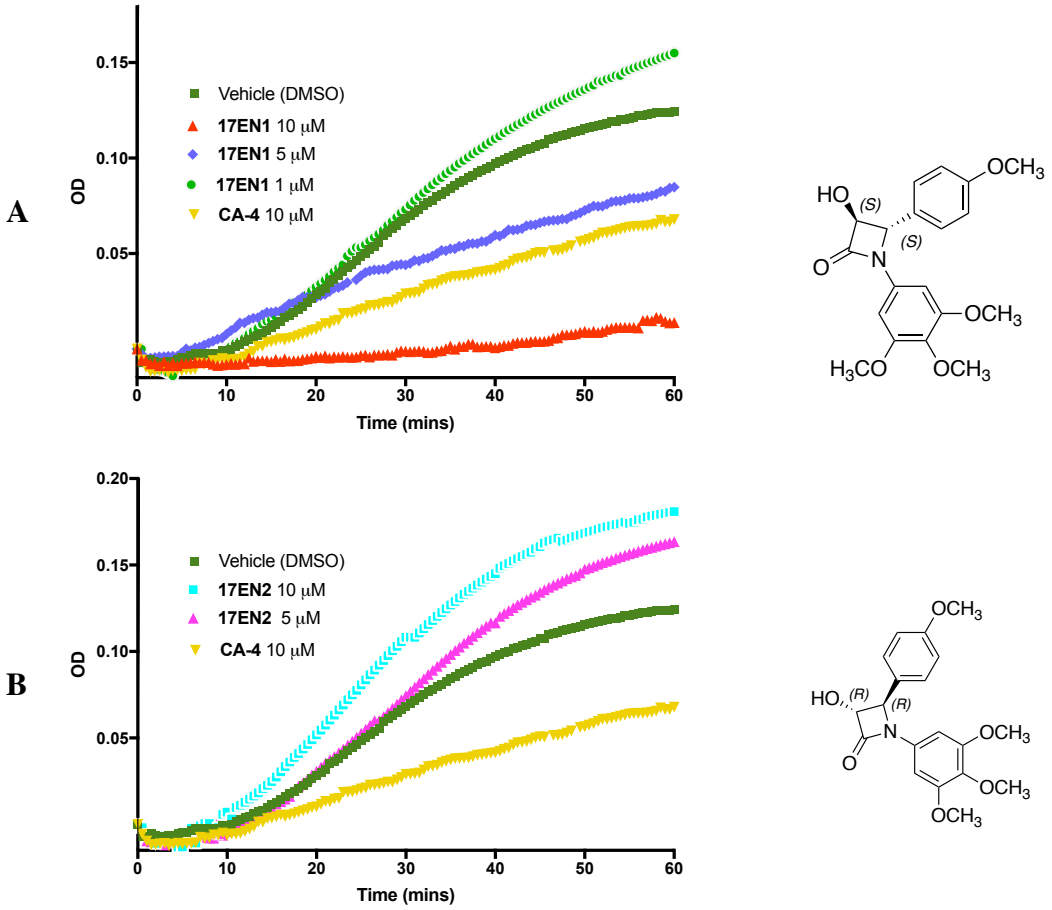

Figure 6.13: Dose response curves for **A**: **17EN1** and **B: 17EN2** for the *in vitro* tubulin polymerisation assay. Graph selected as a representative example of two independent replicates performed in duplicate.

Table 6.16: Effects of **17EN1, 17EN2** and CA-4 on *in vitro* tubulin polymerisation standardised to vehicle control. Results represent the values from two independent experiments performed in duplicate.

Code	Average AUC	Fold reduction in AUC	Average V_{max}	Fold reduction in V_{max}	Average final OD value	% change in OD value [1]
Vehicle (DMSO)	268.33	**-**	2.98	**-**	0.13	**-**
17EN1 10 μM	15.77	**17.0**	0.57	**5.25**	0.02	**87.50**
17EN1 5 μM	156.31	**1.72**	1.49	**2.00**	0.09	**31.60**
17EN1 1 μM	274.05	**0.98**	3.18	**0.94**	0.16	**-25.70**
17EN2 10 μM	356.30	**0.75**	3.76	**0.79**	0.18	**-45.50**
17EN2 5 μM	290.34	**0.92**	3.59	**0.83**	0.17	**-31.60**
CA-4 10 μM	84.98	**3.16**	1.53	**1.95**	0.07	**47.60**

[1] minus represents increase in final OD value relative to vehicle control

6.12.1.2 *Comparative tubulin polymerisation efficacy of **24EN1** versus **24EN2***

The effects of 3*S,*4*R* eutomer **24EN1** compared to its 3*R,*4*S* distomer **24EN2** were also evaluated. **24EN1** was determined as an extremely potent microtubule depolymeriser reducing the AUC by a factor of 64 at 10 μM. V_{max} and final OD for **24EN1** (10 μM) were reduced by a factor of 25 and 100% respectively which was superior to the 3 fold reduction in V_{max} and 70% reduction in final OD for CA-4 (10 μM). **24EN1 (**5 μM) was superior to CA-4 (10 μM) reducing the AUC, V_{max} and final OD by a factor of 16, 11 and 95% respectively. At concentrations as low as 1 μM, **24EN1** was comparable to CA-4 (10 μM), both reducing V_{max} by approximately a factor of 3 (**A,** Figure 6.14 and Table 6.17).

In contrast to the 3-hydroxyl 3*R,*4*R* distomer **17EN2,** which did not demonstrate microtubule inhibition (**B,** Figure 6.13), the 3*R,*4*S* distomer **24EN2** (10 μM) was found to have potent microtubule depolymerising activity, comparable to CA-4 (10 μM) (**B,** Figure 6.14). Both **24EN2 (**10 μM) and CA-4 (10 μM) caused reductions in AUC by a factor of 4, V_{max} by a factor of 3 and comparable % change in final OD [77% and 70% respectively (Table 6.17)]. Despite the unfavourable docking orientation for the *3R,*4*S* **24EN2** distomer at the CBS (Figure 5.17), microtubule depolymerising activity is retained for **24EN2** based on tubulin polyermisation assay findings. Both **24EN1** and **24EN2** are microtubule depolymerisers with eutomer **24EN1** having superior

microtubule destabilising activity due to the more favourable 3*S,4R* absolute configuration and enhanced ligand-receptor interactions (Figure 5.17).

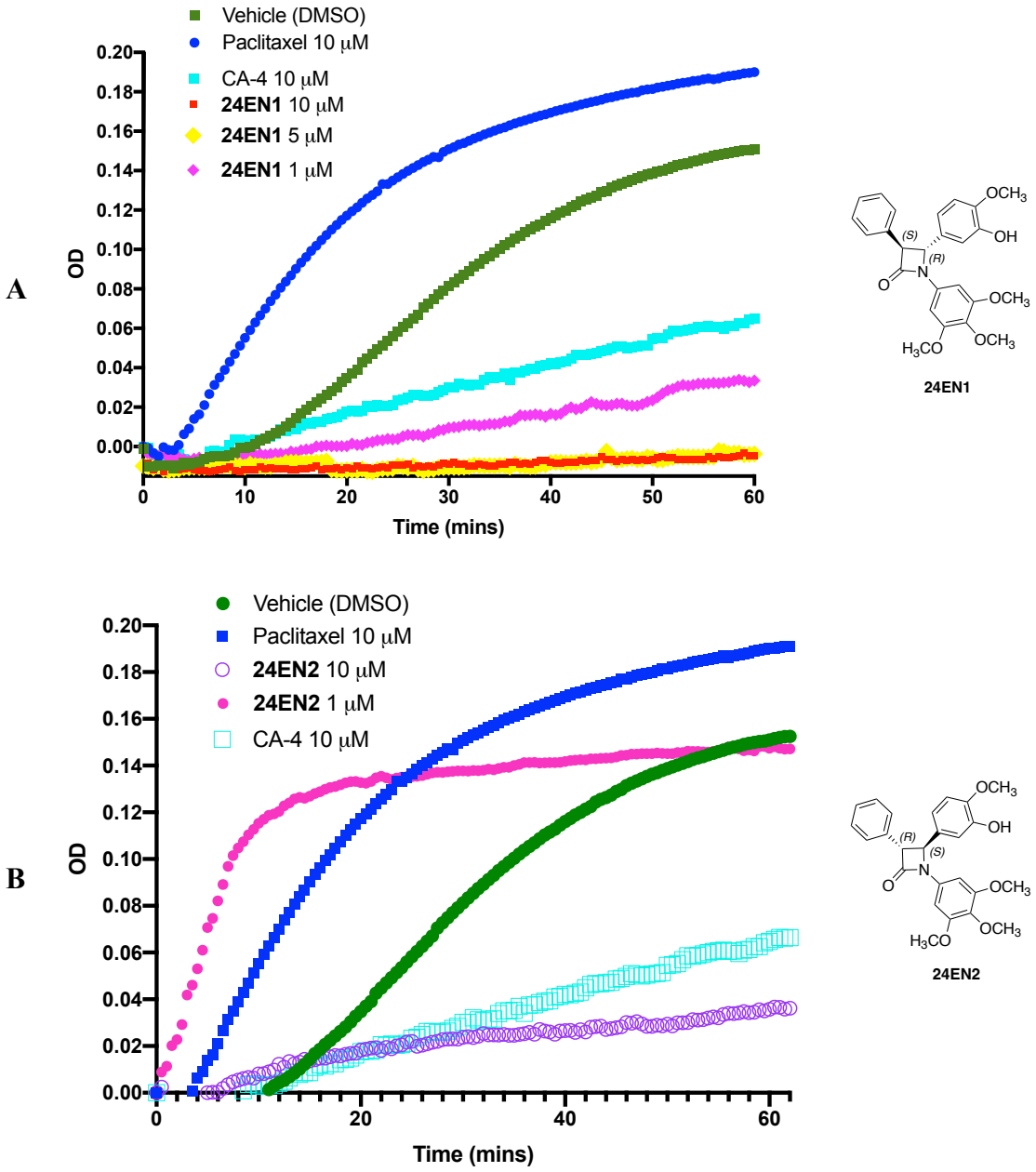

Figure 6.14: Dose response curves for **A: 24EN1** and **B**: **24EN2** for the *in vitro* tubulin polymerisation assay. Graph selected as a representative example of two independent replicates performed in duplicate.

Table 6.17: Effects of 3*S*,4*R* eutomer **24EN1,** 3*R* 4*S* distomer **24EN2** and CA-4 on *in vitro* tubulin polymerisation standardised to vehicle control. Results represent the values from two independent experiments performed in duplicate.

Code	Average AUC	Fold reduction in AUC	Average V_{max}	Fold reduction in V_{max}	Average final OD value	% change in OD value [1]
Vehicle (DMSO)	241.54	-	2.73	-	0.12	-
CA-4 10 µM	65.67	**3.68**	1.07	**2.57**	0.04	**69.90**
24EN1 10 µM	3.80	**63.58**	0.11	**25.31**	0.00	**100.81**
24EN1 5 µM	16.17	**14.94**	0.25	**11.08**	0.01	**95.35**
24EN1 1 µM	83.99	**2.88**	1.01	**2.70**	0.09	**24.80**
24EN2 10 µM	66.14	**3.65**	0.88	**3.12**	0.03	**76.58**
24EN2 1 uM	299.16	**0.81**	1.43	**1.91**	0.15	**-19.56**
Paclitaxel 10 µM	805.81	**0.30**	1.72	**1.59**	0.22	**-80.52**

[1] minus represents an increase in final OD value relative to vehicle control

6.12.1.3 *Determination of IC_{50} for tubulin depolymerisation efficacy for **24EN1***

A dose response curve was obtained for **24EN1** to calculate its IC_{50} for microtubule depolymerisation. 5 µM was selected as the highest concentration due to the 95% reduction observed for the OD during preliminary studies at this concentration (**A,** Figure 6.14 and Table 6.17) in addition to 1 µM, 0.5 µM, 0.1 µM, 0.01 µM and 0.005 µM. Two methods of reporting the IC_{50} were selected as follows:

1) % of the vehicle's V_{max}
2) % of final polymer mass (calculated by subtracting final OD from vehicle OD).

The data was analysed using log[**24EN1** (concentration in µM)] versus response (1 and 2 above) using a variable slope in GraphPad Prism. Table 6.18 outlines parameters and data output for **24EN1**'s dose response in the tubulin polymerisation assay. **A** and **B** (Figure 6.15) illustrate the dose response curves for **24EN1** performed on two independent occasions. Logarithmic dose response curves were constructed (**C-F**, Figure 6.15) and used to calculate IC_{50} values for microtubule depolymerisation, reported in Table 6.19. The IC_{50} value for **24EN1** reported as a % reduction of V_{max} is 0.630 µM ± 0.142. (Table 6.19) The second method for reporting the IC_{50} of **24EN1** as a % reduction of final polymer mass resulted in an IC_{50} of 0.736 µM ± 0.037 (Table

6.19). Both methods for reporting the IC_{50} of **24EN1**'s microtubule depolymerisation are in close agreement and demonstrate that **24EN1** is an extremely potent microtubule depolymerising agent.

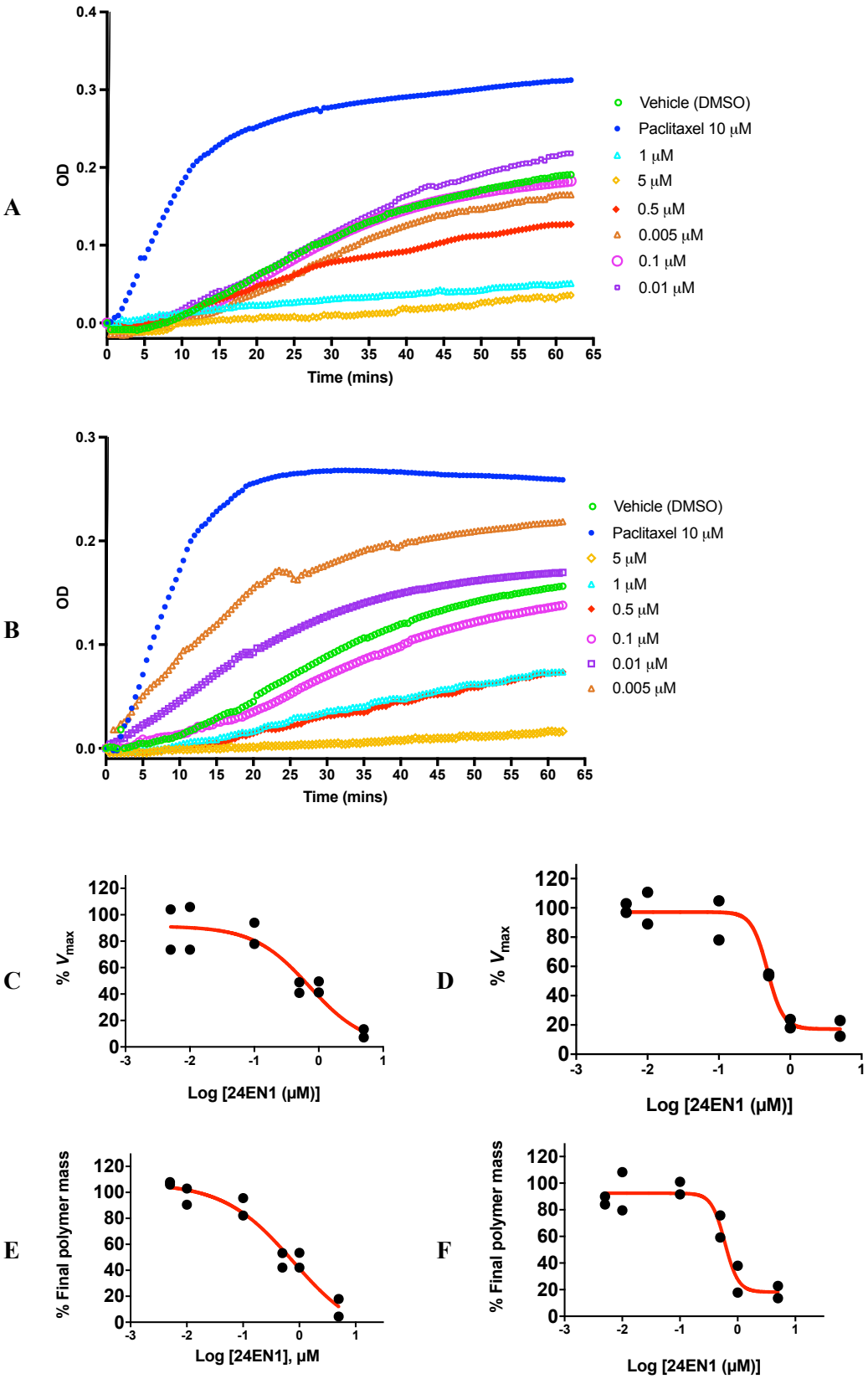

Figure 6.15: Dose response curves for **A**: **24EN1** replicate 1 and **B: 24EN1** replicate 2 for *in vitro* tubulin polymerisation assay. **C:** Calculation of IC_{50} as **%** of V_{max} for replicate 1 **D:** Calculation of IC_{50} as **%** of V_{max} for replicate 2 **D:** Calculation of IC_{50} as **%** of final polymer mass for replicate 1 **E:** Calculation of IC_{50} as % of final polymer mass for replicate 2.

Table 6.18: *In vitro* dose response tubulin polymerisation assay for **24EN1**. Values represent average values of two independent experiments performed in duplicate.

Code	Average AUC	Fold reduction in AUC	Average V_{max}	Fold reduction in V_{max}	Average final OD values	% change in OD value[1]
Vehicle (DMSO)	357.85	-	3.56	-	0.17	
Paclitaxel (10 μM)	837.79	**0.43**	3.04	**1.17**	0.29	**-64.73**
5 μM	21.85	**16.38**	0.50	**7.13**	0.03	**85.02**
1 μM	215.85	**1.66**	1.13	**3.14**	0.06	**64.03**
0.5 μM	121.93	**2.93**	1.72	**2.07**	0.10	**42.19**
0.1 μM	259.32	**1.38**	3.13	**1.14**	0.16	**7.63**
0.01 uM	407.38	**0.88**	3.59	**0.99**	0.19	**-11.81**
0.005 μM	580.68	**0.62**	3.01	**1.18**	0.19	**-10.62**

[1] minus indicates increase in final OD value relative to vehicle control

Table 6.19: IC_{50} values for eutomer **24EN1** calculated as % fold reduction in V_{max} and polymer mass

	IC_{50} value (μM) as calculated as % fold reduction in V_{max}	**IC_{50} value (μM) as calculated as % reduction in final polymer mass**
Replicate 1	0.771	0.773
Replicate 2	0.488	0.699
Average IC_{50}	**0.630 ± 0.143**	**0.735 ± 0.037**

6.12.1.4 *Comparative tubulin polymerisation assays for β-lactam eutomers with B ring meta substitutions*

The eutomers designed for optimal anti-proliferative activity in chemoresistant HT-29 colorectal cancer cells were next investigated at two concentrations: 5 μM **(A,** Figure 6.16) and 1 μM. **(B,** Figure 6.16) At 5 μM **20EN1** and **18EN1** had the greatest microtubule depolymerising effects of the panel analysed. For example, **20EN1 (**5 μM) reduced AUC by 33 fold, V_{max} by a factor of 6 and final OD by 86% (Table 6.20). **19EN1 (**5 μM) was marginally less potent than **20EN1** and **18EN1** with a reduction in AUC by 14 fold (18 and 33 for **18EN1** and **20EN1** respectively). A 6 fold reduction in V_{max} for **19EN1** was comparable to the 5 fold reduction for **18EN1** and **20EN1** each at 5 μM. *Meta* bromine substituted **21EN1** was slightly less potent, reducing the AUC by a factor of 7, V_{max} by a factor of 5 and % change in OD by 80%.

At the lower concentration of 1 μM, **18EN1** was the most potent microtubule depolymeriser of the panel across all three parameters, reducing AUC by 2, V_{max} by 2, and final OD by 7%. **20EN1** ranked a close second with values of 1.9, 2, and 4.38 for the aforementioned parameters. Minimal microtubule inhibition was observed for **19EN1** and **21EN1** at 1 μM. **18EN1** and **20EN1** were determined as the most potent microtubule depolymerisers of the the panel designed for optimal antiproliferative activity in HT-29 cells.

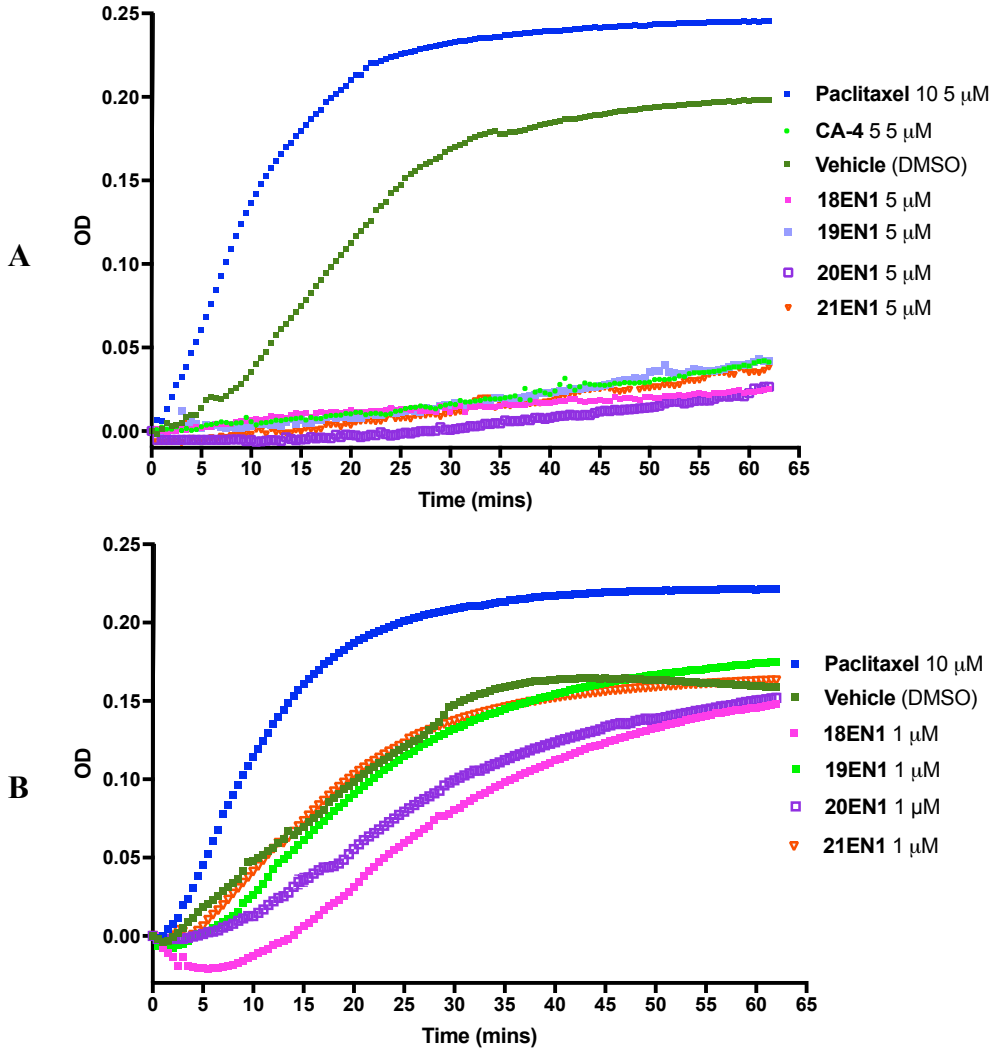

Figure 6.16: Tubulin polymerisation curves for B ring *meta* substituted 3*S*,4*S* eutomers **18EN1**, **19EN1, 20EN1** and **21EN1** with CA-4 (**A, only**) and paclitaxel as positive controls **A:** 5 μM **B:** 1 μM. Graphs selected as a representative example of two independent replicates performed in duplicate.

Table 6.20: Effects on *in vitro* tubulin polymerisation for B ring *meta* substituted 3*S*,4*S* eutomers compared to CA-4. Values represent average values of two independent experiments performed in duplicate.

Code	Average AUC	Fold reduction in AUC	Average V_{max}	Fold reduction in V_{max}	Average final OD value	% change in OD value [1]
Vehicle (DMSO)	469.53	**-**	4.03	**-**	0.19	**-**
Paclitaxel 10 μM	930.60	**0.50**	1.65	2.43	0.24	-26.87
18EN1 5 μM	26.46	**17.75**	0.41	9.82	0.03	87.02
19EN1 5 μM	33.09	**14.19**	0.71	5.66	0.03	86.27
20EN1 5 μM	14.30	**32.84**	0.73	5.45	0.04	78.26
21EN1 5 μM	64/.93	**7.23**	0.75	5.37	0.03	80.21
CA-4 5 μM	70.91	**6.62**	4.03	2.43	0.19	-26.87

[1] minus represents an increase in final OD value relative to vehicle control

Table 6.21: Effects on *in vitro* tubulin polymerisation for B ring *meta* substituted 3*S*,4*S* eutomers compared to CA-4. Values represent average values of two independent experiments performed in duplicate.

Code	Average AUC	Fold reduction in AUC	Average V_{max}	Fold reduction in V_{max}	Average final OD Values	% change in OD value [1]
Vehicle (DMSO)	502.44	**-**	5.82	**-**	0.16	**-**
Paclitaxel 10 µM	771.14	**0.65**	0.72	**8.06**	0.23	**-42.71**
18EN1 1 µM	282.66	**1.8**	2.95	**1.97**	0.15	**6.74**
19EN1 1 µM	424.59	**1.18**	3.14	**1.85**	0.17	**-5.82**
20EN1 1 µM	316.98	**1.9**	2.86	**2.03**	0.15	**4.38**
21EN1 1 µM	478.29	**1.05**	2.76	**2.11**	0.16	**-0.16**

[1] minus represents an increase in final OD value relative to vehicle control

Table 6.22 summarises the microtubule depolymerising activity reported as a fold reduction in V_{max} for B ring *meta* substituted 3*S,* 4*S* eutomers at 1 and 5 µM accompanied by their IC_{50} values in MCF-7, MDA-MB-231 and HT-29 cells. B ring *meta*-fluorine substituted 3*S,*4*S* **18EN1** had the most potent anti-proliferative activity, complimented by the most potent microtubule destabilising activity [6.74 and 94.35% reduction in final

polymer mass (OD value) at 1 and 5 μM (Table 6.22)]. **18EN1** was next selected for comparative tubulin polymerisation studies with its distomer **18EN2** as the most potent anti-proliferative B ring *meta* substituted enantiomer in both HT-29 and breast cancer cells.

Table 6.22: Comparison of anti-proliferative activity for *meta* substituted 3*S*,4*S* eutomers to their microtubule depolymerising activity reported as % reduction in final polymer mass at 1 and 5 μM.

Code	IC_{50} in MCF-7 cells (nM)	IC_{50} in MDA-MB-231 cells (nM)	IC_{50} in HT-29 cells (nM)	% change in final OD value (1 μM)	% change in final OD value (5 μM)
18EN1	0.26 ± 0.15	0.70 ± 0.05	0.51 ± 0.33	6.74	94.35
19EN1	1.11 ± 0.36	12.98 ± 6.65	1.41 ± 0.29	4.38	125.06
20EN1	0.66 ± 0.31	2.44 ± 0.99	0.77 ± 0.22	5.82	108.87
21EN1	2.08 ± 0.92	1.74 ± 0.90	1.44 ± 0.34	-0.16	82.89

6.12.1.5 *Comparative tubulin polymerisation assays for **18EN1** and **18EN2***

18EN1 was compared to distomer 3*R*,4*R* **18EN2** for evaluation of their relative microtubule depolymerising activity. In comparison to the corresponding *meta* unsubstituted 3*R*,4*R* distomer **17EN2**, which did not demonstrate microtubule depolymerisation (**B**, Figure 6.13 and Table 6.16), microtubule destabilising activity was observed for **18EN2** [10 and 5 μM (Table 6.23 and Figure 6.17)]. The distomer **18EN2** (5 μM) however had a much lower magnitude of tubulin inhibition than eutomer **18EN1**, reducing AUC only by a factor of 1.29, V_{max} by a factor of < 2 and final OD value by only 12%. At double this concentration **18EN2** (10 μM) remained less potent as a microtubule depolymeriser with respect to **18EN1** (5 μM), reducing the AUC only by 2, V_{max} by 2 and % change in final polymer mass of 32% [Values were 18, 22 and 94 respectively for **18EN1** [5 μM (Table 6.23). 3*R*,4*R* **18EN2** while observed as a microtubule depolymeriser was found as far less potent than the corresponding 3*S*,4*S* eutomer **18EN1** (**B,** Figure 6.17 and Table 6.23).

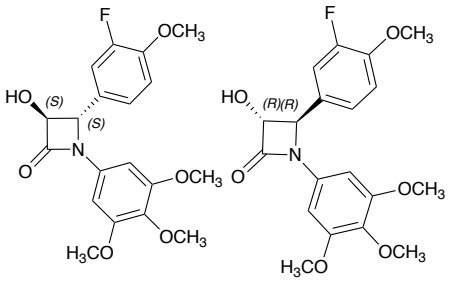

18EN1 18EN2

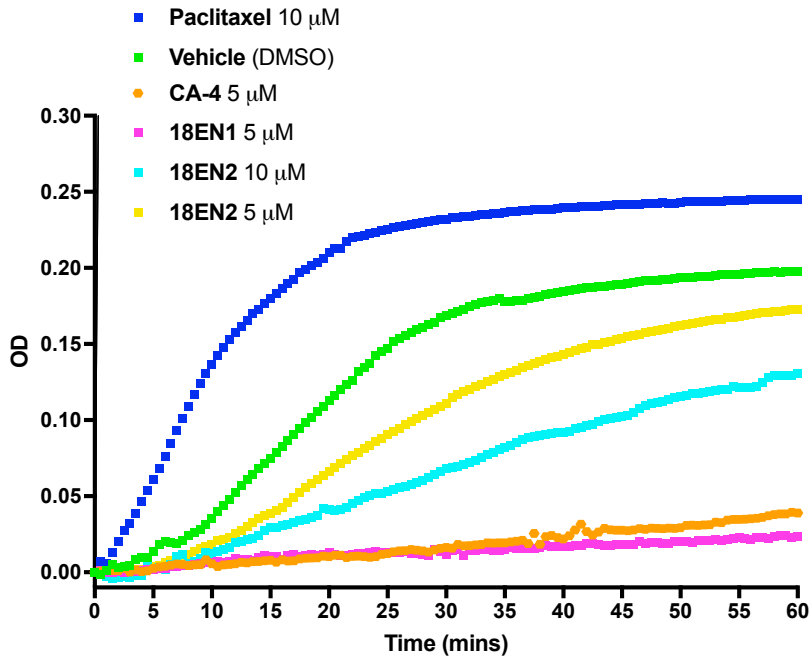

Figure 6.17: Tubulin polymerisation dose response curves for **18EN1** and **18EN2.** Graph selected is a representative example of two independent replicates performed in duplicate.

Table 6.23: Effects on *in vitro* tubulin polymerisation **18EN1** at 5 μM and **18EN2** at 5 and 10 μM. Values represent average values of two independent experiments performed in duplicate.

Compound Code	Average AUC	Fold reduction in AUC	Average V_{max}	Fold reduction in V_{max}	Average final OD Values	% change in OD value [1]
Vehicle (DMSO)	480.55	-	4.46	-	0.19	-
Paclitaxel 10 μM	877.53	**1.83**	1.02	**4.37**	0.26	**-32.06**
18EN1 5 μM	26.71	**17.81**	0.20	**21.96**	0.01	**93.83**
18EN2 10 μM	275.55	**1.75**	2.24	**2.00**	0.13	**32.20**
18EN2 5 μM	371.36	**1.29**	3.16	**1.41**	0.17	**12.12**
CA-4 5 μM	70.91	**6.62**	38.77	**12.11**	25.44	**80.51**

[1] minus represents an increase in final OD value relative to vehicle control

6.12.1.6 *Calculation of IC_{50} of tubulin polymerisation inhibition for 3S,4S **18EN1***

A dose response curve was calculated for **18EN1** (Figure 6.18). The concentrations chosen for each independent replicates were altered [10 μM to 0.5 μM in replicate 1 (**A,C & E,** Figure 6.18) and 5 μM to 0.01 μM in replicate 2 **(B, D & F,** Figure 6.18) in order to obtain an accurate $IC_{50.}$ Log[**18EN1,** μM] versus response as % of the vehicle *V*max and % of final polymer mass or OD value were used as methods for reporting the IC_{50} for tubulin inhibition of **18EN1**. Table 6.24 reports the data obtained for the dose response of enantiomer **18EN1.** The IC_{50} was calculated as 1.864 μM ± 0.54 and 1.626 μM ± 0.72 (Table 6.25) using % V_{max} (**C** and **D**, Figure 6.1) and % of final polymer mass (**E** and **F**, Figure 6.1) as two independent methods of reporting response. **18EN1** demonstrated extremely potent microtubule depolymerising activity with the additional advantage of anti-proliferative activity in HT-29 CA-4 resistant colorectal cancer cells (Table 6.7).

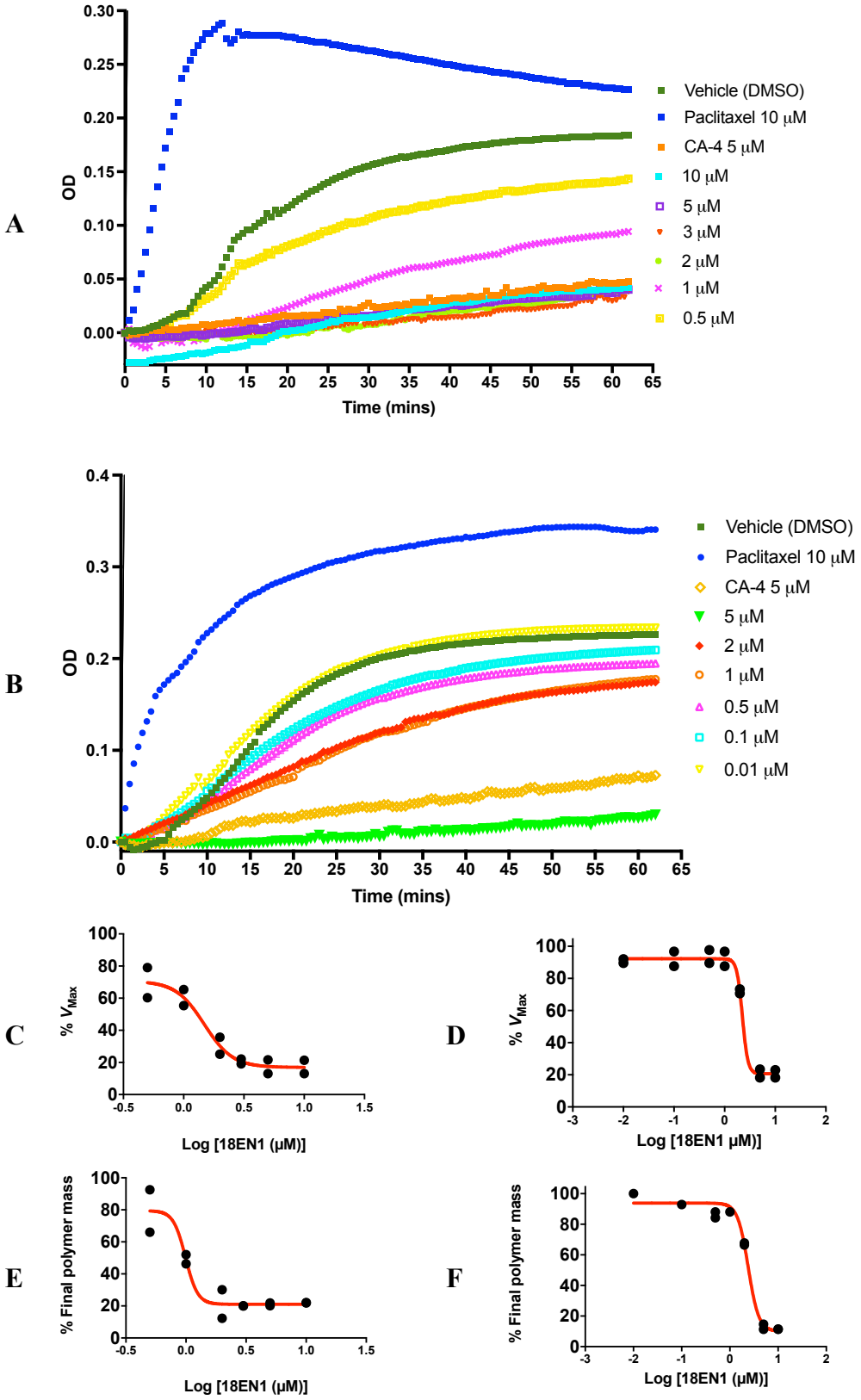

Figure 6.18: Dose response curves for **A: 18EN1** replicate 1 and **B: 18EN1** replicate 2 for the *in vitro* tubulin polymerisation assay. **C:** Calculation of IC_{50} as **%** of V_{max} for replicate 1 **D:** Calculation of IC_{50} as **%** of V_{max} for replicate 2 **E:** Calculation of IC_{50} as **%** of final polymer mass for replicate 1 **F:** Calculation of IC_{50} as **%** of final polymer mass for replicate 2

Table 6.24: Inhibition of *in vitro* tubulin polymerisation for 3*S*,4*S* **18EN1** as a dose response for IC_{50} calculations. Values represent average of two independent experiments performed in duplicate

	Average AUC	Fold reduction in AUC	Average V_{max}	Fold reduction in V_{max}	Average Final OD	% change in OD
Vehicle (DMSO)	602.83	-	3.80	-	0.21	-
Paclitaxel	923.59	**0.65**	0.40	**9.41**	0.27	**-26.91**
18EN1 10 μM	37.46	**16.09**	0.63	**6.00**	0.04	**80.18**
18EN1 5 μM	129.30	**4.66**	1.22	**3.11**	0.04	**82.48**
18EN1 3 μM	223.18	**2.70**	1.85	**2.06**	0.04	**81.99**
18EN1 2 μM	345.88	**1.74**	2.53	**1.50**	0.11	**49.68**
18EN1 1 μM	359.51	**1.68**	2.93	**1.30**	0.13	**37.35**
18EN1 0.5 μM	486.73	**1.24**	2.99	**1.27**	0.17	**19.93**
18EN1 0.1 μM	463.58	**1.30**	3.71	**1.02**	0.16	**25.13**
18EN1 0.01 μM	723.10	**0.83**	3.66	**1.04**	0.25	**-16.77**
CA-4 5 μM	147.10	**4.10**	1.17	**3.24**	0.07	**67.20**

Table 6.25: IC_{50} values for 3*S*, 4*S* **18EN1** calculated as % fold reduction in V_{max} and final polymer mass (OD value)

18EN1	**IC_{50} (μM) calculated as % fold reduction in V_{max}**	**IC_{50} (μM) calculated as % reduction in final polymer mass**
Replicate 1	1.482	1.113
Replicate 2	2.246	2.139
Average IC_{50}	**1.864 ± 0.54**	**1.626 ± 0.725**

6.13 *Cytotoxicity evaluation of enantiomers in non-tumorigenic MCF-10-2A breast cells*

Preliminary cytotoxicity analysis was carried out for the *trans* racemate **17** and its enantiomers and compared to CA-4 in non-tumorigenic MCF-10-2A breast epithelial cells using the AlamarBlue™ antiproliferative assay.[710,689] A further panel of lead eutomers (**16EN1, 18EN1, 19EN1, 20EN1, 21EN1, 24EN1** and **39EN1**) selected by the Swiss ADME webtool with excellent drug-like properties (Chapter 4) were also screened to determine their cytotoxic effects in non-tumorigenic MCF-10-2A cells.

6.13.1.1 *Cytotoxicity evaluation for enantiomers of **17** in MCF-10-2A cells*

Viability values for CA-4, *trans* **17** and **17EN1** at 10 nM were significantly greater in MCF-10-2A (**A, yellow**, Figure 6.19) than in MCF-7 cells (**A, pink**, Figure 6.19) ($p < 0.0001$, 0.0002 and 0.0001 respectively). When treated with **17EN1 (**10 nM) 96% of MCF-10-2A cells were viable in contrast to only 21% of MCF-7 breast cancer cells. At 100 nM, 52 % and 60% of MCF-10-2A cells were viable at 72 h following treatment with **17EN1** and **17EN2** respectively, in comparison to only 23% and 22% of MCF-7 cells. Both enantiomers therefore show some selective toxicity towards breast cancer cells in comparison to MCF-10-2A cells (Figure 6.19).

6.13.1.2 *IC_{50} of **17EN1** and **17EN2** in MCF-10-2A versus MCF-7 cells*

IC_{50} values were calculated for **17EN1, 17EN2** and CA-4 in the MCF-10-2A cells yielding a cytotoxic ratio *i.e* the difference in IC_{50} values between MCF-7 cancer and MCF-10-2A non-tumorigenic cells. The IC_{50} for **17EN1** is 0.7 μM in MCF-10-2A cells compared to 5 nM in MCF-7 cells. A cytotoxic ratio of 138 demonstrates **17EN1**'s semi-selective toxicity toward MCF-7 cancer cells versus non-tumorigenic MCF-10-2A cells (Table 6.26).

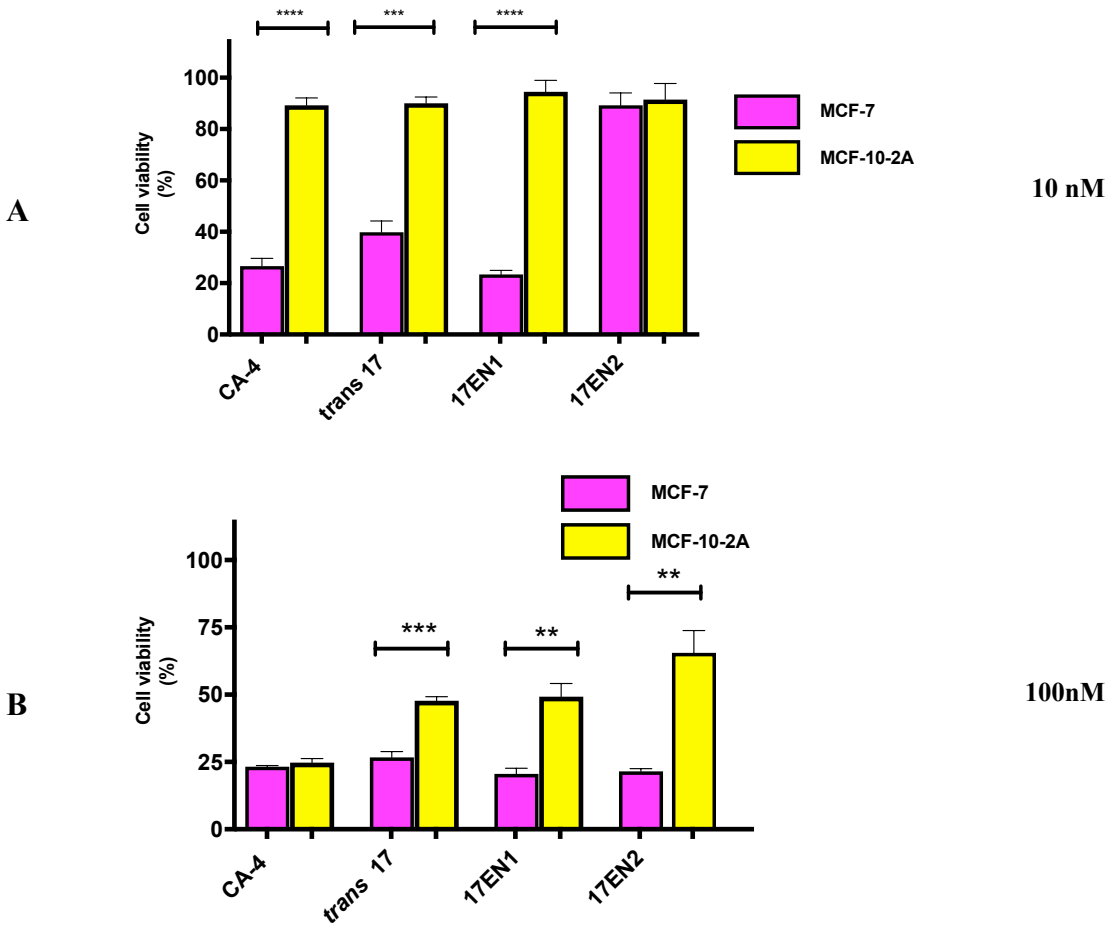

Figure 6.19: % cellular viability measured using AlamarBlue™ assay for CA-4, **17, 17EN1** and **17EN2** at 72 h in MCF-7 (pink) versus MCF-10-2A (yellow) cells at **A:** 10 nM and **B**: 100 nM. Values represent the average of at least three independent experiments performed in triplicate with error bars representing SEM. Statistical analysis performed using unpaired parametric t tests where ** = $p < 0.002$ *** $p = < 0.0002$ **** $p = <0.0001$

Table 6.26: IC_{50} values for enantiomers of racemate **17** and CA-4 in MCF-7 breast cancer cells versus non-tumorigenic endothelial breast MCF-10-2A cells at 72 h. Values represent the average of at least three independent experiments performed in triplicate ± SEM

Code	MCF-10-2A IC_{50} (μM)	MCF-7 IC_{50} (μM)	Cytotoxic ratio[1]
17EN1	0.69 ± 0.15	0.005 ± 0.002	138
17EN2	2.308 ± 1.8	0.032 ± 0.001	72
CA-4	0.058 ± 0.005	0.005 ± 0.002	12

[1]calculated by ratio of IC_{50} in MCF-10-2A : MCF-7 cells

6.13.1.3 *Cytotoxicity for lead eutomers in MCF-10-2A cells*

Eutomers **16EN1, 18EN1, 19EN1, 20EN1, 21EN1, 24EN1** and **39EN1** were subsequently evaluated in MCF-10-2A cells. 22% and 26% of MCF-7 cells remained viable following treatment with 3-phenyl substituted **24EN1** (1 nM) and 3-fluorophenyl **39EN1** (1 nM) respectively. A much larger proportion (75% and 48%) of MCF-10-2A cells were viable. MCF-7 cells treated with **16EN1** (1 nM) were 31% viable in contrast to a larger proportion of 51% for MCF-10-2A cells. MCF-10-2A viability values ranged from 74% - 102% following treatment with the remainder of eutomers at 1nM. 100% of MCF-10-2A cells were viable following treatment with **18EN1** (1 nM) compared to only 22% of MCF-7 cells. 100% of MCF-10-2A cells were also viable after treatment with **20EN1** (1 nM). Similarly **21EN1** (1 nM) and **19EN1 (**1 nM) were minimally cytotoxic towards MCF-10-2A cells with 97% and 95% remaining viable respectively compared to 51% and 35% for MCF-7 cells (**A,** Figure 6.20). Statistically significant differences were observed between viabilities of MCF-7 cancer cells versus MCF-10-2A cells treated with **18EN1, 19EN1, 20EN1** and **21EN1** at 1 nM [p values of <0.0001 (**A,** Figure 6.20)].

18EN1, 19EN1, 20EN1 and **21EN1** were determined as the most selective analogues at 10 nM. MCF-10-2A cells were significantly more viable with 83%, 92%, 94% and 91% cell viability compared to 21%, 25%, 16% and 20% for MCF-7 cells [**B,** Figure 6.20**,** (p values of < 0.0001, 0.0001, 0.0001 and 0.0002 respectively)]. **16EN1** (10 nM) was determined as cytotoxic towards MCF-10-2A cells with only 32% of cells remaining viable following treatment although significantly less toxic versus its effects in MCF-7 cells which were only 16% viable [p < 0.002, (**B,** Figure 6.20)]**.** At 100 nM **18EN1, 19EN1, 20EN1** and **21EN1** were significantly less cytotoxic towards MCF-10-2A cells with 79%, 83%, 80% and 60% viable cells compared to 23%, 25%, 14% and 22% for MCF-7 cells. [p < 0.002, < 0.03, <0.0002, <0.002 respectively, (**C,** Figure 6.20**)]** In contrast MCF-10-2A cells treated with CA-4 (100 nM) were only 24% viable. The B ring *meta* substituted eutomers, **18EN1, 19EN1, 20EN1** and **21EN1** were therefore determined with lower cytotoxicity toward MCF-10-2A cells compared to positive control CA-4.

This data supports the selection of **18EN1** as a lead B ring *meta* substituted eutomer due to its most potent anti-proliferative effects of the 3-hydroxyl eutomer panel (Table 6.3) in addition to minimal cytotoxicity in non-tumorigenic MCF-10-2A cells (Figure 6.20) for further biochemical studies and progression towards testing in pre-clinical *in vivo* models.

MCF-10-2A cells treated with **39EN1** (10 nM) were only 53% viable. Although **39EN1** demonstrated cytotoxicity towards MCF-10-2A cells at 10 nM, there was a significant difference between the % viability of MCF-7 versus MCF-10-2A cells. In contrast MCF-7 cells were only 23% viable ($p < 0.03$), when treated with **39EN1 [**10 nM, (B Figure 6.20)]. 3-phenyl derivative **24EN1 (**1 nM) was determined as slightly more cytotoxic than 3-fluorophenyl **39EN1** (1 nM) towards MCF-10-2A cells with 38% and 78% of viable MCF-10-2A cells respectively observed following 72h treatment. 38% of viable MCF-10-2A cells determined following treatment with **24EN1 (**1 nM) was comparable to 22% of viable MCF-7 cells. [$p > 0.05$, (**B,** Figure 6.20)].

Since the IC_{50} of 0.033 nM for **24EN1** in MCF-7 cells is much lower than the lowest concentration (1 nM) analysed in the cytotoxicity study illustrated in Figure 6.20, viability values in MCF-10-2A cells treated with **24EN1** were next evaluated at much lower concentrations in the range of **24EN1**'s IC_{50} in MCF-7 cells (Figure 6.21). Despite the apparent cytotoxicity of **24EN1** towards MCF-10-2A cells observed at 1 nM (**A,** Figure 6.20), cell viability was determined to be significantly greater in MCF-10-2A cells versus MCF-7 cells at concentrations ranging from 0.25-0.05 nM [($p < 0.0002$ – $p < 0.0001$)Figure 6.21]. Viability values in MCF-10-2A cells were determined as >50% at 0.5 nM ($p < 0.002$) and 82-87% when treated with **24EN1** from 0.05-0.25 nM, which is 2-8 times greater than **24EN1**'s IC_{50} in MCF-7 cells. The data presented in Figure 6.21 therefore demonstrates the semi-selective cytotoxicity of **24EN1** toward breast cancer cells versus non-tumorigenic epithelial breast cells.

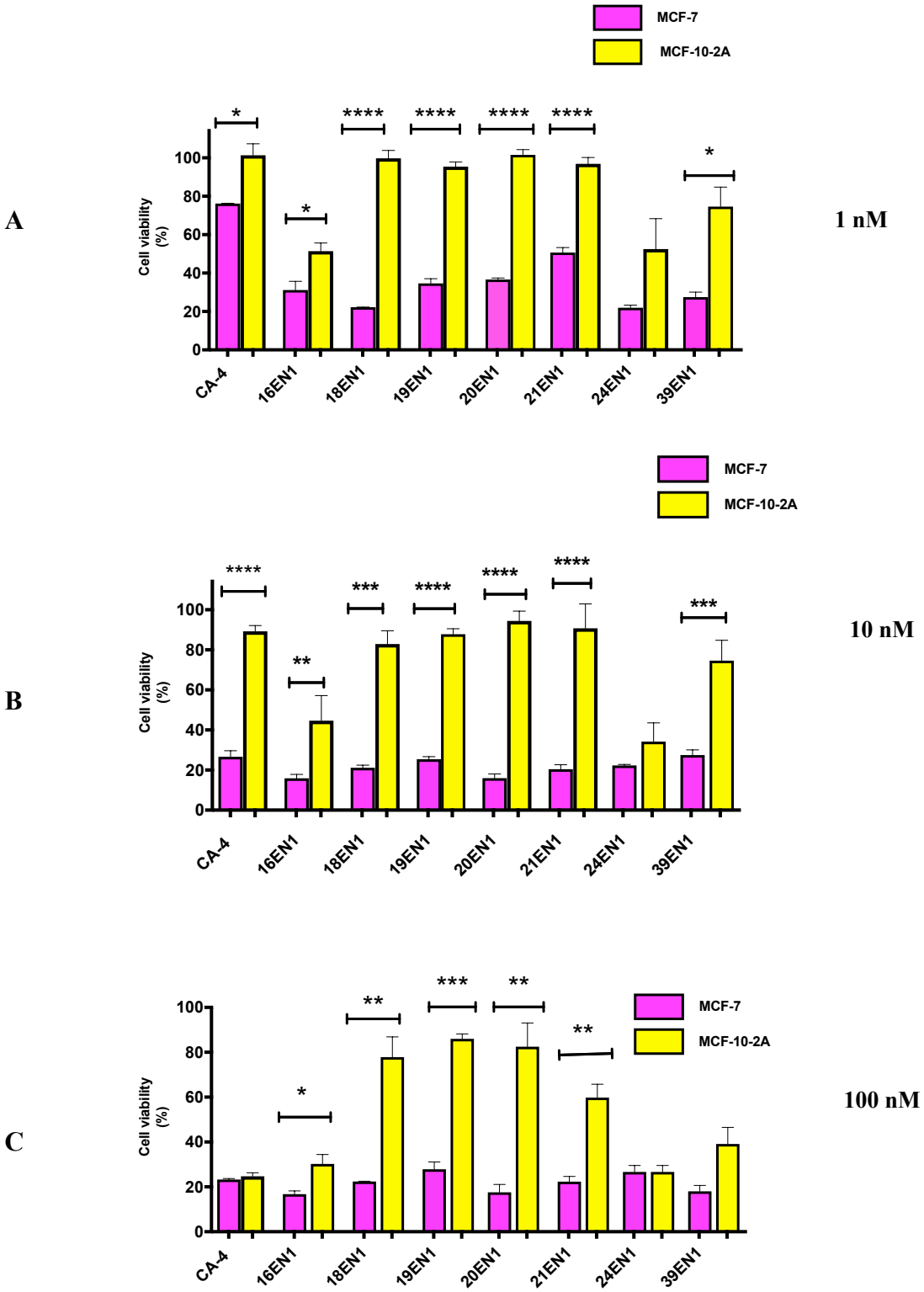

Figure 6.20: % viability for lead eutomers measured using AlamarBlue™ assay at 72h in MCF-7 (pink) versus MCF-10-2A (yellow) cells at **A:** 1 nM . **B:** 10 nM **C:** 100 nM Values represent averages of at least three independent experiments performed in triplicate with error bars representing SEM. Statistical analysis performed using unpaired parametric t tests where * = p < 0.03 ** = p < 0.002 *** p = < 0.0002 **** p = <0.0001

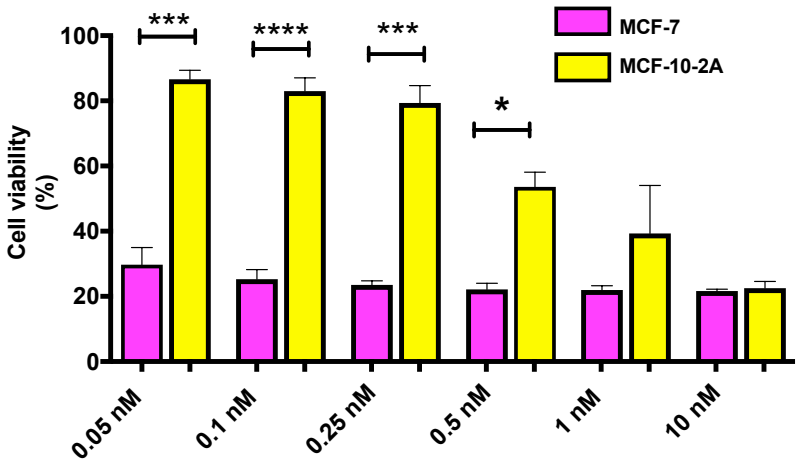

Figure 6.21: % cellular viability of **24EN1** in MCF-7 versus MCF-10-2A cells at 72 h using the AlamarBlue™ cell viability assay. Values represent averages of at least three independent experiments performed in triplicate with error bars representing SEM. Statistical analysis performed using unpaired parametric t tests where * = $p < 0.03$, *** $p = < 0.0002$ ****, $p = <0.0001$.

6.13.1.4 *IC_{50} calculation for eutomers in MCF-10-2A cells*

An IC_{50} value was calculated for selected eutomers in MCF-10-2A cells and compared to the corresponding values in MCF-7 cells **(**Table 6.27). **24EN1** in non-tumorigenic MCF-10-2A breast epithelial cells and MCF-7 cancer cells was found to have IC_{50} values of 0.7 nM and 0.03 nM respectively and a cytotoxic ratio of 23. Additionally, all cytotoxic ratios with the exception of **16EN1** were greater than CA-4 [2.5 for **16EN1** compared to 10 for CA-4, (Table 6.27)]. The majority of the eutomer panel were more selectively toxic toward breast cancer cells compared to CA-4 and are therefore promising agents for targeting cancer cells without undesirable effects on non-tumorigenic breast cells.

Table 6.27: IC_{50} values of selected β-lactam enantiomers in ER positive breast cancer cells (MCF-7) versus non-tumorigenic breast cells (MCF-10-2A)

Code	MCF-10-2A IC_{50} (nM))	MCF-7 IC_{50} (nM))	Cytotoxic Ratio[1]
18EN1	1320 ± 50	0.3 ± 0.03	4400
16EN1	2.0 ± 0.8	0.8 ± 0. 20	2.5
24EN1	0.7 ± 0.2	0.03 ± 0.01	23
39EN1	23 ± 0.6	0.3 ± 0.09	77
CA-4	49 ± 5	5 ± 2	10

[1]calculated *via* ratio of IC_{50} in MCF-10-2A : MCF-7 cells

6.14 *Confocal microscopy*

To support tubulin polymerisation results, immunofluorescence or confocal microscopy was carried out for selected enantiomers in three breast cancer cell lines and HT-29 cells. (Figure 6.22- Figure 6.30).

6.14.1.1 *Confocal microscopy of the microtubule network in three breast cancer cell lines following treatment with **17EN1** and **17EN2***

Confocal microscopy was carried out for **17EN1** and **17EN2** and compared to both CA-4 and paclitaxel as depolymerising and polymerising positive controls respectively in three breast cancer cell lines, MDA-MB-231 (Figure 6.22), MCF-7 (Figure 6.23) and Hs578T(i)8 cells (Fiugre 6.24). Cells were treated for 16 h with CA-4 (100 nM), paclitaxel (1 μM) or **17EN1** and **17EN2** at concentrations based on anti-proliferative IC_{50} values. The selected concentration ranges allowed for direct comparison of microtubule depolymerizing effects of **17EN1** versus **17EN2** at 50 and 100 nM.

6.14.1.2 *Confocal Microscopy of **17EN1** and **17EN2** treated MDA-MB-231 cells*

Representative images for confocal analysis of the effects of **17EN1** versus **17EN2** on the microtubule network of MDA-MB-231 cells are illustrated in Figure 6.22**.** MDA-MB-231 cells demonstrated a well organised microtubule network when stained with an anti-α-tubulin mAb. Tubulin depolymerisation occured for cells treated with CA-4 (100 nM), observed by the absence of a microtubule network with respect to untreated or vehicle treated cells. This contrasted the polymerisation observed in paclitaxel treated cells where microtubules were observed as tight networks surrounding the nuclei of cells**.** The 3*S,*4*S* eutomer, **17EN1 (**50 nM) abolished the microtubule network in MDA-MB-231 cells while a well organized microtubule network remained at 10 nM. The less potent

3*R*,4*R* distomer **17EN2** (50 nM), [in contrast to *in vitro* tubulin polymerisation assays where no effect on tubulin depolymerisation was observed (**B,** Figure 6.13)], disrupted the microtubule network, albeit partially, with evidence of the microtubule network remaining. This contrasted total depolymerisation which was evident for cells treated with a higher concentration of **17EN2** (500 nM and 1 μM) while evidence of the microtubule network remained in cells treated with **17EN2** (100 nM), despite minor disruption of the microtubule network. Confocal microscopy confirms that **17EN2** is a microtubule depolymeriser although less potent than its 3*S,* 4*S* eutomer **17EN1.** This was observed by comparing **17EN1** and **17EN2** at both 50 and 100 nM (Figure 6.22).

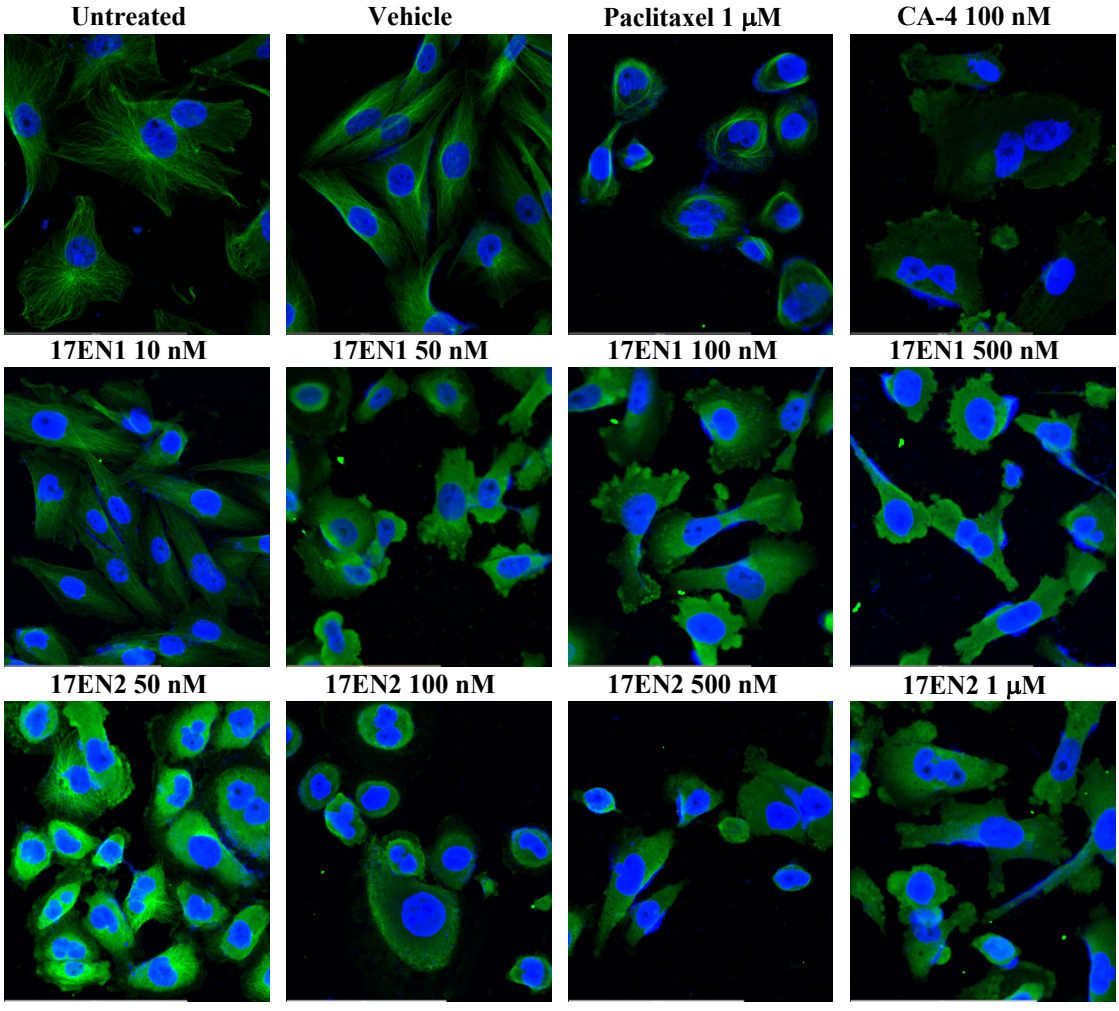

Figure 6.22: Confocal microscopy of the microtubule network in MDA-MB-231 cells. Untreated, vehicle treated (0.6% v/v ethanol) controls paclitaxel (1 μM) and CA-4 (100 nM), 3*S*,4*S* β-lactam eutomer **17EN1** at 10 nM, 50 nM, 100 nM and 500 nM and 3*R*,4*R* β-lactam distomer **17EN2** at 50 nM, 100 nM, 500 nM and 1 μM. Cells were treated for 16 h. Representative confocal micrographs of three independent experiments are shown. Scale bar 100 μm

6.14.1.3 *Confocal Microscopy of the microtubule network for MCF-7 cells treated with **17EN1** and **17EN2***

Figure 6.23 illustrates a representative example of MCF-7 cells treated with **17EN1** and **17EN2**. The microtubule network of MCF-7 cells treated with **17EN1** (50 nM) were observed as partially disrupted with evidence of the microtubule network remaining. This contrasts the abolishment of the microtubule network in MDA-MB-231 cells treated with the same concentration [**17EN1 (**50 nM), (Figure 6.22)]. **17EN1** is at least equally as potent in TNBC MDA-MB-231 cells as in MCF-7 cells (Figure 6.22) with potentially superior microtubule depolymerising activity in MDA-MB-231 cells (Figure 6.23). In contrast little evidence of depolymerisation in MCF-7 cells treated with **17EN2** (50 nM) was observed. **17EN2 (**100 nM) caused partial depolymerisation of the microtubule network in MCF-7 cells. However, the microtubule structures while disorganised remained partially intact in a 'web-like' manner, observed without the typical filamentous network observed for the cytoskeleton of untreated or vehicle treated cells. Direct comparison of **17EN1 (**100 nM) and **17EN2** (100 nM) demonstrated that the effect of **17EN1** on the microtubule network is much more pronounced than the effect of **17EN2**. Little evidence of an intact microtubule network remained for MCF-7 cells treated with **17EN1** (100 nM). These findings demonstrate that both enantiomers are again microtubule depolymerisers in MCF-7 cells (Figure 6.23) with **17EN1** determined as the more potent eutomer, in keeping with findings observed in MDA-MB-231 cells (Figure 6.22)

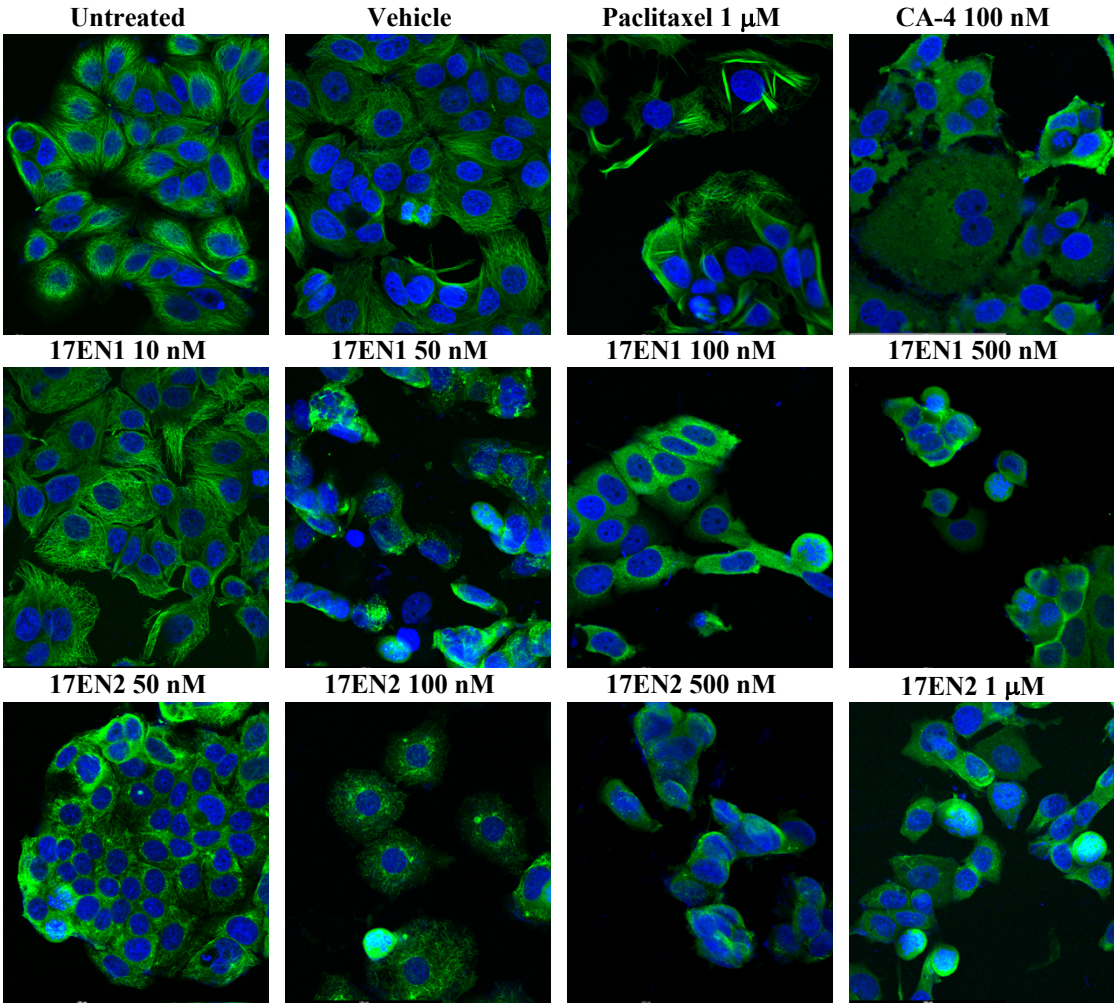

Figure 6.23: Confocal microscopy of the microtubule network in MCF-7 cells. Untreated, vehicle treated (0.6% v/v ethanol), controls paclitaxel (1 μM) and CA-4 (100 nM), 3*S*,4*S* β-lactam eutomer **17EN1** at 10 nM, 50 nM, 100 nM and 500 nM and 3*R*,4*R* β-lactam distomer **17EN2** at 50 nM, 100 nM, 500 nM and 1 μM. Cells were treated for 16 h. Representative confocal micrographs of three independent experiments are shown. Scale bar 100 μM

6.14.1.4 *Confocal Microscopy of the Hs578T(i)8 cell microtubule network treated with **17EN1** and **17EN2***

illustrates a representative example of Hs578T(i)8 cells treated with **17EN1** and **17EN2.** **17EN1** (10 nM) demonstrated evidence of microtubule depolymerisation which was not evident in MCF-7 (Figure 6.23) or MDA-MB-231 cells (Figure 6.22) treated with **17EN1** (10 nM). Cells treated with **17EN1** (50 nM) have little evidence of the microtubule network remaining. This contrasts findings in MCF-7 cells treated with **17EN1** (50 nM)

where evidence of the microtubule network remained (Figure 6.23). Similarly **17EN2** (100 nM) caused disassembly of the Hs578T(i)8 microtubule network (Figure 6.24) which again contrasts MCF-7 cells at this same concentration where the microtubule network was still evident in cells treated with 100 nM of **17EN2** (Figure 6.23). Both **17EN1** and **17EN2** are potentially more potent microtubule depolymerisers in the more aggressively proliferating metastatic breast cancer Hs578T(i)8 cell line (Figure 6.24) in comparison to MCF-7 (Figure 6.23) and MDA-MB-231 (Figure 6.22) cells and at lower concentrations.

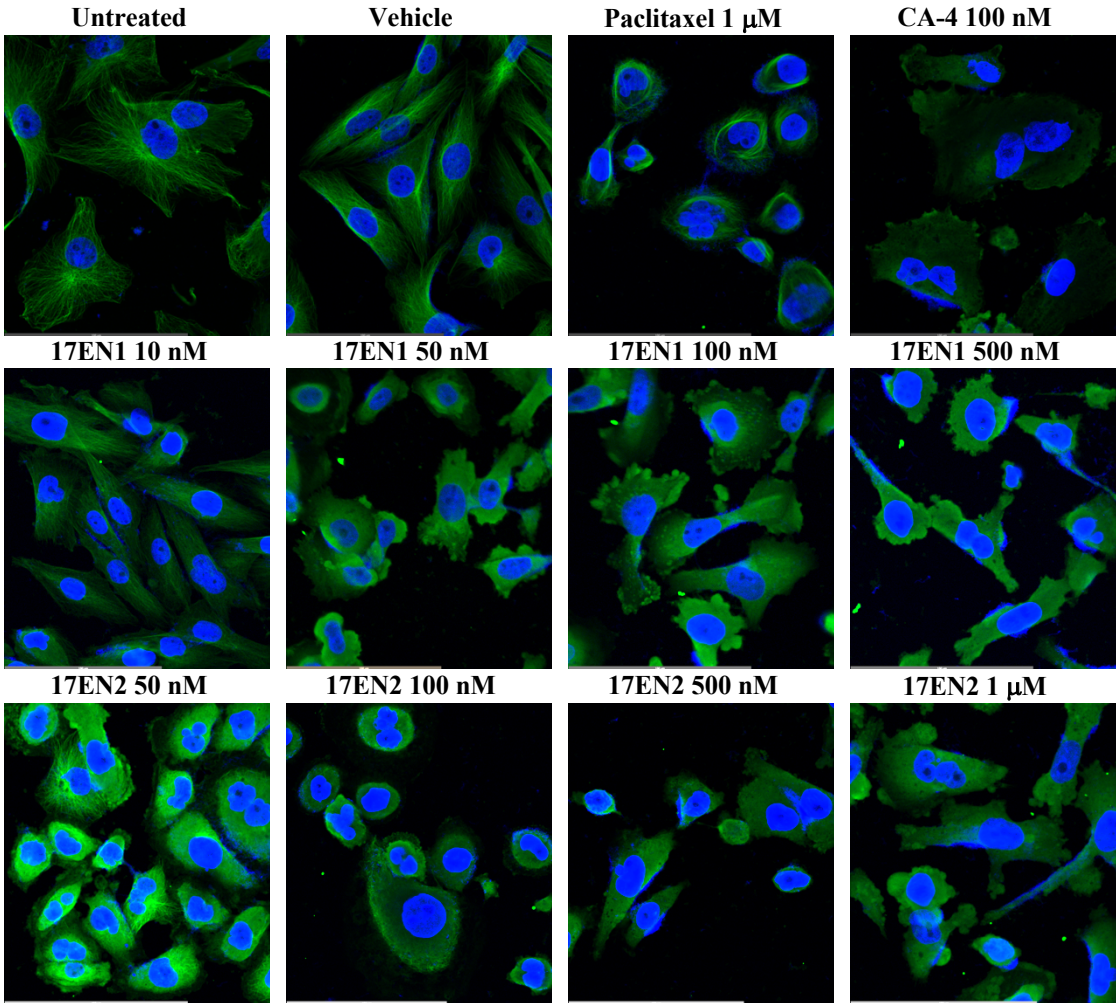

Figure 6.24: Confocal microscopy of the microtubule network in Hs578Ti(8) cells. Untreated, vehicle treated (0.6% v/v), controls paclitaxel (1 μM) and CA-4 (100 nM), 3*S*,4*S* eutomer **17EN1** at 10 nM, 50 nM, 100 nM and 500 nM and 3*R*,4*R* distomer **17EN2** at 50 nM, 100 nM, 500 nM and 1 μM. Cells were treated for 16 h. Representative confocal micrographs of three independent experiments are shown. Scale bar 100 μm

6.14.1.5 *Confocal microscopy of the microtubule network for breast cancer cells treated with 3S,4R eutomer **24EN1***

Confocal microscopy of MDA-MB-231 (Figure 6.25), MCF-7 (Figure 6.26) and Hs578T(i)8 (Figure 6.27) cells was carried out following treatment with 3*S*,4*R* eutomer **24EN1**.

6.14.1.6 *Confocal microscopy for eutomer **24EN1** in MDA-MB-231 cells*

24EN1 (1 nM) had little effect on the microtubule network of MDA-MB-231 cells. (Figure 6.25) However, at 5 nM, the microtubule network commenced disassembly in addition to mitotic catastrophe observed as nuclear fragmentation (breaking up of blue nucleus into smaller nuclei). The microtubule network remained partially intact when following treatment with **24EN1** (5 nM). At 10 nM little evidence of the network remained with microtubule network comparable with cells treated with CA-4 (100 nM). These findings demonstrate that microtubule disassembly commences at 5 nM for **24EN1** following a 16 h treatment period while the microtubule depolymerising effects of **24EN1** at 10 nM are comparable to CA-4 at 10 times this concentration of 100 nM (Figure 6.25).

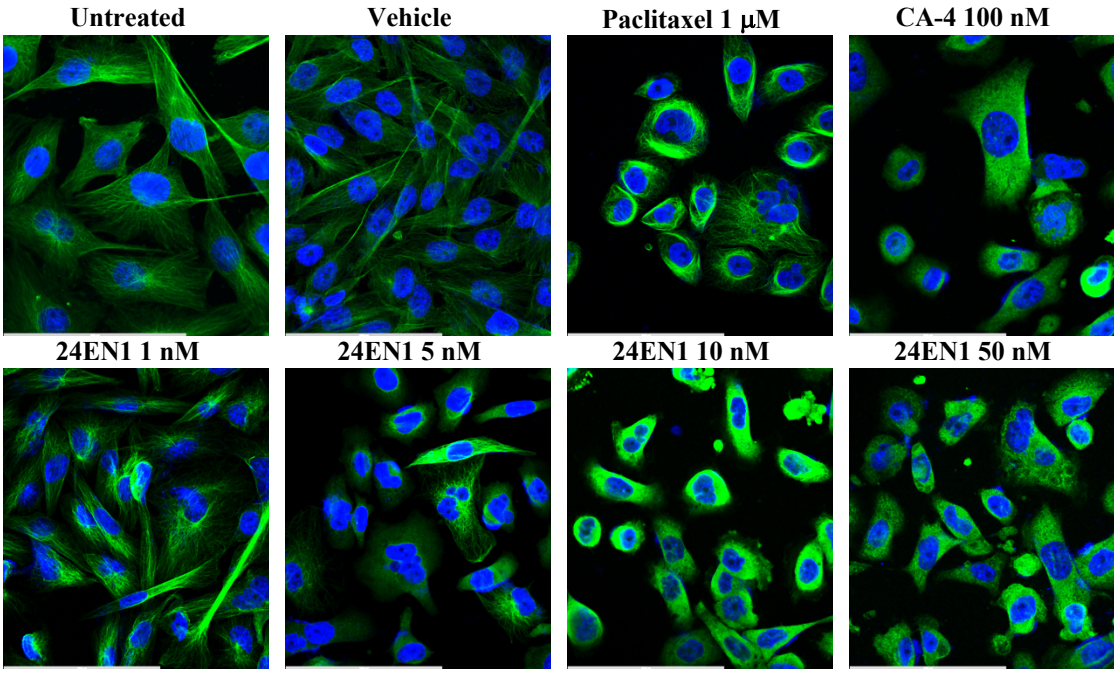

Figure 6.25: Confocal microscopy of the microtubule network of MDA-MB-231 cells. Untreated, vehicle treated (0.6% v/v ethanol), controls paclitaxel (1 μM) and CA-4 (100 nM), 3*S*,4*R* eutomer **24EN1** at 1 nM, 5 nM, 10 nM and 50 nM. Cells were treated for 16 h. Representative confocal micrographs of three independent experiments are shown. Scale bar: 100 μm.

6.14.1.7 *Confocal microscopy of the MCF-7 microtubule network treated with **24EN1***

Similar results were obtained for **24EN1** in MCF-7 cells (Figure 6.26) as observed for MDA-MB-231 cells (Figure 6.25). Microtubule depolymerisation was not observed at 1 nM while at 5 nM, disassembly of the microtubule network commenced. The nuclei are observed breaking into multiple smaller nuclei due to mitotic catastrophe in MCF-7 cells treated with 5 nM of **24EN1**. The effects of **24EN1** on MCF-7 cells at both 10 nM and 50 nM were comparable to CA-4 (100 nM).

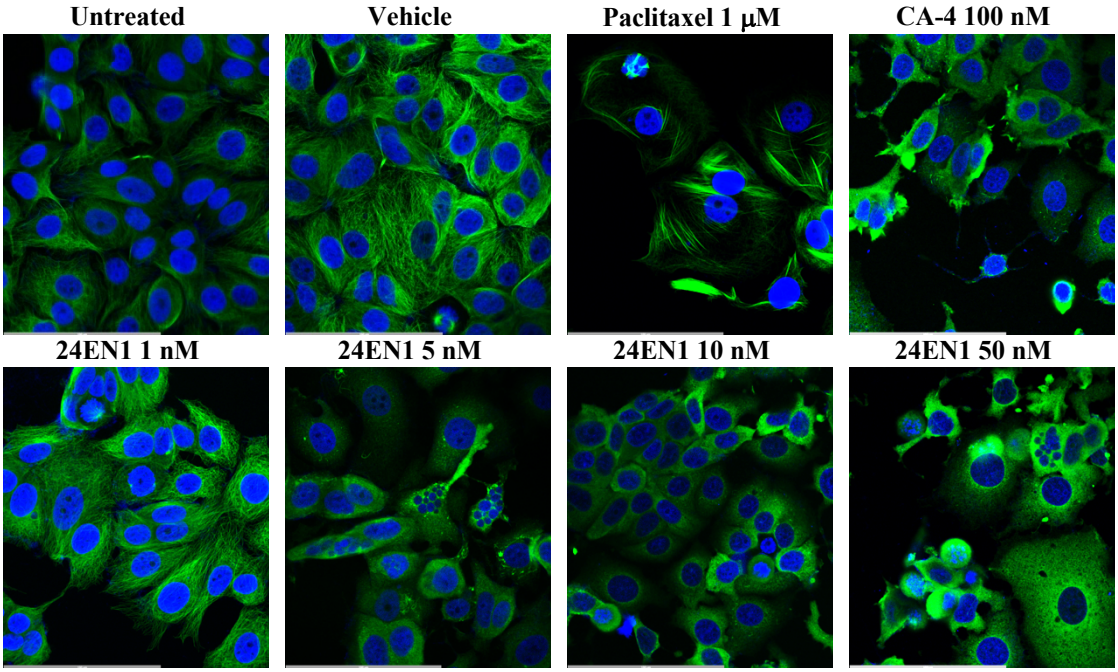

Figure 6.26: Confocal microscopy of the microtubule network of MCF-7 cells. Untreated, vehicle treated 0.6 % (v/v) % ethanol, controls paclitaxel (1 μM) and CA-4 (100 nM), 3*S*,4*R* eutomer **24EN1** at 1 nM, 5 nM, 10 nM and 50 nM. Cells were treated for 16 h. Representative confocal micrographs of three independent experiments are shown. Scale bar: 100 μm.

6.14.1.8 *Confocal microscopy of the Hs578T(i)8 cells microtubule network treated with eutomer **24EN1***

Contrasting observations for **24EN1** in MCF-7 (Figure 6.26) and MDA-MB-231 cells (Figure 6.25), **24EN1** (1 nM) caused disorganisation of the microtubule network in Hs578T(i)8 cells (Figure 6.27) which was not observed in any other breast cancer cell line at this concentration of 1 nM. While the microtubule network of Hs578T(i)8 cells

remained intact following treatment with **24EN1** (1 nM), resolution of the network appeared reduced, inferring that mild tubulin depolymerisation had occurred. The microtubule network underwent total disassembly when treated with 5 nM of **24EN1**. **24EN1** was therefore extremely potent in the invasive Hs578T(i)8 TNBC cell line with comparable activity at 5 nM to MDA-MB-231 and MCF-7 cells (Figure 6.25 and Figure 6.26 respectively).

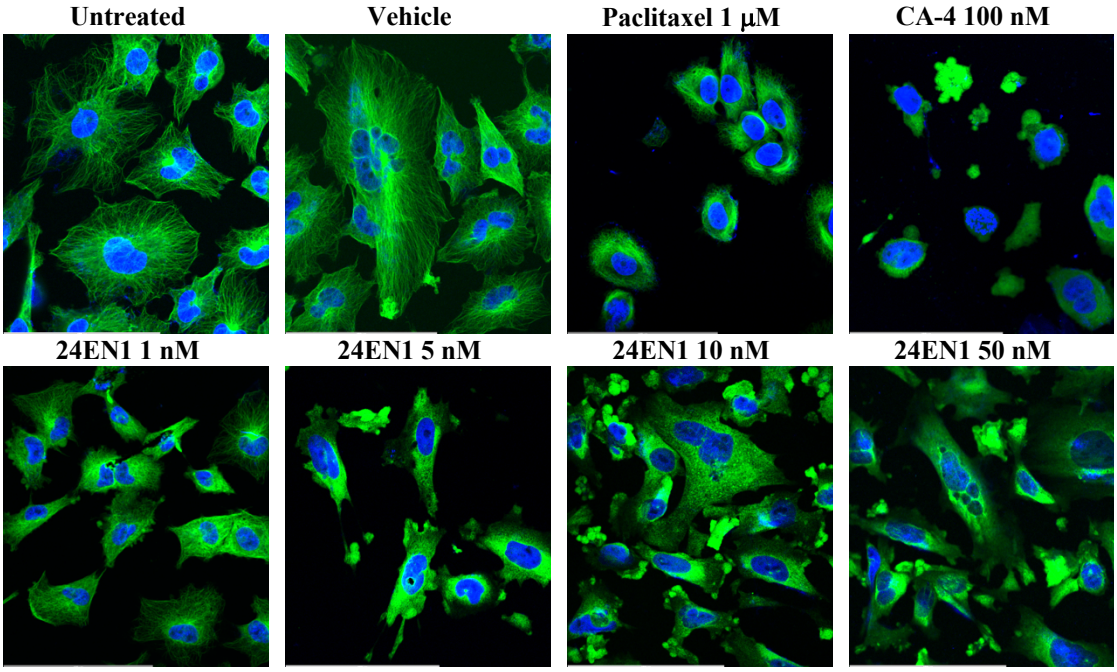

Figure 6.27: Confocal microscopy of the microtubule network of Hs578T(i)8 cells. Untreated, vehicle treated (0.6% v/v), controls paclitaxel (1 μM) and CA-4 (100 nM), 3*S*,4*R* eutomer **24EN1** at 1 nM, 5 nM, 10 nM and 50 nM. Cells were treated for 16 h. Representative confocal micrographs of three independent experiments are shown. Scale bar: 100 μm.

6.14.2 *Confocal microscopy of TNBC cells treated with eutomer **18EN1***

Although the structure of **18EN1** was originally designed for optimal activity in CA-4 resistant HT-29 cells, it has also demonstrated excellent antiproliferative activity in TNBC cell lines (Table 6.3). Therefore confocal microscopy was carried on the microtubule network in two TNBC cell lines, MDA-MB-231 cells (Figure 6.28) and the Hs578T(i)8 cell line following treatment with **18EN1** (Figure 6.29). **18EN1** demonstrated extremely potent microtubule depolymerising activity in MDA-MB-231 TNBC cells (Figure 6.28). 5 nM caused disruption of the MDA-MB-231 microtubule network with only minor evidence of tubulin remaining around nuclei of cells.Tubulin networks remained intact when treated 1 nM of **18EN1** while abolishment of the

microtubule network was observed in cells treated with 10 and 50 nM, comparable to the effects of CA-4 (100 nM). Disruption of the microtubule network was also observed in Hs578T(i)8 cells treated with 5 nM, 10 nM and 50 nM, demonstrating comparable effects in the more aggressive TNBC cell line (Figure 6.29) to the MDA-MB-231 TNBC cell line (Figure 6.28).

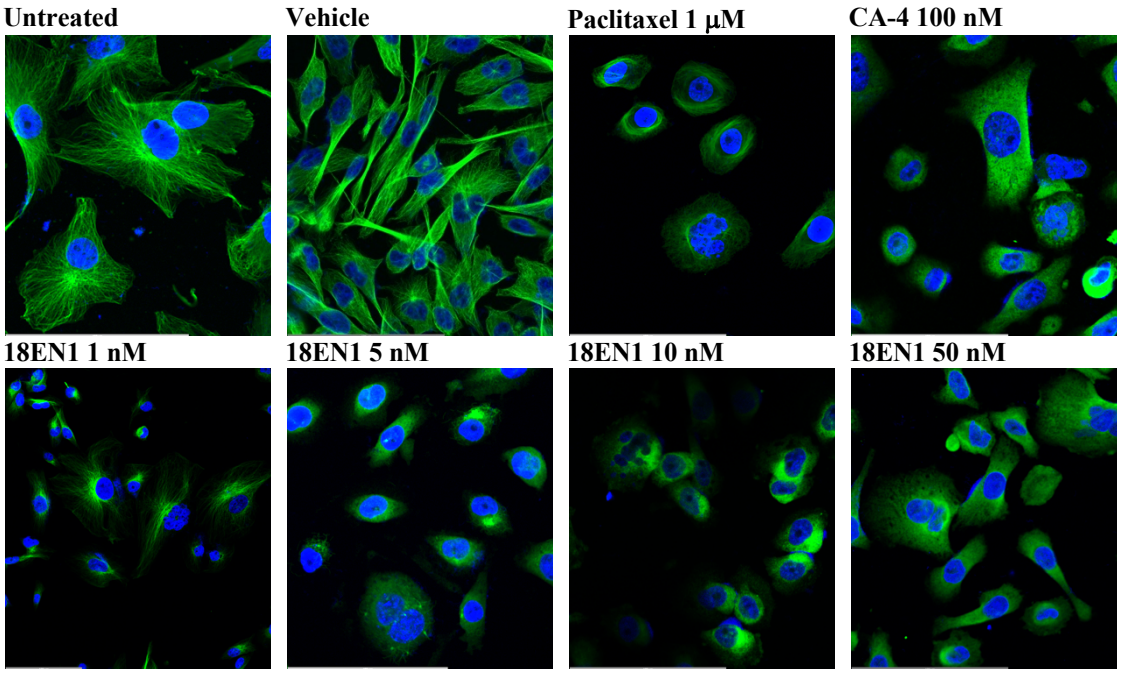

Figure 6.28: Confocal microscopy of the microtubule network in MDA-MB-231 cells. Untreated, vehicle treated (0.6% v/v), controls Paclitaxel (1 μM) and CA-4 (100 nM), 3*S*,4*S* eutomer **18EN1** at 1 nM, 5 nM, 1 nM and 50 nM. Cells were treated for 16 h. Representative confocal micrographs of three independent experiments are shown. Scale bar: 100 μm.

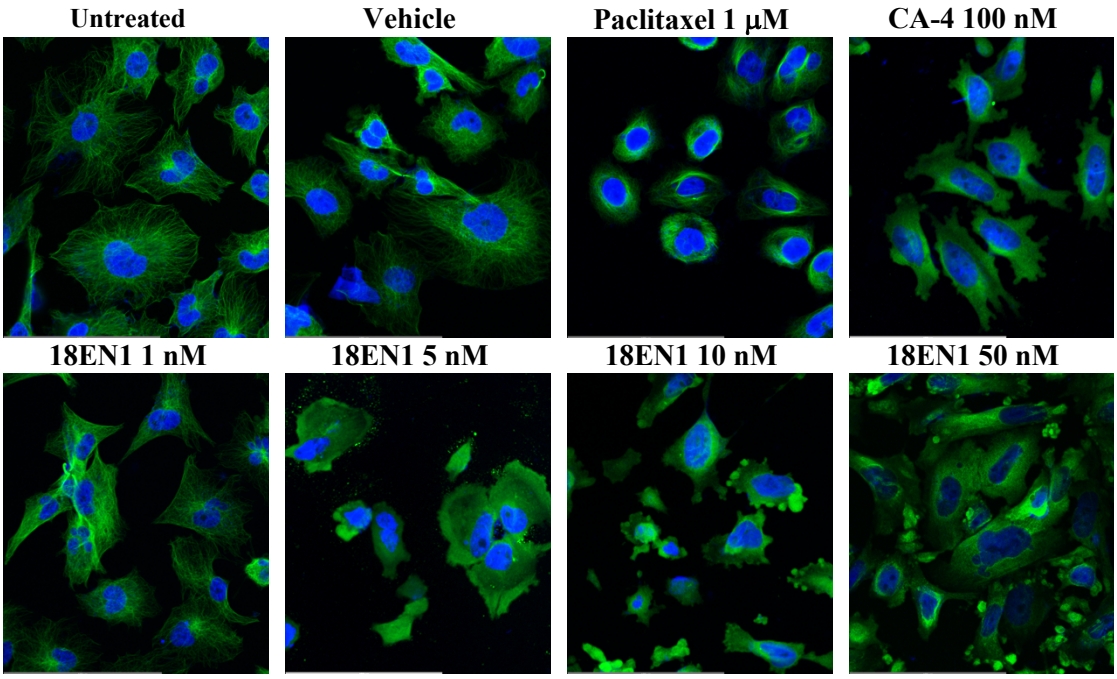

Figure 6.29: Confocal microscopy of the microtubule network in Hs578T(i)8 cells. Untreated, vehicle treated (0.6% v/v), controls paclitaxel (1 μM) and CA-4 (100 nM), 3*S*,4*S* eutomer **18EN1** at 1 nM, 5 nM, 1 nM and 50 nM. Cells were treated for 16 h. Representative confocal micrographs of three independent experiments are shown. Scale bar: 100 μM

6.14.3 *Confocal microscopy of the microtubule network in HT-29 CA-4 resistant colorectal cancer cells treated with **18EN1** or **24EN1***

The antiproliferative potency of the B ring *meta* hydroxyl substituted eutomer **24EN1** was determined as much poorer in HT-29 cells compared to its excellent activity in breast cancer cells. In contrast **18EN1** with a fluorine substitution replacing the B ring *meta* hydroxyl moiety had excellent activity in HT-29 cells. Confocal microscopy aimed to compare the effect of both analogues on the HT-29 microtubule network. Figure 6.30 is a representative example of HT-29 cells treated with either **18EN1** or **24EN1**. Since HT-29 cells are resistant to the microtubule depolymerising effects of CA-4, their appearance following treatment with CA-4 (100 nM), as anticipated, was similar to vehicle control treated cells. Significant differences were observed on the microtubule network of HT-29 cells treated with **18EN1** while effects of **24EN1** on the microtubule network were negligible and comparable to CA-4 and untreated cells. **18EN1** at concentrations as low as 1 nM caused disruption to the microtubule network of HT-29 cells. At 5 nM, 10 nM and 50 nM , little evidence of a viable microtubule network remained. The appearance

of cells treated with any concentration of **24EN1** was similar to CA-4 (100 nM) and vehicle treated cells. These findings demonstrate that while both **18EN1** and **24EN1** are extremely potent anti-proliferative and microtubule depolymerisers in breast cancer cells, only **18EN1** with the metabolically stable fluorine substitution in place of CA-4's and **24EN1**'s B ring *meta* hydroxyl position, has microtubule depolymerising activity in HT-29 cells. These findings confirm that **18EN1** is the most suitable lead eutomer for progression in further pre-clinical studies as a CBSI with dual activity against both breast and CA-4 resistant colorectal cancer.

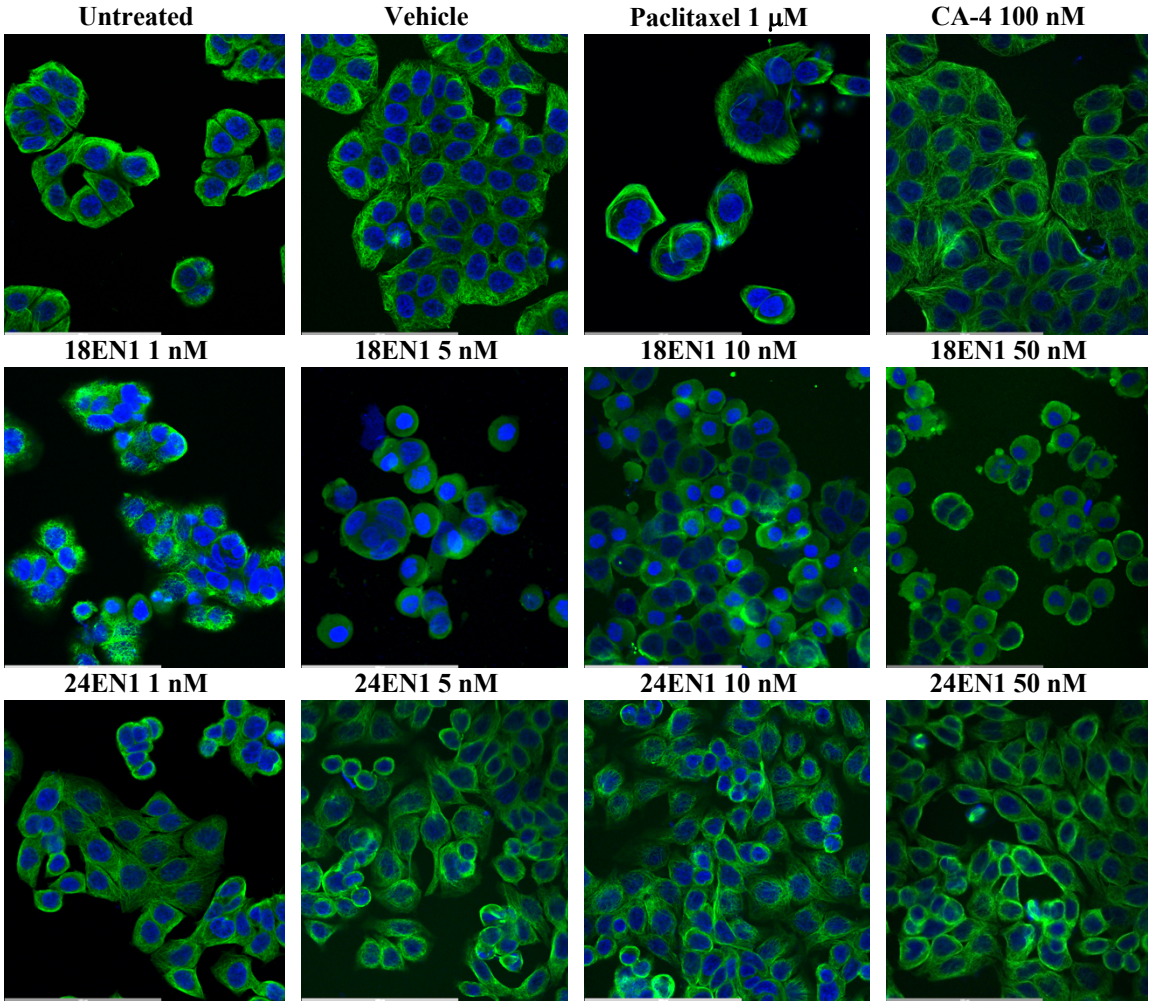

Figure 6.30: Confocal microscopy of the microtubule network in HT-29 cells. Untreated, vehicle treated (0.6% v/v), controls paclitaxel (1 μM) and CA-4 (0.1 μM), 3*S*,4*S* eutomer **18EN1** at 1 nM, 5 nM, 10 nM and 50 nM and 3*S*,4*R* eutomer **24EN1** at 1 nM, 5 nM, 10 nM 50 nM. Cells were treated for 16 h. Representative confocal micrographs of three independent experiments are shown. Scale bar: 100 μm bottom.

6.15 *Cell cycle analysis by flow cytometry*

Cell cycle analysis by flow cytometry aimed to quantify DNA content following treatment with enantiomeric combretazets to determine the percentage of cells undergoing mitotic arrest in G_2/ M phase and additionally cells undergoing apoptosis in the sub G_1/G_0 phase.[711-713] Flow cytometric quantification of DNA content involves use of the DNA-binding fluorochrome, propidium iodide (PI). The fluorescent dye (PI) binds to DNA stoichiometrically to produce a fluorescent signal which is directly proportional to the amount of DNA present.[711, 714] Analysis of DNA content enables accurate discrimination between G_1/G_0, S and G_2/M phases in addition to the sub G_1/G_0 population as a marker of apoptotic cells. Cells must be treated with RNAase to ensure only DNA content is measured.[712] **17EN1** was analysed in MDA-MB-231 cells. (Figure 6.31) **24EN1** was analysed in two TNBC cell lines; MDA-MB-231 cells (Figure 6.32) and Hs578T(i)8 cells (Figure 6.33). **18EN1** was also analysed in both MDA-MB-231 cells (Figure 6.35) in addition to CA-4 resistant HT-29 cells (Figure 6.34) to demonstrate G_2/ M phase arrest in both breast and colorectal cancer cells.[713]

6.15.1 *Cell cycle analysis of MDA-MB-231 TNBC cells following treatment with eutomer **17EN1***

The effect of **17EN1** on the cell cycle of MDA-MB-231 cells was investigated by flow cytometry at six time points [2h 8h, 16h, 24h, 48h and 72h, **(**Figure 6.31 and Table 6.28]. Following treatment with **17EN1** a time and dose dependent increase in cell population within G_2/M phase was observed which coincided with a corresponding decrease in the cell population of G_1/G_0. **17EN1 (**15 nM) induced G_2/M phase arrest as early as 8h (44%) which had increased to 64% by 16h (Table 6.28). At higher concentrations of 20 –100 nM, a dose and time dependent increase was observed in the % of cells arrested in G_2/M phase until 48h which subsequently decreased at 72h. For example at 20 nM, the % of cells treated with **17EN1** in G_2/M phase at 16, 24 and 48 h was 59%, 68% and 70% respectively which decreased to 50% at 72 h . (Table 6.28)This trend is explained by the mitotic arrest that occurs following initial tubulin depolymerisation. When the mitotic spindle disintegrates, an accumulation of cells is typically observed in G_2/M phase. Cells cannot divide and therefore become apoptotic.[715, 716] This is observed as a decrease in % of cells in G_2/M phase accompanied by a simultaneous increase in the % of cells in sub G_1/G_0 *i.e* the apoptotic population. Larger increases in the sub G_1/G_0 population of

apoptotic cells were not observed until 48 -72h. For example, at the highest concentration (100 nM) the % of cells in this population was only 4% by 24 h. The time and concentration dependent increase in sub G_1/G_0 appears most pronounced for **17EN1** in MDA-MB-231 cells between 48h to 72h. At 15 nM, however there was only a small decrease in % of the G_2/M phase population from 57% to 51% between 48 h and 72h, accompanied by a minor increase in % of cells in sub G_1/G_0 of 12% to 13% from 48-72h. However at higher concentrations a larger quantity of cells have become apoptotic between 48-72 h. For example the G_2/M phase population treated with 30 nM of **17EN1** decreased from 74% to 57% from 48-72h with a simultaneous increase of 10% - 18% of sub G_1/G_0 apoptotic cells. At 100 nM, a decrease of cells at G_2/M phase from 66% at 48 h to 54% at 72h was observed accompanied by a simultaneous increase in % of cells in sub G_1/G_0 from 17-27% (Table 6.28). These findings are in keeping with data for the combretazet racemates, however at much lower concentrations than previously reported in the literature.[359, 378]

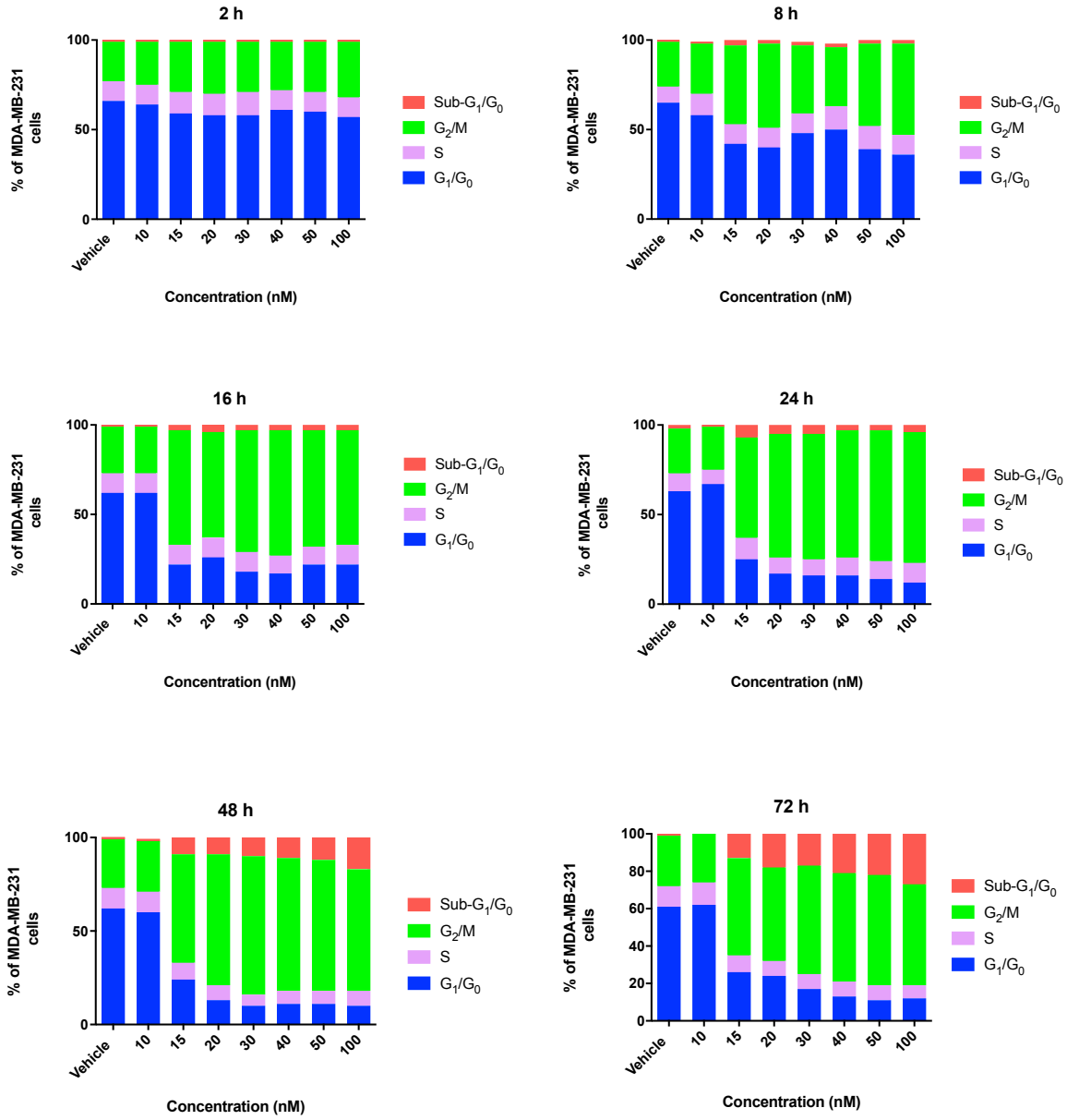

Figure 6.31: **17EN1** induces G_2/M arrest and apoptosis in MDA-MB-231 cells. Cells were treated with either vehicle [1% ethanol (v/v)], or **17EN1** at concentrations of 10, 15, 20, 30, 40, 50 nM or 100 nM for 2, 8, 16, 24, 48 and 72 h. Cells were then fixed, stained with PI, and analysed by flow cytometry. Cell cycle analysis was performed on histograms of gated counts per DNA area (FL2-A). The number of cells with <2N (sub-G_1/G_0), 2N (G_0/G_1), and 4N (G_2/M). DNA content was determined with BD accuri C6. Values represent the mean for three independent experiments.

Table 6.28: **%** of MDA-MB-231 cells in each stage of cell cycle when treated with **17EN1**. Values represent as the mean for three independent experiments ± SEM.

	Vehicle		**17EN1 10 nM**		**17EN1 15 nM**		**17EN1 20 nM**		**17EN1 30 nM**		**17EN1 40 nM**		**17EN1 50 nM**		**17EN1 100 nM**	
G_1/G_0	**%**	**SEM**	**%**	**SEM**	**%**	**SEM**	**%**	**SEM**	**%**	**SEM**	**%**	**SEM**	**%**	**SEM**	**%**	**SEM**
2h	65.6	2.86	63.43	2.21	58.49	4.45	57.88	7.51	57.9	4.25	60.94	7.12	60.4	5.41	56.87	1.59
8h	63.86	3.06	59.47	6.32	42.67	6.97	40.93	9.98	48.9	11.75	51.37	13.01	38.8	14.95	36.45	9.92
16h	61.87	4.12	62.03	0.92	22.21	5.34	25.92	7.59	18.25	6.97	17.46	5.68	21.98	5.43	22.45	4.25
24h	63.41	2.58	66.97	1.42	25.48	10.32	15.12	4.94	15.96	5.79	15.83	7.06	13.72	3.64	12.87	3.09
48h	61.85	3.01	61	1.73	22.81	8.6	14.18	6.51	9.53	0.76	10.5	3.44	10.83	2.99	9.87	5.01
72h	61.46	1.13	61.67	1.25	25.87	8.29	23.95	6.32	17.4	6.91	13.06	7.52	11.42	4.15	12.1	5.49
	Vehicle		**17EN1 10 nM**		**17EN1 15 nM**		**17EN1 20 nM**		**17EN1 30 nM**		**17EN1 40 nM**		**17EN1 50 nM**		**17EN1 100 nM**	
S	**%**	**SEM**	**%**	**SEM**	**%**	**SEM**	**%**	**SEM**	**%**	**SEM**	**%**	**SEM**	**%**	**SEM**	**%**	**SEM**
2h	10.52	3.82	10.83	1.53	12.42	6.13	11.81	3.21	12.66	3.66	10.88	2.92	10.88	3.35	10.59	3.61
8h	8.88	2.75	11.7	1.28	11.27	2.81	10.5	3.45	11.09	3.22	13.17	4.13	13.36	3.81	10.76	2.27
16h	10.75	1.3	10.8	1.36	11.49	0.67	11.17	1.37	10.78	3.34	10.18	1.39	10.05	1.6	10.78	1.71
24h	10.01	2.62	8.43	3.18	11.7	1.5	9.03	2.85	9.05	1.76	9.9	1.42	9.62	2.81	10.68	3.06
48h	10.88	2.12	10.97	2.86	8.28	1.54	7.93	3.13	6.31	1.79	7.25	1.55	7.23	2	7.77	1.68
72h	10.38	0.45	11.63	0.23	9.34	2.79	8.25	2.08	7.5	2.26	8.26	3.69	7.8	3.14	7.13	0.79
	Vehicle		**17EN1 10 nM**		**17EN1 15 nM**		**17EN1 20 nM**		**17EN1 30 nM**		**17EN1 40 nM**		**17EN1 50 nM**		**17EN1 100 nM**	
G_2/M	**%**	**SEM**	**%**	**SEM**	**%**	**SEM**	**%**	**SEM**	**%**	**SEM**	**%**	**SEM**	**%**	**SEM**	**%**	**SEM**
2h	21.7	4.7	23.53	2.76	27.73	9.42	28.9	4.69	27.69	3.92	26.22	8.9	28.41	7.28	30.27	4.34
8h	25.01	2	27.56	6.12	43.9	8.06	47.03	9.03	38.31	9.8	32.99	9.67	45.64	18.6	50.36	12.49
16h	26.09	3.02	26.22	0.85	63.85	5.02	58.64	12.03	67.95	6.29	69.96	3.49	65.53	4.51	64.1	5.2
24h	24.64	2.59	23.9	1.83	57.25	13.62	68.26	7.63	71.25	5.73	71.7	7.21	73.08	3.41	73.35	5.24
48h	26.6	2.42	26.87	3.4	56.8	11.29	69.7	13.68	74.38	2.63	71.55	7.36	71.85	6.07	66.39	11.61
72h	27.3	0.81	26.33	2.11	51.62	3.87	49.8	5.66	57.53	12.94	57.89	16.27	59.17	11.63	53.63	12.07
	Vehicle		**17EN1 10 nM**		**17EN1 15 nM**		**17EN1 20 nM**		**17EN1 30 nM**		**17EN1 40 nM**		**17EN1 50 nM**		**17EN1 100 nM**	
Sub G_1/G_0	**%**	**SEM**	**%**	**SEM**	**%**	**SEM**	**%**	**SEM**	**%**	**SEM**	**%**	**SEM**	**%**	**SEM**	**%**	**SEM**
2h	1.27	0.4	1.27	0.67	0.76	0.21	1.01	0.25	0.89	0.41	1.11	0.61	0.9	0.41	1.06	0.38
8h	1.15	0.56	1.18	0.4	3.09	1.91	2.14	0.86	1.75	1.02	2.39	1.22	2.13	1.01	1.85	0.38
16h	1.43	0.51	1.11	0.34	2.61	0.81	5.03	5.54	2.84	1.28	2.81	1.84	2.61	1.07	2.73	0.93
24h	2.05	1.33	1.07	0.12	6.78	4.93	5.09	1.72	6.08	3.09	3.3	1.5	3.49	1.61	3.66	1.73
48h	1.38	0.78	1.47	0.99	11.55	4.68	8.78	4.62	10.3	3.54	11.25	4.33	11.63	4.23	17.29	6.22
72h	1.74	0.68	1.05	0.53	13.02	7.01	17.63	5.67	17.68	5.73	20.86	6.41	21.61	6.85	26.58	7.32

6.15.2 *Cell cycle analysis of MDA-MB-231 TNBC cells following treatment with **24EN1***

24EN1 demonstrated an increase in G_2/M phase arrest as early as 8h at concentrations as low as 2.5 nM (Figure 6.32). 44% of cells were arrested in G_2/M phase at 8 h compared to 30% for vehicle treated cells (Table 6.29). A concomitant decrease in % of cells in the G_1/G_0 population was observed (43% of cells in G_1/G_0 at 8 h compared to 58% for the vehicle control). **24EN1** is a much more potent anti-mitotic agent compared to **17EN1 (**Table 6.31 and Table 6.28) which demonstrated an increase in G_2/M phase only from concentrations of 15 nM in MDA-MB-231 cells. **24EN1** is therefore estimated as six fold more potent with cell cycle arrest commencing at 2.5 nM and between 2-8 h. A dose and time dependent increase in the % of MDA-MB-231 cells in G_2/M phase from 16-48h treated with **24EN1** was observed (Table 6.29). From 48 – 72h an increase in the % of cells in sub G_1/G_0 was observed representative of cells undergoing apoptosis occurred. At 16h the % of cells in G_2/M phase for concentrations 2.5 -100 nM are similar, between 57- 60% (Table 6.28). However, at 24h a dose dependent rise in the % of cells in the G_2/M phase population began. For example, at 24h, 52%, 65% and 70% of cells treated with 2.5, 8 and 10 nM have arrested in G_2/M phase. Similarly, a dose dependent increase in the sub G_1/G_0 population from 48 – 72h at 5, 10 and 100 nM was observed from 9 - 22%, 8 - 29% and 10-32% respectively. These findings demonstrate that mitotic arrest occurred in MDA-MB-231 cells at concentrations as low as 2.5 nM and as early as 8 h for *3S,4R* eutomer **24EN1**. Between 24-72 h cells were arrested in G_2/M phase, commenced apoptosis at 24h with largest increases in % of sub G_1/G_0 *i.e* apoptotic cells occurring between 48-72h.

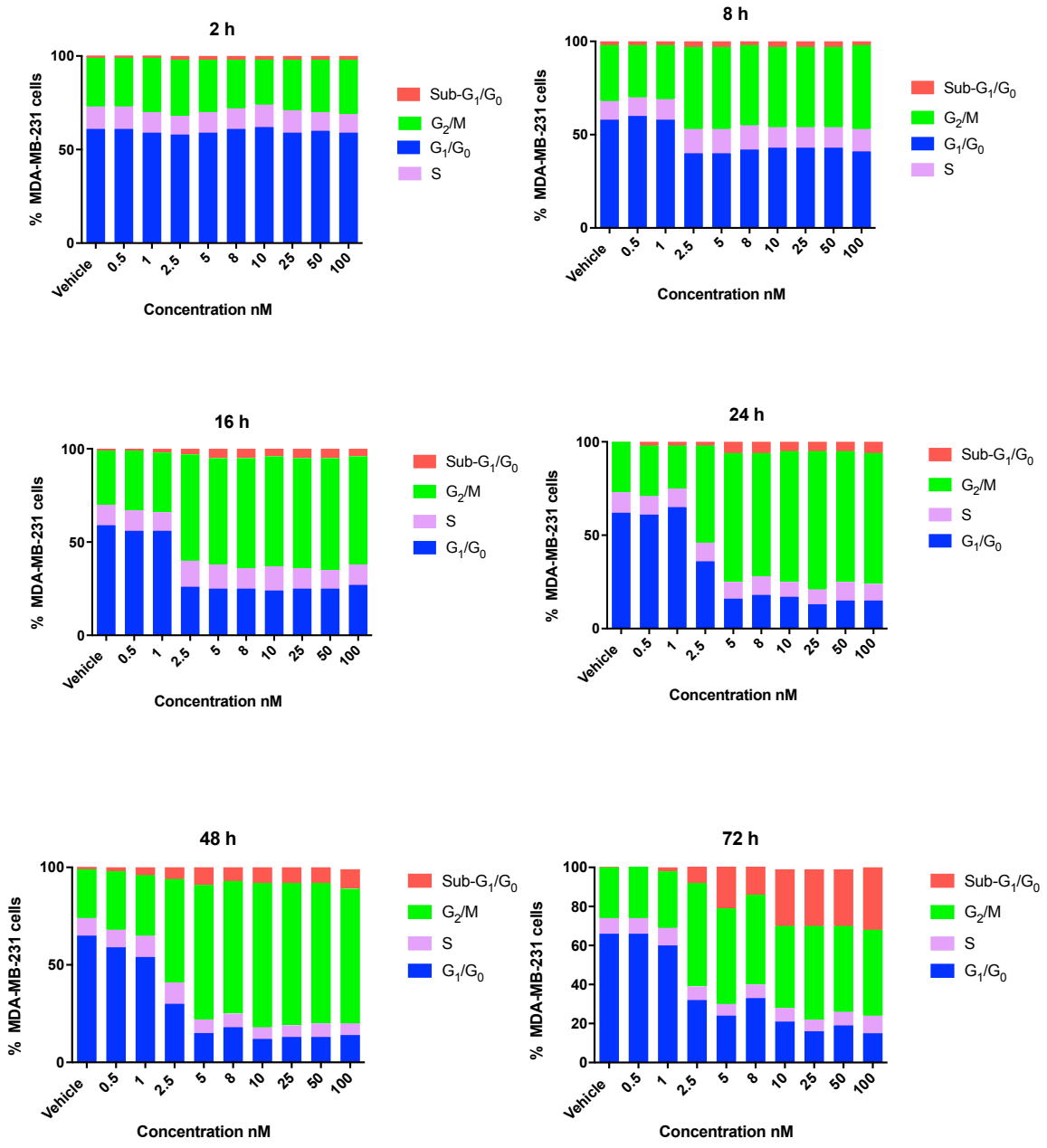

Figure 6.32: **24EN1** induces G_2/M arrest and apoptosis in MDA-MB-231 cells. Cells were treated with either vehicle [1% ethanol (v/v)], or **24EN1** at concentrations of 0.5, 1, 2.5, 5, 8, 10, 25, 50 or 100 nM for 2, 8, 16, 24, 48 and 72 h. Cells were then fixed, stained with PI, and analysed by flow cytometry. Cell cycle analysis was performed on histograms of gated counts per DNA area (FL2-A). The number of cells with <2N (sub-G_1/G_0), 2N (G_0/G_1), and 4N (G_2/M). DNA content was determined with BD accuri C6. Values represent the mean for three independent experiments.

Table 6.29: **%** of MDA-MB-231 cells in each stage of cell cycle when treated with **24EN1**. Values represent as the mean for three independent experiments ± SEM.

	Vehicle		**24EN1 0.5 nM**		**24EN1 1 nM**		**24EN1 2.5 nM**		**24EN1 5 nM**		**24EN1 8 nM**		**24EN1 10 nM**		**24EN1 25 nM**		**24EN1 50 nM**		**24EN1 100 nM**	
G_1/G_0	**%**	**SEM**	**%**	**SEM**	**%**	**SEM**	**%**	**SEM**	**%**	**SEM**	**%**	**SEM**	**%**	**SEM**	**%**	**SEM**	**%**	**SEM**	**%**	**SEM**
2h	61.03	4.39	64.23	1.68	60.38	4.64	57.53	2.98	58.9	4.61	60.8	4.25	61.6	4.75	58.79	6.81	59.68	4.33	60.17	3.53
8h	58.2	6.22	60.42	2.72	54.95	2.31	43.1	2.4	41.53	1.64	42.57	5.33	42.5	1.22	43	1.42	42.1	5.1	40.85	3.89
16h	58.59	3.86	56.44	4.13	53.33	7.15	26.2	6.35	25.17	3.45	23.13	7.96	24.23	5.01	25.42	4.38	23.33	5.84	27.23	1.63
24h	61.87	4.83	57.9	5.75	65.25	1.51	35.92	9.97	15.9	3.91	18.25	4.3	16.57	3.87	13.34	0.96	15.25	4.33	15.08	2.46
48h	69.75	6.01	58.87	9.33	54.47	4.1	30.43	12.44	15.14	2.46	17.6	7.71	11.97	0.67	13.77	1.7	12.73	0.06	15.93	3.49
72h	65.92	3.26	62.59	10.73	60.37	14.43	32.06	19.45	24.41	12.08	33.1	1.91	21.34	0.41	15.93	5.1	19.06	9.5	15.3	4.37
	Vehicle		**24EN1 0.5 nM**		**24EN1 1 nM**		**24EN1 2.5 nM**		**24EN1 5 nM**		**24EN1 8 nM**		**24EN1 10 nM**		**24EN1 25 nM**		**24EN1 50 nM**		**24EN1 100 nM**	
S	**%**	**SEM**	**%**	**SEM**	**%**	**SEM**	**%**	**SEM**	**%**	**SEM**	**%**	**SEM**	**%**	**SEM**	**%**	**SEM**	**%**	**SEM**	**%**	**SEM**
2h	12.14	1.77	11.72	2.24	11.27	0.16	12.15	1.39	11.27	0.47	10.9	1.01	11.87	1.07	11.37	0.71	9.7	2.12	10	1.61
8h	10.21	0.71	9.53	1.04	10.68	2.02	11.53	0.78	11.67	1.5	13.36	2.5	12	1.64	10.78	0.94	11.79	0.81	11.54	0.66
16h	10.7	1.13	12.27	2.01	12.63	1.58	13.85	4.25	12.62	0.93	10.97	2.98	12.59	2.42	11.68	0.62	9.55	1.51	10.64	2.7
24h	10.33	5.25	9.61	3.95	10.47	1.84	9.00	3.06	9.77	4.12	10.24	1.11	9.6	4.22	8	2.86	9.53	2.76	8.79	3.5
48h	9	1.65	8.73	1.67	10.93	5.06	11.07	0.61	7	0.52	5.07	1.26	5.9	0.85	6.33	2.14	9.47	3.67	5.74	0.28
72h	7.5	2.88	7.88	3.03	9.3	4.96	7.16	0.31	5.95	1.54	6.76	2.18	6.8	2.79	6.33	2.08	6.79	1.87	8.9	4.11
	Vehicle		**24EN1 0.5 nM**		**24EN1 1 nM**		**24EN1 2.5 nM**		**24EN1 5 nM**		**24EN1 8 nM**		**24EN1 10 nM**		**24EN1 25 nM**		**24EN1 50 nM**		**24EN1 100 nM**	
G_2/M	**%**	**SEM**	**%**	**SEM**	**%**	**SEM**	**%**	**SEM**	**%**	**SEM**	**%**	**SEM**	**%**	**SEM**	**%**	**SEM**	**%**	**SEM**	**%**	**SEM**
2h	26.21	4.12	23.43	1.8	26.61	2.61	29.5	0.85	28.47	3.93	27.8	4.39	25.3	3.32	28.33	5.35	28.82	4.89	28.25	3.91
8h	30.07	4.12	28.73	4.56	32.18	0.84	43.8	3.29	43.66	1.84	41.9	3.9	42.33	1.64	42.79	4.96	43.25	6.91	45.1	6.88
16h	28.8	4.59	32	4.45	33.15	7.58	58.73	9.51	59.63	5.45	60.21	9.72	59.18	5.24	58.94	2.56	56.46	6.21	56.8	2.5
24h	24.27	5.62	22.69	14.8	23.31	3.11	52.22	11.54	69.55	8.09	65.25	4.36	70.44	6.45	74.3	4.17	70.08	12.1	70.04	7.16
48h	25.42	5.13	31.03	7.94	31.77	6.3	54.93	14.65	69.96	4.44	64.65	17.99	75.32	0.62	72.86	4.46	71.96	2.52	68.81	5.71
72h	26.42	2.92	28	8.11	29.07	7.48	52.97	13.91	48.73	6.24	46.17	2.72	41.95	6.58	48.2	10.32	43.81	9.73	44.13	7.64
	Vehicle		**24EN1 0.5 nM**		**24EN1 1 nM**		**24EN1 2.5 nM**		**24EN1 5 nM**		**24EN1 8 nM**		**24EN1 10 nM**		**24EN1 25 nM**		**24EN1 50 nM**		**24EN1 100 nM**	
Sub G_1/G_0	**%**	**SEM**	**%**	**SEM**	**%**	**SEM**	**%**	**SEM**	**%**	**SEM**	**%**	**SEM**	**%**	**SEM**	**SEM**	**%**	**SEM**	**SEM**	**%**	**SEM**
2h	1.49	0.79	1.4	0.7	2.31	2.23	1.73	1.57	2.23	1.55	2.37	2.23	2.03	1.64	2.33	1.49	2.43	1.7	2.41	1.7
8h	2.1	2.27	3.76	2.46	2.37	2.28	2.77	3.06	2.75	1.83	2.26	1.73	2.77	1.5	3.13	3.61	2.63	2.01	1.71	1.12
16h	1.5	1.3	2.03	1.51	2.82	2.82	3.51	0.95	4.55	4.2	5.73	5.83	3.1	1.31	3.84	2.93	4.07	2.35	3.87	1.12
24h	0.96	0.28	2.16	1.4	1.11	0.17	3.87	0.31	6.00	1.97	6.4	2.98	4.7	2.17	4.54	2.11	5.38	4.12	6.35	2.47
48h	1.33	0.97	2.2	1.21	4.26	3.08	5.6	1.28	9.28	2.38	7.47	0.81	7.99	0.2	8.43	1.23	8.2	0.35	10.25	1.6
72h	0.57	0.15	2.29	2.47	2.27	2.63	9.82	1.9	21.65	6.21	14.61	1.48	29.42	4.84	29.14	3.51	29.32	4.99	32.21	9.4

6.15.2.1 *Cell cycle analysis of Hs578T(i)8 TNBC cells following treatment with **24EN1***

Similar results for **24EN1** were observed during cell cycle studies in Hs578T(i)8 cells (Figure 6.33).The % of cells in G_1/G_0 treated with 2.5 nM decreased from 47% to 37% from 2-8 h with a corresponding increase in the % of cells in G_2/M phase from 38% to 45% (Table 6.30)**.** At 16 h the % of cells treated with 2.5 nM of **24EN1** in G_1/G_0 decreased further to 30%. There was a time dependent increase in the % of cells treated with 2.5 nM accumulating in G_2/M phase increasing from 45% at 8 h to 52% at 48h. The % of cells in G_2/M phase (2.5 nM) decreased from 54% at 48 h to 43% at 72 h accompanied by an increase in the sub G_1/G_0 population (8% -15% from 24 to 48 h). From 10 nM upward, a dose dependent magnitude of mitotic arrest was observed compared to lower concentrations. The % of cells in G_2/M phase at 5 and 10 nM increased from 45 - 52% and 47- 64% from 8 -24h respectively (Table 6.30). This demonstrated equipotent anti mitotic activity for **24EN1** in MDA-MB-231 cells with respect to the more aggressive triple negative Hs578T(i)8 cell line (Table 6.30).

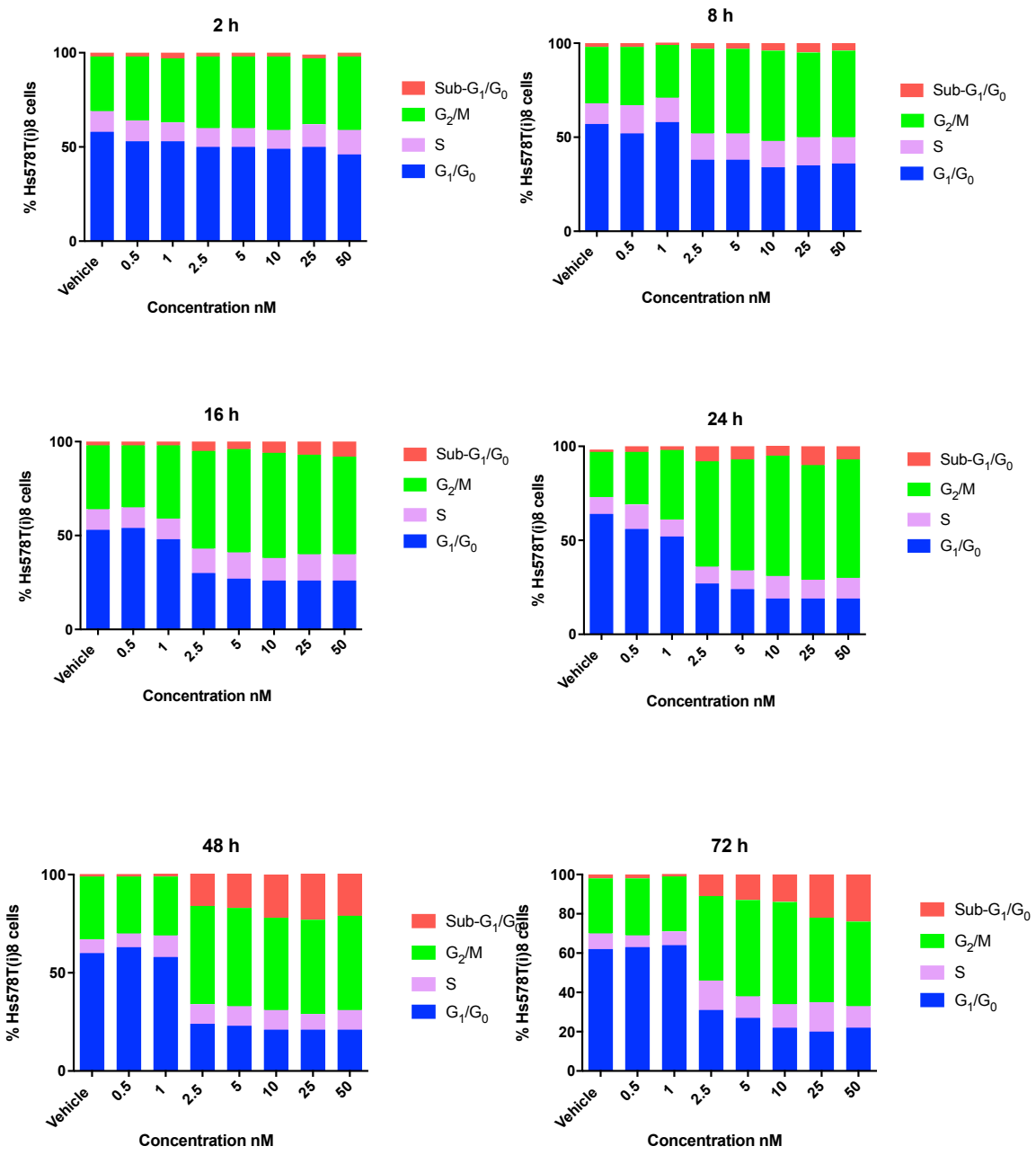

Figure 6.33: **24EN1** induces G_2/M arrest and apoptosis in Hs578T(i)8 cells. Cells were treated with either vehicle [1% ethanol (v/v)], or **24EN1** at concentrations of 0.5, 1, 2.5, 5, 8, 10, 25 or 50 nM for 2, 8, 16, 24, 48 and 72 h. Cells were then fixed, stained with PI, and analysed by flow cytometry. Cell cycle analysis was performed on histograms of gated counts per DNA area (FL2-A). The number of cells with <2N (sub-G_1/G_0), 2N (G_0/G_1), and 4N (G_2/M). DNA content was determined with BD accuri C6. Values represent the mean for three independent experiments.

Table 6.30: **%** of Hs578T(i)8 cells in each stage of cell cycle when treated with **24EN1**. Values represent as the mean for three independent experiments ± SEM.

	Vehicle		**24EN1 0.5 nM**		**24EN1 1 nM**		**24EN1 2.5 nM**		**24EN1 5 nM**		**24EN1 10 nM**		**24EN1 25 nM**		**24EN1 50 nM**	
G_1/G_0	%	SEM	%	SEM	%	SEM	%	SEM	%	SEM	%	SEM	%	SEM	%	SEM
2h	53.84	1.39	49.74	3.94	49.89	2.44	47.97	5.93	46.97	3.45	45.34	4.54	43.24	3.59	43.24	3.59
8h	54.08	3.08	51.02	4.82	55.49	7.28	36.94	5.08	36.94	5.08	32.85	5.07	34.73	6.34	34.73	6.34
16h	51.02	2.05	52.4	1.09	48.07	4.86	30.23	4.9	26.9	6.61	26.27	2.23	25.87	3.79	25.87	3.79
24h	64.4	7.4	56.23	6.28	50.52	9.12	25.83	6.96	22.49	5.84	17.92	5.15	18.98	6.65	18.98	6.65
48h	60.63	2.11	63.45	2.65	57.94	3.72	24.07	4.37	22.73	2.06	21.3	3.12	21.05	0.93	21.05	0.93
72h	60.38	2.82	63.3	2.86	65.13	7.78	30.27	7.85	24.46	3.46	22.4	0.46	21.53	5.45	21.53	5.45
	Vehicle		**24EN1 0.5 nM**		**24EN1 1 nM**		**24EN1 2.5 nM**		**24EN1 5 nM**		**24EN1 10 nM**		**24EN1 25 nM**		**24EN1 50 nM**	
S	%	SEM	%	SEM	%	SEM	%	SEM	%	SEM	%	SEM	%	SEM	%	SEM
2h	11.27	4.1	10.87	3.06	10.27	3.69	10.27	3.23	9.93	3.44	10.21	2.68	10.72	2.66	10.19	2.55
8h	11.38	1.45	15.13	4.21	13.25	3.15	13.71	1.24	13.71	1.24	14.33	2.11	14.93	1.51	14.11	1.7
16h	10.83	2.37	10.98	2.05	11.2	0.99	14.07	1.31	14.07	1.31	11.77	2.42	14.46	1.28	13.96	1.96
24h	9.1	7.41	13.02	1.58	9.12	2.25	8.39	2.95	8.72	3.52	9.33	1.83	9.03	2.55	8.97	3.01
48h	7.08	1.84	6.88	1.72	11.17	2.75	10.36	0.88	10.02	0.33	9.85	1.57	8.05	1.68	10.2	1.72
72h	7.65	1.54	6.21	2.61	6.59	2.6	15.21	2.03	10.94	7.06	11	6.97	9.86	7.24	10.95	6.86
	Vehicle		**24EN1 0.5 nM**		**24EN1 1 nM**		**24EN1 2.5 nM**		**24EN1 5 nM**		**24EN1 10 nM**		**24EN1 25 nM**		**24EN1 50 nM**	
G_2/M	%	SEM	%	SEM	%	SEM	%	SEM	%	SEM	%	SEM	%	SEM	%	SEM
2h	29.43	4	34.17	2.77	34.06	3.44	37.54	3.98	37.54	3.98	39.48	2.51	32.7	16.68	37.88	3.59
8h	29.9	2.53	31.49	5.93	27.71	9.31	44.66	6.59	44.66	6.59	47.51	8.52	44.65	7.85	45.81	7.08
16h	34.33	3.59	33.08	3.23	37.19	5.11	51.89	3.88	55.22	3.76	54.73	3.52	53.68	4.9	52.45	1.64
24h	23.95	7.82	26.83	4.2	36.94	7.46	54.35	5.09	52.1	17.01	64.39	3.94	60.25	11.7	61.8	3.75
48h	31.54	2.27	28.78	2.89	29.69	2.31	51.76	7.73	50.42	9.49	47.2	14.58	47.53	14.88	47.98	11.5
72h	22.47	14.08	29.22	2.98	27.65	5.59	42.61	6.83	48.81	12.24	50.57	8.76	44	9.91	42.93	5.27
	Vehicle		**24EN1 0.5 nM**		**24EN1 1 nM**		**24EN1 2.5 nM**		**24EN1 5 nM**		**24EN1 10 nM**		**24EN1 25 nM**		**24EN1 50 nM**	
Sub G_1/G_0	%	SEM	%	SEM	%	SEM	%	SEM	%	SEM	%	SEM	%	SEM	%	SEM
2h	2.17	1.38	1.2	0.42	2.95	1.93	1.6	0.32	1.93	0.88	1.6	0.61	1.74	1.12	2.26	0.9
8h	1.57	0.36	1.81	1.54	1.15	0.37	2.84	1.22	2.84	1.22	3.88	2.14	4.53	0.7	4.48	0.95
16h	2.41	1.17	1.95	0.3	2.41	1.51	5.05	2.47	5.05	2.47	5.57	2.32	6.52	1.26	8.3	2.16
24h	1.46	0.85	3.06	3.56	1.68	1.53	7.99	3.12	6.78	2.3	6.32	1.54	10.2	7.85	5.97	1.91
48h	0.7	0.63	1.47	1.06	2.05	2.05	14.89	6.71	17.6	6.79	22.4	11.9	30.6	8.69	26.88	6.35
72h	1.99	1.53	1.99	1.91	1.14	0.58	14.5	3.2	12.8	5.08	12.8	3.3	22	10.2	22.36	3.26

6.15.3 *Cell cycle analysis of HT-29 colorectal cancer cells following treatment with **18EN1***

The effect of B ring *meta* fluorine substituted analogue **18EN1** on the cell cycle of CA-4 resistant colorectal HT-29 cancer cells was next investigated by flow cytometry from 0.6 nM to 50 nM. **18EN1** demonstrated excellent biological activity from 1 nM to 50 nM in cell cycle experiments. No effect was seen at 0.6 nM. A dose and time dependent increase in the % of cells in G_2/M phase due to mitotic arrest was observed accompanied by a decrease in % of cells in G_1/G_0 (Figure 6.34 and Table 6.31). G_2/M phase arrest in HT-29 cells commenced at 1 nM at 16 h with an increase from 28% to 49% between 8-16 h. In contrast, at higher concentrations *e.g.* 5 nM, mitotic arrest occurred as early as 8h, with 56% of cells arresting in G_2/M phase. A progressive increase was observed in the G_2/M phase population from 28% at 2 h, to 55%,77%, 82% and 79 % at 8, 16, 24 and 48 h. At the highest concentration (50 nM), a decrease in the G_2/M phase population was once again observed from 48 to 72h (90 to 81%) on account of a corresponding increase in apoptotic cells in sub G_1/G_0 from 4% to 8%. At 5 nM an increase in apoptotic cells in sub G_1/G_0 from 48-72 h was observed, from 4% to 8%. From 5 to 50 nM, **18EN1** demonstrated extremely potent anti-mitotic activity in HT-29 cells (Table 6.31), due to microtubule depolymerising effects which was absent for both CA-4 and **24EN1**.

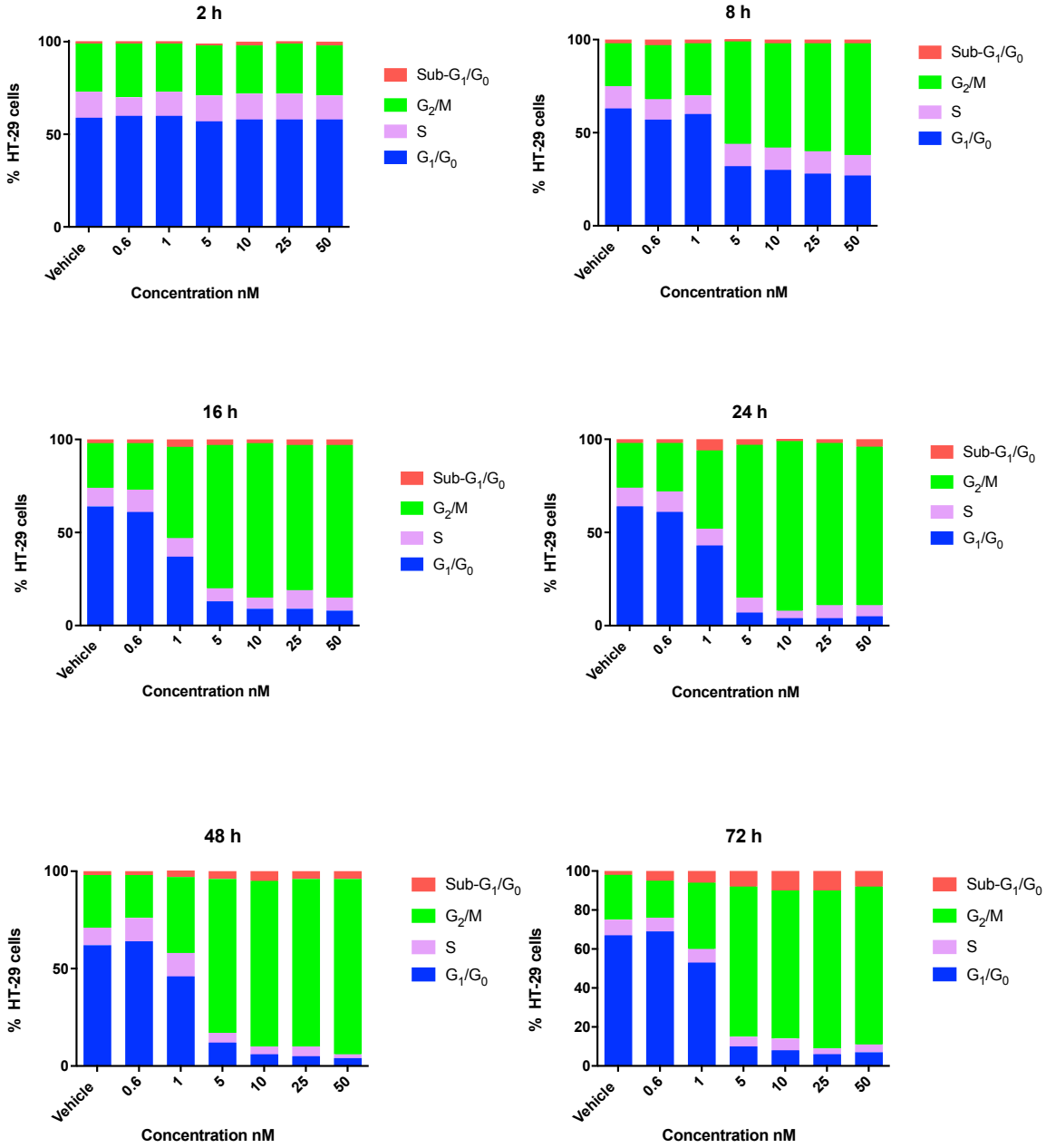

Figure 6.34: **18EN1** induces G_2/M arrest and apoptosis in HT-29 cells. Cells were treated with either vehicle [1% ethanol (v/v)], or **18EN1** at concentrations of 0.6 , 1, 5, 10, 25 or 50 nM for 2, 8, 16, 24, 48 and 72 h. Cells were then fixed, stained with PI, and analysed by flow cytometry. Cell cycle analysis was performed on histograms of gated counts per DNA area (FL2-A). The number of cells with <2N (sub-G_1/G_0), 2N (G_0/G_1), and 4N (G_2/M). DNA content was determined with BD accuri C6. Values represent the mean for three independent experiments

Table 6.31: % of HT-29 cells in each stage of cell cycle when treated with **18EN1**. Values represent as the mean for three independent experiments ± SEM.

	Vehicle		**18EN1 0.6 nM**		**18EN1 1 nM**		**18EN1 5 nM**		**18EN1 10 nM**		**18EN1 25 nM**		**18EN1 50 nM**	
G_1/G_0	%	SEM	%	SEM	%	SEM	%	SEM	%	SEM	%	SEM	%	SEM
2h	59.13	3.74	53.71	5.28	56.27	3.78	54.2	2.55	55.14	3.81	55.04	3.33	54.93	7.98
8h	60.65	5.96	56.63	3.89	57.07	9.88	29.91	3.49	29.91	1.47	28.46	3.95	27.5	0.27
16h	57.13	2.63	60.64	8.15	34.94	9.65	7.93	2.26	7.31	3.92	9.1	6.99	7.87	4.12
24h	61.35	2.13	59.46	4.78	43.19	11.45	7.18	3.34	3.7	0.95	3.63	1.54	5.28	3.39
48h	62.36	3.76	67.4	3.22	45.64	11.3	12.47	8.55	6.08	2.03	4.7	1.68	3.97	2.4
72h	67.48	7.16	68.88	4.01	53.32	12.09	10.43	3.84	7.53	4.21	5.84	1.04	6.99	1.43
	Vehicle		**18EN1 0.6 nM**		**18EN1 1 nM**		**18EN1 5 nM**		**18EN1 10 nM**		**18EN1 25 nM**		**18EN1 50 nM**	
S	%	SEM	%	SEM	%	SEM	%	SEM	%	SEM	%	SEM	%	SEM
2h	13.54	6.6	13	2.91	13.27	2.85	13.64	4.02	13.9	3.29	13.67	2.62	13.27	2.25
8h	11.67	1.92	13.82	6.44	10.09	1.38	11.75	1.78	12.15	1.75	12.41	1.54	11.14	1.46
16h	10.4	4.6	11.59	3.26	10.42	2.53	6.92	2.95	6.35	2.45	6.2	2.74	5.16	1.93
24h	10.03	2.28	10.7	2.79	9.18	5.48	4.73	2.94	3.2	1.33	3.05	0.44	4.95	6.38
48h	9.44	5.51	11.57	2.97	8.89	2.08	3.22	1.19	2.77	0.96	1.79	0.29	1.44	0.51
72h	7.57	1.52	6.94	0.76	7.26	1.48	2.93	0.37	5.09	3.06	1.91	0.51	2.23	0.44
	Vehicle		**18EN1 0.6 nM**		**18EN1 1 nM**		**18EN1 5 nM**		**18EN1 10 nM**		**18EN1 25 nM**		**18EN1 50 nM**	
G_2/M	%	SEM	%	SEM	%	SEM	%	SEM	%	SEM	%	SEM	%	SEM
2h	22.3	7.29	29.39	1.98	25.75	3.13	27.81	2.41	26.2	1.42	27.6	1.83	27.23	2.06
8h	22.81	5.02	25.56	1.05	27.87	8.6	54.98	3.11	54.49	2.07	55.66	5.23	57.22	0.64
16h	24.47	4.69	23.63	7.06	48.74	11.33	77.03	2.49	82.77	8.51	76.1	7.98	81.72	7.24
24h	23.76	1.78	26.17	5.42	41.21	18.66	81.77	10.71	91.39	1.26	87.82	1.38	84.6	11.39
48h	21.7	3.27	21.87	2.47	39.35	15.12	79.09	10.88	84.93	6	88.98	3.36	90.36	4.87
72h	20.36	3.79	18.54	5.62	33.65	9.35	77.39	1.81	75.94	3.02	80.56	0.54	81.22	1.96
	Vehicle		**18EN1 0.6 nM**		**18EN1 1 nM**		**18EN1 5 nM**		**18EN1 10 nM**		**18EN1 25 nM**		**18EN1 50 nM**	
Sub G_1/G_0	%	**SEM**	%	**SEM**	%	**SEM**	%	**SEM**	%	**SEM**	%	**SEM**	%	**SEM**
2h	2.82	2	1.05	0.13	1.21	0.26	0.94	0.1	1.6	0.75	1.27	0.72	1.53	0.15
8h	2.15	0.84	2.67	1.86	2.3	0.37	1.4	0.62	1.73	0.82	1.59	0.74	1.7	0.95
16h	2.07	0.61	1.53	0.53	3.6	2.08	3.24	1.08	1.97	0.89	3.47	1.65	3	1.64
24h	2.21	0.58	1.94	0.93	5.73	4.59	3.39	2.2	1.2	0.3	1.9	0.95	3.46	2.09
48h	1.7	0.53	1.54	0.92	7.06	9.51	4.24	1.83	5.12	3.42	4.01	0.77	3.5	1.64
72h	2.56	2.12	5.61	5.98	4.75	2.35	7.8	1.92	10.24	1.15	9.55	0.78	8.09	1.69

6.15.4 *Cell cycle analysis of MDA-MB-231 TNBC cells following treatment with **18EN1***

Subsequently cell cycle studies were carried out for **18EN1** in the MDA-MB-231 TNBC cells (Figure 6.35) to demonstrate **18EN1**'s dual anti-mitotic activity in both breast cancer and CA-4 resistant HT-29 colorectal cancer cells, complimenting previously discussed anti-proliferative findings (Table 6.3). G2/M phase arrest occurred at 2.5 nM and as early as 16h with an increase in the percentage of cells from 39 to 67% at 8-16h followed by the anticipated decrease to 54% at 24h. This decrease at 24h was accompanied by an increase in the percentage of apoptotic cells in the sub G_1/G_0 population from 5% to 10% from 24-48 h which further increased to 14 % by 72h (Table 6.32). **18EN1** induced apoptosis in MDA-MB-231 cells early as 24-48 h which continued to increase until 72h. For example, at 50 nM, 5% of the MDA-MB-231 cell population treated with **18EN1** resided in sub G_1/G_0 population at 24h, compared to 1.4% for vehicle treated cells. This was followed by an increase to 10% at 48 h and 25 % at 72 h. The dose dependency of the % of apoptotic cells in sub G_1/G_0 was observed by comparing the % of cells in the sub G_1/G_0 population at 72 h of 14% (2.5 nM), 19% (5nM), 22% (10 nM), 25% (25 nM) and 25% (50 nM). This data demonstrates that **18EN1** is active as an anti-mitotic agent due to its microtubule depolymerising effects at concentrations as low as 2.5 nM in MDA-MB-231 cells (Figure 6.35 and Table 6.32) in addition to its G_2/M phase arresting activity in HT-29 cells commencing at 5 nM (Figure 6.34 and Table 6.31).

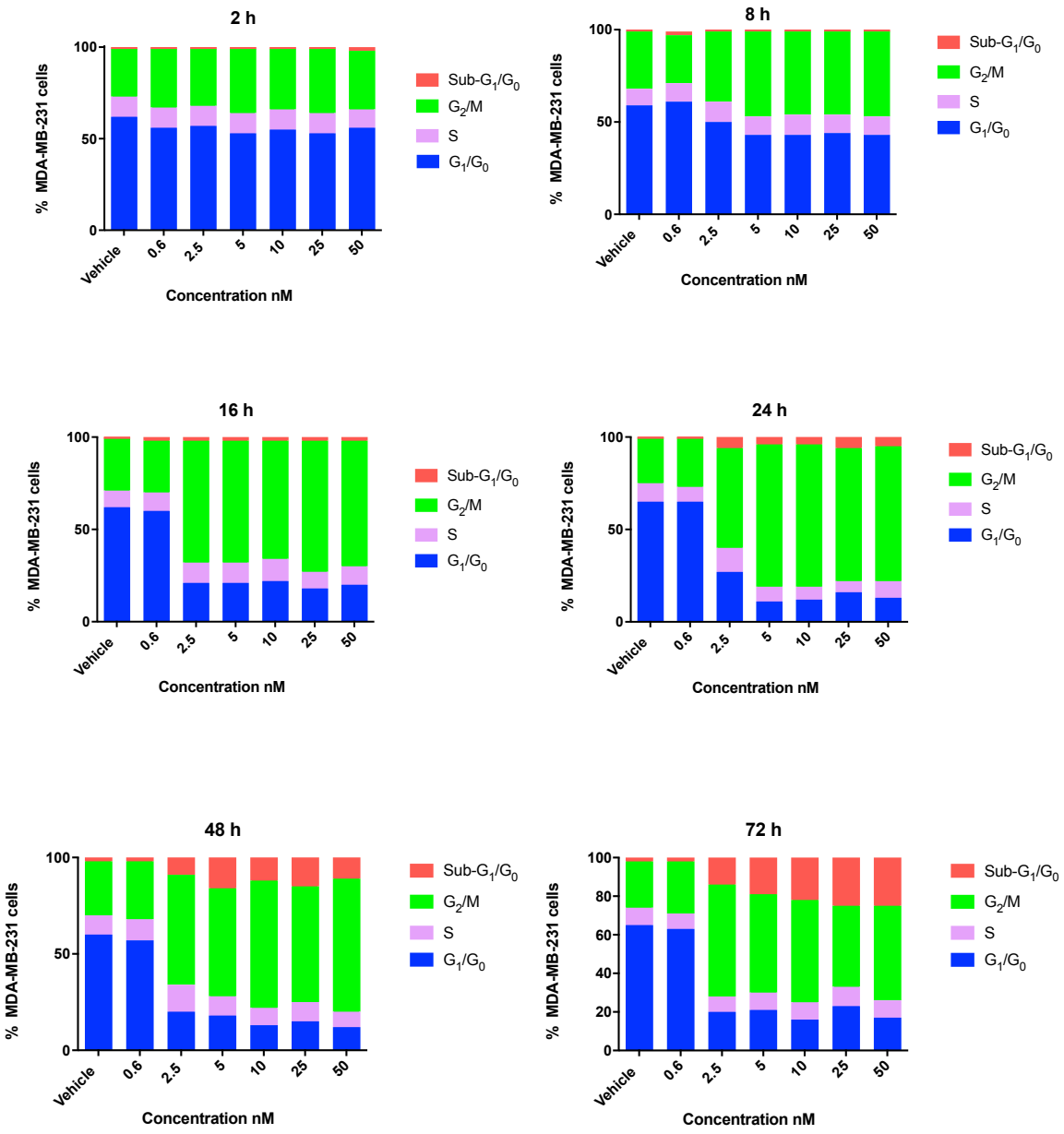

Figure 6.35: **18EN1** induces G_2/M phase arrest and apoptosis in MDA-MB-231cells. Cells were treated with either vehicle [1% ethanol (v/v)], or **18EN1** at concentrations of 0.6 , 2.5, 5, 10, 25, or 50 nM for 2, 8, 16, 24, 48 and 72 h. Cells were then fixed, stained with PI, and analysed by flow cytometry. Cell cycle analysis was performed on histograms of gated counts per DNA area (FL2-A). The number of cells with <2N (sub-G_1), 2N (G_0/G_1), and 4N (G_2/M). DNA content was determined with BD accuri C6. Values represent the mean for three independent experiments

Table 6.32: **%** of MDA-MB-231 cells in each stage of cell cycle when treated with **18EN1**. Values represent as the mean for three independent experiments ± SEM.

	Vehicle		**18EN1 0.6 nM**		**18EN1 2.5 nM**		**18EN1 5 nM**		**18EN1 10 nM**		**18EN1 25 nM**		**18EN1 50 nM**	
G_1/G_0	%	**SEM**	%	**SEM**	%	**SEM**	%	**SEM**	%	**SEM**	%	**SEM**	%	**SEM**
2h	61.67	3.87	56.14	4.66	56.62	1.41	53.19	10.32	55.42	10.59	53.39	7.61	55.72	11.52
8h	58.74	5.82	60.82	3.19	49.96	4.75	44.42	7.93	43.45	9.47	44.49	9.38	43.39	8.78
16h	59.45	3.71	58.8	5.4	20.73	0.64	20.83	5.45	21.61	2.53	17.57	3.68	20.41	4.71
24h	64.61	1.99	64.85	3.32	27.6	8.66	10.56	0.52	12.58	0.85	16.43	6.99	13.83	3.16
48h	60.41	4.89	57.0	7.41	20.43	5.27	17.8	3.5	13.37	4.15	14.67	2.03	11.72	1.4
72h	64.64	2.73	62.57	8.02	20.1	2.72	20.88	5.42	16.1	2.87	22.57	8.89	16.57	4.08
	Vehicle		**18EN1 0.6 nM**		**18EN1 2.5 nM**		**18EN1 5 nM**		**18EN1 10 nM**		**18EN1 25 nM**		**18EN1 50 nM**	
S	%	**SEM**	%	**SEM**	%	**SEM**	%	**SEM**	%	**SEM**	%	**SEM**	%	**SEM**
2h	11.81	2.46	11.99	2.6	11.27	2.27	13.03	3.21	12.06	3.41	12.34	3.5	11.88	2.8
8h	9.77	1.24	9.78	2.48	11.36	0.28	10.48	1.22	10.74	0.95	11.34	0.91	10.4	1.8
16h	8.85	1.21	10.16	3.31	11.42	0.99	10.82	2.5	11.99	4.22	8.84	0.67	10.14	0.9
24h	9.46	2.77	8.24	0.88	13	9.35	8.27	2.57	6.63	1.32	6.05	1.43	8.79	2.17
48h	9.96	2.42	10.51	3.79	13.56	6.69	10.3	2.48	8.54	1.62	9.5	3.3	8.25	2.29
72h	7.78	2.1	7.9	1.04	8.32	2.08	11.05	6.01	8.91	2.76	9.58	2.33	8.93	2.48
	Vehicle		**18EN1 0.6 nM**		**18EN1 2.5 nM**		**18EN1 5 nM**		**18EN1 10 nM**		**18EN1 25 nM**		**18EN1 50 nM**	
G_2/M	%	**SEM**	%	**SEM**	%	**SEM**	%	**SEM**	%	**SEM**	%	**SEM**	%	**SEM**
2h	25.59	5.49	31.72	1.66	32.81	2.2	34.65	5.01	32.58	6.52	35.12	3.21	32.97	5.8
8h	30.75	1.99	26.85	2.65	39.19	4.32	45.82	7.93	46.4	8.19	45.18	7.04	46.01	9.18
16h	27.93	3.29	27.91	2.18	67.03	0.17	63.76	1.56	63.84	3.29	71.83	2.2	66.78	1.76
24h	24.39	0.53	25.6	2.48	54.03	17.06	76.64	4.31	75.86	5.45	71.76	12.58	69.94	8.58
48h	28.08	1.42	31.32	4.2	57.49	5.52	54.78	15.52	66.19	9	60.1	8.13	68.93	4.32
72h	24.38	1.35	26.84	6.09	57.49	4.8	52.13	11.75	52.33	11.95	41.93	15.63	50.07	12.61
	Vehicle		**18EN1 0.6 nM**		**18EN1 2.5 nM**		**18EN1 5 nM**		**18EN1 10 nM**		**18EN1 25 nM**		**18EN1 50 nM**	
Sub G_1/G_0	%	**SEM**	%	**SEM**	%	**SEM**	%	**SEM**	%	**SEM**	%	**SEM**	%	**SEM**
2h	1.15	0.47	1.08	0.46	1.18	0.63	0.96	0.57	1.47	1.49	1.05	0.62	0.76	0.27
8h	1.15	0.61	1.73	1.78	1.2	0.67	0.81	0.28	0.93	0.21	1.04	0.45	0.91	0.33
16h	1.12	0.59	1.69	1.81	2.1	0.65	1.48	0.97	2.1	1.14	1.87	0.6	1.67	0.42
24h	1.38	0.31	1.47	0.67	5.81	4.28	3.7	1.78	3.21	1.85	3.89	1.34	5.24	3.58
48h	1.57	0.37	1.68	0.62	10.32	1.01	15.84	7.4	11.26	3.27	14.63	5.87	9.93	0.75
72h	2.08	0.37	1.73	0.65	13.8	2.05	18.73	3.54	21.6	3.87	25.1	3.64	24.8	5.85

6.16 *Chapter 6 Summary*

In summary, potent anti-proliferative and microtubule depolymerising enantiomers have been identified. Eutomers of the 3-hydroxyl panel were confirmed as of 3*S,*4*S* absolute configuration while eutomers of the 3-substituted B ring *meta* hydroxyl containing panel were determined as of 3*S,*4*R* absolute configuration in Chapter 4. Biochemical studies including anti-proliferative, tubulin polymerisation assays and confocal microscopy confirm that both 3*S,*4*S* eutomers and 3*R,*4*R* distomers are active as anti-proliferative and microtubule destabilising agents. However, 3*R,*4*R* distomers are much less potent microtubule destabilisers with poorer IC_{50} values with respect to the corresponding eutomers. The same trend was observed for 3*S,*4*R* 3-substituted eutomers and their corresponding 3*R,*4*S* distomers. **24EN1** was selected as the lead enantiomer and demonstrated sub nanomolar IC_{50} values in three breast cancer cell lines and disrupted the microtubule network at 5 nM in all three breast cancer cell lines visualised by confocal microscopy. **24EN1** induced mitotic arrest and apoptosis from a concentration of 2.5 nM following cell cycle flow cytometric analysis of two TNBC cell lines. Its IC_{50} for microtubule depolymerisation was calculated as 0.630 μM ± 0.142 and 0.735 μM ± 0.037 as a % reduction of V_{max} and final polymer mass respectively. The activity of **24EN1** was poor in HT-29 CA-4 resistant colorectal cancer cells while the 3-hydroxyl *meta* substituted eutomers were highly active due to increased metabolically stability imparted by the halogen and methyl substitutions. **18EN1** inhibited the microtubule network in confocal microscopy experiments at concentrations ranging from 1-50 nM and caused a dose dependent increase in both mitotic arrest and apoptosis in cell cycle analysis from 5 nM in HT-29 cells and from 2.5 nM in MDA-MB-231 cells. Its IC_{50} for microtubule depolymerisation was slightly less potent than **24EN1,** measured as 1.864 μM ± 0.54 and 1.626 μM ± 0.72 using % of vehicle V_{max} and % of final polymer mass respectively. While **24EN1** demonstrated partial cytotoxicity in non-tumorigenic MCF-10-2A cells, **18EN1** demonstrated minimal cytotoxicity at concentrations as high as 100 nM. **18EN1** was therefore determined as the most suitable lead analogue for further progression as an agent with dual activity in both breast and CA-4 resistant colorectal cancers, with potential for phosphate prodrug derivatisation to further enhance its drug-like properties, due to the presence of the 3-hydroxyl moiety. Future work will focus on synthetic derivatisation of **18EN1** towards phosphate ester prodrugs for progression

toward pre-clinical *in vivo* models as a water soluble and clinically viable lead enantiopure 3*S*,4*S* combretazet.

Table 6.33: Summary table of biochemical data for lead eutomers **18EN1** and **24EN1**

	18EN1 (3*S*,4*S*)		**24EN1 (3*S*,4*R*)**	
IC_{50}	MCF-7	0.26 nM	MCF-7	0.033 nM
	MDA-MB-231	0.70 nM	MDA-MB-231	0.68 nM
	Hs578T(i)8	0.32 nM	Hs578T(i)8	0.27 nM
	HT-29	0.53	HT-29	28 nM
Relative potency MCF-7: HT-29 cells	0.49		0.001	
% Viability in MCF-10-2A cells	1 nM	98%	1 nM	44%
	10 nM	82%	10 nM	25%
	100 nM	79%	100 nM	22%
Fold change in V_{max} of tubulin polymerisation at A) 1 μM and B) 5 μM	A) 3-22 B) 3		A) 7-11 B) 3	
IC_{50} for tubulin polymerisation inhibition	As % fold reduction in V_{max}	As % reduction in final polymer mass	As % fold reduction in V_{max}	As % reduction in final polymer mass
	1.86 μM	1.63 μM	0.63 μM	0.74 μM
Concentration of microtubule inhibition observed in confocal microscopy experiments	MDA-MB-231	5 nM	MDA-MB-231	5 nM
	Hs578T(i)8	5 nM	Hs578T(i)8	1 nM
	HT-29	1 nM	HT-29	**No microtubule inhibition observed (resistance inferred)**
Lowest concentration demonstrating mitotic arrest in cell cycle studies	MDA-MB-231	2.5 n	MDA-MB-231	2.5 nM
	HT-29	1 nM	Hs578T(i)8	1-2.5 nM